



JACC

Basic to Translational Science

*A Journal of the
American College of Cardiology*



EDITOR-IN-CHIEF

Douglas L. Mann, MD,
Washington University School
of Medicine, St. Louis, MO, USA

DEPUTY EDITOR

Coleen A. McNamara, MD,
University of Virginia School of Medicine,
Charlottesville, VA, USA

GUEST EDITOR-IN-CHIEF

Michael R. Bristow, MD, PhD,
University of Colorado Denver and
Anschutz Medical Campus,
Aurora, CO, USA

SCIENTIFIC GRAPHICS EDITOR

Ankit Garg, PhD, MD,
Washington University School of Medicine,
St. Louis, MO, USA

EDITORS-IN-CHIEF

JACC

Valentin Fuster, MD, PhD,
Mount Sinai Health System,
New York, NY, USA

JACC: Cardiovascular Interventions

David J. Moliterno, MD,
University of Kentucky, Lexington, KY, USA

JACC: Cardiovascular Imaging

Y. Chandrashekhar, MD, DM,
University of Minnesota/VAMC,
Minneapolis, MN, USA

JACC: Heart Failure

Bykem Bozkurt, MD, PhD,
Baylor College of Medicine,
DeBakey VA Medical Center,
Houston, TX, USA

JACC: Clinical Electrophysiology

Kalyanam Shivkumar, MD, PhD,
UCLA Cardiac Arrhythmia Center,
UCLA, Health System, Los Angeles, CA, USA

JACC: Case Reports

INTERIM EDITORS-IN-CHIEF

Mary Norine Walsh, MD,
St. Vincent Heart Center,
Indianapolis, IN, USA

Eric R. Bates, MD,
University of Michigan,
Ann Arbor, MI, USA

JACC: CardioOncology

Bonnie Ky, MD, MSCE,
Perelman School of Medicine at the
University of Pennsylvania,
Philadelphia, PA, USA

JACC: Asia

Jian'an Wang, MD, PhD,
Zhejiang University School of Medicine,
Hangzhou, China

JACC: Advances

Candice K. Silversides, MD,
University Health Network,
University of Toronto,
Toronto, Ontario, Canada

ASSOCIATE EDITORS

Brian H. Annex, MD,
University of Virginia,
Charlottesville, VA, USA

Nikolaos G. Frangogiannis, MD,
Albert Einstein College of Medicine,
Bronx, NY, USA

Maria I. Kontaridis, PhD,
Masonic Medical Research Institute,
Utica, NY, USA

Daniel P. Kelly, MD,
Perelman School of Medicine at
the University of Pennsylvania,
Philadelphia, PA, USA

Peter Libby, MD,
Brigham and Women's Hospital,
Harvard Medical School,
Boston, MA, USA

William Robb MacLellan, MD,
University of Washington
School of Medicine,
Seattle, WA, USA

Geoffrey S. Pitt, ScM, MD, PhD,
Weill Cornell Medicine,
New York, NY, USA

Karin R. Sipido, MD, PhD,
KU Leuven,
Leuven, Belgium

STATISTICAL EDITOR

Cindy Green, PhD,
Duke University Medical Center,
Durham, NC, USA

SECTION EDITOR — CARDIAC DEVICES

Juan F. Granada, MD,
CRF-Skirball Center for Innovation,
Orangeburg, NY, USA

SECTION EDITOR — HEMATOLOGY/ THROMBOSIS

Jean M. Connors, MD,
Brigham and Women's Hospital,
Boston, MA, USA

SECTION EDITOR —

PEDIATRIC CARDIOLOGY

Marlene Rabinovitch, MD,
Stanford University
School of Medicine,
Stanford, CA, USA

SECTION EDITOR — TISSUE ENGINEERING

Yibing Qyang, PhD,
Yale University School of Medicine,
New Haven, CT, USA

SENIOR ADVISORY EDITORS

Leslie A. Leinwand, PhD,
University of Colorado Boulder
BioFrontiers Institute,
Boulder, CO, USA

Eric N. Olson, PhD,
UT Southwestern Medical Center,
Dallas, TX, USA

Robert Roberts, MD,
University of Arizona
College of Medicine,
Tucson, AZ, USA

Christine E. Seidman, MD,
Harvard Medical School,
Boston, MA, USA

CME/MOC/ECME EDITOR

Kenneth A. Ellenbogen, MD,
Virginia Commonwealth University
Medical Center,
Richmond, VA, USA

SOCIAL MEDIA EDITORS

Matt Alexander, MD, PhD,
Vanderbilt University School of
Medicine,
Nashville, TN, USA

Jeffrey J. Hsu, MD, PhD,
UCLA Health/West LA
VA Medical Center,
Los Angeles, CA, USA

SOCIAL MEDIA COORDINATORS

Michael A. Raddatz, MD, PhD,
University of California-Los Angeles,
Los Angeles, CA, USA

Jean W. Wassenaar, MD, PhD,
Vanderbilt University Medical Center,
Nashville, TN, USA

EDITORIAL CONSULTANTS IN TRANSLATIONAL CV SCIENCE

Mark Anderson, MD, PhD,
Johns Hopkins University
School of Medicine,
Baltimore, MD, USA

Themistocles Assimes, MD, PhD,
Stanford University
School of Medicine,
Palo Alto, CA, USA

Noel Bairey-Merz, MD,
Cedars-Sinai Heart Institute,
Los Angeles, CA, USA

Craig Basson, MD,
Weill Medical College of
Cornell University,
Needham, MA, USA

Jeffrey Berger, MD,
New York University
School of Medicine,
New York, NY, USA

Don Bers, PhD,
University of California,
Davis, CA, USA

Daniel Burkoff, MD, PhD,
Cardiovascular Research
Foundation,
Framingham, MA, USA

John Burnett, MD,
Mayo Clinic Rochester,
Rochester, MN, USA

John Canty, MD,
University at Buffalo,
Buffalo, NY, USA

Barbara Casadei, MD,
University of Oxford,
Oxford, UK

EDITORIAL CONSULTANTS IN TRANSLATIONAL CV SCIENCE CONTINUED

Karen Christman, PhD,
University of California-San Diego,
San Diego, CA, USA

Peter Crawford, MD, PhD,
University of Minnesota,
Minneapolis, MN, USA

Craig Emter, PhD,
University of Missouri,
Columbia, MO, USA

Zahi Fayad, PhD,
Mount Sinai Medical Center,
New York, NY, USA

Glenn Fishman, MD,
Mount Sinai School of
Medicine,
New York, NY, USA

Peter Ganz, MD,
San Francisco General Hospital,
San Francisco, CA, USA

Roberta Gottlieb, MD,
Cedars-Sinai Medical Center,
Los Angeles, CA, USA

Josh Hare, MD,
University of Miami Miller
School of Medicine,
Miami, FL, USA

Ray Hershberger, MD,
The Ohio State University,
Columbus, OH, USA

Carolyn Ho, MD,
Brigham and Women's Hospital,
Boston, MA, USA

Jennifer Ho, MD,
Massachusetts General Hospital,
Boston, MA, USA

Farouc Jaffer, MD, PhD,
Massachusetts General Hospital,
Harvard Medical School,
Boston, MA, USA

Tim Kamp, MD, PhD,
University of Wisconsin,
Madison, WI, USA

Walter Koch, PhD,
Temple University
School of Medicine,
Philadelphia, PA, USA

David Lanfear, MD,
Henry Ford Hospital,
Heart and Vascular Institute,
Detroit, MI, USA

Jin-Moo Lee, MD,
Washington University
School of Medicine,
St. Louis, MO, USA

Richard Lee, MD,
Brigham and Women's Hospital,
Boston, MA, USA

Jonathan Lindner, MD,
Oregon Health and Science
University,
Portland, OR, USA

Peter Liu, MD,
Institute of Circulatory &
Respiratory Health-Canadian
Institutes of Health Research
University Health Network,
Ottawa, Ontario, Canada

Eduardo Marban, MD, PhD,
Cedars-Sinai Heart Institute,
Los Angeles, CA, USA

Ali Marian, MD,
University of Texas Health Science
Center-Houston,
Houston, TX, USA

Kenneth Margulies, MD,
University of Pennsylvania
Perelman School of Medicine,
Philadelphia, PA, USA

Timothy McKinsey, PhD,
University of Colorado Anschutz
Medical Campus,
Aurora, CO, USA

Javid Moslehi, MD,
Vanderbilt School of Medicine,
Nashville, TN, USA

Jorge Plutzky, MD,
Brigham and Women's Hospital,
Boston, MA, USA

David Port, PhD,
University of Colorado
School of Medicine,
Aurora, CO, USA

Sumanth Prabhu, MD,
University of Alabama at
Birmingham,
Birmingham, AL, USA

Hani Sabbah, PhD,
Henry Ford Hospital,
Washington University
School of Medicine,
Detroit, MI, USA

Paul Simpson, MD,
San Francisco VA Medical
Center and University of
California-San Francisco,
San Francisco, CA, USA

Mark Sussman, PhD,
San Diego State University,
San Diego, CA, USA

Jenny Van Eyk, PhD,
California School of
Health Sciences,
Los Angeles, CA, USA

Richard Vega, MD,
Translational Research Institute,
Orlando, FL, USA

Xander Wehrens, MD, PhD,
Baylor College of Medicine,
Houston, TX, USA

Arthur Wilde, MD, PhD,
Academic Medical Center
University of Amsterdam,
Amsterdam, the Netherlands

Myles Wolf, MD, MMSc,
Northwestern University
Feinberg School of Medicine,
Chicago, IL, USA

Sean Wu, MD, PhD,
Stanford Cardiovascular Institute,
Stanford, CA, USA

AMERICAN COLLEGE OF CARDIOLOGY STAFF

Washington, DC, USA

DIVISIONAL VICE PRESIDENT, PUBLISHING

Justine Varieur Turco, MA

EXECUTIVE MANAGING EDITOR

Monica R. Payne-Emmerson, MS

MANAGING EDITOR

Kimberly Trevey, BA

EDITORIAL ASSISTANT

Jennifer Rapp, BA

DIGITAL PUBLISHING DIRECTOR

**Ron Schmelzer, Jr., MSPM,
PMP, CSM**

DIGITAL CONTENT

MANAGER

Kara McDermott, BA

DIGITAL PRODUCT

MANAGER

Taryn Myers, PMP

MARKETING MANAGER

Colleen Whipple-Erno, BA

SOCIAL MEDIA

COORDINATOR

Sarah Khalaf, BA

EDITORIAL SUPPORT

Ania Bukowski, BAS

Adam Etkin, MA

ETHICS COMMITTEE

Chair: **Richard L. Popp, MD,**
Stanford University School of Medicine,
Palo Alto, CA, USA

Holly Atkinson, MD,
Mount Sinai Health System,
New York, NY, USA

Lawrence S. Cohen, MD,
Yale University School of Medicine,
New Haven, CT, USA

Kim Fox, MD,
National Heart and Lung Institute,
Imperial College, Royal Brompton Hospital,
London, UK

Robert Frye, MD,
Mayo Clinic Rochester,
Rochester, MN, USA

Philip J. Landrigan, MD,
Mount Sinai,
New York, NY, USA

Eric N. Prystowsky, MD,
The Care Group, LLC,
Indianapolis, IN, USA



JACC

Basic to Translational Science

*A Journal of the
American College of Cardiology*

2024-2025 OFFICERS

The American College of Cardiology's (ACC) Board of Trustees (BOT) is the centralized governing authority for the ACC and responsible for overseeing decisions related to the College's mission and strategic direction. The president serves as the head of the BOT.

Cathleen Biga, MSN, FACC, American College of Cardiology (ACC) President, Cardiovascular Management of Illinois, Woodridge, IL, USA

B. Hadley Wilson, MD, MACC, ACC Immediate-Past President, Sanger Heart & Vascular Institute, Atrium Health, Charlotte, NC, USA

Christopher M. Kramer, MD, FACC, ACC Vice President, University of Virginia Health System, Charlottesville, VA, USA

Akshay K. Khandelwal, MD, MBA, FACC, ACC Treasurer, Allegheny Health Network, Wexford, PA, USA

Himabindu Vidula, MD, MS, FACC, ACC Secretary and Board of Governors Chair, Penn Medicine, University of Pennsylvania, Philadelphia, PA, USA

Cathleen C. Gates, MA, ACC Chief Executive Officer, Washington, DC, USA

2024-2025 SCIENTIFIC PUBLICATIONS COMMITTEE (SPC)

The mission of the Scientific Publications Committee (SPC) of the American College of Cardiology (ACC) is to provide oversight and direction for all scientific peer-reviewed journals of the ACC and to advance the mission of the ACC to transform cardiovascular care and improve heart health.

CORRESPONDENCE FOR AMERICAN COLLEGE OF CARDIOLOGY

All correspondence for the College, other than that related to *JACC: Basic to Translational Science* should be sent to Resource Center, American College of Cardiology, 2400 N Street, NW, Washington, DC 20037, USA

Fred M. Kusumoto, MD, FACC, Chair, Department of Cardiovascular Disease, Mayo Clinic, Jacksonville, FL, USA

John A. Bittl, MD, FACC, Boston, MA, USA

Brian Alan Boe, MD, FACC, University Hospitals Cleveland Medical Center and Nationwide Children's Hospital, Columbus, OH, USA

Marc P. Bonaca, MD, FACC, UCHealth University of Colorado Hospital, Aurora, CO, USA

Mark A. Creager, MD, FACC, Chair Elect, Heart and Vascular Center, Dartmouth-Hitchcock Medical Center, Lebanon, NH, USA

Mary M. McDermott, MD, Northwestern Memorial Hospital, Chicago, IL, USA

Glaucia Maria Moraes De Oliveira, MD, MSc, PhD, FACC, Federal University of Rio de Janeiro (UFRJ), Rio de Janeiro, Brazil

Andriana Nikolova, MD, Cedars-Sinai Medical Center, Los Angeles, CA, USA

Kian Keong Poh, MB BCh, FACC, Department of Cardiology, National University Heart Center, Singapore

Karin R. Sipido, MD, PhD, Department of Cardiovascular Sciences, Division of Experimental Cardiology, KU Leuven, Leuven, Belgium

Brittany Weber, MD, Department of Medicine, Brigham Women's Hospital, Harvard Medical, Boston, MA, USA

J. Brendan Mullen, ACC Senior Executive Vice President, Science and Quality Divisions, Washington, DC, USA

Justine Varieur Turco, MA, ACC Divisional Vice President, Publishing, Washington, DC, USA

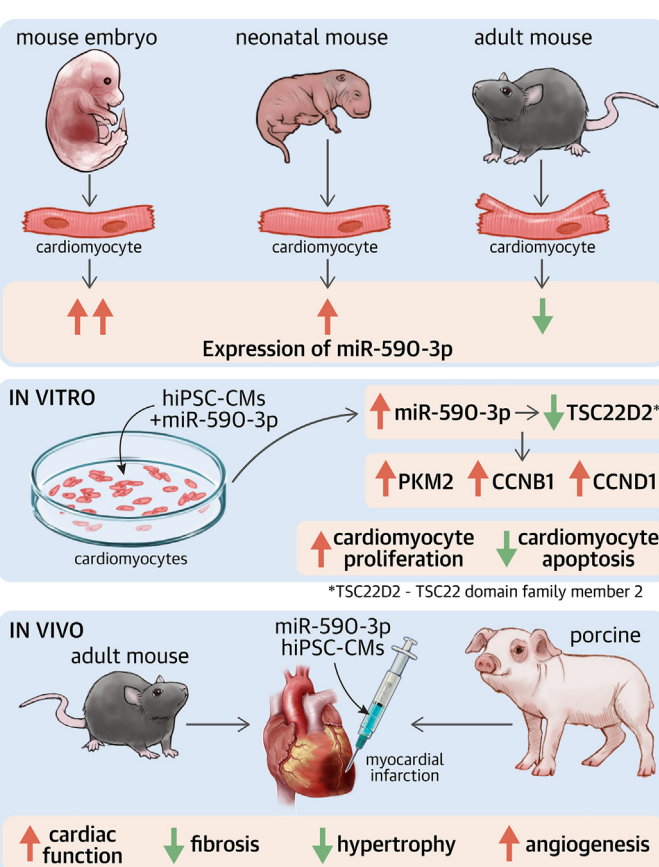
LEADING EDGE TRANSLATIONAL RESEARCH

miR-590-3p Overexpression Improves the Efficacy of hiPSC-CMs for Myocardial Repair



Zhiwei Zhang, MD,^{a,*} Xiaoting Li, MD,^{b,c,*} Jiawei Zhuang, MD,^d Qingwei Ding, MD,^a Hui Zheng, MD,^a Teng Ma, MD,^a Qingyou Meng, MD,^a Ling Gao, PhD^e

VISUAL ABSTRACT



HIGHLIGHTS

- miR-590-3p overexpression increased the proliferative capacity of hiPSC-CMs *in vitro* and *in vivo*.
- miR-590-3p overexpression enhanced the number of engrafted hiPSC-CMs in infarcted mouse hearts.
- miR-590-3p-overexpressing hiPSC-CMs promoted cardiac repair in a preclinical pig MI model.

Zhang Z, et al. J Am Coll Cardiol Basic Trans Science. 2024;9(5):557-573.

From the ^aDepartment of Vascular Surgery, General Surgery Clinical Center, Shanghai General Hospital, Shanghai Jiao Tong University School of Medicine, Shanghai, China; ^bDepartment of Geriatrics, Shanghai General Hospital, Shanghai Jiao Tong University School of Medicine, Shanghai, China; ^cDepartment of Cardiology, Second Affiliated Hospital of Soochow University, Suzhou, China; ^dDepartment of Cardiovascular Surgery, The First Affiliated Hospital of Xiamen University, School of Medicine, Xiamen, China.

**ABBREVIATIONS
AND ACRONYMS****BLI** = bioluminescence live imaging**ECM** = extracellular matrix**HF** = heart failure**hiPSC-CM** = human induced pluripotent stem cell-derived cardiomyocyte**LAD** = left anterior descending coronary artery**LVEDV** = left ventricular end-diastolic volume**LVESV** = left ventricular end-systolic volume**MI** = myocardial infarction**miRNA** = microRNA**OE** = overexpressing**qRT-PCR** = quantitative real-time polymerase chain reaction**UTR** = untranslated region**SUMMARY**

Recent evidence demonstrates that low engraftment rates limit the efficacy of human induced pluripotent stem cell-derived cardiomyocytes (hiPSC-CMs) for cardiac repair after myocardial infarction. In this study, we attempted to overcome this limitation by enhancing the proliferative capacity of transplanted hiPSC-CMs. We found that miR-590-3p overexpression increased the proliferative capacity of hiPSC-CMs. miR-590-3p overexpression increased the number of engrafted cells and had a higher efficacy for myocardial repair than control cells. Moreover, we confirmed the safety of using miR-590-3p-overexpressing hiPSC-CMs in pig hearts. These results indicated that miR-590-3p overexpression stimulated hiPSC-CM cell cycle re-entry to induce cell proliferation and increased the therapeutic efficacy in MI. (J Am Coll Cardiol Basic Trans Science 2024;9:557–573) © 2024 The Authors. Published by Elsevier on behalf of the American College of Cardiology Foundation. This is an open access article under the CC BY-NC-ND license (<http://creativecommons.org/licenses/by-nc-nd/4.0/>).

Despite significant advances in disease management, end-stage heart failure (HF) is the leading cause of mortality worldwide because of the limited regenerative capacity of the adult human heart.¹ In mammals, the proliferative capacity of cardiomyocytes ceases in a short window after birth.² As a result, injured hearts have a limited ability to repair because they produce a limited number of cardiomyocytes after myocardial infarction (MI). Consequently, the ischemic site is replaced by scar tissue without contractile function. In recent years, concerted efforts have been made to develop therapeutic strategies to promote myocardial regeneration. Several advanced approaches, including adult/somatic stem cell transplantation, induction of the proliferation of endogenous cardiomyocytes, and the transdifferentiation of resident cardiac fibroblasts into functional cardiomyocyte-like cells, can improve cardiac function and reduce cardiac fibrosis in animal models of MI.^{3–5} However, the therapeutic efficacy of these methods is limited, and these strategies have safety concerns, such as an increased risk of ventricular arrhythmia.⁶ Therefore, it is crucial to develop novel, efficient, and safe therapeutic strategies to promote cardiac regeneration.

Transplanting human induced pluripotent stem cell-derived cardiomyocytes (hiPSC-CMs) into injured myocardium is promising for end-stage HF treatment. Unlike adult human cardiomyocytes, hiPSCs have

unlimited self-renewal capacity and can readily differentiate into cardiomyocytes *in vitro* under certain induction conditions. Theoretically, producing a clinically relevant number of hiPSC-CMs is feasible through industrialization. CMs derived from hiPSCs are structurally and functionally immature, resembling fetal CMs, with a gene expression profile of a developing heart, small cell size, less organized sarcomeres, small forces of contraction, and low mitochondrial density compared with adult CMs.⁷ In addition, although the long-term culture of hiPSC-CMs stimulates cell maturation to some extent,⁸ metabolic maturation reduces the proliferation of hiPSC-CMs and their ability to tolerate hypoxia.⁷ As a result, only a small percentage of transplanted cells survive at the injection sites, preventing harnessing the full potential of hiPSC-CMs in cardiac regeneration.⁹ Therefore, developing novel approaches to enhance the engraftment rate of hiPSC-CMs during cardiovascular disease treatment is critical.

MicroRNAs (miRNAs) are evolutionarily conserved, single-stranded, noncoding, 18- to 22-nucleotide RNAs that regulate gene expression by directly binding to the 3'-untranslated regions (UTRs) of target messenger RNAs.¹⁰ miRNAs participate in various biological processes, including embryonic development and tissue regeneration.^{11,12} Additionally, miRNAs have essential functions in heart regeneration. For instance, miR-19a/19b promoted endogenous cardiomyocyte proliferation by regulating the expression of phosphatase and tensin

Xiamen University, Xiamen, China; and the ^aTranslational Medical Center for Stem Cell Therapy and Institute for Regenerative Medicine, Shanghai East Hospital, Tongji University School of Medicine, Shanghai, China. *Drs Zhang and Li contributed equally to this work.

The authors attest they are in compliance with human studies committees and animal welfare regulations of the authors' institutions and Food and Drug Administration guidelines, including patient consent where appropriate. For more information, visit the [Author Center](#).

homolog deleted on chromosome 10 (PTEN) in a mouse model of MI.¹³ However, AAV6-miR-199a administration led to uncontrolled cardiac regeneration in a pig model of MI.⁶

The role of miRNAs in regulating hiPSC-CM physiology remains largely unknown. A previous study performed miRNA functional screening and found that miR-590-3p promoted cardiomyocyte proliferation.¹² In addition, Lesizza et al¹⁴ reported that AAV6-miR-590-3p stimulated endogenous cardiomyocyte proliferation and improved cardiac function after MI. However, little is known about the effect of miR-590-3p on hiPSC-CM proliferation. In this study, we investigated: 1) the ability of miR-590-3p to stimulate hiPSC-CM proliferation; 2) the potential to transplant miR-590-3p-overexpressing (OE) hiPSC-CMs into mouse and pig hearts; and 3) the ability of miR-590-3p-OE hiPSC-CMs to promote cardiac repair in mouse and pig models of MI.

METHODS

hiPSC CULTURE AND CARDIOMYOCYTE DIFFERENTIATION.

The hiPSC line RC01001-A (Nuwacell) was used in this study. hiPSCs were maintained in Essential 8 medium (Stemcell Technologies) and differentiated into cardiomyocytes using the GiWi protocol.¹⁵ Differentiated hiPSC-CMs were purified by metabolic selection between day 15 and day 25, as described previously.¹⁵ The purity of hiPSC-CMs was confirmed by flow cytometry using a FACSCalibur flow cytometer (Beckman Coulter). The maturation of differentiated hiPSC-CMs was achieved by prolonging the culture period (up to day 60).

PRODUCTION AND TRANSFECTION OF AAV6-miR-590-3P.

The plasmids AAV6-miR-590-3p and control AAV6 were purchased from GeneChem Technologies. AAV packaging was conducted using AAV-293 cells, and AAV particles were harvested from the supernatant using an AAV Purification Maxi Slurry Kit (AmyJet Scientific). The concentration of particles was adjusted (1:100 to 1:1,000 dilution) to minimize cell toxicity and achieve transfection efficiencies of >80%. After transfection, the expression of miR-590-3p in hiPSC-CMs was detected by quantitative real-time polymerase chain reaction (qRT-PCR).

FLUORESCENCE IN SITU HYBRIDIZATION. Fluorescence in situ hybridization assays were performed to detect miR-590-3p in heart tissues according to the manufacturer's instructions. Briefly, heart samples were embedded in an optimal cutting temperature compound for serial cryosectioning. The sections (8 μm thick) were incubated with proteinase K (15 μg/mL) at 37 °C for 30 minutes. Then, miR-590-3p was

hybridized with a Cy3-labeled oligonucleotide probe (AmyJet Scientific). The sections were stained with 4',6-diamidino-2-phenylindole and imaged under an inverted fluorescence microscope (Leica).

IMMUNOFLUORESCENCE ANALYSES. Cell or tissue samples were fixed with 4% paraformaldehyde and permeabilized with 0.4% Triton X-100 at room temperature for 15 minutes. After nonspecific antigen blocking with 1% bovine serum albumin for 1 hour, the samples were incubated with primary antibodies (for details, see *Supplemental Table 1*) at 4 °C overnight and subsequently incubated with the corresponding secondary antibodies at 37 °C for 2 hours. Wheat germ agglutinin (Thermo Fisher Scientific) and terminal deoxynucleotidyl transferase-mediated deoxyuridinetriphosphate nick-end labeling (Thermo Fisher Scientific) staining were performed using a commercial kit. Nuclei were stained with 4',6-diamidino-2-phenylindole.

MESSENGER RNA PROFILING. RNA sequencing of control and miR-590-3p-OE hiPSC-CMs was performed using an Illumina 2000 and 2 × 100-base pair paired-end sequencing (LC Sciences) as described previously. Gene ontology enrichment analysis of differentially expressed genes was performed using the Lianchuan Biological Cloud Platform (LC Sciences).

ANIMAL EXPERIMENTS. Mice MI was induced in a mouse model by ligating the left anterior descending coronary artery (LAD) as described previously. Briefly, M-NSG (NOD-Prkdc^{scid}Il2rg^{emi}/Smoc) female mice (9–10 weeks old, provided by Shanghai Model Organisms Center) were anesthetized with 2% isoflurane and mechanically ventilated using an animal ventilator (Harvard Apparatus). The heart was exposed by left thoracotomy, and the LAD was ligated using an 8-0 Prolene suture (Ethicon). The animals were randomly divided into 3 groups: an MI group (15 μL of phosphate-buffered saline), a control group (5.0×10^5 wild-type hiPSC-CMs), and an miR-590-3p group (5.0×10^5 miR-590-3p-OE hiPSC-CMs). After cell delivery, the incisions were closed with 6-0 sutures. A sham group underwent all procedures except LAD ligation.

Bama pigs (female; 20–25 kg) were used to evaluate the therapeutic effect of hiPSC-CM transplantation on MI. Briefly, pigs were anesthetized with 2% isoflurane and mechanically ventilated using an animal ventilator (Hallowell EMC). The heart was exposed by left thoracotomy, and the LAD was occluded between the first and second diagonal coronary arteries with a 4-0 Prolene suture for 1 hour and then reperfused. miR-590-3p-OE hiPSC-CMs or control cells (5.0×10^7

cells/heart, 8–10 points in the injured area) were injected into the myocardium, and the incision was closed. The animals received the following immunosuppressants: methylprednisolone sodium succinate (2 mg/kg), tacrolimus (0.3 mg/kg), and mycophenolate mofetil (100 mg/kg). A telemetry device (Ensense Biomedical Technologies) was implanted subcutaneously in the chest wall according to the manufacturer's instructions. The peripheral blood of each pig was collected and analyzed at the Department of Clinical Pathology of Shanghai General Hospital.

CARDIAC FUNCTION ANALYSES. Mice. Cardiac function was assessed by echocardiography at indicated timepoints. Mice were anesthetized with 2% isoflurane and mechanically ventilated. Echocardiography data were measured using a Visual Sonics Vevo2100 system (Visual Sonics). Left ventricular ejection fraction and fractional shortening were calculated using the following equations: ejection fraction percentage = $[(\text{LVEDV} - \text{LVESV})/\text{LVEDV}] \times 100$ and fractional shortening percentage = $[(\text{LVEDD} - \text{LVESD})/\text{LVEDD}] \times 100$, where LVEDV and LVESV are left ventricular end-diastolic and end-systolic volume, respectively, and LVEDD and LVESD are left ventricular end-diastolic and end-systolic diameter, respectively. An operator blinded to the study groups performed all measurements.

Pigs. Cardiac function was assessed by high-resolution computed tomography (Siemens). Briefly, the animals were anesthetized with 2% isoflurane and placed in the supine position. Before computed tomography scanning, an iodinated contrast agent (0.5 mL/kg; Abcam) was injected into the ear vein. Cardiac function was analyzed with Vitrea Enterprise Suite software (Siemens).

CELL ENGRAFTMENT. The engraftment of implanted hiPSC-CMs was evaluated by bioluminescence live imaging (BLI), immunofluorescent staining, and qRT-PCR. In BLI, luciferase-hiPSC-CMs were evaluated using the IVIS Lumina III In Vivo Imaging System (PerkinElmer) 7 and 28 days after cell delivery. The average fluorescence intensity of regions of interest was quantitated. For histologic analysis, hiPSC-CMs were stained with human-specific cardiac troponin T and imaged using an inverted fluorescence microscope. The expression of the sex-determining region Y (SRY) gene in the transplantation site was measured to evaluate the engraftment rate of implanted hiPSC-CMs, as described previously.

QUANTITATIVE REAL-TIME POLYMERASE CHAIN REACTION. Total RNA isolation, reverse transcription, and qRT-PCR were performed as described

previously. Glyceraldehyde-3-phosphate dehydrogenase or U6 small nuclear RNA (for miRNA) served as internal controls. The primer sequences are listed in Supplemental Table 2.

WESTERN BLOT. Protein isolation, quantitation, and electrophoresis were performed as described previously. Glyceraldehyde-3-phosphate dehydrogenase served as a loading control. Protein blots were analyzed by Image Pro Plus version 6.0.

DUAL-LUCIFERASE REPORTER ASSAY. hiPSC-CMs (5.0×10^4 cells/well) were seeded in 24-well plates and cotransfected with TSC22D2 luciferase reporter plasmids and miR-590-3p mimic or negative control using Lipofectamine 3000 (Thermo Fisher Scientific). After 48 hours, luciferase activity was detected using a dual-luciferase reporter assay system (Promega). *Renilla* luciferase activity was used as an internal control.

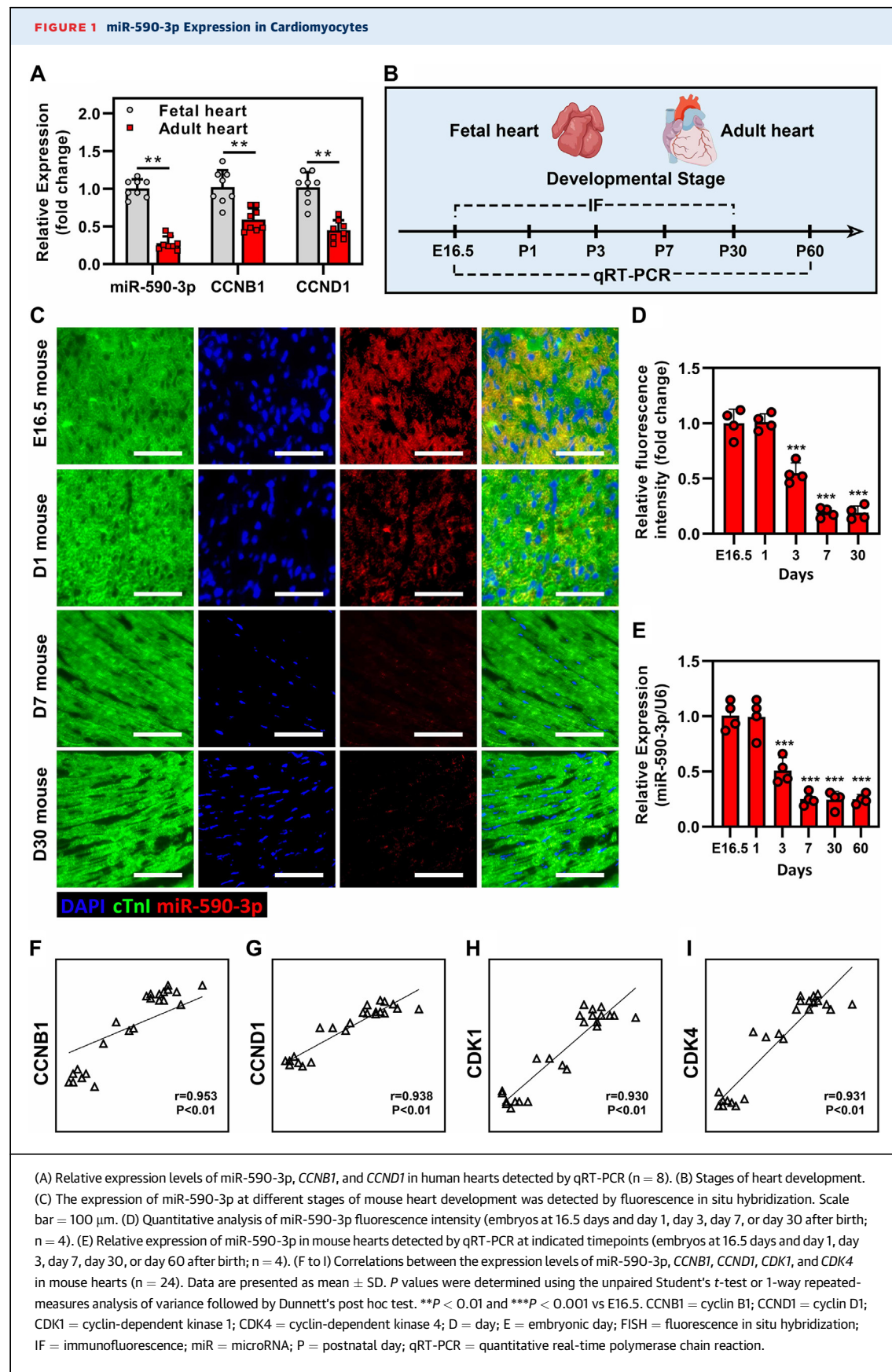
STATISTICAL ANALYSIS. Data are presented as mean \pm SD and analyzed using Graph Pad Prism software version 9.0 (GraphPad Software Inc). The Shapiro-Wilk test was used to assess normality. The unpaired Student's *t*-test was used for comparisons between 2 groups, and 1-way analysis of variance followed by the Tukey's post hoc test for multiple pairwise comparisons was used for comparisons among >2 groups unless otherwise specified. Pearson's correlation coefficient (*r* values with 95% CIs) was used to compare continuous variables. A *P* value of <0.05 was considered statistically significant.

STUDY APPROVAL. Human experiments were approved by the Research Ethics Committee of Shanghai Jiao Tong University. Fetal heart tissues were collected after elective surgical abortions. Adult heart tissues (controls) were obtained from patients who died without cardiac disease. The spouse or immediate family of heart donors provided written informed consent.

All animal experiments were approved by the Institutional Animal Care and Use Committee of Shanghai Jiao Tong University and were performed in accordance with the National Institutes of Health Guide for the Care and Use of Laboratory Animals.

RESULTS

miR-590-3P IS ENRICHED IN THE FETAL HEART. To assess the role of miR-590-3p in the cardiomyocyte cell cycle, we first measured its expression in human hearts. Our results showed that miR-590-3p expression was significantly higher in fetal hearts than in adult hearts. Not surprisingly, the expression of the



proliferation genes cyclin B1 (*CCNB1*) and cyclin D1 (*CCND1*) was also significantly higher in fetal hearts than in adult hearts (Figure 1A). Next, we detected the expression of miR-590-3p during mouse cardiac development by fluorescence *in situ* hybridization and qRT-PCR (Figure 1B). The miRNA fluorescence *in situ* hybridization assay demonstrated that miR-590-3p was enriched in fetal mouse hearts (Figures 1C and 1D). Moreover, our qRT-PCR results demonstrated that miR-590-3p expression was up-regulated in mouse embryonic hearts and decreased after birth (Figure 1E). We also investigated the correlation between the expression of miR-590-3p and proliferation-related genes in mouse hearts at different developmental stages. The expression of *CCNB1*, *CCND1*, cyclin-dependent kinase (CDK) 1, and CDK4 was linearly correlated with that of miR-590-3p (Figures 1F to 1I).

miR-590-3p OVEREXPRESSION PROMOTED hiPSC-CM PROLIFERATION. Next, we investigated whether miR-590-3p overexpression promoted the proliferation of hiPSC-CMs. For this purpose, hiPSCs were differentiated into cardiomyocytes using the GiWi protocol (Supplemental Figure 1A). miR-590-3p overexpression was induced by AAV6-miR-590-3p transfection and confirmed by qRT-PCR 10 days after transfection (Supplemental Figure 1B). We found that miR-590-3p-OE hiPSC-CMs were immature (Supplemental Figures 1C to 1E). Immunofluorescence analyses indicated that miR-590-3p overexpression significantly increased the proportion of cells expressing proliferation markers (Figures 2A to 2D).

We also assessed the effect of miR-590-3p on cell apoptosis. The results revealed that miR-590-3p overexpression reduced the number of apoptotic (transferase-mediated deoxyuridinetriphosphate nick-end labeling-positive) cells in an ischemic and hypoxic environment (Figures 2E and 2F). Moreover, qRT-PCR analysis showed that miR-590-3p overexpression up-regulated G1/S genes (*CCND1* and *CDK4*) and G2/M genes (*CCNA1* and polo-like kinase 1 [*PLK1*]) (Figures 2G and 2H), up-regulated the anti-apoptotic gene *Bcl-2*, and down-regulated the pro-apoptotic gene *Bax* in hiPSC-CMs (Figure 2I).

miR-590-3p overexpression up-regulated 1,304 genes and down-regulated 1,192 genes (Supplemental Figures 2A to 2C). These genes were implicated in cellular structure, excitation-contraction coupling, and metabolism. Gene ontology enrichment analysis showed that miR-590-3p overexpression affected various biological processes, including cell proliferation and apoptosis (Supplemental Figure 2D). These results are consistent with the ability of miR-590-3p

to stimulate cellular proliferation and inhibit apoptosis.

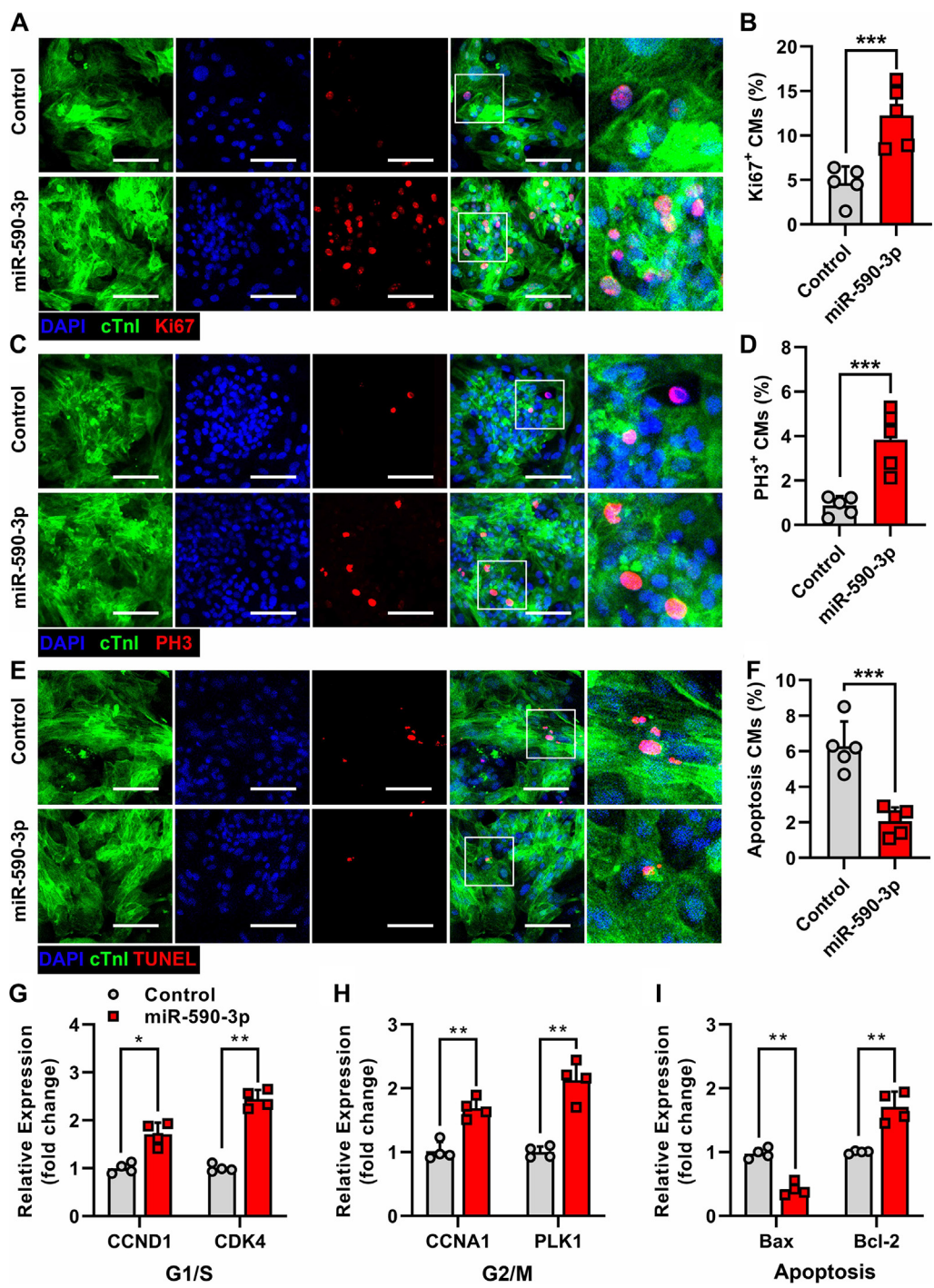
miR-590-3p PROMOTED hiPSC-CM PROLIFERATION BY REGULATING THE TSC22D2/PKM2 PATHWAY.

The molecular mechanism by which miR-590-3p regulates hiPSC-CM proliferation was investigated. We performed a bioinformatics analysis to identify target genes using 4 target gene prediction databases. Ankyrin repeat and SOCS box containing 1 (*ASB1*), transmembrane protein 18 (*TMEM18*), and TSC22 domain family member 2 (*TSC22D2*) were found in all databases (Figure 3A). The results of qRT-PCR showed that miR-590-3p decreased the expression of *TMEM18* and *TSC22D2* in hiPSC-CMs (Figure 3B). Further, *TSC22D2* expression was higher in cardiomyocytes than in cardiac fibroblasts and endothelial cells (Figure 3C). Therefore, we selected *TSC22D2* for further studies and performed a dual-luciferase reporter assay to assess whether *TSC22D2* was a downstream target of miR-590-3p (Figure 3D). Our results showed that the relative luciferase activity decreased significantly in cells expressing *TSC22D2* and miR-590-3p (Figure 3E). A recent study reported that *TSC22D2* inhibited cellular proliferation by regulating pyruvate kinase M2 (PKM2).¹⁶ Relative protein expression was measured by Western blot analysis. The findings demonstrated that miR-590-3p down-regulated *TSC22D2* expression and up-regulated PKM2, cyclin B1, and cyclin D1, which regulate cell proliferation (Figure 3F). Immunofluorescence staining showed that *TSC22D2* overexpression reversed the effect of miR-590-3p on hiPSC-CM proliferation (Figures 3G and 3H).

miR-590-3p-OE hiPSC-CMs IMPROVED CARDIAC FUNCTION IN A MURINE MODEL OF MI.

To investigate whether miR-590-3p overexpression could enhance the therapeutic efficacy of hiPSC-CMs in myocardial repair, we evaluated the cardiac function of mice treated with miR-590-3p-OE hiPSC-CMs (miR-590-3p) or control hiPSC-CMs (control) (Figure 4A). Treatment with control hiPSC-CMs decreased the heart weight/body weight ratio, and miR-590-3p potentiated this effect (Figure 4B). Echocardiographic measurements indicated that control hiPSC-CMs improved cardiac function on day 28 post-MI, and miR-590-3p enhanced this effect (Figures 4C to 4G). The scar size was quantified by histology (Masson's tricolor staining). Control hiPSC-CMs decreased the fibrotic area, and miR-590-3p overexpression enhanced this effect (Figures 4H and 4I). These findings demonstrated that miR-590-3p overexpression increased the

FIGURE 2 miR-590-3p Overexpression Promotes the Proliferation of hiPSC-CMs and Increases Their Ability to Tolerate Hypoxia In Vitro



(A) Representative images of hiPSC-CMs positive for the proliferation marker Ki67. (B) Number of Ki67-positive cells in control and miR-590-3p-overexpressing hiPSC-CMs ($n = 5$; 5 random fields per sample). (C) Representative images of hiPSC-CMs positive for the M-phase marker PH3. (D) Number of PH3-positive cells in control and miR-590-3p-OE hiPSC-CMs ($n = 5$; 5 random fields per sample). (E) Representative images of apoptotic (TUNEL-positive) hiPSC-CMs. (F) Number of TUNEL-positive control and miR-590-3p-OE hiPSC-CMs ($n = 5$; 5 random fields per sample). (G to I) Relative expression levels of (G and H) cell cycle and (I) apoptosis genes in control and miR-590-3p-OE hiPSC-CMs ($n = 4$). Scale bar: 50 μ m. Data are presented as mean \pm SD. P values were determined using the unpaired Student's t -test. * $P < 0.05$, ** $P < 0.01$, and *** $P < 0.001$. Bcl-2 = B-cell lymphoma-2; Bax = Bcl-2 associated X; CM = cardiomyocyte; hiPSC-CM = human induced pluripotent stem cell-derived cardiomyocyte; miR = microRNA; TUNEL = transferase-mediated deoxyuridinetriphosphate nick-end labeling.

ability of hiPSC-CMs to improve cardiac function and reduce fibrosis after MI.

miR-590-3p OVEREXPRESSION INCREASED THE NUMBER OF ENGRAFTED hiPSC-CMs, PROMOTED ANGIOGENESIS, AND INHIBITED CARDIOMYOCYTE HYPERTROPHY IN INFARCTED MOUSE HEARTS. BLI and immunofluorescence staining were performed to investigate whether miR-590-3p overexpression increased the number of engrafted hiPSC-CMs after cell transplantation (**Figure 5A**). Luciferase-hiPSC-CMs (5.0×10^5 cells) were injected into the infarcted myocardium. BLI analysis showed that the luciferin signal was higher in animals receiving miR-590-3p-OE hiPSC-CMs than in controls at day 28 after cell delivery (**Figures 5B and 5C**). In line with this observation, immunofluorescence staining showed that the area occupied by transplanted hiPSC-CMs (stained with human-specific cardiac troponin T [green fluorescence]) was significantly greater in mice receiving miR-590-3p-OE hiPSC-CMs than in controls at day 28 after cell delivery (**Figures 5D and 5E**). qRT-PCR results demonstrated that the expression of the *SRY* gene (transplanted cells indicator) demonstrated that there were more miR-590-3p-OE hiPSC-CMs in the heart than in controls after transplantation (**Supplemental Figure 3**). The results showed that miR-590-3p promoted the proliferation and expansion of the graft *in vivo*.

The ability of miR-590-3p to induce cellular proliferation was assessed by measuring the number of transplanted hiPSC-CMs expressing the proliferation markers Ki67 and PH3 via immunofluorescence staining. The expression levels of Ki67 and PH3 were 2- and 4-fold higher, respectively, in miR-590-3p-OE cells than in control cells (**Figures 6A to 6D**). qRT-PCR analysis indicated that the expression levels of the proliferation-related genes *CCNB1*, *CCND1*, *CDK4*, and *PLK1* were remarkably higher in myocardium treated with miR-590-3p-OE hiPSC-CMs than in hearts treated with control cells (**Supplemental Figures 4A to 4D**). We also assessed whether miR-590-3p-OE hiPSC-CMs could induce the proliferation of endogenous cardiomyocytes. The proportion of Ki67-positive endogenous cardiomyocytes was significantly higher in the infarct border zone of animals treated with miR-590-3p-OE hiPSC-CMs (**Figures 6E and 6F**).

Angiogenesis plays a critical role in myocardial repair following MI. Therefore, we measured microvessel density by CD31 immunofluorescence staining in the infarct border zone at day 28 post-MI. The results showed that microvessel density was almost 2-fold higher in the infarct border zone of animals treated with miR-590-3p-OE hiPSC-CMs than in the

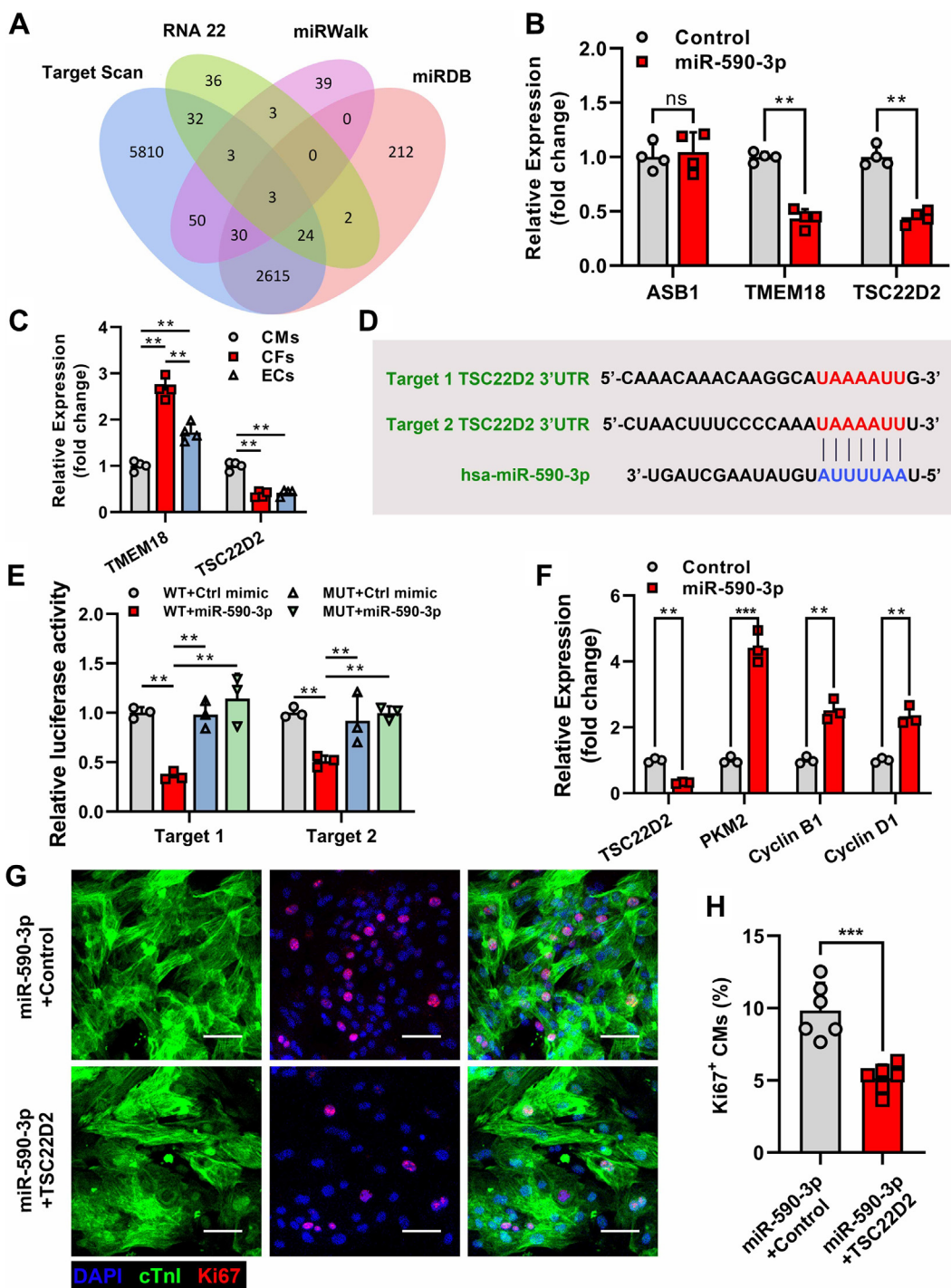
myocardium of animals treated with control cells (**Figures 7A and 7B**).

The protective function of hiPSC-CMs on cardiac hypertrophy was assessed by measuring the cross-sectional surface area of native cardiomyocytes in the infarct border zone. The cross-sectional surface area of cardiomyocytes was significantly smaller in the infarct border zone of animals treated with miR-590-3p-OE hiPSC-CMs than in animals treated with control cells (**Figures 7C and 7D**). These results indicated that miR-590-3p overexpression increased the ability of hiPSC-CMs to promote angiogenesis and inhibit cardiomyocyte hypertrophy.

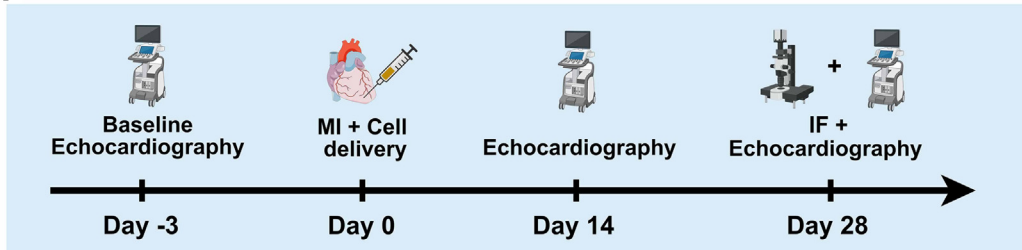
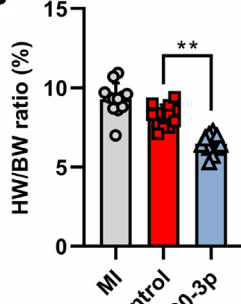
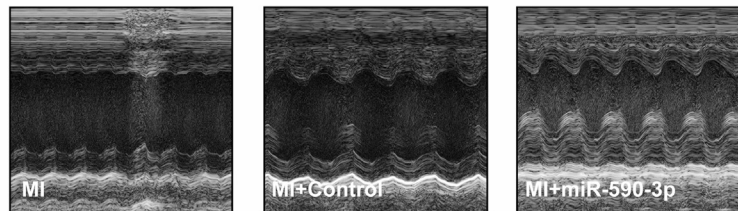
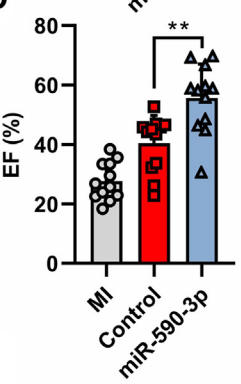
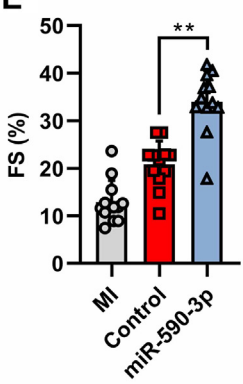
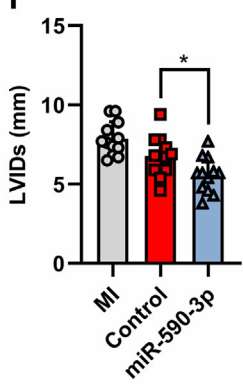
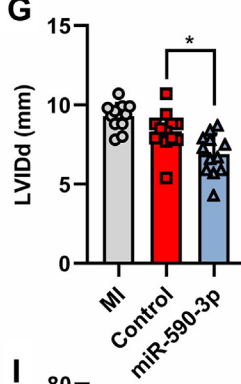
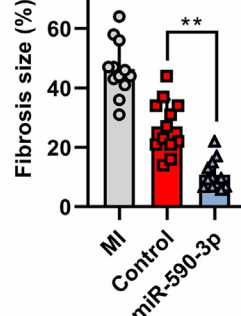
miR-590-3p-OE hiPSC-CM TREATMENT IMPROVED CARDIAC FUNCTION BY STIMULATING hiPSC-CM PROLIFERATION IN A PIG MODEL OF MI. We evaluated the ability of miR-590-3p-OE hiPSC-CMs to repair MI. The experimental workflow is illustrated in **Figure 8A**. Cardiac function was evaluated 28 days after MI by high-resolution computed tomography. Both control hiPSC-CMs and miR-590-3p-OE hiPSC-CMs enhanced left ventricular ejection fraction and left ventricular fractional shortening while reducing LVEDV and LVESV. In addition, cardiac function was better in the miR-590-3p-OE hiPSC-CM group than in the control group (**Figures 8B to 8E**). Similarly, the analyses of fresh heart slides showed that hiPSC-CM transplantation reduced scar size, and miR-590-3p-OE hiPSC-CMs had a stronger effect on scar reduction. Thus, miR-590-3p-OE hiPSC-CM transplantation has therapeutic potential for MI.

Analysis of Ki67 and PH3 expression by immunofluorescence staining showed that miR-590-3p significantly enhanced hiPSC-CM proliferation in porcine hearts. (**Supplemental Figures 5A to 5D**). We next assessed the safety of using miR-590-3p-OE hiPSC-CMs in pig hearts. Blood cell analysis showed that the number of monocytes increased slightly after hiPSC-CM delivery, and this increase might be caused by the surgical procedure (**Supplemental Figures 6A to 6D**). The levels of serum chemistry in hepatic, renal, and cardiac analyses did not change significantly after hiPSC-CM transplantation in the control and miR-590-3p groups (**Supplemental Figures 6E to 6H**). In addition, continuous electrocardiogram recordings detected by a telemetry device showed that miR-590-3p-OE hiPSC-CM transplantation did not cause an increase in arrhythmic events (premature ventricular contractions and nonsustained ventricular tachycardia) (**Supplemental Figures 6I and 6J**). These results demonstrated the safety and efficacy of the transplantation of miR-590-3p-OE hiPSC-CMs.

FIGURE 3 miR-590-3p Promotes the Proliferation of hiPSC-CMs by Regulating the TSC22D2/Pkm2 Pathway

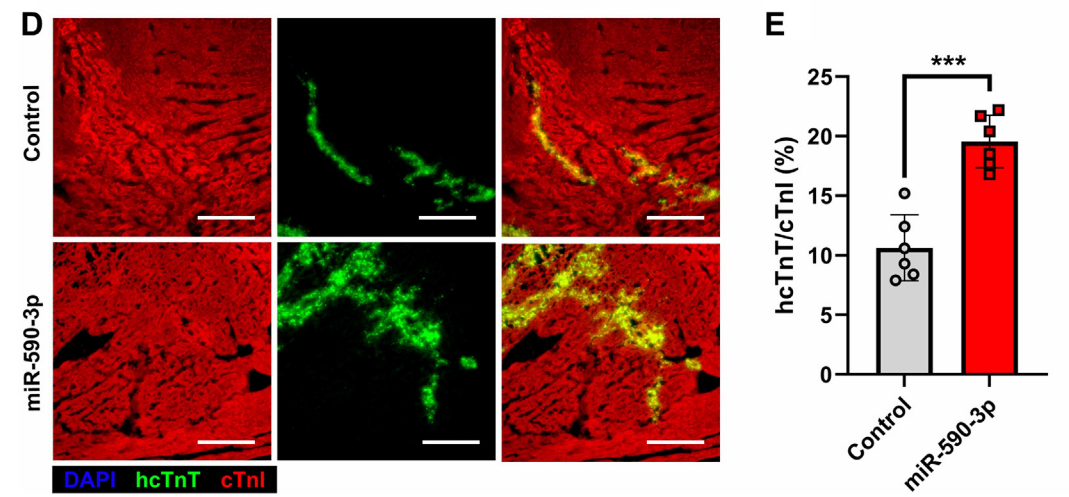
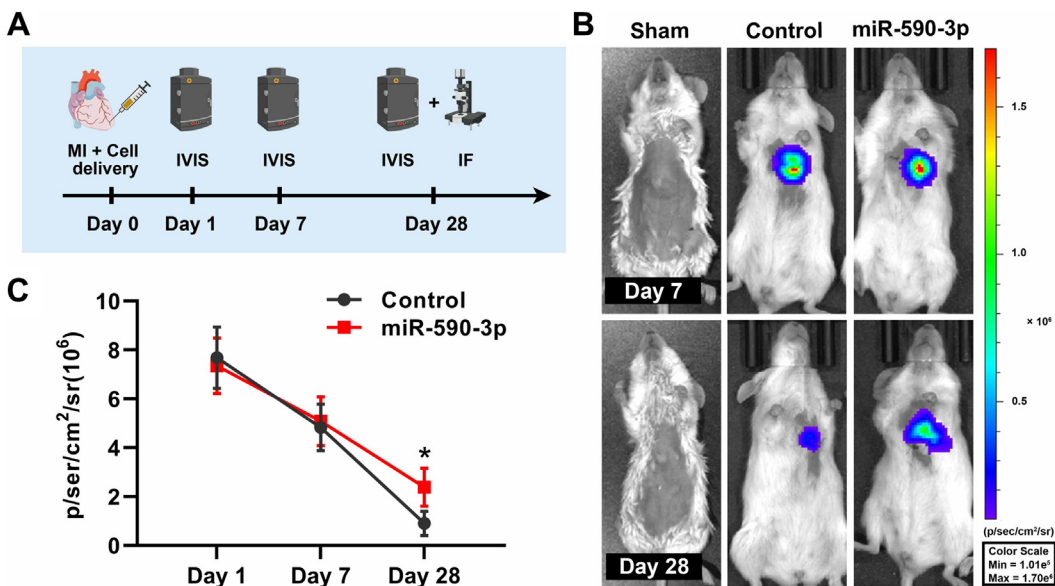


(A) Venn diagram of miR-590-3p potential target genes. (B) Analysis of the relative expression levels of *ASB1*, *TMEM18*, and *TSC22D2* in hiPSC-CMs by qRT-PCR after miR-590-3p treatment ($n = 4$). (C) Relative expression levels of *TMEM18* and *TSC22D2* in CMs, CFs, and ECs ($n = 4$). (D) Potential binding sites for miR-590-3p in the 3'-UTR of *TSC22D2*. (E) Luciferase reporter activity of chimeric vectors carrying the luciferase gene and a fragment of *TSC22D2* containing WT or mutation binding sites for miR-590-3p. (F) Western blot analysis of the protein expression of *TSC22D2*, *PKM2*, cyclin B1, and cyclin D1 ($n = 3$). (G) Representative images of hiPSC-CMs positive for the proliferation marker Ki67. (H) Number of Ki67-positive cells ($n = 5$; 5 random fields per sample). Scale bar: 50 μ m. Data are presented as mean \pm SD. P values were determined using the unpaired Student's *t*-test or 1-way analysis of variance followed by Tukey's post hoc test. ** $P < 0.01$ and *** $P < 0.001$. ASB1 = ankyrin repeat and SOCS box containing 1; CF = cardiac fibroblast; cTnI = cardiac troponin I; Ctrl = control; DAPI = 4',6-diamidino-2-phenylindole; EC = endothelial cell; MUT = mutation; ns = not significant; PKM2 = pyruvate kinase M2; TMEM18 = transmembrane protein 18; TSC22D2 = TSC22 domain family member 2; UTR = untranslated region; WT = wild type; other abbreviations as in Figure 1 and 2.

FIGURE 4 miR-590-3p Overexpression Improves the Therapeutic Effect of hiPSC-CM Transplantation on Cardiac Repair After MI**A****B****C****D****E****F****G****H****I**

(A) Timeline of mouse MI in vivo. (B) Quantification of the HW/BW ratio ($n = 12$). (C) Representative echocardiographic images. (D to G) Echocardiographic assessment of EF%, FS%, LVIDs, and LVIDd ($n = 12$). (H) Fibrotic area in infarcted mouse hearts. (I) Quantification of fibrosis ($n = 12$). Data are presented as mean \pm SD. P values were determined using 1-way analysis of variance followed by Tukey's post hoc test. * $P < 0.05$ and ** $P < 0.01$. BW = body weight; EF = ejection fraction; FS = shortening fraction; HW = heart weight; LVIDd = left ventricular internal diameter at end diastole; LVIDs = left ventricular internal diameter at end systole; MI = myocardial infarction; other abbreviations as in Figures 1 and 2.

FIGURE 5 miR-590-3p Overexpression Increases the Engraftment Rates of hiPSC-CMs in Infarcted Mouse Hearts After Cell Transplantation



(A) Timeline of the *in vivo* study. (B) Representative BLI images of hearts implanted with miR-590-3p-overexpressing hiPSC-CMs or control cells. (C) Quantification of BLI fluorescence intensity ($n = 6$). (D) IF staining of hiPSC-CMs in infarcted hearts. (E) Quantification of the engraftment rates of hiPSC-CMs in infarcted hearts ($n = 6$). Scale bar = 200 μ m. Data are presented as mean \pm SD. P values were determined using unpaired Student's *t*-test. * $P < 0.05$ and *** $P < 0.001$. BLI = bioluminescence live imaging; hcTnT = human cardiac troponin T; IVIS = image visualization and infrared spectroscopy; Max = maximum; Min = minimum; other abbreviations as in Figures 1 to 4.

DISCUSSION

Severe MI usually results in a significant loss of cardiomyocytes. During the early stage of MI, cardiac fibroblasts are activated and produce extracellular matrix (ECM) in response to new hemodynamic conditions.¹⁷ However, the loss of cardiomyocytes and excessive ECM deposition causes changes in cardiac structure, impairing function and ultimately leading

to HF. hiPSC-CM transplantation is a potentially effective therapeutic strategy for heart tissue repair. However, several critical issues need to be resolved before clinical application. Our results demonstrated that miR-590-3p enhanced the ability of hiPSC-CMs to improve MI by regulating the TSC22D2/PKM2 pathway.

Low engraftment rates after cell transplantation are one of the primary obstacles to achieving the

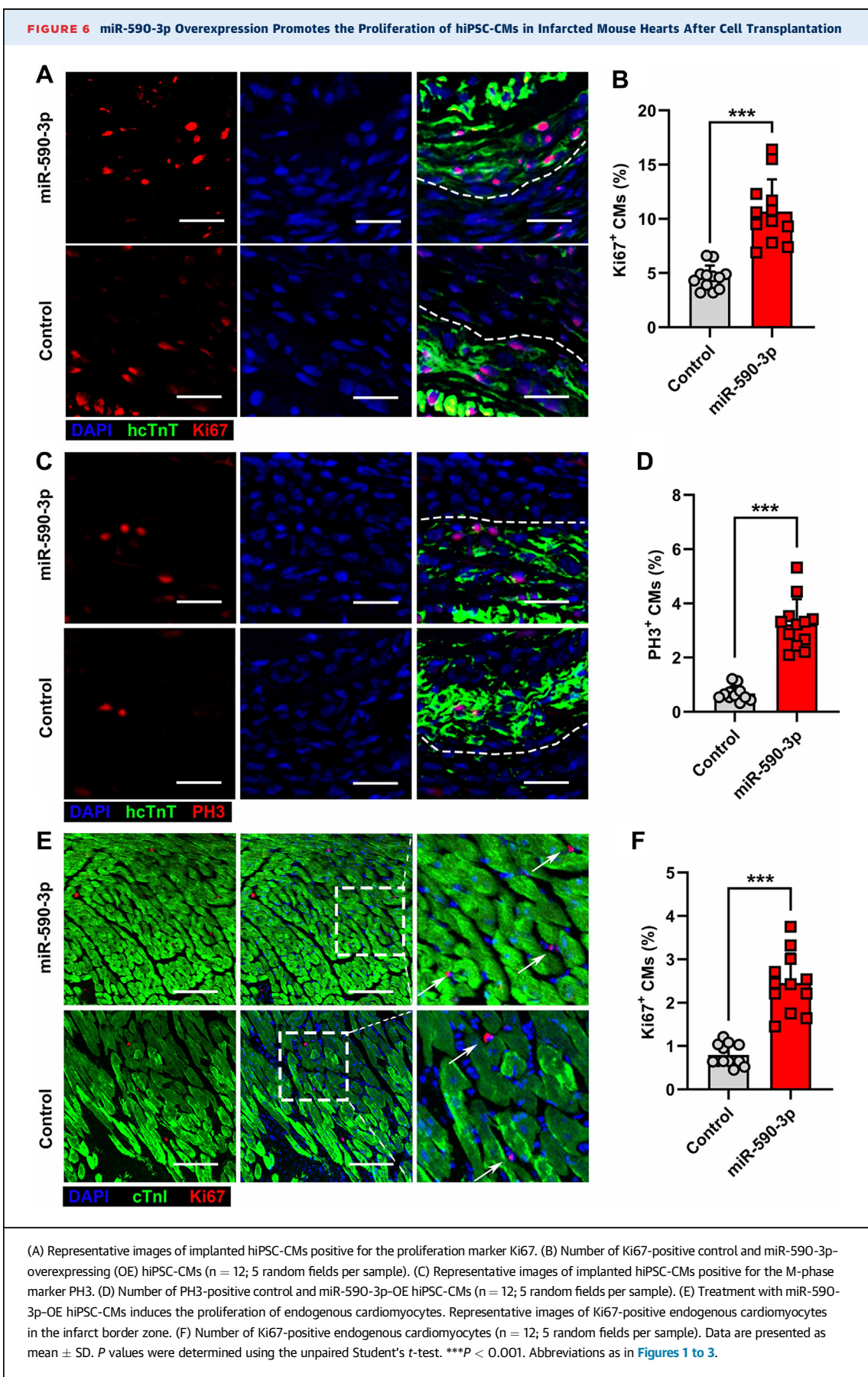
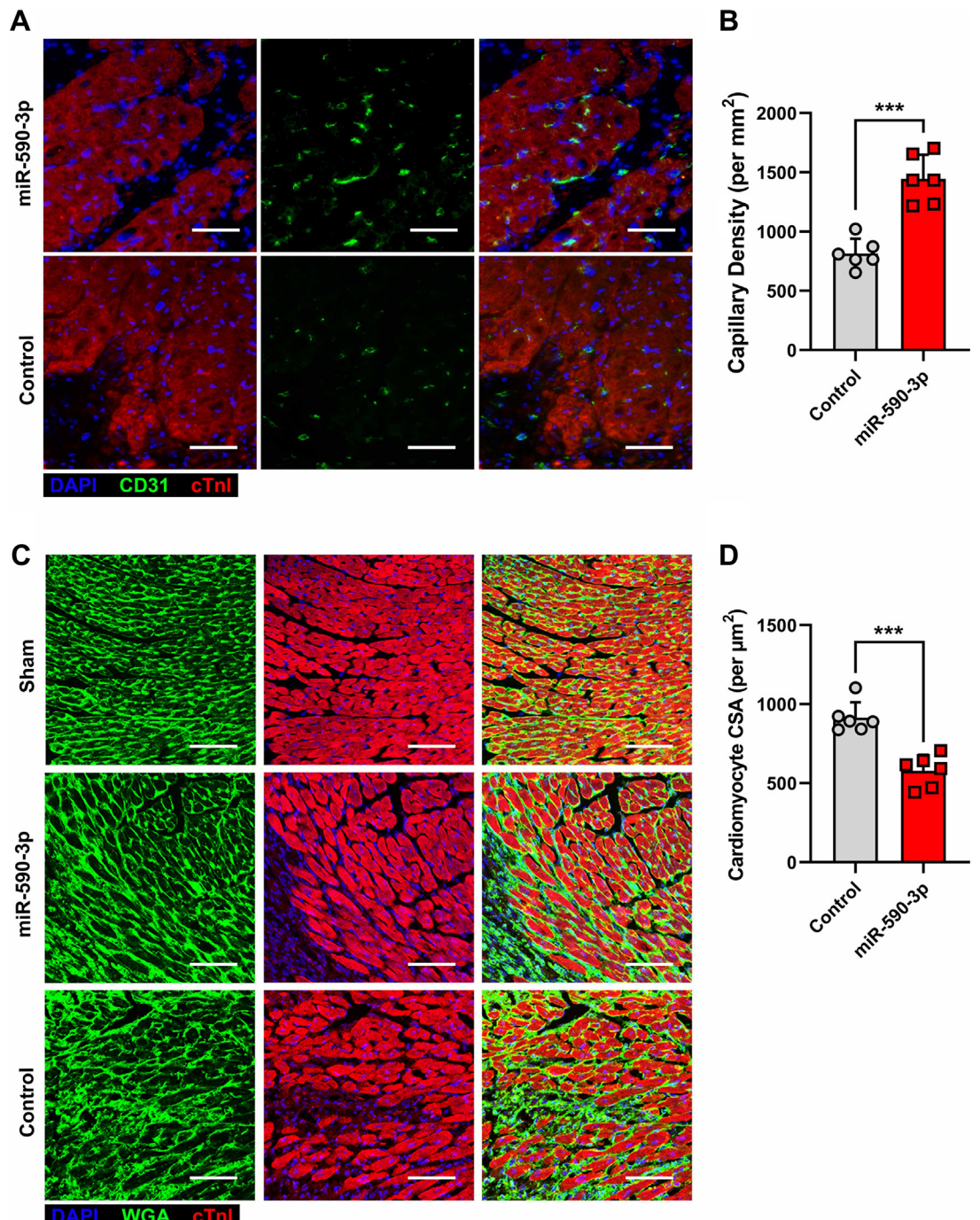
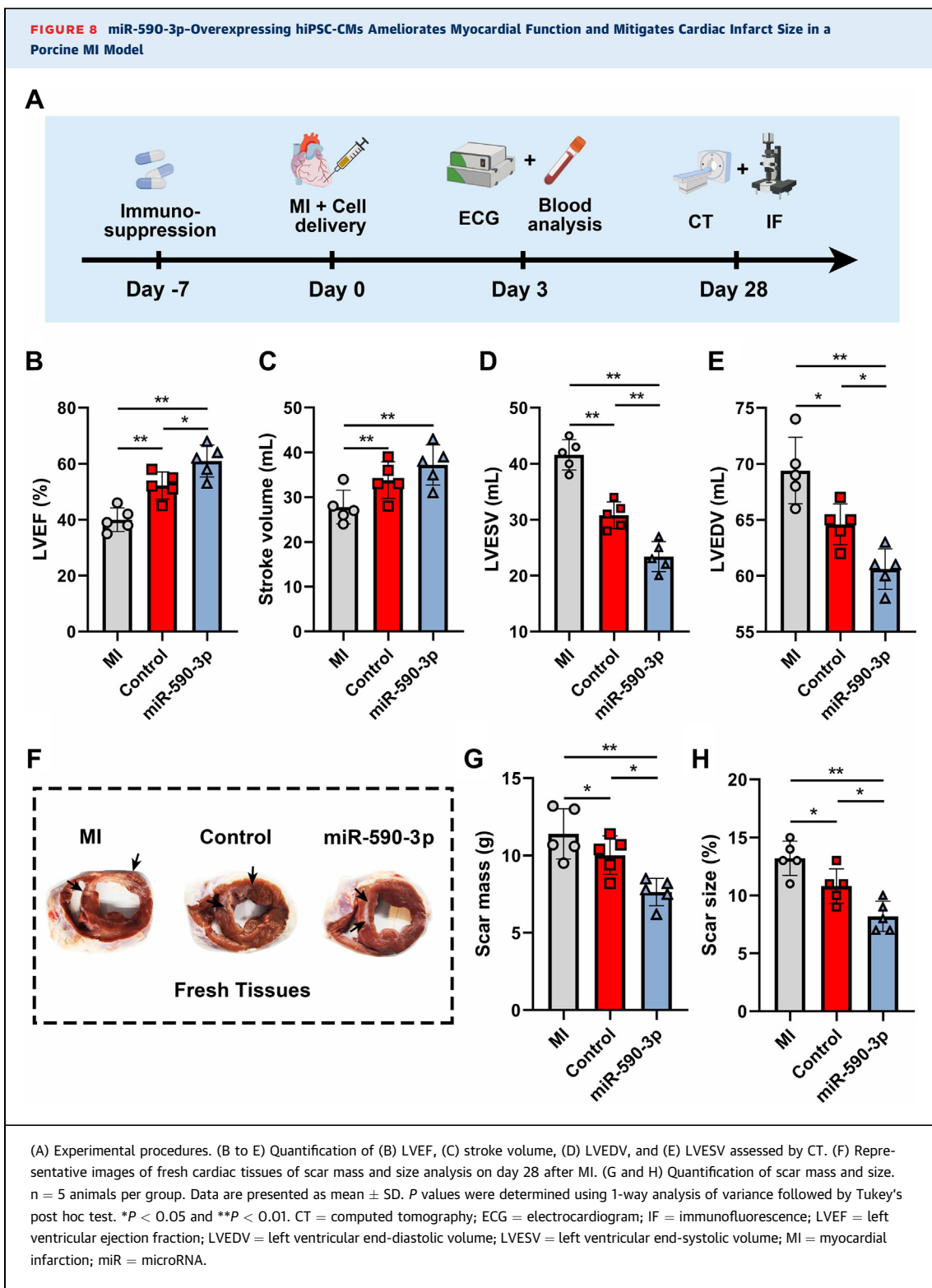


FIGURE 7 Treatment With miR-590-3p-Overexpressing hiPSC-CMs Promotes Angiogenesis and Inhibits Cardiomyocyte Hypertrophy in a Mouse Model of Myocardial Infarction



(A) Representative images of microvessels immunostained with troponin I (red) and CD31 (green). Scale bar: 50 μ m. (B) Quantification of microvessel density by calculating the number of CD31-positive cells per mm^2 ($n = 6$, 5 random fields per sample). (C) Representative images of cardiomyocytes immunostained with WGA-FITC (red) and troponin I (green) in the infarct border zone. Scale bar: 100 μ m. (D) Quantification of the CSA of cardiomyocytes by WGA-FITC staining ($n = 6$, 5 random fields per sample). Data are presented as mean \pm SD. P-values were determined using unpaired Student's *t*-test. *** $P < 0.001$. CSA = cross-sectional area; FITC = fluorescein isothiocyanate; WGA = wheat germ agglutinin; other abbreviations as in Figures 1 and 4.



functional regeneration of injured hearts through stem cell therapy.^{18,19} This study provides the first evidence that miR-590-3p stimulates the proliferation of hiPSC-CMs *in vivo* and *in vitro*. Moreover, miR-590-3p increased the hiPSC-CM engraftment rate, improving cardiac function and reducing cardiac fibrosis and hypertrophy after MI.

In mammalian fetuses, approximately 3% to 15% of cardiomyocytes are in the cell cycle,²⁰ which increases cardiac regeneration capacity by stimulating cardiomyocyte division. Gene expression profiling and proteomics analysis identified several factors that increase the proliferative capacity of cardiomyocytes, and *in vivo* studies demonstrated that proliferative genes stimulated mitosis in adult mammalian cardiomyocytes after MI.²¹ Similar to adult cardiomyocytes, the proliferative capacity of hiPSC-CMs decreases with prolonged culturing, and hiPSC-CMs initiate maturation and exit the cell cycle after transplantation.²² Our results demonstrated the ability of miR-590-3p to promote cellular proliferation. We found that the expression of miR-590-3p decreased during cardiac maturation. Gain-of-function experiments demonstrated that miR-590-3p promoted hiPSC-CM proliferation. miR-590-3p also increased the number of proliferating hiPSC-CMs *in vitro* by more than 2-fold and increased the engraftment rate of implanted hiPSC-CMs by more than 1.5-fold in a mouse model of MI. Furthermore, the expression of proliferation markers Ki67 and PH3 was significantly up-regulated in cardiomyocytes receiving miR-590-3p-OE hiPSC-CMs, suggesting that paracrine factors secreted by hiPSC-CMs induce endogenous cardiomyocyte proliferation.

The effect of miR-590-3p on cell proliferation varies depending on the disease model and cell type. For instance, Salem et al²³ demonstrated that miR-590-3p promoted ovarian cancer growth and metastasis by enhancing tumor cell proliferation.²³ Conversely, Wang et al²⁴ observed that miR-590-3p inhibited osteosarcoma cell proliferation and metastasis by regulating SRY-box transcription factor 9 (SOX9).²⁴ The varying effect of miR-590-3p on tumor cell proliferation in different cancers may be related to the target genes it regulates and the expression of target genes in tumor cells. miR-590-3p promotes endogenous cardiomyocyte proliferation in rodents. However, little is known about the function of miR-590-3p in hiPSC-CM proliferation. Our results showed that miR-590-3p increased hiPSC-CM proliferation, whereas other studies found that miR-590-3p promoted hiPSC-CM proliferation to a small extent. This discrepancy may be attributable to the different iPSC cell lines used across studies and differences in gene

expression and biological functions among cell lines. Therefore, a comprehensive assessment of the role of miR-590-3p in iPSC cell lines can help develop hiPSC-CM-based therapeutic strategies for MI.

Uncontrolled cardiomyocyte proliferation increases the risk of death in patients with MI. Gabisonia et al⁶ reported that the expression of human miRNA-199a in infarcted pig hearts stimulated cardiac repair. However, the persistent and uncontrolled expression of this miRNA resulted in the sudden arrhythmic death of treated pigs. These results indicate that achieving cardiac repair by stimulating endogenous cardiomyocyte proliferation is attainable in large mammals; however, the dosage of this therapy needs to be tightly controlled. In our study, 5.0×10^7 cells were transplanted into infarcted hearts.¹⁹ Previous studies reported that mechanical action and electrical activity promoted hiPSC-CM maturation. Moreover, graft cells matured 30 days after hiPSC-CM transplantation in neonatal mice.²⁵ These results confirm that the proliferative capacity of hiPSC-CMs decreases after transplantation while their contractile and metabolic functions increase. Furthermore, our experimental results confirmed that miR-590-3p-OE hiPSC-CM transplantation was not associated with an increase in arrhythmic events, demonstrating that miR-590-3p-OE hiPSC-CM transplantation is safe and effective for treating MI.

Cardiac fibrosis causes ventricular systolic dysfunction. In addition, cardiac overload and nutrient deficiency contribute to cardiomyocyte hypertrophy in the peri-infarct zone. Therefore, even after recovering from initial infarction, fibrosis affects the viability of peri-infarct zone cardiomyocytes through the disintegration of the ECM and replacement of necrotic tissue by scar tissue.²⁶ We found that hiPSC-CM transplantation restored cardiac function, increased microvessel density, and reduced cardiomyocyte hypertrophy and that miR-590-3p overexpression enhanced these effects.

Because of differences in hemodynamic and electrophysiologic properties between mice and humans, research data from rodent models cannot be translated to humans.²⁷ Nonetheless, preclinical animal models, such as pigs and nonhuman primates, are essential to assess clinical safety. Gabisonia et al⁶ reported that intramyocardial injections of miR-199a induced endogenous cardiomyocyte proliferation, improving functional recovery in a pig model of MI. However, uncontrolled endogenous cardiomyocyte proliferation mediated by miR-199 overexpression predisposed to ventricular arrhythmias, leading to sudden death.⁶ Our study assessed the safety of using miR-590-3p-OE hiPSC-CMs in pig hearts. The number

of blood cells; the levels of inflammatory cytokines in the pericardial fluid; and the levels of hepatic, renal, and cardiac markers have no difference between miR-590-3p-OE hiPSC-CM and control hiPSC-CM administration.

STUDY LIMITATIONS. In the present study, we analyzed the phenotype of the mouse/pig model 4 weeks after MI. Although miR-590-3p-OE hiPSC-CMs showed a restorative effect on cardiac function in the early stages of MI, further research is required to assess myocardial recovery in the long run.

CONCLUSIONS

The results showed that miR-590-3p overexpression promoted hiPSC-CM proliferation in vitro and in vivo. Further, miR-590-3p improved the therapeutic effect of hiPSC-CMs on MI by increasing the engraftment rate. Importantly, we confirmed the safety of using miR-590-3p-OE hiPSC-CMs in pig hearts. These results demonstrate that the transplantation of miR-590-3p-OE hiPSC-CMs is potentially effective for cardiac regeneration.

FUNDING SUPPORT AND AUTHOR DISCLOSURES

This work was supported by the National Key Research and Development Program of China (2020YFA0112600), the National Natural Science Foundation of China (No. 81970397), and the Preresearch Fund Project of the Second Affiliated Hospital of Soochow University (SDFYQN1914). The authors have reported that they have no relationships relevant to the contents of this paper to disclose.

REFERENCES

- Pfeffer MA, Shah AM, Borlaug BA. Heart failure with preserved ejection fraction in perspective. *Circ Res*. 2019;124:1598–1617.
- Mahmoud AI, Kocabas F, Muralidhar SA, et al. Meis1 regulates postnatal cardiomyocyte cell cycle arrest. *Nature*. 2013;497:249–253.
- Ichihara Y, Kaneko M, Yamahara K, et al. Self-assembling peptide hydrogel enables instant epicardial coating of the heart with mesenchymal stromal cells for the treatment of heart failure. *Biomaterials*. 2018;154:12–23.
- Jung JH, Ikeda G, Tada Y, et al. miR-106a-363 cluster in extracellular vesicles promotes endogenous myocardial repair via Notch3 pathway in ischemic heart injury. *Basic Res Cardiol*. 2021;116:19.
- Qian L, Huang Y, Spencer CI, et al. In vivo reprogramming of murine cardiac fibroblasts into induced cardiomyocytes. *Nature*. 2012;485:593–598.
- Gabisonia K, Prosdocimo G, Aquaro GD, et al. MicroRNA therapy stimulates uncontrolled cardiac repair after myocardial infarction in pigs. *Nature*. 2019;569:418–422.
- Kolanowski TJ, Busek M, Schubert M, et al. Enhanced structural maturation of human induced pluripotent stem cell-derived cardiomyocytes under a controlled microenvironment in a microfluidic system. *Acta Biomater*. 2020;102:273–286.
- Ebert A, Joshi AU, Andorf S, et al. Proteasome-dependent regulation of distinct metabolic states during long-term culture of human iPSC-derived cardiomyocytes. *Circ Res*. 2019;125:90–103.
- Shiba Y, Gomibuchi T, Seto T, et al. Allogeneic transplantation of iPS cell-derived cardiomyocytes regenerates primate hearts. *Nature*. 2016;538:388–391.
- Lu TX, Rothenberg ME. MicroRNA. *J Allergy Clin Immunol*. 2018;141:1202–1207.
- Du WW, Yang W, Xuan J, et al. Reciprocal regulation of miRNAs and piRNAs in embryonic development. *Cell Death Differ*. 2016;23:1458–1470.
- Eulalio A, Mano M, Dal Ferro M, et al. Functional screening identifies miRNAs inducing cardiac regeneration. *Nature*. 2012;492:376–381.
- Gao F, Kataoka M, Liu N, et al. Therapeutic role of miR-19a/19b in cardiac regeneration and protection from myocardial infarction. *Nat Commun*. 2019;10(1):1802.
- Lesizza P, Prosdocimo G, Martinelli V, Sinagra G, Zacchigna S, Giacca M. Single-dose intracardiac injection of pro-regenerative microRNAs improves cardiac function after myocardial infarction. *Circ Res*. 2017;120:1298–1304.
- Gao L, Wang L, Wei Y, et al. Exosomes secreted by hiPSC-derived cardiac cells improve recovery from myocardial infarction in swine. *Sci Transl Med*. 2020;12(561):eaay1318.
- Liang F, Li Q, Li X, et al. TSC22D2 interacts with PKM2 and inhibits cell growth in colorectal cancer. *Int J Oncol*. 2016;49:1046–1056.
- Li L, Zhao Q, Kong W. Extracellular matrix remodeling and cardiac fibrosis. *Matrix Biol*. 2018;68–69:490–506.
- Zhao M, Fan C, Ernst PJ, et al. Y-27632 preconditioning enhances transplantation of human-induced pluripotent stem cell-derived cardiomyocytes in myocardial infarction mice. *Cardiovasc Res*. 2019;115:343–356.
- Zhao M, Nakada Y, Wei Y, et al. Cyclin D2 overexpression enhances the efficacy of human induced pluripotent stem cell-derived

ADDRESSES FOR CORRESPONDENCE: Dr Ling Gao, Translational Medical Center for Stem Cell Therapy & Institute for Regenerative Medicine, Shanghai East Hospital, Tongji University School of Medicine, 1800 Yuntai Road, Shanghai 200123, China. E-mail: gao leng5@126.com. OR Dr Qingyou Meng, Department of Vascular Surgery, General Surgery Clinical Center, Shanghai General Hospital, Shanghai Jiao Tong University School of Medicine, 100 Haining Road, Shanghai 200080, China. E-mail: mengqy@163.com.

PERSPECTIVES

COMPETENCY IN MEDICAL KNOWLEDGE: We have demonstrated that miR-590-3p-overexpressed hiPSC-CMs enhance cardiac function 28 days after MI in a preclinical pig model. With potential clinical trials in the near future, the safety of the treatment was also evaluated in this paper. We found that the transplantation of miR-590-3p-overexpressed hiPSC-CMs is potentially effective for cardiac regeneration.

TRANSLATIONAL OUTLOOK: miR-590-3p improved the therapeutic effect of hiPSC-CMs on MI by increasing the engraftment rate. This may present potential new strategies for treating MI, thus helping the development of novel therapeutics.

- cardiomyocytes for myocardial repair in a swine model of myocardial infarction. *Circulation*. 2021;144:210–228.
- 20.** Zhao M, Zhang E, Wei Y, Zhou Y, Walcott GP, Zhang J. Apical resection prolongs the cell cycle activity and promotes myocardial regeneration after left ventricular injury in neonatal pig. *Circulation*. 2020;142:913–916.
- 21.** Magadum A, Singh N, Kurian AA, et al. Pkm2 regulates cardiomyocyte cell cycle and promotes cardiac regeneration. *Circulation*. 2020;141:1249–1265.
- 22.** Feyen DAM, McKeithan WL, Bruyneel AAN, et al. Metabolic maturation media improve physi-
ological function of human iPSC-derived cardiomyocytes. *Cell Rep*. 2020;32:107925.
- 23.** Salem M, O'Brien JA, Bernaudo S, et al. miR-590-3p promotes ovarian cancer growth and metastasis via a novel FOXA2-versican pathway. *Cancer Res*. 2018;78:4175–4190.
- 24.** Wang WT, Qi Q, Zhao P, Li CY, Yin XY, Yan RB. miR-590-3p is a novel microRNA which suppresses osteosarcoma progression by targeting SOX9. *Biomed Pharmacother*. 2018;107:1763–1769.
- 25.** Kadota S, Pabon L, Reinecke H, Murry CE. In vivo maturation of human induced pluripotent stem cell-derived cardiomyocytes in neonatal and adult rat hearts. *Stem Cell Rep*. 2017;8:278–289.
- 26.** Kim GH, Uriel N, Burkhoff D. Reverse remodelling and myocardial recovery in heart failure. *Nat Rev Cardiol*. 2018;15:83–96.
- 27.** Liu S, Li K, Wagner Florencio L, et al. Gene therapy knockdown of Hippo signaling induces cardiomyocyte renewal in pigs after myocardial infarction. *Sci Transl Med*. 2021;13(600):eabd6892.

KEY WORDS cell cycle, human induced pluripotent stem cells, miR-590-3p, myocardial infarction

APPENDIX For supplemental tables and figures, please see the online version of this paper.

EDITORIAL COMMENT

More Bang for the Buck

Using miRNA-Treated Human iPSC-Derived Cardiomyocytes for Cardiac Repair*



Timothy J. Kamp, MD, PhD

Although reperfusion remains the optimal therapy for acute myocardial infarction (MI), a substantial portion of patients are unable to achieve prompt reperfusion, leading to significant MIs. Following an MI, necrotic tissue is replaced by fibrous scar tissue rather than new functional muscle because the adult human heart lacks a regenerative capacity. Such loss of functional muscle can initiate the progressive spiral to heart failure and death despite optimal medical and device therapy. Although heart transplantation remains an option for end-stage heart failure, limited donor organs and lifelong immunosuppression remain major limitations. Thus, the quest to remuscularize the post-MI heart is being actively pursued using a variety of innovative approaches. Broadly, investigators are following 3 general strategies: 1) reactivate proliferation of endogenous cardiomyocytes; 2) reprogram native cardiac cells such as fibroblasts to functional cardiomyocytes; and 3) transplant human pluripotent stem cell-derived cardiomyocytes (hPSC-CMs) or cardiac progenitor cells. However, as the study by Zhang et al¹ in this issue of *JACC: Basic to Translational Science* suggests, a combination of approaches may be the most effective.

Over the past decade, great progress has been made in developing approaches using hPSC-CMs to

regenerate injured heart muscle in a variety of animal models. Despite a handful of phase 1 clinical trials testing the safety of various approaches to deliver hPSC-CMs to treat patients with heart failure, major roadblocks remain before the full potential of this approach can be realized—remuscularization of the damaged heart. Prominent among the challenges are: 1) overcoming immunological barriers for an allogeneic cell product; and 2) dosing and biomanufacturing limitations. The latter challenge relates to the fact that despite efforts at optimizing cell preparation and delivery approaches, intramyocardial delivery of hPSC-CMs leads to a relatively low survival rate for transplanted cells, <10% or lower. Thus, to realize significant remuscularization in large animal models, investigators have used large doses, generally in the range of 1 billion hPSC-CMs. Biomanufacturing approaches continue to improve, but the costs will potentially be prohibitive with current technology given that 1 billion hPSC-CMs must be generated per patient and more than 1 treatment may be needed. Thus, ways to enable smaller doses of hPSC-CMs to provide clinical benefit are of great practical importance to advancing this potential therapeutic avenue.

As in normal development, differentiation of hPSCs to CMs leads to cells that are initially proliferative, but as they mature, the cells exit the cell cycle and stop dividing. The hPSC-CMs that have been tested for cell therapy, although immature, have largely stopped proliferating. If instead of nonproliferating CMs, a population of proliferative CMs could be transplanted and the cells continue to divide, there could be more benefit per dose. A number of experimental approaches have been demonstrated to reactivate proliferation in quiescent CMs, including forced expression of certain

*Editorials published in *JACC: Basic to Translational Science* reflect the views of the authors and do not necessarily represent the views of *JACC: Basic to Translational Science* or the American College of Cardiology.

From the Department of Medicine, Stem Cell and Regenerative Medicine Center, University of Wisconsin, Madison, Wisconsin, USA.
The author attests they are in compliance with human studies committees and animal welfare regulations of the author's institution and Food and Drug Administration guidelines, including patient consent where appropriate. For more information, visit the [Author Center](#).

microRNAs (miRs).² MiRs are small RNAs of 18-22 nucleotides that are noncoding and typically act by binding the 3'-untranslated region of target messenger RNAs, leading to degradation and/or translational repression. Prior research showed that delivery of miR199a-3p or miR-590-3p in the post-MI adult mouse heart induced endogenous cardiomyocyte proliferation, reduced infarct size, and improved cardiac function.² Can forced expression of proliferation-inducing miRs in hPSC-CMs maintain the hPSC-CMs in a proliferative state and improve dosing requirements?

Zhang et al¹ tested AAV6-mediated delivery of miR-590-3p to hiPSC-CMs and demonstrated that forced expression of miR-590-3p did lead to increased proliferation of the hiPSC-CMs in culture. Furthermore, by characterizing the potential targets of miRNA-590-3p, they demonstrated that the target TSC22 domain family member 2 is down-regulated, which leads to up-regulation of pyruvate kinase M2 and downstream cell cycle genes. Next, the investigators tested delivery of hiPSC-CMs transduced with miR-590-3p to mouse hearts at the time of surgically induced MI. They found evidence using bioluminescent imaging of a luciferase reporter as well as histology that the miR-590-3p-expressing hiPSC-CMs formed larger grafts containing proliferating CMs at 28 days, which was accompanied by a significantly greater improvement in cardiac function relative to treatment with nontransduced hiPSC-CMs. The study then tested the same strategy delivering miR-590-3p hiPSC-CMs to pig hearts following surgically induced MI and showed remarkable improvements in cardiac function relative to sham control and improved relative to non-transduced hiPSC-CMs. This was accomplished in the porcine model with a dose of 50 million hiPSC-CMs, which is 10-20-fold lower than effective doses in prior large animal studies. Furthermore, the investigators did not find signals for toxicity, including a lack of induced ventricular tachycardia.

The finding that proliferating hiPSC-CMs are able to form larger grafts than nonproliferating hiPSC-CMs is consistent with recent studies that used an alternative approach to activate proliferation: overexpression of the key cell cycle gene, *CCND2*.³ Interestingly, the

study by Zhao et al³ demonstrated that an effect of *CCND2* overexpression was to stimulate the release of exosomes containing miR302b-3p and miR373-3p, which increase the proliferation of CMs. But uncontrolled proliferation of hiPSC-CMs or native CMs can lead to adverse outcomes, as was highlighted by overexpression of miR-199a-3p in post-MI pig hearts resulting in sustained ventricular tachycardia and death despite significant cardiac regeneration.⁴ Thus, it will be essential to advance strategies that control the degree and timing of hiPSC-CM proliferation. Additionally, not all approaches to induce proliferation of hPSC-CMs will exert equal effects and safety. For example, miRs target large gene regulatory networks, and each “proliferation”-inducing miR may be associated with distinct risk profiles. Perhaps the fact that miR-590-3p has been demonstrated to inhibit proliferation of hepatocellular cancer cells and is being tested as an anticancer therapy suggests that it might help counter a concern from hPSC-related therapy: tumor formation.⁵ Additionally, therapy-induced ventricular tachycardia, whether primarily from the hPSC-CM graft or from continued proliferation of CMs, will be an important safety outcome that undoubtedly will differ among the distinct strategies. Although it is encouraging that Zhang et al¹ did not observe ventricular tachycardia in the porcine post-MI model with 1 month of observation, longer and larger studies are needed to confirm this safety readout. Overall, exciting progress in advancing cardiac regeneration therapies to clinical application continues, but the biological complexities and practical realities require continued effort to fully realize the remarkable promise.

FUNDING SUPPORT AND AUTHOR DISCLOSURES

The author has reported that he has no relationships relevant to contents of this paper to disclose.

ADDRESS FOR CORRESPONDENCE: Dr Timothy J. Kamp, Cellular and Molecular Arrhythmia Research Program, University of Wisconsin-Madison School of Medicine and Public Health, 8459 WIMR II, 1111 Highland Avenue, Madison, Wisconsin 53705, USA. E-mail: tjk@medicine.wisc.edu.

REFERENCES

- 1.** Zhang Z, Li X, Zhuang J, et al. miR-590-3p overexpression improves the efficacy of hiPSC-CMs for myocardial repair. *J Am Coll Cardiol Basic Trans Science*. 2024;9(5):557-573.
 - 2.** Eulalio A, Mano M, Dal Ferro M, et al. Functional screening identifies miRNAs inducing cardiac regeneration. *Nature*. 2012;492(7429):376-381.
 - 3.** Zhao M, Nakada Y, Wei Y, et al. Cyclin D2 overexpression enhances the efficacy of human induced pluripotent stem cell-derived cardiomyocytes for myocardial repair in a swine model of myocardial infarction. *Circulation*. 2021;144(3):210-228.
 - 4.** Gabisonia K, Prosdocimo G, Aquaro GD, et al. MicroRNA therapy stimulates uncontrolled cardiac repair after myocardial infarction in pigs. *Nature*. 2019;569(7756):418-422.
 - 5.** Ge X, Gong L. MiR-590-3p suppresses hepatocellular carcinoma growth by targeting TEAD1. *Tumour Biol*. 2017;39(3):1010428317695947.
-

KEY WORDS cell cycle, human induced pluripotent stem cell, miR-590-3p, myocardial infarction

ORIGINAL RESEARCH - CLINICAL

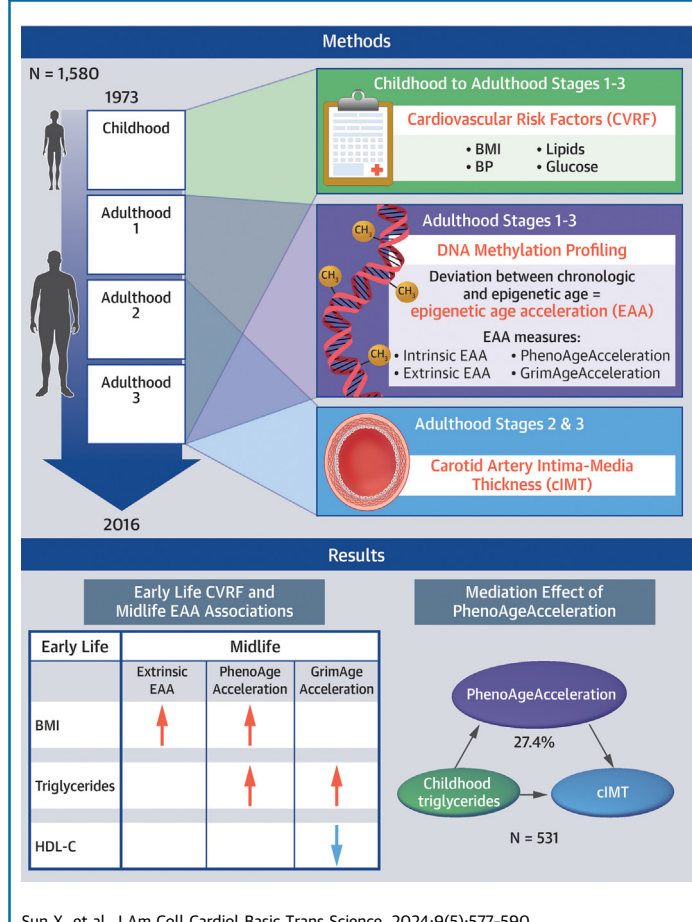


Associations of Epigenetic Age Acceleration With CVD Risks Across the Lifespan

The Bogalusa Heart Study

Xiao Sun, PhD,^{a,d} Wei Chen, MD, PhD,^a Alexander C. Razavi, MD, PhD, MPH,^b Mengyao Shi, PhD, MPH,^c Yang Pan, PhD,^d Changwei Li, MD, PhD,^a Maria Argos, PhD,^e Brian T. Layden, MD,^f Martha L. Daviglus, MD, PhD,^g Jiang He, MD, PhD,^a Owen T. Carmichael, PhD,^h Lydia A. Bazzano, MD, PhD,^a Tanika N. Kelly, PhD, MPHⁱ

VISUAL ABSTRACT



Sun X, et al. J Am Coll Cardiol Basic Trans Science. 2024;9(5):577-590.

HIGHLIGHTS

- Prospective associations between individual CVD risk factors in early life and EAA in midlife suggest that childhood BMI and TGs may affect adulthood EAA, pointing to potential precision strategies to decelerate the biological aging process.
- Simultaneously measured CVD risk factors and EAA provide temporal evidence that CVD risk factors such as BMI, TGs, and HDL-C act as upstream determinants rather than consequences of EAA.
- The mediating effect of EAA in the association between childhood CVD risk factors and subclinical atherosclerosis implicates EAA as a potential molecular link between early life CVD risk and the development of subclinical disease in adulthood.

**ABBREVIATIONS
AND ACRONYMS**

- AUC** = area under the curve
BMI = body mass index
BP = blood pressure
cIMT = carotid intima-media thickness
CVD = cardiovascular disease
CVH = cardiovascular health
DBP = diastolic blood pressure
DNAm = DNA methylation
EAA = epigenetic age acceleration
EEAA = extrinsic epigenetic age acceleration
HDL-C = high-density lipoprotein cholesterol
IEAA = intrinsic epigenetic age acceleration
GrimAgeAccel = GrimAge acceleration
LDL-C = low-density lipoprotein cholesterol
PhenoAgeAccel = PhenoAge acceleration
SBP = systolic blood pressure
TG = triglyceride

SUMMARY

Although epigenetic age acceleration (EAA) might serve as a molecular signature of childhood cardiovascular disease (CVD) risk factors and further promote midlife subclinical CVD, few studies have comprehensively examined these life course associations. This study sought to test whether childhood CVD risk factors predict EAA in adulthood and whether EAA mediates the association between childhood CVD risks and midlife subclinical disease. Among 1,580 Bogalusa Heart Study participants, we estimated extrinsic EAA, intrinsic EAA, PhenoAge acceleration (PhenoAgeAccel), and GrimAge acceleration (GrimAgeAccel) during adulthood. We tested prospective associations of longitudinal childhood body mass index (BMI), blood pressure, lipids, and glucose with EAAs using linear mixed effects models. After confirming EAAs with midlife carotid intima-media thickness and carotid plaque, structural equation models examined mediating effects of EAAs on associations of childhood CVD risk factors with subclinical CVD measures. After stringent multiple testing corrections, each SD increase in childhood BMI was significantly associated with 0.6-, 0.9-, and 0.5-year increases in extrinsic EAA, PhenoAgeAccel, and GrimAgeAccel, respectively ($P < 0.001$ for all 3 associations). Likewise, each SD increase in childhood log-triglycerides was associated with 0.5- and 0.4-year increases in PhenoAgeAccel and GrimAgeAccel ($P < 0.001$ for both), respectively, whereas each SD increase in childhood high-density lipoprotein cholesterol was associated with a 0.3-year decrease in GrimAgeAccel ($P = 0.002$). Our findings indicate that PhenoAgeAccel mediates an estimated 27.4% of the association between childhood log-triglycerides and midlife carotid intima-media thickness ($P = 0.022$). Our data demonstrate that early life CVD risk factors may accelerate biological aging and promote subclinical atherosclerosis. (J Am Coll Cardiol Basic Trans Science 2024;9:577-590) © 2024 The Authors. Published by Elsevier on behalf of the American College of Cardiology Foundation. This is an open access article under the CC BY-NC-ND license (<http://creativecommons.org/licenses/by-nc-nd/4.0/>).

Cardiovascular disease (CVD) remains the leading cause of mortality globally,¹ with major risk factors including high blood pressure (BP), adverse lipid profile, high fasting plasma glucose, and high body mass index (BMI) contributing heavily to its global disease burden.^{2,3} Evidence suggests that CVD events are the consequence of a lifelong atherosclerotic process, starting with the development of related risk factors during early life.⁴ Carotid intima-media thickness (cIMT) is a noninvasive measurement of subclinical atherosclerosis,^{5,6} which has been reproducibly linked to early life CVD risk factors and shown to predict the development of clinical CVD events. Although the associations of CVD risk factors with

subclinical CVD have been well established, the molecular mechanisms underlying these relations remain an area of active investigation. Improved mechanistic understanding is needed for the development of novel therapeutic strategies that might delay or even reverse the lifelong atherosclerotic process. Furthermore, work in this area could enhance early detection efforts.

Unlike the human genome, the methylome can be influenced by environmental factors⁷⁻⁹ in addition to genetics, making it an attractive target for disease prevention research. The past decade has given rise to an abundance of “epigenetic clocks,” which are composed of DNA methylation (DNAm) sites that predict chronological age with remarkable

From the ^aDepartment of Epidemiology, Tulane University School of Public Health and Tropical Medicine, New Orleans, Louisiana, USA; ^bEmory Clinical Cardiovascular Research Institute, Emory University School of Medicine, Atlanta, Georgia, USA; ^cDepartment of Epidemiology, School of Public Health, and Jiangsu Key Laboratory of Preventive and Translational Medicine for Geriatric Diseases Medical College of Soochow University, Jiangsu, China; ^dDivision of Nephrology, Department of Medicine, College of Medicine, University of Illinois at Chicago, Chicago, Illinois, USA; ^eDivision of Epidemiology and Biostatistics, School of Public Health, University of Illinois Chicago, Chicago, Illinois, USA; ^fDivision of Endocrinology, Diabetes and Metabolism, Department of Medicine, College of Medicine, University of Illinois at Chicago, Chicago, Illinois, USA; ^gInstitute for Minority Health Research, College of Medicine, University of Illinois at Chicago, Chicago, Illinois, USA; and the ^hPennington Biomedical Research Center, Baton Rouge, Louisiana, USA.

The authors attest they are in compliance with human studies committees and animal welfare regulations of the authors' institutions and Food and Drug Administration guidelines, including patient consent where appropriate. For more information, visit the [Author Center](#).

accuracy.¹⁰⁻¹⁴ Deviation of chronological age from epigenetic clock age, termed epigenetic age acceleration (EAA), has been identified as a powerful biomarker of aging-related disease and mortality.^{15,16} Most commonly, EAA has been estimated based on clocks derived from Horvath (Horvath DNAmAge),¹¹ Hannum et al (Hannum DNAmAge),¹² Levine et al (PhenoAge),¹⁶ and Lu et al (GrimAge),¹⁷ with each EAA measure composed of distinct methylation sites that reflect both unique and common aging-related processes. For example, intrinsic epigenetic age acceleration (IEAA) represents aging independent of blood immune cell composition,¹⁸ while extrinsic epigenetic age acceleration (EEAA) estimates aging taking into account blood immune cell-type composition. PhenoAge acceleration (PhenoAgeAccel) and GrimAge acceleration (GrimAgeAccel) were developed to correlate with aging-related physiological dysregulation¹⁶ and mortality,¹⁷ respectively. A growing body of published data has reported associations between EAA measures and CVD,¹⁹⁻²¹ along with its risk factors.^{20,22} Despite their potential clinical significance, existing works are predominantly based on cross-sectional associations and lack temporal clarity. Recent studies leveraging longitudinal data have reported prospective associations of EAA with CVD and overall cardiovascular health (CVH).^{19,23} However, longitudinal associations of EAA with individual CVD risk factors remain unknown, and whether EAA could mediate associations between individual CVD risk factors and CVD has not been studied.

Here, we report the results of our investigation into the associations between early life CVD risk factors, EAA measures, and subclinical CVD among a biracial sample of participants from the on-going BHS (Bogalusa Heart Study). Our unique study design leveraged multiple measures of individual CVD risk factors and EAA collected across the life course to examine longitudinal and temporal relationships between these variables. Furthermore, we confirmed associations of EAA with subclinical CVD in the BHS and further explored the mediating effects of EAA on the associations between early life CVD risk factors and the development of subclinical CVD.

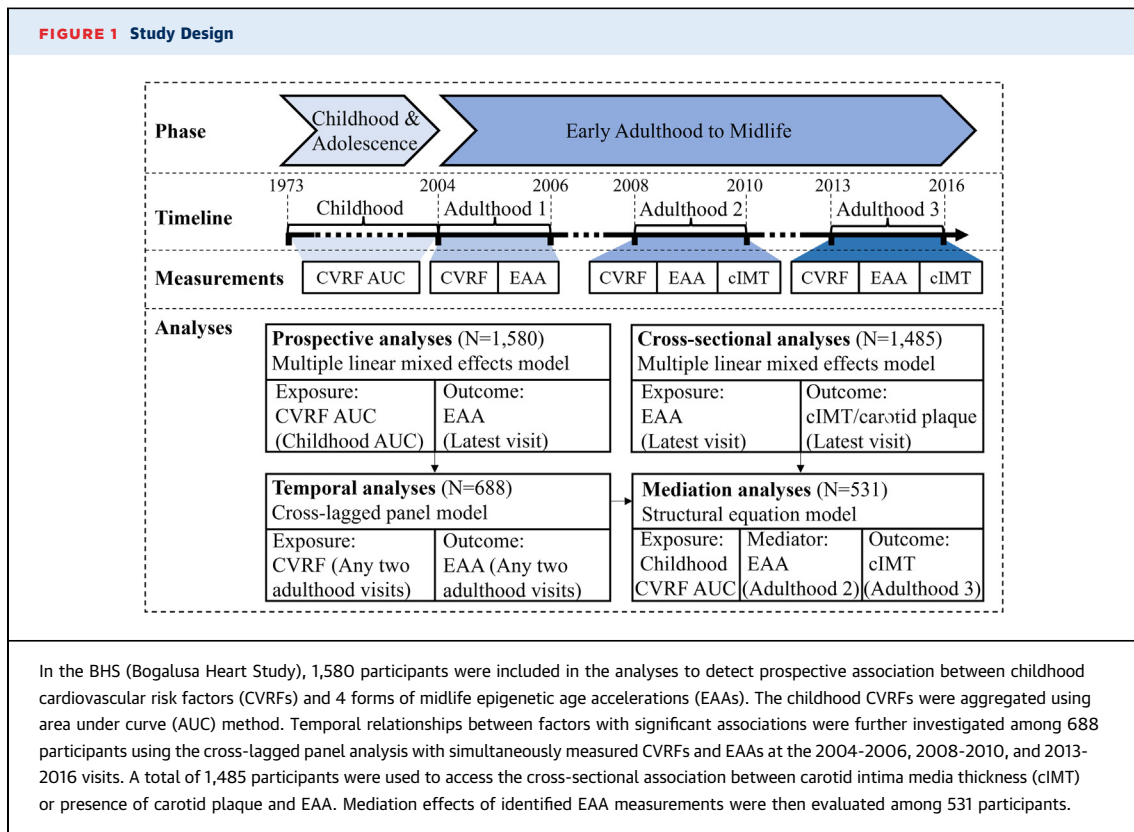
METHODS

STUDY PARTICIPANTS. The BHS is a population-based long-term study examining the natural history of CVD and its risk factors from childhood to adulthood among residents of Bogalusa, Louisiana. From 1973 to today, 9 surveys were conducted in children and adolescents aged 4-17 years, and 11 surveys were conducted among adults aged 18-51 years who had

been examined previously as children. Detailed description of the BHS design and methods have been reported previously.²⁴ This study included a total of 1,580 participants from the BHS who had at least 1 measure of clinical CVD risk factors, including BMI, systolic blood pressure (SBP), diastolic blood pressure (DBP), low-density lipoprotein cholesterol (LDL-C), high-density lipoprotein cholesterol (HDL-C), triglycerides (TGs), and glucose in childhood and at least 1 assessment of genome-wide DNAm in adulthood. Among these participants, we examined the prospective relationship of childhood CVD risk factors with adulthood EAA. Of the 1,580 participants included in the prospective analyses, 688 had at least 2 simultaneously collected measures of identified clinical CVD risk factors and DNAm spanning young adulthood through midlife, contributing to cross-lagged panel analyses that were employed to support causal inference. A total of 1,485 participants had available EAA and subclinical atherosclerosis measurements for cross-sectional analyses aimed to confirm these associations in the BHS, and among them, 531 participants had temporally appropriate CVD risk factor, EAA, and subclinical CVD risk factor data for mediation analyses. **Figure 1** provides a visual schematic of our unique study design.

Informed consents were obtained from all the BHS participants after detailed explanation of the study. The study was approved by the Institutional Review Board at Tulane University.

MEASUREMENT OF EAA. DNAm profiling was conducted using whole blood samples obtained in up to 3 BHS visit cycles, including the 2004-2006, 2008-2010, and 2013-2016 visits, using methods detailed in a previous report.^{18,25} In brief, DNA was extracted from whole blood using the PureLink Pro 96 Genomic DNA Kit (Life Technologies, Thermo Fisher Scientific) following the manufacturer's instructions. Following DNA extraction, the Infinium HumanMethylation450 BeadChip (Illumina) was used for whole genome DNAm quantification. Samples were processed at the Microarray Core Facility, University of Texas Southwestern Medical Center at Dallas. Generated raw data were processed and normalized using Illumina's GenomeStudio Methylation Module software to generate a final matrix of beta estimates for each cytosine-phosphate-guanine site. Following epigenetic profiling and normalization, EEAA, IEAA, PhenoAgeAccel, and GrimAgeAccel at each study visit were calculated using Horvath's online DNA Methylation Age Calculator.²⁶ This calculator incorporates an internal normalization procedure to further control batch effects using a modified beta mixture



quantile dilation normalization method.²⁷ Prior to conduct of statistical analyses, the normality of EAA variable distributions was confirmed.

MEASUREMENT OF CVD RISK FACTORS AND COVARIATES. In the ongoing BHS, demographic characteristics such as age, sex, race, and lifestyle risk factors including smoking and drinking status, as well as medical history are collected using standardized questionnaires at each visit. Smoking and drinking status were categorized as never or ever. During a physical examination, anthropometric measures were obtained with participants in light clothing without shoes. At each visit, body weight and height were measured twice to the nearest 0.1 kg and 0.1 cm, respectively. BMI was calculated by dividing mean body weight in kilograms by mean height in meters squared. In childhood, BP was measured in duplicate from the right arm using a mercury sphygmomanometer while participants were in a relaxed, sitting position. In adulthood, BP was measured in triplicate on the right arm of participants using the Omron HEM 907XL digital BP device after 5 minutes in the sitting position. For 12 hours prior to the study visit, participants were advised to avoid eating, smoking, intake of caffeine and alcohol, and physical activity.^{28,29} Fasting blood samples are collected by venipuncture

by trained personnel. Plasma glucose and serum total cholesterol, HDL-C, and TGs are measured by standard enzymatic procedures. LDL-C is estimated using the Friedewald equation.³⁰

MEASUREMENT OF SUBLINICAL ATHEROSCLEROSIS. Carotid ultrasonography was performed on a subset of BHS participants by trained personnel at the 2008–2010 and 2013–2016 study visits. Ultrasound measurements included maximum cIMT at diastole from the far walls of the common carotid artery, carotid bulb, and internal carotid artery segments bilaterally. The mean of the maximum cIMT test reading from the 3 left and 3 right far walls of the common, bulb, and internal segments were used for the analysis. Carotid plaque was defined as a cIMT ≥ 1.5 mm at any of the 6 measured sites.⁵

STATISTICAL ANALYSIS. Characteristics table description. As shown in Table 1, patient characteristics by visit are presented using the mean \pm SD or median (Q1, Q3) for continuous variables and count (percentage) for categorical variables.

Early life AUC calculations. To leverage repeated childhood measurements of CVD risk factors, early life BMI, SBP, DBP, LDL-C, HDL-C, log-transformed TGs, and fasting plasma glucose were individually summarized as an area under the curve (AUC)

TABLE 1 Characteristics of 1,580 BHS Participants Who Participated at the Baseline Visit and Underwent Epigenetics Profiling in at Least 1 of 3 Most Recent Study Visits

	Baseline (N = 1,580)	2004-2006 Visit (n = 1,114)	2008-2010 Visit (n = 888)	2013-2016 Visit (n = 1,281)
Age, y	9.7 ± 3.9	39.5 ± 4.4	43.5 ± 4.5	48.2 ± 5.3
Male	43.8	43.2	42.7	41.3
African American	32.9	29.3	31.6	34.4
High school or less	—	39.7	42.2	50.9
Drinker	—	60.4	63.0	56.0
Ever smoker	—	56.7	56.2	50.2
BMI, kg/m ²	17.6 ± 3.6	30.4 ± 7.6	30.9 ± 7.7	31.4 ± 7.8
SBP, mm Hg	99.4 ± 10.0	117.8 ± 15.4	118.6 ± 15.7	123.6 ± 17.2
DBP, mm Hg	61.3 ± 8.7	79.4 ± 10.4	82.1 ± 9.9	78.7 ± 11.6
LDL-C, mg/dL	89.8 ± 24.3	126.4 ± 35.5	124.7 ± 34.1	114.8 ± 35.5
HDL-C, mg/dL	65.6 ± 20.7	48.7 ± 13.5	46.8 ± 14.7	51.5 ± 16.3
Triglyceride, mg/dL	61.0 (46.0, 80.0)	110.0 (75.0, 163.0)	109.0 (74.0, 164.0)	109.0 (78.0, 158.0)
Glucose, mg/dL	82.8 ± 9.1	90.5 ± 22.3	91.8 ± 18.9	107.5 ± 38.3
IEAA	—	-0.17 ± 4.6	4.70 × 10 ⁻² ± 4.0	-2.47 × 10 ⁻¹⁷ ± 4.0
EEAA	—	-0.15 ± 4.9	4.09 × 10 ⁻² ± 4.7	1.54 × 10 ⁻¹⁶ ± 5.2
PhenoAgeAccel	—	-0.33 ± 4.9	8.96 × 10 ⁻² ± 5.3	-2.81 × 10 ⁻¹⁶ ± 5.6
GrimAgeAccel	—	-0.31 ± 5.1	8.61 × 10 ⁻² ± 5.2	1.99 × 10 ⁻¹⁶ ± 4.9
cIMT, mm	—	0.84 ± 0.19	0.66 ± 0.15	0.94 ± 0.32
Carotid plaque	—	5.8	3.7	31.9

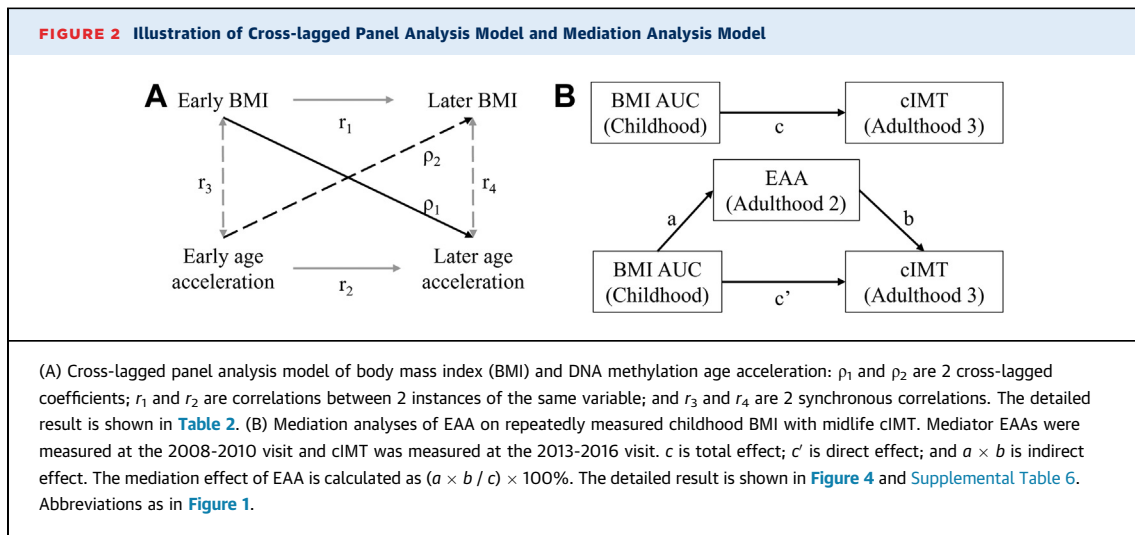
Values are mean ± SD, %, or median (Q1, Q3).

BHS = Bogalusa Heart Study; BMI = body mass index; cIMT = carotid intima-media thickness; DBP = diastolic blood pressure; EEAA = extrinsic epigenetic age acceleration; GrimAgeAccel = GrimAge acceleration; HDL-C = high-density lipoprotein cholesterol; IEAA = intrinsic epigenetic age acceleration; LDL-C = low-density lipoprotein cholesterol; PhenoAgeAccel = PhenoAge acceleration; SBP = systolic blood pressure.

estimate for each participant using methods developed specifically for the BHS and employed extensively in this cohort.³¹⁻³³ In brief, growth curves of CVD risk factors measured multiple times during childhood (when a participant was <18 years of age) were constructed using a random effects model in SAS (version 9.4, SAS Institute, Inc). The mixed model regresses the continuous risk factor on fixed and random effects of age and its higher order terms. The model allows the intercept, linear, and nonlinear parameters to vary from individual to individual, with the random effect coefficients representing the difference between the fixed parameters and the observed values for each individual. To avoid collinearity of age with its higher order terms, age was centered to the mean age of BHS participants in childhood. Quadratic growth curves were fitted for all factors in race-sex groups. The AUCs were calculated as the integral of the curve parameters during the follow-up period for each participant.

Prospective associations of early life CVD risk factors with adulthood EAA. Associations of the early life CVD risk factors (as continuous AUC values) with EAA were tested using multiple linear mixed effects models that leveraged up to 3 repeated adulthood measures of EAA. An autoregressive correlation matrix was used to account for the repeated

measures within individuals. Multiple covariates measured simultaneously with EAA were adjusted. Model 1 was adjusted for age, sex, and race. Model 2 additionally accounted for smoking and drinking status. A Bonferroni correction to account for testing each EAA measure for association with 7 CVD risk factors was employed, with a *P* value threshold of 7.1×10^{-3} used for determining statistical significance. The results of mixed effects models are presented as regression coefficient (beta) and SE. To further support temporal inference for identified associations between clinical CVD risk factors and EAA, simultaneously collected measures of CVD risk factors and EAA at 2 time points, spanning young adulthood through midlife, were leveraged to conduct cross-lagged panel analyses.³⁴ Specifically, participants who attended at least 2 study visits where CVD risk factors and EAA were concurrently measured were included in this analysis. If data were available for more than 2 visits, data from the first and last available visits were used. **Figure 2A** provides a schematic of the conceptual model underlying the cross-lagged analysis approach using BMI as an example. This analysis examines reciprocal, longitudinal relationships between CVD risk factors and EAA and was conducted using the R package Lavaan (R Foundation).³⁵ Two sensitivity analyses were



performed to test whether differences in time intervals between exams influenced results of the cross-lagged analysis. We conducted the first sensitivity analysis among a subset of the cross-lagged analysis participants who attended the 2 most recent study visits between 2008-2010 and 2013-2016. Our second sensitivity analysis utilized data from all participants included in the original cross-lagged modelling approach, additionally including time interval between visits as a covariate in the analysis.

Associations of EAAs with subclinical atherosclerosis. Cross-sectional associations between EAA and the continuous cIMT, as well as the discrete carotid plaque phenotypes, were examined using multiple linear and logistic regression models, respectively. Two multivariable models were utilized: model 1 adjusted for age, sex, and race; and model 2 adjusted for covariates in model 1, along with smoking and drinking status. These analyses were conducted based on data obtained from the most recently completed study visit for each participant.

Mediation effects of EAA. To assess whether identified EAA measures (longitudinally associated with a CVD risk factor and cross-associated with cIMT) mediated the associations between early life CVD risk factors and midlife cIMT, we conducted mediation analyses based on the path diagrams illustrated in [Figure 2B](#), again using BMI as an example. For these analyses, measurement of cIMT at the 2013-2016 visit was assessed as the outcome, the EAA measurement in a visit prior to the cIMT measurement was assessed as the mediator, and the AUC of childhood CVD risk factors, measured when participants were 18 years of age or less, were assessed as the exposure. Here, the beta coefficient for the association between the childhood CVD risk factor AUC

and midlife cIMT is defined as total effect (denoted as c in [Figure 2B](#)). The indirect effect is estimated as the product of coefficients a and b derived from 2 regression models, the first regressing EAA on BMI AUC and adjusting for covariates and the latter regressing of cIMT on EAA after controlling for BMI AUC and covariates. Two sets of covariates measured simultaneously with EAA were included in the mediation analyses. Covariates in model 1 included age, sex, race, and model 2 further included smoking and drinking. Prior to conducting the mediation analyses, continuous variables were standardized using Z-transformation. The mediation effect was estimated as the percentage of the contribution of the indirect effect to the total effect, with statistical significance determined using the bootstrap method with 1,000 bootstrap iterations.³⁶ The analysis was conducted using the R package Mediation.³⁷

RESULTS

DESCRIPTION OF PARTICIPANTS. [Table 1](#) describes the characteristics of the 1,580 BHS participants at their baseline and most recently completed study visits. Among this biracial cohort, 43.8% were male and 32.9% were African American. With a median follow-up of 38.8 (Q1, Q3: 34.9, 40.8) years, the mean ages at baseline, the 2004-2006, 2008-2010, and 2013-2016 study visits were 9.7, 39.5, 43.5, and 48.2 years, respectively. As expected, BMI, SBP, DBP, LDL-C, TGs, and glucose were higher in the 3 midlife visits compared to the baseline visit. In this population, EAA variability was substantial, with each SD increase corresponding to an absolute increase of 4-5 years in accelerated aging across measures of midlife visits. On average, cIMT were 0.8 mm, 0.7 mm, and 0.9 mm,

with 5.8%, 3.7%, and 31.9% of participants demonstrating carotid plaque at the 2004-2006, 2008-2010, and 2013-2016 study visits, respectively.

ASSOCIATION OF EARLY LIFE CVD RISK FACTORS AND EAA. Associations between childhood CVD risk factor AUCs and adulthood EAA are shown in **Figure 3** and **Supplemental Table 1**. Childhood BMI demonstrated significant or nominally significant associations with all measures of EAA. For example, in the fully adjusted model (model 2), each SD increase in early life BMI AUC was associated with 0.27 ($P = 5.402 \times 10^{-3}$), 0.63 ($P = 2.624 \times 10^{-7}$), 0.88 ($P = 6.062 \times 10^{-11}$), and 0.52 ($P = 3.196 \times 10^{-7}$) years increased IEAA, EEAA, PhenoAgeAccel, and GrimAgeAccel, respectively. Early life log-transformed TG AUC consistently associated with both PhenoAgeAccel and GrimAgeAccel across models, with each SD increment increase conferring a respective 0.50 ($P = 5.506 \times 10^{-4}$) and 0.43 ($P = 9.269 \times 10^{-5}$) year increase in the EAA measures. Likewise, early SBP AUC was associated with IEAA (0.27; $P = 6.498 \times 10^{-3}$) and PhenoAgeAccel (0.52; $P = 1.216 \times 10^{-4}$), and each SD increase in early HDL-C was associated with 0.32 ($P = 2.125 \times 10^{-3}$) years decreased GrimAgeAccel in the fully adjusted models. There were no consistent associations of early life DBP, LDL-C, or glucose with adulthood EAA.

To further discern the temporal relationships of BMI, SBP, TGs, and HDL-C with EAA, we carried out cross-lagged panel analyses utilizing simultaneous measurements of these variables collected at the 2 most distant time points in young adulthood through midlife. The path coefficients between selected CVD risk factors and EAA are presented in **Table 2**. In the fully adjusted model, path coefficients from baseline BMI to follow-up EEAA, PhenoAgeAccel, and GrimAgeAccel were statistically significant ($P_{\text{BMI} \rightarrow \text{EEAA}} = 2.795 \times 10^{-3}$, $P_{\text{BMI} \rightarrow \text{PhenoAgeAccel}} = 1.675 \times 10^{-2}$, and $P_{\text{BMI} \rightarrow \text{GrimAgeAccel}} = 1.202 \times 10^{-3}$). Likewise, path coefficients from baseline TGs to follow-up PhenoAgeAccel and GrimAgeAccel were statistically significant ($P_{\log \text{TG} \rightarrow \text{PhenoAgeAccel}} = 1.930 \times 10^{-3}$, and $P_{\log \text{TG} \rightarrow \text{GrimAgeAccel}} = 4.051 \times 10^{-3}$) and path coefficients from baseline HDL-C to follow-up GrimAgeAccel was statistically significant ($P_{\text{HDL-C} \rightarrow \text{GrimAgeAccel}} = 1.527 \times 10^{-2}$). In contrast, path coefficients examining temporal associations of baseline EAA to follow-up BMI, TGs, and HDL-C were not statistically significant in either of the models tested, providing no evidence of EAA temporally preceding these measures. No sex-based differences were present (data not shown). Findings of sensitivity analyses restricting the cross-lagged panel analyses to only those with EAA and CVD risk factor measures at the 2 most recent study

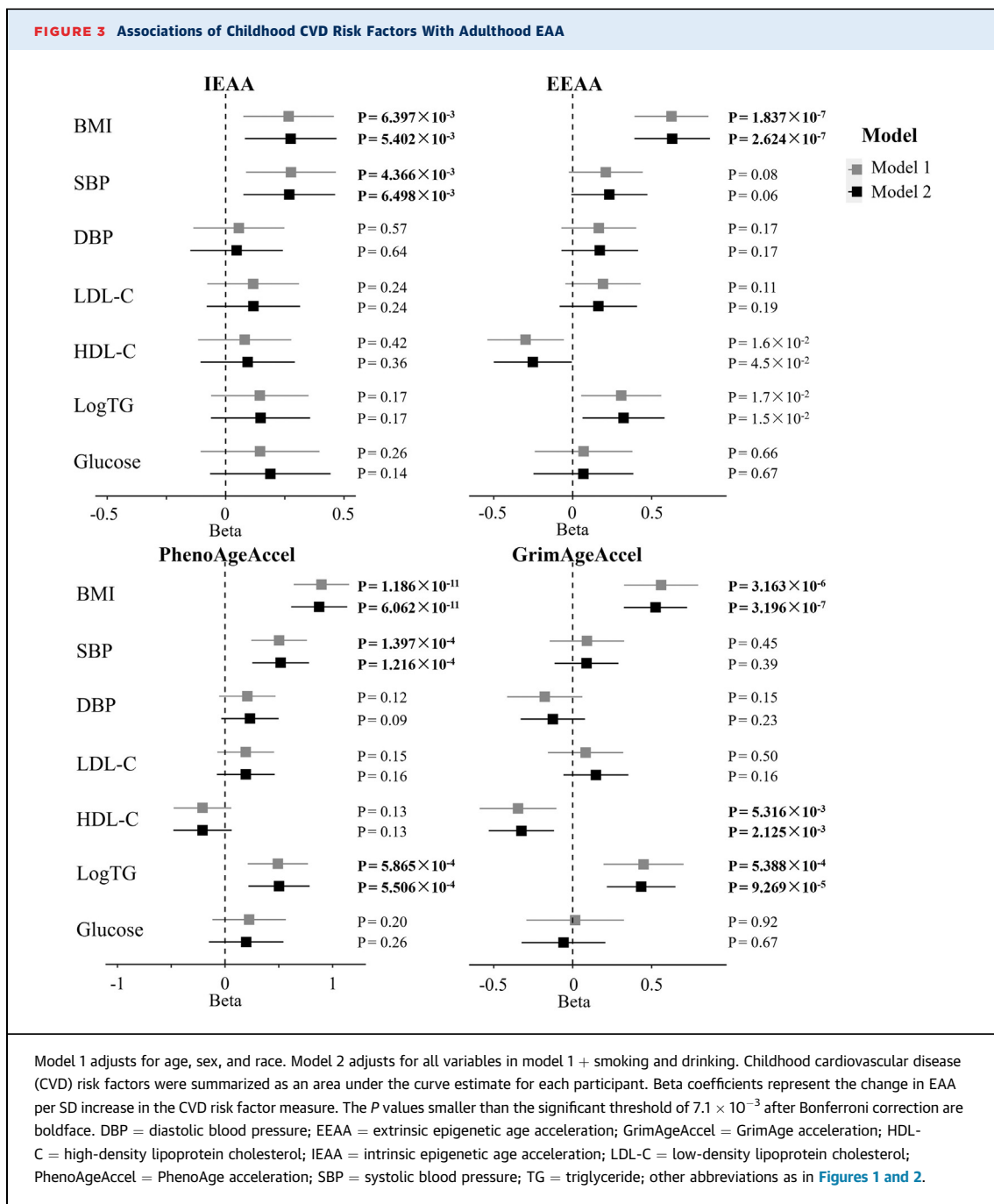
visits (**Supplemental Table 2**) and adjusting for time interval between study visits (**Supplemental Table 3**) were consistent with those of the main analysis.

CROSS-SECTIONAL ANALYSES EXAMINING ASSOCIATIONS OF EAA WITH cIMT AND CAROTID PLAQUE. Associations of EAA with the continuous and discrete measures of subclinical atherosclerosis are shown in **Supplemental Table 4**. Our results demonstrated strong and consistent associations of EEAA, PhenoAgeAccel, and GrimAgeAccel with both cIMT and carotid plaque in the BHS participants. For example, each SD increase in EEAA, PhenoAgeAccel, and GrimAgeAccel was cross-sectionally associated with a 0.034 mm ($P = 1.660 \times 10^{-5}$), 0.034 mm ($P = 1.443 \times 10^{-5}$), and 0.046 mm ($P = 1.031 \times 10^{-6}$) increase in cIMT, respectively, in the fully adjusted model (model 2). Similarly, each SD increase in EEAA, PhenoAgeAccel, and GrimAgeAccel was cross-sectionally associated with 1.26-fold ($P = 3.173 \times 10^{-4}$), 1.39-fold ($P = 2.540 \times 10^{-7}$), and 1.49-fold ($P = 6.902 \times 10^{-8}$) higher odds of carotid plaque in the fully adjusted model. There was no evidence of associations between IEAA and either cIMT or carotid plaque.

MEDIATION ANALYSES. Prior to mediation analyses, we confirmed results of previous studies,³⁸⁻⁴² demonstrating significant associations of childhood BMI, BP, lipids, and glucose AUC with adulthood cIMT in the BHS (**Supplemental Table 5**). The results of analyses investigating the potentially mediating effects of identified EAA measures on known associations of childhood BMI, TGs, and HDL-C with cIMT are shown in **Figure 4** and **Supplemental Table 6**. In model 1, PhenoAgeAccel and GrimAgeAccel had significant mediation effects ($P = 0.014$ and $P = 0.016$, respectively) on the associations between childhood BMI and cIMT, with trends that were similar and marginally significant in model 2. PhenoAgeAccel was identified as a significant mediator of the association between childhood TGs and cIMT ($P = 0.006$) in model 1 and remained significant ($P = 0.022$) in model 2 (**Supplemental Table 6**). Mediation effects of EEAA on BMI-cIMT associations of GrimAgeAccel on TG-cIMT associations and of GrimAgeAccel on HDL-C-cIMT were not observed in this small subsample.

DISCUSSION

In the current study examining the relation of individual early life CVD risk factors with multiple measures of epigenetic aging, we found that increased childhood BMI, SBP, TGs, and HDL-C predicted accelerated epigenetic aging in adulthood. Furthermore, through the implementation of discrete time



structural equation models, our findings support increased BMI, TGs, and HDL-C as upstream determinants, rather than downstream consequences of accelerated epigenetic aging. As expected, EAA measures were cross-sectionally associated with subclinical atherosclerosis in the midlife BHS cohort. Further analyses demonstrated that mediating effects of PhenoAgeAccel on the association of childhood TGs and BMI with subclinical atherosclerosis in midlife. In

total, these findings provide temporal evidence of EAA as a molecular footprint of adverse childhood CVH, while further implicating EAA as a mechanism linking early life CVD risk factors to later life subclinical atherosclerosis.

Our work not only supports but expands on recent findings from the CARDIA (Coronary Artery Risk Development in Young Adults) study.²³ In CARDIA, Joyce et al²³ identified prospective associations

TABLE 2 Results of Cross-lagged Panel Analyses Assessing Temporal Relations Between Identified CVD Risk Factors and EAA in a Subsample With Simultaneously Collected Repeated Measures of CVD Risk Factors and EAA (n = 688)

	Model 1 ^a						Model 2 ^b					
	EAA _{BL} → Risk Factor _{FU}			Risk Factor _{BL} → EAA _{FU}			EAA _{BL} → Risk Factor _{FU}			EAA _{BL} → Risk Factor _{FU}		
	Beta	SE	P Value	Beta	SE	P Value	Beta	SE	P Value	Beta	SE	P Value
BMI (n = 688)												
IEAA	-0.013	0.030	0.67	-0.01	0.016	0.52	-0.018	0.041	0.66	-0.021	0.018	0.23
EEAA	-0.028	0.032	0.39	0.052	0.019	7.634 × 10 ⁻³	-0.001	0.044	0.99	0.066	0.022	2.795 × 10 ⁻³
PhenoAgeAccel	0.046	0.026	0.075	0.052	0.02	9.831 × 10 ⁻³	-0.024	0.033	0.46	0.058	0.024	1.675 × 10 ⁻²
GrimAgeAccel	-0.068	0.027	0.01	-0.012	0.014	0.39	0.042	0.035	0.24	0.054	0.017	1.202 × 10 ⁻³
SBP (n = 688)												
IEAA	0.206	0.124	0.098	-0.001	0.008	0.87	0.332	0.173	0.055	-0.012	0.009	0.21
PhenoAgeAccel	0.079	0.106	0.46	0.012	0.01	0.23	0.061	0.126	0.63	0.000	0.011	1.00
Log triglyceride (n = 678)												
PhenoAgeAccel	0.007	0.003	0.039	1.126	0.237	1.957 × 10 ⁻⁶	0.003	0.004	0.37	0.896	0.289	1.930 × 10 ⁻³
GrimAgeAccel	0.014	0.004	4.587 × 10 ⁻⁵	0.783	0.174	6.627 × 10 ⁻⁶	0.007	0.004	0.067	0.631	0.219	4.051 × 10 ⁻³
HDL-C (n = 688)												
GrimAgeAccel	-0.135	0.104	0.19	-0.016	0.01	0.12	-0.08	0.109	0.46	-0.023	0.009	1.527 × 10 ⁻²

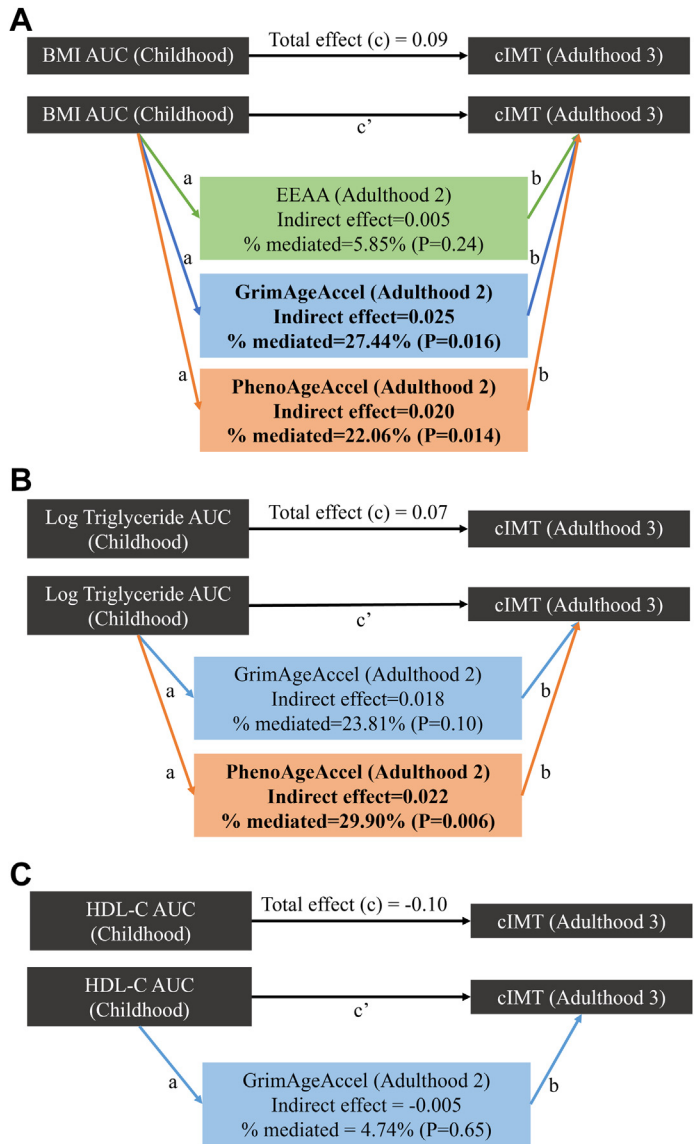
^aModel 1 adjusts for age, sex, and race. ^bModel 2 adjusts for all variables in model 1 + smoking and drinking status simultaneously measured with tested factor.

BL = baseline; CVD = cardiovascular disease; EAA = epigenetic age acceleration; FU = follow-up; other abbreviations as in Table 1.

between a composite CVH score during young adulthood and GrimAgeAccel, with further evidence that GrimAgeAccel mediated associations of CVH score with subclinical atherosclerosis, as measured by coronary artery calcification. We extend CARDIA's findings to demonstrate that prospective associations of clinical CVD risk factors with adulthood EAA can be observed even earlier, starting in childhood. Furthermore, rather than examining a composite CVH score, our study looked at individual CVD risk factors to pinpoint the clinical measures that might be driving CVH-EAA associations. Our analyses suggest that early life BMI and TGs, but not BP and glucose, may be most relevant in accelerating epigenetic aging across the life course. Furthermore, our cross-lagged panel analyses, which leveraged repeated simultaneously measured CVD risk factors and EAA, provides temporal evidence supporting CVD risk factors as upstream determinants rather than consequences of EAA. Like CARDIA, EAA measures in the BHS were also associated with subclinical atherosclerosis, here measured as cIMT and the discrete carotid plaque endpoint. Whereas power was somewhat limited for our mediation analyses, our findings suggest that measures of EAA may, in part, link childhood BMI and TGs to subclinical atherosclerosis in adulthood. In total, these findings continue to highlight the relevance of early life CVD risk factors in subclinical atherosclerosis, while pointing out specific risk factors that might be pivotal in decelerating epigenetic aging for the prevention of CVD.

Although we are among the first to identify prospective and temporal associations between early life BMI and accelerated epigenetic aging in midlife, several studies have reported cross-sectional associations of these 2 variables.^{43–47} For example, Quach et al⁴⁹ identified associations of EEAA and IEAA with higher BMI among participants of the WHI (Women's Health Initiative). In one of the few longitudinal studies in this area, Quach et al⁴⁹ further examined whether BMI at baseline predicted EEAA and IEAA after 2.7 years follow-up among a small subsample of participants of the InCHianti study (N = 239). In contrast to our findings, no associations were observed.⁴⁸ Given the small sample size and limited follow-up time, it is unclear whether this study was sufficiently powered for such analyses. Consistent with our findings that suggest increased EAA as a downstream consequence but not upstream determinant of increased BMI, Simpkin et al⁴⁹ found no associations between EAA (measured at age 7) and change in BMI through 17 years of age using models with or without adjustment for cell counts. Overall, our findings contribute additional information to the growing evidence of an association between obesity and epigenetic aging, providing compelling new data that implicate obesity as precursor to this phenomenon.

Our study also identified prospective and temporal associations of early life TGs and HDL-C with EAA. Like BMI, TGs have been associated with measures of

FIGURE 4 Results of Mediation Analyses

Mediation effects of EAAs on the (A) BMI-cIMT, (B) triglyceride-cIMT, and (C) HDL-C-cIMT associations in childhood and adulthood, respectively, are shown. The examined EAA measurements were selected based on our prospective and temporal analyses. Total effect, direct effect, and indirect effect are indicated as c , c' , and $a \times b$, respectively.

Abbreviations as in Figures 1 to 3.

EAA in several cross-sectional studies,^{16,18,20,21,48,50} including the work of Quach et al⁴⁸ in the WHI. Furthermore, in a recent CARDIA study, Gao et al⁵¹ examined associations of early adulthood lipid levels with midlife GrimAgeAccel. Like us, they identified strong associations between early life TGs and HDL-C with midlife GrimAgeAccel, with their

analyses focused on young adulthood TG levels compared to our focus on childhood.

As expected, increased EAA was associated with subclinical atherosclerosis in our cross-sectional analyses of BHS participants, including both cIMT and carotid plaque. Numerous reports have identified associations between EAA and measures of both subclinical and clinical CVD.^{19,20,23,52-55} For example, a 2018 report by Roetker et al¹⁹ identified baseline cross-sectional associations between EAA and cIMT among African American participants of the ARIC (Atherosclerosis Risk in Communities) study. Likewise, analyses by Joyce et al²³ suggested an association (and mediating effect) of GrimAgeAccel on coronary artery calcification in CARDIA participants. In one of the only studies to investigate prospective associations of EAA with clinical CVD events, the ARIC study went on to demonstrate that each 5-year increase in IEAA and EEAA was associated with, respectively, 17% and 22% increased risks of fatal coronary heart disease.¹⁹ In aggregate, we confirm previous associations and present new evidence for a role of EAA in subclinical CVD in a rural cohort.

We identified a significant mediating effect of EAA on the relationship of increased early life TGs and BMI with midlife subclinical atherosclerosis. We reported the significant mediation effects of both PhenoAgeAccel and GrimAgeAccel on the associations between childhood BMI and midlife cIMT. To our knowledge, only the previous study by Gao et al,⁵¹ which focused specifically on TGs and the GrimAgeAccel measure alone, has investigated mediation of EAA in CVD risk factor-subclinical (or -clinical) CVD associations. In CARDIA, Gao et al⁵¹ showed that GrimAgeAccel mediated 17% of the association between early life TGs and subclinical atherosclerosis. Although this mediation was not significant in the current study, it is worth noting that the estimated effect size was similar to that reported in CARDIA, with a mediation effect of 16.8% in our most comparable model. Given the smaller sample size of the BHS, we may have been underpowered to detect this signal. PhenoAgeAccel was identified as a significant mediator, explaining 27.4% of the association between childhood TGs with midlife cIMT in the BHS. In total, our findings implicate EAA as a potential molecular link between early life CVD risk and the development of subclinical disease in adulthood. Given the small sample size for this analysis and generally marginally significant signals, despite rather large mediation effect sizes, more research in this area is warranted.

The associations of accelerated epigenetic aging with CVD risk factors and subclinical CVD were not

homogeneous across measures. For instance, SBP showed a significant association with IEAA and Phe-noAgeAccel, but no association was found with EEAA or GrimAgeAccel. On the other hand, BMI exhibited strong associations with all 4 EAAs. This was not all together unexpected given a general lack of overlap of methylation sites across the 4 different EAA measures.^{14,56-58} Furthermore, recent work by Liu et al⁵⁶ demonstrated both similarities and differences in the aging processes reflected across various measures of EAA. For example, gene coexpression analyses identified consistent enrichment across epigenetic clocks for biological pathways,⁵⁶ including immunity and inflammation,⁵⁹ chromatin modification,⁶⁰ and autophagy.⁶¹ However, correlations with gene coexpression for these shared biological pathways varied in magnitude across clocks.⁵⁶ Furthermore, in vitro experiments identified strong associations of PhenAge but not other epigenetic clocks with mitochondrial dysfunction and cellular senescence,⁵⁶ molecular mechanisms that may play key roles in the development of CVD.⁶²⁻⁶⁸ In total, these findings provide impetus for future work to integrate EAA measures with other multiomics data, which might reveal further molecular insights into the relationships observed here.

Our study has several important strengths. The unique longitudinal design of the BHS enabled a unique investigation into the influence of childhood CVD risk factors on EAA, as well as the potentially mediating effect of this molecular footprint on subclinical disease. By leveraging an average of 3-4 measures of CVD risk factors in childhood and up to 3 adulthood measures of EAA, our study was able to powerfully and precisely investigate associations between early life CVD risk factors and epigenetic aging in a biracial, rural cohort. Furthermore, the BHS offered simultaneously collected measures of CVD risk factors and EAA to more clearly articulate the temporal relationship between these variables for the first time.

STUDY LIMITATIONS. Blood samples from childhood were not available in BHS participants, so we could not adjust for baseline EAA in our investigation of the association between early life CVD risk factors and midlife EAA. Likewise, whereas apolipoprotein B or direct LDL measurements would offer greater accuracy in our analyses compared to relying on the

Friedewald equation for estimating LDL-C, particularly in cases of hypertriglyceridemia, these data are not available in the BHS.⁶⁹ Furthermore, we note caution in drawing conclusions regarding associations between HDL-C and subclinical CVD given null associations observed in randomized clinical trials and Mendelian randomization studies.⁷⁰ Because only smaller subsamples had appropriate data available for the cross-lagged panel and mediation analyses, nonsignificant findings do not clearly suggest a lack of association and could instead reflect a lack of statistical power. Further research to investigate the promising marginally significant findings identified here may be warranted.

CONCLUSIONS

Our study provides compelling early evidence that accelerated epigenetic aging in adulthood is influenced by childhood BMI and TG levels. Furthermore, our data suggest that EAA may mediate the associations of these childhood CVD risk factors and the development of subclinical disease. In total, our findings provide information on unique strategies that might decelerate the biological aging process early in life, while pointing to potentially modifiable molecular mechanisms that could be targeted for precision disease prevention across the life span.

ACKNOWLEDGMENTS The authors are grateful for the contribution of all staff members who were involved in conducting the Bogalusa Heart Study. The authors extend their gratitude to the participants of Bogalusa Heart Study, many of whom have diligently participated since they were children.

FUNDING SUPPORT AND AUTHOR DISCLOSURES

The Bogalusa Heart Study was supported by the National Institute on Aging of the National Institutes of Health (awards R01AG041200, R01AG062309, R01AG077000, and R33AG057983) and the National Institute of General Medical Sciences of the National Institutes of Health (award P20GM109036). The authors have reported that they have no relationships relevant to the contents of this paper to disclose.

ADDRESS FOR CORRESPONDENCE: Dr Tanika N. Kelly, Division of Nephrology, Department of Medicine, College of Medicine, University of Illinois at Chicago, 820 South Wood Street, Chicago, Illinois 60612, USA. E-mail: tkelly5@uic.edu.

PERSPECTIVES

COMPETENCY IN MEDICAL KNOWLEDGE: CVD remains the leading cause of mortality globally. Evidence suggests that CVD events are the consequence of a lifelong atherosclerotic process, starting with the development of related risk factors during early life. Although the associations of CVD risk factors with subclinical CVD have been well established, the molecular mechanisms underlying these relations remain an area of active investigation. Improved mechanistic understanding is needed for the development of novel therapeutic strategies that might delay or even reverse the lifelong atherosclerotic process. The past decade has given rise to an abundance of epigenetic clocks, which are composed of DNAm sites that accurately predict chronological age. Deviation of chronological age from epigenetic clock age, termed EAA, has been identified as a powerful biomarker of aging-related disease and mortality. Although EAA might serve as a molecular signature of childhood CVD risk factors and further promote midlife subclinical CVD, few studies have comprehensively examined these life course associations.

The current report comprehensively examines these associations, providing compelling early evidence that accelerated epigenetic aging in adulthood is influenced by childhood BMI and TG levels and might further mediate the associations of these childhood CVD risk factors with the development of subclinical disease.

TRANSLATIONAL OUTLOOK: This study highlights epigenetic age acceleration as a molecular signature of suboptimal early life CVH that might promote midlife subclinical disease. Further research is warranted to explore the promising translational potential of this research, which might include assessing interventions targeting EAA to mitigate the risk of accelerated biological aging and subsequent development of subclinical atherosclerosis. Furthermore, investigating the downstream proteins and metabolites that influence EAA could uncover additional novel therapeutic targets for preventing or delaying the onset of CVD in later life.

REFERENCES

- Roth GA, Mensah GA, Johnson CO, et al. GBD-NHLBI-JACC Global Burden of Cardiovascular Diseases Writing Group. Global burden of cardiovascular diseases and risk factors, 1990–2019: update from the GBD 2019 study. *J Am Coll Cardiol.* 2020;76(25):2982–3021.
- GBD 2015 Mortality and Causes of Death Collaborators. Global, regional, and national life expectancy, all-cause mortality, and cause-specific mortality for 249 causes of death, 1980–2015: a systematic analysis for the Global Burden of Disease Study 2015. *Lancet.* 2016;388(10053):1459–1544.
- Joseph P, Leong D, McKee M, et al. Reducing the global burden of cardiovascular disease, part 1: the epidemiology and risk factors. *Circ Res.* 2017;121(6):677–694.
- Pool LR, Aguayo L, Brzezinski M, et al. Childhood risk factors and adulthood cardiovascular disease: a systematic review. *J Pediatr.* 2021;232:118–126.e23.
- Stein JH, Korcarz CE, Hurst RT, et al. Use of carotid ultrasound to identify subclinical vascular disease and evaluate cardiovascular disease risk: a consensus statement from the American Society of Echocardiography Carotid Intima-Media Thickness Task Force. Endorsed by the Society for Vascular Medicine. *J Am Soc Echocardiogr.* 2008;21(2):93–111.
- Iwakiri T, Yano Y, Sato Y, et al. Usefulness of carotid intima-media thickness measurement as an indicator of generalized atherosclerosis: findings from autopsy analysis. *Atherosclerosis.* 2012;225(2):359–362.
- Demerath EW, Guan W, Grove ML, et al. Epigenome-wide association study (EWAS) of BMI, BMI change and waist circumference in African American adults identifies multiple replicated loci. *Hum Mol Genet.* 2015;24(15):4464–4479.
- Joehanes R, Just AC, Marioni RE, et al. Epigenetic signatures of cigarette smoking. *Circ Cardiovasc Genet.* 2016;9(5):436–447.
- Tang Y, Jin B, Zhou L, Lu W. MeQTL analysis of childhood obesity links epigenetics with a risk SNP rs17782313 near MC4R from meta-analysis. *Oncotarget.* 2017;8(2):2800–2806.
- Jylhävä J, Pedersen NL, Hägg S. Biological age predictors. *EBioMedicine.* 2017;21:29–36.
- Horvath S. DNA methylation age of human tissues and cell types. *Genome Biol.* 2013;14(10):R115. <https://doi.org/10.1186/GB-2013-14-10-R115>
- Hannum G, Guinney J, Zhao L, et al. Genome-wide methylation profiles reveal quantitative views of human aging rates. *Mol Cell.* 2013;49(2):359–367.
- Li A, Koch Z, Ideker T. Epigenetic aging: biological age prediction and informing a mechanistic theory of aging. *J Intern Med.* 2022;292(5):733–744.
- Salameh Y, Bejaoui Y, El Hajj N. DNA methylation biomarkers in aging and age-related diseases. *Front Genet.* 2020;11:171. <https://doi.org/10.3389/FGENE.2020.00171>
- Horvath S, Raj K. DNA methylation-based biomarkers and the epigenetic clock theory of ageing. *Nat Rev Genet.* 2018;19(6):371–384.
- Levine ME, Lu AT, Quach A, et al. An epigenetic biomarker of aging for lifespan and healthspan. *Aging (Albany NY).* 2018;10(4):573–591.
- Lu AT, Quach A, Wilson JG, et al. DNA methylation GrimAge strongly predicts lifespan and healthspan. *Aging (Albany NY).* 2019;11(2):303. <https://doi.org/10.1863/AGING.101684>
- Horvath S, Gurven M, Levine ME, et al. An epigenetic clock analysis of race/ethnicity, sex, and coronary heart disease. *Genome Biol.* 2016;17(1):171. <https://doi.org/10.1186/s13059-016-1030-0>
- Roetker NS, Pankow JS, Bressler J, Morrison AC, Boerwinkle E. Prospective study of epigenetic age acceleration and incidence of cardiovascular disease outcomes in the ARIC Study (Atherosclerosis Risk in Communities). *Circ Genom Precis Med.* 2018;11(3):e001937. <https://doi.org/10.1161/CIRCPGEN.117.001937>
- Ammous F, Zhao W, Ratliff SM, et al. Epigenetic age acceleration is associated with cardiometabolic risk factors and clinical cardiovascular disease risk scores in African

- Americans. *Clin Epigenetics*. 2021;13(1):55. <https://doi.org/10.1186/S13148-021-01035-3>
21. Pottinger TD, Khan SS, Zheng Y, et al. Association of cardiovascular health and epigenetic age acceleration. *Clin Epigenetics*. 2021;13(1):42. <https://doi.org/10.1186/S13148-021-01028-2>
22. Horvath S, Erhart W, Brosch M, et al. Obesity accelerates epigenetic aging of human liver. *Proc Natl Acad Sci U S A*. 2014;111(43):15538–15543.
23. Joyce BT, Gao T, Zheng Y, et al. Epigenetic age acceleration reflects long-term cardiovascular health. *Circ Res*. 2021;129(8):770–781.
24. Berenson GS. Bogalusa Heart Study Investigators. Bogalusa Heart Study: a long-term community study of a rural biracial (Black/White) population. *Am J Med Sci*. 2001;322(5):293–300.
25. Sun D, Zhang T, Su S, et al. Body mass index drives changes in DNA methylation: a longitudinal study. *Circ Res*. 2019;125(9):824–833.
26. DNA Methylation Age Calculator. Accessed April 14, 2021. <https://dnamage.genetics.ucla.edu/new>
27. Teschendorff AE, Marabita F, Lechner M, et al. A beta-mixture quantile normalization method for correcting probe design bias in Illumina Infinium 450 k DNA methylation data. *Bioinformatics*. 2013;29(2):189–196.
28. Foster TA, Berenson GS. Measurement error and reliability in four pediatric cross-sectional surveys of cardiovascular disease risk factor variables—the Bogalusa Heart Study. *J Chronic Dis*. 1987;40(1):13–21.
29. Foster TA, Webber LS, Srinivasan SR, Voors AW, Berenson GS. Measurement error of risk factor variables in an epidemiologic study of children—the Bogalusa heart study. *J Chronic Dis*. 1980;33(10):661–672.
30. Friedewald WT, Levy RI, Fredrickson DS. Estimation of the concentration of low-density lipoprotein cholesterol in plasma, without use of the preparative ultracentrifuge. *Clin Chem*. 1972;18(6):499–502.
31. Li S, Chen W, Srinivasan SR, et al. Childhood cardiovascular risk factors and carotid vascular changes in adulthood: the Bogalusa Heart Study. *JAMA*. 2003;290(17):2271–2276.
32. Cook NR, Rosner BA, Chen W, Srinivasan SR, Berenson GS. Using the area under the curve to reduce measurement error in predicting young adult blood pressure from childhood measures. *Stat Med*. 2004;23(22):3421–3435.
33. Chen W, Li S, Cook NR, et al. An autosomal genome scan for loci influencing longitudinal burden of body mass index from childhood to young adulthood in white sibships: the Bogalusa Heart Study. *Int J Obes Relat Metab Disord*. 2004;28(4):462–469.
34. de Jonge J, Dormann C, Janssen PPM, Dollard MF, Landeweerd JA, Nijhuis FJN. Testing reciprocal relationships between job characteristics and psychological well-being: a cross-lagged structural equation model. *J Occup Organ Psychol*. 2001;74(1):29–46.
35. Rosseel Y. lavaan: An R package for structural equation modeling. *J Stat Softw*. 2012;48:1–36.
36. Preacher KJ, Rucker DD, Hayes AF. Addressing moderated mediation hypotheses: theory, methods, and prescriptions. *Multivariate Behav Res*. 2007;42(1):185–227.
37. Tingley D, Yamamoto T, Hirose K, Keele L, Imai K. mediation: R package for causal mediation analysis. *J Stat Softw*. 2014;59(5):1–38.
38. Neuhauser HK, Büschges J, Schaffrath Rosario A, et al. Carotid intima-media thickness percentiles in adolescence and young adulthood and their association with obesity and hypertensive blood pressure in a population cohort. *Hypertension*. 2022;79(6):1167–1176.
39. Yang L, Magnussen CG, Yang L, Bovet P, Xi B. Elevated blood pressure in childhood or adolescence and cardiovascular outcomes in adulthood: a systematic review. *Hypertension*. 2020;75(4):948–955.
40. Ikezaki H, Ai M, Okazaki M, Hayashi J, Shimono N, Schaefer EJ. Relationship between the cholesterol and triglyceride content of lipoprotein subclasses and carotid intima-media thickness: results from the Kyushu and Okinawa Population Study (KOPS). *Clin Chim Acta*. 2023;548:117521.
41. Zhang T, Fan B, Li S, et al. Long-term adiposity and midlife carotid intima-media thickness are linked partly through intermediate risk factors. *Hypertension*. 2022;80(1):160–168.
42. Koskinen J, Juonala M, Dwyer T, et al. Impact of lipid measurements in youth in addition to conventional clinic-based risk factors on predicting preclinical atherosclerosis in adulthood: International Childhood Cardiovascular Cohort Consortium. *Circulation*. 2018;137(12):1246–1255.
43. de Toro-Martín J, Guénard F, Tchernof A, et al. Body mass index is associated with epigenetic age acceleration in the visceral adipose tissue of subjects with severe obesity. *Clin Epigenetics*. 2019;11(1):172. <https://doi.org/10.1186/S13148-019-0754-6>
44. Nevalainen T, Kananen L, Marttila S, et al. Obesity accelerates epigenetic aging in middle-aged but not in elderly individuals. *Clin Epigenetics*. 2017;9:20. <https://doi.org/10.1186/S13148-016-0301-7>
45. Huang RC, Lillycrop KA, Beilin LJ, et al. Epigenetic age acceleration in adolescence associates with BMI, inflammation, and risk score for middle age cardiovascular disease. *J Clin Endocrinol Metab*. 2019;104(7):3012–3024.
46. Kresovich JK, Garval EL, Martinez Lopez AM, et al. Associations of body composition and physical activity level with multiple measures of epigenetic age acceleration. *Am J Epidemiol*. 2021;190(6):984–993.
47. Lundgren S, Kuitunen S, Pietiläinen KH, et al. BMI is positively associated with accelerated epigenetic aging in twin pairs discordant for body mass index. *J Intern Med*. 2022;292(4):627–640.
48. Quach A, Levine ME, Tanaka T, et al. Epigenetic clock analysis of diet, exercise, education, and lifestyle factors. *Aging (Albany NY)*. 2017;9(2):419–446.
49. Simpkin AJ, Cooper R, Howe LD, et al. Are objective measures of physical capability related to accelerated epigenetic age? Findings from a British birth cohort. *BMJ Open*. 2017;7(10):16708. <https://doi.org/10.1136/BMJOPEN-2017-016708>
50. Arpón A, Milagro FI, Santos JL, García-Granero M, Riezu-Boj JL, Martínez JA. Interaction among sex, aging, and epigenetic processes concerning visceral fat, insulin resistance, and dyslipidaemia. *Front Endocrinol (Lausanne)*. 2019;10:496. <https://doi.org/10.3389/FENDO.2019.00496>
51. Gao T, Wilkins JT, Zheng Y, et al. Plasma lipid profiles in early adulthood are associated with epigenetic aging in the Coronary Artery Risk Development in Young Adults (CARDIA) study. *Clin Epigenetics*. 2022;14(1):16. <https://doi.org/10.1186/S13148-021-01222-2>
52. Hillary RF, Stevenson AJ, McCartney DL, et al. Epigenetic measures of ageing predict the prevalence and incidence of leading causes of death and disease burden. *Clin Epigenetics*. 2020;12(1):115. <https://doi.org/10.1186/S13148-020-00905-6>
53. Perna L, Zhang Y, Mons U, Holleczeck B, Saum KU, Brenner H. Epigenetic age acceleration predicts cancer, cardiovascular, and all-cause mortality in a German case cohort. *Clin Epigenetics*. 2016;8:64. <https://doi.org/10.1186/S13148-016-0228-Z>
54. Wang C, Ni W, Yao Y, et al. DNA methylation-based biomarkers of age acceleration and all-cause death, myocardial infarction, stroke, and cancer in two cohorts: The NAS, and KORA F4. *EBioMedicine*. 2021;63:103151. <https://doi.org/10.1016/j.ebiom.2020.103151>
55. Chervova O, Chernysheva E, Panteleeva K, et al. Evaluation of epigenetic age acceleration scores and their associations with CVD-related phenotypes in a population cohort. *Biology*. 2023;12(1):68. <https://doi.org/10.3390/BIOLOGY12010068>
56. Liu Z, Leung D, Thrush K, et al. Underlying features of epigenetic aging clocks in vivo and in vitro. *Aging Cell*. 2020;19(10):e13229. <https://doi.org/10.1111/ace.13229>
57. Gibson J, Russ TC, Clarke TK, et al. A meta-analysis of genome-wide association studies of epigenetic age acceleration. *PLoS Genet*. 2019;15(11):e1008104. <https://doi.org/10.1371/JOURNAL.PGEN.1008104>
58. Bell CG, Lowe R, Adams PD, et al. DNA methylation aging clocks: challenges and recommendations. *Genome Biol*. 2019;20(1):249.
59. Busse M, Michler E, Von Hoff F, et al. Alterations in the peripheral immune system in dementia. *J Alzheimers Dis*. 2017;58(4):1303–1313.
60. Esposito M, Sherr GL. Epigenetic modifications in Alzheimer's neuropathology and therapeutics. *Front Neurosci*. 2019;13:476. <https://doi.org/10.3389/FNINS.2019.00476>
61. Kragh CL, Ubhi K, Wyss-Corey T, Masliah E. Autophagy in dementias. *Brain Pathol*. 2012;22(1):99–109.

- 62.** Ashar FN, Zhang Y, Longchamps RJ, et al. Association of mitochondrial DNA copy number with cardiovascular disease. *JAMA Cardiol*. 2017;2(11):1247-1255.
- 63.** Calabrese C, Pyle A, Griffin H, et al. Heteroplasmic mitochondrial DNA variants in cardiovascular diseases. *PLoS Genet*. 2022;18(4):e1010068. <https://doi.org/10.1371/JOURNAL.PGEN.1010068>
- 64.** Yue P, Jing S, Liu L, et al. Association between mitochondrial DNA copy number and cardiovascular disease: current evidence based on a systematic review and meta-analysis. *PLoS One*. 2018;13(11):e0206003. <https://doi.org/10.1371/JOURNAL.PONE.0206003>
- 65.** Chen MS, Lee RT, Garber JC. Senescence mechanisms and targets in the heart. *Cardiovasc Res*. 2022;118(5):1173-1187. <https://doi.org/10.1093/CVR/CVAB161>
- 66.** Shakeri H, Lemmens K, Gevaert AB, De Meyer GRY, Segers VFM. Cellular senescence links aging and diabetes in cardiovascular disease. *Am J Physiol Heart Circ Physiol*. 2018;315(3):H448-H462.
- 67.** Guo J, Huang X, Dou L, et al. Aging and aging-related diseases: from molecular mechanisms to interventions and treatments. *Signal Transduct Target Ther*. 2022;7(1):391. <https://doi.org/10.1038/s41392-022-01251-0>
- 68.** Hu C, Zhang X, Teng T, Ma ZG, Tang QZ. Cellular senescence in cardiovascular diseases: a systematic review. *Aging Dis*. 2022;13(1):103. <https://doi.org/10.14336/AD.2021.0927>
- 69.** Contois JH, Langlois MR, Cobbaert C, Sniderman AD. Standardization of apolipoprotein B, LDL-cholesterol, and non-HDL-cholesterol. *J Am Heart Assoc*. 2023;12(15):e030405. <https://doi.org/10.1161/JAHA.123.030405>
- 70.** Kjeldsen EW, Nordestgaard LT, Frikke-Schmidt R. HDL cholesterol and non-cardiovascular disease: a narrative review. *Int J Mol Sci*. 2021;22(9):4547. <https://doi.org/10.3390/IJMS22094547>
-
- KEY WORDS** biological aging, cardiovascular disease risk factors, epigenetic age acceleration, life span, subclinical atherosclerosis
-
- APPENDIX** For supplemental tables, please see the online version of this paper.

EDITORIAL COMMENT

Early Life Cardiovascular Risk Factors and Midlife Epigenetic Aging

An Enduring Legacy*



Paul S. de Vries, PhD,^a Anthony S. Zannas, MD, PhD^{b,c}

Aging can be seen as a progressive deterioration of our physiological functions. Although a person's chronological age based simply on their date of birth is a strong predictor of this process, there can be interindividual differences in the speed at which biological aging occurs. To capture such interindividual differences, several composite epigenetic markers have been developed that combine the DNA methylation status of multiple sites across the human genome to predict age-related traits. The first-generation measures of epigenetic aging, such as the ones developed by Horvath¹ and Hannum et al,² were derived by regression models that merely predict chronological age, whereas second-generation measures, such as the widely used PhenoAge and GrimAge, further predicted health span and lifespan by including in their regression health and mortality endpoints.^{3,4} For all these markers, the degree to which epigenetic age outpaces chronological age—that is, the individual's “epigenetic age acceleration”—is used as a measure of biological aging.

Following these developments, an exponentially increasing number of studies have repeatedly found associations between accelerated epigenetic aging and a variety of age-related traits, independent of

chronological age.⁵ For example, studies have shown cross-sectional associations between epigenetic age acceleration and cardiovascular risk factors.⁵ Epigenetic aging has also been associated with measures of subclinical atherosclerosis and with risk of incident clinical coronary heart disease.⁶ What has remained understudied, however, is whether cardiovascular risk factors early in life can result in enduring effects on epigenetic age acceleration that are still detectable later in life.

In this issue of *JACC: Basic to Translational Science*, Sun et al⁷ provide novel insights into this research gap. The investigators used the Bogalusa Heart Study, a population-based, prospective cohort study that has followed 1,580 participating children from 1973 onward. They studied cardiovascular risk factors during childhood in relation to epigenetic age acceleration in midlife. They found that unfavorable metabolic profiles in childhood, including increased body mass index (BMI), systolic blood pressure, and triglycerides, and decreased high-density lipoprotein cholesterol, predicted midlife epigenetic age acceleration, as measured with 3 of the 4 aforementioned markers (Hannum, PhenoAge, GrimAge). They performed cross-lagged panel analyses, a well-suited and sophisticated approach for clarifying temporal relationships, thereby providing evidence that BMI, triglycerides, and high-density lipoprotein cholesterol are more likely to be determinants rather than consequences of epigenetic age acceleration. The investigators further found that cardiovascular risk factors during childhood were associated with carotid intima media thickness, a measure of subclinical atherosclerosis. They found that PhenoAge and GrimAge mediated up to 27% of the associations of BMI and triglycerides with subclinical atherosclerosis. Together these findings extend prior work and suggest a temporal relationship and potential causal

*Editorials published in *JACC: Basic to Translational Science* reflect the views of the authors and do not necessarily represent the views of *JACC: Basic to Translational Science* or the American College of Cardiology.

From the ^aHuman Genetics Center, Department of Epidemiology, The University of Texas Health Science Center at Houston School of Public Health, Houston, Texas, USA; ^bDepartment of Psychiatry, University of North Carolina at Chapel Hill, Chapel Hill, North Carolina, USA; and the ^cDepartment of Genetics, University of North Carolina at Chapel Hill, Chapel Hill, North Carolina, USA.
The authors attest they are in compliance with human studies committees and animal welfare regulations of the authors' institutions and Food and Drug Administration guidelines, including patient consent where appropriate. For more information, visit the [Author Center](#).

pathway through which cardiovascular risk factors early in life can exert enduring effects on epigenetic aging, thereby contributing to atherosclerosis risk later in life.

Although the study by Sun et al⁷ provides valuable insights, it also reveals lingering questions that should be clarified by future research. First, although the longitudinal design reduces the likelihood of reverse causation, these analyses may still be vulnerable to confounding. Orthogonal approaches for causal inferences such as Mendelian randomization for time-varying exposures could further support and clarify the underlying causal relationships.⁸ Second, it is unclear whether the observed association and mediation is explained by an overall effect on biological age or a more specific effect on epigenetic age. This question is relevant because different markers of biological aging have been suggested to have independent or even additive effects on disease risk.⁹ To better characterize such effects, future studies should integrate epigenetic with other established measures of biological age such as telomere length and proteomic age. Finally, the investigators used carotid intima media thickness as a measure of subclinical atherosclerosis. Given that carotid intima media thickness is not a particularly strong predictor of clinical events, it would be worthwhile to demonstrate this same mediation by epigenetic age acceleration with other measures of atherosclerosis

such as coronary artery calcification or harder endpoints of cardiovascular disease such as clinical coronary heart disease events.

Keeping these unresolved questions in mind, the findings from Sun et al⁷ underscore the importance of preventing or ameliorating cardiovascular risk early in life and may help guide health policies. Early studies suggest that epigenetic aging can be modulated by simple lifestyle interventions, such as diet and exercise.¹⁰ Although the clinical benefits of such modulation remain to be determined, evidence to date raises the intriguing possibility that epigenetic aging can be leveraged as a biomarker to monitor early interventions and promote health across the lifespan.

FUNDING SUPPORT AND AUTHOR DISCLOSURES

Dr Zannas was supported by National Heart, Lung, and Blood Institute grant R01HL163031. Dr de Vries has reported that he has no relationships relevant to the contents of this paper to disclose.

ADDRESS FOR CORRESPONDENCE: Dr Paul de Vries, Department of Epidemiology, Human Genetics, and Environmental Sciences, University of Texas Health Science Center at Houston, 1200 Pressler Street, Suite E-429, Houston, Texas 77030, USA. E-mail: Paul.S.DeVries@uth.tmc.edu.

REFERENCES

1. Horvath S. DNA methylation age of human tissues and cell types. *Genome Biol.* 2013;14(10):R115.
2. Hannum G, Guinney J, Zhao L, et al. Genome-wide methylation profiles reveal quantitative views of human aging rates. *Mol Cell.* 2013;49(2):359–367.
3. Lu AT, Quach A, Wilson JG, et al. DNA methylation GrimAge strongly predicts lifespan and healthspan. *Aging (Albany NY).* 2019;11(2):303–327.
4. Levine ME, Lu AT, Quach A, et al. An epigenetic biomarker of aging for lifespan and healthspan. *Aging (Albany NY).* 2018;10(4):573–591.
5. Ammos F, Zhao W, Ratliff SM, et al. Epigenetic age acceleration is associated with cardiometabolic risk factors and clinical cardiovascular disease risk scores in African Americans. *Clin Epigenetics.* 2021;13(1):55.
6. Roetker NS, Pankow JS, Bressler J, Morrison AC, Boerwinkle E. Prospective study of epigenetic age acceleration and incidence of cardiovascular disease outcomes in the ARIC study (Atherosclerosis Risk in Communities). *Circ Genom Precis Med.* 2018;11(3):e001937.
7. Sun X, Chen W, Razavi AC, et al. Associations of epigenetic age acceleration with CVD risks across the lifespan: the Bogalusa Heart Study. *J Am Coll Cardiol Basic Trans Science.* 2024;9(5):577–590.
8. Sanderson E, Richardson TG, Morris TT, Tilling K, Davey Smith G. Estimation of causal effects of a time-varying exposure at multiple time points through multivariable mendelian randomization. *PLoS Genet.* 2022;18(7):e1010290.
9. Jansen R, Han LK, Verhoeven JE, et al. An integrative study of five biological clocks in somatic and mental health. *Elife.* 2021;10:e59479. <https://doi.org/10.7554/elife.59479>
10. Fiorito G, Caini S, Palli D, et al. DNA methylation-based biomarkers of aging were slowed down in a two-year diet and physical activity intervention trial: the DAMA study. *Aging Cell.* 2021;20(10):e13439.

KEY WORDS biological aging, cardiovascular disease risk factors, epigenetic age acceleration, lifespan, subclinical atherosclerosis

ORIGINAL RESEARCH - PRECLINICAL

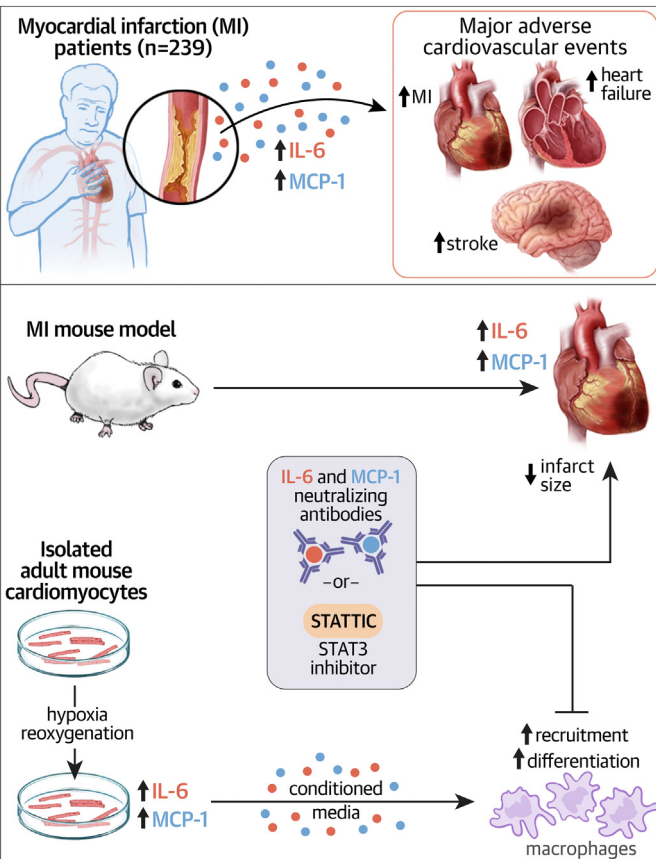


Deleterious Anti-Inflammatory Macrophage Recruitment in Early Post-Infarction Phase

Unraveling the IL-6/MCP-1/STAT3 Axis

Alexandre Paccalet, PhD,^a Sally Badawi, PhD,^a Bruno Pillot, PhD,^a Lionel Augeul, MRes,^a Laura Mechouff, MD, PhD,^a Zeina Harhous, PhD,^a Yves Gouriou, AP, PhD,^a Mélanie Paillard, PhD,^a Marine Breuilly, PhD,^b Camille Amaz, MsRes,^c Yvonne Varillon, MsRes,^c Simon Leboube, MD,^a Camille Brun, MsRes,^a Cyril Prieur, MD, PhD,^c Gilles Rioufol, MD, PhD,^c Nathan Mewton, MD, PhD,^{a,c,d} Michel Ovize, MD, PhD,^a Gabriel Bidault, PhD,^a Thomas Bocheton, MD, PhD,^{a,c,e,*} Claire Crola Da Silva, PhD^{a,*}

VISUAL ABSTRACT



HIGHLIGHTS

- MCP-1 and IL-6 blood levels peak at 24 hours in STEMI patients and are associated with an increased risk of MACE.
- Blood levels of MCP-1 and IL-6 peak at 3 hours in a mouse model of STEMI. The mRNA level of both cytokines was increased in the ischemic heart, suggesting a local production.
- Cardiac myocytes produce MCP-1 and IL-6 that play a synergistic role in macrophage recruitment and polarization via STAT3 signaling pathway.
- Use of anti-IL-6 and anti-MCP-1 neutralizing antibodies mix or a inhibitor of STAT3 pathway (STATTIC) at the onset of reperfusion reduces infarct size in a mouse model of STEMI.
- This study highlights the potential deleterious role of anti-inflammatory macrophages recruitment during the early phase of myocardial infarction.

Paccalet A, et al. J Am Coll Cardiol Basic Trans Science. 2024;9(5):593-604.

**ABBREVIATIONS
AND ACRONYMS****CMA** = adult cardiac myocyte**ELISA** = enzyme-linked immunosorbent assay**HR** = hypoxia-reoxygenation**IL** = interleukin**IR** = ischemia-reperfusion**JAK** = Janus kinase**MACE** = major adverse cardiovascular events**MCP** = monocyte chemoattractant protein**MI** = myocardial infarction**PCI** = percutaneous coronary intervention**STAT3** = signal transducer and activator of transcription 3**STEMI** = ST-segment elevation myocardial infarction**SUMMARY**

Using a translational approach with an ST-segment myocardial infarction (STEMI) cohort and mouse model of myocardial infarction, we highlighted the role of the secreted IL-6 and MCP-1 cytokines and the STAT3 pathway in heart macrophage recruitment and activation. Cardiac myocytes secrete IL-6 and MCP-1 in response to hypoxic stress, leading to a recruitment and/or polarization of anti-inflammatory macrophages via the STAT3 pathway. In our preclinical model of myocardial infarction, neutralization of IL-6 and MCP-1 or STAT3 pathway reduced infarct size. Together, our data demonstrate that anti-inflammatory macrophages can be deleterious in the acute phase of STEMI. (J Am Coll Cardiol Basic Trans Science 2024;9:593–604) © 2024 The Authors.

Published by Elsevier on behalf of the American College of Cardiology Foundation. This is an open access article under the CC BY-NC-ND license (<http://creativecommons.org/licenses/by-nc-nd/4.0/>).

Despite recent advancements in post-myocardial infarction (MI) care, many patients continue to experience complications such as heart failure or stroke in the following years. MI has reportedly triggered sterile inflammation, potentially contributing to adverse effects. Circulating cytokines have been broadly studied for their potential role as prognostic/diagnostic biomarkers post-MI^{1–4} because some of them, such as interleukin (IL)-6 or monocyte chemoattractant protein (MCP)-1, have been demonstrated to be correlated with worsening post-MI recovery.^{5–10}

Encouraging outcomes have emerged using the IL-6 receptor inhibitor tocilizumab, exhibiting improved myocardial salvage index in ST-segment elevation MI (STEMI) patients,¹¹ as well as attenuated inflammatory response, primarily percutaneous coronary intervention (PCI)-related troponin-T release in non-STEMI patients.¹² Despite these promising results, it is noteworthy that these clinical trials targeted the IL6-receptor rather than directly addressing the cytokine IL-6 itself. Thus, a comprehensive understanding of IL-6 and MCP-1 roles in sterile inflammation occurring during MI is imperative for optimizing therapeutic approaches.

In the context of MI, it is reported that IL-6 and MCP-1 are released by cardiac fibroblasts or by

resident, as well as circulating, immune cells, whereas cardiomyocytes are mainly described to release damage-associated molecular pattern molecules.¹³ Although few studies have demonstrated the secretion of IL-6 and MCP-1 by adult cardiomyocytes (CMA) in normal conditions,¹⁴ only 1 study using human atrial cardiomyocytes has shown IL-6 production.¹⁵ However, no studies under hypoxia-reoxygenation (HR) conditions have investigated the secretion of IL-6 and MCP-1 by CMA. Both IL-6 and MCP-1 are recognized for attracting leukocytes to sites of damage or infection.^{16–18} Among the downstream signaling pathways activated by MCP-1 and IL-6, the Janus kinase/signal transducer and activator of transcription 3 (JAK/STAT3) pathway has been identified in nonischemic diseases^{19,20} and serves as a key regulator of immune and inflammatory pathways.²¹ JAK/STAT3 signaling has also been described to drive the polarization of macrophages. However, depending on the pathologies, either inhibition or activation of this pathway increases anti-inflammatory polarization.²² Although a study on rats demonstrated that the inhibition of JAK/STAT3 leads to anti-inflammatory macrophage polarization in MI,²³ the role of this signaling pathway must be well understood. Macrophages' polarization is usually described as undergoing dynamic changes after reperfusion in MI, transitioning from a proinflammatory phase in the early days to a subsequent

From the ^aLaboratoire CarMeN-IRIS Team, INSERM, INRA, Université Claude Bernard Lyon-1, INSA-Lyon, University of Lyon, Bron, France; ^bCIQLE, LyMIC, LABEX CORTEX, Université Claude Bernard Lyon 1, Structure Fédérative de Recherche santé Lyon-Est CNRS UAR3453/Inserm US7, Lyon, France; ^cCentre d'Investigation Clinique de Lyon (CIC 1407 Inserm), Hospices Civils de Lyon, Lyon, France; ^dIntensive Cardiological Care Division, Louis Pradel Hospital, Hospices Civils de Lyon, Lyon, Bron, France; and the ^eUniversity Claude Bernard Lyon 1, Lyon, France. *Drs Bochaton and Crola Da Silva contributed equally to this work as senior authors.

The authors attest they are in compliance with human studies committees and animal welfare regulations of the authors' institutions and Food and Drug Administration guidelines, including patient consent where appropriate. For more information, visit the [Author Center](#).

anti-inflammatory phase starting around 3 to 4 days post-MI.^{24,25} However, this dichotomous classification has been questioned by studies reporting that macrophage infiltration can be advantageous and deleterious depending on the kinetics of infiltration and on the activation states.^{26,27}

In this study, we investigated whether high levels of IL-6 and MCP-1, along with the activation of their respective downstream signaling pathways, orchestrate macrophage recruitment and differentiation and exacerbate MI injuries. Initially, we establish a correlation between the circulating levels of IL-6 and MCP-1 and the occurrence of major adverse cardiovascular events (MACE) such as all-cause mortality, MI, hospitalization for heart failure or stroke within the first year post-STEMI. Using a murine model of MI and an in vitro coculture model, we showed that injured cardiomyocytes release IL-6 and MCP-1, consequently triggering the recruitment and differentiation of anti-inflammatory macrophages via the STAT3 signaling pathway. Finally, our study demonstrated that inhibiting IL-6/MCP-1/STAT3 pathways reduced the population of anti-inflammatory macrophages and decreased the infarct size.

METHODS

A HUMAN COHORT OF STEMI PATIENTS. Sera samples from patients of a previously described HIBISCUS cohort (coHort of patients to Identify Biological and Imaging markerS of CardiovascUlar outcomes in ST elevation myocardial infarction) was used.¹ Briefly, 239 patients were included with STEMI and underwent coronary angiography with a subsequent primary PCI for revascularization. The primary endpoint was all-cause of death, rehospitalization for heart failure, recurrent infarction, and stroke. MACE was assessed within the 12 months after the index hospitalization.

Clinical follow-up was prospectively recorded. MCP-1 and IL-6 concentrations were quantified using enzyme-linked immunosorbent assays (ELISA) and biochemical analyses (C-reactive protein and troponin I) were performed at the Hospices Civil de Lyon Laboratory. Further details are provided in the *Supplemental Methods*.

MOUSE MODEL OF ISCHEMIA-REPERFUSION IN VIVO AND TISSUE COLLECTION.

All animal procedures were performed following the guidelines from Directive 2010/63/EU of the European Parliament of the protection of animals used for scientific purposes. The study was approved by the Lyon 1 Claude Bernard University ethics committee

(N°2018032216064965). The *in vivo* model of ischemia-reperfusion (IR) developed in the laboratory was used to perform the study.²⁸ Details of the surgery procedure are described in the *Supplemental Methods*.

MOUSE CYTOKINES QUANTIFICATION. Circulating concentrations of IL-6 and MCP-1 in mouse sera stored at -80°C were quantified at different time points using ELISA according to the manufacturers' instructions (Invitrogen for IL-6 and R&D systems for MCP-1). The minimum detectable concentration is 0.666 pg/mL for MCP-1 and 4 pg/mL for IL-6.

HEART mRNA QUANTIFICATION. Mice (n = 8/group) were randomly assigned to 2 groups: a control group without ischemia (normoxia) and a second group corresponding to IR 1 hour. At T = 0 and T = 1 hour, mice were anesthetized and then euthanized. RNA extracted from hearts were used to quantify the expression of IL-6 and MCP-1 (*Supplemental Methods*).

IN VITRO HR ON CMA. The HR sequence was performed using a hypoxia incubator (Eppendorf Galaxy 48R). CMA were isolated from hearts as described in the *Supplemental Methods*. CMA were then incubated in 500 μL of hypoxia buffer (140 mmol/L NaCl, 5 mmol/L KCl, 1 mmol/L MgCl₂, 10 mmol/L HEPES, 2 mmol/L CaCl₂) for 1.5 hours at 0.5% of oxygen. Following hypoxia, reoxygenation was performed by adding 1.5 mL of complete medium (DMEM F12, 10% fetal bovine serum, 1% penicillin-streptomycin). CMA then were placed in a normoxic incubator for 24 hours, and the conditioned medium was collected and directly frozen at -20°C until use.

IN VITRO MACROPHAGE PHENOTYPING. Macrophages isolated from bone marrow, as detailed in the *Supplemental Methods*, were cultured in 12-well plates at a concentration of 300,000 cells/mL for 7 days. Macrophages were stimulated with CMA conditioned medium diluted to one-half in complete medium for 24 hours. Macrophages were then harvested, and the cell suspension was stained for 30 minutes at 4°C with CD206 and CD86 (BioLegend, ref 141710 and 105043, respectively) at 1:100 in phosphate-buffered saline, 4% bovine serum albumin. Data were acquired on an LSR Fortessa X20 (BD Bioscience) and analyzed with FlowJo software (V10.8.0, Becton, Dickinson & Company).

Treatment with STATTIC inhibitor at 2.5 μmol/L (Sigma Aldrich, S7946)²⁹ or neutralizing antibodies against IL-6 at 0.3 μg/mL (R&D Biosystems, AF-406-NA) or against MCP-1 at 2.5 μg/mL (R&D Biosystems,

AF-479-NA) were performed at the same time as the stimulation with CMA conditioned medium.

IN VITRO MACROPHAGE RECRUITMENT BY CMA.

For recruitment experiments, macrophages were cultured on Millicell hanging cell culture inserts (Merck, MCEP12H48) at 110,000 cells/mL for 7 days. After polarization in pro- or anti-inflammatory macrophages, recruitment experiments were conducted under a confocal microscope. Experiments are detailed in the *Supplemental Methods*.

STATISTICS. Continuous human data are expressed as median and 95% CI, median (IQR), or mean \pm SD according to their distribution.

Within-group comparisons were performed using a paired *t*-test or Wilcoxon signed rank test, whereas differences between groups used the Wilcoxon rank sum test or unpaired *t*-test.

Kaplan-Meier methods (log-rank test) were used to compare MACE between groups. Cox proportional hazards models were used to obtain the HR and 95% CI for adjusted models predicting MACE.

For in vitro macrophage recruitment experiments, 2-way repeated measures analysis of variance with Sidak's post hoc test for multiple pairwise comparisons was performed. For in vitro macrophage activation experiments at 24 hours, 2-way repeated measures analysis of variance with Dunnett's post hoc test for multiple pairwise comparisons was performed. Linear regression was used to evaluate slope differences for infarct size. Statistical analyses were performed using GraphPad Prism 8.01 (GraphPad Software). A *P* value <0.05 was considered significant.

RESULTS

ELEVATED LEVELS OF IL-6 AND MCP-1 IN THE BLOOD POSITIVELY CORRELATE TO WORSE OUTCOMES AMONG STEMI PATIENTS. Supplemental Tables 1 and 2 provide an overview of the demographic characteristics of the study population (*Supplemental Appendix*). The mean age was 59 ± 12 years, and 79.5% of the cohort was composed of men. There were 160 patients with TIMI flow grades 0 or 1 at admission (66.9%), and 231 had TIMI flow grades ≥ 2 after PCI (96.7%).

We first assessed the temporal variation of IL-6 and MCP-1 concentrations in STEMI patients' sera over the course of the first month. As illustrated in **Figure 1A**, the IL-6 level reached a peak at 24 hours, median value of 5.4 pg/mL (95% CI: 4.2-6.0 pg/mL),

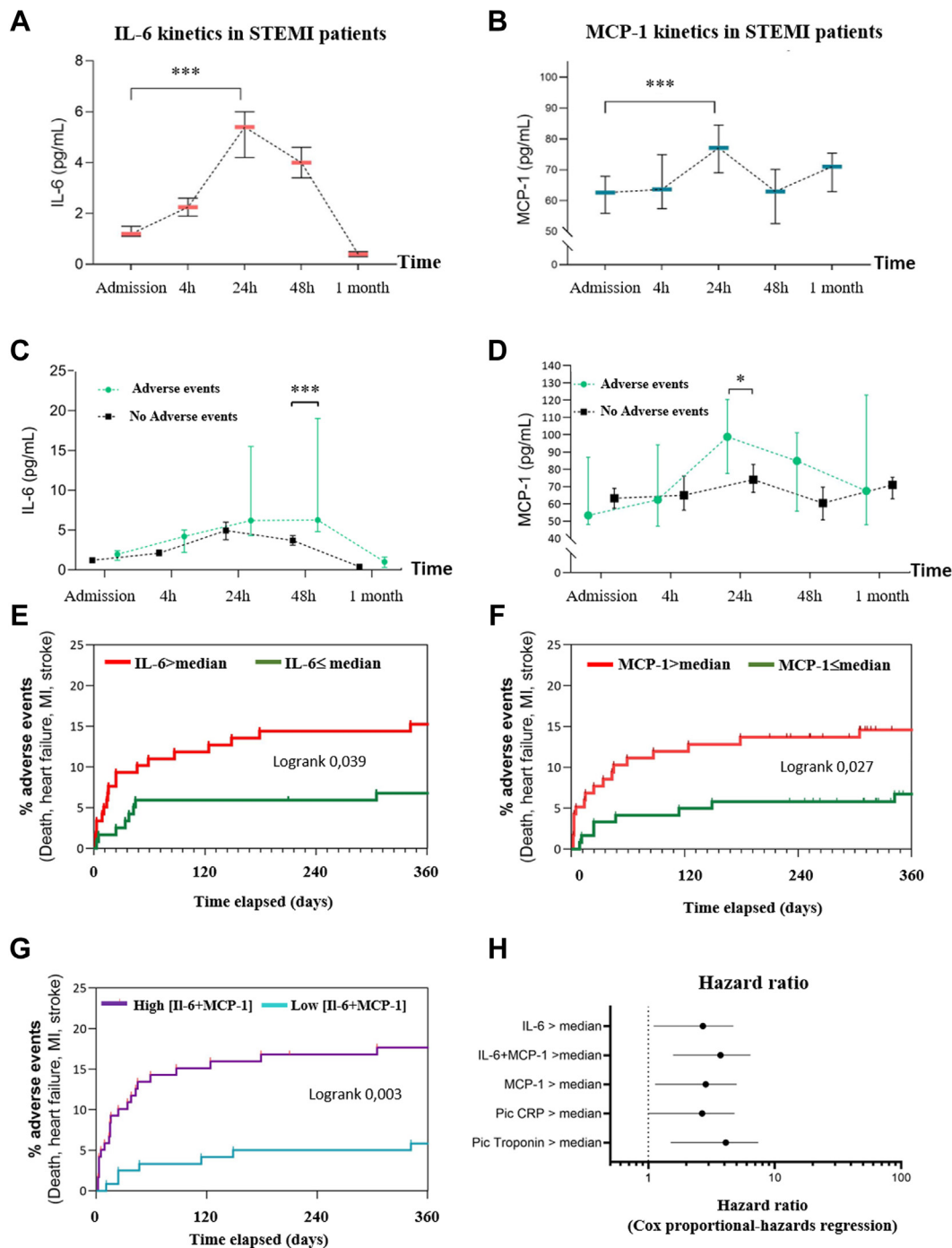
compared with the admission level value of 1.2 pg/mL (95% CI: 1.1-1.5 pg/mL; *P* < 0.001). Likewise, the circulating level of MCP-1 was also increased (**Figure 1B**) compared with the admission level with a median value of 77.1 pg/mL (95% CI 69-84.5 pg/mL; *P* < 0.001 at 24 hours).

Across the entire cohort, a total of 32 patients encountered MACE during the 12-month follow-up. As shown in **Figure 1C**, patients who experienced at least 1 adverse cardiac event within the 12-month follow-up period exhibited elevated blood IL-6 levels in their blood (median value of 6.3 pg/mL; 95% CI: 4.8-19 pg/mL) at 48 hours compared with patients without clinical outcomes (median value of 3.7 pg/mL; 95% CI: 3.1-4.3 pg/mL; *P* < 0.001). Additionally, blood MCP-1 levels were higher in patients who experienced MACE (median value of 98.7 pg/mL; 95% CI: 77.6-120.4 pg/mL) at 24 hours than in patients without MACE (median value at 74.0 pg/mL; 95% CI: 66.6-82.8 pg/mL) at 24 hours; *P* = 0.021 (**Figure 1D**).

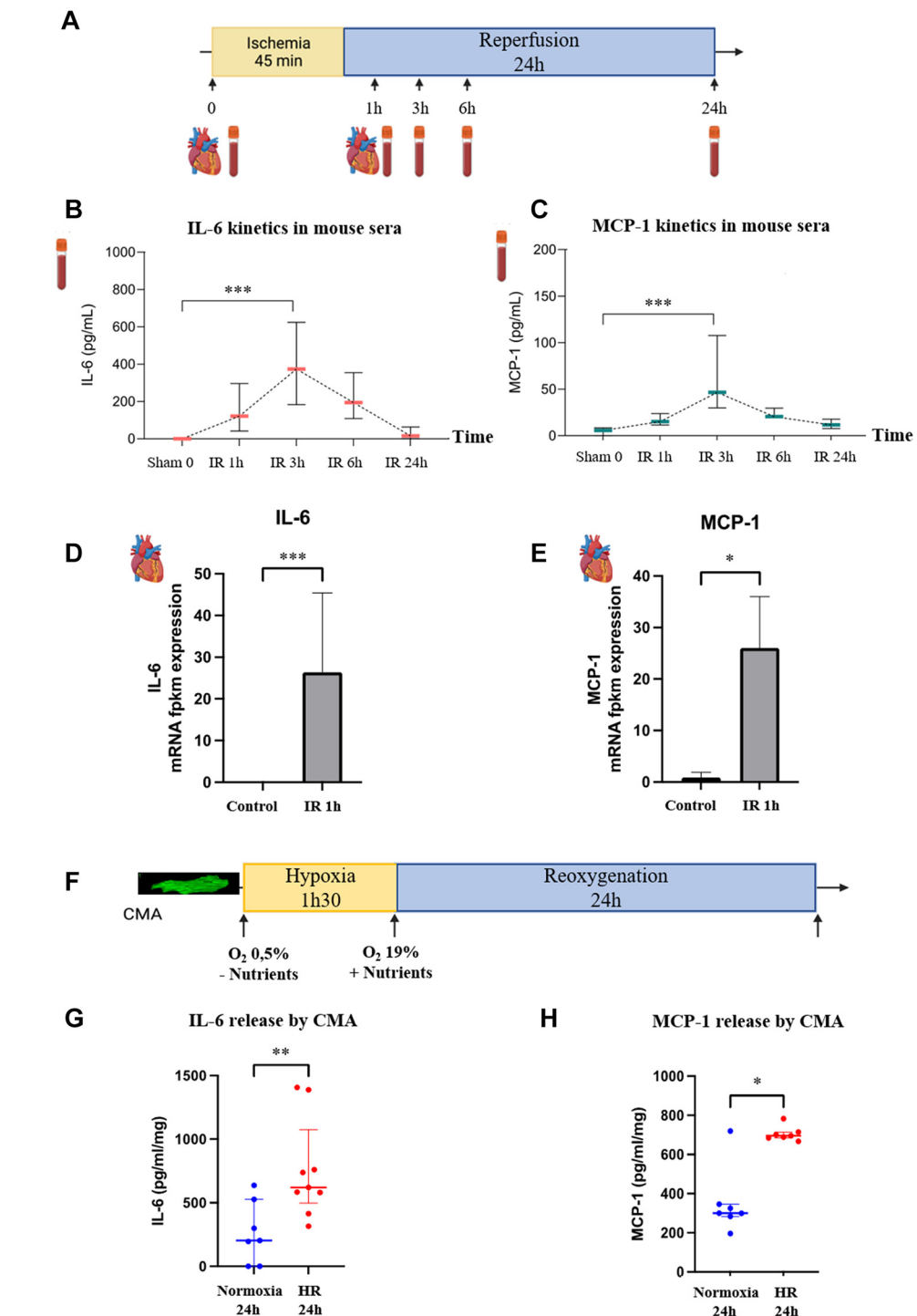
When patients were dichotomized according to the median value of IL-6 or MCP-1 concentration in blood at 24 hours, patients with an IL-6 value above the median had a significantly larger infarct size and a reduced left ventricular ejection fraction than those with a low level of IL-6 (*Supplemental Figures 1A and 1B*). Moreover, MCP-1 level was not associated with significant differences neither in infarct size (*Supplemental Figure 1C*) nor in left ventricular ejection fraction (*Supplemental Figure 1D*).

As displayed in **Figures 1E and 1F** for IL-6 and MCP-1, respectively, patients with IL-6 or MCP-1 levels that exceeded the median were observed to more likely experience MACE over the 12 months' follow-up (unadjusted HR: 2.3; 95% CI: 1.1-4.8; *P* = 0.039 and unadjusted HR: 2.4; 95% CI: 1.1-5.0; *P* = 0.027, respectively). With a Cox proportional hazards model incorporating IL-6 and MCP-1 levels at 24 hours, we successfully illustrated that patients with IL-6 or MCP-1 levels above the median were more at risk of experiencing an adverse cardiac event within the ensuing 2 years in contrast to patients with a level under the median value (HR: 3.2; 95% CI: 1.6-6.4; *P* = 0.003) as shown in **Figure 1G**. In a multivariable Cox regression model including age >65 years, sex, troponin peak level, TIMI flow grade >2 after PCI, ischemic time, and anterior MI, IL-6+MCP-1 serum level at 24 hours above the median value remained associated with an increased risk of experiencing the composite HR endpoint during the follow-up (adjusted HR: 5.3; 95% CI: 1.9-14.4; *P* = 0.003).

FIGURE 1 IL-6 and MCP-1 Levels Peak 24 Hours After Admission for a STEMI and Are Associated With Adverse Clinical Outcomes

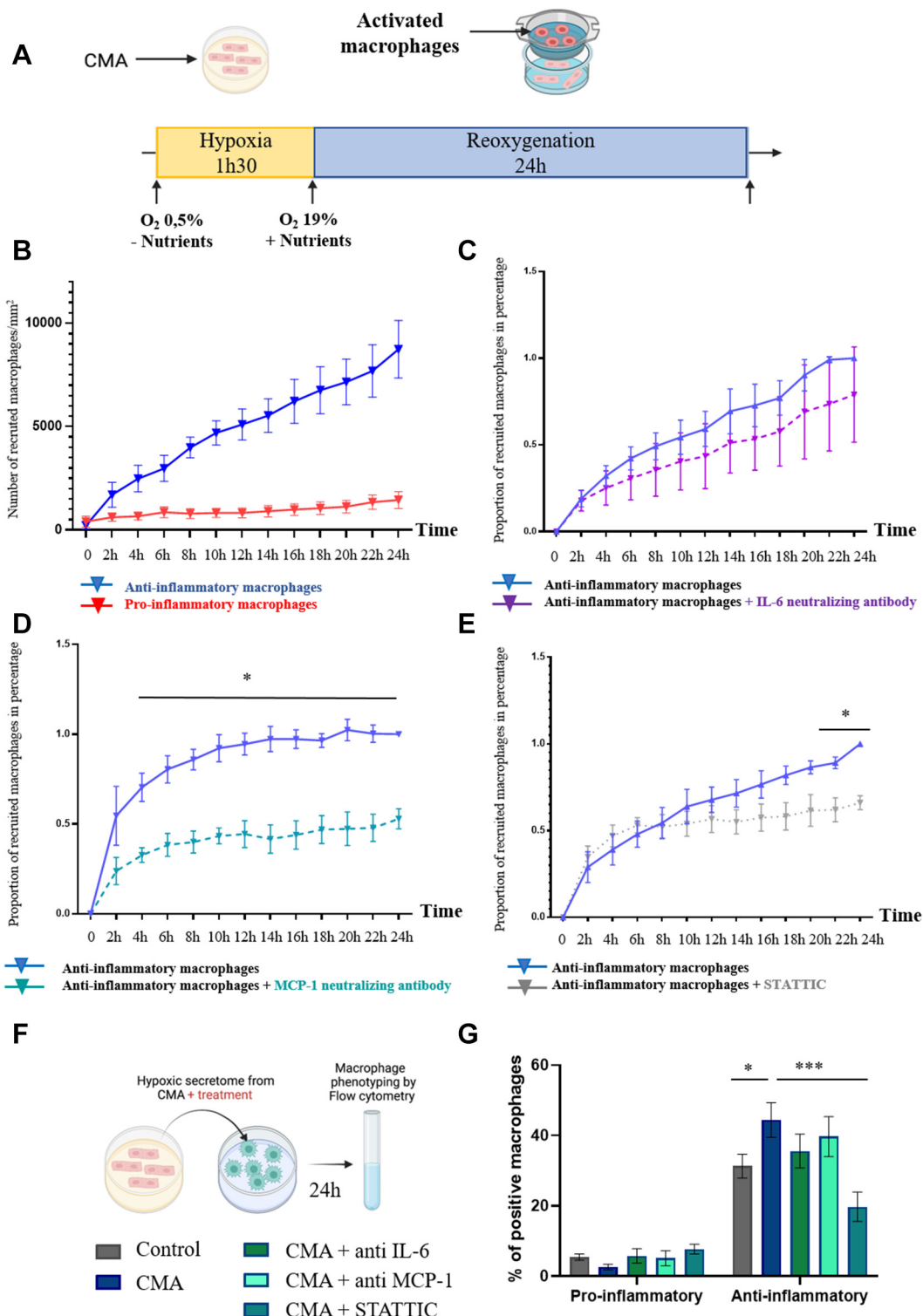


(A and B) Kinetics of IL-6 and MCP-1 concentrations in ST-segment elevation myocardial infarction (STEMI) patient sera measured by enzyme-link immunosorbent assay. (C and D) Major adverse cardiovascular events are presented according to IL-6 or MCP-1 serum levels. Data are presented as median with 95% CI. Wilcoxon rank sum test was used for statistical analysis. (E to G) Kaplan-Meier curves (log-rank test) are used to present adverse cardiac events according to the median concentration of IL-6 or MCP-1 independently or additionally at 24 hours. (H) Unadjusted HR and 95% CI for experiencing a composite endpoint during the median of 24 months of follow-up when having high IL-6 level (>median) or high MCP-1 (>median), both high IL-6 and MCP-1, elevated C-reactive protein (CRP >median), and high troponin peak (>median). The peak used is the maximum value of troponin, or CRP, measured for each patient individually. N = 239. *P < 0.05, **P < 0.01, and ***P < 0.001.

FIGURE 2 IL-6 and MCP-1 Levels Peak at 3 Hours in the Mouse STEMI Model

(A) Experimental outline: peripheral blood and heart were collected at different time points of the ischemia-reperfusion (IR) sequence. (B and C) Kinetics of IL-6 and MCP-1 cytokine levels were quantified by enzyme-link immunosorbent assay from mouse sera after ischemia-reperfusion times; $n = 3$ to 8 mice. (D and E) IL-6 and MCP-1 mRNA expression expressed in fragments per kilobase million (fpkm) in the area at risk normalized by the healthy area. $n = 3$ to 8 mice. (F) Experimental outline, isolated cardiac myocytes adult (CMA) underwent in vitro hypoxia-reoxygenation (HR) sequence. Conditioned mediums were collected at 24 hours post-reperfusion. (G and H) IL-6 and MCP-1 levels in the conditioned medium were measured by enzyme-link immunosorbent assay under normoxia or HR. $n = 7$ to 9 independent experiments. * $P < 0.05$, ** $P < 0.01$, and *** $P < 0.001$. Data were represented as median + interquartile range. Wilcoxon rank sum test for unpaired data with Dunnert's post hoc test was used for statistical analysis. STEMI = ST-segment elevation myocardial infarction.

FIGURE 3 CMA Release IL-6 and MCP-1 in Response to HR Stress to Recruit and Differentiate Macrophages



Continued on the next page

Interestingly, the HR indicated that the combined association of MCP-1 and IL-6 served as a better predictor of secondary events than either cytokine considered independently, to a similar extent as the troponin peak (**Figure 1H**).

Together, these results demonstrate that IL-6 and MCP-1 levels collected at 24 hours after STEMI are associated with worse clinical outcomes. However, mechanistic explanations were lacking, prompting us to utilize preclinical models of MI to address the question.

TEMPORAL SERUM AND EXPRESSION PROFILES OF IL-6 AND MCP-1 IN A MURINE MI MODEL. In a mouse model of MI, blood samples were collected at different time points as displayed in **Figure 2A**. Both IL-6 and MCP-1 median blood levels peaked 3 hours after reperfusion (373.7 pg/mL; Q1-Q3: 183.3–624.5 pg/mL; $P = 0.001$ and 46.6 pg/mL; Q1-Q3: 30.1–107.8 pg/mL; $P = 0.001$, respectively) when compared with sham 0 control (**Figures 2B and 2C**).

Furthermore, both IL-6 and MCP-1 mRNA median expression was significantly increased in the ischemic compared with the sham hearts (26.4; Q1-Q3: 11.0–45.4 vs 0.04; Q1-Q3: 0.03–0.04; $P < 0.001$ and 26.0; Q1-Q3: 15.4–36.0 vs 0.9; Q1-Q3: 0.8–1.9; $P = 0.011$, respectively) (**Figures 2D and 2E**).

IL-6 AND MCP-1 RELEASED BY INJURED CMA TRIGGER MACROPHAGE RECRUITMENT AND DIFFERENTIATION MACROPHAGES VIA ACTIVATING THE STAT3 SIGNALING PATHWAY. Using an in vitro model of isolated CMA subjected to HR sequence (**Figure 2F**), we observed an increase in both IL-6 (**Figure 2G**) and MCP-1 (**Figure 2H**) concentrations, quantified by ELISA, in comparison to the normoxic condition ($P < 0.010$ for IL-6 and $P < 0.050$ for MCP-1).

We tested whether IL-6 and MCP-1 could trigger macrophage recruitment using conditioned medium obtained from CMA exposed to 24 hours of

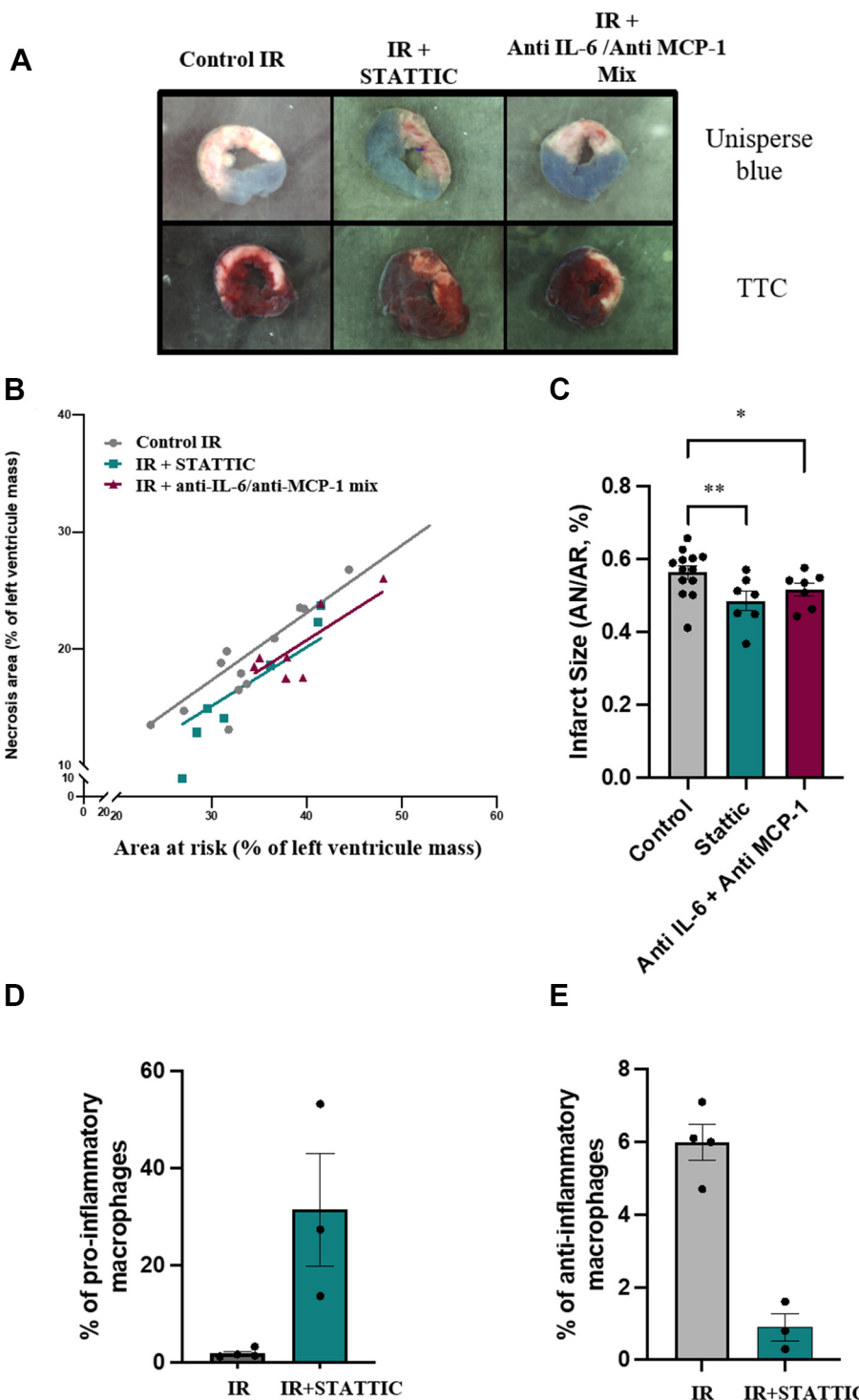
HR in vitro (**Figure 3A**). We specifically measured the effect on pro- or anti-inflammatory macrophages following macrophages phenotype validation by flow cytometry (**Supplemental Figure 2A**). As illustrated in **Figure 3B**, in vitro injured CMA preferentially recruited anti-inflammatory macrophages (median 9,563 macrophages/mm²; Q1-Q3: 5,240–11,737 macrophages/mm²) compared with proinflammatory macrophages (median 1,519 macrophages/mm²; Q1-Q3: 52–2,250 macrophages/mm²; $P < 0.001$). This effect was partially inhibited by neutralizing antibodies against IL-6 or MCP-1. The IL-6 neutralizing antibody led to a 32.1% reduction of anti-inflammatory macrophage recruitment by CMA at 24 hours (**Figure 3C**), without impairing proinflammatory macrophage recruitment (**Supplemental Figure 2B**). Meanwhile, the MCP-1 neutralizing antibody led to a 44.2% reduction of anti-inflammatory macrophages ($P = 0.002$) and 29.8% reduction of proinflammatory macrophages ($P = 0.005$) (**Figure 3D**, **Supplemental Figure 2C**). The inhibition of the STAT3 signaling pathways by the STATTIC antagonist reduced anti-inflammatory macrophage recruitment at 24 hours ($P = 0.044$) (**Figure 3E**), whereas it had no significant effect on proinflammatory macrophage recruitment (**Supplemental Figure 2D**). These results suggest that IL-6- and MCP-1-mediated anti-inflammatory macrophage recruitment mostly relies on STAT3-dependent pathways.

Subsequently, we treated naive macrophages (Mo) with conditioned medium obtained from injured CMA with or without neutralizing antibodies (anti-IL-6 and anti-MCP-1) or STATTIC (**Figure 3F**). The conditioned medium specifically stimulated the differentiation of anti-inflammatory (CD86⁻, CD206⁺) macrophages compared with the control medium (**Figure 3G**). This effect was slightly mitigated by the presence of the neutralizing antibodies (19.84%; $P = 0.1316$ for IL-6 and 11.3%; $P = 0.6611$ for MCP-1).

FIGURE 3 Continued

(A) Experimental outline of recruitment experiment. After hypoxia, a cell culture insert containing PKH-labeled macrophages was added to the CMA well for 24 hours. The dynamic recruitment of macrophages was followed and quantified by confocal microscopy. (B) Proinflammatory (blue line) vs anti-inflammatory (red line) macrophage recruitment by CMA in response to HR sequence. Data are expressed as numbers of macrophages/mm². $n = 10$ independent experiments. (C to E) Effects of the presence of neutralizing antibody against IL-6 (C), MCP-1 (D) or STATTIC inhibitor on the recruitment of anti-inflammatory macrophages when they are added in the medium at reoxygenation time. $n = 4$ independent experiments. (F) Experimental outline of differentiation experiment. Neutralizing antibodies or STATTIC inhibitor was added at the time of macrophages stimulation with the conditioned medium. (G) Characterization of macrophage phenotype following the treatments by flow cytometry. Data are presented as median + SEM. For statistical analysis, 2-way repeated measures analysis of variance with Sidak's post hoc test (B to E) and Wilcoxon rank sum test for unpaired data with Dunnnett's post hoc test (G). * $P < 0.05$, ** $P < 0.01$, and *** $P < 0.001$. Abbreviations as in **Figure 2**.

FIGURE 4 The Early Recruitment of Anti-Inflammatory Macrophages Is Deleterious in Vivo During the First Hours of MI



(A) Infarct size quantification using Unisperse blue to measure perfused area followed by triphenyl tetrazolium chloride (TTC) staining to measure necrosis area after treatment by STATTIC or the mix of IL-6 and MCP-1 neutralizing antibodies. (B and C) Effect of treatments on infarct size are represented by plotted necrosis area as a function of the area at risk (expressed as a percentage of left ventricular mass) or expressed by a ratio of necrosis area on area at risk in percentages. $n = 8$ to 10 per group. (D and E) Impact of STATTIC treatment on the phenotype of macrophages evaluated by flow cytometry; $P = 0.057$ (D and E). Data are presented as median \pm SEM. Mann-Whitney test with Sidak's post hoc test was used for statistical analysis * $P < 0.05$, ** $P < 0.01$, and *** $P < 0.001$. Abbreviations as in Figure 2.

In comparison, STATTIC more efficiently reduced macrophage polarization (56%; $P < 0.001$) (**Figure 3G**).

REDUCING THE RECRUITMENT AND ACTIVATION OF ANTI-INFLAMMATORY MACROPHAGES AT THE ONSET OF REPERFUSION DECREASED INFARCTION SEVERITY. Combined anti-IL-6 and anti-MCP-1 neutralizing antibodies or STATTIC treatment were injected 5 minutes before reperfusion. Infarct size quantification was performed after 24 hours of reperfusion (**Figure 4A**). The distribution of infarct size as a function of the area at risk was slightly, but significantly, decreased in the groups treated with STATTIC or the combination of neutralizing antibodies compared to control IR ($P = 0.0061$ and $P = 0.0081$, respectively) (**Figure 4B**). Calculation of the infarct size as a ratio of area of necrosis over area at risk confirmed a significant effect of both STATTIC and neutralizing antibody treatment; $P = 0.0148$ and $P = 0.0484$, respectively (**Figure 4C**). These results demonstrate that IL-6, MCP-1, and the STAT3 signaling pathway are involved in worsening reperfusion injuries.

The isolation of immune cells from area at risk from ischemic hearts provided further validation that the STATTIC treatment seems to increase the proportion of proinflammatory macrophages while efficiently decreasing the number of anti-inflammatory macrophages (**Figures 4D and 4E**).

DISCUSSION

The present study demonstrates that IL-6 and MCP-1 blood levels positively correlate with worsened outcomes in STEMI patients. This cytokine release at a systemic level is partly due to the capacity of injured CMA to release IL-6 and MCP-1 in the acute phase of MI. Our study highlights the substantial contribution of IL-6, MCP-1, and the STAT3 pathway in both the recruitment and the activation of anti-inflammatory macrophages. Consequently, our findings unveil an unexpected perspective where rapid activation of anti-inflammatory macrophages is detrimental in the context of MI.

Indeed, 1 study⁹ has described that the time course of 3.5 days induced considerable variability concerning the kinetics we describe in the present study. Within our investigation, we observed that the peak of blood MCP-1 concentration occurred 24 hours post-MI and reverted to its basal level after 48 hours. It is worth noting that a single blood sampling within these first 3.5 days would have missed the variation in

MCP-1 level. However, this study has also described that an elevated level of MCP-1 is associated with MACE.

Only 1 translational study assessed MCP-1 levels in both mice and 21 human MI samples.¹⁴ This study showed that the heart produces MCP-1 in healthy states and post-MI conditions. However, the investigators chose an animal model of permanent ligation which, in the absence of reperfusion, was not representative of STEMI patients.

Regarding IL-6, a canine model of MI showed upregulation of IL-6 mRNA in the myocardium following MI.³⁰ In dobutamine stress echocardiography, IL-6 has been associated with an increased risk of cardiovascular events in patients with coronary artery disease,³¹ and IL-6 is also correlated with hemodynamic impairment after injection of dobutamine in patients with chronic heart failure.³² Elevated IL-6 levels have been described in unstable coronary artery disease and are associated with an increased risk of cardiac events and mortality.^{33,34} Plasma levels of IL-6 was elevated after surgery in pulmonary venous effluents from 7 patients immediately and after uncomplicated coronary artery bypass grafting.³⁵ These studies show the elevation of IL-6 during a coronary artery disease.

The novelty of our study is presenting 5 sampling times to obtain the kinetics for each cytokine. Moreover, the study considers only STEMI patients, not all causes of coronary artery disease. We highlight that the combined association of MCP-1 and IL-6 served as a better predictor of secondary events than either cytokine considered independently, to a similar extent as the troponin peak. Our methodology and selected models enabled us to unravel the reasons and consequences of the burst of IL-6 and MCP-1 in STEMI patients.

Data from our in vitro model show that injured CMA release IL-6 and MCP-1 in response to IR. Although the primary characterization of CMA revolves around their contractile function, their role in cytokine production remains poorly described. A limited number of studies have shown that myocytes can release IL-6,^{15,36} but none has investigated this mechanism under hypoxic conditions. Our study is the first to demonstrate that CMA secrete both MCP-1 and IL-6 in response to an IR stress. Besides, we show a synergistic interplay between these 2 cytokines in terms of macrophage recruitment and activation. Indeed, MCP-1, and to a lesser extent IL-6, drives the recruitment of macrophages by CMA. In parallel, IL-6 and STAT3 participate in differentiating anti-inflammatory macrophages by

CMA. Much like preceding studies, we could not confirm STAT3 involvement in MCP-1-mediated recruitment of anti-inflammatory macrophages. However, we successfully demonstrate its involvement in the polarization of macrophages.^{37–39} In vivo, our results reveal that STAT3 inhibition by STATTIC proves comparably efficacious to the dual inhibition achieved by anti-IL-6 and anti-MCP-1 neutralizing antibodies. Consistent with our in vitro results, the in vivo results indicate that the reduction of anti-inflammatory macrophages in the area at risk is mainly attributed to the inhibition of the IL-6/MCP-1/STAT3 pathways.

Surprisingly, our results challenge the conventional notion that anti-inflammatory macrophages are inherently beneficial while proinflammatory ones are deleterious. Instead, the kinetics of intervention are likely the key. Indeed, it has been shown that a decrease in proinflammatory macrophages, paralleled by an increase of anti-inflammatory macrophages 6 days post-MI, reduced fibrosis and increased cardiac function.¹² This may suggest a dynamic shift in the role of the anti-inflammatory macrophages where their function during early reperfusion phase differs from their role during the subsequent remodeling phase.

STUDY STRENGTHS AND LIMITATIONS. The strength of the present study lies in its translational approach. We have used a cohort of 239 well-characterized STEMI patients with a clinical follow-up combined with in vitro and in vivo preclinical models in mouse.

However, we can see some limitations in our study. Even if we consider that the rate at 1 month for each cytokine could indicate a reference close to basal level, the study lacks a control population. Moreover, the phenotype of anti-inflammatory macrophage subtypes is complex and could benefit from more refined characterization in future studies.

CONCLUSIONS

Our study demonstrates the significance of timing of therapeutic targeting as pivotal factors in the success of clinical studies aiming to target

inflammatory processes. Furthermore, our experimental findings propose that the simultaneous targeting of multiple functions, encompassing both recruitment and differentiation, could yield synergistic effects. These insights shed light on potential avenues for refining therapeutic strategies in the context of inflammation-related interventions.

FUNDING SUPPORT AND AUTHOR DISCLOSURES

This work was supported by “Fédération Française de Cardioologie,” and LABEX CORTEX (ANR-11-LABX-0042) and FRM (FD202012010540). The authors have reported that they have no relationships relevant to the contents of this paper to disclose.

ADDRESS FOR CORRESPONDENCE: Dr Claire Crola Da Silva, Laboratoire CarMeN-IRIS Team, Groupe-ment Hospitalier EST, Bâtiment B13, 59 Boulevard Pinel, 69500 Bron, France. E-mail: claire.crola-da-silva@univ-lyon1.fr.

PERSPECTIVES

COMPETENCY IN MEDICAL KNOWLEDGE: Targeting inflammation in cardiovascular disease could pave a new way in therapeutic treatment, but a better understanding of the phenomena remains necessary. Our present study describes the early kinetics of 2 cytokines highly involved in MI response: IL-6 and MCP-1. We demonstrate the highly dynamic release of those 2 cytokines within the first month post-STEMI. Elevated levels of IL-6 and MCP-1 24 hours post-admission are correlated to MACE. Using a pre-clinical model of STEMI, we demonstrated that IL-6 and MCP-1 kinetics are similar in mice. With our in vitro model, we show that cytokines are released by injured cardiac myocytes and induce anti-inflammatory macrophage recruitment and differentiation via the STAT3 signaling pathway. Counter-intuitively, we demonstrate that this anti-inflammatory signaling in the acute phase of MI can be deleterious, highlighting once more the complexity of targeting inflammation in cardiovascular diseases.

TRANSLATIONAL OUTLOOK: Two important points for future clinical trials can be highlighted in this study. First, the precise description of the kinetics of IL-6 and MCP-1 can help in the design of future studies targeting those cytokines to define the right time of treatment. Secondly, our pre-clinical data suggest that synergistic approaches targeting several cytokines could be of interest to improve treatment efficacy.

REFERENCES

1. Paccalet A, Crola Da Silva C, Mechtaouf L, et al. Serum soluble tumor necrosis factor receptors 1 and 2 are early prognosis markers after ST-segment elevation myocardial infarction. *Front Pharmacol.* 2021;12:656928.
2. Hayek A, Paccalet A, Mechtaouf L, et al. Kinetics and prognostic value of soluble VCAM-1 in ST-segment elevation myocardial infarction patients. *Immun Inflamm Dis.* 2021;9:493–501.
3. Mitsis A, Kadoglou NPE, Lambadiari V, et al. Prognostic role of inflammatory cytokines and novel adipokines in acute myocardial infarction: an updated and comprehensive review. *Cytokine.* 2022;153:155848.
4. Bochaton T, Paccalet A, Jeantet P, et al. Heat shock protein 70 as a biomarker of clinical outcomes after STEMI. *J Am Coll Cardiol.* 2020;75:122–124.
5. Ferencik M, Mayrhofer T, Lu MT, et al. Coronary atherosclerosis, cardiac troponin, and interleukin-6 in patients with chest pain: the

- PROMISE trial results. *J Am Coll Cardiol Img.* 2022;15:1427–1438.
- 6.** Schmitz T, Harmel E, Heier M, Peters A, Linseisen J, Meisinger C. Inflammatory plasma proteins predict short-term mortality in patients with an acute myocardial infarction. *J Transl Med.* 2022;20:457.
 - 7.** Borrero-Sánchez G, Pacheco-Bouthillier A, Mendoza-Valdez L, Isordia-Salas I, Argüero-Sánchez R, Careaga Reyna G. Prognostic value of serum levels of interleukin-6 in patients with ST-segment elevation acute myocardial infarction. *Cir Cir.* 2010;78:25–30.
 - 8.** Mossmann M, Wainstein MV, Mariani S, et al. Increased serum IL-6 is predictive of long-term cardiovascular events in high-risk patients submitted to coronary angiography: an observational study. *Diabetol Metab Syndr.* 2022;14:125.
 - 9.** de Lemos JA, Morrow DA, Sabatine MS, et al. Association between plasma levels of monocyte chemoattractant protein-1 and long-term clinical outcomes in patients with acute coronary syndromes. *Circulation.* 2003;107:690–695.
 - 10.** Fanola CL, Morrow DA, Cannon CP, et al. Interleukin-6 and the risk of adverse outcomes in patients after an acute coronary syndrome: observations from the SOLID-TIMI 52 (Stabilization of Plaque Using Darapladib–Thrombolysis in Myocardial Infarction 52) trial. *J Am Heart Assoc Cardiovasc Cerebrovasc Dis.* 2017;6:e005637.
 - 11.** Broch K, Anstensrud AK, Woxholt S, et al. Randomized trial of interleukin-6 receptor inhibition in patients with acute ST-segment elevation myocardial infarction. *J Am Coll Cardiol.* 2021;77:1845–1855.
 - 12.** Mia MM, Cibi DM, Abdul Ghani SAB, et al. YAP/TAZ deficiency reprograms macrophage phenotype and improves infarct healing and cardiac function after myocardial infarction. *PLoS Biol.* 2020;18:e3000941.
 - 13.** Ghigo A, Franco I, Morello F, Hirsch E. Myocyte signalling in leucocyte recruitment to the heart. *Cardiovasc Res.* 2014;102:270–280.
 - 14.** Boyle AJ, Yeghiazarians Y, Shih H, et al. Myocardial production and release of MCP-1 and SDF-1 following myocardial infarction: differences between mice and man. *J Transl Med.* 2011;9:150.
 - 15.** Ancey C, Corbi P, Froger J, et al. Secretion of IL-6, IL-11 and LIF by human cardiomyocytes in primary culture. *Cytokine.* 2002;18:199–205.
 - 16.** Frangogiannis NG. Cardiac fibrosis. *Cardiovasc Res.* 2021;117:1450–1488.
 - 17.** Jones SA, Hunter CA. Is IL-6 a key cytokine target for therapy in COVID-19? *Nat Rev Immunol.* 2021;21:337–339.
 - 18.** Morimoto H, Takahashi M. Role of monocyte chemoattractant protein-1 in myocardial infarction. *Int J Biomed Sci IJBS.* 2007;3:159–167.
 - 19.** Liu Q, Ji S, Xia T, et al. MCP-1 priming enhanced the therapeutic effects of human mesenchymal stromal cells on contact hypersensitivity mice by activating the COX2/PGE2/STAT3 pathway. *Stem Cells Dev.* 2020;29:1073–1083.
 - 20.** Zegeye MM, Lindkvist M, Fälker K, et al. Activation of the JAK/STAT3 and PI3K/AKT pathways are crucial for IL-6 trans-signaling-mediated pro-inflammatory response in human vascular endothelial cells. *Cell Commun Signal CCS.* 2018;16:55.
 - 21.** Harhous Z, Booz GW, Ovize M, Bidaut G, Kurdi M. An update on the multifaceted roles of STAT3 in the heart. *Front Cardiovasc Med.* 2019;6:150.
 - 22.** Xia T, Zhang M, Lei W, et al. Advances in the role of STAT3 in macrophage polarization. *Front Immunol.* 2023;14:1160719.
 - 23.** Xu M, Li X, Song L. Baicalin regulates macrophages polarization and alleviates myocardial ischaemia/reperfusion injury via inhibiting JAK/STAT pathway. *Pharm Biol.* 2020;58:655–663.
 - 24.** Yan X, Anzai A, Katsumata Y, et al. Temporal dynamics of cardiac immune cell accumulation following acute myocardial infarction. *J Mol Cell Cardiol.* 2013;62:24–35.
 - 25.** Nahrendorf M, Swirski FK, Aikawa E, et al. The healing myocardium sequentially mobilizes two monocyte subsets with divergent and complementary functions. *J Exp Med.* 2007;204:3037–3047.
 - 26.** Yang M, Song L, Wang L, et al. Deficiency of GATA3-positive macrophages improves cardiac function following myocardial infarction or pressure overload hypertrophy. *J Am Coll Cardiol.* 2018;72:885–904.
 - 27.** Shiraishi M, Shintani Y, Shintani Y, et al. Alternatively activated macrophages determine repair of the infarcted adult murine heart. *J Clin Invest.* 2016;126:2151–2166.
 - 28.** Chatonnet T, Crola-Da-Silva C, Pillot B, et al. Inhibition of myocardial reperfusion injury by ischemic postconditioning requires sirtuin 3-mediated deacetylation of cyclophilin D. *J Mol Cell Cardiol.* 2015;84:61–69.
 - 29.** Harhous Z, Badawi S, Bona NG, et al. Critical appraisal of STAT3 pattern in adult cardiomyocytes. *J Mol Cell Cardiol.* 2019;131:91–100.
 - 30.** Kukielka GL, Smith CW, Manning AM, Youker KA, Michael LH, Entman ML. Induction of interleukin-6 synthesis in the myocardium. *Circulation.* 1995;92:1866–1875.
 - 31.** Ikonomidou I, Athanassopoulos G, Stamatelopoulos K, et al. Additive prognostic value of interleukin-6 at peak phase of dobutamine stress echocardiography in patients with coronary artery disease. A 6-year follow-up study. *Am Heart J.* 2008;156:269–276.
 - 32.** Deng MC, Erren M, Lütgen A, et al. Interleukin-6 correlates with hemodynamic impairment during dobutamine administration in chronic heart failure. *Int J Cardiol.* 1996;57:129–134.
 - 33.** James SK, Oldgren J, Lindbäck J, Johnston N, Siegbahn A, Wallentin L. An acute inflammatory reaction induced by myocardial damage is superimposed on a chronic inflammation in unstable coronary artery disease. *Am Heart J.* 2005;149:619–626.
 - 34.** Fisman EZ, Benderly M, Esper RJ, et al. Interleukin-6 and the risk of future cardiovascular events in patients with angina pectoris and/or healed myocardial infarction. *Am J Cardiol.* 2006;98:14–18.
 - 35.** Finkel MS, Hoffman RA, Shen L, Oddis CV, Simmons RL, Hattler BG. Interleukin-6 (IL-6) as a mediator of stunned myocardium. *Am J Cardiol.* 1993;71:1231–1232.
 - 36.** Fredj S, Bescond J, Louault C, Potreau D. Interactions between cardiac cells enhance cardiomyocyte hypertrophy and increase fibroblast proliferation. *J Cell Physiol.* 2005;202:891–899.
 - 37.** Lee T-M, Harn H-J, Chiu T-W, et al. Pre-conditioned adipose-derived stem cells ameliorate cardiac fibrosis by regulating macrophage polarization in infarcted rat hearts through the PI3K/STAT3 pathway. *Lab Investig J Tech Methods Pathol.* 2019;99:634–647.
 - 38.** Löhrner H, Pöling J, Gajiwada P, et al. Myocardial healing requires Reg3β-dependent accumulation of macrophages in the ischemic heart. *Nat Med.* 2015;21:353–362.
 - 39.** Shirakawa K, Endo J, Kataoka M, et al. IL (Interleukin)-10-STAT3-galectin-3 axis is essential for osteopontin-producing reparative macrophage polarization after myocardial infarction. *Circulation.* 2018;138:2021–2035.

KEY WORDS IL-6, inflammation, macrophages, MCP-1, myocardial infarction, STAT3

APPENDIX For an expanded Methods section and supplemental figures and tables, please see the online version of this paper.

EDITORIAL COMMENT

Dysregulation of IL-6/MCP-1/STAT3 Axis A Promising Therapeutic Postinfarction Inflammation Strategy?*



Andreas Mitsis, MD, MSc, PhD(c),^a Stergios Tzikas, MD, PhD,^b George Kassimis, MD, PhD^c

In recent decades, there has been a progressive understanding of the complex interplay between cytokines and chemokines released after an acute myocardial infarction (AMI) and their prognostic role during the post-myocardial infarction (MI) period.¹ The acknowledgment of inflammation's crucial role in prognosis has steered the scientific community's efforts toward identifying the optimal target, potentially through inhibition, to mitigate the extent of adverse outcomes resulting from inflammation after an AMI.

Various inflammatory pathways have been described to be used in the post-MI phase. From a pathophysiology viewpoint, these pathways can be separated into those acting via interleukin (IL)-6 and those operating independently of it.² IL-6 plays a pivotal role in the inflammatory signaling implicated in the initiation and progression of cardiovascular disease. IL-6 orchestrates the recruitment of immune cells to the damaged myocardium, while also stimulating the production of acute-phase proteins such as C-reactive protein, which act as inflammation markers. Furthermore, IL-6 influences the differentiation and activation of immune cells, thereby contributing to the inflammatory environment within the infarcted tissue. Increased levels of IL-6 are related to adverse clinical events following AMI,³ while IL-6 inhibition with tocilizumab has been

correlated with improved myocardial salvage index in patients with ST-segment elevation MI.⁴ Similarly, monocyte chemoattractant protein (MCP)-1, a chemokine released by cardiac fibroblasts, contributes to the recruitment of monocytes and macrophages to the site of injury and promote inflammation. Of note, an elevated baseline MCP-1 level is linked to traditional atherosclerosis risk factors and an elevated risk for death or MI, regardless of baseline variables.⁵

One of the downstream pathways through which IL-6/MCP-1 can act is the Janus kinase protein/signal transducer and activator of transcription 3 (STAT3) pathway. Janus kinase protein/STAT3 plays a multi-faceted role in AMI. Following an AMI, STAT3 activation has been associated with both cardioprotective and detrimental effects. On one hand, it can promote cell survival, reduce apoptosis, and facilitate cardiac repair and regeneration after injury. However, excessive STAT3 activation can contribute to adverse cardiac remodeling, fibrosis, and inflammation. The intricate balance of STAT3 signaling in AMI suggests its potential as a therapeutic target for modulating postinfarction outcomes.⁶

In a study reported in this issue of *JACC: Basic to Translational Science*, Paccalet et al⁷ examined the prognostic role of IL-6 and MCP-1 in patients with ST-segment elevation MI, showing that the levels of IL-6 and MCP-1 in the blood levels peak at 24 hours and positively correlate to worse outcomes, respectively. This knowledge might be already well recognized, but the investigators went a step further; using a murine model of MI and an in vitro coculture model, they proved that the production of IL-6/MCP-1 by the injured cardiomyocytes acts via the STAT3 pathway, and this signaling pathway is involved in worsening reperfusion injuries. The investigators found that the use of IL-6-neutralizing antibody led to a 32.1% reduction of anti-inflammatory macrophage recruitment by cardiac myocytes at 24 hours post-MI, without impairing proinflammatory macrophage

*Editorials published in *JACC: Basic to Translational Science* reflect the views of the authors and do not necessarily represent the views of *JACC: Basic to Translational Science* or the American College of Cardiology.

From the ^aCardiology Department, Nicosia General Hospital, Nicosia, Cyprus; ^bThird Department of Cardiology, Aristotle University of Thessaloniki, Thessaloniki, Greece; and the ^cSecond Department of Cardiology, Aristotle University of Thessaloniki, Thessaloniki, Greece. The authors attest they are in compliance with human studies committees and animal welfare regulations of the authors' institutions and Food and Drug Administration guidelines, including patient consent where appropriate. For more information, visit the [Author Center](#).

recruitment. Likewise, the MCP-1-neutralizing antibody led to a 44.2% reduction of anti-inflammatory macrophages ($P = 0.002$) and a 29.8% reduction of proinflammatory macrophages ($P = 0.005$). Furthermore, the inhibition of the STAT3 signaling pathways by the STATTIC antagonist reduced anti-inflammatory macrophage recruitment at 24 hours post-MI ($P = 0.044$), whereas it had no significant effect on proinflammatory macrophage recruitment.

The investigators conclude that these results suggest that IL-6- and MCP-1-mediated anti-inflammatory macrophage recruitment relies mostly on STAT3-dependent pathways. Finally, they report that reducing the recruitment and activation of anti-inflammatory macrophages at the onset of reperfusion, either by treatment with STATTIC or with the combination of neutralizing antibodies, the severity of the infarction decreases ($P = 0.0061$ and $P = 0.0081$, respectively).

The major advantage of this research is the use of the translational nature of research, merging pre-clinical and clinical studies. The investigators show that this is probably one of the ways to improve the translational aspect of research, as understanding the underlying mechanism using a preclinical model could massively accelerate therapeutic research. An additional benefit of this study compared with previous research is the examination of the secretion kinetics of the 2 cytokines, IL-6 and MCP-1, at 5 different sampling times, with the last one at 1 month, which allowed temporal distance from the acute event and a better understanding of these cytokines' secretion kinetics. Besides, the study demonstrates that the combination of IL-6 and MCP-1 has a more robust predictive power than either cytokine alone. A limitation of the study is the absence of a

control group, while the complex phenotype of anti-inflammatory macrophage subtypes may require more refined characterization in future studies.

Finally, the big question that arises with this study is again the complexity of targeting inflammation in cardiovascular diseases. The study results challenge the traditional belief that anti-inflammatory macrophages are inherently advantageous, while proinflammatory ones are harmful, showing the dynamic shift in the role of the anti-inflammatory macrophages whereby their function during the early reperfusion phase differs from their role during the subsequent remodeling phase.

Undoubtedly, future areas of development remain, and further investigations are necessary to address unresolved inquiries. However, a significant conclusion from this study is that effectively targeting molecular inflammation mediators demands a thorough comprehension of the dynamic inflammatory process and the involvement of these mediators in its various stages. Despite significant advances, our understanding of cardiac immunity remains incomplete, highlighting a significant gap in achieving safe and effective treatments for patients with heart inflammation.

FUNDING SUPPORT AND AUTHOR DISCLOSURES

The authors have reported that they have no relationships relevant to the contents of this paper to disclose.

ADDRESS FOR CORRESPONDENCE: Dr Andreas Mitsis, Nicosia General Hospital, Cardiology Department, Limassol Old Road No. 215, 2029, Nicosia, Cyprus. E-mail: andymits7@gmail.com.

REFERENCES

1. Mitsis A, Kadoglou NPE, Lambadiari V, et al. Prognostic role of inflammatory cytokines and novel adipokines in acute myocardial infarction: an updated and comprehensive review. *Cytokine*. 2022;153:155848.
2. Ridker PM, Lüscher TF. Anti-inflammatory therapies for cardiovascular disease. *Eur Heart J*. 2014;35:1782-1791.
3. Tøllefsen IM, Shetelig C, Seljeflot I, Eritsland J, Hoffmann P, Andersen GØ. High levels of interleukin-6 are associated with final infarct size and adverse clinical events in patients with STEMI. *Open Heart*. 2021;8:e001869.
4. Broch K, Anstensrud AK, Woxholt S, et al. Randomized trial of interleukin-6 receptor inhibition in patients with acute ST-segment elevation myocardial infarction. *J Am Coll Cardiol*. 2021;77:1845-1855.
5. de Lemos JA, Morrow DA, Sabatine MS, et al. Association between plasma levels of monocyte chemoattractant protein-1 and long-term clinical outcomes in patients with acute coronary syndromes. *Circulation*. 2003;107:690-695.
6. Zhang Q, Wang L, Wang S, et al. Signaling pathways and targeted therapy for myocardial infarction. *Signal Transduct Target Ther*. 2022;7:78.
7. Paccalet A, Badawi S, Pillot B, et al. deleterious anti-inflammatory macrophage recruitment in early post-infarction phase: unraveling the IL-6/MCP-1/STAT3 axis. *J Am Coll Cardiol Basic Trans Science*. 2024;9(5):593-604.

KEY WORDS IL-6, inflammation, macrophages, MCP-1, myocardial infarction, STAT3

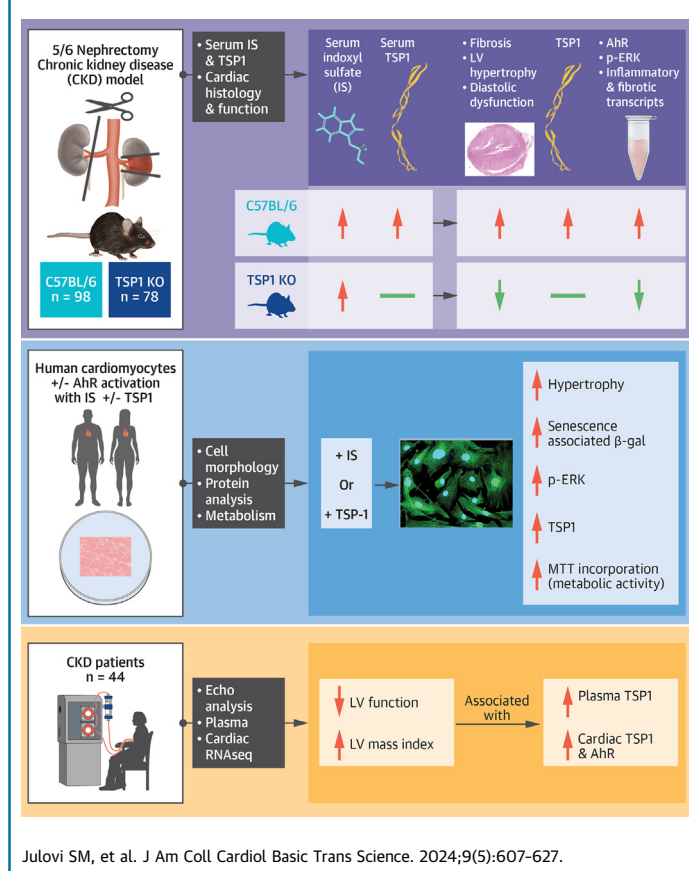
ORIGINAL RESEARCH - PRECLINICAL



Thrombospondin-1 Drives Cardiac Remodeling in Chronic Kidney Disease

Sohel M. Julovi, MBBS, PhD,^{a,b} Katie Trinh, BSc(Adv), MBBS,^a Harry Robertson, BMEDSc(HONS-I),^{a,b,c} Cuicui Xu, BSc, PhD,^a Nikita Minhas, PhD,^a Seethalakshmi Viswanathan, MBBS,^{b,d} Ellis Patrick, BSc(HONS), PhD,^{a,c,e,f} John D. Horowitz, MBBS, PhD,^{g,h,i} Daniel N. Meijles, PhD,^g Natasha M. Rogers, MBBS(HONS), PhD^{a,b,j}

VISUAL ABSTRACT



HIGHLIGHTS

- CRS type 4 is characterized by CKD, cardiac fibrosis, LVH, and diastolic dysfunction, which can lead to HF.
- The uremic toxin IS disrupts cellular and molecular pathways in both CKD and CVDs.
- The matricellular protein TSP1 is known to be elevated in patients with CKD and the disruption of TSP1 signaling provides cardioprotection in preclinical studies.
- For the first time, this study has identified the role of TSP1 as a mediator of cardiac fibrosis, LVH, and diastolic dysfunction in CKD, as well as its link to IS.
- Further studies are required in large clinical studies to confirm the translational role of TSP1 in patients with CKD.

From the ^aKidney Injury Group, Centre for Transplant and Renal Research, Westmead Institute for Medical Research, Westmead, New South Wales, Australia; ^bFaculty of Medicine and Health, The University of Sydney, Camperdown, New South Wales, Australia; ^cSydney Precision Data Science Centre, University of Sydney, New South Wales, Australia; ^dTissue Pathology and Diagnostic Oncology, Institute of Clinical Pathology and Medical Research, Westmead Hospital, Westmead, New South Wales, Australia; ^eSchool of Mathematics, University of Sydney, New South Wales, Australia; ^fLaboratory of Data Discovery for Health Limited (D24H), Science Park, Hong Kong Special Administrative Region, China; ^gMolecular and Clinical Sciences Research Institute, St George's University of London, London, United Kingdom; ^hCardiovascular Pathophysiology and Therapeutics Research Group, Basil Hetzel Institute, Woodville, South Australia, Australia; ⁱDepartment of Medicine, The University of Adelaide, Adelaide, South Australia, Australia; and the ^jRenal and Transplantation Unit, Westmead Hospital, New South Wales, Australia.

ABBREVIATIONS AND ACRONYMS

- 5/6Nx** = 5/6 nephrectomy
AhR = aryl hydrocarbon receptor
CKD = chronic kidney disease
CRS = cardiorenal syndrome
CVD = cardiovascular disease
DEG = differentially expressed gene
EF = ejection fraction
ERK = extracellular signal-related protein kinase
HF = heart failure
HFpEF = heart failure with preserved ejection fraction
HCM = human cardiomyocyte
IS = indoxyl sulfate
LV = left ventricular
LVH = left ventricular hypertrophy
MAPK = mitogen activated protein kinase
MHC = myosin heavy chain
MTT = 3-(4,5-dimethylthiazol-2-yl)-2,5-diphenyl-2H-tetrazolium bromide
p = phosphorylated
p53 = tumor protein p53
SASP = senescence-associated secretory phenotype
siRNA = small interfering RNA
TSP1 = thrombospondin 1
TSP1Ab = anti-thrombospondin 1 antibody
TSP1KO = thrombospondin 1 knockout
WT = wild type

SUMMARY

Patients with chronic kidney disease (CKD) face a high risk of cardiovascular disease. Previous studies reported that endogenous thrombospondin 1 (TSP1) involves right ventricular remodeling and dysfunction. Here we show that a murine model of CKD increased myocardial TSP1 expression and produced left ventricular hypertrophy, fibrosis, and dysfunction. TSP1 knockout mice were protected from these features. In vitro, indoxyl sulfate is driving deleterious changes in cardiomyocyte through the TSP1. In patients with CKD, TSP1 and aryl hydrocarbon receptor were both differentially expressed in the myocardium. Our findings summon large clinical studies to confirm the translational role of TSP1 in patients with CKD. (J Am Coll Cardiol Basic Trans Science 2024;9:607–627) © 2024 The Authors. Published by Elsevier on behalf of the American College of Cardiology Foundation. This is an open access article under the CC BY-NC-ND license (<http://creativecommons.org/licenses/by-nc-nd/4.0/>).

Chronic kidney disease (CKD) is a global public health problem that significantly shortens lifespan primarily by increasing the risk of cardiovascular disease (CVD),¹ particularly manifesting as myocardial ischemia and/or heart failure (HF). Patients with CKD are more likely to die from CVD than progress to end-stage kidney disease, with 50% of deaths due to cardiac events.² CKD resulting in chronic HF is known as cardiorenal syndrome (CRS) type 4³ and has been increasingly identified as a marker of higher morbidity and mortality.^{1,4} Left ventricular hypertrophy (LVH) and diastolic dysfunction are the major factors contributing to development of heart failure with preserved ejection fraction (HFpEF) and sudden cardiac death through ischemia and arrhythmia.⁵ A linear relationship between worsening glomerular filtration rate and LV function confers poor clinical outcomes and the highest mortality.^{6,7}

The molecular pathways that coordinate pathophysiological changes and development of LVH continue to expand and involve mitogen-associated protein kinases ([MAPKs], especially extracellular signaling-related kinase [ERK] 1/2),⁸ oxidative stress, and the aryl hydrocarbon receptor (AhR).⁹ More recently, cardiac stress has been shown to initiate metabolic alterations in cardiomyocytes that promote senescence, leading to a functional decline that includes hypertrophic growth, β-galactosidase expression, and secretion of proinflammatory cytokines (senescence-associated

secretory phenotype [SASP]).¹⁰ A growing body of evidence indicates that uremic toxins represent important, nontraditional cardiovascular risk factors in CKD because they have demonstrable cytotoxic effects,¹¹ are associated with cardiovascular mortality,¹² and fail to be effectively cleared by dialysis, particularly protein-bound subgroups such as indoxyl sulfate (IS).¹³ IS is the best characterized toxin, derived from dietary intake of the essential amino acid tryptophan and converted to indole by the intestinal microbiome. In the absence of effective tubular secretion, serum concentrations are >50× higher in CKD compared to healthy control subjects¹² and are associated with LV dysfunction and cardiovascular mortality.^{12,14} Regression of LVH after kidney transplantation and normalization of cardiac parameters suggests that CKD-specific uremia is a primary driver of cardiac pathology.¹⁵ Thrombospondin 1 (TSP1) is a well-characterized extracellular matrix glycoprotein secreted by cells. However, rather than providing structural integrity, it preferentially regulates signaling pathways to alter cell adhesion, proliferation, and viability in response to injury.¹⁶ The cardiac extracellular matrix provides scaffolding for cardiomyocyte attachment, ventricular geometry, and function, which regulates diastolic performance and inflammation.¹⁷ We recently reported induction of right ventricular TSP1 expression in an animal model of pulmonary hypertension and disruption of TSP1 signaling provided protection.¹⁸

Plasma TSP1 is elevated in patients with CKD;¹⁹ however, the protein did not appear to be derived from fibrotic renal parenchyma. Further work has confirmed high plasma TSP1 concentrations in

The authors attest they are in compliance with human studies committees and animal welfare regulations of the authors' institutions and Food and Drug Administration guidelines, including patient consent where appropriate. For more information, visit the [Author Center](#).

dialysis-dependent patients with CRS compared to those without, and levels were predictive of cardiovascular mortality.¹⁴ However, little is known about the specific effects of TSP1 on the LV or cardiomyocytes in the context of CKD. We now implicate TSP1 in a mouse model of CRS, where the hypertrophied LV is a significant source of TSP1 expression, accompanied by oxidative stress, fibrosis, and SASP. These findings were mitigated in thrombospondin-1 knockout (TSP1KO) mice. In vitro we demonstrate a direct relationship of IS, induction of TSP1, and AhR activation in cardiomyocytes that drives hypertrophy and SASP, highlighting this pathway as a driver of uremic cardiomyopathy.

METHODS

ANIMALS. TSP1KO (B6.129S2-^{Thbs1tm1Hyn/J}) mice on a C57BL/6J background (back-crossed for 15 generations) were originally purchased from the Jackson Laboratory and were maintained by Australian Bio-Resources. Age-matched (6–8 weeks) male littermate control (wild-type [WT]) and (homozygous) TSP1KO mice were transferred to Westmead Institute for Medical Research, housed, and acclimatized for 2 weeks in the biological facility under a 12-hour light/dark cycle with access to standard chow and water ad libitum under approved protocols (no. 4281 Western Sydney Local Health District and no. 1594 University of Sydney). All animal studies were performed in accordance with the Australian code for the care and use of animals for scientific purposes developed by the National Health and Medical Research Council.

CRS MODEL USING 5/6NX. In this study, 156 mice were used, including 98 WT mice and 58 TSP1KO mice (Supplemental Table 1). Age-matched (8- to 10-week-old) male mice were randomly assigned to sham and 5/6 nephrectomy (5/6Nx) groups. The 5/6Nx model is characterized by high mortality.²⁰ We altered the conventional method of nephrectomy,²¹ which significantly reduced mortality to 10% to ~15% (Supplemental Figure 1A). Animals were anesthetized with isoflurane and oxygen, the left kidney exposed and exteriorized through a left flank subcostal incision, and connective tissue and adrenal gland separated by using normal saline-soaked cotton bud instead of iris scissors to prevent the injury to renal pedicle.²¹ The upper and lower renal poles were removed using iris scissors. Hemostasis was achieved with direct pressure, the kidney returned to the abdomen, and the incision closed with 5/0 monofilament nylon. At day 8 following the initial surgery, a right total nephrectomy was performed through a separate flank incision. In sham-operated mice, the

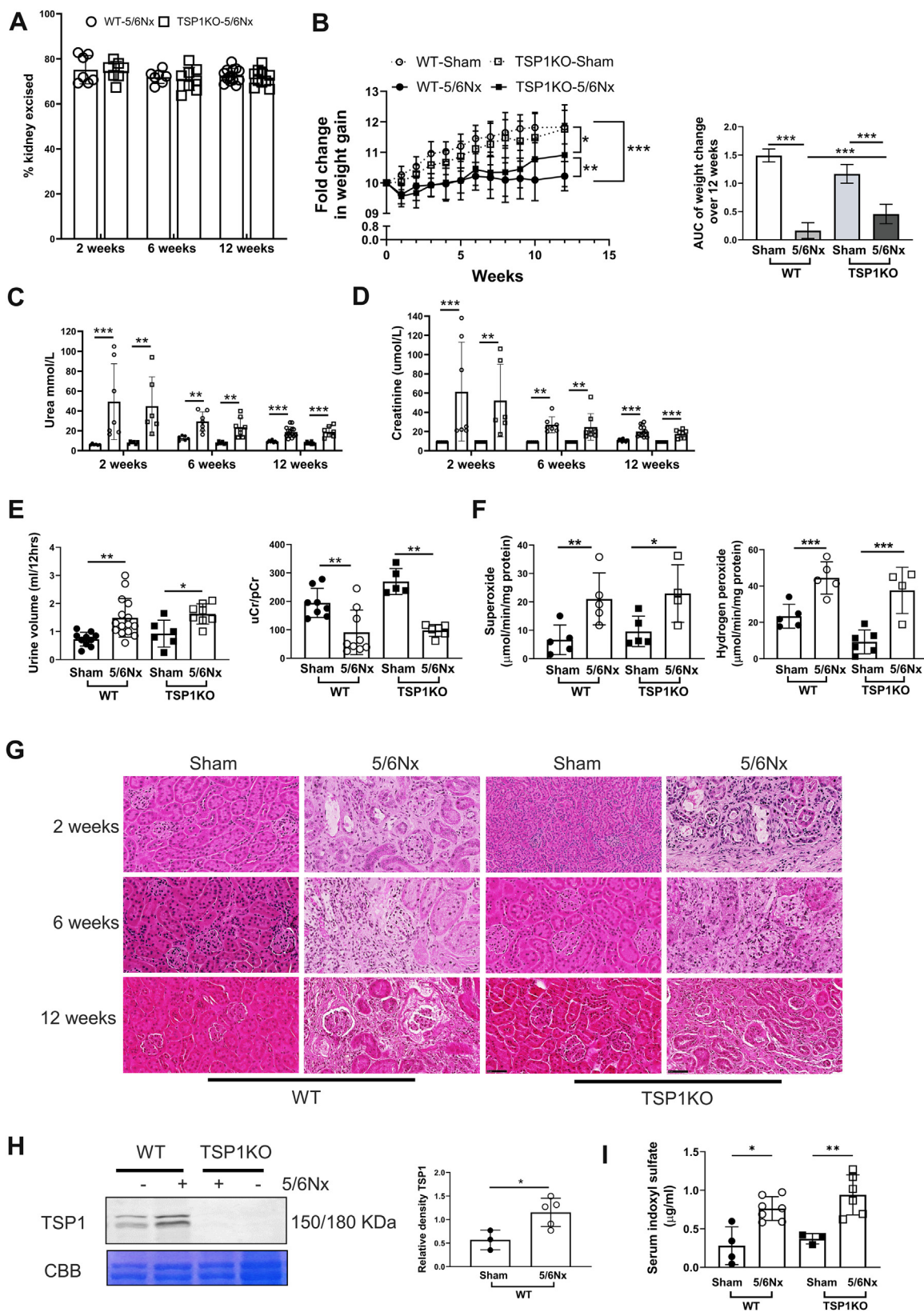
kidneys were exposed in 2 separate surgeries but not resected, as described previously.^{19,21} Among 108 mice receiving 5/6Nx, 25 were euthanized (mostly on the second postoperative day) owing to illness and/or >25% body weight loss and were excluded from analysis (Supplemental Table 1). Additional data were also excluded in some experiments because of histological artifact, poor resolution of echocardiography images, or an insufficient quantity of serum/urine specimens collected.

Body weight and blood pressure using the tail-cuff plethysmography (CODA machine, Kent Scientific Corporation) were measured weekly.²¹ In some experiments, mice were euthanized at week 2 or 6, and tissues were harvested as illustrated in the study design (Supplemental Figure 1B). Metabolic caging was performed at week 10 before transferring to Sydney Imaging Facility at the Charles Perkins Centre for an additional 2 weeks of acclimatization and echocardiography. At week 12, echocardiography was performed (Vevo 2100 Echocardiography Imaging System, VisualSonics), and then mice were euthanized. Heart and wet lung weights were recorded along with tibial length. Organs, plasma, and urine were then processed for analysis and stored at -80 °C. The estimated percentage of removed kidney was calculated by following formula: percentage of removed kidney = weight of excised kidneys (left excised kidney + right kidney) × 100 / total weight of 2 kidneys (left excised + left remnant + right kidney), as described in our recent report.²¹

ASSESSMENT OF RENAL FUNCTION AND PROTEINURIA. Blood urea nitrogen and creatinine, alkaline phosphatase, serum calcium, urinary protein, and creatinine were determined using the Siemens Atellica System (Westmead Hospital).

ENZYME-LINKED IMMUNOSORBENT ASSAY. Mouse plasma IS was measured by enzyme-linked immunosorbent assay according to manufacturer protocol (#MBS720905, MyBioSource, Inc). Briefly, kit contents and samples were brought to room temperature. One hundred microliters (100 µL) of IS standards or samples were added to the enzyme-linked immunosorbent assay plate in duplicate and incubated at 37 °C for 1 hour. The plate was washed 5× with buffer, followed by the addition of conjugate and incubation at 37 °C for 20 minutes. Following addition of stop solution, the plate was read at 450 nm.

HIGH-FREQUENCY ULTRASOUND ECHOCARDIOGRAPHY. Animals were assessed at week 12 under general anesthesia induced with isoflurane and O₂ titrated to effect. Animals were placed supine on an adjustable stage with the tail of the animal facing toward

FIGURE 1 Development of CKD in WT and TSP1KO Mice

Continued on the next page

the operator and limbs secured to electrocardiogram probes. The Vevo2100 ultrasound system (VisualSonics) and linear transducer (MS550D, MicroScan, 40 MHz, VisualSonics) were used to acquire LV parasternal long-axis B-mode/echocardiogram-gated kilohertz visualization images and short-axis mid-papillary echocardiogram-gated kilohertz visualization/M-mode images. Pulse-wave and tissue Doppler images were obtained in apical 4-chamber view using a linear transducer 57 MHz (VevoF2, VisualSonics) as previously described.²² All images were acquired by an operator blinded to the treatment group. Short-axis mid-papillary M-mode analyses (Supplemental Figure 1C) were carried by selecting autoLV from 3 cycles of each cine loop. Pulse-wave and tissue Doppler images (Supplemental Figures 1D and 1E) analyses were carried out to measure diastolic (dys)function. VevoLAB software (VisualSonics) was used for data analysis, and average data from 3 cine loops are presented for each mouse.

HEART HISTOPATHOLOGY. Formalin-fixed kidney and heart tissue embedded in paraffin were sectioned at 4 µm and stained with hematoxylin and eosin or picrosirius red using standard methods.^{19,21} Slides were viewed under brightfield conditions. Picosirius red staining area and intensity were measured and quantified using ImageJ (National Institutes of Health) as previously described.¹⁹ Picosirius red stained images (magnified 80×) were also used to measure the cross-sectional area of cardiomyocytes using ImageJ. Assessors were blinded to treatment groups.

CELL CULTURE. Human primary cardiomyocytes (PromoCell) were subcultured according to manufacturer's instructions. Cells were used at passages 3-6. Cells at ~70% confluence in 6-well plates were treated with recombinant human TSP1 (Athens Research and Technology), IS (Sigma Aldrich) for 24 hours. In some experiments, cells were pretreated with anti-TSP1 (#ab85762) and sarcomeric (#ab68167) antibodies were from Abcam at 1 µg/mL or mouse

immunoglobulin G₁ isotype control (#02-6100, Invitrogen) prior to treatment. For small interfering RNA (siRNA) experiments, cells were plated in media without antibiotics and transfection performed at 50%-60% confluence using Lipofectamine 2000 and TSP1 or control siRNA (Invitrogen) in Opti-MEM (Thermo Fisher Scientific) according to the manufacturer's instructions. Cells were exposed to siRNA for 48 hours prior to experimental use.

Human aortic vascular smooth muscle cells (Clonetech, Lonza) were used in subsequent experimental work owing to the unavailability of human cardiomyocytes (HCMs) in Australia. Human aortic vascular smooth muscle cells were subcultured according to manufacturer's instructions to detect the involvement of AhR in IS-induced TSP1 expression. Cells were used among passages 3-6. For this experiment, cells were pretreated with AhR inhibitor (StemRegenin 1, ab142174, Abcam) (10 µmol/L) for 2 hours and then treated with IS (10 µmol/L) for 24 hours.

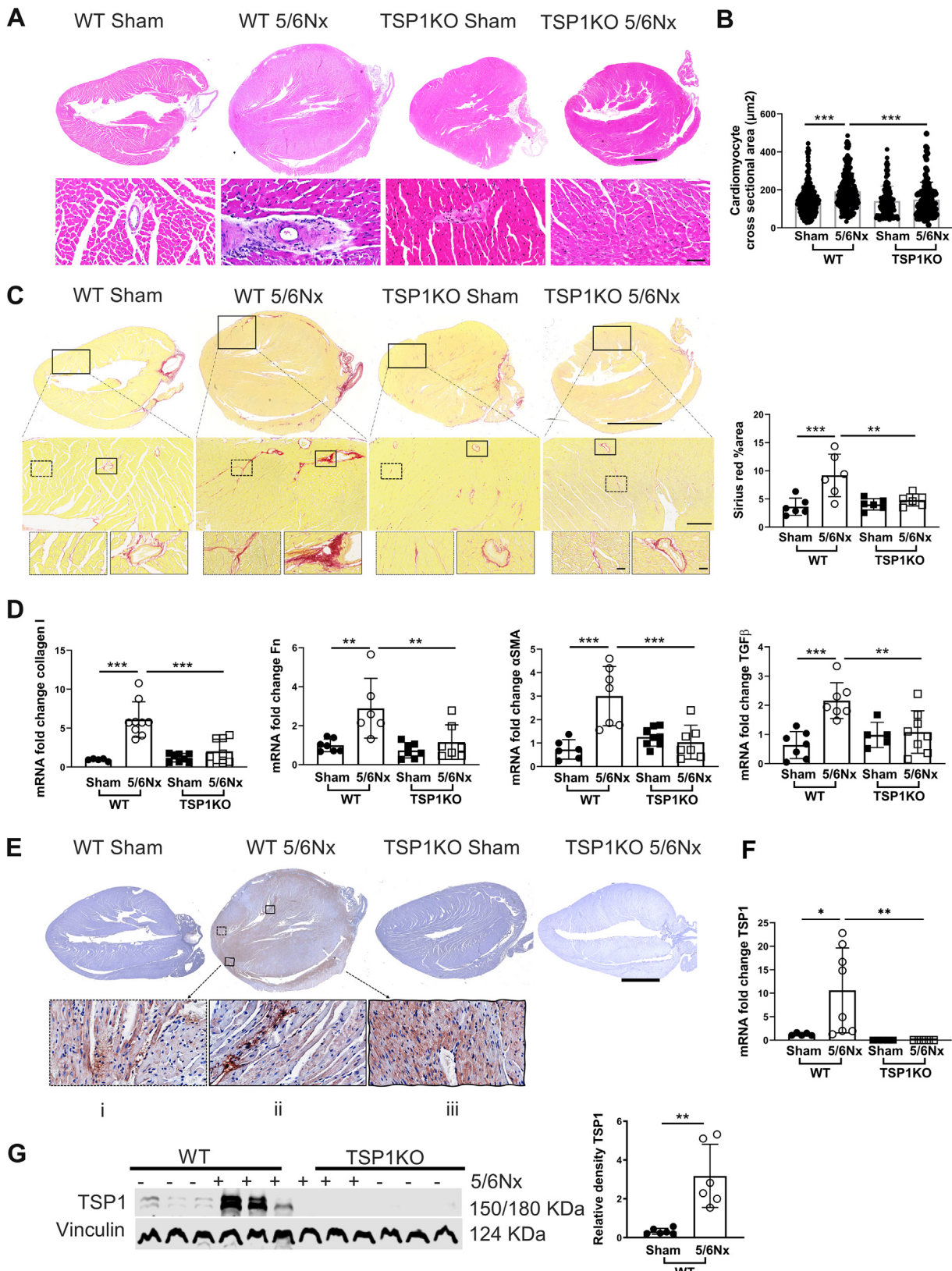
Human cardiac fibroblasts (Lonza) were subcultured according to manufacturer's instructions. Cells were used among passages 4-8. Cells at ~70% confluence were treated with recombinant human TSP1 (Athens Research and Technology) for 24 hours.

Cell viability and senescence assays. Cell metabolic activity was measured using a XTT Cell Viability Kit (Cell Signaling Technology), and senescence was assessed with a Mammalian β-Galactosidase Assay Kit (Thermo Fisher Scientific). Briefly, 10⁴ cells/well were seeded into a 96-well microplate. Serum-starved cells were treated with TSP1 (0.2-10.0 nmol/L) or IS (1-500 µmol/L) for 48 hours. Cell proliferation and senescence were determined at the 450 nm and 405 nm, respectively, using Proteomics SpectraMax iD5 Plate Reader (VWR International).

Cells were stained using a Senescence-β-Galactosidase Staining Kit (Cell Signaling Technology) according to manufacturer's instructions. Samples were then washed in phosphate-buffered saline, and images were captured at random using a light

FIGURE 1 Continued

Wild-type (WT) and thrombospondin-1 knockout (TSP1KO) mice were subjected to sham surgery or 5/6-nephrectomy (5/6Nx). (A) Percentage of kidney excised following 5/6Nx at 2, 6, and 12 weeks ($n = 7-13$). (B) Fold change in body weight over 12 weeks ($n = 6-21$). Serum urea (C) and serum creatinine (D) at 2, 6, and 12 weeks ($n = 6-14$), and (E) urine volume and urinary/plasma creatinine ratios (uCr/pCr) at 10 weeks ($n = 5-15$). (F) Detection of superoxide and H₂O₂ moieties in WT and TSP1KO kidney homogenates ($n = 4-6$). (G) Representative hematoxylin and eosin-stained kidney histology (bar = 50 µm). (H) Expression of plasma TSP1 by Western blotting in sham-operated and 5/6Nx mice. The band density of the protein is normalized with Coomassie brilliant blue (CBB) and combined densitometries are shown ($n = 3-5$). (I) Serum indoxyl sulfate at week 12 was detected by enzyme-linked immunosorbent assay ($n = 3-6$). All data are mean ± SD. * $P < 0.05$, ** $P < 0.01$, and *** $P < 0.001$ by 2-way analysis of variance with Tukey post hoc test (A to F [at each time point], I), and the representing graph (H) was analyzed by unpaired Student's t-test. AUC = area under the curve; CKD = chronic kidney disease.

FIGURE 2 CKD in Mice Induces TSP1-dependent LVH

Continued on the next page

microscope (CKX41, Olympus). At least 5 images were captured from each well and blindly assessed for senescence-associated β -galactosidase (blue)-positive cells.

WESTERN BLOTTING. Tissue or cells were homogenized in cold radio immunoprecipitation assay buffer (Cell Signaling Technology) that contained protease inhibitor cocktail (Sigma-Aldrich) and phosphatase inhibitor cocktail (Roche Applied Science). Protein was quantified using a DC assay (BioRad), resolved by sodium dodecyl sulfate polyacrylamide gel electrophoresis and then transferred onto nitrocellulose membranes (BioRad). Blots were probed at 4 °C overnight with the following primary antibodies: phospho-p44/42 MAPK (pERK1/2) (#4370), p44/42 MAPK (ERK1/2) (#9107), tumor protein p53 (p53) (#2524), p21^{Waf1/Cip1} (#64016), p27^{Kip1} (#3698), AhR (#83200), vinculin (#13901), and β -actin (#4970) all from Cell Signaling Technology. TSP1 (#ab85762), sarcomeric α -actinin (#ab68167) were from Abcam. Atrial natriuretic peptide (#PA5-29559), brain natriuretic protein (#PA5-98294), and cardiac myosin heavy chain (#MA1-26180) were from Invitrogen. Myosin heavy chain (MHC)- β (#sc-53089) was from Santa Cruz Biotechnology. Protein was visualized on an Odyssey LCx Imaging System (Licor). Expression was normalized to the levels of total protein loading or housekeeping gene. Protein band intensity was evaluated using ImageJ.

RNA EXTRACTION AND QUANTIFICATION BY REAL-TIME QUANTITATIVE POLYMERASE CHAIN REACTION.

RNA was extracted using ISOLATE-II RNA MiniKits (Bioline) with on-column DNase treatment. RNA was quantified using a Nanodrop (BioTek) and reverse-transcribed using a SensiFAST cDNA synthesis kit (Bioline). Complementary DNA was amplified in triplicate with commercially available gene-specific primers (Invitrogen) using a CFX384 PCR machine (BioRad). Thermal cycling conditions

were 95 °C for 2 minutes, followed by 40 cycles of 95 °C for 10 seconds and 60 °C for 30 seconds. Data were analyzed using the $\Delta\Delta Ct$ (cycle threshold) method with expression normalized to the house-keeping gene and sham-operated WT animals/control cells used as referent control animals/cells.

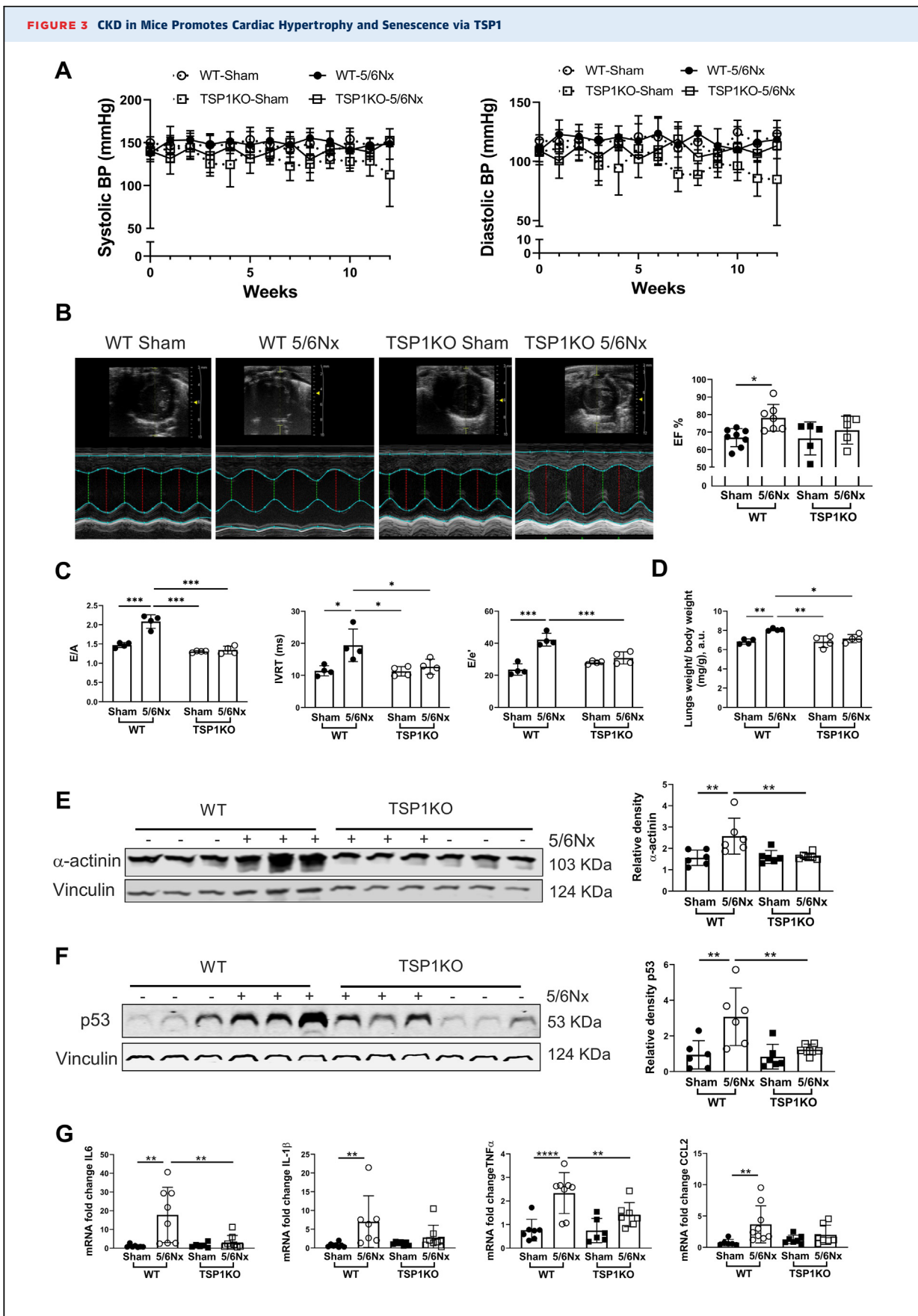
IMMUNOHISTOCHEMISTRY. Immunostaining was performed as previously described.^{19,21} Four-micrometer sections of paraffin-embedded mouse heart tissues were incubated with TSP1 (Abcam), AhR (#LS-B4900, LSBio) or isotype-matched immunoglobulin G. For immunodetection, Dako EnVision+ System-HRP labeled polymer detection kit (Dako) was used with ImmPACT NovaRED Peroxidase (HRP) Substrate (Vector Laboratories) and counterstained by Mayer hematoxylin and Scott bluing solution. After mounting, slides were viewed by Nano Zoomer (Hamamatsu). All samples were stained, imaged, and analyzed simultaneously to exclude between-run variability. AhR staining intensity was calculated from the 5 randomly selected areas at 10 \times magnification, as published previously.²³

REACTIVE OXYGEN SPECIES CHARACTERIZATION.

Measurement of superoxide ($O_2^{•-}$) and H_2O_2 was performed using cytochrome c and Amplex Red assays, respectively, as published previously.^{24,25} Tissues were homogenized in lysis buffer and centrifuged at 1,000g; membranes were resuspended in lysis buffer; and protein concentration was measured using the Bradford microplate method. $O_2^{•-}$ production was initiated by the addition of 180 μ mol/L nicotinamide adenine dinucleotide phosphate hydrogen and was calculated from the initial linear rate of superoxide dismutase (150 U/mL)-inhibitable cytochrome c reduction quantified at 550 nm and using an extinction coefficient of 21.1 mmol/L $^{-1}$ cm $^{-1}$ (BioTek Synergy 4 Hybrid Multi-Mode Microplate Reader). To detect H_2O_2 , protein was added to the wells containing the assay

FIGURE 2 Continued

(A) Representative left ventricle hematoxylin and eosin-stained histology (bars = 1 mm [top panel] and 50 μ m [bottom panel]) and (B) cross-sectional surface area of individual cardiomyocytes. Measurements are from randomly chosen cells (n = 310 WT-sham, 279 WT-5/6Nx, 298 TSP1KO-sham, 214 TSP1KO-Nx) from 4 mice. Regions of interest at the margin of images or incomplete regions of interest were excluded from the counting. (C) Representative left ventricular picrosirius red staining with accompanying histogram of staining area from 5 independent fields of view (n = 6) (bars = 2.5 mm [top], 250 μ m [middle], and 25 μ m [bottom]). (D) Left ventricular messenger RNA (mRNA) expression of fibrosis markers collagen 1, fibronectin (Fn), α -smooth muscle actin (SMA), and TGF- β by quantitative polymerase chain reaction, normalized to HPRT1 with WT sham-operated left ventricle set as the referent control (n = 6-7). (E) Representative left ventricular immunohistochemical staining for TSP1 (bar = 2.5 mm) with high magnification areas (bars = 50 μ m): (i) injured area, (ii) interstitial space, and (iii) cardiomyocytes. (F) Left ventricular mRNA expression of TSP1 by quantitative polymerase chain reaction, normalized to HPRT1 with WT sham-operated left ventricle set as the referent control (n = 5-8). (G) Left ventricular homogenates were analyzed for TSP1 expression by Western blotting. Band density was normalized with vinculin and combined densitometries are shown (n = 6). All data are mean \pm SD; *P < 0.05, **P < 0.01, and ***P < 0.001 by 2-way analysis of variance with Tukey post hoc test (A to D) or unpaired Student's t-test (G). HPRT1 = hypoxanthine phosphoribosyltransferase 1; LVH = left ventricular hypertrophy; other abbreviations as in Figure 1.



Continued on the next page

mixture, and the reaction was initiated by the addition of 36 μmol/L nicotinamide adenine dinucleotide phosphate hydrogen. Fluorescence was detected using the BioTek Synergy 4 Hybrid Multi-Mode Microplate Reader with a 530/25 excitation and a 590/35 emission filter. The reaction was monitored for 30 minutes at 25 °C. To confirm the H₂O₂ signal, catalase (300 U/mL) was added in parallel wells, and the catalase-inhibitable rate of H₂O₂ production was quantified from a H₂O₂ standard curve.

HUMAN DATA. The raw expression data were accessed from the Gene Expression Omnibus using the accession code GSE160145 and imported into R version 4.2.0 (R Foundation).²⁶ The raw reads were normalized using DESeq's Median of Ratios method and variance stabilization transformation performed using the DESeq2 package in R. Differential genes were identified between patients listed with CKD and healthy patients. Genes with a log-fold change >2, and an adjusted *P* < 0.05 using the Benjamini-Hochberg false discovery rate were determined to be differentially expressed. A Wilcoxon rank-sum test was used to identify enriched Kyoto Encyclopedia of Genes and Genomes pathways²⁷ between healthy and patients with CKD. Gene Set Enrichment Analyses was executed using the clusterProfiler package in R²⁸ on the list of differentially expressed genes (DEGs) between healthy and patients with CKD using Gene Ontology pathway database.²⁹ Data used for this study are publicly available using the Gene Expression Omnibus accession code listed. The code used to generate analysis and figures is available online.³⁰ No other clinical data or demographics were available for this patient cohort.

HUMAN PLASMA TSP1 AND ECHOCARDIOGRAPHY CORRELATION. The study was approved by the Human Research Ethics Committee of Western Sydney Local Health District (HREC LNR/12/WMEAD/114 and LNRSSA/12/WMEAD/117 [3503]). In brief, patients were recruited from nephrology outpatient clinics at Westmead Hospital and did not have an intercurrent

illness. All subjects were previously recruited, and their plasma TSP1 levels were measured and published.¹⁹ Patients with echocardiography studies within 3 months of venupuncture and not associated with acute illness or cardiovascular deterioration were used for analysis.

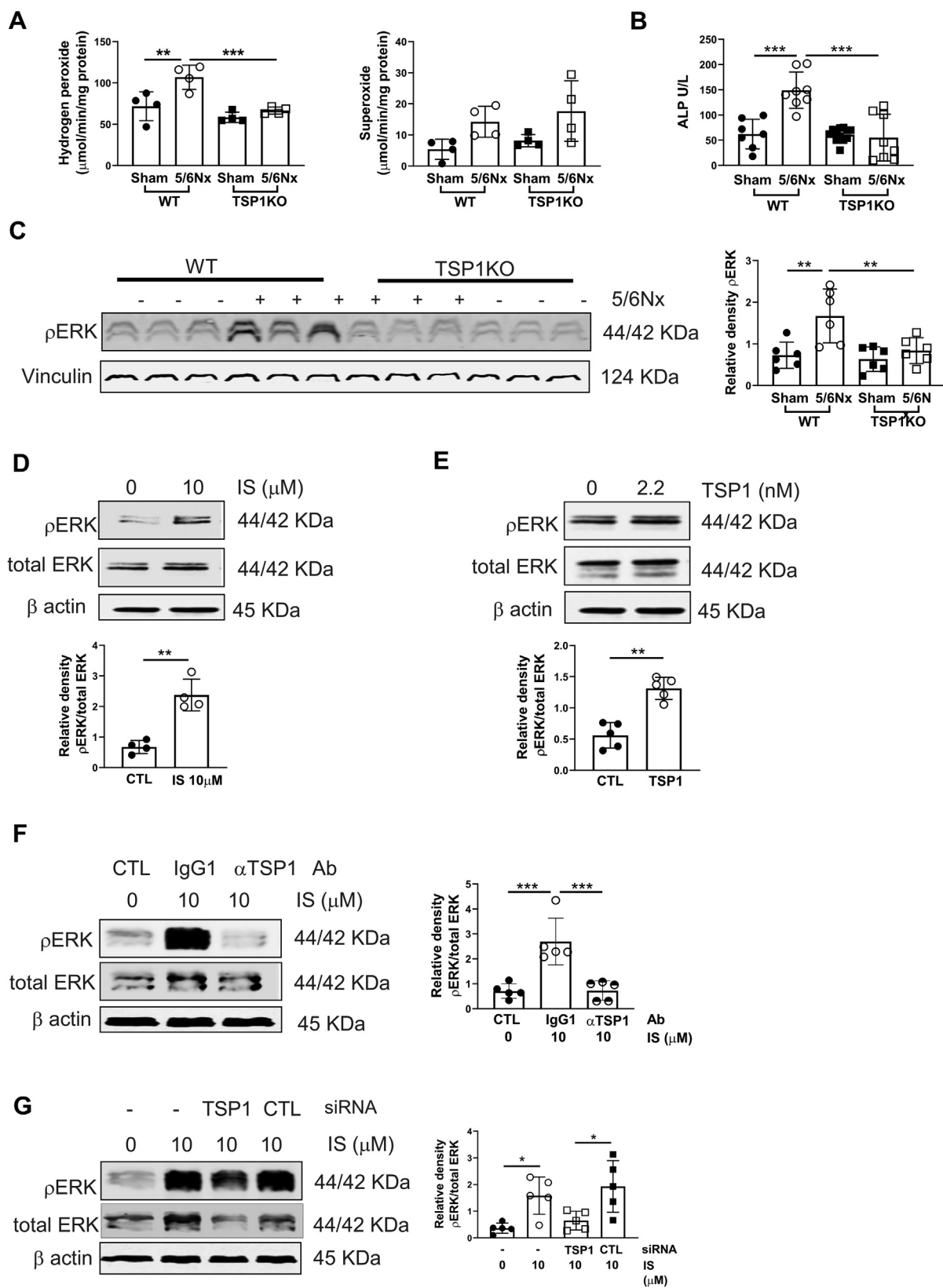
STATISTICAL ANALYSIS. Statistical analyses were performed using GraphPad Prism software (version 10.0.3; GraphPad Software Inc). Data are presented as mean ± SD or median (25th, 75th percentiles) (box plot) dependent on data distribution. Between-group comparisons used unpaired Student's *t*-test or Wilcoxon rank-sum test, whereas within-group comparisons used paired Student's *t*-tests. One- or 2-way analysis of variance was used to compare >2 groups with Sidak's or Tukey's post hoc test for multiple pairwise comparisons. Spearman's correlation coefficient (*r*) was used to evaluate the association of 2 continuous variables as determined through linear regression. Kaplan-Meier methods were used to present survival curves with groups compared using the log-rank test. A value of *P* < 0.05 was considered statistically significant.

RESULTS

DEVELOPMENT OF EQUIVALENT CKD IN WT AND TSP1KO MICE. A 5/6Nx model recapitulates features of CKD and induces cardiac remodeling. Removal of 70%-80% of total kidney mass at multiple time points (Figure 1A) demonstrated reduced body weight in WT- and TSP1KO-5/6Nx mice compared to sham-operated control mice, although weight reduction was less in TSP1KO-5/6Nx mice compared to WT-5/6Nx mice (Figure 1B). Acute elevation of serum urea and creatinine was seen at 2 weeks post-5/6Nx (Figures 1C and 1D), which reduced with time. Serum urea, serum creatinine, polyuria, and decreased urine creatinine/plasma creatinine ratio was equivalent in both genotypes post-5/6Nx (Figures 1C to 1E). TSP1 is a well-recognized activator of oxidative stress,²³ but

FIGURE 3 Continued

Systolic and diastolic blood pressure (BP) using tail-cuff plethysmography over 12 weeks in WT or TSP1KO mice following 5/6Nx or sham operation (n = 20–23). (B) Representative images of left ventricle echocardiography and measurement of ejection fraction (EF) at 12 weeks (n = 5–8). (C) Four apical view echocardiography analysis. E/A ratio of early mitral flow velocity (E) and late diastolic transmural flow velocity (A), isovolumic relaxation time (IVRT), and E/e' ratio of early mitral flow velocity (E) and diastolic septal mitral annulus velocity (e') (n = 4). (D) Lung weight normalized by the tibial length (n = 4). Mice left ventricular homogenates were analyzed by Western blotting for expression of (E) α-actinin, and (F) senescence markers tumor protein p53 (p53). Band density was normalized with vinculin and combined densitometries were shown (n = 6). (G) Left ventricular messenger RNA expression of senescence-associated secretory phenotype cytokines interleukin (IL)-6, IL-1β, TNF-α, and CCL2 by quantitative polymerase chain reaction, normalized to HPRT1 with WT sham-operated left ventricle set as the referent control (n = 6–9). All data are mean ± SD; *P < 0.05, **P < 0.01, and ***P < 0.001 by 2-way analysis of variance with Tukey post hoc test. a.u. = arbitrary units; other abbreviations as in Figure 1.

FIGURE 4 CKD in Mice Promotes Cardiac Oxidative Stress, Inflammation, and MAPK Up-Regulation via TSP1

Continued on the next page

there were no differences in reactive oxygen species in the remnant kidney of WT- and TSP1KO-5/6Nx mice (**Figure 1F**). Photomicrographs of the remnant kidney over time are demonstrated in **Figure 1G**. At 12 weeks following 5/6Nx, the renal parenchyma demonstrated fibrosis and tubular atrophy in addition to changes in glomerular morphology that included tuft shrinkage and glomerulosclerosis in both genotypes (**Figure 1G**). Plasma TSP1 was up-regulated only in WT-5/6Nx mice (**Figure 1H**). As expected, plasma IS was up-regulated in WT-5/6Nx and TSP1KO-5/6Nx mice compared to WT-sham and TSP1KO-sham mice, respectively (**Figure 1I**).

GENETIC DISRUPTION OF TSP1 SIGNALING LIMITS CARDIAC PATHOLOGY IN A MOUSE MODEL OF CRS. Given equivalent renal dysfunction between WT- and TSP1KO-5/6Nx mice, we then explored changes in cardiac phenotype. Representative sections demonstrated LVH (**Figure 2A**) and increased cardiomyocyte cross-sectional area only in WT-5/6Nx mice (**Figure 2B**, *Supplemental Figure 2A*), accompanied by increased heart weight (compared to tibial length) (*Supplemental Figure 2B*). Perivascular and interstitial fibrosis was demonstrated in WT-5/6Nx hearts (**Figure 2C**), which was corroborated by significantly elevated collagen I, fibronectin, α -smooth muscle actin, and transforming growth factor- β (**Figure 2D**). LVH and fibrosis were abrogated in TSP1KO-5/6Nx hearts. Immunohistochemical staining revealed marked myocardial TSP1 expression, localized to the cardiomyocytes and interstitial, vascular, and perivascular spaces only in WT-5/6Nx mice (**Figure 2E**, *Supplemental Figure 2C*), confirmed by quantitative polymerase chain reaction (**Figure 2F**) and Western blotting (**Figure 2G**) of LV tissue.

TSP1 IS REQUIRED TO PROMOTE LVH, DIASTOLIC DYSFUNCTION, AND SENESCENCE IN MICE WITH CRS. Systolic and diastolic pressure and mean

arterial pressure and heart rate were not statistically significantly lower in TSP1KO mice compared to WT mice (**Figure 3A**, *Supplemental Figure 2D*). Echocardiography performed at week 12 confirmed the histological evidence of LVH, with increased EF and fractional shortening exclusively in WT-5/6Nx mice (**Figure 3B**, *Supplemental Figure 2E*). Consistent with previous reporting,³¹ this was accompanied by decreased LV systolic internal diameter and systolic volume (*Supplemental Figure 2F*). LV diastolic internal diameter and volume were preserved in TSP1KO-5/6Nx mice (*Supplemental Figure 2G*).

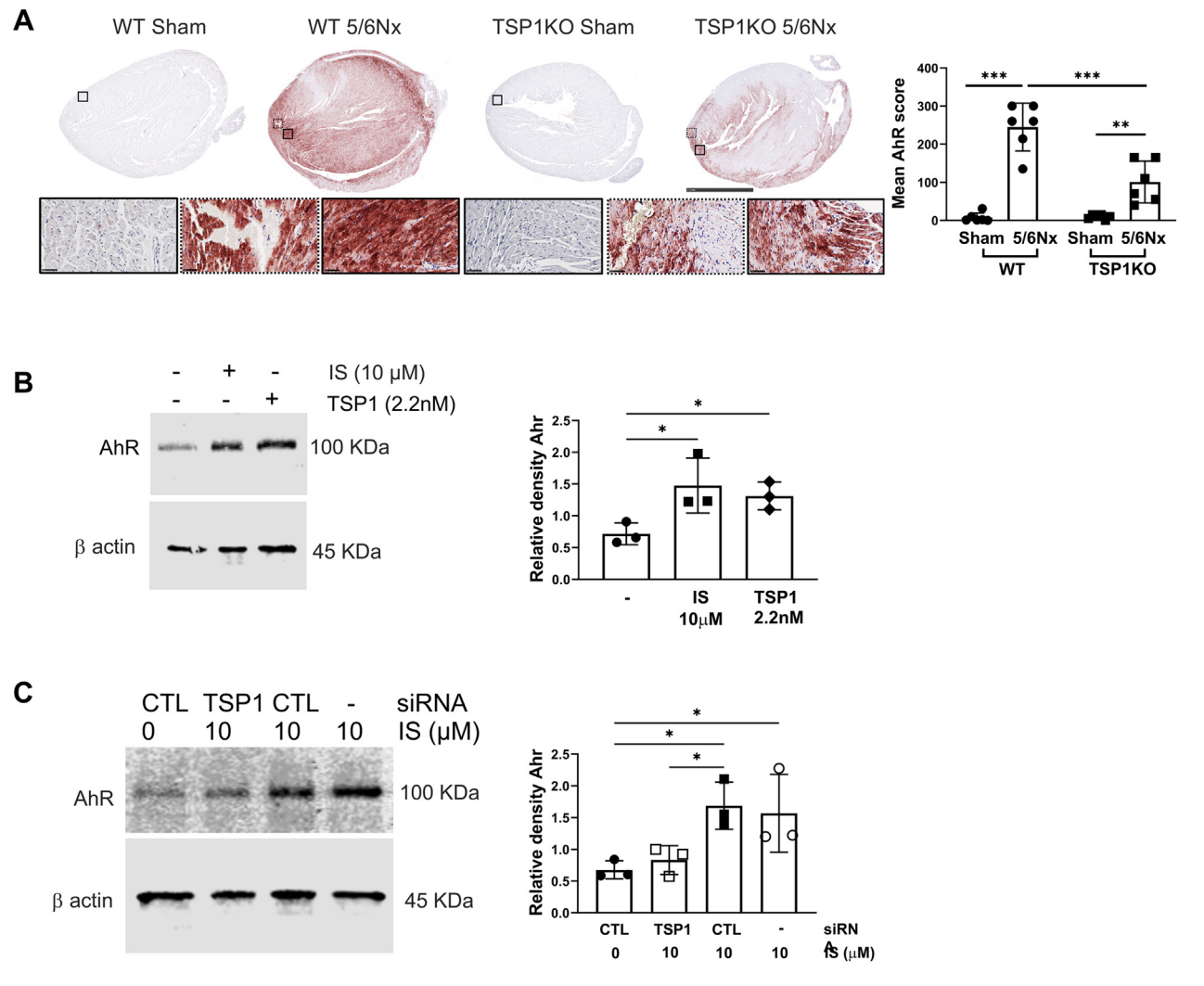
Diastolic dysfunction frequently correlates with heightened interstitial fibrosis, concentric hypertrophy, and atrial enlargement. The early flow velocity (E) of the mitral valve exhibited no significant variance among the groups (*Supplemental Figure 3A*). Doppler assessment of LV filling velocity, determined by the ratio of early (E) to late (A) diastolic transmitral Doppler flow velocities (E/A), and isovolumetric relaxation time was significantly increased in WT-5/6Nx mice compared to sham-operated mice, but not in TSP1KO-5/6Nx mice (**Figure 3C**).

The septal mitral annular velocity (e') demonstrated a significant reduction in WT-5/6Nx, TSP1KO sham, and TSP1KO-5/6Nx mice when compared to WT-sham mice (*Supplemental Figure 3B*). Moreover, the E/e' ratio was significantly increased solely in WT-5/6Nx mice (**Figure 3C**), indicating the onset of diastolic dysfunction, with no such elevation observed in TSP1KO-5/6Nx mice. Furthermore, lung weight was increased in WT-5/6Nx mice (**Figure 3D**), which is suggestive of increased lung congestion and HFpEF.

LVH increases cardiomyocyte contractile machinery³² that is governed by overexpression of MHC and α -actinin, which provide adenosine triphosphate hydrolysis³³ and anchor actin filaments to the sarcomeric Z-disk,³⁴ respectively. WT-5/6Nx hearts demonstrated significantly up-regulated α -actinin

FIGURE 4 Continued

Measurement of (A) superoxide and H₂O₂ (n = 4) in left ventricular tissue, and (B) serum alkaline phosphatase (ALP) (n = 7–12). (C) Expression of phosphorylated extracellular regulated kinase (pERK), and vinculin by Western blotting in the left ventricle from WT or TSP1KO hearts following 5/6Nx or sham operation (n = 6). Band density was normalized with vinculin. (D,E) Human cardiomyocyte cells at ~70% confluence in 6-well plates were treated with indoxyl sulfate (IS) (10 μ mol/L) (D, n = 4) and TSP1 (2.2 nmol/L) (E, n = 5) for 24 hours. pERK and total ERK were measured by Western blotting in whole-cell lysates. β -actin was used as an internal control. (F) Human cardiomyocyte cells were pretreated treated with immunoglobulin G₁ (IgG₁) (1 μ g/mL) or anti-TSP1 antibody (α TSP1Ab) (1 μ g/mL) for 2 hours and then treated with IS (10 μ mol/L) for 24 hours. pERK and total ERK were measured by Western blotting in whole-cell lysates. β -actin was used as an internal control (n = 5). (G) Human cardiomyocyte cells were pretreated with control (CTL) siRNA (50 nmol/L) or TSP1small interfering RNA (siRNA) (50 nmol/L) for 48 hours and then treated with IS (10 μ mol/L) for 24 hours. pERK and total ERK were measured by Western blotting in whole-cell lysates. β -actin was used as an internal control (n = 5). Band density was normalized with total ERK. Graphs are mean \pm SD; *P < 0.05, **P < 0.01, and ***P < 0.001 by 1-way analysis of variance (F to H) and 2-way analysis of variance with Tukey Post hoc test (A to C, F, G) or unpaired Student's t-test (D, E). CTRL = control; MAPK = mitogen activated protein kinase; other abbreviations as in **Figure 1**.

FIGURE 5 Myocardial Activation of AhR Is Up-Regulated in CRS

(A) Representative left ventricle immunohistochemical staining for aryl hydrocarbon receptor (AhR) (bar = 2.5 mm) with high magnification areas (bars = 50 μ m), with the accompanying histogram of mean AhR scoring (n = 6). (B) Human cardiomyocyte cells at ~70% confluence in 6-well plates were treated with IS (10 μ mol/L) or TSP1 (2.2 nmol/L) for 24 hours. AhR was measured by Western blotting in whole-cell lysates. β -actin was used as an internal control (n = 3). (C) Human cardiomyocyte cells were pretreated with CTL (50 nmol/L) or TSP1 siRNA (50 nmol/L) for 48 hours and then treated with IS for 24 hours. AhR was measured by Western blotting in whole-cell lysates. β -actin was used as an internal control (n = 3). Band density was normalized with β -actin. All data are mean \pm SD; *P < 0.05, **P < 0.01, and ***P < 0.001 by 2-way analysis of variance with Tukey post hoc test (A) or 1-way analysis of variance with Sidak multiple comparisons test (B, C). CRS = cardiorenal syndrome; other abbreviations as in Figures 1 and 4.

(Figure 3E) and β -MHC, with reduced α -MHC (Supplemental Figure 3C). Expression of both atrial and brain natriuretic peptides was elevated in WT-5/6Nx mice compared to TSP1KO-5/6Nx mice, with no difference in α -MHC expression (Supplemental Figure 3C). WT-5/6Nx hearts also showed amplified expression of senescence markers p53, p21^{Cip1}, and p27^{Kip1} (Figure 3F, Supplemental Figure 3D), which was associated with up-regulated proinflammatory

cytokines (Figure 3G). Senescence and proinflammatory markers were mitigated in TSP1KO-5/6Nx mice (Figure 3G).

DISRUPTION OF TSP1 SIGNALING IN MICE WITH CRS MITIGATES LV OXIDATIVE STRESS AND THE MAPK/ERK PATHWAY. Growing evidence implicates redox pathways³⁵ and chronic inflammation³⁶ in the development of LVH and contractile dysfunction. WT-5/6Nx

LV tissue demonstrated significantly greater oxidative stress in the form of H₂O₂, which was mitigated in TSP1KO-5/6Nx tissue; superoxide moiety measurements were equivalent (**Figure 4A**). Tissue nonspecific alkaline phosphatase is associated with systemic inflammation³⁷ and positively correlates with cardiovascular events.³⁸ WT-5/6Nx mice demonstrated elevated serum alkaline phosphatase, which was abrogated in TSP1KO-5/6Nx animals (**Figure 4B**). Histologic examination also revealed areas of heterotopic ossification only seen in WT-5/6Nx hearts (**Supplemental Figure 3E**).

Reactive oxygen species and inflammation activate a broad variety of hypertrophy signaling kinases,³⁹ including MAPK signaling cascades, which are central regulators of pathological LVH.⁴⁰ MAPK ERK is also linked to TSP1 activity and H₂O₂ availability.⁴¹ pERK expression was up-regulated only in WT-5/6Nx hearts (**Figure 4C**). To demonstrate that this effect could be replicated in vitro, we incubated HCMs with IS or TSP1, and both up-regulated pERK (**Figures 4D and 4E**), which was mitigated with anti-thrombospondin 1 antibody ([α TSP1Ab], which demonstrates direct inhibitory⁴² and steric hindrance⁴³ effects on TSP1 activity) or siRNA (**Figures 4F and 4G**). These data suggest that the effect of IS was dependent on intact TSP1 signaling.

CRS IS ASSOCIATED WITH AhR ACTIVATION. IS is a ligand and potent agonist of AhR, and this interaction is clinically relevant in CKD⁴⁴ because it regulates the cell cycle and responsiveness to oxidative stress.⁴⁵ AhR regulates TSP1 gene promoter activity,⁴⁶ and MAPK activation has also been shown to facilitate AhR activity,⁴⁷ suggesting bidirectional potentiation of signaling. Immunohistochemical staining revealed marked myocardial AhR activation in WT-5/6Nx hearts, which was mitigated in TSP1KO-5/6Nx hearts (**Figure 5A**). IS and TSP1 were both capable of up-regulating AhR activation in HCMs (**Figure 5B**), and IS-induced AhR activation was mitigated by TSP1 siRNA (**Figure 5C**). Human vascular smooth muscle cells exposed to an AhR inhibitor demonstrated reduced TSP1 expression, even when concurrently treated with IS (**Supplemental Figure 4A**), supporting the notion that AhR is required for TSP1 activation. The proinflammatory cytokine profile characteristic of SASP remained intact with induction of TNF- α , interleukin-6, interleukin-1 β , and CCL2 with IS, but this was limited in the presence of AhR inhibitors (**Supplemental Figure 4B**).

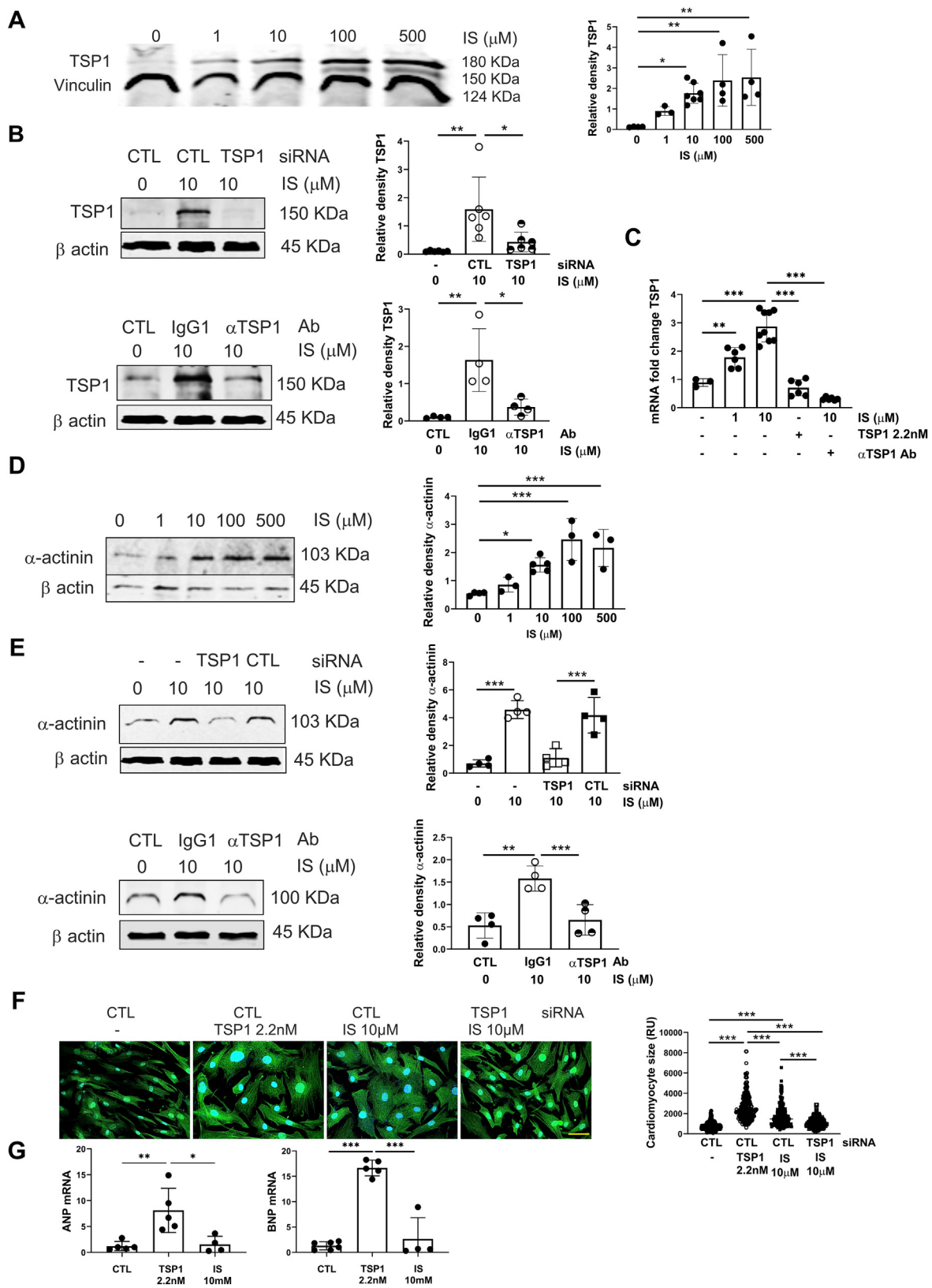
IS INDUCES CARDIOMYOCYTE HYPERSTROPHY AND SASP MEDIATED BY TSP1. Our global KO mouse did not distinguish which cells were driving LVH in CRS;

however, we initially focused on pathologic signaling within cardiomyocytes. We evaluated the response of HCMs to IS and TSP1, demonstrating up-regulation of TSP1 in response to both (**Figure 6A, Supplemental Figure 5A**) at concentrations found in patients with CKD.⁴⁸ A positive feedback loop in response to exogenous TSP1 is counterintuitive to cellular response to injury, but this remains a robust observation in other cell types.^{18,49} IS-mediated induction of TSP1 was limited by TSP1 siRNA and [α TSP1Ab] at protein (**Figure 6B**) and transcript levels (**Figure 6C**). Similar to our in vivo findings, α -actinin expression increased with exogenous IS (**Figure 6D**) or TSP1 (**Supplemental Figure 5B**), and the response was decreased by TSP1 siRNA or [α TSP1Ab] (**Figure 6E**). Morphometric analysis revealed significant increases in HCM surface area in response to TSP1 or IS, and effect of IS was again mitigated with TSP1 siRNA (**Figure 6F**). TSP1, but not IS, significantly increases the messenger level of atrial and brain natriuretic peptides in HCMs (**Figure 6G**).

IS down-regulated HCM metabolic activity (measured via MTT [3-(4,5-dimethylthiazol-2-yl)-2,5-diphenyl-2H-tetrazolium bromide] incorporation) at all concentrations (**Figure 7A**), and TSP1 demonstrated an effect at 2.2 nmol/L (**Figure 7B**). TSP1 siRNA treatment reduced IS-induced effects (**Figure 7C**). Limited synthetic capability reflects cellular senescence, and prematurely senescent cardiomyocytes accumulate in cardiomyopathies,⁵⁰ becoming pathogenic by introducing chronic inflammation (also known as SASP). HCM senescence in the context of uremic toxins has not been previously explored. IS (**Figure 7D**) and TSP1 (**Figure 7E**) significantly increased senescence-associated β -galactosidase in HCMs, and the effect was abrogated by siRNA (**Figure 7F**) or [α TSP1Ab] (**Figure 7G**). Messenger RNA levels of interleukin-6 and -1 β , TNF- α , and CCL2 were increased following incubation with IS (**Figure 7H**) and decreased when cells were pretreated with [α TSP1Ab].

We also investigated the effect of TSP1 on human cardiac fibroblasts, demonstrating a small, but significant decreased MTT incorporation (**Supplemental Figure 6A**) and increased senescence (**Supplemental Figure 6B**).

TSP1 AND AhR ARE RELEVANT IN HUMAN CRS. We have previously published that plasma TSP1 levels inversely correlate with estimated glomerular filtration rate.¹⁹ Analysis of a subgroup of these patients (**Supplemental Table 2**) demonstrated an inverse relationship between plasma TSP1 and LVEF, as well as a direct correlation between plasma TSP1 and LV mass index (**Figure 8A**). There was no significant correlation between plasma TSP1 and fractional

FIGURE 6 IS Induces Cardiomyocyte Hypertrophy That Is Dependent on TSP1

Continued on the next page

shortening, LV internal end-diastolic diameter, or end-systolic diameter ([Supplemental Figure 7A](#)).

The publicly available data set GSE160145 (Gene Expression Omnibus) provides gene expression data from explanted hearts from healthy or dialysis-dependent patients with CRS. The principal component analysis is shown in [Supplemental Figure 7B](#). TSP1 and AhR gene expression was significantly up-regulated in patients with CKD compared to healthy control subjects ([Figure 8B](#)). DEGs between healthy and CRS hearts, including TSP1 and AhR, were identified in a volcano plot ([Figure 8C](#)). A heatmap from a subset of CRS patients also demonstrates the distribution of DEGs ([Supplemental Figure 7C](#)). The top 12 DEGs in CRS hearts are listed in [Supplemental Table 3](#). A Wilcoxon rank-sum test was performed on candidate DEGs to establish enriched pathways in the Kyoto Encyclopedia of Genes and Genomes database ([Figure 8D](#)). DEGs were predominantly enriched in cytokine- and ECM-receptor interactions, as well as p53 signaling. Gene set enrichment analysis was also used to determine enriched pathways within the Gene Ontology database ([Supplemental Figure 7D](#)), demonstrating changes in cell cycle processes, oxidative stress, and senescence.

DISCUSSION

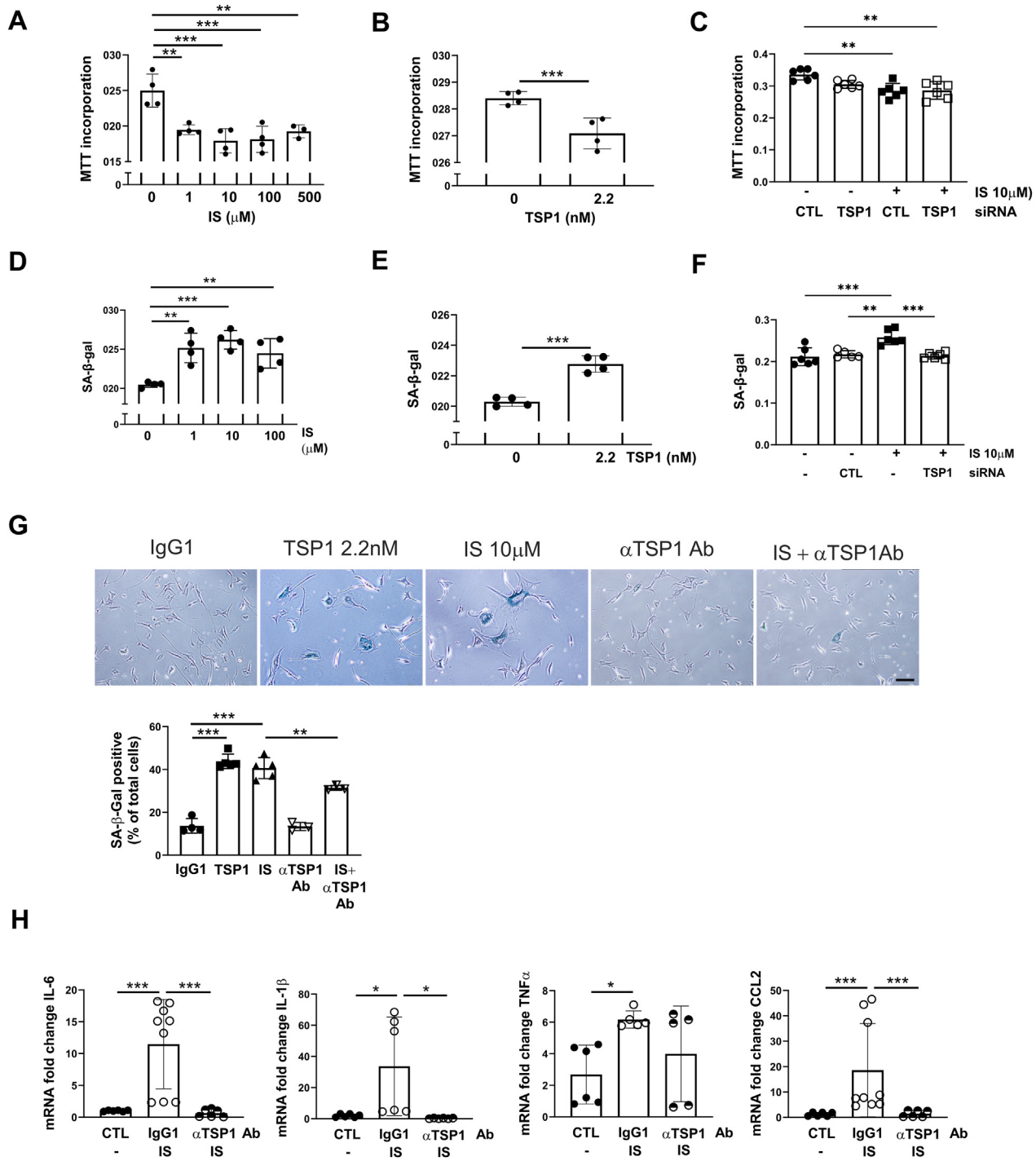
The excess burden of cardiac disease in renal impairment is well established, and patients experience morbidity and mortality from cardiovascular events rather than renal failure per se.¹ Uremia-specific toxins, particularly IS, are involved in the pathogenesis of CRS, and here we show, for the first time, that the matrix protein TSP1 is necessary to drive cardiac pathology. In vivo, WT mice subject to 5/6Nx demonstrated LVH, diastolic dysfunction, up-

regulated myocardial TSP1 and AhR expression, maladaptive oxidative stress, SASP, and fibrosis. TSP1KO mice were protected from cardiac pathology despite equivalent renal dysfunction. Our *in vitro* results demonstrated that IS, through TSP1, promoted cardiomyocyte hypertrophy and SASP with activation of ERK and up-regulated AhR. Importantly, blockade of TSP1 signaling reversed abnormal cardiomyocyte findings associated with IS exposure. Analysis of an independent RNA-sequencing data set from explanted human hearts showed increased expression of TSP1 and AhR in samples with CRS patients (compared to healthy control subjects). Differential gene expression analysis in CRS hearts were linked with cytokine, extracellular matrix, and p53 signaling pathways, which we identified as relevant signaling pathways *in vivo* and *in vitro*. We believe these data uncover a novel mechanism that implicates TSP1 as a driver of LVH, positioning it as a potential biomarker of disease and a prospective target for clinical intervention.

Our findings are clinically relevant: we have previously published that plasma TSP1 correlated inversely with estimated glomerular filtration rate.¹⁹ We extended these findings to demonstrate correlation with both reduced EF and increased LV mass. Large cohort studies have previously published that patients with CKD can present with HFpEF or HF with reduced EF, and similar relationships were observed for estimated glomerular filtration rate and proteinuria in terms of all-cause hospitalization regardless of EF.^{51,52} There are also reports of bimodal presentations of EF in CKD patient populations with an increased prevalence of HFpEF.^{52,53} Consistent with a recent report,⁵⁴ we observed diastolic dysfunction and markers of HFpEF only in WT-5/6Nx mice, which might be a function of animal age (<6 months old),

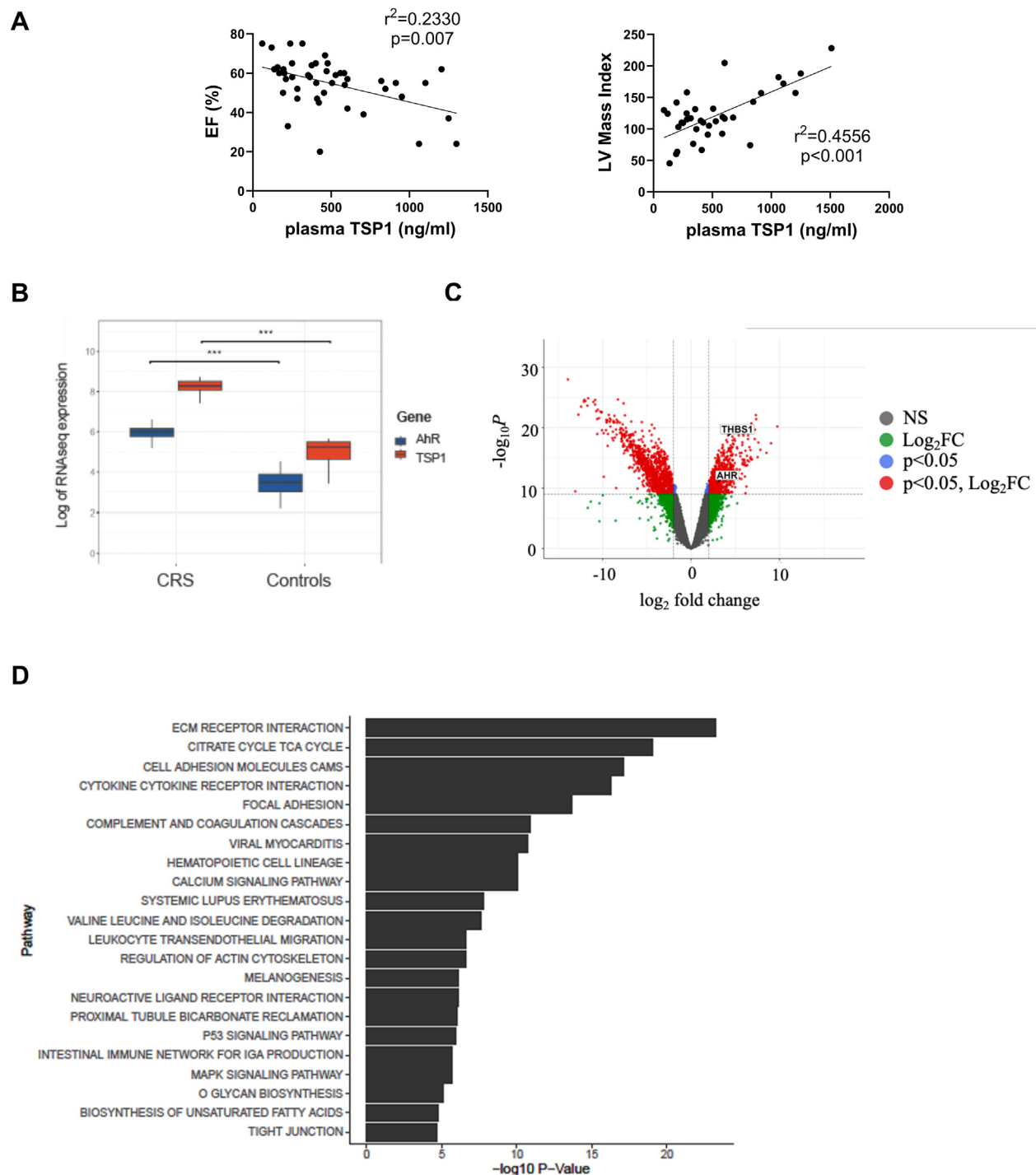
FIGURE 6 Continued

(A) Human cardiomyocytes were treated with IS at 0 μmol/L (n = 3), 1 μmol/L (n = 3), 10 μmol/L (n = 7), 100 μmol/L (n = 4), and 500 μmol/L (n = 4) for 24 hours. TSP1 and vinculin were measured by Western blotting in whole-cell lysates. Band density was normalized with vinculin. (B) Human cardiomyocytes were transfected with CTL or TSP1 siRNA (50 nmol/L), or treated with isotype control IgG₁ or αTSP1Ab antibody (1 μg/mL), incubated with IS (10 μmol/L), then probed for TSP1 protein or TSP1 mRNA expression (C). (D) Human cardiomyocytes were treated with increasing doses of IS and probed for α-actinin. (E) Human cardiomyocytes were transfected with CTL or αTSP1 siRNA (50 nmol/L) or treated with IgG₁ or αTSP1Ab (1 μg/mL), incubated with IS (10 μmol/L), then probed for α-actinin. Band density was normalized with β-actin. Representative Western blots and combined densitometry are shown (n = 3–7). (F) Human cardiomyocyte surface area after treatment with TSP1 (2.2 nmol/L) or IS (10 μmol/L) for 48 hours, following transfection with CTL or TSP1 siRNA (50 nmol/L) for 48 hours. Cells were stained for α-actinin (green) and 4',6-diamidino-2-phenylindole (blue) (original magnification 40×; bar = 50 μm). Measurements are from 233 to 259 randomly chosen cells from 4 independent experiments. (G) Human cardiomyocytes were treated with TSP1 (2.2 nmol/L) and IS (10 μmol/L) for 24 hours and were probed for atrial natriuretic peptide (ANP) and brain natriuretic peptide (BNP) mRNA (n = 4–6). All data are mean ± SD; *P < 0.05, **P < 0.01, and ***P < 0.001 by 1-way analysis of variance with Sidak multiple comparisons test. RU = relative units; other abbreviations as in [Figures 1, 2, and 4](#).

FIGURE 7 IS induces HCM SASP That Is Dependent on TSP1

Incorporation of 3-(4,5-dimethylthiazol-2-yl)-2,5-diphenyl-2H-tetrazolium bromide (MTT) in human cardiomyocytes (HCMs) following incubation with (A) IS (1, 10, 100, and 500 $\mu\text{mol/L}$), (B) TSP1 (2.2 nmol/L), or (C) IS (10 $\mu\text{mol/L}$) following transfection with CTL or TSP1 siRNA (50 nmol/L) ($n = 3-6$). HCM senescence-associated β -galactosidase (SA- β -gal) activity following (D) IS (1, 10, and 100 $\mu\text{mol/L}$), (E) TSP1 (2.2 nmol/L), or (F) IS pretreated with CTL or TSP1 siRNA (50 nmol/L) ($n = 5-6$). (G) SA- β -gal staining following incubation with TSP1 (2.2 nmol/L) ($n = 5$), IS (10 $\mu\text{mol/L}$) ($n = 5$), IgG1 antibody (1 $\mu\text{g/mL}$) ($n = 4$) or α TSP1Ab (1 $\mu\text{g/mL}$) ($n = 3$). Measurements are from 5 randomly chosen images from independent experiments (bar = 200 μm). (H) Transcript expression of IL-6, IL-1 β , TNF α , and CCL2 from HCMs treated with IS, CTL antibody or α TSP1Ab ($n = 3$ independent experiments, normalized to 18S ribosome). All data are mean \pm SD; * $P < 0.05$, ** $P < 0.01$, and *** $P < 0.001$ by 1-way analysis of variance with Sidak multiple comparisons test (A, C, D, F to H) or Student's *t*-test (B, E). SASP = senescence-associated secretory phenotype; other abbreviations as in Figures 1 to 4.

FIGURE 8 TSP1 and AhR Expression Is Up-Regulated in Diseased Human Hearts



(A) Linear regression analysis of plasma TSP1 levels and percentage of EF or left ventricular (LV) mass index in patients with chronic kidney disease. (B) Range of TSP1 and AhR gene expression in explanted hearts from healthy patients compared to those with cardiorenal syndrome. Data are expressed as median with 25th and 75th percentiles (box plot); *** $P < 0.001$ by Wilcoxon rank-sum test. (C) Volcano plot of differentially expressed genes from RNA-seq-analyzed explanted hearts from healthy patients or those with cardiorenal syndrome. (D) Kyoto Encyclopedia of Genes and Genomes pathway of differentially expressed genes. CAMS = cell-cell adhesion molecules; ECM = extracellular matrix; FC = fold change; IGA = immunoglobulin A; NS = not significant; TCA = citric acid cycle; other abbreviations as in Figures 1 and 3 to 5.

genotype (C57BL/6 background), diet (standard chow), and duration of CKD (12 weeks). Other features, including impaired exercise capacity caused by skeletal muscle weakness, malnutrition (failure to gain weight), inflammation, and dehydration (due to polyuria),^{55,56} may be additional confounding factors, and these require further investigation.

TSP1 is a matrix glycoprotein produced by numerous cell types^{18,25,57} that activates transforming growth factor- β to induce fibrosis,⁵⁷ limits cellular proliferation,⁴⁹ increases redox stress,²⁵ and promotes inflammatory responses,⁵⁸ all of which we demonstrate in the cardiac pathology of our murine CRS model. In this study, we also establish that TSP1 is upstream of ERK1/2 activation and AhR (with likely bidirectional signaling), which are complicit in the development of SASP and cardiac dysfunction. Our use of a global TSP1KO mouse did not define the cell type responsible for TSP1 secretion, although we focused on cardiomyocyte phenotype in vitro. However, all nucleated cells produce TSP1 in response to external stressors⁵⁹ (eg, hypoxia, inflammation, hyperglycemia), and it may be that paracrine signaling, particularly SASP-derived products,¹⁰ among cardiomyocytes, fibroblasts, and endothelial cells, cooperatively contributes to adverse cardiac remodeling.⁶⁰

We were able to definitively demonstrate a permissive cardiorenal phenotype following 5/6Nx in WT mice. The 5/6Nx model is typically associated with high mortality,²⁰ presumably due to acute uremia following excision of the contralateral kidney. However, alterations in our surgical technique significantly improved survival to >85%-90%. TSP1KO mice are resistant to acute kidney injury;⁶¹ therefore, the induction of equivalent renal injury through a reduction in functional renal parenchyma was only possible using a 5/6Nx model. Measurements of renal dysfunction were equivalent, supporting the use of global KO animals for this study.

Accumulated toxins are the cause of uremia in CKD, and robust evidence establishes uremic toxins as central to the deranged molecular pathways in both CVD and CKD.¹⁴ IS is the best characterized uremic toxin, from both epidemiologic and molecular perspectives. It promotes expression of profibrotic genes (through Smad-dependent transforming growth factor- β),^{57,62} up-regulating inflammation⁶³ and cellular senescence^{64,65} via reactive oxygen species and p53 pathways^{66,67} (although not demonstrated in cardiomyocytes). Interestingly, the cellular effects of IS mimic those seen with TSP1, but the role of TSP1 in CKD-induced cardiac pathology is unexplored. In this study, absence of TSP1 attenuated

features of CRS-induced LVH and mitigated expression of deranged molecular pathways without altering blood pressure, supporting a cardiac effect that is independent of the vasculature (but not necessarily vascular responsiveness).

We have previously reported the induction of cardiac TSP1 in animal models with right ventricular dysfunction,¹⁸ and disruption of TSP1 signaling provided cardioprotection in the same setting.⁶⁸ However, the role of TSP1 in preclinical models of pressure overload-induced LV dysfunction is discordant,^{69,70} with TSP1KO mice exhibiting early hypertrophy and late dilation despite less type 1 collagen deposition.^{69,70} However, our CRS model is not defined by increased afterload (hypertension), which is consistent with published reports.^{21,71,72} Histopathologic studies have shown that cardiomyocyte diameter and resting tension are both increased in HFP EF.⁷³⁻⁷⁵ Higher cardiomyocyte resting tension has been presumably related to sarcomeric protein phosphorylation that was observed in patients⁷⁵ and preclinical models.⁷⁶ In our study, both myocyte diameter and sarcomeric actinin were increased in WT-5/6Nx mice, but were mitigated in TSP1KO-5/6Nx mice. Diastolic dysfunction can result from abnormal relaxation and/or increased myocardial stiffness, ultimately leading to elevated LV filling pressures and HFP EF. LV filling pressure is assessed by E/A, isovolumetric relaxation time, and the E/e' ratio, which constitutes key hemodynamic abnormalities associated with diastolic dysfunction. These parameters can effectively stratify HF phenotypes, including those with both reduced and preserved EF,⁷⁷⁻⁷⁹ and have been applied in small animal studies.⁸⁰ In our study, E/A, isovolumetric relaxation time, and E/e' ratio were increased in WT-5/6Nx mice but not in TSP1KO-5/6Nx mice.

STUDY LIMITATIONS. Uremia is a complex condition with multiple systemic abnormalities, including cardiomyopathy. Animal models, including 5/6Nx may not fully mimic the progressive nature of human uremic cardiomyopathy owing to differences in comorbid conditions, including hypertension. Differences in disease duration and severity of kidney injury can also affect the relevance of research findings.

The tissue architecture and mechanical cues in the heart and blood vessels influence cellular phenotype and cross-talk, but these factors are absent in cell culture systems, limiting the relevance of findings. Uremic cardiomyopathy involves interactions among multiple cell types, which may not be fully captured when studying cell types individually. Further

studies are required to accurately define the culprit cell promoting the cardiac pathology seen in CRS. In addition, lack of concurrent clinical details in the patient cohort warrant large clinical studies that will appropriately define the place of TSP1 as a potential biomarker of disease.

CONCLUSIONS

Collectively our results suggest that TSP1 is driving the cellular effects of IS through activation of ERK and AhR, supporting our hypothesis that TSP1 is a missing link between CKD and development of CVD, particularly LVH. The mechanisms that underscore its development include oxidative stress, senescence, and inflammation.

ACKNOWLEDGMENTS The authors are grateful to Pre-Clinical Imaging Facility, Sydney Imaging Core Research Facility (Charles Perkins Centre, The University of Sydney) for small animal imaging. The authors appreciate the facilities, resources, and professional assistance provided by the Westmead Institute for Medical Research Histology and Cell Imaging Facilities. The authors thank Drs Jennifer Li and Kedar Ghimire (Westmead Institute for Medical Research) for valuable assistance with the manuscript.

FUNDING SUPPORT AND AUTHOR DISCLOSURES

This work was supported by a National Health Medical Research Council grant (GNT2007991) to awarded to Dr Rogers, a National Heart Foundation Vanguard Grant (106035) to Drs Rogers and Julovi, and a Westmead Medical Research Foundation grant to Dr Julovi. All other authors have reported that they have no relationships relevant to the contents of this paper to disclose.

REFERENCES

1. Jha V, Garcia-Garcia G, Iseki K, et al. Chronic kidney disease: global dimension and perspectives. *Lancet*. 2013;382(9888):260–272.
2. Vanholder R, Massy Z, Argiles A, et al. Chronic kidney disease as cause of cardiovascular morbidity and mortality. *Nephrol Dial Transplant*. 2005;20(6):1048–1056.
3. Rangaswami J, Bhalla V, Blair JEA, et al. Cardiorenal syndrome: classification, pathophysiology, diagnosis, and treatment strategies: a scientific statement from the American Heart Association. *Circulation*. 2019;139(16):e840–e878.
4. Taveira Gomes T, Santos Araujo C, Valente F, et al. Cardiorenal syndrome and death risk in patients with heart failure or chronic kidney disease: an unmet cardiorenal need? *Eur Heart J*. 2021;42(suppl 1):819.
5. Deo R, Fyr CL, Fried LF, et al. Health ABC study. Kidney dysfunction and fatal cardiovascular disease—an association independent of atherosclerotic events: results from the Health, Aging, and Body Composition (Health ABC) study. *Am Heart J*. 2008;155(1):62–68.
6. Unger ED, Dubin RF, Deo R, et al. Association of chronic kidney disease with abnormal cardiac mechanics and adverse outcomes in patients with heart failure and preserved ejection fraction. *Eur J Heart Fail*. 2016;18(1):103–112.
7. Hillege HL, Nitsch D, Pfeffer MA, et al. CHARM Investigators. Renal function as a predictor of outcome in a broad spectrum of patients with heart failure. *Circulation*. 2006;113(5):671–678.
8. Gallo S, Vitacolonna A, Bonzano A, Comoglio P, Crepaldi T. ERK: a key player in the pathophysiology of cardiac hypertrophy. *Int J Mol Sci*. 2019;20(9):2164.
9. Anderson G, Mazzoccoli G. Left ventricular hypertrophy: roles of mitochondria CYP1B1 and melatonergic pathways in co-ordinating wider pathophysiology. *Int J Mol Sci*. 2019;20(16):4068.
10. Mehdizadeh M, Aguilar M, Thorin E, Ferreyre G, Nattel S. The role of cellular senescence in cardiac disease: basic biology and clinical relevance. *Nat Rev Cardiol*. 2022;19(4):250–264.
11. Tumur Z, Niwa T. Indoxyl sulfate inhibits nitric oxide production and cell viability by inducing oxidative stress in vascular endothelial cells. *Am J Nephrol*. 2009;29(6):551–557.
12. Barreto FC, Barreto DV, Liabeuf S, et al. EUTox Work Group. Serum indoxyl sulfate is associated with vascular disease and mortality in chronic kidney disease patients. *Clin J Am Soc Nephrol*. 2009;4(10):1551–1558.
13. Lekawanijit S. Cardiotoxicity of uremic toxins: a driver of cardiorenal syndrome. *Toxins (Basel)*. 2018;10(9):352.
14. Hung SC, Kuo KL, Wu CC, Targ DC. Indoxyl sulfate: a novel cardiovascular risk factor in chronic kidney disease. *J Am Heart Assoc*. 2017;6(2):e005022.

- 15.** Parfrey PS, Harnett JD, Foley RN, et al. Impact of renal transplantation on uremic cardiomyopathy. *Transplantation*. 1995;60(9):908-914.
- 16.** Rogers NM, Sharifi-Sanjani M, Csanyi G, Pagano PJ, Isenberg JS. Thrombospondin-1 and CD47 regulation of cardiac, pulmonary and vascular responses in health and disease. *Matrix Biol*. 2014;37:92-101.
- 17.** Frangogiannis NG. The extracellular matrix in ischemic and nonischemic heart failure. *Circ Res*. 2019;125(1):117-146.
- 18.** Rogers NM, Sharifi-Sanjani M, Yao M, et al. TSP1-CD47 signaling is upregulated in clinical pulmonary hypertension and contributes to pulmonary arterial vasculopathy and dysfunction. *Cardiovasc Res*. 2017;113(1):15-29.
- 19.** Julovi S, Sanganeria B, Minhas N, Ghimire K, Nankivell B, Rogers NM. Blocking thrombospondin-1 signaling via CD47 mitigates renal interstitial fibrosis. *Lab Invest*. 2020;100(9):1184-1196.
- 20.** Rosendahl A, Kabiri R, Bode M, et al. Adaptive immunity and IL-17A are not involved in the progression of chronic kidney disease after 5/6 nephrectomy in mice. *Br J Pharmacol*. 2019;176(12):2002-2014.
- 21.** Julovi SM, Dao A, Trinh K, et al. Disease-modifying interactions between chronic kidney disease and osteoarthritis: a new comorbid mouse model. *RMD Open*. 2023;9(3):e003109.
- 22.** Zucchiigna S, Paldino A, Falcão-Pires I, et al. Towards standardization of echocardiography for the evaluation of left ventricular function in adult rodents: a position paper of the ESC Working Group on Myocardial Function. *Cardiovasc Res*. 2021;117(1):43-59.
- 23.** Julovi SM, Martin JL, Baxter RC. Nuclear insulin-like growth factor binding protein-3 as a biomarker in triple-negative breast cancer xenograft tumors: effect of targeted therapy and comparison with chemotherapy. *Front Endocrinol (Lausanne)*. 2018;9:120.
- 24.** Meijles DN, Sahoo S, Al Ghouléh I, et al. The matricellular protein TSP1 promotes human and mouse endothelial cell senescence through CD47 and Nox1. *Sci Signal*. 2017;10(501):eaa1784.
- 25.** Yao M, Rogers NM, Csanyi G, et al. Thrombospondin-1 activation of signal-regulatory protein-alpha stimulates reactive oxygen species production and promotes renal ischemia reperfusion injury. *J Am Soc Nephrol*. 2014;25(6):1171-1186.
- 26.** Love MI, Huber W, Anders S. Moderated estimation of fold change and dispersion for RNA-seq data with DESeq2. *Genome Biol*. 2014;15(12):550.
- 27.** KEGG pathway database: wiring diagrams of molecular interactions, reactions and relations. Kyoto Encyclopedia of Genes and Genomes. Accessed February 15, 2021. <https://www.genome.jp/kegg/pathway.html>
- 28.** Yu G, Wang LG, Han Y, He QY. clusterProfiler: an R package for comparing biological themes among gene clusters. *OMICS*. 2012;16(5):284-287.
- 29.** The Gene Ontology Resource. Gene Ontology. Accessed February 15, 2021. <http://geneontology.org>
- 30.** Robertson H. Thrombospondin-1-drives-cardiac-remodelling-in-chronic-kidney-disease. Accessed February 15, 2021. <https://github.com/Harry25R/Thrombospondin-1-drives-cardiac-remodelling-in-chronic-kidney-disease>
- 31.** Kennedy DJ, Vetteeth S, Periyasamy SM, et al. Central role for the cardiotonic steroid marinobufagenin in the pathogenesis of experimental uremic cardiomyopathy. *Hypertension*. 2006;47(3):488-495.
- 32.** Izumo S, Lompre AM, Matsuoka R, et al. Myosin heavy chain messenger RNA and protein isoform transitions during cardiac hypertrophy. Interaction between hemodynamic and thyroid hormone-induced signals. *J Clin Invest*. 1987;79(3):970-977.
- 33.** van Bilsen M, Chien KR. Growth and hypertrophy of the heart: towards an understanding of cardiac specific and inducible gene expression. *Cardiovasc Res*. 1993;27(7):1140-1149.
- 34.** Kostin S, Hein S, Arnon E, Scholz D, Schaper J. The cytoskeleton and related proteins in the human failing heart. *Heart Fail Rev*. 2000;5(3):271-280.
- 35.** Takimoto E, Kass DA. Role of oxidative stress in cardiac hypertrophy and remodeling. *Hypertension*. 2007;49(2):241-248.
- 36.** Yokoyama T, Nakano M, Bednarczyk JL, McIntyre BW, Entman M, Mann DL. Tumor necrosis factor-alpha provokes a hypertrophic growth response in adult cardiac myocytes. *Circulation*. 1997;95(5):1247-1252.
- 37.** Damera S, Raphael KL, Baird BC, Cheung AK, Greene T, Beddu S. Serum alkaline phosphatase levels associate with elevated serum C-reactive protein in chronic kidney disease. *Kidney Int*. 2011;79(2):228-233.
- 38.** Kunutsor SK, Apekey TA, Khan H. Liver enzymes and risk of cardiovascular disease in the general population: a meta-analysis of prospective cohort studies. *Atherosclerosis*. 2014;236(1):7-17.
- 39.** Sabri A, Hughie HH, Lucchesi PA. Regulation of hypertrophic and apoptotic signaling pathways by reactive oxygen species in cardiac myocytes. *Antioxid Redox Signal*. 2003;5(6):731-740.
- 40.** Muslin AJ. MAPK signalling in cardiovascular health and disease: molecular mechanisms and therapeutic targets. *Clin Sci (Lond)*. 2008;115(7):203-218.
- 41.** Chen Y, Leask A, Abraham DJ, et al. Thrombospondin 1 is a key mediator of transforming growth factor beta-mediated cell contractility in systemic sclerosis via a mitogen-activated protein kinase kinase (MEK)/extracellular signal-regulated kinase (ERK)-dependent mechanism. *Fibrogenesis Tissue Repair*. 2011;4(1):9.
- 42.** Suchard SJ, Burton MJ, Dixit VM, Boxer LA. Human neutrophil adherence to thrombospondin occurs through a CD11/CD18-independent mechanism. *J Immunol*. 1991;146(11):3945-3952.
- 43.** Annis DS, Murphy-Ullrich JE, Mosher DF. Function-blocking antithrombospondin-1 monoclonal antibodies. *J Thromb Haemost*. 2006;4(2):459-468.
- 44.** Dou L, Poitevin S, Sallee M, et al. Aryl hydrocarbon receptor is activated in patients and mice with chronic kidney disease. *Kidney Int*. 2018;93(4):986-999.
- 45.** Kim JB, Pjanic M, Nguyen T, et al. TCF21 and the environmental sensor aryl-hydrocarbon receptor cooperate to activate a pro-inflammatory gene expression program in coronary artery smooth muscle cells. *PLoS Genet*. 2017;13(5):e1006750.
- 46.** Dabir P, Marinic TE, Kruckovets I, Stenina OI. Aryl hydrocarbon receptor is activated by glucose and regulates the thrombospondin-1 gene promoter in endothelial cells. *Circ Res*. 2008;102(12):1558-1565.
- 47.** Tan Z, Chang X, Puga A, Xia Y. Activation of mitogen-activated protein kinases (MAPKs) by aromatic hydrocarbons: role in the regulation of aryl hydrocarbon receptor (AHR) function. *Biochem Pharmacol*. 2002;64(5-6):771-780.
- 48.** Vanholder R, De Smet R, Glorieux G, et al, EUTox Work Group. Review on uremic toxins: classification, concentration, and interindividual variability. *Kidney Int*. 2003;63(5):1934-1943.
- 49.** Rogers NM, Zhang ZJ, Wang JJ, Thomson AW, Isenberg JS. CD47 regulates renal tubular epithelial cell self-renewal and proliferation following renal ischemia reperfusion. *Kidney Int*. 2016;90(2):334-347.
- 50.** Predmore JM, Wang P, Davis F, et al. Ubiquitin proteasome dysfunction in human hypertrophic and dilated cardiomyopathies. *Circulation*. 2010;121(8):997-1004.
- 51.** Smith DH, Thorp ML, Gurwitz JH, et al. Chronic kidney disease and outcomes in heart failure with preserved versus reduced ejection fraction: the Cardiovascular Research Network PRESERVE Study. *Circ Cardiovasc Qual Outcomes*. 2013;6(3):333-342.
- 52.** Owan TE, Hodge DO, Herges RM, Jacobsen SJ, Roger VL, Redfield MM. Trends in prevalence and outcome of heart failure with preserved ejection fraction. *N Engl J Med*. 2006;355(3):251-259.
- 53.** Borlaug BA, Redfield MM. Diastolic and systolic heart failure are distinct phenotypes within the heart failure spectrum. *Circulation*. 2011;123(18):2006-2013 [discussion: 2014].
- 54.** Sárközy M, Watzinger S, Kovács Z, et al. Neuregulin-1β improves uremic cardiomyopathy and renal dysfunction in rats. *J Am Coll Cardiol Basic Trans Science*. 2023;8(9):1160-1176. <https://doi.org/10.1016/j.jacbtbs.2023.03.003>
- 55.** Himmelfarb J, Stenvinkel P, Izkizler TA, Hakim RM. The elephant in uremia: oxidant stress as a unifying concept of cardiovascular disease in uremia. *Kidney Int*. 2002;62(5):1524-1538.
- 56.** Stohr EJ, Gonzalez-Alonso J, Pearson J, et al. Dehydration reduces left ventricular filling at rest and during exercise independent of twist mechanics. *J Appl Physiol (1985)*. 2011;111(3):891-897.
- 57.** Murphy-Ullrich JE, Pocztak M. Activation of latent TGF-beta by thrombospondin-1: mechanisms and physiology. *Cytokine Growth Factor Rev*. 2000;11(1-2):59-69.
- 58.** Frangogiannis NG, Ren G, Dewald O, et al. Critical role of endogenous thrombospondin-1 in preventing expansion of healing myocardial infarcts. *Circulation*. 2005;111(22):2935-2942.

- 59.** Stenina-Adognravi O. Invoking the power of thrombospondins: regulation of thrombospondins expression. *Matrix Biol.* 2014;37:69-82.
- 60.** Tang X, Li PH, Chen HZ. Cardiomyocyte senescence and cellular communications within myocardial microenvironments. *Front Endocrinol (Lausanne)*. 2020;11:280.
- 61.** Thakar CV, Zahedi K, Revelo MP, et al. Identification of thrombospondin 1 (TSP-1) as a novel mediator of cell injury in kidney ischemia. *J Clin Invest.* 2005;115(12):3451-3459.
- 62.** Lekawavijit S, Adrahtas A, Kelly DJ, Kompa AR, Wang BH, Krum H. Does indoxyl sulfate, a uremic toxin, have direct effects on cardiac fibroblasts and myocytes? *Eur Heart J.* 2010;31(14):1771-1779.
- 63.** Sun CY, Hsu HH, Wu MS. p-Cresol sulfate and indoxyl sulfate induce similar cellular inflammatory gene expressions in cultured proximal renal tubular cells. *Nephrol Dial Transplant.* 2013;28(1):70-78.
- 64.** Adijiang A, Higuchi Y, Nishijima F, Shimizu H, Niwa T. Indoxyl sulfate, a uremic toxin, promotes cell senescence in aorta of hypertensive rats. *Biochem Biophys Res Commun.* 2010;399(4):637-641.
- 65.** Shimizu H, Yisireyili M, Nishijima F, Niwa T. Indoxyl sulfate enhances p53-TGF-beta1-Smad3 pathway in proximal tubular cells. *Am J Nephrol.* 2013;37(2):97-103.
- 66.** Adelbizek Y, Shimizu H, Saito S, Mironova R, Niwa T. Indoxyl sulfate counteracts endothelial effects of erythropoietin through suppression of Akt phosphorylation. *Circ J.* 2013;77(5):1326-1336.
- 67.** Shimizu H, Yisireyili M, Higashiyama Y, Nishijima F, Niwa T. Indoxyl sulfate upregulates renal expression of ICAM-1 via production of ROS and activation of NF-kappaB and p53 in proximal tubular cells. *Life Sci.* 2013;92(2):143-148.
- 68.** Ochoa CD, Yu L, Al-Ansari E, Hales CA, Quinn DA. Thrombospondin-1 null mice are resistant to hypoxia-induced pulmonary hypertension. *J Cardiothorac Surg.* 2010;5:32.
- 69.** Xia Y, Dobaczewski M, Gonzalez-Quesada C, et al. Endogenous thrombospondin 1 protects the pressure-overloaded myocardium by modulating fibroblast phenotype and matrix metabolism. *Hypertension.* 2011;58(5):902-911.
- 70.** Belmadani S, Bernal J, Wei CC, et al. A thrombospondin-1 antagonist of transforming growth factor-beta activation blocks cardiomyopathy in rats with diabetes and elevated angiotensin II. *Am J Pathol.* 2007;171(3):777-789.
- 71.** Bongartz LG, Braam B, Gaillard CA, et al. Target organ cross talk in cardiorenal syndrome: animal models. *Am J Physiol Renal Physiol.* 2012;303(9):F1253-F1263.
- 72.** Nakano T, Katsuki S, Chen M, et al. Uremic toxin indoxyl sulfate promotes proinflammatory macrophage activation via the interplay of OATP2B1 and Dll4-Notch signaling. *Circulation.* 2019;139(1):78-96.
- 73.** van Heerebeek L, Borbely A, Niessen HW, et al. Myocardial structure and function differ in systolic and diastolic heart failure. *Circulation.* 2006;113(16):1966-1973.
- 74.** Borbely A, van der Velden J, Papp Z, et al. Cardiomyocyte stiffness in diastolic heart failure. *Circulation.* 2005;111(6):774-781.
- 75.** van Heerebeek L, Hamdani N, Handoko ML, et al. Diastolic stiffness of the failing diabetic heart: importance of fibrosis, advanced glycation end products, and myocyte resting tension. *Circulation.* 2008;117(1):43-51.
- 76.** Sheng JJ, Feng HZ, Pinto JR, Wei H, Jin JP. Increases of desmin and alpha-actinin in mouse cardiac myofibrils as a response to diastolic dysfunction. *J Mol Cell Cardiol.* 2016;99:218-229.
- 77.** Paulus WJ, Tschope C, Sanderson JE, et al. How to diagnose diastolic heart failure: a consensus statement on the diagnosis of heart failure with normal left ventricular ejection fraction by the Heart Failure and Echocardiography Associations of the European Society of Cardiology. *Eur Heart J.* 2007;28(20):2539-2550.
- 78.** Guazzi M, Dixon D, Labate V, et al. RV contractile function and its coupling to pulmonary circulation in heart failure with preserved ejection fraction: stratification of clinical phenotypes and outcomes. *J Am Coll Cardiol Img.* 2017;10(10 Pt B):1211-1221.
- 79.** Mohammed SF, Hussain I, AbouEzzeddine OF, et al. Right ventricular function in heart failure with preserved ejection fraction: a community-based study. *Circulation.* 2014;130(25):2310-2320.
- 80.** Hamdani N, Franssen C, Lourenco A, et al. Myocardial titin hypophosphorylation importantly contributes to heart failure with preserved ejection fraction in a rat metabolic risk model. *Circ Heart Fail.* 2013;6(6):1239-1249.

KEY WORDS aryl hydrocarbon receptor, cardiac fibrosis, chronic kidney disease, left ventricular hypertrophy, thrombospondin 1

APPENDIX For supplemental figures and tables, please see the online version of this paper.

EDITORIAL COMMENT

Thrombospondin-1 in Chronic Kidney Disease Driven Cardiac Dysfunction



More Than Just a Biomarker?*

Attila Kiss, MD

Chronic kidney disease (CKD) affects 15% to 20% of adults globally and increases the risk of various cardiovascular diseases (CVDs); consequently, cardiorenal syndromes encompasses conditions in which failure of either the kidneys or the heart leads to failure of the other organ.¹ In general, progressive deterioration of the left ventricular (LV) pump function leads to insufficient perfusion of the kidney and renal dysfunction entails increased blood pressure, fluid retention, and elevation of uremic toxins levels in the circulation, which eventually foists increased workload on the heart and results in cardiomyocyte hypertrophy, stiffness, metabolic alterations, and extracellular matrix (ECM) remodeling with concomitant cardiac fibrosis.¹ Current treatments for chronic CKD involve lifestyle changes, medication, and dialysis, which can delay disease progression but they do not usually rescue the adverse cardiac remodeling. Consequently, CKD-driven cardiac dysfunction is still largely incurable; therefore, there is an urgent need for evidence-based therapies to identify, treat, and significantly improve both the cardiovascular and kidney dysfunction among patients with CKD.

To better understand the progression of cardiovascular dysfunction in CKD, and eventually reduce

the premature mortality in patients with CKD, it is also important to identify one or likely more highly sufficient/selective circulating biomarkers. Accordingly, previous studies summarized the use of serum biomarkers (eg, atrial and B-type natriuretic peptide, isoforms of troponins, adiponectin, plasma growth differentiation factor-15, ECM proteins) for cardiovascular disease risk prediction in CKD.^{2,3} Most cardiovascular diseases (eg, CKD) involve severe remodeling of the ECM, culminating in the formation of fibrotic tissue that is deleterious to organ function and ECM protein may serve as a biomarker for disease progression⁴ and targeted therapy for heart failure in CKD. In addition, the accumulation of non-hemodialyzable uremic toxins, such as indoxyl sulfate and p-cresyl sulfate, in the circulation and in tissues serves as a biomarker and is associated with the progression of CKD, and CVD in patients with CKD.⁵

The ECM network is composed mainly of collagen, which provides a scaffold for the cellular constituents of the heart and, furthermore, contributes to the effective transmission of the contractile force. Collagen type I and type III are highly abundant in the heart, and responsible for the elasticity of the matrix network as well as cardiomyocyte stiffness and mechanical compliance. Besides collagens, the ECM also includes nonstructural proteins such as glycosaminoglycans, proteoglycans, and glycoproteins. However, despite its high clinical significance, the exact underlying signaling mechanisms of cardiac ECM remodeling, fibrosis still remains elusive in CKD.

A recent study in this issue of *JACC: Basic to Translational Science* by Julovi et al⁶ demonstrated for the first time that the disruption of ECM glycoprotein thrombospondin (TSP)-1, which in general may be secreted by various cells, including

*Editorials published in *JACC: Basic to Translational Science* reflect the views of the authors and do not necessarily represent the views of *JACC: Basic to Translational Science* or the American College of Cardiology.

From the Ludwig Boltzmann Institute for Cardiovascular Research at the Center for Biomedical Research and Translational Surgery, Medical University of Vienna, Vienna, Austria.
The author attests they are in compliance with human studies committees and animal welfare regulations of the author's institution and Food and Drug Administration guidelines, including patient consent where appropriate. For more information, visit the [Author Center](#).

cardiomyocytes, fibroblasts, and smooth muscle cells in the myocardium, provides cardioprotection in a mouse model of CKD.

When extrapolating from preclinical (animal study and using human cardiomyocytes) findings to patients with CKD, the authors also issue the differential protein levels of circulating TSP-1 and myocardial gene expression of TSP-1 among patients with CKD in comparison with healthy patients, consequently higher levels of TSP-1 in plasma associated with a lower LV ejection fraction and an increase in LV mass index, respectively. Surprisingly, TSP-1 knockout mice do not show renal protection, despite its detrimental role in renal fibrosis⁷ and ischemic acute kidney injury. Furthermore, TSP-1 upregulation in the kidneys is associated with aging, and subsequently renal dysfunction.⁷ Accordingly, CKD and CVD are common in older people, and their prevalence increases in parallel with age. This is a very important and thought-provoking issue with regard to the findings of Julovi et al,⁶ and one can speculate whether TSP-1 upregulation in plasma may reflect renal failure rather than cardiomyocyte dysfunction/cardiac ECM remodeling in patients with CKD. Consequently, using renal tissue-specific TSP-1 knockout mice with advanced age theoretically poses an attractive alternative to clarifying the unrealized renal benefits of TSP-1 downregulation and simultaneously raise awareness of the progression of CKD-driven LV hypertrophy and dysfunction.

One of the greatest fundamental findings by Julovi et al⁶ was to recognize the molecular signaling mechanism that mitigates TSP-1 upregulation in cardiomyocytes. Accordingly, nonhemodialyzable uremic toxins, for example, indoxyl sulfate binds to aryl hydrocarbon receptor in cardiomyocytes, a ligand activated transcription factor that may be involved in the regulation of TSP-1. Consequently, its overexpression resulted in cardiomyocyte hypertrophy and diastolic dysfunction in association with cardiac fibrosis in a mouse model of CKD and isolated human cardiomyocytes, respectively. Consistent with that finding, the observed impaired LV function and hypertrophy are associated with plasma indoxyl sulfate upregulation in a rat model of CKD.⁸ Although not explicitly stated in the report, we raise the question of whether indoxyl sulfate solely regulates the expression of TSP-1 in cardiomyocytes or whether its overexpression also contributes to the enhancement of pro-inflammatory and pro-fibrotic mechanisms in different cell types in the heart tissue? The authors did not provide further evidence or investigate why the high levels of indoxyl sulfate even in TSP-1

knockout mice still resulted in a strong cardioprotection. A question that emerges from these findings is whether and to what extent the TSP-1 plays a role in cardiac dysfunction in CKD, whether TSP-1 in cardiomyocytes affects the phenotypes of neighboring cells and microenvironment (eg, in cardiac fibroblasts). Indeed, cardiomyocytes are critical contributors to the myocardial fibrotic programs,⁹ in response to injurious stimuli (mechanical stress, metabolic dysfunction, and inflammatory cytokines) that might induce the cardiac fibroblast activation (fibroblasts to myofibroblast transition) and eventually cardiac fibrosis as well as cardiomyocyte stiffness.

A final question addressed by the present study⁶ is whether TSP-1 might be a trigger for senescence in the heart and demonstrated that senescence and pro-inflammatory markers in the heart tissue were mitigated in TSP-1 knockout mice with CKD. In line with that, differentially expressed gene expression analysis in the human dataset also confirmed the potential role of senescence in the progression of CKD and the risk for CVD in CKD. These findings raise the question of the probability of senolytic treatment¹⁰ to alleviate the effects of TSP-1 in adverse cardiac remodeling in CKD.

In summary, the findings of Julovi et al⁶ provide a first piece of evidence that a novel signaling pathway drives uremic toxin; for example, indoxyl sulfate-induced cardiomyocyte dysfunction through the upregulation of the ECM protein TSP-1. These findings were also confirmed in patients with CKD, lending support to the premise that further stimulation of testing monoclonal antibodies or inhibitors that block the actions of TSP-1. However, further multicenter, randomized clinical trials are warranted to confirm the interaction between indoxyl sulfate and TSP-1 and to prove evidence that TSP-1 levels are gradually increasing in CKD and CKD-driven cardiac hypertrophy and diastolic dysfunction.

FUNDING SUPPORT AND AUTHOR DISCLOSURES

The author has reported that he has no relationships relevant to the contents of this paper to disclose.

ADDRESS FOR CORRESPONDENCE: Dr Attila Kiss, Ludwig Boltzmann Institute for Cardiovascular Research at the Center for Biomedical Research and Translational Surgery, Medical University of Vienna, Währinger Gürtel 18-20, 1090 Vienna, Austria. E-mail: attila.kiss@meduniwien.ac.at.

REFERENCES

- 1.** Scheffold JC, Filippatos G, Hasenfuss G, Anker SD, von Haehling S. Heart failure and kidney dysfunction: epidemiology, mechanisms and management. *Nat Rev Nephrol*. 2016;12:610–623.
- 2.** D'Marco L, Bellasi A, Raggi P. Cardiovascular biomarkers in chronic kidney disease: state of current research and clinical applicability. *Dis Markers*. 2015;2015:586569.
- 3.** Junho CVC, Frisch J, Soppert J, Wollenhaupt J, Noels H. Cardiomyopathy in chronic kidney disease: clinical features, biomarkers and the contribution of murine models in understanding pathophysiology. *Clin Kidney J*. 2023;16:1786–1803.
- 4.** Barallobre-Barreiro J, Radovits T, Fava M, et al. Extracellular matrix in heart failure: role of ADAMTS5 in proteoglycan remodeling. *Circulation*. 2021;144:2021–2034.
- 5.** Lim YJ, Sidor NA, Tonial NC, Che A, Urquhart BL. Uremic toxins in the progression of chronic kidney disease and cardiovascular disease: mechanisms and therapeutic targets. *Toxins (Basel)*. 2021;13:142.
- 6.** Julovi SM, Trinh K, Robertson H, et al. Thrombospondin-1 drives cardiac remodeling in chronic kidney disease. *J Am Coll Cardiol Basic Trans Science*. 2024;9(5):607–627.
- 7.** Kang DH, Anderson S, Kim YG, et al. Impaired angiogenesis in the aging kidney: vascular endothelial growth factor and thrombospondin-1 in renal disease. *Am J Kidney Dis*. 2001;37:601–611.
- 8.** Sarkozy M, Watzinger S, Kovacs ZZA, et al. Neuregulin-1beta improves uremic cardiomyopathy and renal dysfunction in rats. *J Am Coll Cardiol Basic Trans Science*. 2023;8:1160–1176.
- 9.** Frangogiannis NG. Cardiac fibrosis: cell biological mechanisms, molecular pathways and therapeutic opportunities. *Mol Aspects Med*. 2019;65:70–99.
- 10.** Owens WA, Walaszczyk A, Spyridopoulos I, Dookun E, Richardson GD. Senescence and senolytics in cardiovascular disease: promise and potential pitfalls. *Mech Ageing Dev*. 2021;198:111540.

KEY WORDS cardorenal syndrome, chronic kidney disease, HFP EF, left ventricular hypertrophy, thrombospondin 1

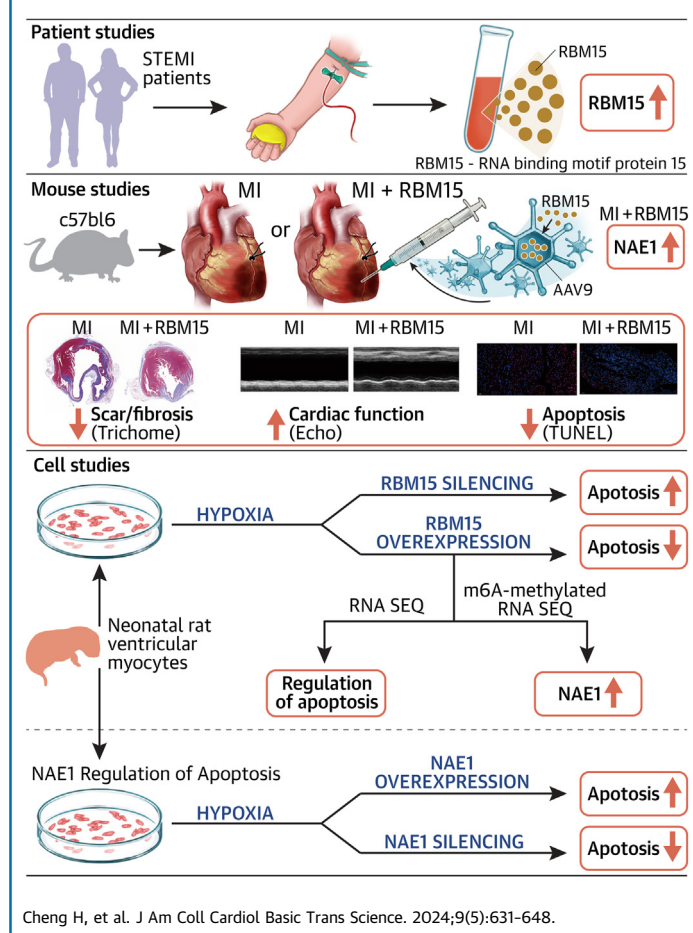
ORIGINAL RESEARCH - PRECLINICAL



RBM15 Protects From Myocardial Infarction by Stabilizing NAE1

Hao Cheng, MD, PhD,^{a,b,c,d,*} Jian Wu, MD, PhD,^{a,b,c,d,*} Linnan Li, MD, PhD,^{a,b,c,d} Xiaoyue Song, MD, PhD,^{a,b,c,d} Junqiang Xue, MD, PhD,^{a,b,c,d} Yuekai Shi, MD, PhD,^{a,b,c,d} Yunzeng Zou, MD, PhD,^{a,b,c,d,e} Jianying Ma, MD, PhD,^{a,b,c,d} Junbo Ge, MD, PhD^{a,b,c,d,e}

VISUAL ABSTRACT



HIGHLIGHTS

- RBM15, as a RNA-binding protein, participates in m⁶A regulation in MI.
- RBM15 can attenuate cardiomyocyte apoptosis and improve heart function after MI.
- RBM15 exerts myocardial protection through stabilizing NAE1 mRNA.

From the ^aDepartment of Cardiology, Zhongshan Hospital, Fudan University, Shanghai, China; ^bShanghai Institute of Cardiovascular Diseases, Shanghai, China; ^cKey Laboratory of Viral Heart Diseases, National Health Commission, Shanghai, China; ^dKey Laboratory of Viral Heart Diseases, Chinese Academy of Medical Science, Shanghai, China; and the ^eInstitutes of Biomedical Sciences, Fudan University, Shanghai, China. *Drs Cheng and Wu contributed equally to this work.

**ABBREVIATIONS
AND ACRONYMS**

- AAV9** = adeno-associated virus 9
- GO** = Gene Ontology
- KEGG** = Kyoto Encyclopedia of Genes and Genomes
- m⁶A** = N6-methyladenosine
- MeRIP-seq** = methylated RNA immunoprecipitation sequencing
- METTL** = methyltransferase-like
- MI** = myocardial infarction
- mRNA** = messenger RNA
- NAE1** = NEDD8 activating enzyme E1 subunit 1
- NRVMs** = neonatal rat left ventricle myocytes
- NS** = normal saline
- qPCR** = quantitative polymerase chain reaction
- RBM15** = RNA binding motif protein 15
- si** = small interfering
- TUNEL** = terminal uridine nick-end labeling
- WTAP** = Wilms tumor 1-associated protein

SUMMARY

RNA-binding proteins play multiple roles in several biological processes. However, the roles of RBM15—an important RNA-binding protein and a significant regulator of RNA methylation—in cardiovascular diseases remain elusive. This study aimed to investigate the biological function of RBM15 and its fundamental mechanisms in myocardial infarction (MI). Methylated RNA immunoprecipitation sequencing was used to explore the N6-methyladenosine (m^6A) difference between MI and normal tissues. Our findings showed the elevated level of m^6A in MI, and its transcription profile in both MI and normal tissues. RBM15 was the main regulator and its overexpression attenuated apoptosis in cardiomyocytes and improved cardiac function in mice after MI. Then, we used one target NEDD8 activating enzyme E1 subunit and its inhibitor (MLN4924) to investigate the impact of RBM15 targets on cardiomyocytes. Finally, the enhanced m^6A methylation in the presence of RBM15 overexpression led to the increased expression and stability of NEDD8 activating enzyme E1 subunit. Our findings suggest that the enhanced m^6A level is a protective mechanism in MI, and RBM15 is significantly upregulated in MI and promotes cardiac function. This study showed that RBM15 affected MI by stabilizing its target on the cell apoptosis function, which might provide a new insight into MI therapy.

(J Am Coll Cardiol Basic Trans Science 2024;9:631–648) © 2024 The Authors. Published by Elsevier on behalf of the American College of Cardiology Foundation. This is an open access article under the CC BY-NC-ND license (<http://creativecommons.org/licenses/by-nc-nd/4.0/>).

Coronary heart disease, leading to myocardial infarction (MI), is a major contributor to morbidity and mortality on a global scale.¹ In the United States, severe ischemia and loss of cardiomyocytes cause nearly 735,000 annual incidences of irreversible tissue damage, resulting in hypertrophy, ventricular remodeling, dilatation, and heart failure.² After the ischemic injury, the myocardium undergoes a sequence of molecular and cellular interactions after different stages of tissue repair.³ The pathophysiology and pathogenesis of MI are complex and diverse, mainly including the production of reactive oxygen species, apoptosis, autophagy, inflammatory response, mitochondrial dysfunction, and immune response.⁴ Some useful clinical biomarkers and key molecules for MI diagnosis, including NPPB, TNNT2, ANGPT2, and THBS2, have been identified already.^{5–9} Although advances in MI treatment, such as stem cell therapies, have improved the prognosis of MI, patients with extensive myocardial injury are still at a high risk of chronic heart failure.^{10–12} In recent years, multiple studies have found that epigenetic regulation is not only involved in the progression of cardiac hypertrophy, hypertension, heart failure, and other cardiovascular diseases, but also plays an important role in MI.¹³

Epigenetics refers to the heritable changes in the phenotype when the DNA methylation, histone modification, noncoding RNAs, and N6-methyladenosine (m^6A) methylation occur on. An essential epigenetic change known as m^6A takes place when the adenine base is methylated at the N6 position.^{14,15} Evidence has shown that m^6A -related proteins play a critical role in diverse biological functions, especially in the development and progression of diseases, such as in promoting gastric cancer progression, inhibiting pancreatic cancer tumorigenesis, or promoting proliferation and tumorigenicity of endometrial cancer.^{16–18} Consistent with its roles, m^6A is emerging as an important pathway mediating cardiovascular diseases.^{19–21} Significant functions are performed by regulators of m^6A , the most common kind of RNA modification. These functions include destruction, translation, localization, transportation, and RNA processing.^{22,23} The m^6A RNA editing was discovered in the 1970s and has recently emerged as a significant regulator in gene expression.^{24,25} It is a dynamic and reversible modification mechanism, and its biological functions are mediated through m^6A -related proteins, named “writer,” “eraser,” and “reader.”²⁶ The formation of m^6A was modulated by 3 categories of proteins: 9 readers (CBLL1, RNA binding motif protein 15

The authors attest they are in compliance with human studies committees and animal welfare regulations of the authors' institutions and Food and Drug Administration guidelines, including patient consent where appropriate. For more information, visit the [Author Center](#).

[RBM15]B, RBM15, ZC3H13, VIRMA, WTAP, METTL16, METTL14, and METTL3), 2 erasers (ALKBH5 and FTO), and 15 readers (IGF2BP1, ELAVL1, RBMX, IGFBP3, IGFBP2, IGFBP1, HNRNPA2B1, LRPPRC, FMR1, HNRNPC, YTHDF3, YTHDF2, YTHDF1, YTHDC2, and YTHDC1).²³ The methyltransferase complex includes methyltransferase-like 3 (METTL3), METTL14, and Wilms tumor 1-associated protein (WTAP) plays an important role on the cardiac function after MI.²⁷ However, there is less research about other methylation regulators, such as RBM15. Therefore, in the present research, we investigated the role of RBM15 in the incidence and progression of MI and provided a novel insight toward myocardial protection.

RBM15 is an RNA-binding protein that can alternatively splice c-Mpl messenger RNA (mRNA) to influence the process of acute megakaryocytic leukemia.²⁸ Moreover, RBM15 is a methylation regulator, although it is named m⁶A methylase, the real function of adding m⁶A is from METTL3.^{29,30} Thus, we investigated whether the role of RBM15 in myocardial protection is significant and whether it could regulate m⁶A process in MI. In this regard, we found that MI tissues exhibited much higher m⁶A methylation levels compared with normal myocardium tissues. The expression of RBM15 was substantially upregulated among m⁶A-related proteins. The developmental expression of RBM15 decreased cell apoptosis both in vitro and in vivo. Then, m⁶A-seq characterization of MI tissues revealed that RBM15 regulated a target gene NEDD8 activating enzyme E1 subunit 1 (NAE1) involving the p53 signaling pathway. Moreover, the expression of NAE1 decreased apoptosis via the mechanism of increased m⁶A methylation. Taken together, these results characterize RBM15 as a significant factor attenuating the apoptosis of cardiomyocytes under MI.

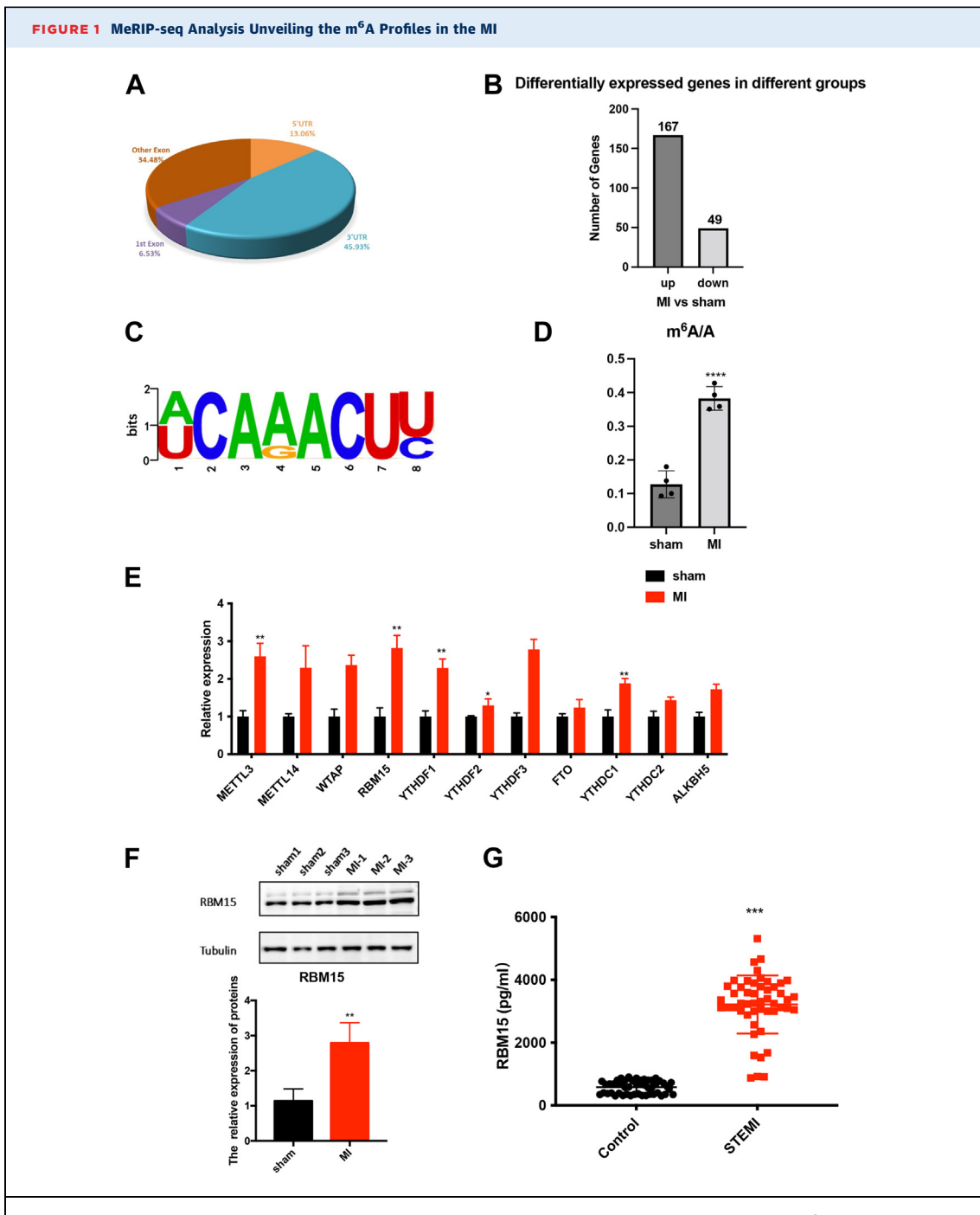
METHODS

HUMAN INCLUSION AND EXCLUSION CRITERIA. In this study, patients with ST-elevation MI who underwent emergent percutaneous catheter interventions in the catheter room of Zhongshan Hospital Affiliated with Fudan University from January 2019 to June 2022 were selected as the experimental group, and healthy individuals matched with the age of the experimental group were selected as the control group (*Supplemental Table 1*). Blood sample collection and experiments were approved by the hospital ethics committee. The inclusion criteria of experimental group and control groups are as follows. 1) The experimental group standard was a male, 18 to 70 years old with obvious pain symptoms in the

anterior chest area were. The time was >30 minutes, rest or sublingual nitroglycerin cannot alleviate the pain, which may be accompanied by nausea and vomiting; electrocardiography showed elevated ST-segment in 2 (or more) leads, pathological Q-wave, or dynamic change; new left bundle branch block; cardiac troponin T, cardiac troponin I, or creatine kinase-myocardial band increase (>99% of the upper limit of the normal reference range); angiography showed coronary stenosis of >70%; chest pain time of <12 hours; no recent history of infectious diseases, malignant tumors, and so on; and informed consent has been signed. 2) The control group standard was a male, age 18 to 70 years with no chest pain caused by physical labor or excitement. There was no significant change in electrocardiography under normal conditions; cardiac troponin T, cardiac troponin I, or creatine kinase-myocardial band are normal; no recent history of infectious diseases or malignant tumors; and informed consent has been signed.

QUANTIFICATION OF mRNA METHYLATION WITH m⁶A-IMMUNOPRECIPITATION AND QUANTITATIVE POLYMERASE CHAIN REACTION. The m⁶A modification level of a gene was assessed using the Magna methylated RNA immunoprecipitation (MeRIP) Kit (Millipore, cat. #CR203146). For this purpose, cells were collected, double-washed with ice-cold PBS, and centrifuged at a centrifugation rate of 1,500 rpm for 5 minutes at 4 °C. Then, the supernatant was discarded, and the cells were mixed with RIP lysis buffer (100 µL) and incubated on ice for 5 minutes. The obtained cell preparation was stocked at -80°C for future analysis. Then, the m⁶A antibody (8 µg) was added to a tube containing magnetic beads, which was then subjected to rotation at room temperature for 30 minutes. Antibody-coated beads were double-washed with RIP buffer and resuspended in RIP buffer (900 µL) mixed with cell lysate (100 µL), followed by centrifugation at 14,000 rpm for 10 minutes at 4 °C and rotation at 4 °C overnight. Subsequently, the beads were again washed with a high-salt buffer, and RNAs were extracted with RIP wash buffer. Finally, the RNA enrichment analysis was performed by quantitative polymerase chain reaction (qPCR).

METHYLATED RNA IMMUNOPRECIPITATION SEQUENCING LIBRARY CONSTRUCTION AND SEQUENCING. For this purpose, total RNA extraction was performed by TRIZOL reagent (Invitrogen) and was quantified by Bioanalyzer 2100 and RNA 6000 Nano LabChip Kit (Agilent) with the RIN number more than 7.0. Then, almost 200 µg of the total RNA was used for the purpose of isolating and purifying the poly(A) mRNA with poly(T) oligonucleotides content attached to the



(A) There were different peaks between MI and sham samples. (B) The differentially expressed genes were targeted by m⁶A modification in MI and sham groups. (C) The m⁶A consensus sequence motif was identified in NRVMs. (D) The total m⁶A level was increased in MI. (E) Relative m⁶A-related proteins increased in MI. (F) The protein expression of RBM15 increased notably in MI. (G) The RBM15 quantification of serum from patients with STEMI and the healthy individuals, as assessed by ELISA. (n = 50). Data are presented as mean \pm SEM. *P < 0.05, **P < 0.01, ***P < 0.001. In data D, E, and F, differences were compared between sham and MI. In data G, difference was compared between controls and STEMI. All data were analyzed using unpaired Student's t test. ELISA = enzyme-linked immunoassay; m⁶A = N6-methyladenosine; MI = myocardial infarction; MeRIP-seq = methylated RNA immunoprecipitation sequencing; STEMI = ST-segment elevation myocardial infarction.

magnetic beads (Invitrogen). Then, the poly(A) mRNA fractions were fragmented into ~100-nt-long oligonucleotides using divalent cations at an elevated temperature. The RNA fragments were then filtered and subjected to incubation with an m⁶A-specific antibody (No. 202003, Synaptic Systems) in immunoprecipitation buffer (50 mM Tris-HCl, 750 mM NaCl, and 0.5% Igepal CA-630) supplemented with 0.5 µg/µL bovine serum albumin at 4 °C. After 2 hours, the RNA-antibody mixture was further incubated with protein-A beads. Moreover, RNA was washed with elution buffer (1 × immunoprecipitation buffer and 6.7 mM m⁶A) and precipitated using ethanol (75%). The immunoprecipitation fragments containing m⁶A and untreated input control fragments were converted to the final complementary DNA library by means of the deoxyuridine triphosphate method complying with strand-specific library preparation. The average insert size for the paired-end libraries was ~100 ± 50 bp. Finally, an Illumina Novaseq 6000 platform was performed for the paired-end 2 × 150 bp sequencing.

METHYLATED RNA IMMUNOPRECIPITATION SEQUENCING DATA ANALYSIS. First, Cutadapt and Perl scripts were used for the quality control of the reads to remove the adaptor, low-quality bases, and undetermined bases.³¹ HISAT2 was used for the purpose of mapping reads to the genome with default parameters.³² The m⁶A peaks were obtained by the R package exomePeak.³³ The peak annotation was done with gene architecture by ChIPseeker.³⁴ Then, StringTie was performed to measure the expression levels for all mRNAs from input libraries by calculating the fragments per kilobase of transcript per million mapped reads.³⁵ Finally, the differentially expressed mRNAs with a fold-change of 2 and a *P* value of <0.05 were selected with the aid of the edgeR package in R.³⁶

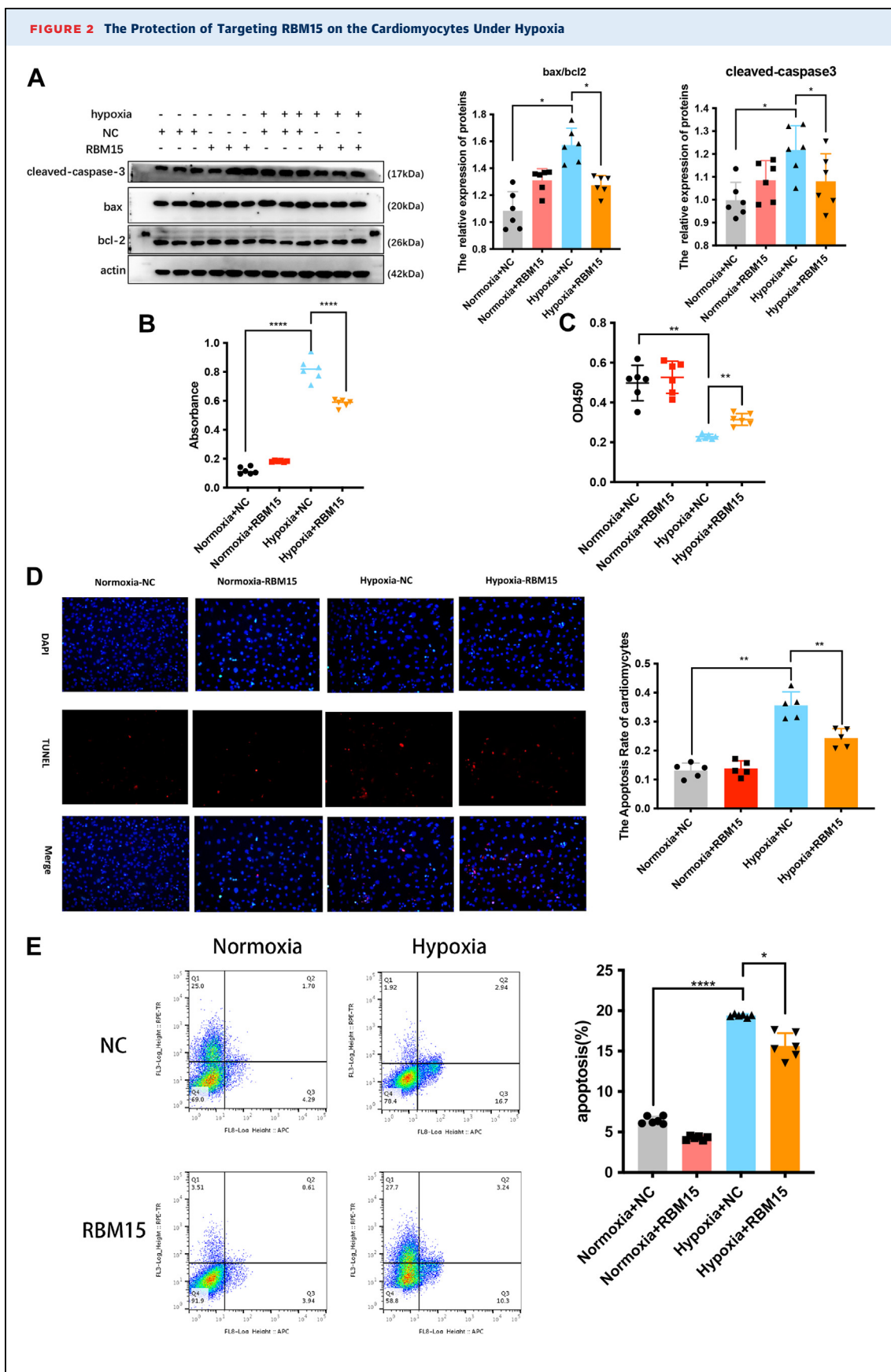
QUANTIFICATION AND STATISTICAL ANALYSIS. All data are shown as mean ± SEM. All statistical analyses, unless otherwise indicated, were performed by GraphPad Prism 9.0 (GraphPad Software). Statistical significance was calculated by 2-tailed unpaired Student's *t* test if 2 independent groups were compared. One-way analysis of variance was used for comparisons among multiple groups. Post hoc analyses were performed using Holm-Sidak's post hoc test for multiple pairwise comparisons or by controlling the false discovery rate using the method of Benjamini, Krieger, and Yekutieli. Kaplan-Meier survival analysis was used to reveal the survival rate of each group *in vivo*. *P* values of <0.05 were considered statistically significant (**P* < 0.05, ***P* < 0.01, ****P* < 0.001). The

significant threshold in multiple tests were set by a false discovery rate of <0.05.

RESULTS

HIGHLY EXPRESSED m⁶A-RELATED PROTEIN RBM15 IN MI. To study the presence of the m⁶A modification during MI, we successfully constructed mice models of MI. We confirmed the occurrence of the m⁶A modification during the MI process by methylated RIP sequencing (MeRIP-Seq); specifically, 1,538 m⁶A peaks were observed in MI compared with the control, and 45.93% of the m⁶A peaks occurred in the 3' untranslated region (Figure 1A). We found 167 upregulated genes and 49 downregulated genes (Figure 1B). In total, the m⁶A sequence identified that 397 transcripts were upregulated, while 252 transcripts were downregulated (Supplemental Figure 1A). Gene Ontology (GO) analysis showed that the differentially expressed m⁶A-related transcripts were enriched in gene sets involved in extracellular space, extracellular matrix, and positive regulation of apoptosis cell clearance, revealing that m⁶A regulation might have an impact on apoptosis (Supplemental Figure 1B). Moreover, Kyoto Encyclopedia of Genes and Genomes (KEGG) analysis showed that the differentially expressed m⁶A-related transcripts were involved in histidine metabolism, hypoxia-inducible factor-1 signaling pathway, complement and coagulation cascades, and extracellular matrix-receptor interaction (Supplemental Figure 1C). When mapping the m⁶A methylomes, the m⁶A consensus sequence RRACH motif was identified to be highly enriched within m⁶A sites in the immuno-purified mRNA (Figure 1C).

Furthermore, an elevated total m⁶A mRNA level was identified in MI (Figure 1D). Then, the expressions of m⁶A-related proteins such as some "writers" (METTL3, METTL14, WTAP and RBM15), "erasers" (FTO and ALKBH5), and "readers" (YTHDF1, YTHDF2, YTHDF3, YTHDC1, and YTHDC2) in MI tissues were assessed with qPCR (Figure 1E). The expression of METTL3 and RBM15 increased dramatically in MI among other methylase-related proteins (Figure 1E). Because we have investigated the role of METTL3 in MI, in this research we paid attention to RBM15. Then, we assessed the protein expression of RBM15 by Western blotting, which also showed a highly elevated expression level in MI tissues (Figure 1F). To investigate potential diagnosis or treatment roles of RBM15 in a clinical context, we examined serum from patients with ST-segment elevation MI and healthy individuals using enzyme-linked immunoassay. Finally, we observed that the RBM15 level increased



Continued on the next page

remarkably (**Figure 1G**). To imitate the MI circumstances, neonatal rat left ventricle myocytes (NRVMs) under hypoxia conditions at different time points (1, 3, 6, 12, and 24 hours) were set to assess the expression of RBM15; we found the highly elevated expression level after 3 hours (**Supplemental Figure 1D**). These results proved that RBM15 might have an important role in the m⁶A modification in MI.

THE EFFECTS OF OVEREXPRESSING RBM15 ON CARDIOMYOCYTES UNDER HYPOXIA. To investigate the biological roles of RBM15 in cardiomyocytes, RBM15 silencing and overexpression were established via transfection into NRVMs (**Supplemental Figures 2A to 2D**). Subsequently, loss- and gain-of-function assays were carried out for the purpose of identifying the role of RBM15 in NRVMs under hypoxic conditions. Considering the key role of bcl-2, cleaved-caspase3, and bax in mediating apoptosis, Western blotting analysis confirmed that RBM15 overexpression attenuated apoptosis activity of NRVMs when treated in hypoxic conditions (**Figure 2A**). Furthermore, lactate dehydrogenase release assays showed that RBM15 overexpression also decreased apoptosis of NRVMs (**Figure 2B**). The results from the CCK8 assay also suggested that RBM15 decreased the apoptosis of NRVMs under hypoxic conditions (**Figure 2C**). Subsequently, we used a terminal uridine nick-end labeling (TUNEL) assay and flow cytometry to further demonstrate the protective effect of RBM15. After hypoxia treatment, there were few TUNEL-positive nuclei in NRVMs that overexpressed RBM15 (**Figure 2D**). Representative flow cytometry plots were generated for control and NRVMs overexpressing RBM15; they demonstrated a decreased number of apoptotic cells in the RBM15-overexpressing treated group (**Figure 2E**). Hence, those *in vitro* results showed that RBM15 could ameliorate hypoxia-induced cell death.

APOPTOSIS OF NRVMs WITH SILENCED RBM15 UNDER HYPOXIC CONDITIONS. To further investigate the functional role of RBM15 in NRVMs, we used small

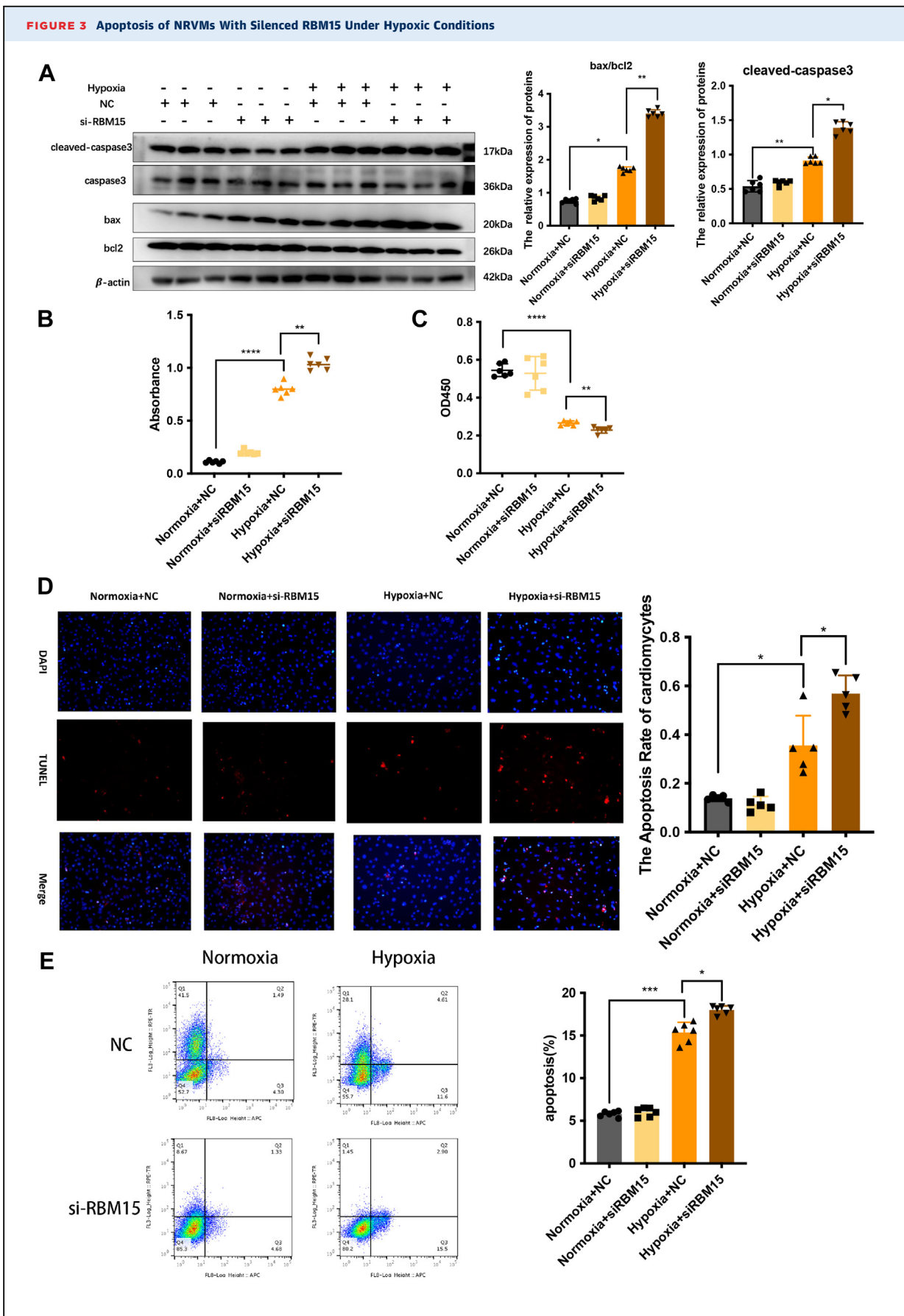
interfering (si)-RBM15 to demonstrate whether the effects of RBM15 knockdown are the opposite from those of RBM15 overexpression. To this end, we performed Western blotting and identified the apoptosis-related markers including bax/bcl-2 and cleaved-caspase3. We found that the RBM15 knockdown remarkably promoted NRVMs apoptosis following hypoxia (**Figure 3A**). Similar to the Western blotting results, the lactate dehydrogenase release assay and CCK8 assay showed that RBM15 silencing increased cell death (**Figures 3B and 3C**). The TUNEL assay and flow cytometry showed the same results, indicating that RBM15 knockdown promoted NRVMs apoptosis after hypoxic treatment (**Figures 3D and 3E**).

IMPROVED HEART FUNCTION AND ATTENUATED CARDIAC FIBROSIS AFTER OVEREXPRESSING RBM15. The protective effects of RBM15 overexpression in cells under hypoxia allowed us to further analyze its effect on the infarction-induced cardiac dysfunction. Then, we successfully established the mouse MI model overexpressing RBM15 (**Supplemental Figures 2E and 2F**). Given that glycogen consumption can cause hypoxia- and glycolysis-induced damage of NRVMs at the very beginning of MI, apoptosis was assessed through Western blot and TUNEL assays on the infarcted tissues and remote areas. We found that, 1 week after MI, the expression levels of cleaved-caspase3 and bax significantly decreased, whereas the expression level of bcl-2 increased in the RBM15-adeno-associated virus 9 (AAV9) group (**Figures 4A to 4F**). The TUNEL assay showed that the number of TUNEL-positive nuclei in the RBM15-AAV9 group was lower than that of the NC-AAV9 group (**Figure 4G**). Thus, the *in vivo* results showed that RBM15 was able to ameliorate MI-induced cell death.

At weeks 1, 2, and 4 after MI, serial echocardiography and hemodynamic measurements were used to evaluate the cardiac function in mice from the indicated groups. We found that the cardiac function was improved by RBM15 overexpression, as indicated by

FIGURE 2 Continued

(A) The apoptosis markers cleaved-caspase3 and bax, and the antiapoptotic marker bcl-2 were assessed by Western blotting (left); the relative ratios of cleaved-caspase3 and bax/bcl-2 protein levels were calculated based on Western blotting results (middle and right). (B, C) Cell injury was determined by the LDH release assay and CCK8 assay ($n = 6$). (D) Representative images of TUNEL staining of NRVMs for DNA fragmentation showing the apoptotic cells (nuclei stained in blue with DAPI, apoptotic cells stained in red) (left) ($n = 5$). Statistical results of TUNEL-positive cells per field indicated that RBM15 decreased treatment-induced cell apoptosis (right). (E) The representative images of flow cytometry using APC and 7-AAD staining (left); statistical analysis of apoptosis ratio of the flow cytometry data (right) ($n = 6$). Scale bar, 100 μ m. $n = 3$. Data are presented as mean \pm SEM. * $P < 0.05$, ** $P < 0.01$, **** $P < 0.0001$. In data A (right), B, C, D (right), and E (right), differences were compared between Normoxia + NC, Hypoxia + NC, and Hypoxia + RBM15. All data were analyzed using One-way analysis of variance followed by Tukey's post hoc analysis. DAPI = 4'-6-diamidino-2-phenylindole; LDH = lactate dehydrogenase; NC = normal control; NRVM = neonatal rat left ventricle myocyte; TUNEL = terminal uridine nick-end labeling.



higher EF%, FS% and lower LVIDd, LVIDs at week 4 after MI (**Figures 5A to 5E**, *Supplemental Figures 3A to 3E*, *Supplemental Table 5*). The effects of RBM15 on the post-MI outcomes were further confirmed by assessing smooth muscle/collagen through Masson staining. The smooth muscle/collagen ratio in the normal saline (NS) group was considerably lower than that in the sham group (**Figures 5F and 5G**). Furthermore, hematoxylin and eosin staining was performed to evaluate the cell morphology of the myocardium. For example, the cardiomyocytes were arranged regularly in the sham group, showing obvious nuclei and no inflammatory cell infiltration. In contrast, the MI, MI with NS, and MI with NC-AAV9 groups displayed major myocardial cell necrosis, disordered myocardial fiber arrangement, and quantities of inflammatory cell infiltrations. The cardiomyocytes in MI within the RBM15-AAV9 group showed a much more orderly arrangement with a remarkable reduction in the range and degree of cell necrosis (**Figure 5H**). Finally, the probability of survival of each group was analyzed and showed that the mortality rate of mice with injection RBM15 after MI was decreased at the final point (**Figure 5I**, *Supplemental Table 6*). Taken together, these *in vivo* data indicated that RBM15 dramatically decreased infarction and improved cardiac function.

ANALYSIS OF DOWNSTREAM TARGETS OF RBM15 IN CARDIOMYOCYTES. To investigate downstream targets of RBM15, the precise mechanisms of the observed RBM15-dependent phenotypes were further investigated with the aid of an integrated combined MeRIP-seq and RNA-seq. MeRIP-seq revealed 1,538 differential m⁶A peaks with increased abundance, whereas RNA-seq uncovered 851 upregulated transcripts (*Supplemental Tables 7 and 8*). We focused more on oncogenes whose methylation and expression profiles were regulated by RBM15. Thus, only those transcripts that had both hypo-m⁶A peaks and elevated expression levels upon RBM15 overexpression were considered. All differentially

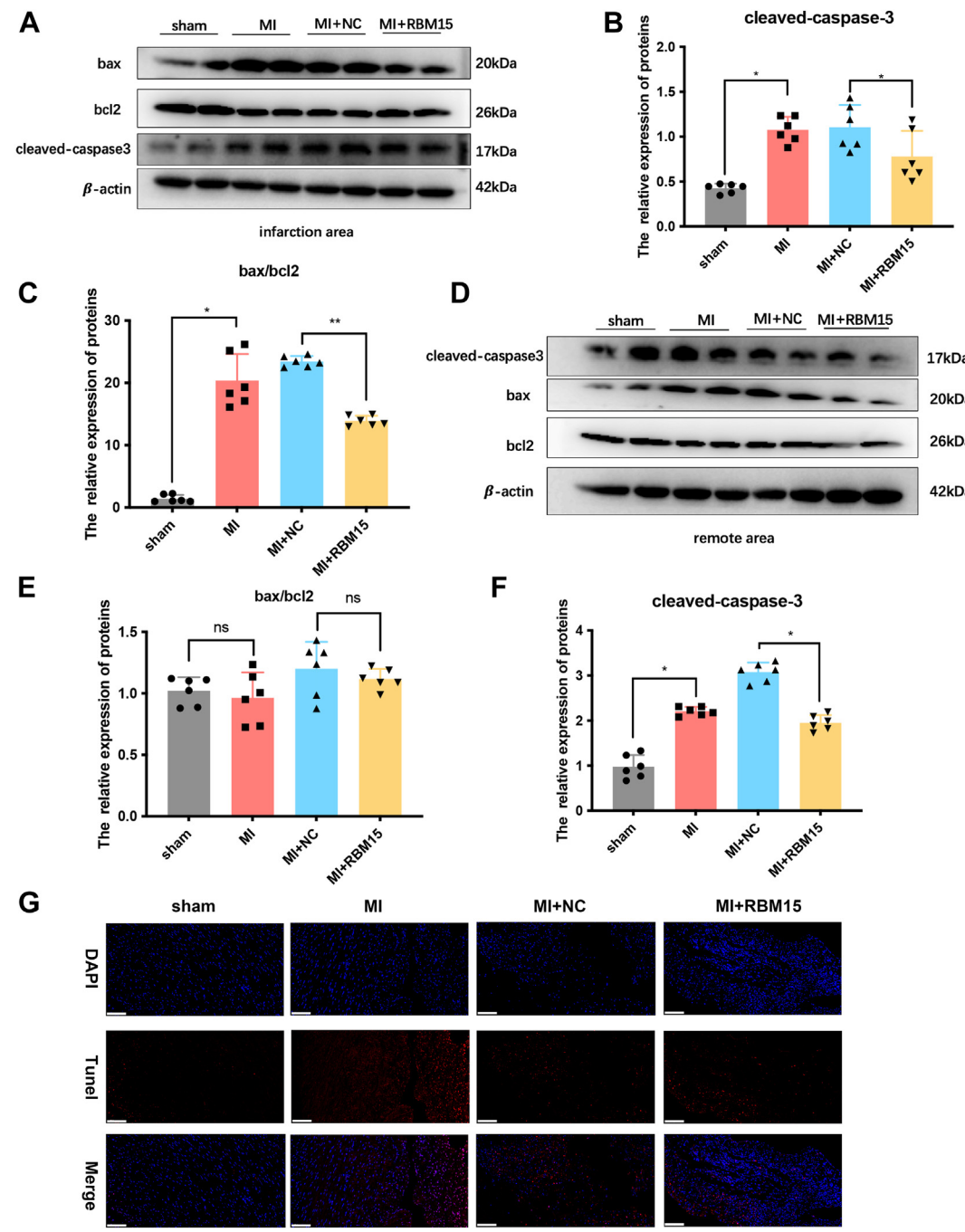
expressed gene fold changes are shown in **Figure 6A**. Then, we conducted the enrichment analysis of all the RBM15-upregulated genes into GO term annotation. The top 10 enrichment GO terms are shown in **Figure 6B**, and we found that gene sets were mainly involved in iron-sulfur cluster assembly, negative regulation of phosphorylation, and regulation of apoptosis process. Moreover, we performed text mining to find any relationship between MI and the significantly enriched GO terms. For example, it has been reported that the ischemic-reperfusion injury results in oxidative damage led by cysteine ligands of the iron-sulfur cluster.³⁷ In MI, PPM1L could inhibit IKK β 's phosphorylation and activation by binding to it, thereby leading to the impairment of nuclear factor κ B signaling activation and inflammatory suppression.³⁸

To further systematically screen biological functions, we searched for all differentially expressed genes in the protein-protein interaction network (**Figure 6C**). Each protein cluster is shown in a distinct color, and the cluster enrichment function is labeled in the corresponding colored boxes. Moreover, KEGG analysis showed that localization, immune response, and metabolic process were related to the RBM15 regulation process (**Figure 6D**). Importantly, filtering the 1538 increased m⁶A peaks with the 851 upregulated genes resulted in the identification of 25 genes (**Figure 6E**). Among these 25 genes, we chose one of the highly conserved genes, named NAE1, in the regulation of the apoptotic process to investigate the details of the regulation (*Supplemental Figures 4A and 4B*).

ENHANCED NAE1 EXPRESSION BY RBM15 THROUGH STABILIZING ITS mRNA. To demonstrate whether RBM15 regulates NAE1 mRNA, we first found that the NAE1 mRNA expression level increased dramatically in the infarction area in the MI model (**Figure 7A**), and its level decreased after silencing RBM15 in NRVMs under hypoxic conditions (**Figure 7B**). In contrast, NAE1 mRNA expression level increased dramatically

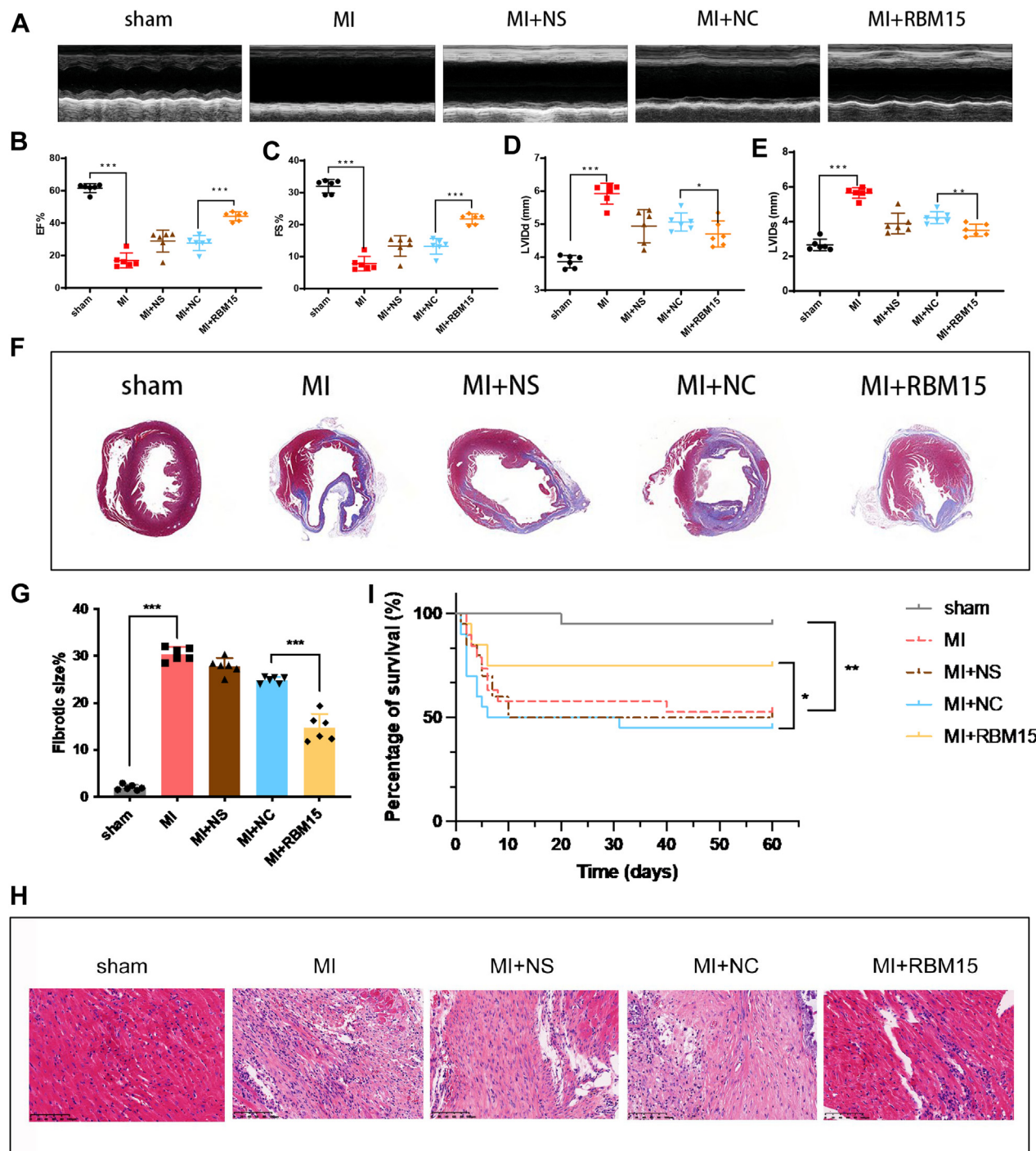
FIGURE 3 Continued

(A) The apoptosis marker bax and the anti-apoptosis marker bcl-2 were assessed by Western blotting (left); the relative ratio of bax/bcl2 protein levels was calculated (middle and right). (B, C) The LDH release assay and CCK8 assay were used to elucidate the cell injury. (B) LDH release assay, (C) CCK8 assay (n = 6). (D) Representative images of TUNEL staining of NRVMs for DNA fragmentation showing the apoptotic cells (nuclei stained in blue with DAPI and apoptotic cells stained in red) (left). Statistical results of TUNEL-positive cells per field indicated that RBM15 decreased treatment-induced cell apoptosis (right) (n = 5). (E) The representative images of flow cytometry using APC and 7-AAD staining (left); statistical analysis of apoptosis ratio of the flow cytometry data (right) (n = 6). Scale bar, 100 μ m. n = 3. Data are presented as mean \pm SEM. *P < 0.05, **P < 0.01, ***P < 0.001. In data A (right), B, C, D (right), and E (right), differences were compared between Normoxia + NC, Hypoxia + NC, and Hypoxia + si-RBM15. All data were analyzed using one-way analysis of variance followed by Tukey's post hoc analysis. 7-AAD = 7-aminoactinomycin D; APC = allophycocyanin; si-RBM15 = small interfering RBM15; other abbreviations as in **Figure 2**.

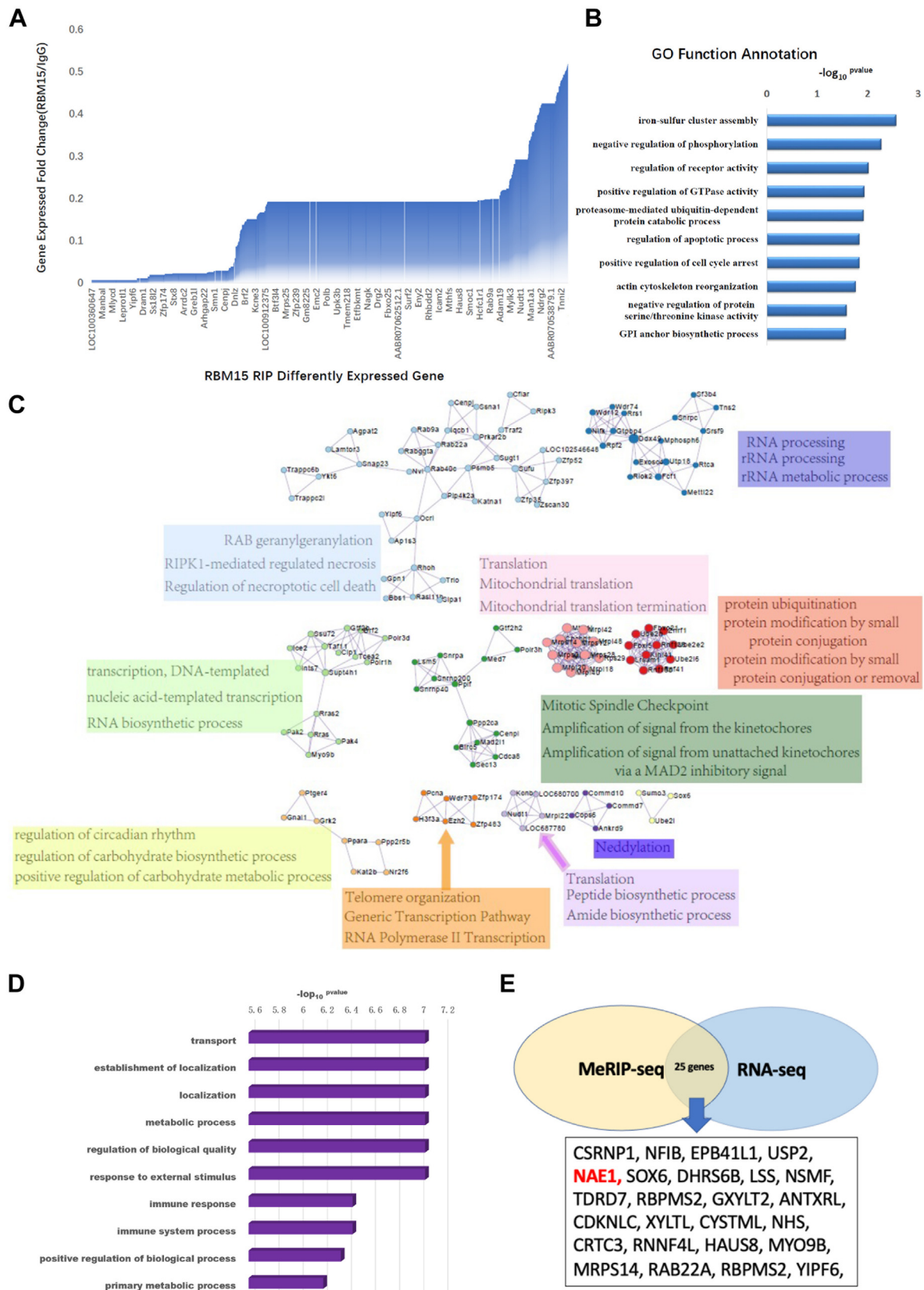
FIGURE 4 Decreased Apoptosis After Injecting RBM15-AAV9 Into the Myocardium after MI

(A to F) The apoptosis markers cleaved-caspase3 and bax, and the anti-apoptosis marker bcl-2 were assessed by Western blotting in the infarct area and remote area, and the relative ratios of cleaved-caspase3, bax/bcl-2 protein levels were calculated. (G) Histochemical identification of TUNEL-positive cells in the post-MI heart on day 7. Infarcted area of TUNEL and DAPI (left) and the rate of TUNEL-positive cells (right) ($n = 6$). Scale bar, 100 μ m. Data are presented as mean \pm SEM. * $P < 0.05$, ** $P < 0.01$, **** $P < 0.0001$. In data B, C, E, F, and G (down), differences were compared between sham and MI, or between MI + NC and MI + RBM15. All data were analyzed using unpaired Student's t test. Abbreviations as in Figures 1 and 2.

FIGURE 5 Improved Heart Function and Attenuated Cardiac Fibrosis After Overexpressing RBM15



(A) Representative echocardiography images on week 4 post-MI ($n = 6$). (B to E) The measurement of left EF%, FS%, LVIDd, and LVIDs on week 4 post-MI and NS injection, NC injection, and RBM15 injection. (F) The representative images of Masson's trichrome staining. (G) Percentage of left ventricle area occupied by scar tissue 4 weeks post-MI and NS injection, NC injection, and RBM15 injection, ($n = 6$). (H) HE staining of myocardial tissue in the marginal zone of MI. Scale bar, 100 μ m. (I) MI + RBM15 group showed improved overall survival. Kaplan-Meier curves were generated, log-rank (Mantel-Cox) test ($n = 20$). Data are presented as mean \pm SEM. *** $P < 0.001$. In data B, C, D, E, G, and I, differences were compared between sham and MI, or between MI + NC and MI + RBM15. All data were analyzed using unpaired Student's *t* test. EF% = ejection fraction %; FS% = fraction shortening %; HE = hematoxylin and eosin; LVIDd = left ventricular internal dimension-diastole; LVIDs = left ventricular internal dimension-systole; NS = normal saline; other abbreviations as in Figures 1 and 2.

FIGURE 6 Analysis of Downstream Targets of RBM15 in Cardiomyocytes

Continued on the next page

after overexpressing RBM15 in NRVMs under hypoxic condition (**Figure 7C**). To investigate the RNA-binding role of RBM15 in NAE1 mRNA, we performed RIP-qPCR, and found that RBM15 could bind quantities of NAE1 mRNA (**Figure 7D**). After treatment with actinomycin D (a transcription inhibitor), the qPCR analysis revealed that the expression of NAE1 significantly decreased after silencing RBM15, indicating that RBM15 can maintain the stability of NAE1 (**Figure 7E**). Taken together, our findings revealed that RBM15 enhanced NAE1 expression via stabilizing its mRNA.

APOPTOSIS OF CARDIOMYOCYTES AFTER INHIBITION OF NAE1. Given that the GO and KEGG analyses showed that NAE1 might be involved in the apoptosis pathway, we further investigated whether NAE1, a downstream target of RBM15, has an effect on cardiomyocyte apoptosis under hypoxia. The role of NAE1 in the protective effect on NRVMs was validated by infecting the cells with adenoviruses expressing NAE1 or siRNA. The Western blotting data proved the upregulated expression of NAE1 and a remarkable decrease in proapoptosis markers (cleaved-caspase3, bax) in NRVMs (**Figure 8A**). In contrast, we used siNAE1-1 and siNAE1-2 to infect NRVMs, and after hypoxia treatment, we found that the NAE1 knockdown promoted apoptosis of NRVMs (**Figure 8B**). Furthermore, the lactate dehydrogenase release and CCK8 assays were used to assess the NRVMs apoptosis, and the results indicated that the NAE1 overexpression was able to decrease apoptosis of NRVMs (**Figures 8C to 8F**). To further examine the proapoptosis effect of the NAE1 knockdown, NRVMs were treated with MLN4924 (the NAE1 inhibitor) at different concentration points. We found that the levels of NAE1 significantly decreased and proapoptosis markers, including cleaved-caspase3 and bax significantly increased (**Figure 8G**). These data demonstrated that NAE1 inhibition enhanced the death of NRVMs.

DISCUSSION

Despite significant advances made in early detection and treatment over the course of the last decade, MI

continues to be a primary cause of death and disabilities.³⁹ Many investigators are actively looking for potential markers and investigating the components of immune cell infiltration of MI, both of which have the potential to have a significantly beneficial impact on the long-term survival of patients with MI. Many studies have reported the potential of using mRNA as a potentially useful indicator of diseases in the cardiovascular field, particularly MI. A growing body of data shows that m⁶A regulators exhibit a wide range of regulatory effects on the diversity of biological activity. However, few people have been able to understand the role of m⁶A regulators in MI.⁴⁰ The m⁶A plays a modulatory role in nearly all stages of the RNA life cycle, including mRNA processing, nuclear export, translation modulation, and even the phase separation potential of mRNA.⁴¹⁻⁴³ It has been reported that m⁶A plays an important role in cardiovascular diseases, not only as a biomarker in diagnosis of MI, but also as a medicine in treatment of cardiac remodeling.^{44,45} Shi et al⁴⁴ used comprehensive analysis of m⁶A regulators expression to identify distinct molecular subtypes of MI, and they found several genes were significantly related to the development of MI, with being regulated by m⁶A methyltransferases. In the present research, we also observed the differences in m⁶A modification in MeRIP of MI and sham control tissues. Moreover, RBM15 was screened as a dramatically changed m⁶A-related protein. Given that we have demonstrated METTL3, the main m⁶A methyltransferase regulated the myocardial remodeling after MI, we investigated the role of RBM15 in MI. We found that the expression level of RBM15 was significantly upregulated in MI. The GO analysis and KEGG analysis revealed that many apoptosis-related genes during MI were remarkably regulated by m⁶A. Overexpression of RBM15 decreased the cardiomyocytes' apoptosis. This observation was further corroborated by in vivo findings that the heart function was improved in the MI mice overexpressing RBM15. Later, NAE1—an RBM15 target—was found by filtering MeRIP-seq and RBM15-RIP-seq. We found that RBM15 positively regulated the stability of the target NAE1 mRNA. Notably, similar to RBM15, the overexpression of

FIGURE 6 Continued

(A) The 851 m⁶A upregulated genes are shown in the bar plot. The x axis indicates the differentially expressed genes, and the Y-axis shows the expression fold change. (B) The top 10 enrichment GO terms of the RBM15-upregulated gene was shown. The y axis indicates the GO terms, the x axis shows the -log P value of enrichment analysis. (C) The protein-protein interaction motifs are shown. The circle node indicates the gene, while the line depicts the interaction between the two proteins. Each colored group of nodes shows a certain motif. The motif function is listed in the corresponding box. (D) The top 10 enrichment KEGG terms of the RBM15-upregulated genes are shown. (E) Filtering the increased genes in MeRIP-seq and RBM15-RIP-seq identified NAE1 as a direct target of RBM15. GO = Gene Ontology; KEGG = Kyoto Encyclopedia of Genes and Genomes; NAE1 = NEDD8 activating enzyme E1 subunit 1; other abbreviations as in **Figure 1**.

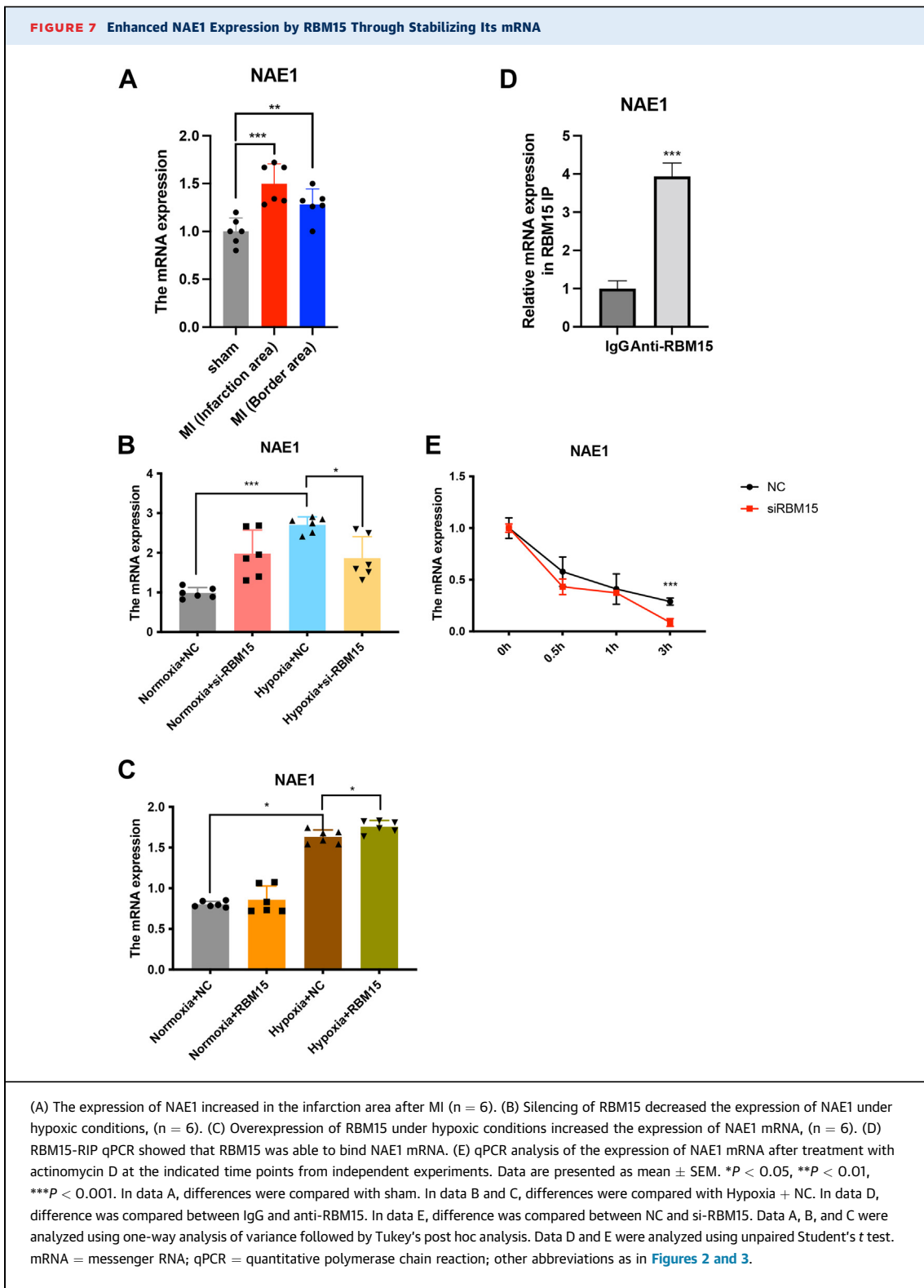
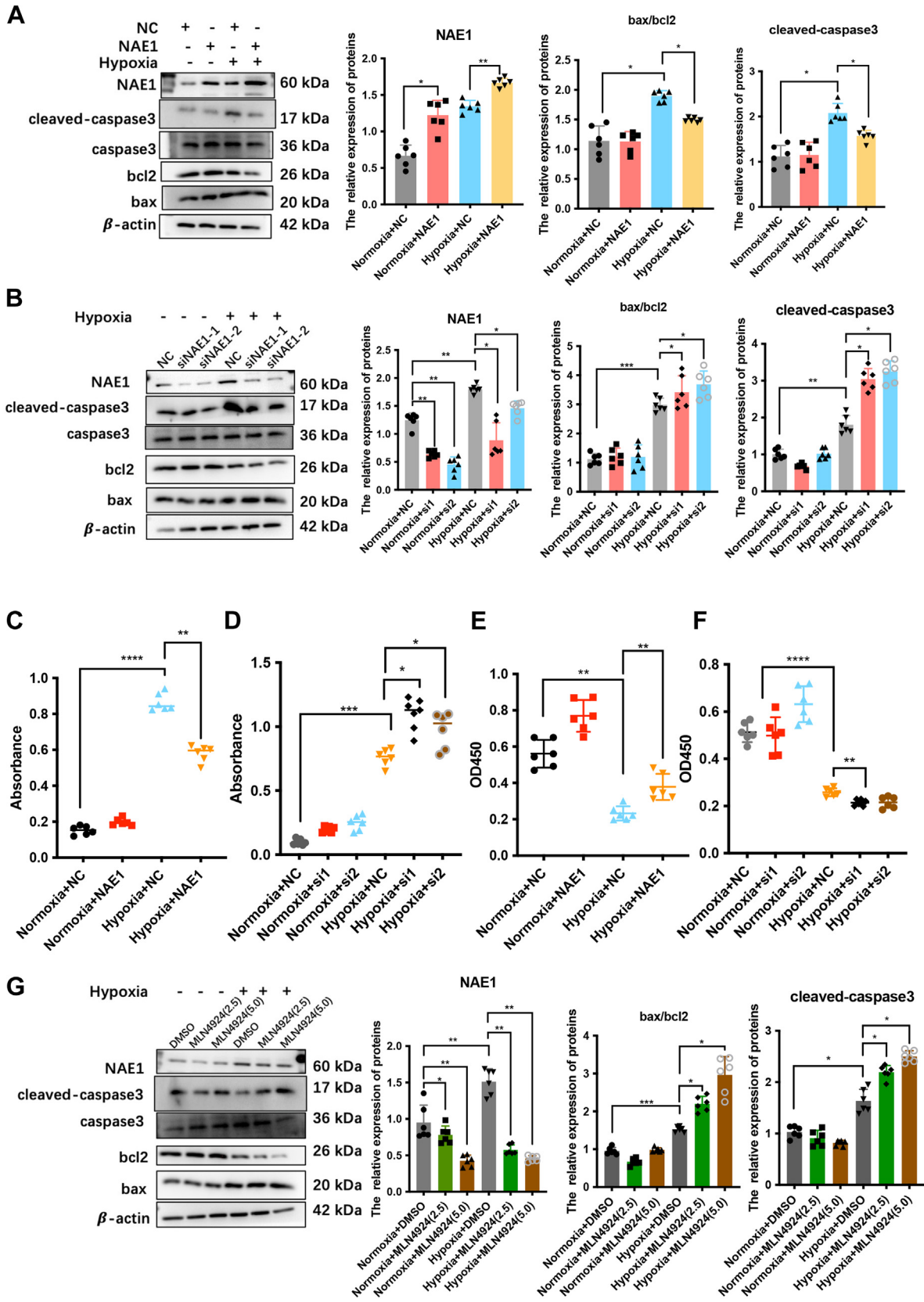


FIGURE 8 Apoptosis of Cardiomyocytes After Inhibition of NAE1



Continued on the next page

NAE1 showed a protective effect on NRVMs apoptosis under hypoxic conditions. Furthermore, functional evaluations such as NAE1 silencing and using MLN4924 (NAE1 inhibitor) demonstrated that NAE1 played a key role in MI. However, in addition to NAE1, other potential downstream targets of RBM15 might play crucial roles in mediating RBM15 functions in MI protection. Nevertheless, clarifying the exact underlying mechanisms requires further systematic investigations.

Recently, a growing body of work has indicated the essential role of m⁶A in human diseases.^{46–48} The regulation process involves 3 major m⁶A regulators, including methyltransferase, demethylase, and methylation recognition enzymes. The methyltransferases include METTL3, METTL14, WTAP, RBM15, and RBM15b, but the latter 3 do not have the ability to transfer m⁶A to mRNA. By adding m⁶A to related mRNAs, METTL3 affects the alternative splicing, stable or translation of those mRNA to regulate various diseases.^{43,49–51} During this process, METTL14 mainly binds to some sites in METTL3 to form a new complex, but WTAP and other proteins such as RBM15 or RBM15b probably recruit some factors to assist in the m⁶A regulation process.^{52–54} Although some researchers have reported that WTAP and RBM15 can add m⁶A to mRNA to regulate some diseases, they have only found that related phenotypes changed, but they have not investigated whether the exact process of adding m⁶A involves WTAP or RBM15 or not.^{55,56} Therefore, we preferred to name RBM15 as the m⁶A regulator, which can assist the m⁶A adding process.

The present research discussed the regulatory role of RBM15 in the protection from MI and the upregulation of the expression of its targets. It has been reported that RBM15 can facilitate the access of DEP5 to mRNA with its nuclear export factor function.⁵⁷ Yang et al⁵⁸ have demonstrated that Circ-CTNNB1 facilitates RBM15-mediated m⁶A modification to drive aerobic glycolysis and osteosarcoma progression.

Additionally, studies related to RBM15 have focused mainly on its function as an RNA-binding protein, and RBM15 has a great effect on megakaryoblastic leukemia and hematopoietic development.^{59–61} Therefore, in this study, we used RIP assays and multiple loss- or gain-of-function experiments to show that RBM15 can bind NAE1 mRNA and stabilize mRNA to decrease cardiomyocytes apoptosis. NAE1 decreases cell apoptosis mainly through inhibiting the p53 pathway and Akt pathway to regulate the myocardial function in MI.^{62–64} Moreover, we found that RBM15 promoted Akt pathway to exert myocardial protective effect (*Supplemental Figures 5A and 5B*). Finally, these findings envision the RBM15 as a candidate drug for the treatment of MI.

STUDY LIMITATIONS. Although we also found that overexpressing RBM15 could increase the total m⁶A level in cells, and NAE1 was screened from MeRIP-seq, which could be regulated by RBM15, we only drew a conclusion that RBM15 participated in NAE1's m⁶A regulation process because the main methyltransferase was METTL3. Lacking the advanced technologies, we merely showed that RBM15 participated in NAE1's m⁶A regulation process. In terms of the present m⁶A research, how to study the dynamic regulation of m⁶A is extremely important, because the dynamic regulation of methylation and demethylation should be involved in the occurrence and development of diseases. In the future, we will explore more mechanisms of RBM15 in assisting NAE1's m⁶A regulation process. However, our study successfully demonstrated the role of RBM15 in MI protection, suggesting a viable potential for developing targeted therapies against MI.

CONCLUSIONS

The present research shed light on an RNA-binding protein, namely, RBM15, which plays a modulatory function in the regulation of NAE1 mRNA. Regarding

FIGURE 8 Continued

(A) NRVMs were transfected with adenovirus overexpressing NAE1 for 48 hours, and then subjected to hypoxia. The apoptosis markers cleaved-caspase3 and bax, the anti-apoptosis marker bcl-2, and NAE1 protein were assessed by Western blotting; the relative ratios of cleaved-caspase3, bax/bcl-2, NAE1 protein levels were calculated based on the Western blotting result. (n = 6). (B) NRVMs were transfected with si-NAE1 for 48 hours, and then subjected to hypoxia. The apoptosis markers were assessed by Western blotting, and the relative ratios of cleaved-caspase3, bax/bcl2, and NAE1 protein levels were calculated based on the Western blotting results. (n = 6). (C to F) Cell injury was determined by LDH release assay and CCK8 assay. (n = 6). (G) NRCMs were treated with MLN4924 for 24 hours with different concentrations (0.0, 2.5, and 5.0 μM), then the apoptosis markers cleaved-caspase3 and bax, the anti-apoptosis marker bcl-2, and NAE1 protein levels were assessed by Western blotting, and the relative ratios of cleaved-caspase3, bax/bcl2, and NAE1 protein levels were calculated based on Western blotting results. (n = 6). Data are presented as mean ± SEM. *P < 0.05, **P < 0.01, ***P < 0.001. In data A, B, C, D, E, and F, differences were compared with Hypoxia + NC. In data G, difference was compared with Hypoxia + DMSO. All data were analyzed using One-way analysis of variance followed by Tukey's post hoc analysis. si-NAE1 = small interfering NAE1; NRVM = neonatal rat left ventricle myocyte; other abbreviations as in *Figures 2 and 7*.

the functional implication of NAE1 in MI protection, these findings emphasize the key role of m⁶A in MI. Moreover, the findings of the present research suggest the regulating role of RBM15 as a general mechanism underlying a variety of biological events in MI, which warrants further investigation.

FUNDING SUPPORT AND AUTHOR DISCLOSURES

The work was supported by the Major Research Plan of the National Natural Science Foundation of China (91639104 to Dr Ge), the National Natural Science Fund of China (81521001 to Dr Ge), The Key Research and Development Program sponsored by the Ministry of Science and Technology (2022YFC2407002 to Dr Ma). All other authors have reported that they have no relationships relevant to the contents of this paper to disclose.

ADDRESS FOR CORRESPONDENCE: Dr Jianying Ma, Department of Cardiology, Zhongshan Hospital, Fudan University, 180 Fenglin Road, Shanghai 200032, China. E-mail: ma.jianying@zs-hospital.sh.cn. OR Dr Junbo Ge, Department of Cardiology, Zhongshan Hospital, Fudan University, 180 Fenglin Road, Shanghai 200032, China. E-mail: jbge@zs-hospital.sh.cn.

REFERENCES

- Writing Group M, Mozaffarian D, Benjamin EJ, et al. Heart disease and stroke statistics-2016 update: a report from the American Heart Association. *Circulation*. 2016;133:e38–360.
- McMurray JJ. Clinical practice. Systolic heart failure. *N Engl J Med*. 2010;362:228–238.
- Sanders LN, Schoenhard JA, Saleh MA, et al. BMP antagonist gremlin 2 limits inflammation after myocardial infarction. *Circ Res*. 2016;119:434–449.
- Kiefer JJ, Augoustides JG. Acute myocardial infarction with cardiogenic shock: navigating the invasive options in clinical management. *J Cardiothorac Vasc Anesth*. 2021;35:3154–3157.
- Chen QQ, Ma G, Liu JF, et al. Neuraminidase 1 is a driver of experimental cardiac hypertrophy. *Eur Heart J*. 2021;42:3770–3782.
- Madan A, Viswanathan MC, Woulfe KC, et al. TNNT2 mutations in the tropomyosin binding region of TNT1 disrupt its role in contractile inhibition and stimulate cardiac dysfunction. *Proc Natl Acad Sci U S A*. 2020;117:18822–18831.
- Chen Z, Zhu S, Hong J, et al. Gastric tumour-derived ANGPT2 regulation by DARPP-32 promotes angiogenesis. *Gut*. 2016;65:925–934.
- Hobohm L, Kolmel S, Niemann C, et al. Role of angiopoietin-2 in venous thrombus resolution and chronic thromboembolic disease. *Eur Respir J*. 2021;58.
- Carpino G, Cardinale V, Di Giambardino A, et al. Thrombospondin 1 and 2 along with PEDF inhibit angiogenesis and promote lymphangiogenesis in intrahepatic cholangiocarcinoma. *J Hepatol*. 2021;75:1377–1386.
- Benjamin EJ, Virani SS, Callaway CW, et al. Heart disease and stroke statistics-2018 update: a report from the American Heart Association. *Circulation*. 2018;137:e67–e492.
- Paik DT, Chandy M, Wu JC. Patient and disease-specific induced pluripotent stem cells for discovery of personalized cardiovascular drugs and therapeutics. *Pharmacol Rev*. 2020;72:320–342.
- Yamanaka S. Pluripotent stem cell-based cell therapy—promise and challenges. *Cell Stem Cell*. 2020;27:523–531.
- Wang K, Li Y, Qiang T, Chen J, Wang X. Role of epigenetic regulation in myocardial ischemia/reperfusion injury. *Pharmacol Res*. 2021;170:105743.
- Lee M, Kim B, Kim VN. Emerging roles of RNA modification: m(6)A and U-tail. *Cell*. 2014;158:980–987.
- Roundtree IA, Evans ME, Pan T, He C. Dynamic RNA modifications in gene expression regulation. *Cell*. 2017;169:1187–1200.
- Zaccara S, Jaffrey SR. A unified model for the function of YTHDF proteins in regulating m(6)A-modified mRNA. *Cell*. 2020;181:1582–1595 e18.
- Zhang B, Wu Q, Li B, Wang D, Wang L, Zhou YL. m(6)A regulator-mediated methylation modification patterns and tumor microenvironment infiltration characterization in gastric cancer. *Mol Cancer*. 2020;19:53.
- Hu L, Wang J, Huang H, et al. YTHDF1 regulates pulmonary hypertension through translational control of MAGED1. *Am J Respir Crit Care Med*. 2021;203:1158–1172.
- Mathiyalagan P, Adamia M, Mayourian J, et al. FTO-dependent N(6)-methyladenosine regulates cardiac function during remodeling and repair. *Circulation*. 2019;139:518–532.
- Dorn LE, Lasman L, Chen J, et al. The N(6)-methyladenosine mRNA methylase METTL3 controls cardiac homeostasis and hypertrophy. *Circulation*. 2019;139:533–545.
- Gao XQ, Zhang YH, Liu F, et al. The piRNA CHAPIR regulates cardiac hypertrophy by controlling METTL3-dependent N(6)-methyladenosine methylation of Parp10 mRNA. *Nat Cell Biol*. 2020;22:1319–1331.
- Wiener D, Schwartz S. The epitranscriptome beyond m(6)A. *Nat Rev Genet*. 2021;22:119–131.
- Wang X, Wu Y, Guo R, Zhao L, Yan J, Gao C. Comprehensive analysis of N6-methyladenosine RNA methylation regulators in the diagnosis and subtype classification of acute myocardial infarction. *J Immunol Res*. 2022;2022:5173761.
- Desrosiers R, Friderici K, Rottman F. Identification of methylated nucleosides in messenger RNA from Novikoff hepatoma cells. *Proc Natl Acad Sci U S A*. 1974;71:3971–3975.

PERSPECTIVES

COMPETENCY IN MEDICAL KNOWLEDGE: Despite the large number of drug therapies available for the treatment of MI, there remains a compelling need for establishing a novel and effective therapies to improve the efficacy of existing ones. Among many antitumor drugs, the pharmacological basis of many drugs is to promote the apoptosis of tumor cells or inhibit the proliferation of corresponding blood vessels through RNA modification. However, in the cardiovascular field, there is no RNA modification drug for the treatment of MI.

TRANSLATIONAL OUTLOOK: The enhanced m⁶A methylation in the presence of RBM15 overexpression led to the increased expression and stability of NAE1, contributing to less myocardial fibrosis, cell apoptosis, and cardiac dysfunction. Our findings suggest that the enhanced m⁶A level is a protective mechanism in MI, setting the stage for the therapeutic targeting of the MI. Finally, pharmacological inhibitors of the molecules involved the pathway are being tested and are primed for testing for the beneficial effects in patients with MI.

- 25.** Zhao BS, Roundtree IA, He C. Post-transcriptional gene regulation by mRNA modifications. *Nat Rev Mol Cell Biol.* 2017;18:31-42.
- 26.** Liu N, Pan T. N6-methyladenosine-encoded epitranscriptomics. *Nat Struct Mol Biol.* 2016;23:98-102.
- 27.** Gong R, Wang X, Li H, et al. Loss of m(6)A methyltransferase METTL3 promotes heart regeneration and repair after myocardial injury. *Pharmacol Res.* 2021;174:105845.
- 28.** Xiao N, Laha S, Das SP, Morlock K, Jesneck JL, Raffel GD. Ott1 (Rbm15) regulates thrombopoietin response in hematopoietic stem cells through alternative splicing of c-Mpl. *Blood.* 2015;125:941-948.
- 29.** Wang T, Kong S, Tao M, Ju S. The potential role of RNA N6-methyladenosine in Cancer progression. *Mol Cancer.* 2020;19:88.
- 30.** Deng X, Su R, Weng H, Huang H, Li Z, Chen J. RNA N(6)-methyladenosine modification in cancers: current status and perspectives. *Cell Res.* 2018;28:507-517.
- 31.** Kechin A, Boyarskikh U, Kel A, Filipenko M. cutPrimers: a new tool for accurate cutting of primers from reads of targeted next generation sequencing. *J Comput Biol.* 2017;24:1138-1143.
- 32.** Kim D, Langmead B, Salzberg SL. HISAT: a fast spliced aligner with low memory requirements. *Nat Methods.* 2015;12:357-360.
- 33.** Meng J, Lu Z, Liu H, et al. A protocol for RNA methylation differential analysis with MeRIP-Seq data and exomePeak R/Bioconductor package. *Methods.* 2014;69:274-281.
- 34.** Yu G, Wang LG, He QY. ChIPseeker: an R/Bioconductor package for ChIP peak annotation, comparison and visualization. *Bioinformatics.* 2015;31:2382-2383.
- 35.** Pertea M, Pertea GM, Antonescu CM, Chang TC, Mendell JT, Salzberg SL. StringTie enables improved reconstruction of a transcriptome from RNA-seq reads. *Nat Biotechnol.* 2015;33:290-295.
- 36.** Robinson MD, McCarthy DJ, Smyth GK. edgeR: a Bioconductor package for differential expression analysis of digital gene expression data. *Bioinformatics.* 2010;26:139-140.
- 37.** Kang PT, Chen CL, Lin P, Zhang L, Zweier JL, Chen YR. Mitochondrial complex I in the post-ischemic heart: reperfusion-mediated oxidative injury and protein cysteine sulfonation. *J Mol Cell Cardiol.* 2018;121:190-204.
- 38.** Wang B, Zhou Q, Bi Y, et al. Phosphatase PPM1L prevents excessive inflammatory responses and cardiac dysfunction after myocardial infarction by inhibiting IKK β activation. *J Immunol.* 2019;203:1338-1347.
- 39.** Mehta LS, Beckie TM, DeVon HA, et al. Acute myocardial infarction in women: a scientific statement from the American Heart Association. *Circulation.* 2016;133:916-947.
- 40.** Henry TD, Tomey MI, Tamis-Holland JE, et al. Invasive management of acute myocardial infarction complicated by cardiogenic shock: a scientific statement from the American Heart Association. *Circulation.* 2021;143:e815-e829.
- 41.** Su R, Dong L, Li C, et al. R-2HG exhibits anti-tumor activity by targeting FTO/m(6)A/MYC/CEBPA signaling. *Cell.* 2018;172:90-105 e23.
- 42.** Ries RJ, Zaccara S, Klein P, et al. m(6)A enhances the phase separation potential of mRNA. *Nature.* 2019;571:424-428.
- 43.** Barbieri I, Tzelepis K, Pandolfini L, et al. Promoter-bound METTL3 maintains myeloid leukaemia by m(6)A-dependent translation control. *Nature.* 2017;552:126-131.
- 44.** Shi X, Cao Y, Zhang X, et al. Comprehensive analysis of N6-methyladenosine RNA methylation regulators expression identify distinct molecular subtypes of myocardial infarction. *Front Cell Dev Biol.* 2021;9:756483.
- 45.** Choy M, Xue R, Wu Y, Fan W, Dong Y, Liu C. Role of N6-methyladenosine modification in cardiac remodeling. *Front Cardiovasc Med.* 2022;9:774627.
- 46.** Deng LJ, Deng WQ, Fan SR, et al. m6A modification: recent advances, anticancer targeted drug discovery and beyond. *Mol Cancer.* 2022;21:52.
- 47.** Li Y, Gu J, Xu F, Zhu Q, Chen Y, Ge D, Lu C. Molecular characterization, biological function, tumor microenvironment association and clinical significance of m6A regulators in lung adenocarcinoma. *Brief Bioinform.* 2021;22.
- 48.** Zhang B, Chen Z, Tao B, et al. m(6)A target microRNAs in serum for cancer detection. *Mol Cancer.* 2021;20:170.
- 49.** Vu LP, Pickering BF, Cheng Y, et al. The N(6)-methyladenosine (m(6)A)-forming enzyme METTL3 controls myeloid differentiation of normal hematopoietic and leukemia cells. *Nat Med.* 2017;23:1369-1376.
- 50.** Yankova E, Blackaby W, Albertella M, et al. Small-molecule inhibition of METTL3 as a strategy against myeloid leukaemia. *Nature.* 2021;593:597-601.
- 51.** Liu P, Li F, Lin J, et al. m(6)A-independent genome-wide METTL3 and METTL14 redistribution drives the senescence-associated secretory phenotype. *Nat Cell Biol.* 2021;23:355-365.
- 52.** Chen XY, Zhang J, Zhu JS. The role of m(6)A RNA methylation in human cancer. *Mol Cancer.* 2019;18:103.
- 53.** Zhao Z, Meng J, Su R, Zhang J, Chen J, Ma X, Xia Q. Epitranscriptomics in liver disease: Basic concepts and therapeutic potential. *J Hepatol.* 2020;73:664-679.
- 54.** Jiang X, Liu B, Nie Z, et al. The role of m6A modification in the biological functions and diseases. *Signal Transduct Target Ther.* 2021;6:74.
- 55.** Wang X, Tian L, Li Y, et al. RBM15 facilitates laryngeal squamous cell carcinoma progression by regulating TMBM6 stability through IGF2BP3 dependent. *J Exp Clin Cancer Res.* 2021;40:80.
- 56.** Li ZX, Zheng ZQ, Yang PY, et al. WTAP-mediated m(6)A modification of lncRNA DIAPH1-AS1 enhances its stability to facilitate nasopharyngeal carcinoma growth and metastasis. *Cell Death Differ.* 2022;29:1137-1151.
- 57.** Zolotukhin AS, Uranishi H, Lindtner S, Bear J, Pavlakis GN, Felber BK. Nuclear export factor RBM15 facilitates the access of DBP5 to mRNA. *Nucleic Acids Res.* 2009;37:7151-7162.
- 58.** Yang F, Liu Y, Xiao J, et al. Circ-CTNNB1 drives aerobic glycolysis and osteosarcoma progression via m6A modification through interacting with RBM15. *Cell Prolif.* 2022;e13344.
- 59.** Kawaguchi H, Hitzler JK, Ma Z, Morris SW. RBM15 and MKL1 mutational screening in megakaryoblastic leukemia cell lines and clinical samples. *Leukemia.* 2005;19:1492-1494.
- 60.** Raffel GD, Mercher T, Shigematsu H, et al. Ott1(Rbm15) has pleiotropic roles in hematopoietic development. *Proc Natl Acad Sci U S A.* 2007;104:6001-6006.
- 61.** Tran NT, Su H, Khodadadi-Jamrayan A, et al. The AS-RBM15 lncRNA enhances RBM15 protein translation during megakaryocyte differentiation. *EMBO Rep.* 2016;17:887-900.
- 62.** Ai TJ, Sun JY, Du LJ, et al. Inhibition of neddylation by MLN4924 improves neointimal hyperplasia and promotes apoptosis of vascular smooth muscle cells through p53 and p62. *Cell Death Differ.* 2018;25:319-329.
- 63.** Guihard S, Ramolu L, Macabre C, Wasylkyk B, Noel G, Abecassis J, Jung AC. The NEDD8 conjugation pathway regulates p53 transcriptional activity and head and neck cancer cell sensitivity to ionizing radiation. *Int J Oncol.* 2012;41:1531-1540.
- 64.** Ferris J, Espina-Fiedler M, Hamilton C, et al. Pevonedistat (MLN4924): mechanism of cell death induction and therapeutic potential in colorectal cancer. *Cell Death Discov.* 2020;6:61.

KEY WORDS apoptosis, MI therapy, m⁶A, RBM15

APPENDIX For an expanded Methods section as well as supplemental tables and figures, please see the online version of this paper.

EDITORIAL COMMENT

Potential of Epigenetic Therapy in Alleviating Cardiac Death and Fibrotic Remodeling in Myocardial Infarction*



Olivier Morel, MD, PhD^{a,b,c}

Despite significant advancements in the management of ST-segment elevation myocardial infarction (STEMI), the development of effective cardioprotective strategies remains an ongoing challenge. Although prompt reperfusion therapy, primarily achieved through primary percutaneous coronary intervention, has transformed the acute management of STEMI by salvaging jeopardized myocardium and improving patient outcomes, patients often experience postreperfusion adverse cardiac events. These events, including myocardial stunning, reperfusion injury, and adverse ventricular remodeling, contribute to ongoing morbidity and mortality. Despite various pharmacological and nonpharmacological approaches targeting the renin-angiotensin-aldosterone system, sympathetic nervous system, inflammation, angiogenesis, mitochondrial function, cytochrome c release, and delivery of supersaturated oxygen, clinical trials have yielded limited success, emphasizing the need for novel strategies to enhance cardioprotection.^{1,2}

Over the past decade, we have gathered significant insight into how epigenetic events contribute to the pathogenesis of cardiovascular disease.^{3,4}

Epigenetics involves regulatory networks governing gene expression and cellular behavior through reversible modifications of genomic DNA and histones.⁵ An essential epigenetic change, known as N6-methyladenosine (m6A), occurs when the adenosine base is methylated at the N6 position. The m6A modification is a dynamic and reversible post-transcriptional modification process regulated by 3 distinct protein complexes: writers (enzymes that add chemical modifications), readers (effector proteins that bind to modified macromolecules), and erasers (enzymes that delete chemical modifications), which tune important biological processes by adding or removing the m6A sites. Among the proteins involved in m6A modification, methyltransferases play a crucial role in catalyzing the methylation of RNAs. Writers consist of large methyltransferase complexes in which the RNA-binding protein (RBM15) acts as a scaffold for methyltransferase-like proteins such as METTL3 and METTL4, facilitating their recruitment and the methylation of mRNA molecules. Significant functions performed by regulators of m6A include destruction, translocation, transportation, and RNA processing.^{5,6}

In this issue of *JACC: Basic to Translational Science*, Cheng et al⁷ provide pioneering data on the protective role of RBM15 in limiting cardiomyocyte apoptosis following myocardial infarction (MI).⁷ Using mouse models of MI, the investigators highlighted the significance of m6A modification during the progression of myocardial ischemia, identifying 1,538 m6A peaks in MI tissues compared with control tissues. Additional analysis revealed the up-regulation of 167 genes and the down-regulation of 49 genes. Through Gene Ontology (GO) analysis, the investigators emphasized the enrichment of differentially expressed m6A-related transcripts in genes

*Editorials published in *JACC: Basic to Translational Science* reflect the views of the authors and do not necessarily represent the views of *JACC: Basic to Translational Science* or the American College of Cardiology.

From the ^aDepartment of Cardiology, University Hospital of Strasbourg, Strasbourg, France; ^bUR3074 Translational Cardiovascular Medicine, University of Strasbourg, Strasbourg, France; and the ^cMedical University of Hanoi, Hanoi, Vietnam.

The author attests they are in compliance with human studies committees and animal welfare regulations of the author's institution and Food and Drug Administration guidelines, including patient consent where appropriate. For more information, visit the [Author Center](#).

involved in extracellular matrix remodeling and apoptosis. Moreover, Kyoto Encyclopedia of Genes and Genomes (KEGG) analysis highlighted the involvement of differentially expressed m6A-related transcripts in pathways such as histidine metabolism, the HIF-1 signaling pathway, complement and coagulation cascades, and extracellular matrix-receptor interactions.

To ascertain the relevance of this pathway in humans, RBM15 levels were quantified by enzyme-linked immunosorbent assay in 50 STEMI patients and 50 age-matched control patients with comparable cardiovascular risk factors, revealing a significant increase of RBM15 in STEMI patients. Overexpression of RBM15 attenuated cardiomyocyte apoptosis under hypoxic conditions *ex vivo* and adverse myocardial remodeling in mice, whereas silencing RBM15 (*si*-RBM15) provided the opposite effect. The importance of this pathway was underscored in mice through a functional approach using serial echocardiography and hemodynamic measurements coupled with histological analysis. To establish a model of cardiac overexpression of RBM15, adenovirus-RBM15 was injected into the mouse myocardial tissue at 3 to 5 points using an insulin needle. Western blot and quantitative polymerase chain reaction analyses were conducted to determine the peak expression of RBM15 3 weeks after injection. Subsequently, MI was induced using left coronary artery ligation, unveiling delayed improvement in heart function, reduced cardiac fibrosis at 4 weeks, and enhanced 60-day survival associated with RBM15 overexpression. Furthermore, analysis of downstream targets of RBM15 in neonatal rat left ventricle cardiomyocytes identified NEDD8 activating enzyme E1 subunit 1 (NAE1) as a crucial regulator of apoptosis. Elevated NAE1 mRNA expression within the infarct area tissue, coupled with *ex vivo* analysis illustrating enhancement of NAE1 via RBM15-mediated mRNA stabilization, provided additional insight into the mechanistic basis of RBM15-mediated cardioprotection. Finally, the inhibition of NAE1 demonstrated a noteworthy reduction in cardiomyocyte apoptosis, underscoring the significance of this pathway in post-MI remodeling.

Although a translational approach was undertaken, the study faced challenges in obtaining extensive human data regarding RBM15 expression throughout the progression of MI. The study lacked information on RBM15's expression in human ischemic myocardial tissue, and this could be a valuable addition to future studies. The characterization of STEMI patients would have benefited from further elaboration, particularly in assessing coronary reperfusion

(TIMI flow grade, blush), infarct size, left ventricular ejection fraction. A key point, likely to drive future study design, is the relationship between RBM15 levels and key prognostic biomarkers of MI, such as natriuretic peptides, cardiac troponin I, C-reactive protein, or interleukin 6. Although not reported here, this warrants further discussion and exploration. Despite these limitations, this study elucidated a novel and important pathway involved in mitigating cardiac death and fibrotic myocardial remodeling. It aligns with previous research demonstrating the significance of METTL3 up-regulation in heart failure and m6A modifications in various experimental models and human tissues, emphasizing the potential clinical relevance of targeting these pathways in the context of MI.^{3,6} Whereas the Cheng et al⁷ study focused on the primary role of writers in regulating m6A modification and lacked evidence for any modification of erasers proteins within myocardial tissue, another recent study provided convincing data showing a key role for the eraser fat mass and obesity-associated protein (FTO), an m6A demethylase.⁸ FTO expression was found to be downregulated in heart failure, leading to an aberrant increase in global cardiac m6A levels, as well as m6A levels in selective contractile transcripts, resulting in decreased protein expression. Loss of FTO resulted in abnormal calcium handling and sarcomere dynamics, leading to impaired contractile function. By contrast, overexpression of FTO in failing murine myocardium attenuated ischemia-induced cardiac remodeling and loss of cardiac contractile function, demonstrating the therapeutic potential of FTO.⁸

Beyond apoptosis regulation and calcium handling, recent evidence highlighted the importance of epigenetically regulated networks in governing the functional phenotype shift of cardiac macrophages.⁹ The transition of cardiac macrophages to a reparative phenotype plays a crucial role in resolving inflammatory responses and facilitating efficient tissue repair following MI. Notably, nucleophosmin 1 (NPM1) has been implicated in promoting atherosclerosis through the induction of vascular inflammation via the nuclear factor- κ B signaling pathway.¹⁰ Conversely, NPM1 plays a critical role in controlling the inflammatory phenotype of cardiac macrophages, thereby antagonizing cardiac repair. Macrophage-specific deletion of NPM1 emerges as a promising strategy for promoting cardiac repair and alleviating post-MI cardiac dysfunction and adverse remodeling. The epigenetic machinery, mediated by the NPM1-KDM5b interaction, governs cardiac macrophages transition and post-MI tissue repair via metabolic reprogramming. NPM1 acts as an epigenetic factor

targeting the *Tsc1* gene, then recruiting histone demethylase KDM5b, to form an inhibitory epigenetic complex that ultimately suppresses reparative transition via the mTOR pathway. Antisense oligonucleotides and NPM1 inhibitors demonstrated therapeutic efficacy in promoting cardiac repair in wild-type mice after MI.⁹

Collectively, these innovative studies offer novel and pertinent insights into how epigenetic therapy could mitigate adverse cardiac remodeling in MI and alleviate inflammation-related damage. Historically, many therapies that showed promise in experimental models failed to translate successfully from bench to

bedside and have consequently been consigned to the graveyard of therapies. Let us remain hopeful that the fate of epigenetic therapies will diverge from this trend.

FUNDING SUPPORT AND AUTHOR DISCLOSURES

The author has reported that he has no relationships relevant to the contents of this paper to disclose.

ADDRESS FOR CORRESPONDENCE: Dr Olivier Morel, Nouvel Hôpital Civil, University Hospital of Strasbourg, 1 place de l'Hôpital, 67000 Strasbourg, France. E-mail: olivier.morel@chru-strasbourg.fr.

REFERENCES

1. Kloner RA, Creech JL, Stone GW, O'Neill WW, Burkhoff D, Spears JR. Update on cardioprotective strategies for STEMI: focus on supersaturated oxygen delivery. *J Am Coll Cardiol Basic Trans Science*. 2021;6:1021-1033.
2. Morel O, Perret T, Delarche N, et al. Pharmacological approaches to reperfusion therapy. *Cardiovasc Res*. 2012;94:246-252.
3. Shi X, Cao Y, Zhang X, et al. Comprehensive analysis of N6-methyladenosine RNA methylation regulators expression identify distinct molecular subtypes of myocardial infarction. *Front Cell Dev Biol*. 2021;9:756483.
4. Felisbino MB, McKinsey TA. Epigenetics in cardiac fibrosis: emphasis on inflammation and fibroblast activation. *J Am Coll Cardiol Basic Trans Science*. 2018;3:704-715.
5. Pagiatakis C, Condorelli G. The RNA methylome blackboard. *Circulation*. 2019;139:546-548.
6. Choy M, Xue R, Wu Y, Fan W, Dong Y, Liu C. Role of N6-methyladenosine modification in cardiac remodeling. *Front Cardiovasc Med*. 2022;9:774627.
7. Cheng H, Wu J, Li L, et al. RBM15 protects from myocardial infarction by stabilizing NAE1. *J Am Coll Cardiol Basic Trans Science*. 2024;9(5):631-648.
8. Mathiyalagan P, Adamik M, Mayourian J, et al. FTO-dependent N(6)-methyladenosine regulates cardiac function during remodeling and repair. *Circulation*. 2019;139:518-532.
9. Zhang S, Zhang Y, Duan X, Wang B, Zhan Z. Targeting NPM1 epigenetically promotes post-infarction cardiac repair by reprogramming reparative macrophage metabolism. *Circulation*. Published online February 23, 2024. <https://doi.org/10.1161/CIRCULATIONAHA.123.065506>.
10. Rao C, Liu B, Huang D, et al. Nucleophosmin contributes to vascular inflammation and endothelial dysfunction in atherosclerosis progression. *J Thorac Cardiovasc Surg*. 2021;161:e377-e393.

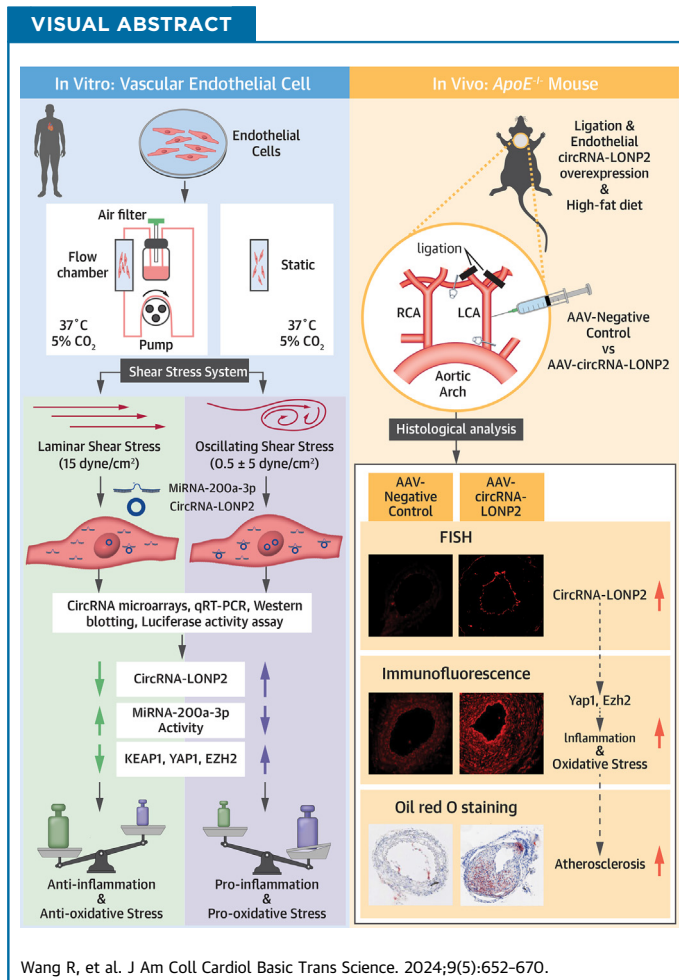
KEY WORDS apoptosis, m6A, MI therapy, RBM15

ORIGINAL RESEARCH - PRECLINICAL



Shear-Sensitive circRNA-LONP2 Promotes Endothelial Inflammation and Atherosclerosis by Targeting NRF2/HO1 Signaling

Ruoyu Wang, MM,^{a,b,*} Yue Zeng, MM,^{a,b,*} Ziqi Chen, PhD,^{a,b} Dongwei Ma, MM,^{a,b} Xiaozhe Zhang, PhD,^{a,b} Guifu Wu, MD, PhD,^{a,b,c} Wendong Fan, PhD^{b,d}

**HIGHLIGHTS**

- CircRNA-LONP2 modulates the flow-dependent inflammatory response.
- CircRNA-LONP2 accelerates atherosclerosis progression.
- CircRNA-LONP2 induces oxidative stress and endothelial inflammation through miR-200a-3p.
- Species-specific differences exist in circRNA-LONP2-regulated nuclear factor erythroid 2-related factor 2 signaling.

SUMMARY

Hemodynamic shear stress is a frictional force that acts on vascular endothelial cells and is essential for endothelial homeostasis. Physiological laminar shear stress (LSS) suppresses endothelial inflammation and protects arteries from atherosclerosis. Herein, we screened differentially expressed circular RNAs (circRNAs) that were significantly altered in LSS-stimulated endothelial cells and found that circRNA-LONP2 was involved in modulating the flow-dependent inflammatory response. Furthermore, endothelial circRNA-LONP2 overexpression promoted endothelial inflammation and atherosclerosis in vitro and in vivo. Mechanistically, circRNA-LONP2 competitively sponged miR-200a-3p and subsequently promoted Kelch-like ECH-associated protein 1, Yes-associated protein 1, and enhancer of zeste homolog 2 expression, thereby inactivating nuclear factor erythroid 2-related factor 2/heme oxygenase-1 signaling, promoting oxidative stress and endothelial inflammation, and accelerating atherosclerosis. LSS-induced down-regulation of circRNA-LONP2 suppresses endothelial inflammation, at least in part, by activating the miR-200a-3p-mediated nuclear factor erythroid 2-related factor 2/heme oxygenase-1 signaling pathway. CircRNA-LONP2 may serve as a new therapeutic target for atherosclerosis. (J Am Coll Cardiol Basic Trans Science 2024;9:652-670) © 2024 The Authors. Published by Elsevier on behalf of the American College of Cardiology Foundation. This is an open access article under the CC BY-NC-ND license (<http://creativecommons.org/licenses/by-nc-nd/4.0/>).

Hemodynamic shear stress is a frictional force that acts on vascular endothelial cells (ECs) and is essential for endothelial homeostasis under normal physiological conditions. The physiological level of laminar shear stress (LSS) inhibits atherosclerosis by reducing the expression of inflammatory molecules, including adhesion molecules, that guide leukocytes to migrate through arterial walls.¹ Conversely, low oscillating shear stress (OSS) promotes endothelial inflammation and the development of atherosclerosis.²⁻⁴ However, the molecular mechanisms underlying the flow-dependent regulation of vascular function are not fully understood.

Circular RNAs (circRNAs) are a novel class of endogenous noncoding RNAs that present a covalently closed loop structure via back-splicing the 3' end of RNAs with the 5' end.⁵⁻⁸ Previous studies have shown that circRNAs regulate gene expression through various mechanisms, including acting as microRNA (miRNA) sponges, interacting with proteins, and encoding proteins.⁹⁻¹¹ circRNAs play crucial regulatory roles in cardiovascular diseases, including

atherosclerosis.¹²⁻¹⁴ However, the role of circRNAs in mediating the effects of shear stress on endothelial inflammation remains unclear.

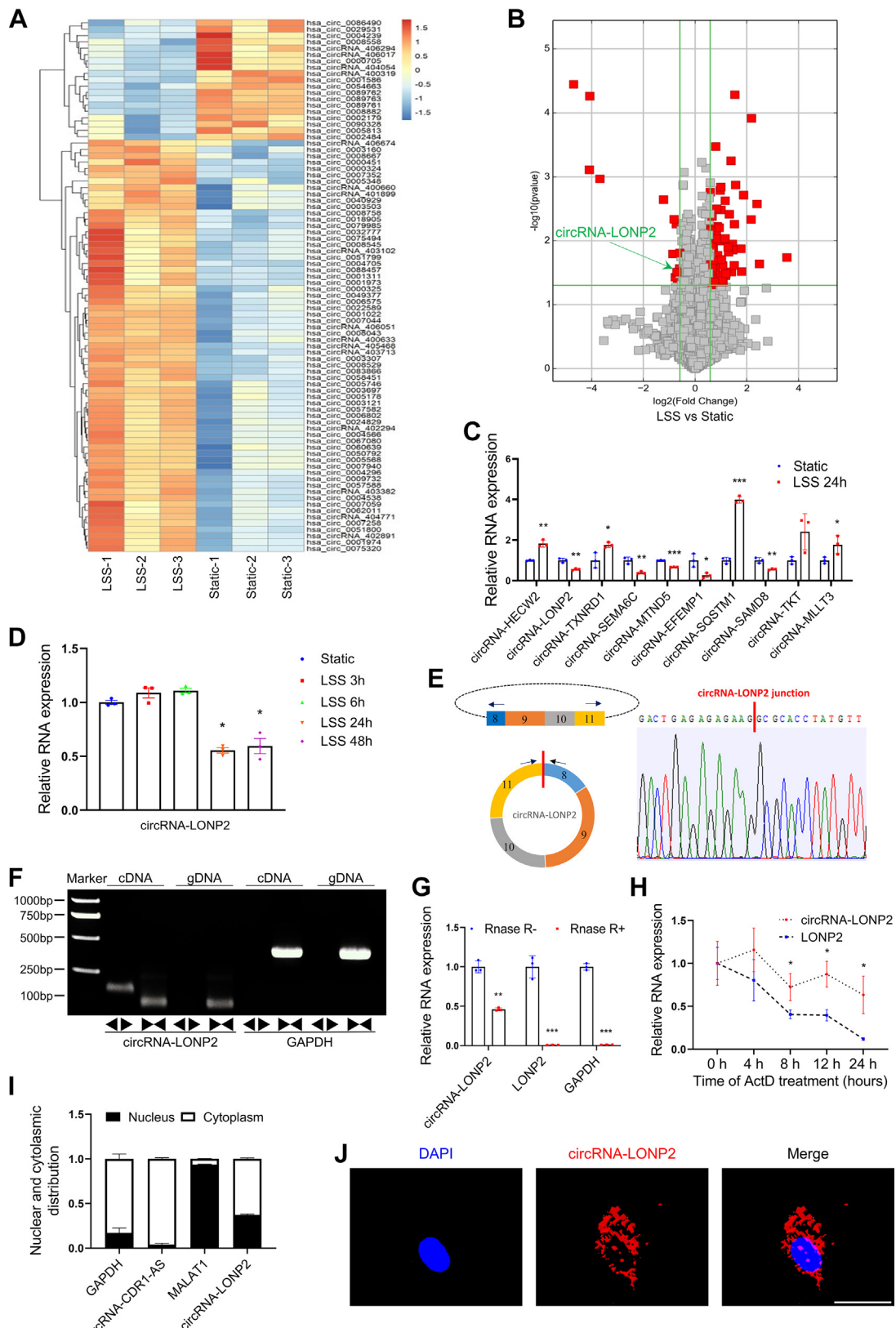
In the current study, we first screened differentially expressed circRNAs that were significantly altered in LSS-stimulated ECs and identified that circRNA-LONP2 may be involved in modulating the flow-dependent inflammatory response. Furthermore, endothelial circRNA-LONP2 overexpression promoted endothelial inflammation and the development of atherosclerosis in vitro and in vivo. Mechanistically, we found that circRNA-LONP2 acts as a competing endogenous RNA (ceRNA) to sponge miR-200a-3p, thereby increasing Kelch-like ECH-associated protein 1 (KEAP1), Yes-associated protein 1 (YAP1), and enhancer of zeste homolog 2 (EZH2) expression, inactivating nuclear factor erythroid 2-related factor (NRF2) signaling and promoting oxidative stress and endothelial inflammation.

ABBREVIATIONS AND ACRONYMS

- AAV9** = adeno-associated virus vector 9
ceRNA = competing endogenous RNA
EC = endothelial cell
EZH2 = enhancer of zeste homolog 2
HO = heme oxygenase
HUVEC = human umbilical vein endothelial cell
ICAM = intercellular adhesion molecule
KEAP1 = Kelch-like ECH-associated protein 1
LCA = left carotid artery
MAEC = mouse aortic endothelial cell
mRNA = messenger RNA
miRNA = microRNA
MUT = mutant
LSS = laminar shear stress
OSS = low oscillating shear stress
NF- κ B = nuclear factor- κ B
NRF2 = nuclear factor erythroid 2-related factor
qRT-PCR = quantitative reverse transcription-polymerase chain reaction
siRNA = small interfering RNA
TNF = tumor necrosis factor
VCAM = vascular cell adhesion molecule
YAP1 = Yes-associated protein 1
WT = wild-type

From the ^aDepartment of Cardiology, the Eighth Affiliated Hospital of Sun Yat-sen University, Shenzhen, Guangdong, People's Republic of China; ^bNHC Key Laboratory of Assisted Circulation and Vascular Diseases (Sun Yat-sen University); ^cGuangdong Innovative Engineering and Technology Research Center for Assisted Circulation, Shenzhen, Guangdong, People's Republic of China; and the ^dDepartment of Cardiology, the First Affiliated Hospital of Sun Yat-sen University, Guangzhou, Guangdong, People's Republic of China. *Drs Wang and Zeng contributed equally to this work and are joint first authors.

The authors attest they are in compliance with human studies committees and animal welfare regulations of the authors' institutions and Food and Drug Administration guidelines, including patient consent where appropriate. For more information, visit the [Author Center](#).

FIGURE 1 CircRNA-LONP2 Is Down-Regulated by Atheroprotective LSS

METHODS

CELL CULTURE. Human umbilical vein ECs (HUVECs) (catalog no. 8000) and human aortic ECs (catalog no. 6100) were purchased from ScienCell Research Laboratories and cultured in an EC culture medium containing 5% fetal bovine serum, 1% EC growth supplement, and 1% penicillin/streptomycin (catalog no. 1001; ScienCell Research Laboratories). HUVECs from passages 5 to 7 were used for all experiments. The cells were cultured in a carbon dioxide incubator (5% carbon dioxide) at 37°C.

Mouse aortic ECs (MAECs) (catalog no. BNCC359881; Bena Culture Collection) and Lenti-X 293T cells (catalog no. 632180; Takara Bio) were cultured in high-glucose Dulbecco's modified Eagle medium (catalog no. C11995500BT; Gibco) containing 10% fetal bovine serum (catalog no. A31608-02; Gibco) and 1% penicillin/streptomycin (catalog no. 15140122; Gibco).

THP-1 cells (catalog no. SCSP-567) were purchased from National Collection of Authenticated Cell Cultures and cultured in RPMI 1640 (catalog no. 21875034; Gibco) containing 10% fetal bovine serum, 1% penicillin/streptomycin (catalog no. 15140122; Gibco), 250 ng/mL amphotericin B, 1 mM glutamine, and 0.05 mM 2- mercaptoethanol (catalog no. 31350010; Gibco).

ANIMAL STUDIES. Animal experiments complied with animal welfare regulations. The animal experimental protocol was reviewed and approved by the Institutional Animal Care and Use Committee (Sun Yat-Sen University, approval no. SYSU-IACUC-2021-000608) and by the Animal Research Committee of the Eighth Affiliated Hospital of Sun Yat-sen

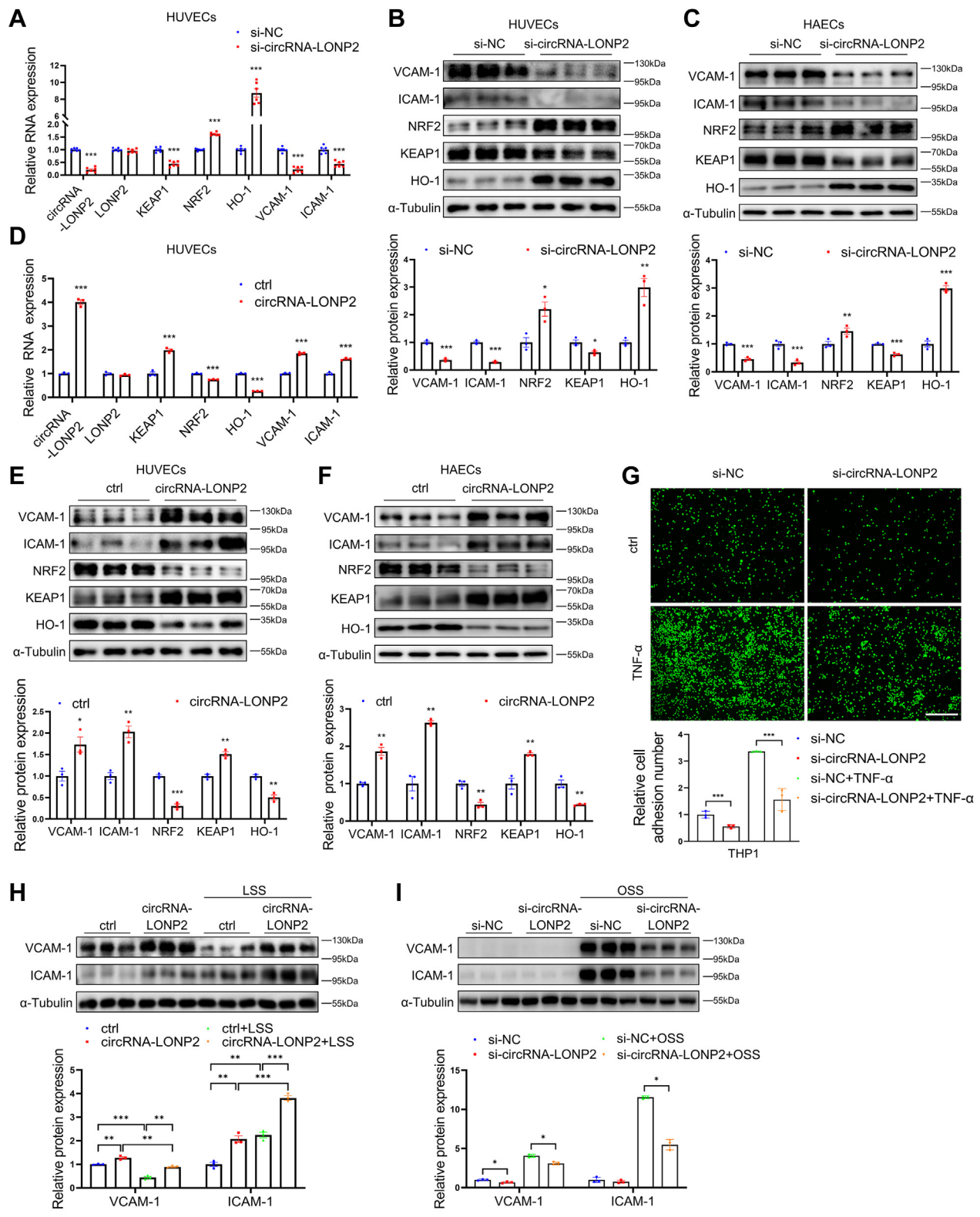
University (approval no. 2021-010-01). Male *ApoE*^{-/-} genetically engineered mice (7-8 weeks old, weighing 32 ± 3 g) were bred following the guidelines of the China Animal Protection Association. *ApoE*^{-/-} mice were carefully kept in a specific pathogen-free grade animal facility at the Animal Center of Sun Yat-Sen University and fed a high-fat diet from the time of purchase.

ApoE^{-/-} mice were subjected to partial carotid artery ligation surgery¹⁵ on the left carotid artery (LCA) 5 weeks later; they were simultaneously injected *in situ* with recombinant adeno-associated virus vector 9 (AAV9) with SLRSPPS peptide modification (AAV9^{SLRSPPS}-Tie2-circRNA-LONP2 (1×10^{10} vector genomes) or AAV9^{SLRSPPS}-Tie2-control (1×10^{10} vector genomes). High-fat feeding continued for 6 weeks postoperatively. The *ApoE*^{-/-} mice were then sacrificed, and the bilateral carotid arteries were harvested for further histologic and immunofluorescent staining analyses. Atherosclerotic plaques of the LCA and right coronary artery were identified by using Oil Red O staining; the intima and media areas of the LCA and right coronary artery were examined by using hematoxylin and eosin staining. Further details are provided in the *Supplemental Appendix*.

STATISTICAL ANALYSIS. All experiments were independently repeated at least 3 times, and the data were statistically processed with GraphPad Prism 8.0 (GraphPad Software). Data were tested for normality by using the Shapiro-Wilk test. Data are presented as mean ± SEM, and differences between groups were tested for significance by using the two-tailed Student's *t*-test (two groups). One-way analysis of variance (>2 groups) or 2-way analysis of variance

FIGURE 1 Continued

(A) Heatmap of the top 84 differentially expressed circular RNAs (circRNAs) in human umbilical vein endothelial cells (HUVECs) exposed to atheroprotective laminar shear stress (LSS) (15 dyne/cm² for 24 hours). (B) Volcano plots showing the variation in circRNA expression between the 2 groups. The vertical lines indicated 1.5 fold change (log2 scaled) up and down, respectively, and the horizontal line represents the *P* value of 0.05, as determined by the Student's *t*-test (-log10 scaled). The red dots in the volcano plot indicate the differentially expressed circRNAs that were statistically significant. (C) Quantitative reverse transcription-polymerase chain reaction (qRT-PCR) verification of 10 significantly expressed circRNAs. (D) Expression of circRNA-LONP2 in HUVECs was detected after exposure to atheroprotective LSS (15 dyne/cm²) for 3, 6, 24, and 48 hours. Glyceraldehyde 3-phosphate dehydrogenase (GAPDH) was used as an internal control. (E) Exon information of circRNA-LONP2 (circBase identifier: hsa_circ_0008558). The back-splice junction sequences of circRNA-LONP2 were amplified by divergent primers and verified using Sanger sequencing. The red vertical line indicates the backsplice site. Divergent and convergent primers are indicated by the arrows. (F) Divergent primers amplify circRNA-LONP2 in complementary DNA (cDNA) but not in genomic DNA (gDNA). GAPDH was used as a linear control. (G) Relative RNA levels of circRNA-LONP2, LONP2, and GAPDH were detected by qRT-PCR after treatment with RNase R. (H) Relative RNA levels of circRNA-LONP2 and LONP2 were detected by qRT-PCR after treatment with actinomycin D (ActD) (5 ng/ml) at the indicated time points in HUVECs. (I) Cellular RNA fractionation assays were used to analyze cellular distribution of circRNA-LONP2. MALAT1 served as a positive control for the nucleus, and circRNA-CDR1-AS1 and GAPDH served as positive controls for the cytoplasm. (J) RNA-fluorescence *in situ* hybridization assay was performed to detect circRNA-LONP2 expression in HUVECs using 5' and 3' Cy-3 labeled probes (circRNA-LONP2). Nuclei were stained with 4',6-diamidino-2-phenylindole (DAPI). Scale bar = 25 μm. Statistical analyses were performed applying unpaired 2-tailed Student's *t*-test (C, G, H, and I) or 1-way analysis of variance with Tukey's post hoc test (D). Values are mean ± SEM. *n* = 3. **P* < 0.05; ***P* < 0.01; ****P* < 0.001 versus control.

FIGURE 2 CircRNA-LONP2 Modulation of the Flow-Dependent Inflammatory Response

(>2 groups) with Tukey's post hoc test were used for multiple pairwise comparisons. A *P* value <0.05 was considered statistically significant.

An expanded Methods section and *Supplemental Tables 1 to 6* are presented in the *Supplemental Appendix*.

RESULTS

CircRNA-LONP2 IS DOWN-REGULATED BY ATHEROPROTECTIVE LSS. To identify the changes in circRNA expression patterns after shear stress stimulation, we conducted circRNA microarray analysis using RNA extracted from HUVECs cultured for 24 hours under static or LSS conditions. A total of 84 differentially expressed circRNAs were detected with >1.5 fold change and *P* < 0.05, including 65 up-regulated and 19 down-regulated circRNAs (**Figures 1A and 1B**). We confirmed that several circRNAs do have differential expression, including the highly abundant circRNA-LONP2 (circBase identifier: hsa_circ_0008558), which was significantly down-regulated in LSS-stimulated ECs compared with the static control (**Figure 1C**). circRNA-LONP2 was selected for further investigation because of its relatively high expression level in ECs (*Supplemental Figure 1*) and important impact on EC function (**Figure 2**, *Supplemental Figure 2*).

Upon examining ECs at different time points after LSS stimulation, we found that long-term (24 hours and 48 hours) LSS stimulation reduced circRNA-LONP2 expression, whereas short-term LSS (3 hours and 6 hours) had no effect (**Figure 1D**). The levels of linear LONP2 messenger RNA (mRNA) did not change in ECs that received LSS stimulation for 24 hours compared with those in static controls. These results suggest that circRNA-LONP2, but not the linear LONP2 transcripts, may be related to mediate the effects of LSS.

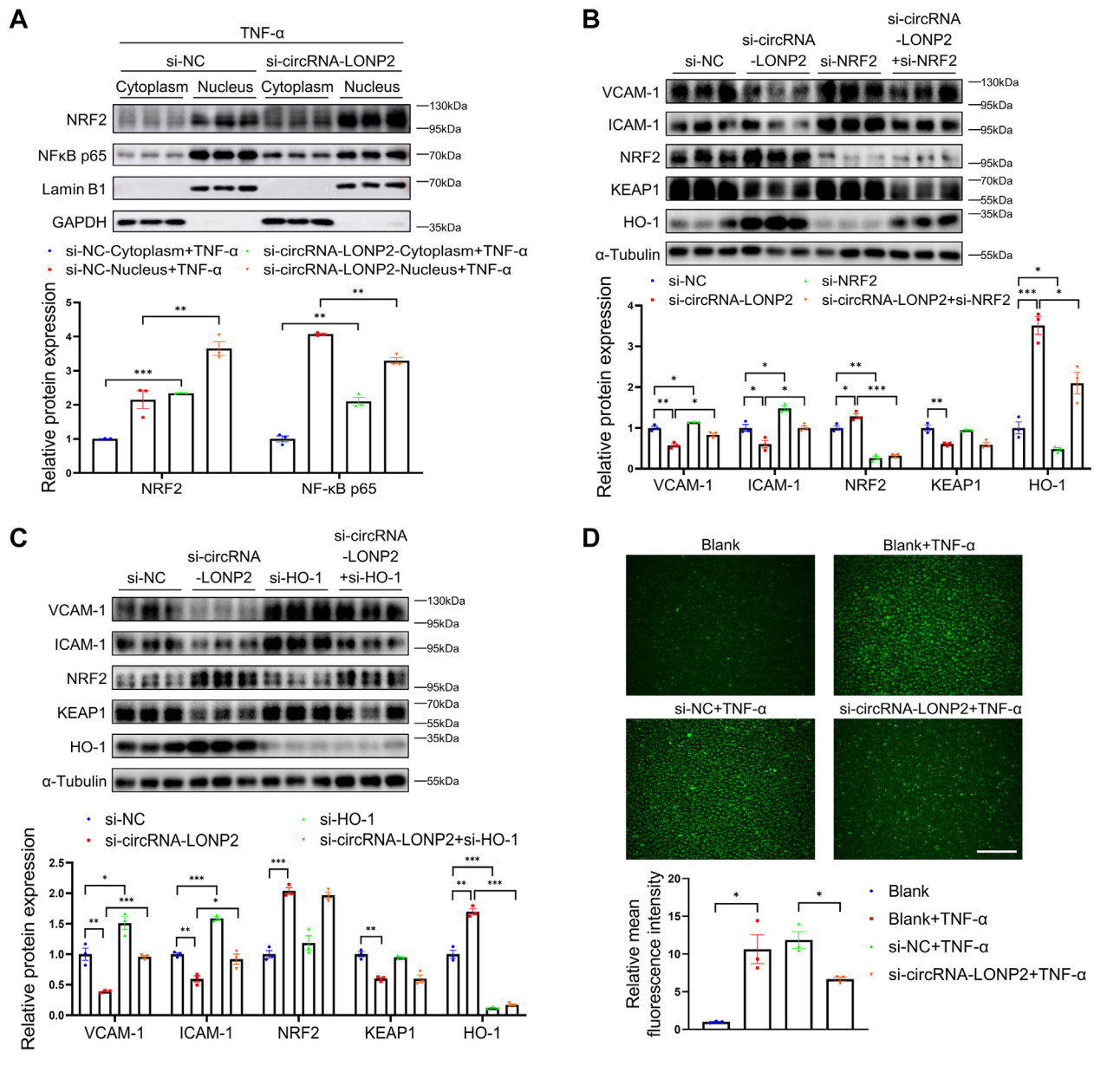
Several RNA-binding proteins have been reported to be involved in circRNA production, including quaking (QKI),¹⁶ fused in sarcoma (FUS),¹⁷ double-stranded RNA-specific adenosine deaminase (ADAR), and ATP-dependent RNA helicase A (DHX9).¹⁸ Therefore, we investigated the mRNA expression of these RNA-binding proteins in response to different shear stress stimuli. Our results reveal the opposite effects of LSS and OSS on the mRNA levels of ADAR, DHX9, FUS, and QKI in ECs (*Supplemental Figure 3*), suggesting that shear stress regulates circRNA-LONP2 expression through the aforementioned proteins.

We then assessed the exon structure of circRNA-LONP2, which is derived from exons 8, 9, 10, and 11 of LONP2. Using divergent primers and Sanger sequencing, we confirmed head-to-tail splicing of circRNA-LONP2 and validated the whole structure of circRNA-LONP2 (**Figure 1E**, *Supplemental Figure 4*). Polymerase chain reaction analysis revealed that divergent primers could amplify circRNA-LONP2 in reverse-transcribed RNA (complementary DNA), but not in genomic DNA, indicating that this RNA is circular in form (**Figure 1F**). **Figures 1G and 1H** illustrate the resistance of circRNA-LONP2 to exonucleolytic degradation, confirming its circular nature. In addition, nuclear-cytoplasmic fractionation (**Figure 1I**) and RNA-fluorescence *in situ* hybridization (**Figure 1J**) showed that circRNA-LONP2 was preferentially located in the cytoplasm of ECs, indicating that the cytoplasm is the main site for the biological effects of circRNA-LONP2.

CircRNA-LONP2 MODULATION OF THE FLOW-DEPENDENT INFLAMMATORY RESPONSE. To investigate the biological functions of circRNA-LONP2, small interfering RNAs (siRNAs) targeting the back-spliced junction of circRNA-LONP2 were used to specifically knock down circRNA-LONP2 expression in ECs. Quantitative reverse transcription-polymerase chain reaction

FIGURE 2 Continued

(A) RNA levels of circRNA-LONP2, LONP2, Kelch-like ECH-associated protein 1 (KEAP1), nuclear factor erythroid 2-related factor (NRF2), heme oxygenase (HO)-1, vascular cell adhesion molecule (VCAM)-1, and intercellular cell adhesion molecule (ICAM)-1 in HUVECs transfected with circRNA-LONP2 small interfering RNA (siRNA) (si-circRNA-LONP2) or control siRNA (si-NC) were measured by using qRT-PCR. *n* = 6. (B and C) Protein levels of KEAP1, NRF2, HO-1, VCAM-1, and ICAM-1 in endothelial cells transfected with si-circRNA-LONP2 or si-NC were detected by using Western blot analysis. *n* = 3. (D) RNA levels of circRNA-LON2, LONP2, KEAP1, NRF2, HO-1, VCAM-1, and ICAM-1 in HUVECs transfected with circRNA-LONP2 or control (ctrl) lentivirus were measured by RT-qPCR. GAPDH served as an internal reference. *n* = 3. (E and F) Protein levels of KEAP1, NRF2, HO-1, VCAM-1, and ICAM-1 in endothelial cells transfected with circRNA-LONP2 or ctrl lentivirus were evaluated by using Western blot analysis. *n* = 3. (G) HUVECs were transfected with si-circRNA-LONP2 or si-NC for 48 hours and then exposed to tumor necrosis factor (TNF)- α (5 ng/ml) for 4 hours. A monocyte adhesion assay was performed by incubating HUVECs with fluorescently labeled THP-1 cells. Scale bar: 1 mm. *n* = 3. (H) HUVECs were transfected with circRNA-LONP2 or ctrl lentivirus for 72 hours and subsequently exposed to atheroprotective LSS (15 dyne/cm²) for another 24 hours. Protein levels of VCAM-1 were detected by using Western blot analysis. *n* = 3. (I) HUVECs were transfected with si-circRNA-LONP2 or si-NC for 24 hours and were subsequently exposed to oscillatory shear stress (OSS) (\pm 5 dyne/cm² at 1 Hz) for another 24 hours. Protein levels of VCAM-1 and ICAM-1 were detected by using Western blot analysis. *n* = 3. Statistical analyses were performed applying the unpaired 2-tailed Student's *t*-test (A to G) or 1-way analysis of variance with Tukey's post hoc test (H and I). Values are mean \pm SEM. *n* \geq 3. **P* < 0.05; ***P* < 0.01; ****P* < 0.001 versus ctrl. Abbreviations as in **Figure 1**.

FIGURE 3 CircRNA-LONP2 Regulated Endothelial Inflammation via NRF2/HO-1 Pathway

(A) HUVECs were transfected with si-circRNA-LONP2 or si-NC for 48 hours and subsequently treated with TNF- α (5 ng/mL) for an additional 4 hours. Western blot analysis on cellular proteins separated into nuclear and cytoplasmic fractions from HUVECs. Lamin B1 and GAPDH were considered as markers for nucleus and cytoplasm, respectively. (B) HUVECs were transfected with si-circRNA-LONP2 or si-NC with or without NRF2 siRNA (si-NRF2) for 48 hours. Protein levels of KEAP1, NRF2, HO-1, VCAM-1, and ICAM-1 were determined by Western blot analysis. (C) HUVECs were transfected with si-circRNA-LONP2 or si-NC with or without HO-1 siRNA (si-HO-1) for 48 hours. Protein levels of KEAP1, NRF2, HO-1, VCAM-1, and ICAM-1 were determined by Western blot analysis. (D) HUVECs were transfected with si-circRNA-LONP2 or si-NC for 48 hours and then exposed to TNF- α (5 ng/mL) for 4 hours. Intracellular reactive oxygen species levels were detected by 2,7-dichlorodihydrofluorescein diacetate and were observed with a fluorescence microscope. Scale bar: 1 mm. Statistical analyses were performed by applying the unpaired 2-tailed Student's *t*-test (A and D) or the 1-way analysis of variance with Tukey's post hoc test (B and C). Values are mean \pm SEM. $n = 3$. * $P < 0.05$; ** $P < 0.01$; *** $P < 0.001$ versus control. Other abbreviations as in Figures 1 and 2.

(qRT-PCR) showed that circRNA-LONP2 silencing reduced the mRNA levels of KEAP1, and inflammatory genes vascular cell adhesion molecule-1 (VCAM-1) and intercellular cell adhesion molecule-1 (ICAM-1) increased the mRNA levels of the antioxidative stress and anti-inflammatory genes NRF2 and heme oxygenase-1 (HO-1), and had no significant effects on the mRNA levels of LONP2 (Figure 2A). Interestingly, Western blot analysis revealed that circRNA-LONP2 silencing reduced the protein levels of VCAM-1, ICAM-1, and KEAP1 while promoting the protein expression of NRF2 and HO-1 in HUVECs and human aortic ECs (Figures 2B and 2C).

After confirming the high circularization efficiency (approximately 75%) (Supplemental Figure 5) and high splicing accuracy (approximately 92.5%) (Supplemental Figure 6) of transcripts generated from the circRNA-LONP2 overexpression vector, we investigated whether circRNA-LONP2 overexpression had opposite effects. As expected, circRNA-LONP2 overexpression significantly up-regulated the mRNA and protein levels of VCAM-1, ICAM-1, and KEAP1 but down-regulated those of NRF2 and HO-1 (Figures 2D to 2F).

To distinguish the effects of circRNA-LONP2 from its linear counterpart, a plasmid with the reverse circularization sequence deletion (R-deletion) was constructed, allowing the plasmid to produce only linear transcripts for use as a control in circRNA-LONP2 overexpression experiments (Supplemental Figure 7A). qRT-PCR showed that the wild-type (WT) vector, but not the R-deletion mutant (MUT), significantly overexpressed circRNA-LONP2, whereas the R-deletion MUT significantly overexpressed the linear transcript (Supplemental Figure 7B). As expected, no significant differences were detected between the R-deletion group and the control group (Supplemental Figures 7B and 7C), suggesting that the linear counterpart of circRNA-LONP2 does not modulate endothelial inflammation and oxidative stress. Furthermore, circRNA-LONP2 silencing significantly reversed the inflammation and oxidative stress of ECs induced by circRNA-LONP2 overexpression but had no effect on the expression of the linear transcripts (Supplemental Figures 7D and 7E). These results suggest that circRNA-LONP2, but not its counterpart, is the major cause of inflammation and oxidative stress in ECs.

In addition, knockdown of endogenous circRNA-LONP2 attenuated tumor necrosis factor- α (TNF- α)-induced protein expression of VCAM-1 and ICAM-1 in ECs, which brought about reduced adhesion of monocytes to ECs (Figure 2G). Consistently, circRNA-LONP2 overexpression partially counteracted

LSS-induced repression of VCAM-1, monocyte chemoattractant protein 1, and E-Selectin (SELE) expression (Figure 2H, Supplemental Figure 8). Considering that oscillatory shear stress (OSS, 0.5 ± 5 dyne/cm 2) up-regulated the expression levels of circRNA-LONP2 (Supplemental Figure 9), we investigated whether knockdown of circRNA-LONP2 could partially reverse the pro-inflammatory effects of OSS. As expected, circRNA-LONP2 silencing partially attenuated the OSS-induced VCAM-1 and ICAM-1 protein expression in ECs (Figure 2I). Taken together, our results suggest that circRNA-LONP2 regulates flow-dependent inflammatory responses.

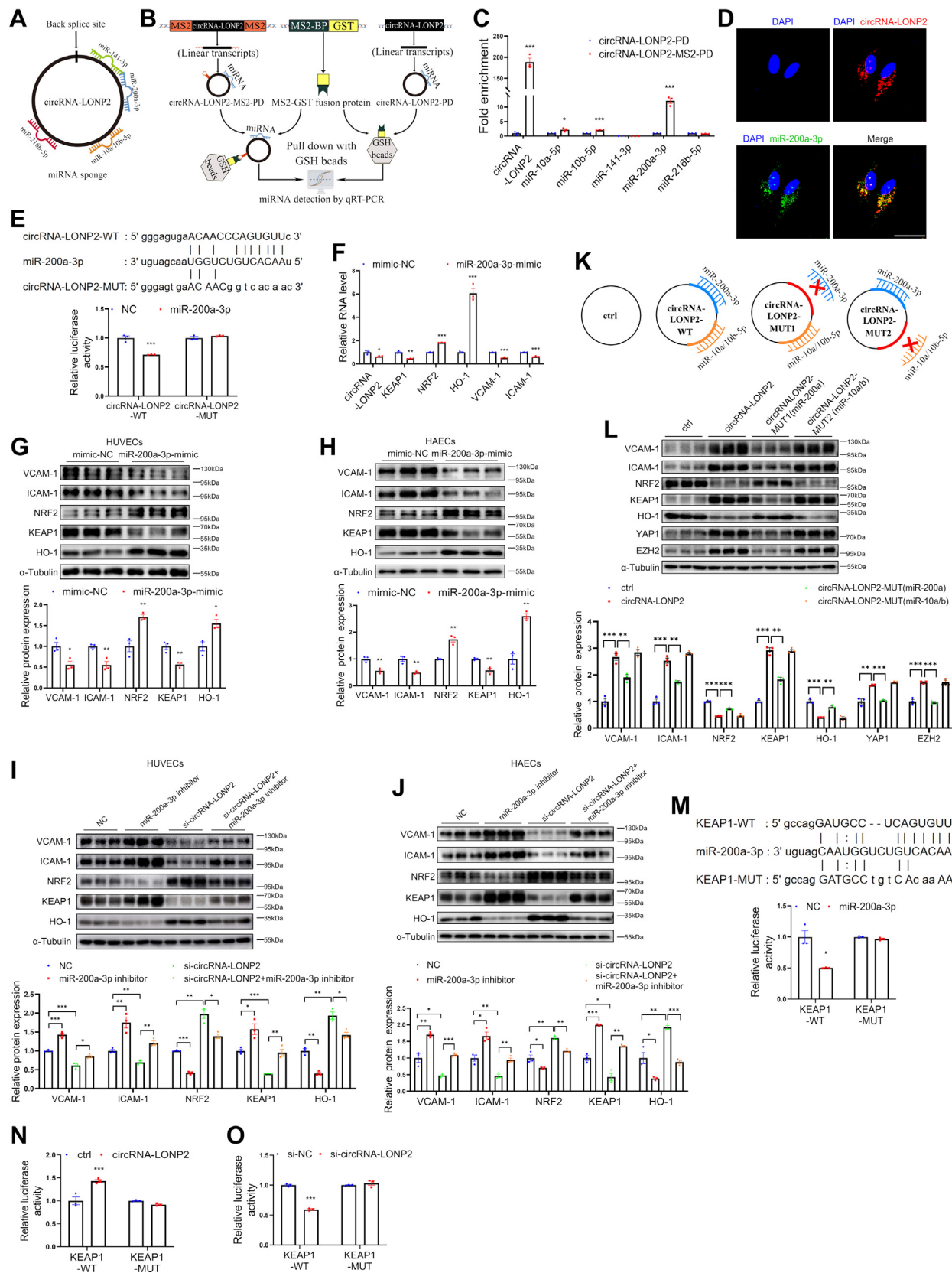
CircRNA-LONP2 REGULATED ENDOTHELIAL INFLAMMATION VIA THE NRF2/HO-1 AXIS.

Because circRNA-LONP2 is derived from the back-splicing of its linear transcript, we tested whether the linear LONP2 transcript mediates the function of circRNA-LONP2. Our data show that silencing or overexpression of circRNA-LONP2 has no effect on mRNA levels of linear LONP2 (Figures 2A and 2D). Consistently, LSS down-regulated the expression of circRNA-LONP2 without affecting the mRNA level of linear LONP2 (Supplemental Figure 10). These results suggest that shear-sensitive circRNA-LONP2 modulates endothelial inflammation independently from linear LONP2.

To investigate the possible mechanisms underlying circRNA-LONP2-induced endothelial inflammation, we further performed Western blot analysis of the nuclear and cytoplasmic fractions of ECs transfected with circRNA-LONP2 siRNA or control siRNA. The purity of the nuclear and cytosolic fractions was confirmed by Western blot analysis using antibodies against the nuclear (Lamin B1) and cytoplasmic (GAPDH [glyceraldehyde 3-phosphate dehydrogenase]) marker proteins. As expected, the knockdown of circRNA-LONP2 attenuated TNF- α -stimulated nuclear factor- κ B (NF- κ B) p65 translocation into the nucleus, while promoting NRF2 nuclear translocation, suggesting that circRNA-LONP2 may induce endothelial inflammation by modulating the nuclear translocation of NRF2 and NF- κ B (Figure 3A).

A previous study reported that the NRF2/HO-1 pathway has anti-inflammatory properties.¹⁹ We therefore explored whether circRNA-LONP2 regulates endothelial inflammation through the NRF2/HO-1 axis. As expected, inhibition of NRF2 or its downstream target, HO-1, by siRNA significantly abrogated the anti-inflammatory effects of circRNA-LONP2 siRNA in ECs (Figures 3B and 3C). Collectively, these data show that circRNA-LONP2 regulates endothelial inflammation via the NRF2/HO-1 axis.

Given that circRNA-LONP2 works through the NRF2/HO-1 axis, we performed a reactive oxygen

FIGURE 4 CircRNA-LONP2 Induced Endothelial Inflammation Through the miR-200a-3p/KEAP1/NRF2 Pathway

species assay to determine if oxidative stress was reduced after circRNA-LONP2 silencing in HUVECs. As shown in **Figure 3D**, silencing of circRNA-LONP2 reduced the TNF- α -induced reactive oxygen species levels in ECs. These results suggest that circRNA-LONP2 modulates endothelial inflammation by regulating the oxidative stress state of ECs.

CircRNA-LONP2 INDUCED ENDOTHELIAL INFLAMMATION THROUGH THE miR-200A-3p/KEAP1/NRF2 PATHWAY.

Because circRNA-LONP2 was observed to be preferentially located in the cytoplasm of ECs, we hypothesized that circRNA-LONP2 may regulate gene expression by acting as miRNA sponges. The starBase database²⁰ was used to predict the targets of circRNA-LONP2, and 5 broadly conserved miRNAs (miR-10a-5p, miR-10b-5p, miR-141-3p, miR-200a-3p, and miR-216b-5p) that directly bind to circRNA-LONP2 were selected for further analysis (**Figure 4A**). To identify miRNAs that might bind to circRNA-LONP2, we designed an MS2 RNA pull-down assay. A vector was constructed expressing circRNA-LONP2 labeled with MS2 RNA hairpins (circRNA-LONP2-MS2-PD) and a control vector expressing circRNA-LONP2 (circRNA-LONP2-PD). By labeling circRNA-LONP2 with the MS2 structure and co-expressing MS2-binding protein (ie, MS2-BP) fused to a GST tag (ie, MS2-BP-GST), we were able to use glutathione magnetic beads to pull down miRNAs that interact with circRNA-LONP2.

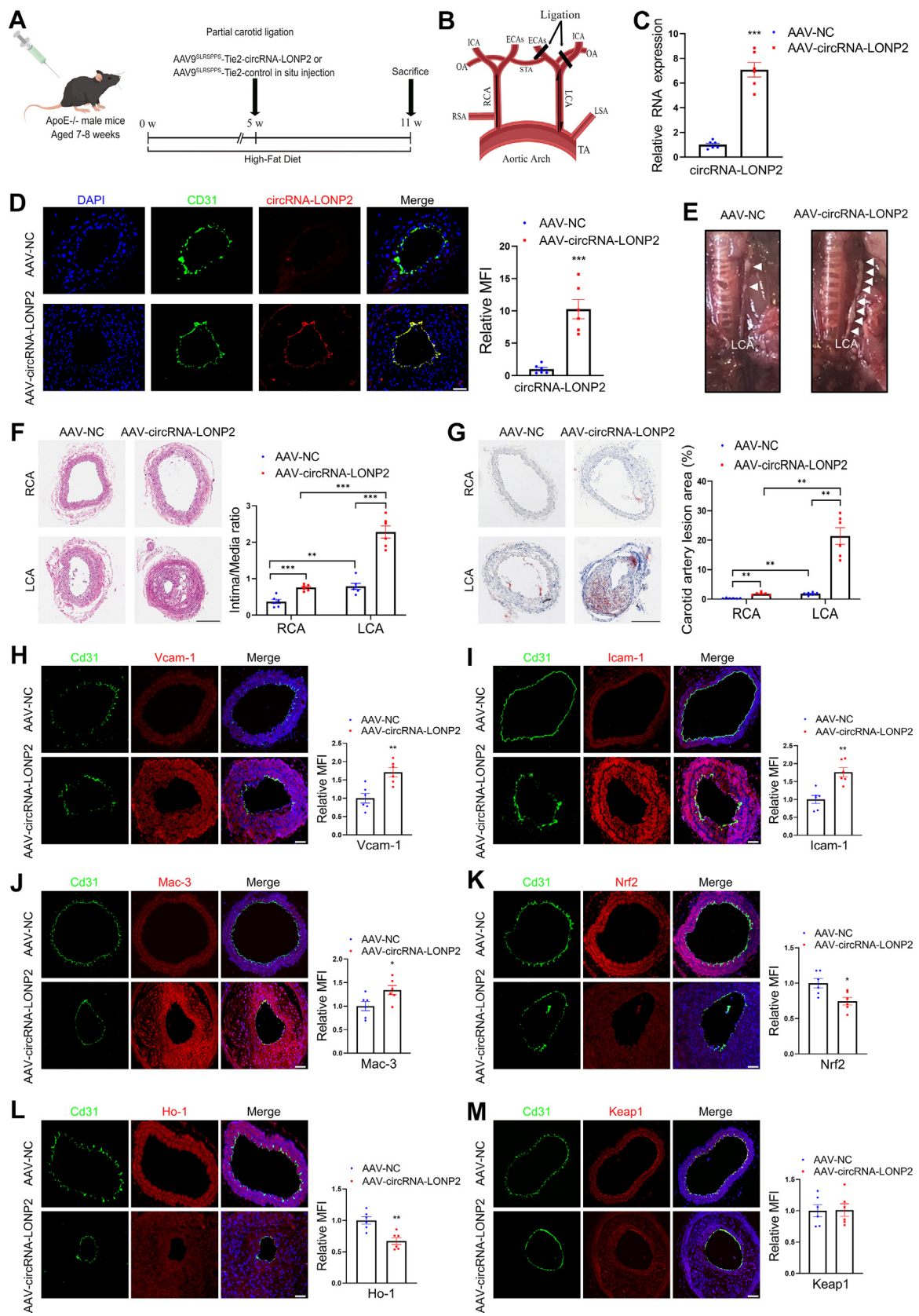
In addition, to avoid nonspecific pull-down of linear transcripts, one-half of the MS2 sequence was cloned at the 5' end of circRNA-LONP2 and the other

half at the 3' end; thus, only circRNA-LONP2 (whose 5' end and 3' end are connected to form a closed loop by back-splicing) transcripts, rather than its linear transcripts, can form intact MS2 (**Figure 4B, Supplemental Figure 11A**). The results showed specific enrichment of circRNA-LONP2 and miR-200a-3p, miR-10a-5p, and miR-10b-5p in the MS2-labeled circRNA-LONP2-MS2-PD group compared with the control (**Figure 4C, Supplemental Figure 11B**). Because miR-200a-3p was the most enriched miRNA in the circRNA-LONP2 pull-down assay, fluorescence in situ hybridization assays were performed to confirm the interaction, revealing the co-localization of circRNA-LONP2 and miR-200a-3p (**Figure 4D**). We further performed dual-luciferase assays using reporters containing WT and MUT miR-200a-3p binding sites of circRNA-LONP2 to verify the interaction between circRNA-LONP2 and miR-200a-3p. The results proved that miR-200a-3p mimics could significantly down-regulate the luciferase activity of the WT group, but not the MUT group, indicating that circRNA-LONP2 may indeed bind miR-200a-3p (**Figure 4E**).

Given the apparent interaction between circRNA-LONP2 and miR-200a-3p, we investigated the biological function of miR-200a-3p. We found that transfection of ECs with miR-200a-3p mimics significantly down-regulated the RNA levels of circRNA-LONP2, KEAP1, VCAM-1, and ICAM-1 while up-regulating the RNA levels of NRF2 and HO-1 (**Figure 4F**). In addition, overexpression of miR-200a-3p promoted NRF2 and HO-1 protein expression while suppressing the protein expression of VCAM-1, ICAM-1, and KEAP1 (**Figures 4G and 4H**). The

FIGURE 4 Continued

(A) Starbase online database provided predicted putative binding sites of several broadly conserved miRNAs with circRNA-LONP2. (B) Schematic illustrating that circRNA-LONP2 with MS2 stem-loop was pulled down by glutathione (GSH) magnetic beads. circRNA-LONP2 without MS2 stem-loop structure served as a control. (C) Fold enrichment of miRNAs pulled down by magnetic beads was detected by using qRT-PCR. (D) RNA fluorescence in situ hybridization assay illustrating the co-localization of circRNA-LONP2 and miR-200a-3p in HUVECs using 5' and 3' Cy-3 labeled probes (circRNA-LONP2) and 5' and 3' FAM-labeled probes (miR-200a-3p). Nuclei were stained with DAPI. Scale bar = 25 μ m. (E) The predicted wild-type (WT) or mutated (MUT) miR-200a-3p binding site in circRNA-LONP2. Luciferase reporter activity of circRNA-LONP2-WT or circRNA-LONP2-MUT in Lenti-X 293T cells co-transfected with miR-200a-3p mimic or mimic control (mimic-NC) was detected by the Dual-Luciferase Reporter Assay System. (F) RNA levels of circRNA-LONP2, KEAP1, NRF2, HO-1, VCAM-1, and ICAM-1 in HUVECs transfected with miR-200a-3p-mimic or mimic-NC for 48 hours were measured by RT-qPCR. (G and H) ECs were transfected with miR-200a-3p-mimic or mimic-NC for 48 hours. KEAP1, NRF2, HO-1, VCAM-1, and ICAM-1 protein levels were detected by using Western blot analysis. (I and J) ECs were transfected with si-circRNA-LONP2 or si-NC with or without miR-200a-3p inhibitor for 48 hours. Protein levels of KEAP1, NRF2, HO-1, VCAM-1, and ICAM-1 were determined by Western blot analysis. (K) The schematic depicts WT circRNA-LONP2 (circRNA-LONP2-WT), circRNA-LONP2 with a MUT miR-200a-3p binding site (circRNA-LONP2-MUT1), and circRNA-LONP2 with a MUT miR-10a/10b-5p binding site (circRNA-LONP2-MUT2). Circ-pL05 served as a ctrl. (Diagrams obtained using Figdraw) (L) Protein levels of VCAM-1, ICAM-1, NRF2, KEAP1, HO-1, Yes-associated protein 1 (YAP1), and enhancer of zeste homolog 2 (EZH2) in HUVECs transfected with circRNA-LONP2, circRNA-LONP2-MUT (miR-200a), circRNA-LONP2-MUT (miR-10a/b), or ctrl lentivirus were analyzed by Western blot analysis. (M) Schematic representation of predicted WT or MUT miR-200a-3p binding sites in KEAP1 mRNA. Luciferase reporter activity of KEAP1-WT or KEAP1-MUT in Lenti-X 293T cells co-transfected with miR-200a-3p mimic or mimic ctrl was detected by using the Dual-Luciferase Reporter Assay System. (N) Luciferase reporter activity of KEAP1-WT or KEAP1-MUT in Lenti-X 293T cells co-transfected with circRNA-LONP2 or control plasmids was detected by using the Dual-Luciferase Reporter Assay System. (O) Luciferase reporter activity of KEAP1-WT or KEAP1-MUT in Lenti-X 293T cells co-transfected with si-circRNA-LONP2 or si-NC was detected by using the Dual-Luciferase Reporter Assay System. Statistical analyses were performed by applying the unpaired 2-tailed Student's t-test (C, E, F, G, H, M, N, and O) or the 2-way analysis of variance with Tukey's post hoc test (I, J and L). Values are mean \pm SEM. n = 3. *P < 0.05; **P < 0.01; ***P < 0.001 versus control. A, B, and K were created by using Figdraw. Abbreviations as in **Figures 1 and 2**.

FIGURE 5 CircRNA-LONP2 Accelerates the Progression of Atherosclerosis

cell phenotype induced by miR-200a-3p was similar to that induced by circRNA-LONP2 silencing, suggesting that miR-200a-3p mediates the regulatory effect of circRNA-LONP2 on EC function. As expected, transfection with miR-200a-3p inhibitors significantly rescued the inhibitory effects of circRNA-LONP2 silencing on KEAP1, VCAM-1, and ICAM-1 protein expression, while abolishing circRNA-LONP2 silencing-induced NRF2 and HO-1 protein expression (**Figures 4I and 4J**). Thus, the antioxidative and anti-inflammatory effects of circRNA-LONP2 silencing in ECs were mediated by miR-200a-3p.

Interestingly, we found that miR-10a-5p and miR-10b-5p could also be pulled down by circRNA-LONP2, although not as efficiently as miR-200a-3p. Previous studies have shown that miR-10a exerts anti-inflammatory effects in cultured human aortic ECs.^{21–23} To test whether circRNA-LONP2 also regulates endothelial inflammation by sponging miR-10a-5p and miR-10b-5p and to further show that the anti-inflammatory effects of circRNA-LONP2 silencing in ECs are mediated by miR-200a-3p, circRNA-LONP2-MUT1 (circRNA-LONP2 with mutated miR-200a-3p binding sites) vectors and circRNA-LONP2-MUT2 (circRNA-LONP2 with mutated miR-10a/b-5p binding sites) vectors (**Figure 4K**) were constructed. Western blot analysis revealed that a mutation in the miR-200a-3p binding site largely blocked the pro-oxidative and pro-inflammatory effects of circRNA-LONP2, whereas a mutation in the miR-10a/b binding site had no effect (**Figure 4L**), suggesting that circRNA-LONP2 promotes oxidative stress and endothelial inflammation by sponging miR-200a-3p.

Notably, previously studies reported that circRNA-LONP2 directly interacts with pri-miR-17 and miR-27b-3p.^{24,25} Consistent with these findings, our data indicated that primary miR-17 and miR-27b-3p, but

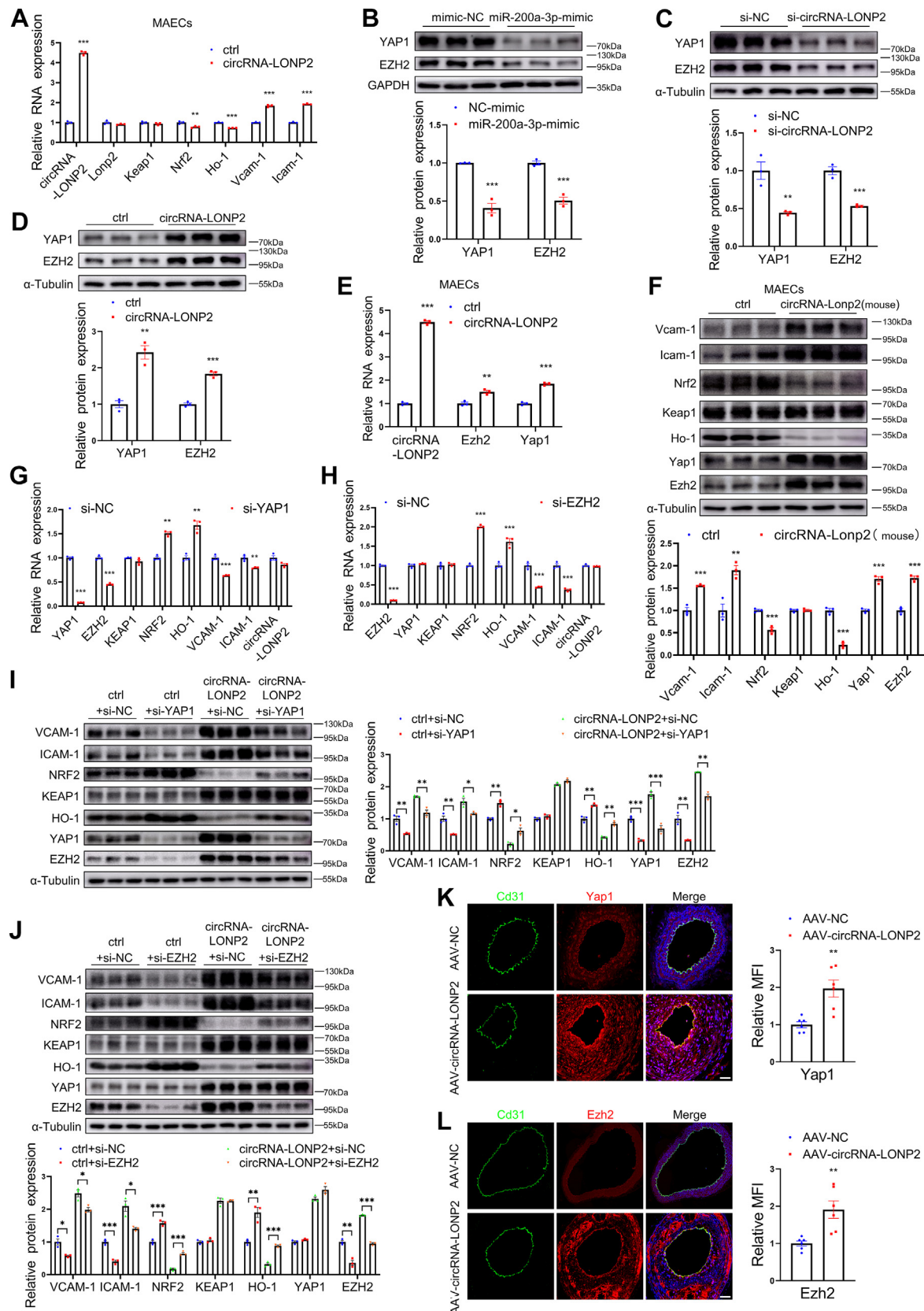
not miR-17-3p or miR-17-5p, were pulled down by circRNA-LONP2 in HUVECs, albeit with lower enrichment compared with miR-200a-3p (**Supplemental Figure 11B**). To examine the roles of pri-miR-17 and miR-27b-3p in circRNA-LONP2-induced endothelial oxidative stress and inflammation, circRNA-LONP2-MUT3 (circRNA-LONP2 with mutated miR-27b-3p binding sites) vectors and circRNA-LONP2-MUT4 (circRNA-LONP2 with mutated pri-miR-17 binding sites) vectors (**Supplemental Figure 11C**) were constructed. Western blot analysis revealed that these mutations had no effect on the pro-oxidative and pro-inflammatory effects of circRNA-LONP2 (**Supplemental Figure 11D**), suggesting that pri-miR-17 and miR-27b-3p are not involved in circRNA-LONP2-induced endothelial oxidative stress and inflammation.

We further investigated whether the expression levels of miR-200a-3p can be regulated by circRNA-LONP2 or LSS. As shown in **Supplemental Figures 12 and 13A to 13C**, although circRNA-LONP2 was more abundant than miR-200a-3p, knockdown or over-expression of circRNA-LONP2 had no effect on the expression of miR-200a-3p. Furthermore, LSS had no effect on the expression of miR-200a-3p (**Supplemental Figure 13D**). These data indicate that shear-sensitive circRNA-LONP2 modulates endothelial inflammation without affecting the expression of miR-200a-3p.

Because miR-200a-3p was found to target KEAP1,²⁶ we hypothesized that circRNA-LONP2 induced endothelial inflammation through the miR-200a-3p/KEAP1/NRF2 pathway. To confirm that KEAP1 is regulated by miR-200a-3p, luciferase reporters containing WT or MUT 3'-untranslated region of KEAP1 were constructed. Dual-luciferase reporter assays showed that the luciferase activities of the KEAP1 WT

FIGURE 5 Continued

(A) Schematic figure showing the experimental strategy (by Figdraw). Seven- to eight-week-old male *ApoE*^{−/−} mice were fed a high-fat diet and subjected to partial ligation of the left common carotid artery (LCA) at week 5. During the ligation, the LCA was infused with Endo-AAV9-Tie2-circRNA-LONP2 or Endo-AAV9-Tie2-control lentiviruses. (B) Schematic representation of partial left carotid artery ligation (Diagrams obtained using Figdraw). (C) qRT-PCR analysis of circRNA-LONP2 in arterial tissues from mice treated with Endo-AAV9-Tie2-circRNA-LONP2 or Endo-AAV9-Tie2-control lentiviruses; n = 6. (D) RNA fluorescence in situ hybridization for circRNA-LONP2 and immunofluorescence staining for Cd31 and DAPI in the ligated LCA of *ApoE*^{−/−} mice. Scale bar: 40 μm. Quantification of relative mean fluorescent intensity of circRNA-LONP2 (n = 6). (E) After 6 weeks, the LCAs were separated to examine atherosclerotic lesions. Representative images of carotid arteries are shown. White arrows indicate plaque lesions. (F) Carotid arteries were harvested 6 weeks after ligation for hematoxylin and eosin staining (left). Representative images are shown. The areas of the intima and media were quantified by using ImageJ software (right). Scale bar: 200 μm, n = 6. (G) Oil Red O staining of carotid arteries (left). Representative images are shown. Plaque areas were quantified by using ImageJ software (right). Scale bar: 200 μm; n = 6. (H to M) Immunofluorescence staining for Vcam-1 (H), Icam-1 (I), Mac-3 (J), Nrf2 (K), Ho-1 (L), Keap1 (M), Cd31, and DAPI in the ligated LCA of *ApoE*^{−/−} mice. Scale bar: 40 μm. Quantification of relative mean fluorescent intensity of Vcam-1, Icam-1, Mac-3, Nrf2, Ho-1, and Keap1 (n = 6). The unpaired 2-tailed Student's t-test was used for statistical analyses (C, D, and F to M). Values are mean ± SEM. *P < 0.05; **P < 0.01; ***P < 0.001 versus control. A was created by using Figdraw. AAV9 = adeno-associated virus vector 9; RCA = right carotid artery; other abbreviations as in **Figures 1 and 2**.

FIGURE 6 CircRNA-LONP2 Modulates Oxidative Stress and Endothelial Inflammation via the miR-200a-3p/YAP1/EZH2 Axis

Continued on the next page

reporter (but not MUT reporter) were significantly decreased when transfected with miR-200a-3p mimics compared with the control group (**Figure 4M**). In addition, we found that circRNA-LONP2 overexpression or knockdown further increased or reduced the luciferase activity of the KEAP1 WT reporter (**Figures 4N and 4O**). These results revealed that circRNA-LONP2 serves as a sponge for miR-200a-3p to regulate KEAP1 and promote endothelial inflammation via the ceRNA mechanism in ECs.

CircRNA-LONP2 ACCELERATES THE PROGRESSION OF ATHEROSCLEROSIS. A previous report showed that AAV9^{SLRSPPS} could efficiently target ECs.²⁷ To study the function of endothelial circRNA-LONP2 in atherogenesis, *ApoE*^{-/-} mice with partial ligation of the LCA were infected with AAV9^{SLRSPPS}-Tie2-circRNA-LONP2 or AAV9^{SLRSPPS}-Tie2-control (**Figures 5A and 5B**). The murine Tie2 promoter was used to drive endothelial circRNA-LONP2 expression in *ApoE*^{-/-} mice. Endothelial overexpression of circRNA-LONP2 was confirmed by qRT-PCR and fluorescence in situ hybridization (**Figures 5C and 5D**). Six weeks after ligation, the plaque area, neointima size, and intimal lipid deposition in *ApoE*^{-/-} mice infected with AAV9^{SLRSPPS}-Tie2-circRNA-LONP2 were significantly aggravated compared with those in the control group (**Figures 5E to 5G, Supplemental Figure 14**). In addition, immunofluorescence staining showed that circRNA-LONP2 increased the protein levels of the pro-inflammatory markers Vcam-1 (**Figure 5H**) and Icam-1 (**Figure 5I**) and mononuclear phagocytes marker Mac-3 substantially (**Figure 5J**) in the ligated LCA of *ApoE*^{-/-} mice, while decreasing the protein levels of antioxidative and anti-inflammatory Nrf2 (**Figure 5K**) and Ho-1 (**Figure 5L**), without significantly affecting the protein expression of Keap1 (**Figure 5M**). These data suggest that circRNA-LONP2 accelerates the progression of atherosclerosis by

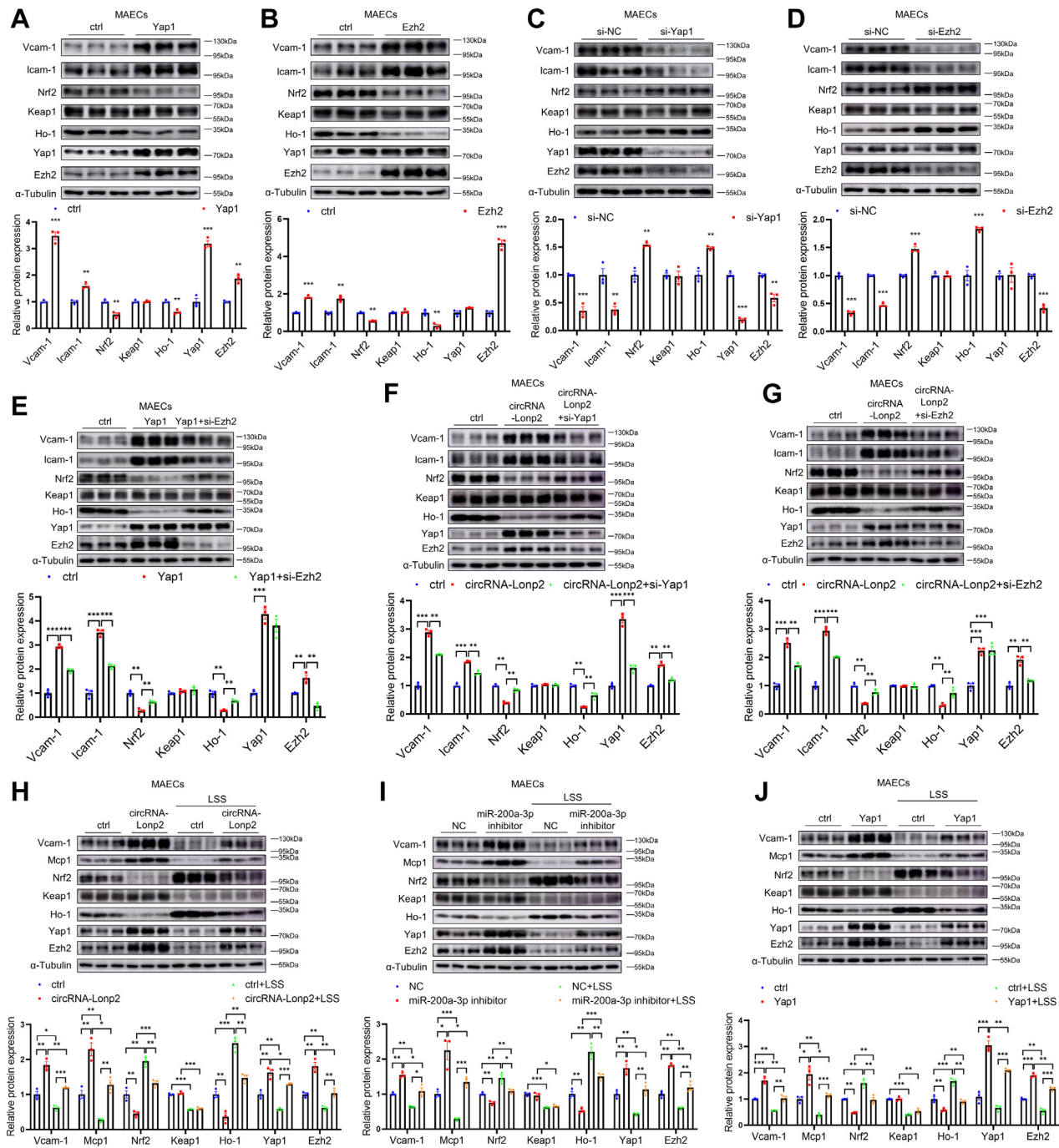
inducing oxidative stress and endothelial inflammation. Furthermore, these results reveal that there is an additional pathway by which circRNA-LONP2 regulates NRF2 signaling without affecting KEAP1 expression.

CircRNA-LONP2 MODULATES OXIDATIVE STRESS AND ENDOTHELIAL INFLAMMATION VIA THE miR-200A-3p/YAP1/EZH2 AXIS. Although miR-200a-3p was conserved across most vertebrates, the miR-200a-3p binding site was not conserved in mouse *Keap1*, suggesting that mouse *Keap1* mRNA is not a target of miR-200a-3p. Indeed, although the overexpression of circRNA-LONP2 increased the mRNA levels of Vcam-1 and Icam-1 while reducing the mRNA levels of Nrf2 and Ho-1, it did not affect the mRNA levels of *Keap1* in MAECs (**Figure 6A**). Consistently, immunofluorescence staining showed that circRNA-LONP2 has no effect on protein levels of *Keap1* in mice (**Figure 5M**). These data suggested that the regulatory effects of circRNA-LONP2 on the progression of atherosclerosis in mice are not mediated by *Keap1* but by other miR-200a-3p targets.

A previous report has shown that miR-200a-3p inhibits inflammation and the formation of atherosclerotic lesions by targeting EZH2.²⁸ EZH2 functions as a histone H3 Lys27 (H3K27) trimethyltransferase that transcriptionally represses NRF2 expression in lung cancer.²⁹ In addition, YAP1, which promotes the development of atherosclerotic lesions,³⁰ has been identified as a target of miR-200a-3p.³¹ YAP1/TAZ promotes the transcription of EZH2 in lung cancer.³² Therefore, we further explored whether EZH2 and YAP1 are involved in the pro-oxidative and pro-inflammatory effects of circRNA-LONP2. As expected, overexpression of miR-200a-3p decreased EZH2 and YAP1 protein expression (**Figure 6B**). Consistently, silencing circRNA-LONP2 down-regulated YAP1 and EZH2 (**Figure 6C**), whereas the overexpression of circRNA-LONP2 had the opposite effect

FIGURE 6 Continued

(A) RNA levels of circRNA-LON2, LONP2, Keap1, Nrf2, Ho-1, Vcam-1, and Icam-1 in mouse aortic endothelial cells (MAECs) transfected with human circRNA-LONP2 or control (ctrl) lentivirus were measured by RT-qPCR. Gapdh served as an internal reference; n = 3. (B) HUVECs were transfected with miR-200a-3p-mimic or mimic-NC (control) for 48 hours. YAP1 and EZH2 protein levels were detected by Western blot analysis; n = 3. (C) Protein levels of YAP1 and EZH2 in HUVECs transfected with si-circRNA-LONP2 or si-NC (control) were detected by Western blot analysis; n = 3. (D) Protein levels of YAP1 and EZH2 in HUVECs transfected with circRNA-LONP2 or ctrl lentivirus were analyzed by Western blot analysis; n = 3. (E) RNA levels of circRNA-LON2, Yap1, and Ezh2 in MAECs transfected with human circRNA-LONP2 or ctrl lentivirus were measured by RT-qPCR. Gapdh served as an internal reference; n = 3. (F) Protein levels of Keap1, Nrf2, Ho-1, Vcam-1, Icam-1, Yap1, and Ezh2 in MAECs transfected with mouse circRNA-LONP2 (mouse) or ctrl lentivirus were detected by using Western blot analysis; n = 3. (G and H) RNA levels of YAP1, EZH2, KEAP1, NRF2, HO-1, VCAM-1, ICAM-1, and circRNA-LONP2 in HUVECs transfected with YAP1 or EZH2 siRNA (si-YAP1 or si-EZH2) or si-NC were measured by RT-qPCR; n = 3. (I and J) HUVECs overexpressing circRNA-LONP2 were co-transfected with si-YAP1 or si-EZH2 for 72 hours. Protein levels of KEAP1, NRF2, HO-1, VCAM-1, ICAM-1, YAP1, and EZH2 were determined by Western blot analysis; n = 3. (K and L) Immunofluorescence staining for Yap1 (K), Ezh2 (L), Cd31, and DAPI in the ligated LCA of *ApoE*^{-/-} mice. Scale bar: 40 μm. Quantification of relative mean fluorescent intensity of Yap1 and Ezh2 (n = 6). Statistical analyses were performed by using the unpaired 2-tailed Student's t-test (A-H, K, and L) or the 1-way analysis of variance with Tukey's post hoc test (I and J). Values are mean ± SEM. *P < 0.05; **P < 0.01; ***P < 0.001 versus control. Abbreviations as in **Figures 1 to 3**.

FIGURE 7 Shear Stress Modulates MAEC Oxidative Stress and Inflammation Via the circRNA-LONP2/miR-200a-3p/YAP1/EZH2 Axis

(A and B) Protein levels of Keap1, Nrf2, Ho-1, Vcam-1, Icam-1, Yap1, and Ezh2 in MAECs transduced with mouse Yap1 (A), mouse Ezh2 (B), or ctrl lentivirus were analyzed by using Western blot analysis. (C and D) Protein levels of Keap1, Nrf2, Ho-1, Vcam-1, Icam-1, Yap1, and Ezh2 in MAECs transfected with mouse Yap1 siRNA (si-Yap1), mouse Ezh2 siRNA (si-Ezh2), or si-NC were analyzed by using Western blot analysis. (E) MAECs transduced with mouse Yap1 or mCherry (ctrl) lentivirus for 24 hours were transfected with mouse Ezh2 siRNA or control siRNA for an additional 48 hours. Protein levels of Keap1, Nrf2, Ho-1, Vcam-1, Icam-1, Yap1, and Ezh2 were determined by using Western blot analysis. (F and G) MAECs transduced with mouse circRNA-Lonp2 or mCherry (ctrl) lentivirus for 24 hours were transfected with mouse si-Yap1 (F), mouse si-Ezh2 (G), or control siRNA for an additional 48 hours. Protein levels of Keap1, Nrf2, Ho-1, Vcam-1, Icam-1, Yap1, and Ezh2 were determined by using Western blot analysis. (H to J) MAECs transfected with circRNA-Lonp2 or ctrl lentivirus (H), miR-200a-3p inhibitor or negative control (NC) inhibitor (I), Yap1 or ctrl lentivirus (J) were exposed to atherosprotective LSS (15 dyne/cm²) for 24 hours. The protein levels of Vcam-1, Mcp1, Nrf2, Keap1, Ho-1, Yap1, and Ezh2 were detected by using Western blot analysis. Unpaired 2-tailed Student's t-test was used for statistical analyses. Values are mean ± SEM. n = 3. *P < 0.05; **P < 0.01; ***P < 0.001 versus control. Abbreviations as in Figures 1, 2, and 6.

(Figure 6D). Furthermore, the overexpression of human circRNA-LONP2 increased mRNA levels of Yap1 and Ezh2 in MAECs (Figure 6E). Collectively, these data suggest that EZH2 and YAP1 are conserved downstream targets of circRNA-LONP2.

We further explored whether mouse circRNA-Lonp2 has a similar function. Although there were some mismatches between the human and mouse Lonp2 genome sequences, the binding sites of miR-200a-3p in human circRNA-LONP2 and mouse circRNA-Lonp2 were conserved (Supplemental Figure 15). We found that circRNA-Lonp2 was expressed in MAECs and in the mouse aorta (Supplemental Figure 16). The overexpression of mouse circRNA-Lonp2 up-regulated Ezh2, Yap1, Vcam-1, and Icam-1, while down-regulating Nrf2 and Ho-1 at the protein level, without affecting Keap1 expression in MAECs (Figure 6F). These data suggest that, in mice, circRNA-Lonp2 promotes oxidative stress and endothelial inflammation by targeting Yap1 and Ezh2 rather than Keap1.

Next, we investigated whether circRNA-LONP2 functions by targeting YAP1/EZH2 in both humans and mice. Silencing YAP1 or its downstream target EZH2 decreased the mRNA and protein levels of VCAM-1 and ICAM-1, while increasing the mRNA and protein levels of NRF2 and HO-1, without affecting the mRNA and protein levels of KEAP1 in HUVECs (Figures 6G to 6J). Moreover, silencing of YAP1 or EZH2 by siRNA significantly abrogated the pro-oxidative and pro-inflammatory effects of circRNA-LONP2 in HUVECs (Figures 6I and 6J). Consistent with these data, immunofluorescence staining showed that circRNA-LONP2 significantly up-regulated Yap1 and Ezh2 in mice (Figures 6K and 6L). Collectively, these data suggest that circRNA-LONP2 functions by targeting YAP1/EZH2 in both humans and mice.

To show the causal relationship between Yap1/Ezh2 expression and Nrf2 activation in mouse ECs, we conducted a series of gain-of-function and loss-of-function experiments as well as rescue experiments. Overexpression of Yap1 or its downstream target Ezh2 increased the protein levels of Vcam-1 and Icam-1, while decreasing the protein levels of Nrf2 and Ho-1, without affecting Keap1 protein expression in MAECs (Figures 7A and 7B). Silencing of Yap1 or Ezh2 had the opposite effect (Figures 7C and 7D). Moreover, silencing of Ezh2 significantly abrogated the pro-oxidative and pro-inflammatory effects of Yap1 in MAECs (Figure 7E). Consistent with these data, silencing of Yap1 or Ezh2 significantly abrogated the pro-oxidative and pro-inflammatory effects of mouse circRNA-Lonp2 in

MAECs (Figures 7F and 7G). In addition, circRNA-Lonp2 overexpression partially counteracted the LSS-induced repression of Vcam-1, Mcp-1, Yap1, and Ezh2 protein expression, as well as partially attenuated the LSS-induced up-regulation of Nrf2 and Ho1 protein expression, with no effect on Keap1 protein expression in MAECs (Figure 7H). Consistently, miR-200a-3p inhibitor transfection or Yap1 overexpression partially counteracted the anti-oxidative and anti-inflammatory effects of LSS in MAECs (Figures 7I and 7J). Taken together, these results indicate that shear-sensitive circRNA-LONP2 regulates oxidative stress and endothelial inflammation via a conserved signaling mechanism, the miR-200a-3p/YAP1/EZH2 axis.

DISCUSSION

LSS inhibits endothelial inflammation and protects arteries from atherosclerosis,³³⁻³⁵ however, the mechanism of this effect is unclear. CircRNAs are key regulators of vascular homeostasis and atherosclerosis,^{36,37} but their role in mediating the action of LSS has not been explored. In this study, we first revealed that LSS down-regulated circRNA-LONP2 expression, inhibiting oxidative stress and endothelial inflammation by activating the miR-200a-3p-mediated NRF2/HO-1 signaling pathway. These findings provide strong evidence for the atherogenic effects of endothelial circRNA-LONP2 and suggest it as potential target for atherosclerotic therapy.

Although atherosclerosis is associated with many systemic risk factors, such as hypercholesterolemia, hypertension, diabetes, smoking, and aging, this process primarily occurs near arterial branches, bifurcations, and curvatures, where the blood flow is disturbed, generating OSS that drives atherosclerosis by inducing vascular inflammation and oxidative stress.³⁸ OSS triggers endothelial inflammation by up-regulating the expression of endothelial adhesion molecules (VCAM-1 and ICAM-1), facilitating monocyte adhesion to ECs.³⁹ Activation of NF- κ B signaling is crucial in OSS-induced inflammation.⁴⁰ NRF2 is activated by LSS, which induces activation of anti-inflammatory and antioxidant gene expression and protects cells from oxidative stress and inflammatory damage.⁴¹⁻⁴³ NRF2 activates the transcription of a series of antioxidant genes and is the main regulator of the cellular antioxidant defense system.⁴⁴ Under normal conditions, NRF2 is sequestered in the cytoplasm by KEAP1, which prevents NRF2 from nuclear translocation and facilitates its proteasomal degradation.⁴⁵ In response to LSS stimulation, NRF2 is activated by dissociation from KEAP1 and

translocation into the nucleus, which induces the expression of antioxidant genes.^{41,43}

In addition to its antioxidant effects, NRF2 inhibits the NF- κ B signaling pathway through a variety of mechanisms. First, NRF2 inhibits oxidative stress-mediated NF- κ B activation by reducing intracellular reactive oxygen species levels.⁴⁶ Second, NRF2 induces up-regulation of cellular HO-1 expression, preventing degradation of I κ B- α .⁴⁷ Thus, targeted activation of NRF2 may protect the arterial vascular system from atherosclerosis through its antioxidant and anti-inflammatory effects. We found that LSS-induced down-regulation of circRNA-LONP2 suppresses endothelial inflammation, at least in part by activating the NRF2/HO-1 signaling pathway. These findings suggest that circRNA-LONP2 can serve as a therapeutic target in atherosclerosis.

miRNAs are a class of small, noncoding RNAs, each about 22 nucleotides long, that are active in post-transcriptional gene silencing.^{48,49} miRNAs respond to shear stress regulation and participate in vascular EC inflammation.⁵⁰⁻⁵² miR-200a-3p is highly conserved among vertebrate species and reportedly targets KEAP1,^{26,53-55} YAP1,^{31,56,57} and EZH2.²⁸ However, the role of miR-200a-3p in mediating the effects of shear stress on endothelial inflammation remains unclear. LSS suppresses YAP1, which interrupts inflammatory signaling pathways and prevents atherosclerosis progression.⁵⁸ EZH2 is down-regulated by LSS to prevent apoptosis in ECs⁵⁹; EZH2 down-regulation also enhances activation of atherosclerosis-protective MAPK7 signaling, conferring an antiatherosclerotic effect.⁶⁰ Consistent with these previous findings, we found that miR-200a-3p targets and inhibits KEAP1, YAP1, and EZH2 expression in ECs and that transfection with miR-200a-3p mimics activated NRF2 signaling. In addition, knockdown of NRF2 or its downstream HO-1 significantly attended the anti-inflammation effect of circRNA-LONP2 knockdown. Together, these results establish the previously unknown functions of circRNA-LONP2 in regulating NRF2 signaling via sponging miR-200a-3p and endothelial inflammation via NRF2 signaling. Interestingly, we uncovered 2 mechanisms (conserved and species-specific mechanisms) by which circRNA-LONP2 modulates NRF2 signaling. First, circRNA-LONP2 regulates the nuclear transport of NRF2 via the miR-200a-3p/KEAP1 axis (human-specific regulatory mechanism). Second, circRNA-LONP2 regulates NRF2 expression via the miR-200a-3p/YAP1/EZH2 axis (a conserved regulatory mechanism in both humans and mice). Our findings

highlight species-specific differences in circRNA-LONP2-regulated NRF2 signaling.

Previous studies reported that circRNA-LONP2 directly interacts with and promotes the processing of primary microRNA-17 in colorectal carcinoma cells²⁴ and directly interacts with miR-27b-3p to accelerate the progression of esophageal squamous cell carcinoma through the miR-27b-3p-ZEB1 axis.²⁵ Although our data confirm that circRNA-LONP2 can interact with pri-miR-17 or miR-27-3p, the mutation experiments rule out a role for pri-miR-17 or miR-27-3p in mediating circRNA-LONP2-induced vascular endothelial inflammation and oxidative stress. Further research is needed to explore the role of circRNA-LONP2 in vascular ECs through its interaction with pri-miR-17 or miR-27-3p.

STUDY LIMITATIONS. First, although most of the circRNA-LONP2 was located in the cytoplasm, a small number of circRNA-LONP2 were still located in the nucleus. Further experiments are required to explore the function of circRNA-LONP2 in the nucleus. Second, the mechanism of how LSS mediates circRNA-LONP2 reduction remains unclear. Further studies are needed to explore the potential role of ADAR, DHX9, FUS, and QKI in shear stress-mediated circRNA-LONP2 regulation. Third, the ceRNA hypothesis suggests that gene expression is optimally regulated when miRNA and ceRNA are expressed almost equally.^{61,62} However, our study showed that circRNA-LONP2 is approximately twice as abundant as miR-200a-3p in HUVECs. Further studies are needed to explore the effects of other factors on ceRNA activity, such as the subcellular location of circRNA-LONP2 and miR-200a-3p, miR-200a-3p/circRNA-LONP2 affinity, RNA editing, and RNA-binding proteins. Finally, although our *in vitro* and *in vivo* experiments showed that circRNA-LONP2 promotes oxidative stress and endothelial inflammation and accelerates the progression of atherosclerosis, further research is needed to explore the clinical value of circRNA-LONP2.

CONCLUSIONS

The current study found that antiatherosclerotic LSS significantly down-regulated the expression of circRNA-LONP2, and the reduction of circRNA-LONP2 alleviated oxidative stress and endothelial inflammation by enhancing the activity of miR-200a-3p, which targets KEAP1, YAP1, and EZH2 mRNA for degradation and subsequently activates the NRF2/HO-1 pathway. Our findings suggest that

circRNA-LONP2 could serve as a new therapeutic target for atherosclerosis.

FUNDING SUPPORT AND AUTHOR DISCLOSURES

This work was supported by the National Key R&D Program of China (2020YFC2004400); the National Natural Science Foundation of China (81970367, 82270477, 82270437, 81500361, and 81670417); the Natural Science Foundation of Guangdong Province (No. 2023A1515030110); the Shenzhen Key Medical Discipline Construction Fund (SZXK002); and Shenzhen Key Clinical Discipline Funds (ZDXKF-01002). The authors have reported that they have no relationships relevant to the contents of this paper to disclose.

ADDRESS FOR CORRESPONDENCE: Dr Wendong Fan, Department of Cardiology, the First Affiliated Hospital of Sun Yat-sen University, No. 58 Zhongshan 2nd Road, Guangzhou 510080, Guangdong, People's Republic of China. E-mail: fanwd3@mail.sysu.edu.cn. OR Dr Guifu Wu, Department of Cardiology, the Eighth Affiliated Hospital of Sun Yat-sen University, No. 3025 Shennan Zhong Road, Shenzhen 518033, Guangdong, People's Republic of China. E-mail: wuguifu@mail.sysu.edu.cn.

REFERENCES

1. Demos C, Johnson J, Andueza A, et al. Sox13 is a novel flow-sensitive transcription factor that prevents inflammation by repressing chemokine expression in endothelial cells. *Front Cardiovasc Med.* 2022;9:979745.
2. Dardik A, Chen L, Frattini J, et al. Differential effects of orbital and laminar shear stress on endothelial cells. *J Vasc Surg.* 2005;41(5):869–880.
3. Souilhol C, Serbanovic-Canic J, Fragiadaki M, et al. Endothelial responses to shear stress in atherosclerosis: a novel role for developmental genes. *Nat Rev Cardiol.* 2020;17(1):52–63.
4. Cunningham KS, Gotlieb AI. The role of shear stress in the pathogenesis of atherosclerosis. *Lab Invest.* 2005;85(1):9–23.
5. Salzman J, Chen RE, Olsen MN, et al. Cell-type specific features of circular RNA expression. *PLoS Genet.* 2013;9(9):e1003777.
6. Memczak S, Jens M, Elefsinioti A, et al. Circular RNAs are a large class of animal RNAs with regulatory potency. *Nature.* 2013;495(7441):333–338.
7. Starke S, Jost I, Rossbach O, et al. Exon circularization requires canonical splice signals. *Cell Rep.* 2015;10(1):103–111.
8. Kosik KS. Molecular biology: circles reshape the RNA world. *Nature.* 2013;495(7441):322–324.
9. Zhang M, Zhao K, Xu X, et al. A peptide encoded by circular form of LINC-PINT suppresses oncogenic transcriptional elongation in glioblastoma. *Nat Commun.* 2018;9(1):4475.
10. Han D, Li J, Wang H, et al. Circular RNA circMTO1 acts as the sponge of microRNA-9 to suppress hepatocellular carcinoma progression. *Hepatology.* 2017;66(4):1151–1164.
11. Zang J, Lu D, Xu A. The interaction of circRNAs and RNA binding proteins: an important part of circRNA maintenance and function. *J Neurosci Res.* 2020;98(1):87–97.
12. Zhang M, Zhu Y, Zhu J, et al. circ_0086296 induced atherosclerotic lesions via the IFIT1/STAT1 feedback loop by sponging miR-576-3p. *Cell Mol Biol Lett.* 2022;27(1):80.
13. Tong KL, Tan KE, Lim YY, et al. CircRNA-miRNA interactions in atherogenesis. *Mol Cell Biochem.* 2022;477(12):2703–2733.
14. Huang X, Zhao Y, Zhou H, et al. Circular RNAs in atherosclerosis. *Clin Chim Acta.* 2022;531:71–80.
15. Jia X, Bai X, Yang X, et al. VCAM-1-binding peptide targeted cationic liposomes containing NLRP3 siRNA to modulate LDL transcytosis as a novel therapy for experimental atherosclerosis. *Metabolism.* 2022;135:155274.
16. Conn SJ, Pillman KA, Toubia J, et al. The RNA binding protein quaking regulates formation of circRNAs. *Cell.* 2015;160(6):1125–1134.
17. Errichelli L, Dini MS, Laneve P, et al. FUS affects circular RNA expression in murine embryonic stem cell-derived motor neurons. *Nat Commun.* 2017;8:14741.
18. Kristensen LS, Andersen MS, Stagsted L, et al. The biogenesis, biology and characterization of circular RNAs. *Nat Rev Genet.* 2019;20(11):675–691.
19. Chen XL, Dodd G, Thomas S, et al. Activation of Nrf2/ARE pathway protects endothelial cells from oxidant injury and inhibits inflammatory gene expression. *Am J Physiol Heart Circ Physiol.* 2006;290(5):H1862–H1870.
20. Li JH, Liu S, Zhou H, et al. starBase v2.0: decoding miRNA-ceRNA, miRNA-ncRNA and protein-RNA interaction networks from large-scale CLIP-Seq data. *Nucleic Acids Res.* 2014;42(database issue):D92–D97.
21. Lee DY, Yang TL, Huang YH, et al. Induction of microRNA-10a using retinoic acid receptor- α and retinoid X receptor- α agonists inhibits atherosclerotic lesion formation. *Atherosclerosis.* 2018;271:36–44.
22. Kuo JT, Tsai HE, Lin CT, et al. Low levels of MicroRNA-10a in cardiovascular endothelium and blood serum are related to human atherosclerotic disease. *Cardiol Res Pract.* 2021;2021:1452917.
23. Fang Y, Shi C, Manduchi E, et al. MicroRNA-10a regulation of proinflammatory phenotype in atherosusceptible endothelium in vivo and in vitro. *Proc Natl Acad Sci U S A.* 2010;107(30):13450–13455.
24. Han K, Wang FW, Cao CH, et al. CircLONP2 enhances colorectal carcinoma invasion and metastasis through modulating the maturation and exosomal dissemination of microRNA-17. *Mol Cancer.* 2020;19(1):60.
25. Zhu C, Bi W, Li H, et al. CircLONP2 accelerates esophageal squamous cell carcinoma progression via direct MiR-27b-3p-ZEB1 axis. *Front Oncol.* 2022;12:822839.
26. Wei J, Zhang Y, Luo Y, et al. Aldose reductase regulates miR-200a-3p/I41-3p to coordinate Keap1-Nrf2, Tgf β 1/2, and Zeb1/2 signaling in renal mesangial cells and the renal cortex of diabetic mice. *Free Radic Biol Med.* 2014;67:91–102.
27. Varadi K, Michelfelder S, Korff T, et al. Novel random peptide libraries displayed on AAV

PERSPECTIVES

COMPETENCY IN MEDICAL KNOWLEDGE: Hemodynamic shear stress is a frictional force that acts on vascular ECs and is essential for endothelial homeostasis under normal physiological conditions. circRNAs are powerful regulators of vascular homeostasis and atherosclerosis; however, their roles in mediating the effects of LSS remain unexplored. This study provides the first evidence that circRNA-LONP2 modulates the flow-dependent endothelial inflammatory response and accelerates the progression of atherosclerosis, suggesting a clinical significance of circRNA-LONP2 in atherosclerosis.

TRANSLATIONAL OUTLOOK: OSS induces circRNA-LONP2 expression and promotes atherosclerosis; however, LSS inhibits circRNA-LONP2 expression and has anti-atherosclerosis properties. We propose that endothelial-specific knockdown of circRNA-LONP2, or its downstream targets KEAP1, YAP1 or EZH2, might be a promising therapeutic strategy to prevent or treat atherosclerosis.

- serotype 9 for selection of endothelial cell-directed gene transfer vectors. *Gene Ther.* 2012;19(8):800-809.
- 28.** Wang J, Li P, Xu X, et al. MicroRNA-200a inhibits inflammation and atherosclerotic lesion formation by disrupting EZH2-mediated methylation of STAT3. *Front Immunol.* 2020;11:907.
- 29.** Li Z, Xu L, Tang N, et al. The polycomb group protein EZH2 inhibits lung cancer cell growth by repressing the transcription factor Nrf2. *FEBS Lett.* 2014;588(17):3000-3007.
- 30.** Wang KC, Yeh YT, Nguyen P, et al. Flow-dependent YAP/TAZ activities regulate endothelial phenotypes and atherosclerosis. *Proc Natl Acad Sci U S A.* 2016;113(41):11525-11530.
- 31.** Yu SJ, Hu JY, Kuang XY, et al. MicroRNA-200a promotes anoikis resistance and metastasis by targeting YAP1 in human breast cancer. *Clin Cancer Res.* 2013;19(6):1389-1399.
- 32.** Lo SF, Pulito C, Sacconi A, et al. YAP/TAZ and EZH2 synergize to impair tumor suppressor activity of TGFBR2 in non-small cell lung cancer. *Cancer Lett.* 2021;500:51-63.
- 33.** Sun Y, Zhang B, Xia L. Effect of low wall shear stress on the morphology of endothelial cells and its evaluation indicators. *Comput Methods Programs Biomed.* 2021;208:106082.
- 34.** Pu L, Meng Q, Li S, et al. Laminar shear stress alleviates monocyte adhesion and atherosclerosis development via miR-29b-3p/CX3CL1 axis regulation. *J Cell Sci.* 2022;135(14).
- 35.** Meng Q, Pu L, Qi M, et al. Laminar shear stress inhibits inflammation by activating autophagy in human aortic endothelial cells through HMGB1 nuclear translocation. *Commun Biol.* 2022;5(1):425.
- 36.** Liu Z, Zhou Y, Xia J. CircRNAs: key molecules in the prevention and treatment of ischemic stroke. *Biomed Pharmacother.* 2022;156:113845.
- 37.** Wang Z, Wang H, Guo C, et al. Role of hsa_circ_0000280 in regulating vascular smooth muscle cell function and attenuating neointimal hyperplasia via ELAVL1. *Cell Mol Life Sci.* 2022;80(1):3.
- 38.** Tamargo IA, Baek KI, Kim Y, et al. Flow-induced reprogramming of endothelial cells in atherosclerosis. *Nat Rev Cardiol.* 2023;20(11):738-753.
- 39.** Chiu JJ, Chien S. Effects of disturbed flow on vascular endothelium: pathophysiological basis and clinical perspectives. *Physiol Rev.* 2011;91(1):327-387.
- 40.** Nagel T, Resnick N, Dewey CJ, et al. Vascular endothelial cells respond to spatial gradients in fluid shear stress by enhanced activation of transcription factors. *Arterioscler Thromb Vasc Biol.* 1999;19(8):1825-1834.
- 41.** Chen XL, Varner SE, Rao AS, et al. Laminar flow induction of antioxidant response element-mediated genes in endothelial cells. A novel anti-inflammatory mechanism. *J Biol Chem.* 2003;278(2):703-711.
- 42.** Warabi E, Wada Y, Kajiwara H, et al. Effect on endothelial cell gene expression of shear stress, oxygen concentration, and low-density lipoprotein as studied by a novel flow cell culture system. *Free Radic Biol Med.* 2004;37(5):682-694.
- 43.** Hosoya T, Maruyama A, Kang MI, et al. Differential responses of the Nrf2-Keap1 system to laminar and oscillatory shear stresses in endothelial cells. *J Biol Chem.* 2005;280(29):27244-27250.
- 44.** Han J, Shi X, Xu J, et al. DL-3-n-butylphthalide prevents oxidative stress and atherosclerosis by targeting Keap-1 and inhibiting Keap-1/Nrf-2 interaction. *Eur J Pharm Sci.* 2022;172:106164.
- 45.** Kim MJ, Jeon JH. Recent advances in understanding Nrf2 agonism and its potential clinical application to metabolic and inflammatory diseases. *Int J Mol Sci.* 2022;23(5).
- 46.** Soares MP, Seldon MP, Gregoire IP, et al. Heme oxygenase-1 modulates the expression of adhesion molecules associated with endothelial cell activation. *J Immunol.* 2004;172(6):3553-3563.
- 47.** Chen LG, Zhang YQ, Wu ZZ, et al. Peanut arachidin-1 enhances Nrf2-mediated protective mechanisms against TNF- α -induced ICAM-1 expression and NF- κ B activation in endothelial cells. *Int J Mol Med.* 2018;41(1):541-547.
- 48.** Guo H, Ingolia NT, Weissman JS, et al. Mammalian microRNAs predominantly act to decrease target mRNA levels. *Nature.* 2010;466(7308):835-840.
- 49.** Bartel DP. MicroRNAs: target recognition and regulatory functions. *Cell.* 2009;136(2):215-233.
- 50.** Schober A, Nazari-Jahantigh M, Wei Y, et al. MicroRNA-126-5p promotes endothelial proliferation and limits atherosclerosis by suppressing Dlk1. *Nat Med.* 2014;20(4):368-376.
- 51.** Loyer X, Potteaux S, Vion AC, et al. Inhibition of microRNA-92a prevents endothelial dysfunction and atherosclerosis in mice. *Circ Res.* 2014;114(3):434-443.
- 52.** Fan W, Fang R, Wu X, et al. Shear-sensitive microRNA-34a modulates flow-dependent regulation of endothelial inflammation. *J Cell Sci.* 2015;128(1):70-80.
- 53.** Kamble D, Mahajan M, Dhat R, et al. Keap1-Nrf2 pathway regulates ALDH and contributes to radioresistance in breast cancer stem cells. *Cells.* 2021;10(1).
- 54.** Sun X, Zuo H, Liu C, et al. Overexpression of miR-200a protects cardiomyocytes against hypoxia-induced apoptosis by modulating the kelch-like ECH-associated protein 1-nuclear factor erythroid 2-related factor 2 signaling axis. *Int J Mol Med.* 2016;38(4):1303-1311.
- 55.** Liu QL, Zhang J, Liu X, et al. Role of growth hormone in maturation and activation of dendritic cells via miR-200a and the Keap1/Nrf2 pathway. *Cell Prolif.* 2015;48(5):573-581.
- 56.** Wang D, Luo Y, Wang G, et al. CircATRNL1 promotes epithelial-mesenchymal transition in endometriosis by upregulating Yes-associated protein 1 in vitro. *Cell Death Dis.* 2020;11(7):594.
- 57.** Wu DM, Wang S, Wen X, et al. LncRNA SNHG15 acts as a ceRNA to regulate YAP1-Hippo signaling pathway by sponging miR-200a-3p in papillary thyroid carcinoma. *Cell Death Dis.* 2018;9(10):947.
- 58.** Yuan P, Hu Q, He X, et al. Laminar flow inhibits the Hippo/YAP pathway via autophagy and SIRT1-mediated deacetylation against atherosclerosis. *Cell Death Dis.* 2020;11(2):141.
- 59.** Zhang P, Yan X, Zhang X, et al. TMEM215 prevents endothelial cell apoptosis in vessel regression by blunting BIK-regulated ER-to-mitochondrial Ca influx. *Circ Res.* 2023;133(9):739-757.
- 60.** Maleszewska M, Vanchin B, Harmsen MC, et al. The decrease in histone methyltransferase EZH2 in response to fluid shear stress alters endothelial gene expression and promotes quiescence. *Angiogenesis.* 2016;19(1):9-24.
- 61.** Denzler R, Agarwal V, Stefano J, et al. Assessing the ceRNA hypothesis with quantitative measurements of miRNA and target abundance. *Mol Cell.* 2014;54(5):766-776.
- 62.** Bosson AD, Zamudio JR, Sharp PA. Endogenous miRNA and target concentrations determine susceptibility to potential ceRNA competition. *Mol Cell.* 2014;56(3):347-359.

KEY WORDS atherosclerosis, circRNA-LONP2, endothelial inflammation, microRNA-200a-3p, shear stress

APPENDIX For an expanded Methods section and supplemental figures, please see the online version of this paper.

EDITORIAL COMMENT

Stressing the Circle

Circular RNA-LONP2 Role in Atherosclerosis*



Simona Greco, PhD, Fabio Martelli, PhD

Atherosclerosis is a chronic inflammatory disease affecting the vascular wall of large- and medium-sized arteries. This disease leads to myocardial infarction, ischemic stroke, and peripheral arterial disease, representing the leading cause of morbidity and mortality in developed countries.¹ Hypercholesterolemia, hypertension, and diabetes mellitus are among the systemic risk factors predisposing to atherosclerosis. Atheromas preferentially form in arterial regions in which the blood flow is disturbed, whereas arterial regions exposed to stable flow remain healthy.² In particular, early atherosclerotic lesions appear nonrandomly in the artery, with a strikingly localized pattern that follows the geometry of branched or curved points. In light of this finding, it is possible to classify the near-wall shear stress profiles in atheroprone and atheroprotected arterial geometries.²

The blood flow imposes a stress on the endothelium with frictional forces or wall shear stresses. There are several blood flow patterns, ranging from a time-averaged unidirectional laminar flow, usually occurring in unbranched arterial regions, to a disturbed flow, occurring in branched or curved arteries. These flow patterns result in laminar shear stress (LSS) and low-magnitude and oscillatory shear stress (OSS), respectively.

Shear stress stimulates various mechanosensors, such as ion channels, nicotinamide adenine dinucleotide phosphate oxidase and xanthine oxidase, receptor tyrosine kinases, G proteins, and cell/cell

and cell/matrix adhesion complexes. These mechanotransduction mechanisms link the externally applied mechanical stress to intracellular and intranuclear events.³

Different spatial and temporal patterns of shear stresses, despite the common mechanosensors and mechanotransducers, trigger distinguishable gene expression patterns. Indeed, LSS upregulates atheroprotective genes, such as endothelial nitric oxide synthase, the Krüppel-like factor family (*KLF2* and *KLF4*), nuclear factor erythroid 2-related factor 2-like bZIP transcription factor 2 (*NRF2* or *NFE2L2*), and superoxide dismutases (*MN-SOD* and *EC-SOD*), and downregulates proatherogenic genes, such as those related to coagulation, leukocyte diapedesis, and smooth muscle cell proliferation. Conversely, OSS enhances proatherogenic genes, such as vascular cell adhesion protein 1 and intercellular adhesion molecule 1 and suppresses atheroprotective genes. Thus, LSS plays a crucial role in vascular homeostasis, whereas OSS leads to vascular dysfunction and disease.

Although the interconnection between hemodynamics, endothelial pathobiology, and aterogenesis has been extensively investigated, more in-depth research is needed to understand the molecular mechanisms underpinning the responses to different flow patterns. Specifically, among the emerging players, noncoding RNAs (ncRNAs) are particularly promising⁴; ncRNAs are mainly categorized according to their sequence length into small or long ncRNAs.⁵ Small ncRNAs include microRNAs (miRNAs), and long ncRNAs include linear long ncRNAs and circular RNAs (circRNAs). circRNAs identify single-strand covalently closed molecules generated through the back-splicing of linear RNA precursors. Accordingly, circRNAs are resistant to exonucleases, which makes them significantly more stable than their linear counterparts and promising biomarkers. circRNAs can act as miRNA sinks or sponges, thus actively

*Editorials published in *JACC: Basic to Translational Science* reflect the views of the authors and do not necessarily represent the views of *JACC: Basic to Translational Science* or the American College of Cardiology.

From the Molecular Cardiology Laboratory, IRCCS Policlinico San Donato, San Donato Milanese, Milan, Italy.

The authors attest they are in compliance with human studies committees and animal welfare regulations of the authors' institutions and Food and Drug Administration guidelines, including patient consent where appropriate. For more information, visit the [Author Center](#).

competing with miRNA targets.⁶ Several flow-sensitive miRNAs and few long ncRNAs have been found to regulate endothelial function and atherosclerosis,⁴ whereas the role of circRNAs remains unclear.

In this issue of *JACC: Basic to Translational Science*, Wang et al⁷ report that flow-sensitive circRNA-LONP2 modulates the inflammatory response induced by shear stress and the development of atherosclerosis both *in vitro* and *in vivo*. By microarray profiling in human umbilical vein endothelial cells (ECs), they identified several circRNAs modulated by LSS compared to the static condition, among which circRNA-LONP2 was significantly downregulated. Reverse transcription quantitative polymerase chain reaction experiments showed instead that the linear form of LONP2 was not modulated, indicating independent circRNA-LONP2 modulation, a telltale of significant biological function. Importantly, the circRNA exon structure was confirmed by divergent primers and Sanger's sequencing, whereas the exonucleases degradation resistance proved the circular structure, and the *in situ* hybridization results indicated the cytoplasmic localization.

The atheroprotective LSS and the atheropromoting OSS had a different impact on circRNA-LONP2 expression; the former reduced and the latter increased the circRNA expression. Gain- and loss-of-function experiments showed that in human ECs the inhibition of circRNA-LONP2 expression reduced the messenger RNA levels of the proinflammatory *VCAM-1* and *ICAM-1* and increased the messenger RNA levels of the antioxidative stress and anti-inflammatory genes *NRF2* and heme oxygenase 1, whereas circRNA-LONP2 overexpression had opposite effects. The increase of *ICAM-1* and *VCAM-1* messenger RNA levels mediated by OSS was counteracted by circRNA silencing. The effects of the circRNA-LONP2-mediated generation of reactive oxygen species on endothelial inflammation was demonstrated by silencing circRNA-LONP2 expression, which attenuated the tumor necrosis factor alpha-induced expression of *VCAM-1* and *ICAM-1* in ECs, reduced reactive oxygen species levels, and reduced the adhesion of monocytes to the cocultured ECs. These data suggest that circRNA-LONP2 regulates flow-dependent inflammatory responses.

The ability of circRNAs to act as a miRNA sink or sponge, thus actively competing with miRNA targets, has been demonstrated in several cardiovascular systems.^{5,6} An MS2-RNA tagging strategy was used to pull down miRNAs interacting with circRNA-LONP2; among them, miR-200a-3p was particularly promising and was further characterized. First, the

phenotype induced by miR-200a-3p that mimics transfection in ECs was similar to that induced by circRNA-LONP2 silencing. Moreover, miR-200a-3p inhibition prevented the anti-inflammatory effects of circRNA-LONP2 silencing. miR-200a-3p levels did not change in circRNA-LONP2 gain- and loss-of-function or under LSS, indicating that circRNA-LONP2 inflammatory action is mediated by miR-200a-3p interaction without affecting the expression of the miRNA. This is an interesting mechanistic detail because miRNA/circRNA interaction has often been reported to lead to the decrease of miRNA levels.^{5,6}

Under normal conditions, NRF2 is retained in the cytoplasm by kelch-like Ech-associated protein 1 (KEAP1), which triggers NRF2 proteasomal degradation. Upon ECs exposure to LSS, NRF2 dissociates from KEAP1 and translocates into the nucleus, inducing the expression of antioxidant genes and inhibiting nuclear factor kappa-light-chain-enhancer of activated B cells signaling pathway through multiple mechanisms.

KEAP1 messenger RNA was experimentally demonstrated as a circRNA-LONP2 target; accordingly, miR-200a-3p mimics significantly downregulated KEAP1 and upregulated NRF2, indicating that circRNA-LONP2 induced endothelial inflammation through a miR-200a-3p/KEAP1/NRF2 pathway in humans.

The apolipoprotein E-deficient (*ApoE*^{-/-}) mouse model displays impaired lipoprotein clearance causing the increase of cholesterol ester-enriched particles in the blood, which, in turn, facilitates the development of atherosclerotic plaques. In the experimental model adopted by Wang et al,⁷ *ApoE*^{-/-} mice, 6 weeks after the partial ligation of the left common carotid artery, developed a plaque-laden area. The overexpression of circRNA-Lonp2 by an endothelial-retargeted adeno-associated virus vector 9 under the control of the endothelial-specific Tie2 promoter expanded the plaque area, the neointima size, and the lipid deposition. Moreover, the circRNA-forced expression increased the proinflammatory markers Vcam-1 and Icam-1 and the mononuclear phagocytes marker Mac-3, whereas it reduced Nrf2 and Ho-1 without affecting the expression of Keap1. Interestingly, circRNA-Lonp2 regulated Nrf2 expression in mice via an alternative pathway (present in mice and humans). The mechanotransducer and transcription factor yes-associated protein 1 (Yap1) regulates the transcription of enhancer of zeste homolog 2 (Ezh2), a histone-H3 Lys27 (H3K27) trimethyl transferase that represses the transcription of Nrf2.⁸ Gain- and loss-of-function and rescue

experiments in mouse aortic ECs showed that circRNA-Lonp2 regulated oxidative stress and endothelial inflammation via a miR-200a-3p/Yap1/Ezh2 axis. The mechanistic redundancy of NRF2 regulation by circRNA-LONP2 is indicative of the importance of the identified pathway upon shear stress.

The study limitations are well considered by the authors, including the need for further investigations to evaluate the potential role of RNA-binding proteins in flow-mediated circRNA-LONP2 expression. Moreover, the clinical significance of circRNA-LONP2 dysregulation needs to be investigated in humans. However, this study constitutes a significant advancement in the field, being the first to identify an arterial flow-sensitive circRNA with a role in vascular remodeling, suggesting circRNA-LONP2 as a potential antiatherosclerotic therapeutic target. This is particularly relevant in the prospect of the rapidly

evolving field of RNA therapy, exploring approaches to target the circRNA back-splicing junction with techniques such as RNA interference and antisense oligonucleotides.⁹

FUNDING SUPPORT AND AUTHOR DISCLOSURES

Dr Martelli is supported by the Italian Ministry of Health, Ricerca Corrente 2024 1.07.128, RF-2019-12368521, and POS-T4 CAL.HUB.RIA T4-AN-09 and by the Next Generation EU-NRRP M6C2 Inv. 2.1 PNRR-MAD-2022-12375790 and EU PNRR/2022/C9/MCID/18, European Commission. Drs Martelli and Greco have reported that they have no relationships relevant to the contents of this paper to disclose.

ADDRESS FOR CORRESPONDENCE: Dr Fabio Martelli, IRCCS Policlinico San Donato, Via Morandi 30, 20097 San Donato Milanese, Milan, Italy. E-mail: fabio.martelli@grupposandonato.it.

REFERENCES

1. World Health Organization. Cardiovascular diseases (CVDs). Fact sheet. 2021. Accessed April 17, 2024. [https://www.who.int/news-room/fact-sheets/detail/cardiovascular-diseases-\(cvds\)](https://www.who.int/news-room/fact-sheets/detail/cardiovascular-diseases-(cvds))
2. Gimbrone MA, García-Cardeña G. Vascular endothelium, hemodynamics, and the pathobiology of atherosclerosis. *Cardiovasc Pathol*. 2013;22:9-15.
3. Baeyens N, Bandyopadhyay C, Coon BG, Yun S, Schwartz MA. Endothelial fluid shear stress sensing in vascular health and disease. *J Clin Invest*. 2016;126:821-828.
4. Kumar S, Williams D, Sur S, Wang J-Y, Jo H. Role of flow-sensitive microRNAs and long noncoding RNAs in vascular dysfunction and atherosclerosis. *Vasc Pharmacol*. 2019;114:76-92.
5. Robinson EL, Baker AH, Brittan M, et al. Dissecting the transcriptome in cardiovascular disease. *Cardiovasc Res*. 2022;118:1004-1019.
6. Madè A, Bibi A, Garcia-Manteiga JM, et al. circRNA-miRNA-mRNA deregulated network in ischemic heart failure patients. *Cells*. 2023;12:2578-2602.
7. Wang R, Zeng Y, Chen Z, et al. Shear-sensitive circRNA-LONP2 promotes endothelial inflammation and atherosclerosis by targeting NRF2/HO1 signaling. *J Am Coll Cardiol Basic Trans Science*. 2024;9(5):652-670.
8. Li Z, Xu L, Tang N, et al. The polycomb group protein EZH2 inhibits lung cancer cell growth by repressing the transcription factor Nrf2. *FEBS Lett*. 2014;588:3000-3007.
9. Caporali A, Anwar M, Devaux Y, et al. Non-coding RNAs as therapeutic targets and biomarkers in ischemic heart disease. *Nat Rev Cardiol*. Published online March 18, 2024. <https://doi.org/10.1038/s41569-024-01001-5>

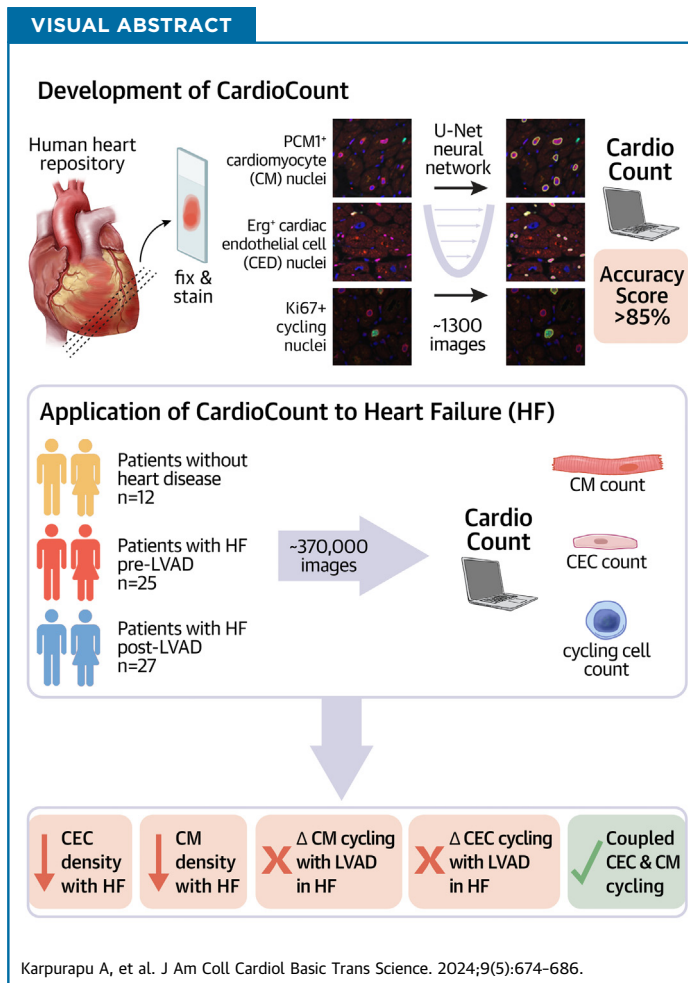
KEY WORDS atherosclerosis, circRNA-LONP2, endothelial inflammation, microRNA-200a-3p, shear stress

NOVEL TRANSLATIONAL METHODS

Deep Learning Resolves Myovascular Dynamics in the Failing Human Heart



Anish Karpurapu, BS,^a Helen A. Williams, BS,^a Paige DeBenedittis, PhD,^a Caroline E. Baker, BS,^a Simiao Ren, PhD,^b Michael C. Thomas, BS,^a Anneka J. Beard, MS,^a Garth W. Devlin, BS,^c Josephine Harrington, MD,^a Lauren E. Parker, BS,^a Abigail K. Smith,^a Boyla Mainsah, PhD,^b Michelle Mendiola Pla, MD,^c Aravind Asokan, PhD,^c Dawn E. Bowles, PhD,^c Edwin Iversen, PhD,^d Leslie Collins, PhD,^b Ravi Karra, MD, MHS^{a,e,f}



From the ^aDivision of Cardiology, Department of Medicine, Duke University Medical Center, Durham, North Carolina, USA; ^bDepartment of Electrical and Computer Engineering, Duke University, Durham, North Carolina, USA; ^cDivision of Surgical Sciences, Department of Surgery, Duke University Medical Center, Durham, North Carolina, USA; ^dDepartment of Statistical Science, Duke University, Durham, North Carolina, USA; ^eDepartment of Pathology, Duke University Medical Center, Durham, North Carolina, USA; and the ^fDuke Regeneration Center, Durham, North Carolina, USA.

SUMMARY

The adult mammalian heart harbors minute levels of cycling cardiomyocytes (CMs). Large numbers of images are needed to accurately quantify cycling events using microscopy-based methods. CardioCount is a new deep learning-based pipeline to rigorously score nuclei in microscopic images. When applied to a repository of 368,434 human microscopic images, we found evidence of coupled growth between CMs and cardiac endothelial cells in the adult human heart. Additionally, we found that vascular rarefaction and CM hypertrophy are interrelated in end-stage heart failure. CardioCount is available for use via GitHub and via Google Colab for users with minimal machine learning experience. (J Am Coll Cardiol Basic Trans Science 2024;9:674–686) © 2024 The Authors. Published by Elsevier on behalf of the American College of Cardiology Foundation. This is an open access article under the CC BY-NC-ND license (<http://creativecommons.org/licenses/by-nc-nd/4.0/>).

ABBREVIATIONS AND ACRONYMS

CEC	= cardiac endothelial cell
CM	= cardiomyocyte
CNN	= convolutional neural network
FN	= false negative
FP	= false positive
HF	= heart failure
LVAD	= left ventricular assist device
PBST	= phosphate-buffered saline and Tween
TP	= true positive

Although the innate regenerative capacity of the mammalian heart is limited, multiple groups have identified a low, but present, level of cardiomyocyte (CM) turnover in the adult human heart.^{1–4} While such a low level of cycling has largely been considered insignificant, recent genetic ablation experiments in adult mice suggest that rare cycling CMs promote functional recovery after injury.⁵ However, the impact of CM cycling on human cardiovascular outcomes is unknown.

Elegant transgenic, fate-mapping methods have been developed to trace and quantify CM proliferation in adult mice and zebrafish.^{5–8} However, such methods are not feasible for assaying CM cycling in the human heart. Traditional methods to quantify cycling cells from human tissue sections require manual curation of microscopic images. However, for low-frequency events, such as CM cycling, manual methods are often insufficient. Because of the sheer labor required to score thousands of images, manually curated assessments often lack the sensitivity to identify subtle phenotypes and could be subject to biases if readers are not sufficiently blinded. Not surprisingly, there can be wide variance in the frequency estimates of rare events such as CM cycling from lab to lab.⁹ A potential solution is to apply automated image segmentation routines to score microscopy images more quickly, reproducibly, and objectively. Once computationally prohibitive, better computing power has reinvigorated computer vision by enabling deep learning methods. Deep learning has

subsequently been widely applied to various applications in biology, including image segmentation.¹⁰ However, these image analysis tools, although highly accurate, can be sensitive to imaging conditions and often require significant computational resources.

To address these issues, we developed CardioCount, a deep learning routine to score CM cycling in the human heart. CardioCount is a U-Net-based deep learning model with a ResNet50 backbone that was previously utilized to identify solar panels from drone imagery.¹¹ CardioCount identifies nuclei from antibody-labeled fluorescent images and can colocalize nuclear objects from multiple image channels. Inspired by the DeepLearning4Mic project, the software can run on Google Colab's cloud resources and score thousands of images with few local computational tools.¹² We show that CardioCount is highly versatile and can be adapted to different image acquisition setups and to different species via transfer learning. To demonstrate the functionality of our deep learning model, we used CardioCount to assay 10,305 mm² of human cardiac tissue obtained from patients with and without end-stage heart failure (HF), including some who received left ventricular assist devices (LVADs). Using this tool, we confirm that loss of capillary density marks end-stage HF, but vascular rarefaction results from the proportional changes of cardiac endothelial cells (CECs) and CMs. Additionally, we demonstrate that as in zebrafish and mice, CM cycling is coupled with CEC cycling in the human heart.

The authors attest they are in compliance with human studies committees and animal welfare regulations of the authors' institutions and Food and Drug Administration guidelines, including patient consent where appropriate. For more information, visit the [Author Center](#).

METHODS

HUMAN CARDIAC SAMPLES. Human tissue samples were obtained from the Duke Human Heart Repository.¹³ Heart tissue was collected from unused donor hearts without HF (control hearts), from patients with end-stage HF who underwent LVAD implantation (pre-LVAD), and from LVAD recipients who underwent LVAD explantation (post-LVAD).

HISTOLOGY AND IMMUNOSTAINING. Cryosections of fresh, frozen, human cardiac tissue were fixed with 4% paraformaldehyde, washed and permeabilized with 0.1% Tween (phosphate-buffered saline and Tween [PBST]), and subjected to heat-induced antigen retrieval with citrate buffer. After additional washing with PBST, the samples were blocked with 5% bovine serum albumin for an hour and incubated overnight with primary antibodies. Samples were then washed with PBST and incubated with secondary antibodies and DAPI (1:5,000) for 1 hour. Cryosections from neonatal mouse hearts were processed as previously described.¹⁴ Primary antibodies used for this work included: anti-PCM1 (Sigma-Aldrich, HPA023370, 1:100); anti-Erg (Abcam, ab92513, 1:25); anti-CD31 (BD Bioscience, 553370, 1:100), anti-Ki67 (Thermo Fisher Scientific, 4-5698-82, 1:100), anti-Tnnt (Developmental Studies Hybridoma Bank, CT3, 1:25), and anti-Cre (Cell Signaling Technologies, 15036, 1:50). Secondary antibodies were conjugated to Alexa-488 (Invitrogen, A21208, 1:1000), Alexa-594 (Invitrogen, A11037, 1:200), Alexa-633 (Invitrogen, A21052, 1:200), or Alexa-647 (Invitrogen, A21472, 1:200). To ensure quality control within each staining batch, a human colon tissue sample was included as a positive control for anti-Ki67 immunostaining.

MICROSCOPY. Stained human tissue samples were imaged with a Zeiss CSU-X1 spinning disk confocal microscope or a Zeiss LSM 510 confocal microscope. Stained murine sections were imaged with a Zeiss CSU-X1 spinning disk confocal microscope, a Zeiss AxioImager M1 epifluorescent microscope, or a Zeiss LSM 510 confocal microscope.

DEVELOPMENT OF CardioCount. Images ($N = 1,333$) stratified across all patients were manually curated for ground truth by generating ground truth masks with Fiji/ImageJ (330 images for the Erg model, 330 images for the PCM1 model, and 667 images for the Ki67 model).¹⁵ Ten percent of the annotated data set was set aside for testing, 70% was used for training, and the last 20% was held for validation and hyperparameter selection. Raw RGB images (red: Erg or PCM1 for cell identity of CECs or CMs respectively, green: Ki67 for cell cycling, blue: DAPI for nuclei)

were converted to 2 channel images (either RB to train the Erg and PCM1 models, or GB to train the Ki67 model). Two channel images and their corresponding ground truth masks were used to train a U-Net-based convolutional neural network (CNN), as described previously.^{11,16}

After training CNNs for each marker, the entire data set of 368,434 images was passed through each model. The probability map outputs from the CNN for these images were converted to object maps through a postprocessing pipeline by binarizing the images, grouping positive pixels into objects, and assigning a confidence score to each object. An object confidence threshold score was used to classify each object as a true positive (TP), false positive (FP), or false negative (FN) based on an intersection over union of 0.2 calculated as $TP/(TP+FP+FN)$. Precision ($TP/[TP+FP]$), and recall [$TP/(TP+FN)$] were used to determine the F1 score ($2TP/[2TP+FP+FN]$), which was used to measure model accuracy and was calculated for each set of hyperparameters on the validation set. Hyperparameters that were tuned included: architecture type, learning rate, class weight ratio, loss weights, and the ratio between loss weights. Final models were selected by the highest F1 score on the validation set. To colocalize nuclear objects and identify double-positive cells, nuclei of Ki67⁺ cells were filtered by the presence of a centroid of an Erg or PCM1 nucleus within the borders of the Ki67⁺ nucleus. All code scripts are available on GitHub.

MURINE CARDIAC SAMPLES. Cardiac tissue from neonatal mice was collected and processed as previously described.¹⁴ For AAV experiments, neonatal ICR mice were intraperitoneally injected with 10^{11} vg of AAV.cc47 encoding Cre recombinase carrying pAAV.cTNT.iCre.^{17,18} Neonatal hearts were collected 9 days after injection. pAAV.cTNT.iCre was a gift from William Pu (Addgene plasmid # 69916).

ADAPTATION OF CardioCount TO MURINE CARDIAC IMAGES. CNNs for murine cardiac images were initially trained using optimized hyperparameters and model weights from the corresponding human data set. A total of 50 murine images were annotated and used as input. Five images were held out for the test set, while the training and validation sets were split in a 7:2 ratio. For transfer learning, a learning rate sweep was performed for the encoder (1E-2, 5E-3, 2.5E-3, 1E-3, 5E-4, 2.5E-4, 1E-4, and 5E-5). The learning rate for the decoder was set as 10 times that of the encoder. Following the learning rate sweep, a class weight ratio sweep was performed with various background-to-foreground ratios (1:500, 1:250, 1:100, 1:50, 1:25, 1:10, 1:5, 1:2, 1:1, and 2:1). Postprocessing

was done as described for the human nuclear segmentation pipeline. The optimal model on the validation set was then run on the testing set for the F1 statistics.

DEVELOPMENT OF AREA SEGMENTATION PIPELINE. To compute tissue area for nuclear density calculations, we developed an area calculation algorithm that calculates percent tissue coverage, defined as the number of pixels covered by tissue divided by the total number of pixels in the image. Segmentation and calculation of percent tissue coverage in images were calculated using an algorithm developed using the scikit-image, NumPy, and OpenCV libraries in Python.¹⁹⁻²¹ First, images were normalized by multiplying pixels by 255 and dividing by the 95th percentile of the pixel in the thresholded image, unless the image was considered a background image (more than 97% of pixels are near black). A series of dilation, area closing, binary erosion, area opening, binary dilation, binary erosion, area opening, and area closing was used in sequence to obtain the segmented image. Human verification of a set of random samples was conducted to ensure the areas calculated were appropriate.¹⁹⁻²¹

STATISTICAL ANALYSIS. Continuous data are presented as mean \pm SD or median with 25th and 75th percentiles (Q1-Q3). Statistical analyses between unpaired data were conducted using Welch's *t*-test for normally distributed data or a Wilcoxon rank sum test otherwise. Shapiro-Wilk's test was used to evaluate data distribution. Categorical data are presented as count (%) and were analyzed using the Fisher exact test. Paired data were analyzed by fitting generalized additive models with random effects. Pearson's correlation coefficient (*r*) was used to evaluate the association between continuous variables using linear regression. If data were not log scalable due to zero-valued datapoints, a small positive constant was added to each datapoint to ensure normally distributed axes after log transformation. Statistical analyses and plot generation were performed in R software (R Project for Statistical Computing) using the dplyr, ggpurr, ggplot2, and mgcv packages.²²⁻²⁵ An a priori *P* value <0.05 was used to determine statistical significance.

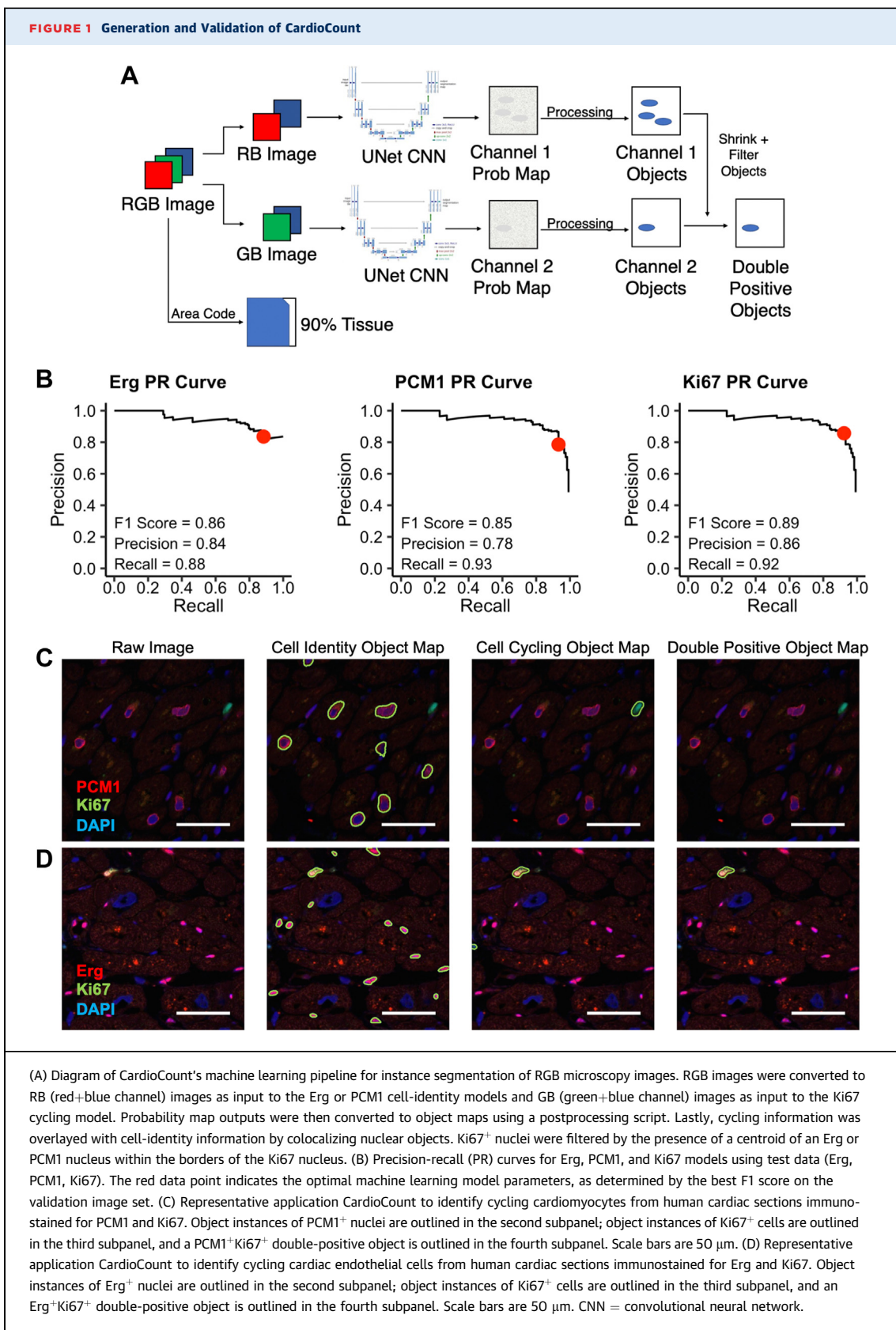
STUDY APPROVAL. All human subjects research was approved by the Duke University Medical Center Institutional Review Board (Prooooo05621). Informed consent was obtained for all subjects. All animal studies were approved by the Duke University Institutional Animal Care and Use Committee.

RESULTS

A DEEP LEARNING MODEL TO SCORE CYCLING CELLS IN THE HUMAN HEART.

Based on the low rates of CM cycling previously reported, we reasoned that large amounts of cardiac tissue would need to be assayed to determine whether intrinsic rates of CM cycling vary between individuals. We leveraged the Duke Human Heart Repository, a bank of cardiac tissue specimens that contains tissues from individuals with various etiologies of HF as well as nonfailing cardiac tissue samples.¹³ Baseline characteristics for the population evaluated are provided in *Supplemental Table 1*. We assayed a total of 12 non-failing control hearts and 32 hearts from patients undergoing LVAD implantation for end-stage HF (*Supplemental Table 1, Supplemental Figure 1*). Patients with HF were age matched to patients without HF, with an average age of 54.1 ± 9.7 years for the 32 HF patients and 53.6 ± 8.7 years for the patients without HF. In general, patients with HF had a lower left ventricular ejection fraction (17.5% [10.0%-20.0%] vs 55.0% [55.0%-62.5%]; *P* < 0.001, Wilcoxon rank sum test), had larger left ventricular diameters as measured by left ventricular internal end-diastolic diameter (6.60 [5.90-6.85] cm vs 4.50 [4.48-4.58] cm; *P* < 0.001, Wilcoxon rank sum test), and were more likely to have type II diabetes mellitus (56.3% vs 8.3%; *P* = 0.006, Fisher exact test). On average, patients with LVADs were diagnosed with HF 4.9 ± 5.8 years before LVAD implantation.

From each individual, we immunostained cryosections with PCM1 to mark CM nuclei, Erg to mark CEC nuclei, and Ki67 to mark cycling nuclei.^{2,26,27} In total, we imaged $83.1 \pm 36.9 \text{ mm}^2$ of cardiac tissue per individual, for a total of $10,305 \text{ mm}^2$ across 368,434 images. To score such a large number of images, we developed a customized U-Net-based deep learning algorithm based on prior work used to identify solar panels from satellite images (*Figure 1*).¹¹ Broadly, we established an approach to identify specific types of nuclei by colocalization of a cycling marker with a cell-type specific nuclear marker. We adapted this framework to develop specific models for resolving $\text{PCM}1^+$ CM nuclei, Erg^+ CEC nuclei, and $\text{Ki}67^+$ cycling nuclei. As ground truth for model training and validation, we manually curated a library of 1,333 images (330 images for Erg, 330 images for PCM1, and 667 images for Ki67). Seventy percent of each data set was used for model training, with 20% set aside for validation and hyperparameter testing and 10% held out for final model F1 score statistics. Training data were



passed through a U-Net CNN to determine model weights and to generate probability maps of nuclei locations. Raw probability maps were then converted into nuclei objects. Models were optimized based on precision-recall curves and tuned by sweeping across hyperparameters for learning rate, loss weights, loss-weight ratio, and class-weight ratio ([Supplemental Figure 2A](#)). Final models for identifying CM, CEC, and cycling nuclei achieved F1 scores of 0.85, 0.86, and 0.89, respectively ([Figure 1](#), [Supplemental Figure 2B](#)).

MYOVASCULAR RATIO IS LARGELY MAINTAINED DURING DISEASE. HF is a progressive disease, marked by CM hypertrophy and loss of CMs. Numerous studies have cited vascular rarefaction, or the loss of capillary density, as a marker of more advanced disease.^{28–30} However, whether this decrease in capillary density is associated with CEC loss or CM hypertrophy has yet to be resolved. To address this outstanding question, we used CardioCount to compare CEC and CM densities from pre-LVAD implantation HF samples to control samples. CEC and CM densities were computed by dividing nuclei counts by tissue areas calculated by a custom area segmentation pipeline. As expected, based on the CM hypertrophy known to occur in HF ([Figures 2A and 2B](#)), the density of CM nuclei was decreased by ~33% in samples from patients with HF (135.1 [102.0–155.5] CM nuclei/mm² vs 201.5 [181.6–229.3] CM nuclei/mm²; $P < 0.001$, Wilcoxon rank sum test) ([Figure 2C](#)). When we evaluated CECs, we noted a similar decrease in nuclear density, with a ~54.8% decrease in patients with HF compared with control patients (306.1 ± 60.9 CECs/mm² vs 138.2 ± 61.2 CECs/mm²; $P < 0.001$, 2-sided unpaired *t*-test) ([Figure 2D](#)). Based on the overall similarity in this decline, we compared the ratio of CEC:CM nuclei across patients. Patients without HF had largely the same ratio as those with HF (1.45 ± 0.46 CECs/CM vs 1.16 ± 0.53 CECs/CM; $P = 0.123$, 2-sided *t*-test) ([Figure 2E](#)), indicating that vascular rarefaction is either secondary to CM hypertrophy or due to a proportional loss of CECs and CMs. However, we noted a wider spread in the CEC:CM ratio among patients with HF compared with control patients, suggesting heterogeneity in the CEC:CM ratio within HF patients. When we evaluated which clinical factors might be related to CEC:CM ratio, only N-terminal pro-B-type natriuretic peptide (NT-proBNP) levels—a marker clinically used to mark ventricular stress and identify HF patients at high risk^{31,32}—were significantly correlated, with a decrease of 0.562

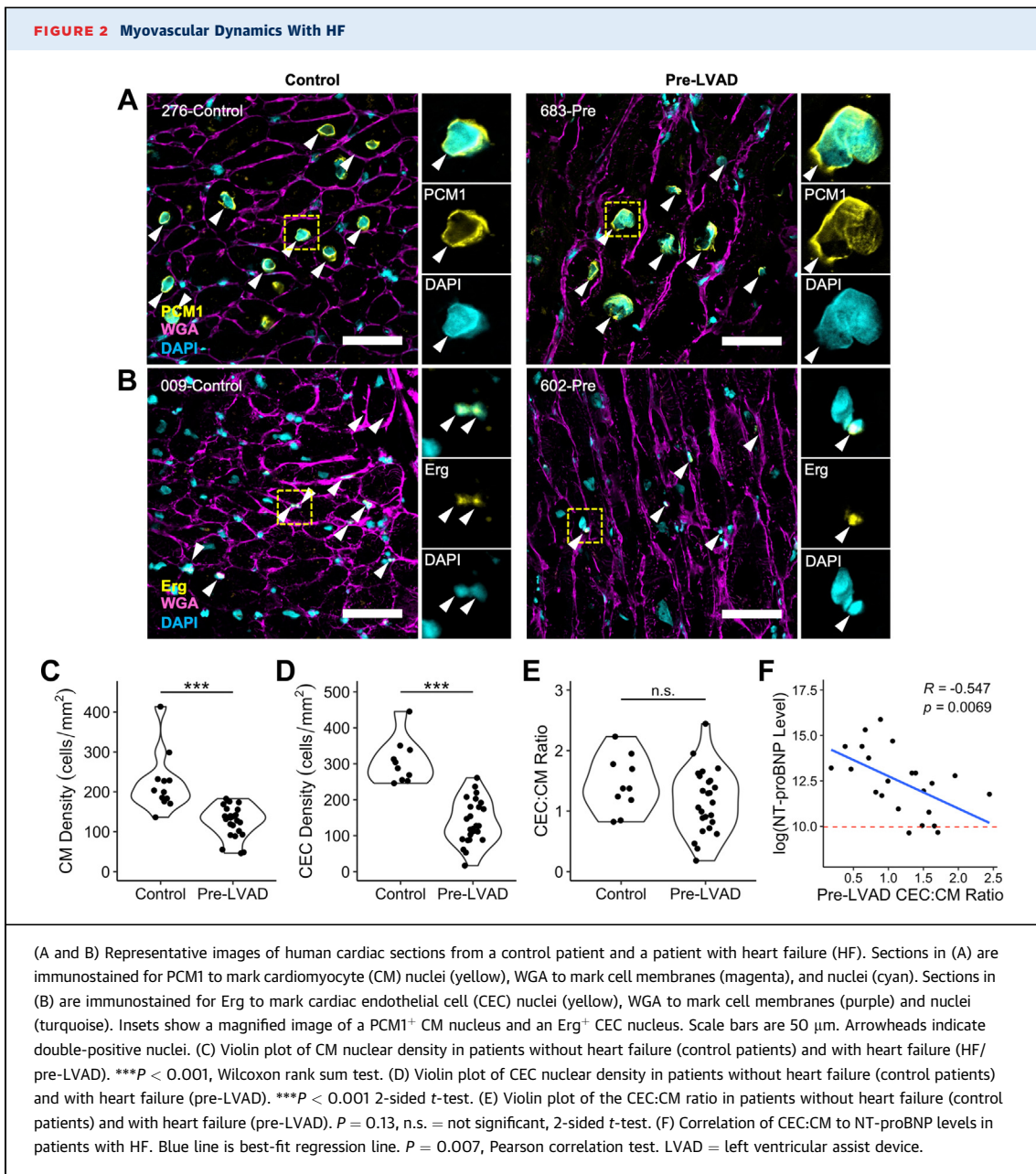
CECs per CM per doubling of NT-proBNP ($r = -0.547$; $P = 0.007$) ([Figure 2F](#)).

MYOVASCULAR DYNAMICS ON LVAD SUPPORT.

LVADs are surgically implanted pumps that improve survival in patients with advanced HF. Blood is drawn into the LVAD from the left ventricle through an inflow cannula and propelled into the aorta, effectively decompressing the left ventricle. In select patients, LVADs have been associated with reverse remodeling and recovery of ventricular function.³³ Histologically, LVAD support leads to regression of CM hypertrophy and increased capillary density.³⁴ Because our samples from the LVAD cohort were collected at the time of LVAD insertion, we had a unique opportunity to use CardioCount to evaluate myovascular dynamics after LVAD support in individuals by also assaying LVAD explantation samples from the same individual. We obtained 20 matched pre-LVAD and post-LVAD cardiac tissue samples from the same patient along with an additional 5 unmatched pre-LVAD tissue samples and 7 unmatched post-LVAD tissue samples. On average, sex, age, race, and heart size measured by left ventricular internal end-diastolic diameter were consistent. However, post-LVAD patients compared with pre-LVAD patients had lower NT-proBNP levels (3,550 ± 4,040 pg/mL vs 11,300 ± 14,600 pg/mL) ([Supplemental Table 2](#)).

Consistent with prior work, we found that LVAD support resulted in an increase in the density of CM nuclei (126.6 ± 39.3 CMs/mm² vs 177.7 ± 50.9 CMs/mm²; $P < 0.001$, 2-sided paired *t*-test) and the density of CEC nuclei (138.2 ± 61.2 CECs/mm² vs 222.1 ± 116.8 CECs/mm²; $P = 0.002$, 2-sided paired *t*-test) ([Figures 3A to 3D](#)).³⁴ We did not observe any changes in CEC:CM ratio with LVAD support (1.16 ± 0.53 CECs/CM vs 1.27 ± 0.59 CECs/CM) ([Figure 3E](#)).

Although CMs in the postnatal mammalian heart have largely exited the cell cycle, recent work has measured a low, but present, rate of CM turnover in the adult human heart,¹ including a recent report that the rate of CM cycling increases with LVAD support.⁴ Thus, we sought to characterize cellular cycling in our cohort by colocalizing Ki67⁺ nuclei with CECs and CM nuclei. Overall, we found evidence for rare cycling CMs and CECs either before or after LVAD support ([Figures 4A to 4D](#)). However, we noted considerable heterogeneity among patients with regards to CM and CEC cycling. We have recently described that coupled expansion of CMs and CECs is required for cardiac growth and regeneration in neonatal mice.¹⁴ To determine whether CEC and CM cycling might be

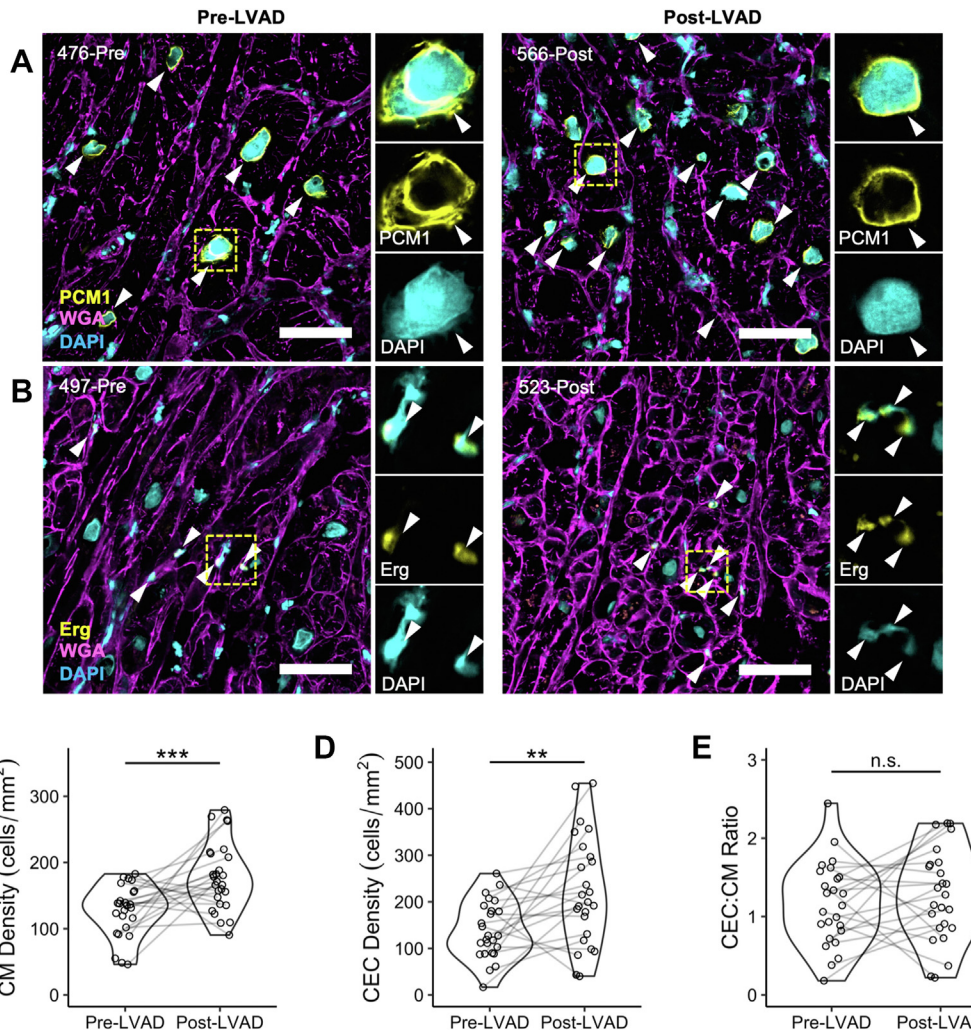


coupled in the adult human heart, we regressed CEC and CM cycling rates for each patient. We found a modest correlation between CM cycling rate and CEC cycling rate ($r = 0.59$; $P = 0.002$) (Figure 4E), with a doubling in CEC cycling rate corresponding to a 1.47-fold increase in CM cycling rate, suggesting that coupled expansion of CECs and CMs also occurs in diseased human hearts.

TRANSFER LEARNING ALLOWS CardioCount TO BE GENERALIZED TO OTHER DATA SETS. Because our models for CMs, CECs, and cycling cells have the same underlying architecture and perform similarly

despite different staining morphologies, we reasoned that our models could be repurposed for additional applications using transfer learning. We first assayed the ability to score neonatal mouse hearts, which have smaller nuclear morphology and higher cell density than human myocardial tissue. Starting with the machine learning models trained on the human data set, we tuned the model hyperparameters with limited training/validation sets of neonatal mouse heart images (Figures 5A to 5C, Supplemental Figure 3). Combined training and validation set sizes of 0, 10, 15, 30, and 45 were used to train the model,

FIGURE 3 Myovascular Changes After LVAD Support

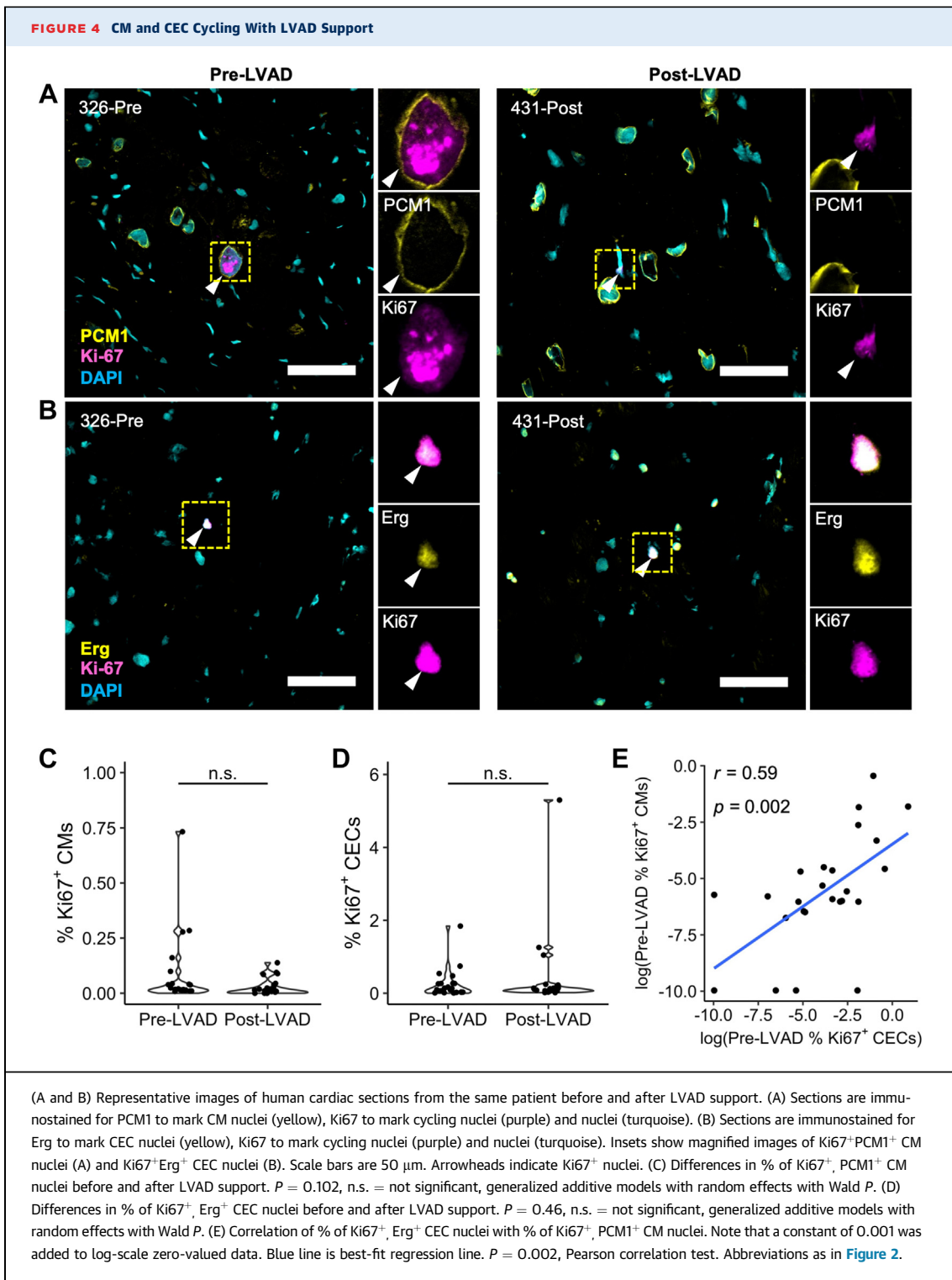


(A and B) Representative images of human cardiac sections from a control patient and a patient with heart failure. (A) Sections are immunostained for PCM1 to mark CM nuclei (yellow), WGA to mark cell membranes (purple) and nuclei (turquoise). (B) Sections are immunostained for Erg to mark CEC nuclei (yellow), WGA to mark cell membranes (purple) and nuclei (turquoise). Insets show a magnified image of a $\text{PCM}1^+$ CM nucleus and Erg^+ CEC nuclei. Scale bars are 50 μm . Arrowheads indicate $\text{PCM}1^+$ and Erg^+ nuclei. (C) Violin plot of CM nuclear density in patients pre-LVAD and post-LVAD. *** $P < 0.001$, generalized additive models with random effects with Wald P . (D) Violin plot of CEC nuclear density in patients pre-LVAD and post-LVAD. ** $P = 0.002$, generalized additive models with random effects with Wald P . (E) Violin plot of CEC:CM ratio in patients pre-LVAD and post-LVAD. $P = 0.44$, n.s.= not significant, generalized additive models with random effects with Wald P . For C to F, lines connect paired samples from the same patient. Abbreviations as in Figure 2.

whereas a testing set of 5 images was used to evaluate the transfer learning trained model. As expected, the model without transfer learning performed consistently worse than the other models; however, we did see a plateau in F1 score improvement after a transfer learning data set size of 15 images (Figure 5B). The neonatal mouse Erg data set consisted of images with $2,752 \times 2,208$ pixel dimensions instead of the standard

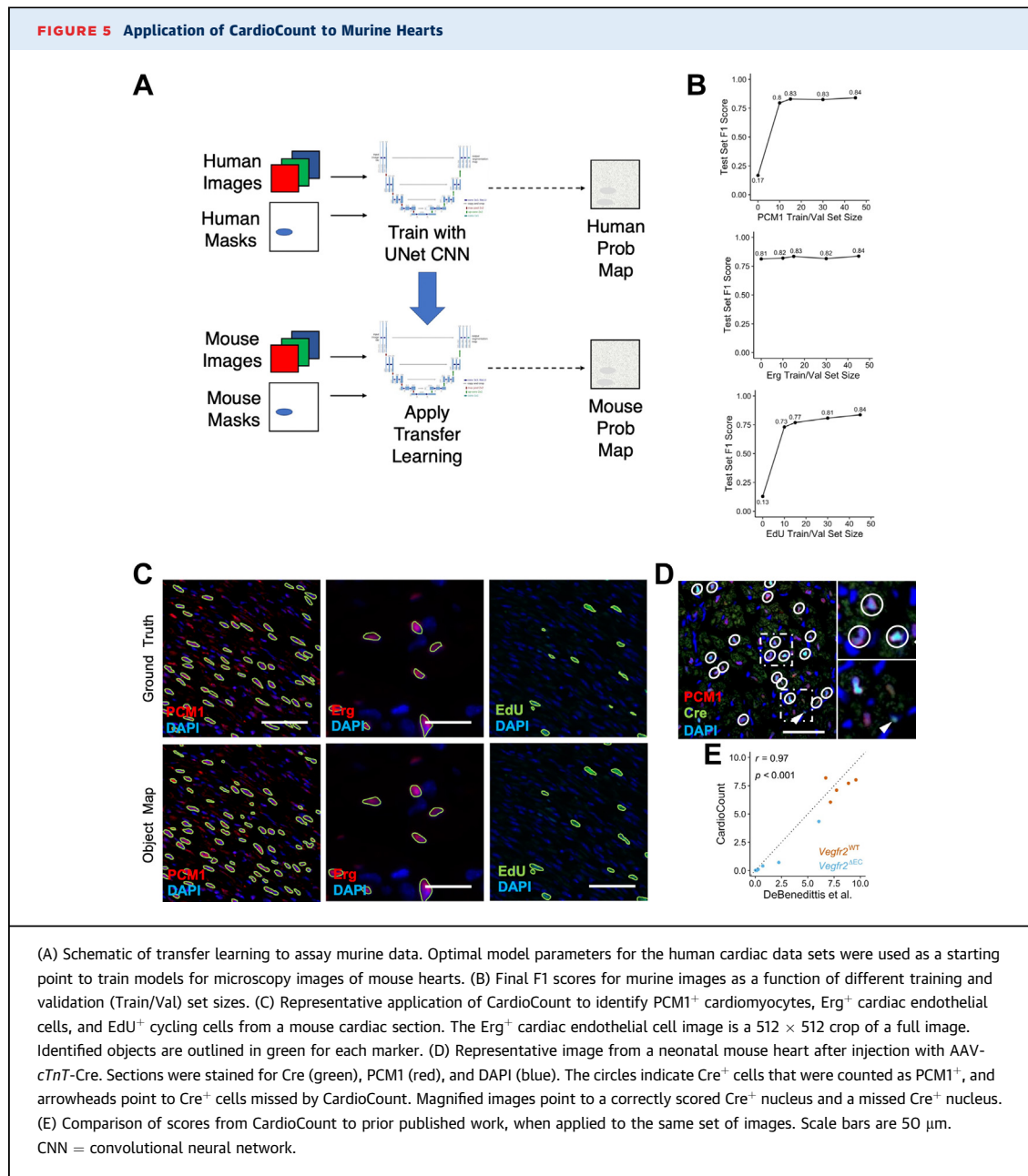
512×512 dimensions of the images used to train the human data set, suggesting that our modeling approach can be transferred to diverse imaging conditions.

We next sought to benchmark our data against other data sets. We first tested the sensitivity of CardioCount for detecting CM nuclei based on PCM1 immunostaining. Neonatal mice were injected with



AAV encoding Cre recombinase under the control of a CM-specific chicken troponin T promoter, followed by immunostaining of sections for Cre and PCM1 (Figure 5D).¹⁸ CardioCount was used to identify CM

nuclei using the PCM1 and DAPI channels, and manually corroborated with Cre signals. Of 7,834 CM nuclei that were labeled with Cre, 7,685 nuclei were correctly scored as CM nuclei, giving a



(A) Schematic of transfer learning to assay murine data. Optimal model parameters for the human cardiac data sets were used as a starting point to train models for microscopy images of mouse hearts. (B) Final F1 scores for murine images as a function of different training and validation (Train/Val) set sizes. (C) Representative application of CardioCount to identify PCM1⁺ cardiomyocytes, Erg⁺ cardiac endothelial cells, and EdU⁺ cycling cells from a mouse cardiac section. The Erg⁺ cardiac endothelial cell image is a 512 × 512 crop of a full image. Identified objects are outlined in green for each marker. (D) Representative image from a neonatal mouse heart after injection with AAV-*cTnT-Cre*. Sections were stained for Cre (green), PCM1 (red), and DAPI (blue). The circles indicate Cre⁺ cells that were counted as PCM1⁺, and arrowheads point to Cre⁺ cells missed by CardioCount. Magnified images point to a correctly scored Cre⁺ nucleus and a missed Cre⁺ nucleus. (E) Comparison of scores from CardioCount to prior published work, when applied to the same set of images. Scale bars are 50 μm. CNN = convolutional neural network.

sensitivity of 98.1%. Of note, the Cre⁺ cells that were missed tended to be out of plane or have atypical PCM1 immunostaining patterns. Finally, we compared CM cycling rates determined by CardioCount against our prior work that used a 2-step process to identify CM nuclei with a random forest model (ilastik),³⁵ followed by segmentation and colocalization with EdU signals in CellProfiler. Across 528 images scored for PCM1⁺ EdU⁺ cells, CardioCount produced a nearly identical output ($r = 0.97$; $P < 0.001$) (Figure 5E).

To enhance use, we developed an easy-to-use user interface for CardioCount in Google Colab, a free, cloud-based notebook environment that provides GPU access and directly integrates with Google Drive. The Google Colab implementation of CardioCount is aimed towards users with minimal machine learning experience or command line expertise. Users can upload their images to Google Drive and directly run the previously described human or mouse models on data sets through the Google Colab interface. Users can also perform transfer learning or train machine learning

models from scratch without the need for any software setup on their local computers. One caveat to using the software is that it remains limited by Google's resource partitioning, including memory and computational resources. The Google Colab CardioCount software works optimally for smaller image sets where fewer computational resources are needed to process the images. The full code scripts needed to run the machine learning pipelines on larger data sets are available on GitHub and can be implemented locally.

DISCUSSION

Assays of cellular cycling and proliferation are fundamental for tissue regeneration research. Organs, such as the heart, with low basal proliferation rates are particularly problematic because an accurate assessment of rare events requires surveying large amounts of tissue to quantify enough events for accurate estimates, much less to be able to compare treatment effects. To address the need for automated and accurate scoring of cellular cycling, we developed CardioCount, a deep learning-powered pipeline to score cells from antibody-labeled immunofluorescent cardiac tissue. We adapted a prior machine learning platform used to identify solar panels from satellite images to identify labeled nuclei. We were able to use this framework to develop highly accurate models for identifying and scoring CMs, CEC, and Ki67⁺ cells in cardiac tissue sections with test set F1 scores of >0.85 on each of the 3 data sets. Our work differs from prior machine learning approaches that identify CM nuclei after immunostaining for sarcomeric proteins—specifically our models are based on nuclear markers and enable colocalization of different immunostains.³⁶ Our approach compares well with other prominent deep learning and cell segmentation techniques such as Cellpose, Mesmer, and CellProfiler, which regularly segment cells on data sets with F1 scores of 0.4 to 0.9 on general segmentation tasks with broad, diverse data sets.^{37–40} Of note, our model assays CM cycling and cannot differentiate CM proliferation from endocycling, which typically requires lineage tracing approaches or cardiac dissociation to determine cellular ploidy.

To test the utility of our tool, we sought to address a long-standing question regarding the cellular basis for the vascular rarefaction that occurs in progressive HF. Consistent with prior work, we were able to identify decreases in both CM and CEC nuclear density in patients with HF. When we evaluated the

overall CEC:CM ratio, we did not observe significant differences between end-state HF and control hearts, with approximately 1.2 to 1.3 CECs/CM, a figure that compares favorably with other approaches^{1,41} (Figure 2). Our data suggest that vascular rarefaction may be a marker of CM hypertrophy or an indicator of proportional loss of CECs and CMs. However, we also noted that the CEC:CM ratio is highly related to NT-proBNP levels, a biomarker that clinically relates to higher filling pressure and worse prognosis (Figure 2F). Thus, our work is also consistent with prior studies suggesting that reduced coronary flow is related to worse HF and may further suggest that individuals with extremely elevated NT-proBNP levels might benefit from mechanical or molecular revascularization approaches. One potential confounder to our work is we assume that the proportion of mononuclear (~74% in the normal heart) and multinucleated CMs stays constant during HF.⁴² Finally, we evaluated cellular dynamics of mechanical unloading with LVAD support. Unlike prior work, we did not identify a significant increase in CM cycling after LVAD support (Figure 4). However, different patient populations and different pump management strategies might partially explain why our results differ from prior work. Importantly, we did note that CEC and CM cycling are associated in the human heart, consistent with prior work in pre-clinical models and raising the possibility that revascularization strategies might be an important adjunct to tissue regeneration approaches (Figure 4E).¹⁴

Our goal was to establish a platform that could broadly be used to score tissue sections. Towards that goal, we have made our platform available using Google Colab to minimize the entry barrier in terms of computational resources and setup. We have also developed a transfer learning module to enable users to develop customized models for their own tissues of interest and imaging setups. As proof of principle, we applied our method to neonatal mouse section images under different microscopy conditions and show that our platform can be highly accurate even when trained with a small number of training images utilizing transfer learning. Overall, the use of accurate and reproducible algorithms for image quantification has the potential to improve experimental rigor and precision.

Although our models are highly promising, we acknowledge several limitations. CardioCount is a nuclei-based model, meaning that CM counts

reported are only a proxy for the total number of CM cells obtained in the images. For this reason, the model works best on nuclear markers and may not be readily transferable to other types of markers. Additionally, though we expect the general approach of our model to work for other data sets, our models were specifically trained on human and mouse cardiac data and therefore may require larger amounts of training data if transfer learning were to be applied to noncardiac contexts. Finally, our Google Colab implementation of the machine learning training remains limited by the hardware Google provides on its free tier to Google Colab users. The Colab notebook works optimally only on smaller image sets, and for larger image sets, the scripts likely need to be run locally.

CONCLUSIONS

We developed CardioCount, a deep learning-based computational pipeline that can be used to segment nuclei and count cells from diverse microscopy setups. Using this tool on a large data set of human myocardium, we were able to make unique observations regarding the composition of human cardiac tissue, including coupled growth between CECs and CMs, the lack of any association between LVAD support and CM cycling, and findings suggestive of vascular rarefaction as a marker of CM hypertrophy. CardioCount is publicly accessible via GitHub or Google Colab, and we hope this platform can be used broadly for similar applications of tissue segmentation.

ACKNOWLEDGMENTS The authors would like to acknowledge all the patients who graciously provided samples that made this work possible.

FUNDING SUPPORT AND AUTHOR DISCLOSURES

This work was funded by a Stead Society Grant (Dr Karra), a Duke University Strong Start Physician Scientist Award (Dr Karra), and

NHLBI grant R01 HL15777 (Dr Karra). The authors have reported that they have no relationships relevant to the contents of this paper to disclose.

ADDRESS FOR CORRESPONDENCE: Dr Ravi Karra, Division of Cardiology, Department of Medicine, Duke University Medical Center, Box 102152 DUMC, Durham, North Carolina 27710, USA. E-mail: ravi.karra@duke.edu.

PERSPECTIVES

COMPETENCY IN MEDICAL KNOWLEDGE: Cardiovascular disease is a leading cause of death worldwide, and understanding cardiac tissue composition and cycling is essential for developing effective therapies. Current methods to quantitatively assay cardiac tissue composition by histology rely on manual scoring, often limiting the amount of tissue that can be assayed. We built a deep learning tool to score large amounts of cardiac tissue. When applied to images of failing hearts, we find that end-state heart failure is associated with a decrease in capillary density, but that this is proportional to changes in myocyte nuclear density. We also show that there is coupled cycling of cardiac endothelial cells with cardiomyocytes in the human heart, like our previous observations in zebrafish and mice. Taken together, we find that the cellular makeup of the failing heart is dynamic and provides a resource for largescale histologic assessment of the heart.

TRANSLATIONAL OUTLOOK: We developed an objective and consistent machine learning model that can segment and count nuclei in thousands of microscopic images. Tools like this will allow for rigorous assessment of cardiac cell composition and will allow for robust, and unbiased, estimates of rare events such as cardiomyocyte cycling. This resource can enhance the rigor of translational studies that rely on quantitative assessments of cardiac tissue. Due to the generalizability of the CardioCount framework, CardioCount may also be applied more broadly for nuclear segmentation of tissue sections in other contexts.

REFERENCES

- Bergmann O, Bhardwaj RD, Bernard S, et al. Evidence for cardiomyocyte renewal in humans. *Science*. 2009;324(5923):98–102.
- Bergmann O, Zdunek S, Alkass K, Druid H, Bernard S, Frisén J. Identification of cardiomyocyte nuclei and assessment of ploidy for the analysis of cell turnover. *Exp Cell Res*. 2011;317(2):188–194.
- Mollova M, Bersell K, Walsh S, et al. Cardiomyocyte proliferation contributes to heart growth in young humans. *Proc Natl Acad Sci U S A*. 2013;110(4):1446–1451.
- Canseco DC, Kimura W, Garg S, et al. Human ventricular unloading induces cardiomyocyte proliferation. *J Am Coll Cardiol*. 2015;65(9):892–900.
- Bradley LA, Young A, Li H, Billcheck HO, Wolf MJ. Loss of endogenously cycling adult cardiomyocytes worsens myocardial function. *Circ Res*. 2021;128(2):155–168.
- Sereti KI, Nguyen NB, Kamran P, et al. Analysis of cardiomyocyte clonal expansion during mouse heart development and injury. *Nat Commun*. 2018;19(1):754. <https://doi.org/10.1038/s41467-018-02891-z>
- Mohamed TMA, Ang YS, Radzinsky E, et al. Regulation of cell cycle to stimulate adult cardiomyocyte proliferation and cardiac regeneration. *Cell*. 2018;173(1):104–116.e12.
- Ali SR, Hippenmeyer S, Saadat LV, Luo L, Weissman IL, Ardehali R. Existing cardiomyocytes generate cardiomyocytes at a low rate after birth in mice. *Proc Natl Acad Sci U S A*. 2014;111(24):8850–8855.
- Eschenhagen T, Bolli R, Braun T, et al. Cardiomyocyte regeneration: a consensus statement. *Circulation*. 2017;136(7):680–686.

- 10.** Durkee MS, Abraham R, Clark MR, Giger ML. Artificial intelligence and cellular segmentation in tissue microscopy images. *Am J Pathol*. 2021;191(10):1693-1701.
- 11.** Ren S, Malof J, Fetter R, Beach R, Rineer J, Bradbury K. Utilizing geospatial data for assessing energy security: mapping small solar home systems using unmanned aerial vehicles and deep learning. *ISPRS Int J Geoinf*. 2022;11(4):222. <https://doi.org/10.3390/ijgi11040222>
- 12.** von Chamier L, Laine RF, Jukkala J, et al. Democratizing deep learning for microscopy with ZeroCostDL4Mic. *Nat Commun*. 2021;12(1):2276. <https://doi.org/10.1038/s41467-021-22518-0>
- 13.** Schechter MA, Hsieh MK, Njoroge LW, et al. Phosphoproteomic profiling of human myocardial tissues distinguishes ischemic from non-ischemic end stage heart failure. *PLoS One*. 2014;9(8):e104157. <https://doi.org/10.1371/journal.pone.0104157>
- 14.** DeBenedittis P, Karpurapu A, Henry A, et al. Coupled myovascular expansion directs cardiac growth and regeneration. *Development*. 2022;149(18):dev200654. <https://doi.org/10.1242/dev.200654>
- 15.** Schindelin J, Arganda-Carreras I, Frise E, et al. Fiji: an open-source platform for biological-image analysis. *Nat Methods*. 2012;9(7):676-682.
- 16.** Paszke A, Gross S, Massa F, et al. PyTorch: an imperative style, high-performance deep learning library. 2019. In: Wallach H, Larochelle H, Beygelzimer A, d'Alché-Buc F, Fox E, Garnett R, eds. *Advances in Neural Information Processing Systems 32 (NeurIPS 2019)*. Curran Associates; 2019. Accessed August 1, 2022. https://proceedings.neurips.cc/paper_files/paper/2019/file/bdbca288fee7f92f2bf9f7012727740-Paper.pdf
- 17.** Gonzalez TJ, Simon KE, Blondel LO, et al. Cross-species evolution of a highly potent AAV variant for therapeutic gene transfer and genome editing. *Nat Commun*. 2022;13(1):5947. <https://doi.org/10.1038/s41467-022-33745-4>
- 18.** Lin Z, Zhou P, von Gise A, et al. Pi3kcb links Hippo-YAP and PI3K-AKT signaling pathways to promote cardiomyocyte proliferation and survival. *Circ Res*. 2015;116(1):35-45.
- 19.** van der Walt S, Schönberger JL, Nunez-Iglesias J, et al. the scikit-image contributors. scikit-image: image processing in Python. *PeerJ*. 2014;2:e453. <https://doi.org/10.7717/peerj.453>
- 20.** Harris CR, Millman KJ, van der Walt SJ, et al. Array programming with NumPy. *Nature*. 2020;585(7825):357-362.
- 21.** Bradski G. The openCV library. *Dr Dobbs J*. 2000;25(11):120-123.
- 22.** Wickham H, François R, Henry L, Müller K. dplyr: a grammar of data manipulation. *R package version 0.4*. 2015;3:1-156.
- 23.** Wood S, Wood MS. Package 'mgcv'. *R package version*. 2015;1(29):1-729.
- 24.** Kassambara A. ggpubr: 'ggplot2' Based Publication Ready Plots. *R package version 0.6.0*. 2023. Accessed August 1, 2022. <https://rpkg.org/datanovia.com/ggpubr/>
- 25.** Wickham H, Chang W, Henry L, et al. H ggplot2: Create Elegant Data Visualisations Using the Grammar of Graphics. 2016. Accessed August 1, 2022. <https://ggplot2.tidyverse.org/reference/ggplot2-package.html>
- 26.** Alkass K, Panula J, Westman M, Wu TD, Guerquin-Kern JL, Bergmann O. No evidence for cardiomyocyte number expansion in preadolescent mice. *Cell*. 2015;163(4):1026-1036.
- 27.** Das S, Goldstone AB, Wang H, et al. A unique collateral artery development program promotes neonatal heart regeneration. *Cell*. 2019;176(5):1128-1142.e18.
- 28.** Parodi O, De Maria R, Oltrona L, et al. Myocardial blood flow distribution in patients with ischemic heart disease or dilated cardiomyopathy undergoing heart transplantation. *Circulation*. 1993;88(2):509-522.
- 29.** Benjamin EJ, Virani SS, Callaway CW, et al. Heart disease and stroke statistics-2018 update: a report from the American Heart Association. *Circulation*. 2018;137(12):e67-e492.
- 30.** Mosseri M, Schaper J, Admon D, et al. Coronary capillaries in patients with congestive cardiomyopathy or angina pectoris with patent main coronary arteries. Ultrastructural morphometry of endomyocardial biopsy samples. *Circulation*. 1991;84(1):203-210.
- 31.** Kang SH, Park JJ, Choi DJ, Registry KorHF, et al. Prognostic value of NT-proBNP in heart failure with preserved versus reduced EF. *Heart*. 2015;101(23):1881-1888.
- 32.** Maeder MT, Mariani JA, Kaye DM. Hemodynamic determinants of myocardial B-type natriuretic peptide release: relative contributions of systolic and diastolic wall stress. *Hypertension*. 2010;56(4):682-689.
- 33.** Kanwar MK, Selzman CH, Ton VK, et al. Clinical myocardial recovery in advanced heart failure with long term left ventricular assist device support. *J Heart Lung Transplant*. 2022;41(10):1324-1334.
- 34.** Drakos SG, Kfoury AG, Hammond EH, et al. Impact of mechanical unloading on microvasculature and associated central remodeling features of the failing human heart. *J Am Coll Cardiol*. 2010;56(5):382-391.
- 35.** Berg S, Kutra D, Kroeger T, et al. ilastik: interactive machine learning for (bio)image analysis. *Nat Methods*. 2019;16:1226-1232.
- 36.** Ali SR, Nguyen D, Wang B, Jiang S, Sadek HA. Deep learning identifies cardiomyocyte nuclei with high precision. *Circ Res*. 2020;127(5):696-698.
- 37.** Stringer C, Wang T, Michaelos M, Pachitariu M. Cellpose: a generalist algorithm for cellular segmentation. *Nat Methods*. 2021;18(1):100-106.
- 38.** Greenwald NF, Miller G, Moen E, et al. Whole-cell segmentation of tissue images with human-level performance using large-scale data annotation and deep learning. *Nat Biotechnol*. 2022;40(4):555-565.
- 39.** Carpenter AE, Jones TR, Lamprecht MR, et al. CellProfiler: image analysis software for identifying and quantifying cell phenotypes. *Genome Biol*. 2006;7(10):R100. <https://doi.org/10.1186/gb-2006-7-10-r100>
- 40.** Lee MY, Bedia JS, Bhate SS, et al. CellSeg: a robust, pre-trained nucleus segmentation and pixel quantification software for highly multiplexed fluorescence images. *BMC Bioinformatics*. 2022;23(1):46. <https://doi.org/10.1186/s12859-022-04570-9>
- 41.** Pinto AR, Ilinykh A, Ivey MJ, et al. Revisiting cardiac cellular composition. *Circ Res*. 2016;118(3):400-409.
- 42.** Bergmann O, Zdunek S, Felker A, et al. Dynamics of cell generation and turnover in the human heart. *Cell*. 2015;161(7):1566-1575.

KEY WORDS cardiomyocyte cell cycle, heart failure, LVAD, UNets, vascular rarefaction

APPENDIX For supplemental figures and tables, please see the online version of this paper.

EDITORIAL COMMENT

Deep Image Segmentation for Cardiomyocyte Proliferation*



Md Abul Hassan Samee, PhD,^a James F. Martin, MD, PhD^{a,b,c,d}

The adult mammalian heart has limited regenerative capacity, which derives from the long-lived nature of adult cardiomyocytes (CMs). Indeed, CM renewal occurs at a minimal, albeit measurable, level in the adult human heart.¹ Investigating whether CM renewal is associated with other measures of improved cardiovascular outcomes is challenged by the technical difficulty in accurately quantifying CM cell division. Current methods for counting CMs, although rigorous in the right hands, are technically challenging and error prone. In mice, the technical challenges are helped by advanced transgenic fate-mapping techniques, which enable more precise tracking and quantification of CM division but are obviously unavailable to human samples.

Manual curation can compromise sensitivity; introduce potential bias; and, unsurprisingly, lead to substantial interlaboratory discrepancies in CM cycling estimates. One solution to these challenges lies at the intersection of cardiovascular biology and machine learning. The exponential growth in computational power and advancements in deep learning-based image analysis have catalyzed the adoption of automated image segmentation techniques, propelling the field toward more rapid, reproducible, and unbiased analyses. In this issue of

JACC: Basic to Translational Science, Karpurapu et al² have demonstrated some significant advances in this direction.

Karpurapu et al² focused on the dynamics of myovascular cells, specifically CMs and cardiac endothelial cells (CECs), in human heart failure and after mechanical unloading by a ventricular assist device.² The authors developed CardioCount, a deep learning-based pipeline for identifying nuclei from antibody-labeled fluorescent images and colocalizing nuclear objects from multiple image channels. CardioCount leverages the U-Net architecture³ with a ResNet50 backbone.⁴ Briefly, the U-Net is an “encoder-decoder” architecture. First, an input image is gradually down-sampled (reducing the spatial resolution) while maintaining necessary contextual information. This part of the model is called an encoder. Next, from reduced images, a decoder restores the spatial resolution and combines features newly discovered by the encoder to produce a “segmentation mask.” U-Net is a classical and widely adopted convolutional neural network architecture for biomedical image segmentation. Residual networks have also been shown to work well for U-Nets. Thus, CardioCount’s success is intuitive. As training data, the authors manually curated the segmentation masks in about 1,000 images. These images used specific markers to identify CM and CEC nuclei and Ki67 to mark nuclei in the cell cycle. They applied the trained model on ~368,000 images obtained from the Duke Human Heart Repository.

Karpurapu et al² found an interesting coupling between CMs and CECs in the adult human heart, suggesting that the dynamics of these cell types are inter-related in the heart failure samples. They found that CM and CEC nuclear density in the failing heart decrease proportionately, suggesting a biologic link between vascular rarefaction and CM hypertrophy. Furthermore, in failing hearts exhibiting cell cycling,

*Editorials published in *JACC: Basic to Translational Science* reflect the views of the authors and do not necessarily represent the views of *JACC: Basic to Translational Science* or the American College of Cardiology.

From the ^aDepartment of Integrative Physiology, Baylor College of Medicine, Houston, Texas, USA; ^bCardiomyocyte Renewal Laboratory, The Texas Heart Institute, Houston, Texas, USA; ^cMcGill Gene Editing Laboratory, The Texas Heart Institute, Houston, Texas, USA; and the ^dCenter for Organ Repair and Renewal, Baylor College of Medicine, Houston, Texas, USA.

The authors attest they are in compliance with human studies committees and animal welfare regulations of the authors’ institutions and Food and Drug Administration guidelines, including patient consent where appropriate. For more information, visit the [Author Center](#).

individuals with higher levels of CM cycling also had higher levels of CEC cycling, supporting a coordinated growth dynamic between CMs and CECs in the adult human heart.

Overall, CardioCount is an impressive feat and an important addition to the list of tools deploying deep learning methods in cardiovascular research. Further advancements will require addressing a few aspects of the methodological approach and selecting best practices. First, as the authors noted, manual curation is a source of bias, yet they started with manually curated “ground truth” images. When multiple human annotators perform curation, which is preferred to a single annotator, unavoidable variations are introduced into the model. Uncertainty-aware Bayesian segmentation approaches could help build a more rigorous model in these cases. Another approach to minimize the variability is “scribble segmentation.”⁵ Rather than drawing precise boundaries, human annotators draw small scribbles within the objects of interest, and the model identifies boundaries. However, we acknowledge that addressing these issues is difficult, and an optimal approach probably does not currently exist.

We think the field essentially needs “human-in-the-loop artificial intelligence” in which human experts remain and iteratively improve models like CardioCount. An initial model is trained using the best available options and resources, but groups of human experts continue providing feedback to the model, and the model is retrained to incorporate that feedback. Building a supportive framework for the CardioCount user community will be crucial for the tool’s success.

Another methodological concern is the limited training data size, but in the future, researchers following up on CardioCount can use generative adversarial networks-based approaches.⁶ Thirdly, in

the current work, the authors could have offered a more careful inspection of the cases in which CardioCount “makes mistakes.” The model’s precision, recall, and F1 score are satisfactory, but it is a missed opportunity not to ask how the accuracy metrics could be improved. Inspecting a model’s mistakes is often a rewarding experience. It reveals the model’s limitation and indicates if there is any fundamentally challenging aspect of the data that requires a different type of model. Finally, although there is a strong rationale for using U-Net, we think it is another missed opportunity not to try alternative methods such as Mask R-CNN.⁷ Benchmarking multiple methods can reveal the relative strengths and weaknesses of the primarily chosen method and lead to a better solution.

In conclusion, the community welcomes tools like CardioCount. These tools can open new avenues for therapeutic intervention and offer unprecedented insights into the development and regeneration of the human heart. Future studies will incorporate improved statistical and machine learning methodologies and validate the findings of these tools.

FUNDING SUPPORT AND AUTHOR DISCLOSURES

Dr Martin is a cofounder and owns shares in YAP Therapeutics. Dr Samee has reported that he has no relationships relevant to the contents of this paper to disclose.

ADDRESS FOR CORRESPONDENCE: Dr Md Abul Hassan Samee, Department of Integrative Physiology, Baylor College of Medicine, One Baylor Plaza, Houston, Texas 77030, USA. E-mail: samee@bcm.edu. OR Dr James F. Martin, Department of Integrative Physiology, Baylor College of Medicine, One Baylor Plaza, Houston, Texas 77030, USA. E-mail: jfmartin@bcm.edu.

REFERENCES

1. Bergmann O, Zdunek S, Felker A, et al. Dynamics of cell generation and turnover in the human heart. *Cell*. 2015;161(7):1566–1575.
2. Karpurapu A, Williams HA, DeBenedittis P, et al. Deep learning resolves myovascular dynamics in the failing human heart. *J Am Coll Cardiol Basic Trans Science*. 2024;9(5):674–686.
3. Ronneberger O, Fischer P, Brox T. *U-Net: Convolutional Networks for Biomedical Image Segmentation*. Springer International Publishing; 2015:234–241.
4. He K, Zhang X, Ren S, Sun J. Deep residual learning for image recognition. 2016 IEEE Conference on Computer Vision and Pattern Recognition (CVPR); 2016:770–778.
5. Lin D, Dai J, Jia J, He K, Sun J. ScribbleSup: scribble-supervised convolutional networks for semantic segmentation. 2016 IEEE Conference on Computer Vision and Pattern Recognition (CVPR); 2016:3159–3167.
6. Mahmood F, Borders D, Chen RJ, et al. Deep adversarial training for multi-organ nuclei segmentation in histopathology images. *IEEE Trans Med Imaging*. 2020;39:3257–3267.
7. Vuola AO, Akram SU, Kannala J. *Mask-RCNN and U-Net ensembled for nuclei segmentation*. 2019 IEEE 16th International Symposium on Biomedical Imaging (ISBI 2019); 2019:208–212.

KEY WORDS cardiomyocyte, deep learning, left ventricular assist device, regeneration

Letter

RESEARCH LETTER

Soluble Programmed Death-1 Predicts Clinical Outcome After STEMI

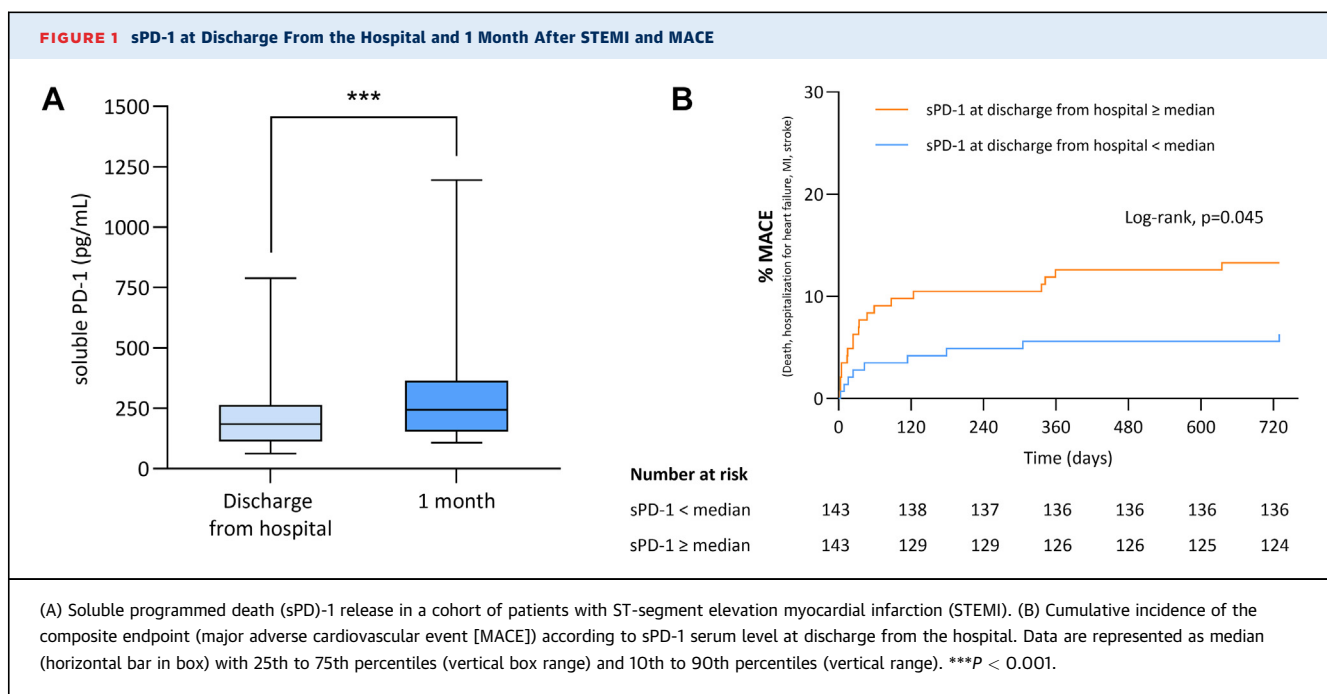


In the aftermath of ST-segment elevation myocardial infarction (STEMI), an inflammatory response occurs, and it is now considered an important prognostic element and a predictor of mortality. Programmed death (PD)-1 is an inhibitory receptor of the CD28 family and is expressed on antigen-activated T lymphocytes. PD-1 inhibits T-cell receptor kinase-dependent signals after binding with its ligands.¹ It is considered as a checkpoint protein, down-regulating effector T cells and maintaining immune tolerance.² We hypothesized that PD-1, through its immune exhaustion function, may have a role at the acute phase of STEMI. Our aim was to determine the plasma level of soluble PD (sPD)-1 after STEMI and its relation with infarct size and clinical events.

We conducted a prospective monocentric study including 286 patients from 2016 to 2020. The study was approved by our ethics committee (Hospices Civils de Lyon, CPP Sud-Est-III). A cohort of STEMI patients who underwent primary percutaneous coronary intervention were included. Plasma samples were collected and stored at -80°C. We assessed sPD-1 levels at 2 time points: discharge from hospital (48 hours after admission) and 1 month. An enzyme-linked immunosorbent assay (R&D Systems) was used for analysis. Patients underwent cardiac magnetic resonance imaging at 1 month in which infarct size and left ventricular ejection fraction (LVEF) were assessed. Clinical events were prospectively collected. Statistical analyses were conducted by using GraphPad Prism version 10.2.0 (GraphPad). The Wilcoxon signed rank test (matched pairs) was used to compare sPD-1 levels at different time points. Comparison of Kaplan-Meier curves for the cumulative incidence of the composite endpoint was performed by using the log-rank test. A *P* value <0.05 was considered statistically significant.

The mean age of the study cohort was 59 ± 12 years; 53.2% had anterior MI. Median LVEF was 53% (25th to 75th percentiles [Q1-Q3]: 46%-59%), and infarct size was 14.0% of the left ventricle (Q1-Q3: 7.0%-23.2%). Median plasma sPD-1 levels were 183.8 pg/mL (Q1-Q3: 112.5-264.5 pg/mL) at discharge from the hospital with a significant increase 1 month after STEMI (244.4 ng/mL; Q1-Q3: 154.3-364.7 ng/mL; *P* < 0.001) (Figure 1A). No correlation between sPD-1 and infarct size (*r* = 0.02; *P* = 0.75) or LVEF (*r* = -0.04; *P* = 0.55) was found at discharge. Similar results were observed at 1 month. There were 28 major adverse cardiovascular events (MACE) during the 2 years of follow-up (7 MIs, 3 ischemic strokes, 14 hospitalizations for heart failure, and 4 all-cause deaths). Patients with sPD-1 levels greater than or equal to the median value (183.8 pg/mL) were more likely to experience MACE at 2 years after STEMI (HR: 2.2; 95% CI: 1.05-4.6; *P* = 0.045) (Figure 1B). In a multivariate model including age, sex, creatinine kinase peak, and Thrombolysis In Myocardial Infarction flow, sPD-1 level at discharge greater than or equal to the median value was an independent factor of increased risk of adverse events (adjusted HR: 2.3; 95% CI: 1.01-5.1; *P* = 0.048). Similarly, sPD1 levels greater than or equal to the median value at 1 month after STEMI was associated with an increased risk of experiencing MACE in univariable and multivariable models, respectively (HR: 4.0 [95% CI: 1.5-11.1; *P* = 0.02]; adjusted HR: 3.5 [95% CI: 1.1-11.3; *P* = 0.04]).

Myocardial injury after MI leads to the activation of the immune system to promote tissue repair and restore homeostasis. PD-1 is viewed as an immune gatekeeper with studies describing its role in preventing an uncontrolled inflammatory reaction.³ We showed, for the first time, that STEMI leads to an increase in sPD1 plasma level between hospital discharge and 1 month. Our preliminary data suggest that sPD1 plasma level in STEMI patients might be an independent prognosis biomarker, reflecting the magnitude of the T-cell inhibition process. These results are in line with previous data exploring the role of immune checkpoint inhibitors in cancer therapies.⁴ It remains uncertain whether the measured sPD-1 was biologically active, including its potential to



(A) Soluble programmed death (sPD)-1 release in a cohort of patients with ST-segment elevation myocardial infarction (STEMI). (B) Cumulative incidence of the composite endpoint (major adverse cardiovascular event [MACE]) according to sPD-1 serum level at discharge from the hospital. Data are represented as median (horizontal bar in box) with 25th to 75th percentiles (vertical box range) and 10th to 90th percentiles (vertical range). ***P < 0.001.

modulate the PD-1 axis, with attention to associated risks such as induced myocarditis.⁵ Because of the relatively small sample size, low number of events, and the lack of a replication cohort, the findings must be regarded as provisional.

Ahmad Hayek, MD^{a,b,†}
 Camille Brun, PhD^{a,†}
 Simon Leboube, MD^b
 Florentin Moulin, PhD^a
 Nathan Mewton, MD, PhD^b
 Gabriel Bidaux, PhD^a
 Sylvie Ducreux, PhD^a
 Mélanie Paillard, PhD^a
 Claire Crola Da Silva, PhD^a
 *Thomas Bochaton, MD, PhD^{a,b}

*Louis Pradel Hospital
 Intensive Care Unit
 28 avenue Doyen Lépine
 69677 Bron, France
 E-mail: thomas.bochaton@chu-lyon.fr
 @BochatonThomas

From the ^aINSERM, INRA, INSA Lyon, Université Claude Bernard Lyon 1, Groupement Hospitalier Est, Bron, France; and the ^bHôpital Louis Pradel, Hôpitaux Civils de Lyon, Bron, France.

†Drs Hayek and Brun contributed equally to this work.

This work was supported by the RHU MARVELOUS (ANR-16-RHUS-0009) of Université de Lyon, within the program “Investissements d’Avenir” operated by the French National Research Agency (Agence Nationale de la Recherche). It was also supported by the Fédération Française de Cardiologie. The authors have reported that they have no relationships relevant to the contents of this paper to disclose. The authors thank the Clinical Investigation Center (William Abrard, Ghoulam Tabdjoun, Yvonne Varillon, Camille Amaz, and Charles de Bourguignon), NeuroBioTec (Nathalie Dufay and Guillaume Fiard), and Régine Cartier, Cyril Prieur, and Gilles Rioufol for all the work that has been performed in data collection and management for this study. They also thank Murielle Robert for her help.

The authors attest they are in compliance with human studies committees and animal welfare regulations of the authors’ institutions and Food and Drug Administration guidelines, including patient consent where appropriate. For more information, visit the [Author Center](#).

REFERENCES

1. Patsoukis N, Wang Q, Strauss L, Boussiotis VA. Revisiting the PD-1 pathway. *Sci Adv*. 2020;6(38):eabd2712.
2. Kythreotou A, Siddique A, Mauri FA, Bower M, Pinato DJ. PD-L1. *J Clin Pathol*. 2018;71(3):189–194.
3. Hayashi T, Tiwary SK, Lavine KJ, et al. The programmed death-1 signaling axis modulates inflammation and LV structure/function in a stress-induced cardiomyopathy model. *J Am Coll Cardiol Basic Trans Science*. 2022;7(11):1120–1139.
4. Tan S, Day D, Nicholls SJ, Segelov E. Immune checkpoint inhibitor therapy in oncology: current uses and future directions: JACC: CardioOncology State-of-the-Art Review. *J Am Coll Cardiol CardioOnc*. 2022;4(5):579–597.
5. Rikhi R, Karnuta J, Hussain M, et al. Immune checkpoint inhibitors mediated lymphocytic and giant cell myocarditis: uncovering etiological mechanisms. *Front Cardiovasc Med*. 2021;8:721333.

STATE-OF-THE-ART REVIEW

Nitric Oxide Releasing Nanomaterials for Cardiovascular Applications



Tanveer A. Tabish, PhD,^a Mark J. Crabtree, PhD,^{a,b} Helen E. Townley, PhD,^{c,d} Paul G. Winyard, PhD,^e Craig A. Lygate, PhD^a

HIGHLIGHTS

- NO-based therapeutics remain a cornerstone of cardiovascular pharmacology, but would benefit from targeted and controlled delivery.
- Nanomaterials can function as highly tunable platforms for drug delivery including NO via catalytic and noncatalytic approaches.
- Multiple nanomaterials have been investigated for NO delivery in vascular stents and grafts, reperfusion injury, and tissue engineering.
- Clinical translation will require multidisciplinary cooperation to optimize material properties, address safety concerns, and test in large animal models.

SUMMARY

A central paradigm of cardiovascular homeostasis is that impaired nitric oxide (NO) bioavailability results in a wide array of cardiovascular dysfunction including incompetent endothelium-dependent vasodilatation, thrombosis, vascular inflammation, and proliferation of the intima. Over the course of more than a century, NO donating formulations such as organic nitrates and nitrites have remained a cornerstone of treatment for patients with cardiovascular diseases. These donors primarily produce NO in the circulation and are not targeted to specific (sub)cellular sites of action. However, safe, and therapeutic levels of NO require delivery of the right amount to a precise location at the right time. To achieve these aims, several recent strategies aimed at therapeutically generating or releasing NO in living systems have shown that polymeric and inorganic (silica, gold) nanoparticles and nanoscale metal-organic frameworks could either generate NO endogenously by the catalytic decomposition of endogenous NO substrates or can store and release therapeutically relevant amounts of NO gas. NO-releasing nanomaterials have been developed for vascular implants (such as stents and grafts) to target atherosclerosis, hypertension, myocardial ischemia-reperfusion injury, and cardiac tissue engineering. In this review, we discuss the advances in design and development of novel NO-releasing nanomaterials for cardiovascular therapeutics and critically examine the therapeutic potential of these nanoplates to modulate cellular metabolism, to regulate vascular tone, inhibit platelet aggregation, and limit proliferation of vascular smooth muscle with minimal toxic effects. (J Am Coll Cardiol Basic Trans Science 2024;9:691-709) © 2024 The Authors. Published by Elsevier on behalf of the American College of Cardiology Foundation. This is an open access article under the CC BY license (<http://creativecommons.org/licenses/by/4.0/>).

From the ^aDivision of Cardiovascular Medicine, Radcliffe Department of Medicine, British Heart Foundation (BHF) Centre of Research Excellence, University of Oxford, Oxford, United Kingdom; ^bDepartment of Biochemical Sciences, School of Biosciences & Medicine, University of Surrey, Guildford, United Kingdom; ^cNuffield Department of Women's and Reproductive Health, John Radcliffe Hospital, University of Oxford, Oxford, United Kingdom; ^dDepartment of Engineering Science, University of Oxford, Oxford, United Kingdom; and the ^eUniversity of Exeter Medical School, College of Medicine and Health, St. Luke's Campus, University of Exeter, Exeter, United Kingdom.

The authors attest they are in compliance with human studies committees and animal welfare regulations of the authors' institutions and Food and Drug Administration guidelines, including patient consent where appropriate. For more information, visit the [Author Center](#).

Manuscript received May 12, 2023; revised manuscript received July 27, 2023, accepted July 27, 2023.

ABBREVIATIONS AND ACRONYMS

cGMP = cyclic guanosine monophosphate

MOF = metal-organic framework

NO = nitric oxide

NOS = nitric oxide synthase

NP = nanoparticle

NONOates = *N*-diazeniumdiolates

SNAP = S-nitroso-*N*-acetylpenicillamine

PCL = poly(ϵ -caprolactone)

Despite the increasing use and significant advances made in interventional and surgical procedures, cardiovascular disease (CVD) has remained a major cause of morbidity and mortality globally for decades.¹ The ageing population in both developed and developing countries has also led to a significant rise in the prevalence of cardiovascular diseases. The endothelium plays a crucial role in maintaining vessel homeostasis, regulating the delicately balanced processes of vascular tone and platelet activation. Vessel homeostasis is maintained by the release of various vasoactive factors from the endothelium. Vasoactive factors can be vasodilatory, including nitric oxide (NO), prostacyclin, endothelium-derived hyperpolarizing factor, or vasoconstrictive, including thromboxane A2 and endothelin-1.^{2,3} NO is one of the most important vasodilatory factors in coronary endothelium and is constitutively generated through the conversion of L-arginine and molecular oxygen to NO and L-citrulline catalyzed by the enzyme nitric oxide synthase (NOS). The essential cofactor tetrahydrobiopterin is a key regulator of cellular redox signaling and is crucial for the maintenance of vascular function, because tetrahydrobiopterin deficiency causes uncoupling of the NOS enzyme resulting in production of the superoxide anion radical (O_2^-) instead of NO.⁴ The 3 distinct isoforms of NOS in mammals are neuronal NOS, inducible NOS, and endothelial nitric oxide synthase (eNOS).⁵ In the vasculature, eNOS in endothelial cells is the primary source of NO and is a crucial regulator of blood pressure, cellular proliferation, and vascular tone. NO continuously diffuses to vascular smooth muscle cells where it stimulates soluble guanylate cyclase (sGC) to produce cyclic guanosine monophosphate (cGMP), thereby activating protein kinase G, which then phosphorylates multiple target proteins resulting in smooth muscle relaxation and vasodilation.^{2,5} Neuronal NOS, the main endogenous source of myocardial NO, regulates cardiac inotropy and relaxation, and modulates intracellular Ca^{2+} homeostasis and signaling pathways including nitroso-redox balance.⁶ Hence, it is no surprise that low bioavailability of NO critically drives the progression of CVD. A full exploration of the critical roles of NO and the mechanisms that regulate NO bioavailability in cardiovascular systems are beyond the scope of this review, but these topics have been extensively reviewed elsewhere.^{5,7,8}

NO down-regulates the expression of the prothrombotic protein tissue factor and inhibits the gene

expression of adhesive proteins by endothelial cells, thereby exerting anti-inflammatory effects by inhibiting the adhesion of leukocytes. NO also inhibits mast cell activation and mast cell-dependent inflammatory events that contribute to destabilization of the atherosclerotic plaque.^{9,10} NO has anti-proliferative effects on smooth muscle cells (SMCs) and therefore prevents neointima hyperplasia in response to injury.¹¹ Thus, NO has wide-ranging vasoprotective, antiatherosclerotic, and antithrombotic roles.¹¹ Drugs that may release or produce NO locally represent a significant breakthrough for the control and treatment of CVD. However, their overall success is limited by the physicochemical properties of NO, which as a diatomic gaseous molecule with one unpaired electron, is highly reactive with free radical oxygen-centered species.¹² Thus, NO has a high diffusion rate, but a short biological half-life (in the order of 0.5–5 seconds), thereby limiting the diffusion distance to around 200 μ m. NO can be rapidly oxidized to highly toxic nitrogen dioxide in the presence of molecular oxygen. Due to such limitations, there is a growing interest in developing novel formats for the controlled, predictable, and targeted release of NO. Over the last few decades, different NO delivery systems have been devised and investigated in the form of NO donors (such as organic nitrates, nitrites, thionitrites, S-nitrosothiols (RSNOs), *N*-diazeniumdiolates (NONOates), metal-NO complexes,^{13,14} NO-releasing nonsteroidal anti-inflammatory drugs,¹⁵ small molecule gas-releasing prodrugs,¹⁶ peptides,¹⁷ proteins,¹⁸ polymeric membranes,¹⁹ hydrogels,²⁰ scaffolds, and nanoparticles (silica, gold, liposomes, dendrimers, and so on)²¹ to store and release NO in a controlled and therapeutically meaningful manner.

Among the previously listed approaches, nanoparticles (NPs) have garnered attention recently because of their remarkable features, which include ultra-small size, high surface area, chemical reactivity, and ease of functionalization. The storage and release of NO by NPs heavily depends on these fundamental features as well as the NO source. NPs offer several advantages over conventional donor drugs, such as the ability to control release rates and to target specific sites of action. Targeted delivery of NO-releasing NPs has been widely reviewed for cancer,²² antimicrobial,²³ and medical devices²⁴; however, the study of NO-releasing/generating NPs for CVD is still in its infancy. In this review, we explore the basic concept of NPs and their key characteristics for use in biomedical applications. In particular, we highlight recent developments in the field of NO-releasing/generating NPs for the targeted,

controlled, and long-term release kinetics of NO along with potential future directions.

CLINICAL APPLICATIONS OF NO DONOR DRUGS

To provide context, we will first briefly discuss the most clinically important NO interventions for the treatment of CVD. At the simplest level, NO is used, nonformulated, as a medical gas for the treatment of pulmonary arterial hypertension and hypoxic newborns.²⁵ Administration by inhalation provides selectivity, particularly because NO is rapidly inactivated in blood, which minimizes systemic adverse effects but also limits the utility of this approach for other conditions.⁸

Low molecular weight organic nitrates, eg, glyceryl trinitrate (GTN), have been in clinical use since the 1870s, although the NO-dependent mechanism was not understood until the late 1970s.⁸ GTN releases 1 molar equivalent of NO upon activation by mitochondrial enzymes, and sublingual GTN has been extensively used to treat acute angina pectoris providing rapid relief of symptoms for a short duration. Other nitrates, such as isosorbide dinitrate and isosorbide-5-mononitrate, are slower onset, but with a prolonged duration of action making them more suitable for angina prophylaxis (eg, via oral or transdermal delivery).²⁶

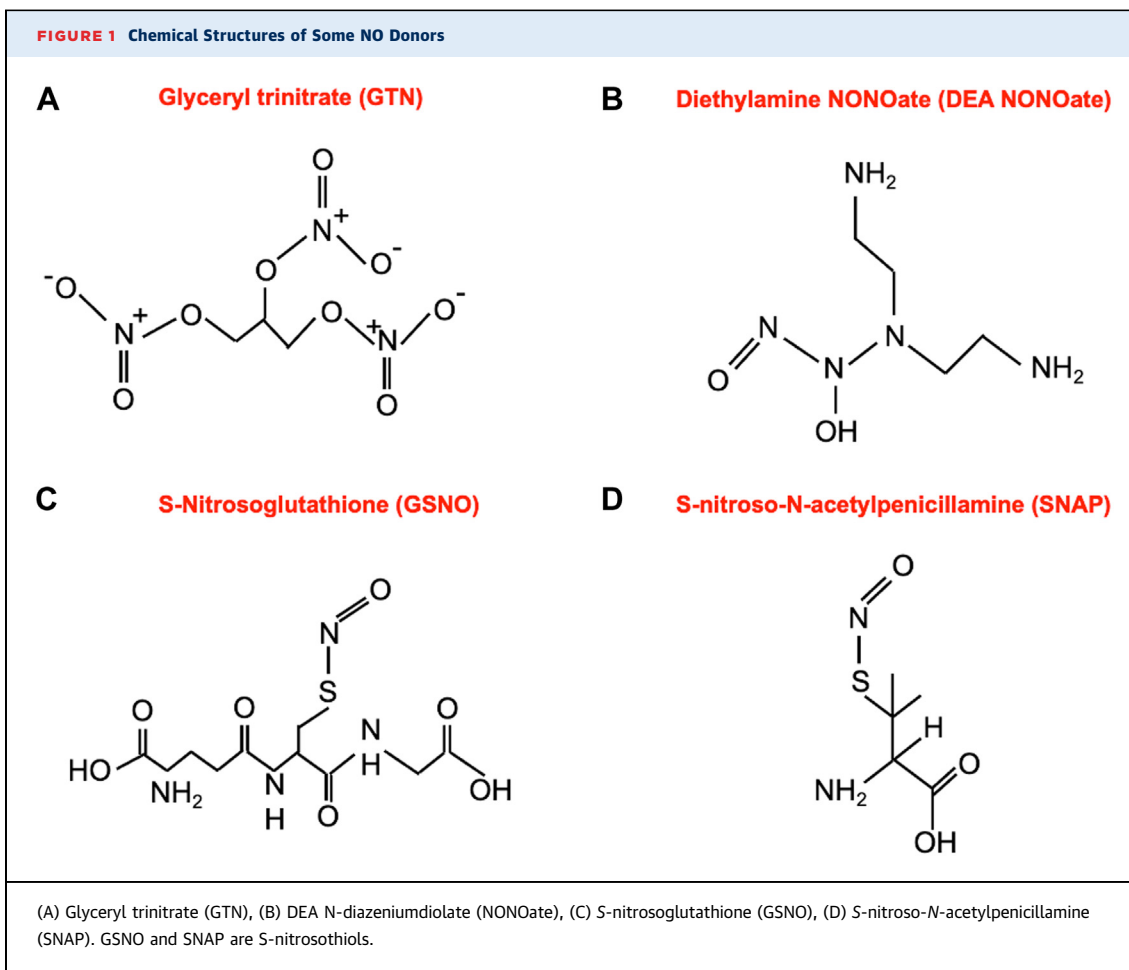
Nitrates are also used in the treatment of heart failure, because they cause vasodilation, thereby reducing venous return, unloading the heart and increasing stroke volume.²⁷ The combined use of oral isosorbide dinitrate and hydralazine has been shown to improve cardiac function and survival in patients with chronic congestive heart failure,²⁸ particularly in African-American patients, in whom NO bioavailability may be disproportionately impaired.²⁹ Intravenous nitrates may also be used for the treatment of acute heart failure to alleviate pulmonary congestion. However, caution is required in conditions where excessive cardiac unloading may result in hypotension, eg, left ventricular hypertrophy and severe aortic stenosis.²⁷

Continuous administration of virtually all organic nitrates results in gradual loss of efficacy because of a complex and multifaceted phenomenon termed nitrate tolerance (reviewed by Munzel et al³⁰). Classically, this is observed as a rebound effect, whereby withdrawal of nitrates results in anginal symptoms that are worse than before treatment. Hence, dosing regimens for angina typically incorporate a nitrate-free period (eg, overnight) to minimize tolerance, but with the commensurate loss of 24-hour

protection. Multiple mechanisms are likely to contribute to nitrate tolerance; these include impaired enzymatic drug activation resulting in reduced NO production, and nitrate resistance caused by desensitization of the sGC signaling pathway.^{31,32} Another key contributor is nitrate pseudotolerance, which arises from overcompensation by neurohormonal pathways in response to sustained vasodilation, eg, increased sympathetic stimulation, activation of the renin-angiotensin-aldosterone system, and increased sensitivity to endogenous vasoconstrictors. It is likely that an increase in oxidative stress underpins many of these mechanisms, with nitrate treatment shown to increase production of superoxide anion via nicotinamide adenine dinucleotide phosphate oxidases and mitochondria. This superoxide rapidly reacts with NO, effectively reducing NO bioavailability, but also forming peroxynitrite (ONOO^-), which promotes NOS uncoupling and a vicious cycle of more superoxide generation. In addition, superoxide and peroxynitrite inhibit sGC in smooth muscle cells and reduce generation of the vasodilator prostacyclin.^{30,33} Hence, the administration of organic nitrates that also have antioxidant activity (eg, pentaerythritol tetranitrate) or in combination with antioxidant compounds may be particularly advantageous. Common but debilitating adverse effects such as headache and hypotension also limit the use of nitrates with severity varying dependent on pharmacokinetic profile and vascular selectivity.³⁰

Other associated classes of drug augment NO signaling, eg, phosphodiesterase inhibitors, which increase cGMP levels by preventing enzymatic degradation, or Vericiguat, which stimulates soluble guanylate cyclase to restore cGMP levels. These agents may have utility in circumventing nitrate tolerance by improving NO sensitivity alongside the use of neurohormonal inhibitors to combat pseudotolerance. For example, Vericiguat is currently licensed in the United Kingdom for the treatment of heart failure with reduced ejection fraction, with the advantage over nitro-vasodilators that long-term administration does not produce tolerance.²⁷ Other NO donors available in clinical settings include a lozenge for lowering blood pressure in patients with prehypertension, nitroprusside for the treatment of hypertension, and latanoprostene bunod for lowering of intraocular eye pressure in patients with glaucoma.³⁴

Nitrates and nitrites are also the breakdown products of NO metabolism, but recycling pathways exist for the regeneration of NO. Nitrates in the



bloodstream accumulate in saliva where oral bacteria convert it to nitrite, which in turn can be reduced to NO in blood and tissues via a variety of mechanisms.⁵

NO-RELEASING COMPOUNDS IN DEVELOPMENT

Over the past few decades, NO donors and precursors, such as diazeniumdiolates (NONOates), S-nitrosothiols (RSNOs), and arginine, have emerged as potent enhancers of NO signaling. The chemical structures of the most commonly used NO donors are shown in Figure 1. Among these, NONOates are commonly studied because of their capability to release NO rapidly under physiological conditions (37 °C, pH 7.4). NONOates are adducts of NO dimer bound to nucleophilic residue via a nitrogen atom. When hydrolyzed, they release 2 molar equivalents of NO per mole of donor,³⁵ and the release rate can be precisely controlled from seconds to days by changing the amount and degree of both hydrogen bonding and amine precursors.

RSNOs represent the addition of NO to a cysteine peptide via a S-NO bond. They can be low or high molecular weight depending on the “R” group, which will therefore greatly influence the biological properties. RSNOs can be endogenous or laboratory synthesized and act as NO donors and/or mediators of NO-signaling via post-translational modification of proteins. Important examples include S-nitroso-N-acetylpenicillamine (SNAP), S-nitrosoalbumin, S-nitrosohemoglobin, S-nitrosocysteine, and S-nitrosoglutathione (GSNO).^{36,37} RSNOs do not undergo spontaneous release of NO because of the low energy S-NO bond ($\approx 150 \text{ kJ mol}^{-1}$).³⁸ However, NO release can be facilitated in several ways: 1) transition metal ion-mediated catalysis (eg, by Cu^{+}); 2) interactions with ascorbate; and 3) photocatalysis.³⁹

Despite the clinical utility of low molecular weight NO donors, they have a number of limitations, eg, their stability under biologically relevant conditions and limited NO payloads. NO release is typically uncontrolled and nonspecific, limiting the delivery of

FIGURE 2 Dimensions (0D, 1D, 2D, and 3D) and Classes of Nanomaterials (Organic, Inorganic)

Dimensions	Organic	Inorganic
Zero-dimensional	Polymer nanoparticle	Mesoporous silica nanoparticle
One-dimensional	Dendrimer	Quantum dot
Two-dimensional	Lipid nanoparticle	Carbon nanotube
Three-dimensional	Liposome	Metal-organic framework
0D: Quantum dots, nanocrystals 1D: Nanotubes 2D: Graphene and related materials 3D: Hydrogels, foams and aerogels	Advantages <ul style="list-style-type: none">Simple fabricationHigh payload capacityEase of surface functionalisationBiocompatibility Disadvantages <ul style="list-style-type: none">Possibility of aggregation	Advantages <ul style="list-style-type: none">Exceptional electrical, mechanical, optical propertiesTunability in size and morphology Disadvantages <ul style="list-style-type: none">Toxicity and limited solubility in solutions

Each class has advantages and disadvantages in terms of synthesis, functionalization, solubility, toxicity, and drug loading. D = dimension.

therapeutic doses to the target site. However, to address these clinical challenges, low molecular weight NO donors can be conjugated or loaded to a variety of nanoparticles for targeted, controlled, and sustained delivery of NO.

NANOMATERIALS AND THEIR FUNDAMENTAL PROPERTIES

Nanomaterials are very small-scale chemical substances, typically 1 to 100 nm in at least 1 dimension. Nanomaterials can be classified based on their origin (natural or synthetic/engineered), composition (organic, inorganic), size, or applications (biomaterials, electronic materials, magnetic materials).⁴⁰ NPs are further classified by dimensions, such as zero-dimensional (eg, quantum dots),⁴¹ 1-dimensional (eg, nanotubes, nanorods),⁴² 2-dimensional (eg, graphene, boron nitride, molybdenum disulfide), or 3-dimensional (eg, foam, aerogels, hydrogels, polymeric nanocomposites).⁴³ The archetypal examples of organic NPs are polymeric, dendrimer, liposomes, and lipid NPs, whereas the archetypal examples of inorganic NPs are mesoporous silica NPs, quantum dots,

carbon nanotubes, and metal-organic frameworks (MOFs) (Figure 2).

Engineered nanomaterials are designed and assembled to optimize interactions with functional payloads and to take advantage of the unique properties of their ultra-small size and high surface-to-volume ratios. These result in high chemical reactivity and quantum confinement effects,⁴⁰ whereby the motion of electrons is restricted to specific energy levels, which significantly enhances optical, electrical, and magnetic properties.^{44,45} Thus, NPs possess physicochemical and mechanical properties that are unique and tuneable.⁴⁶

Nanomaterials are generally prepared by 2 main wet chemical methods: the top-down and bottom-up approaches. The top-down approach involves the decomposition of larger precursors into smaller units, and then these units are converted into NPs. Typical examples of this approach are grinding,⁴⁷ chemical vapor deposition,⁴⁸ or physical vapor deposition.⁴⁹ The bottom-up approach, also known as the “building-up” approach, involves the disintegration of a molecular precursor into smaller constituent parts that are then grown into colloids. Typical examples of

this approach are chemical reduction,⁵⁰ the sol-gel method,⁵¹ biochemical synthesis,⁵² and spinning.⁵³ To date, a large number of nanomaterials have been used in a wide variety of commercial applications including sunscreens, cosmetics, sporting goods, stain-resistant clothing, tires, and electronics, as well as in medicine.

Polymeric NPs can be assembled to precisely control drug release, and they have good biocompatibility. Different drugs and biomolecules can be incorporated into the core of NPs, which are conjugated to a polymeric matrix or nanofiber. The conjugation of particles with polymers improves their drug loading efficacy for both hydrophobic and hydrophilic molecules. Such NPs can be further classified into different morphologies such as micelles or dendrimers, which are highly branched, highly symmetrical, tree-like macromolecules also referred to as hyperbranched polymers.⁵⁴ Dendrimers have widely been reported to have high drug storage capacity and to transport the drug with minimal toxicity to normal cells.⁵⁵ Liposomes have been one of the most widely used nanocarriers because of their multilayered morphologies that are largely adaptable to cellular environments⁵⁶ and the layered morphologies also allow rapid cell infiltration.⁵⁷ Excellent biocompatibility and biodegradability, as well as an inert nature, make liposomes a viable nanocarrier material without further modifications. Liposomal formulations have been reported as drug carriers for the controlled release of biomolecules and some have been approved for clinical applications, eg, liposomal amphotericin is used to reduce side-effects.

Inorganic NPs, such as silica, silver, gold, iron, titanium, carbon nanotubes, and graphene, have been developed in a wide variety of sizes and shapes and have also been utilized for drug delivery, light-mediated therapeutics (photodynamic therapy and photothermal therapy), and diagnostics (cardiac magnetic resonance, fluorescence imaging). Among the new class of nanomaterials, MOFs, comprising metal ions coordinated to organic linkers to form 1-, 2-, or 3-dimensional structures, have also received attention because of their exceptionally high specific surface area, tunable surface chemistry, and ease of functionalization with biomolecules.⁵⁸

The ease of chemical modification on the surface of NPs facilitates the tailoring of the storage/release capacity, flux, and duration of NO. An early study on the development of NO-releasing materials was reported by Larry Keefer and his team⁵⁹ where they used a polymeric matrix for the storage of NO (in the form of $N_2O_2^-$) to adjust the time course of NO release. Organic NPs largely comprise polymeric NPs,

micelles, liposomes, dendrimers, nanofiber composites, and hydrogels.⁶⁰ Typical examples of NO-releasing inorganic NPs are metallic NPs (gold,⁶¹ silver,⁶² copper⁶³), mesoporous silica,⁶⁴ zeolites,⁶⁵ and MOFs.⁶⁶ An early study on the therapeutic potential of NO-releasing NPs in CVD was reported by Taite and West⁶⁷ in 2006. They used a peptide synthesis approach in which 9-fluorenylmethoxycarbonyl (Fmoc groups) were used to protect the N-terminus, thereby allowing the formation of a branching structure of dendrimers. Dendrimers prepared in this way were used for the targeted release of NO over approximately 60 days to control vascular SMC proliferation and inhibit platelet adhesion to thrombogenic surfaces. In 2009, Nishikawa et al⁶⁸ fabricated polysiloxane NPs (average size of 80 nm) by the reaction of sugar-lactones with amine-functionalized polysiloxane and studied localized NO release triggered by polysiloxane NPs in human aortic endothelial cells, revealing that NPs entered into cells via pinocytosis vesicles and that the cellular uptake of NPs mediated NO release, ie, that the enzymatic activity of eNOS can be triggered by targeting caveolae with NPs.

STRATEGIES FOR NO RELEASING AND GENERATING NANOMATERIALS

There are 2 major approaches to exploit the therapeutic release or generation of NO using NPs: catalytic and noncatalytic.⁶⁶ Within the catalytic approach there are 4 main strategies:

1. *Enzyme prodrug systems*—In these systems, NO-releasing prodrugs are immobilized onto the surface of NPs for subsequent enzymatic activation. For example, prodrugs that are converted *in vivo* to spontaneous NO-releasing compounds via the action of esterases⁶⁹ or glycosylated NONOates that are activated by endogenous β -galactosidase. To provide greater tissue specificity, glycosylated NONOates have been chemically modified so they are only cleaved by a specific mutant galactosidase. This mutant enzyme was implanted in tissues within a hydrogel, such that systemic delivery of glycosylated NONOate produced only local NO generation.⁷⁰

2. *The attachment of transition-metal ions to NPs*—Endogenous S-nitrosothiols can spontaneously decompose to NO in a reaction that is catalyzed by Cu^{2+} .⁷¹ Using this approach, Jiang et al⁷² reported the generation of NO from a layer-by-layer structure of copper-loaded titanium nanotubes (average diameter 30 nm).

3. *Nanozymes*—These are nanomaterial-based artificial enzymes which effectively mimic the catalytic sites of natural enzymes. They offer advantages in terms of cost-efficient synthesis, stability in biological media, and biodegradability (see specialized reviews for more on this topic⁷³⁻⁷⁵).
4. *External stimuli*—Several external stimuli, such as light, ultrasound, and x-rays, have also been used to achieve control over the NO release kinetics. The NO release profile from the donors can be changed by varying the intensity of these stimuli. There has been widespread interest in developing such external stimuli responsive NO release in cancer and infections; however, they have not been explored for CVD (see specialized reviews for more on this topic^{76,77}). A few studies have reported the catalytic generation of NO by incorporating nanozymes such as titanium dioxide films,⁷⁸ a copper-catecholic-selenocystamine framework,⁷⁹ electrospun Cu-MOF NPs into poly(ϵ -caprolactone) (PCL),⁸⁰ and PCL-based vascular graft under the catalysis of ascorbic acid.⁸¹

The noncatalytic approach involves chemical modification of NPs to store NO sources (eg, NO gas, NONOates, SNAP) via encapsulation into the cavities or surface, which is then released in tissues upon interaction with moisture, light, or ultrasound. For example, to achieve the controlled, slow, and sustained release of NO, studies have demonstrated the use of sequestered NO gas⁸² and of RSNOs using thiol functionalized dendrimers⁸³ or gadolinium-oxide-based paramagnetic NPs.⁸⁴ Because of their high specific surface area, nanomaterials such as MOFs have the ability to store the largest amounts of NO. This storage capacity is also dictated by the type of NO source, stability, and storage conditions. Hence, leaching of the payload is a limitation when using low molecular weight NO donors such as organic nitrates.

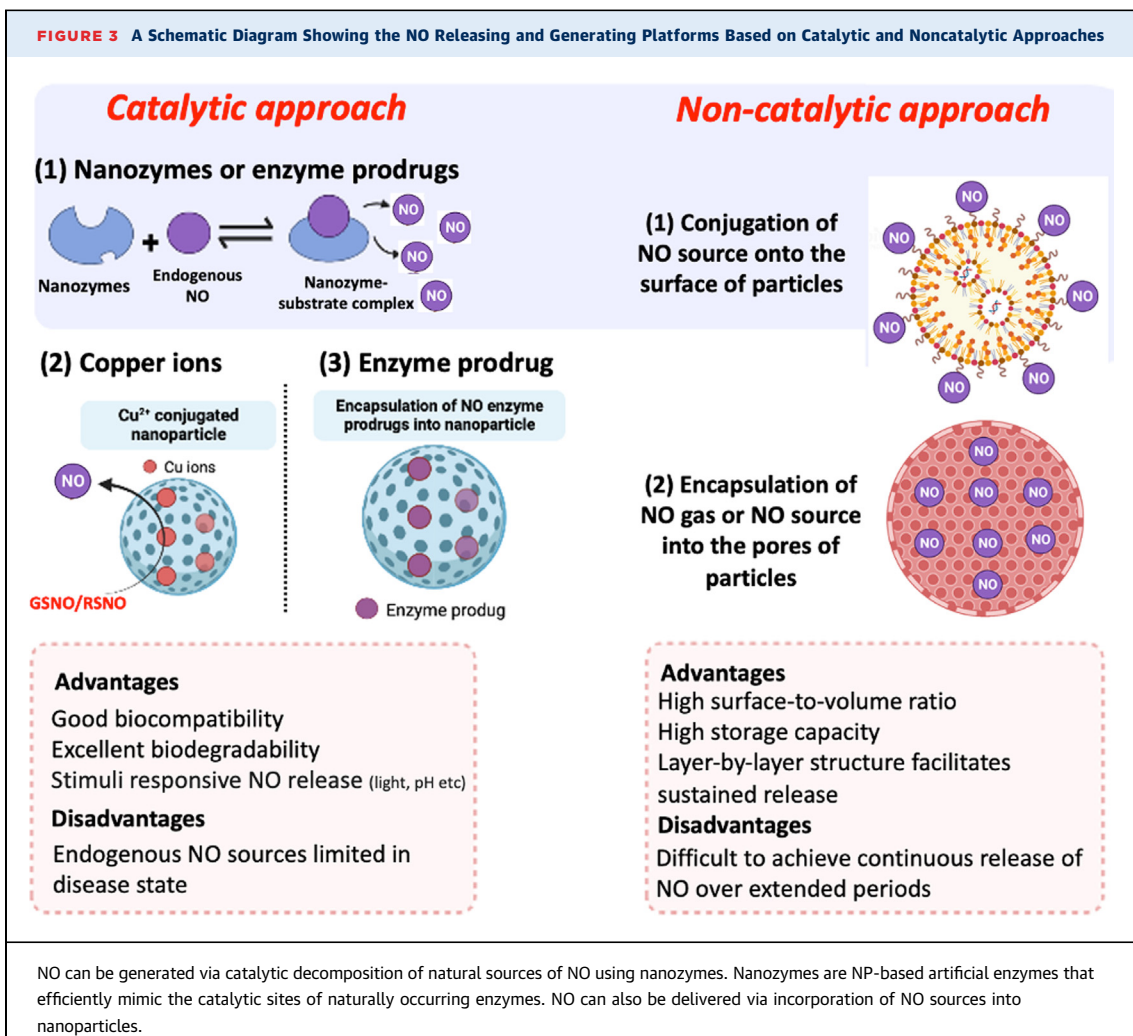
One unique approach has utilized magnetic NPs complexed to lentivirus for targeted gene delivery of eNOS specifically to endothelial cells (ECs). In an initial study, aortic ECs were transfected under cell culture conditions, such that they became strongly magnetic and overexpressed functional eNOS protein. These cells were then administered into the lumen of a perfused aorta where the endothelium had been injured and a specially designed array of magnets used to encourage EC recolonization in the desired radial formation on the vessel wall. In both ex vivo and in vivo experiments, improvements were observed in endothelial layer regeneration and in endothelial-dependent relaxation.⁸⁵ Subsequent experiments eschewed the cell therapy approach for

direct administration of lentiviral-magnetic NP complexes to isolated perfused vessels. Application of the magnetic field was able to enhance contact time and improve gene transfection efficiency without the need to stop flow, resulting in improved vascular function.⁸⁶ These strategies have the potential to greatly improve targeting of gene therapy to the damaged endothelium. However, transgenic eNOS may still become uncoupled and dysfunctional if there is an insufficient supply of substrates and cofactors in the damaged vessel.

Both catalytic and noncatalytic approaches offer advantages and limitations (schematically shown in **Figure 3**). For instance, low concentrations of endogenous NO substrates at diseased sites restrict the clinical use of some catalytic approaches (eg, for the prevention of restenosis). Similarly, the requirement for continuous release of NO over extended periods, such as days, weeks, and months, has not been fully demonstrated using noncatalytic approaches. **Table 1** summarizes the NO release profiles of various types of nanoformulations for use in different cardiovascular disease models.

APPLICATION OF NO-RELEASING AND -GENERATING NANOPARTICLES FOR CARDIOVASCULAR THERAPEUTICS

CARDIOVASCULAR STENTS. In the cardiovascular field, stents are the most widely investigated application for NO-releasing NPs. Stents are inserted following angioplasty and conventionally consist of a metal expandable tubular mesh, which acts as a scaffold to hold open the vessel and thereby maintain blood flow.⁸⁷ Although a substantial improvement on balloon angioplasty alone, bare-metal stents may themselves induce vascular damage and inflammation leading to thrombosis, intimal hyperplasia (characterized by SMC proliferation and collagen deposition), and renarrowing of the blood vessel, a phenomenon known as in-stent restenosis.⁸⁸ Restenosis is most common within 12 months of stent implantation when it affects up to 20% of patients.⁸⁹ In the last 2 decades this has been reduced to ~2% by the use of drug-eluting stents, eg, paclitaxel and sirolimus analogues,⁹⁰ which suppress local immune responses and are potent inhibitors of SMC proliferation. These drugs are incorporated into a polymer coating between 4 and 22 μm thick,⁸⁹ from which they are eluted at a controlled rate. However, issues remain with drug-eluting stents, and the cumulative risk of restenosis creeps up after the first year because of neoatherosclerosis, which is driven by a number of factors, such as chronic inflammation and suboptimal



endothelialization, but also by hypersensitivity reactions to polymer components and flow disturbances caused by the stent itself, leading to platelet activation and stent thrombosis.^{91,92} Given that millions of patients worldwide receive a stent annually, even a 1% to 2% restenosis rate is a sizeable problem, with 10% to 20% of these patients going on to develop recurrent restenosis.⁸⁹

It should be noted that the use of drugs to inhibit SMC proliferation may also inhibit endothelial cell adhesion and proliferation.⁹² Therefore, current approaches can be viewed as a double-edged sword. Timely endothelialization of the vessel wall and the stent surface is important because a healthy, confluent endothelial layer produces NO to reduce vascular permeability, inflammatory cell activation, platelet aggregation, and SMC hyperplasia.^{93,94} Multiple preclinical studies have shown that exogenous NO promotes EC proliferation and migration, both in cell culture and in response to vascular injury.⁹⁵ In

part, this reflects an effect of NO to promote EC survival by preventing apoptosis, via both cGMP-mediated mechanisms to modulate anti-apoptotic protein kinases and by S-nitrosation of caspases to prevent activation.⁹⁶ Hence, an ideal treatment would *enhance* healing and rapid endothelialization as well as *reduce* SMC *hyperproliferation* and thrombogenesis, which makes the use of stent coatings that release or generate NO an attractive proposition.

Stents are typically fabricated by laser cutting stainless steel, titanium-nickel, tantalum, or platinum-iridium alloys.⁹² Nanomaterial-based coatings have been devised to release or generate NO in a controlled manner. In particular, layer-by-layer coating using polymers, polymeric NPs, and other classes of NPs have the potential to extend the NO release profile from hours to days and weeks.⁶⁰ Modifying the surfaces of cardiovascular implants to release NO depends on the mechanical properties of

the materials, such as stiffness, hardness, mechanical strength, viscoelasticity, shape memory behavior, and surface chemistry, which in turn determine the biological fate of such materials.⁹⁷ The Seifalian laboratory has pioneered the use of NO-releasing NPs for stents and vascular grafts,⁹⁸ demonstrating polymeric NPs, nanofibers, and hydrogels for the storage of SNAP and GSNO and the controlled release of NO. The results of these preclinical studies are discussed in the following text and in the next section.

Elnaggar et al⁹⁹ used a method based on layer-by-layer deposition of liposomes (of sizes ≈120 and 20 nm) for the sustained release of NO from a modified stent. They coated stents with liposomes (the thickness of the layer was higher than ≈10 nm) encapsulating NONOate, which was trapped between layers of poly-L-lysine and hyaluronic acid-dopamine, providing a NO release profile of up to 5 days. In vitro results using human umbilical vein endothelial cells (HUVECs) exhibited significantly more endothelial cell proliferation and distinctly inhibited SMC proliferation. Scanning electron microscopy (SEM) analysis of on-stent endothelial layer formation demonstrated the effects of NO on rapid reendothelialization. Studies in pigs demonstrated efficacy in promoting arterial healing and preventing neointimal thickening.

Fan et al¹⁰⁰ reported the immobilization of nano-scale copper-based MOF (size range 10–500 nm) onto the surface of a titanium stent using polydopamine as a coating matrix, thereby allowing the copper-catalyzed generation of NO from endogenous sources. Cu-MOF were prepared by conversion of Cu(OH)₂ to CuBTC (BTC-1,3,5-benzenetricarboxylic acid) through an acid base reaction. Copper-catalyzed generation of NO from the surface of modified 316 L stainless stent resulted in suppression of platelet aggregation via NO-cGMP signaling and considerably reduced thrombosis in an *ex vivo* extracorporeal circulation model (Figure 4), as well as reducing neointimal hyperplasia in an arteriovenous shunt model. However, this approach relies on a plentiful supply of endogenous RSNO around the implanted stent, and further optimization is required to generate therapeutically relevant amounts of NO at the site of action. The efficacy of *in vivo* endothelialization of this copper-based MOF coating was demonstrated by the formation of an endothelial layer on the stent (confirmed by SEM) in comparison to the attachment of red blood cells and platelets on the uncoated stent.

In a similar approach, a copper-catecholamine-selenocystamine framework crosslinked with 3,4-dihydroxy-L-phenylalanine was coated onto the surface of a stainless-steel stent through a dip-

coating method by immersing the framework and stent into the reaction solution (dissolving Dopa hydrochloride, selenocystamine hydrochloride, and CuCl₂·2H₂O in Tris buffer) at room temperature for 24 h. This framework facilitates the interface with glutathione peroxidase (GPx) to promote catalytic activity, thereby resulting in controlled and slow release of NO from the coating.⁷⁹ This conferred good antithrombogenic activity, improved HUVEC migration, and inhibited proliferation of human umbilical artery smooth muscle cells in vitro, as well as improved antithrombogenicity, anti-restenosis, and endothelialization in rats *in vivo*. The formation of an endothelial layer on the stent surface was confirmed morphologically by SEM. Thus, effective suppression of restenosis and promotion of reendothelialization can be achieved by the continuous generation of NO in a controlled manner with a copper-catecholamine framework coated stent.

Microscale polymeric materials or fibers that release or generate NO have also been explored for stent applications. Examples include poly(lactic-co-glycolic acid) (PLGA),¹⁰¹ poly(vinyl alcohol) and poly(vinyl pyrrolidone),¹⁰² thermoplastic polyurethanes,¹⁰³ poly(methyl methacrylate),¹⁰⁴ and metallic thin films including titanium dioxide,⁷⁸ and readers are referred to specialized reviews on this topic.^{98,105,106} Such polymeric materials have shown promising results on re-endothelialization, but have limitations because of the accumulation of acidic degradation by-products, which alter pH and NO release kinetics. The NP approach advocated in this review provides additional benefits in terms of tunable properties, ease of functionalization, and high specific surface area to carry large quantities of NO. It is notable that the release rate of NO from NP-based stent coatings was similar to that of endothelial cells, ie, in the range of 0.5 to 4.0×10^{-10} mol cm⁻² min⁻¹.¹⁰⁰

Despite promising results using NO-producing stents in vitro and in animal models, the clinical translation of this approach presents a number of challenges and issues for further study. For example, efficacy may be limited by uneven distribution of catalytic complexes, limited NO source reservoir or NO-release kinetics, coating stability, biocompatibility, and, in particular, the potential formation of toxic nitrosamines and peroxynitrite during degradation.⁹⁸ Formulations must also be stable during storage and robust enough for percutaneous application even in difficult to reach vessels.

VASCULAR GRAFTS. The most frequently used synthetic polymer for vascular grafts is PCL due to its biocompatibility and advantageous mechanical

TABLE 1 Examples of NO-Releasing NPs for Cardiovascular Applications					
Application	Source of NO	Key Design Features	NO Release Profile Measured in PBS	Model System	Outcomes
Stent ¹⁴⁰	NO gas	Assembly of nanofibers (7–8 nm diameter) coating a 316 L stainless steel stent	4.8 μmol NO over 30 days	In vitro: HUVECs and aortic SMCs	Increased proliferation of endothelial cells and inhibited the proliferation of SMCs
Stent ^{78,141,142}	Various coatings with catalytic decomposition of endogenous GSNO	TiO ₂ film Metal-catecholamine assembly Copper-dopamine (Cu ^{II} -DA) network Immobilization of selenocystamine on nanomaterials followed by coating on a 316 stainless steel stent	TiO ₂ film: Generation of NO with a rate of $1 \times 10^{-10} \text{ mol cm}^{-2} \text{ min}^{-1}$ Metal-catecholamine assembly: over 30 days ranging $0.5\text{--}4 \times 10^{-10} \text{ mol cm}^{-2} \text{ min}^{-1}$ Cu ^{II} -DA network: NO release rate: $50 \times 10^{-10} \text{ mol cm}^{-2} \text{ min}^{-1}$	In vitro: smooth muscle cells In vivo: adult dog restenosis model and rabbit arteriovenous shunt model.	In vitro: NO generation in vitro inhibited platelet activation and aggregation In vivo: selenocystamine immobilized stents are endothelialized and showed significant antiproliferation properties ⁷⁰ Promoted re-endothelialization and improved antirestenosis ^{107,109}
Stent ⁹⁹	DETA NONOate	Liposomes Size: ≈120 and 20 nm Layer-by-layer coating on a stent	50% ^a of NO released over 16 h	In vitro: HUVEC In vivo: castrated male pig coronary injury model.	In vitro: Increased proliferation of endothelial cells and inhibited the proliferation of SMCs In vivo: NO stent induced higher endothelial coverage of $94\% \pm 4\%$ vs $34\% \pm 3\%$ for bare-metal stent
Stent ¹⁴³	SNAP	SeCA/Dopa coating onto 316 L stainless steel stent. Coating thickness: 9.1–16.1 nm	$0.5\text{--}4 \times 10^{-10} \text{ mol cm}^{-2} \text{ min}^{-1}$ over 60 days	In vitro: HUASMC and HUVECs In vivo: New Zealand white rabbit arteriovenous shunt model Ex vivo: New Zealand white rabbit circulation thrombogenicity model	In vitro: Increased proliferation of endothelial cells and inhibited the proliferation of SMCs via up-regulation of cGMP synthesis In vivo: release of NO induced by coated stents enhanced re-endothelialization and reducing in-stent restenosis
Stent ^{69,79,128,144}	Various coatings utilizing GSNO	Titanium dioxide nanotube Hydrogels (composed of alginate and gelatin). Nanoscale copper-based MOF Polymeric NPs: PLGA, PEG, and PCL coated onto the surface of stainless-steel stent	Ti ₂ O nanotubes: NO release rate: $\sim 1.5 \times 10^{-10} \text{ mol cm}^{-2} \text{ min}^{-1}$. Hydrogels: NO release rate: $6.2 \times 10^{-10} \text{ mol cm}^{-2} \text{ min}^{-1}$ MOF: $2.4 \times 10^{-10} \text{ mol cm}^{-2} \text{ min}^{-1}$ Polymeric NPs: NO generation up to $61 \pm 10\%$ from GSNO	In vitro: HUVECs, HUASMCs, and Mouse macrophage lineage cells In vivo: rats and rabbits arteriovenous shunt model; male Bama miniature pig of arteriovenous shunt model	In vitro: coated surface significantly improved endothelial cell growth and inhibited SMC proliferation In vivo: modified stents have rapid re-endothelialization, anti-inflammation, and anti-intimal hyperplasia abilities, compared with the unmodified stents
Artificial blood vessel ⁸⁰	NO-generating coatings, Source: GSNO	Cu-MOF nanoparticles into PCL fibers Size: 438 nm		In vitro: HUVECs Ex vivo: male Sprague Dawley rats of abdominal artery replacement model	Embedded Cu-MOFs for slow release of copper ions and sustained NO production. Significantly increased endothelial cell growth while largely inhibited SMC proliferation
Vascular graft ^{81,138,145,146}	Catalytic decomposition of GSNO and S-nitrosated keratin	PCL based nanofiber assembly Diameter: 263 ± 90 nm POSS-PCU NO-eluting polymer-based small diameter bypass graft	NO release rate: 250 $\mu\text{g}/\text{mL}$, $\sim 1.4 \text{ mmol/L}$ at 24 h	In vitro: HUVECs and HASMCs In vivo: rabbit carotid artery replacement; mouse model of atherosclerosis	Modified graft significantly increased endothelial cell growth while largely inhibited SMC proliferation both in vitro ^{73,101,110,111} and in vivo models ^{73,101}
Vascular injury ⁸²	NO gas	Liposomes of phospholipids and cholesterol	Release: 1.6 μmol over 60 min from NO/argon-containing liposomes. NO release was measured in PBS	In vitro: VSMC In vivo: male New Zealand White rabbits fed an atherogenic diet 2 wks before balloon injury of carotid artery	Liposomes taken up by SMC and significantly inhibited proliferation In vivo: NPs incubated at time of injury reduced neointimal hyperplasia and reduced arterial wall thickening 14 d postinjury

Continued on the next page

TABLE 1 Continued

Application	Source of NO	Key Design Features	NO Release Profile Measured in PBS		Model System	Outcomes
Blood vessel ¹⁴⁷	NO gas	PEG-Lys ₅ -NO hydrogels	PEG-Lys ₅ -NO hydrogels released 89% of NO over 60 d	In vitro: bovine aortic endothelial cells and rat aortic smooth muscle cells In vivo: rat carotid balloon injury model	In vitro: promoted endothelial cell growth and inhibited smooth muscle cell proliferation In vivo: NO-releasing hydrogels were applied to the outer surfaces of carotid. NO was allowed to diffuse into the vessel and intimal thickening was reduced by ~90%	
Hypoxia/reoxygenation model of cardiomyocyte injury ¹⁴⁸	DETA NONOate	Nanofibers	NO release: 1.26 μmol·mg ⁻¹	In vitro: H9c2 cells (immortalized embryonic rat heart myoblasts)	NO-releasing nanofibers prior to hypoxia induction were cytoprotective against reoxygenation injury. Inhibited the generation of hydrogen peroxide, a major contributor to oxidative damage	
Myocardial ischemia/reperfusion injury ⁸³	SNAP + GSH	Nanometer scale 4- polyamidoamine dendrimers	NO release rate: 1,429 ppb NO mg ⁻¹ of SNAP s ⁻¹ (191 pmol NO mg ⁻¹ s ⁻¹ after 45 min)	In vitro: HUVEC and pulmonary artery endothelial cells (CPA-47 cells-calf pulmonary artery 47) Ex vivo: perfused heart of male Sprague-Dawley rats	Dendrimers localized near the cell surface and exposed to levels of GSH sufficient to initiate NO release resulting in high local concentrations of NO. Increased cell survival and reduced myocardial injury	
Cardiac tissue engineering ^{117,124,125}	Catalytic decomposition of GSNO	Electrospun PCL/PK based nanofibrous mats PCL/keratin/Gold NP mats	10 μmol up to 36 h	In vitro: HUVECs and HUASMCs	The biocomposite selectively enhanced adhesion, migration, and growth of ECs while suppressing proliferation of SMCs in the presence of glutathione (GSH) and GSNO	
Atherosclerotic plaque ¹³⁸	SNO-phospholipid	High-density lipoprotein (HDL-like) NPs Size: 13.1 ± 0.7 nm	NO release rate: 80% ^a at 24 h	In vitro: AoSMCs In vivo: ApoE knockout fed high-fat diet for 18 weeks. NPs given 3× per wk IV for final 6 wks	In vitro: NO-releasing NPs reduced SMC migration In vivo: atherosclerotic area was 42% lower in NP-treated mice compared with controls, thereby demonstrating reduction in plaque burden	

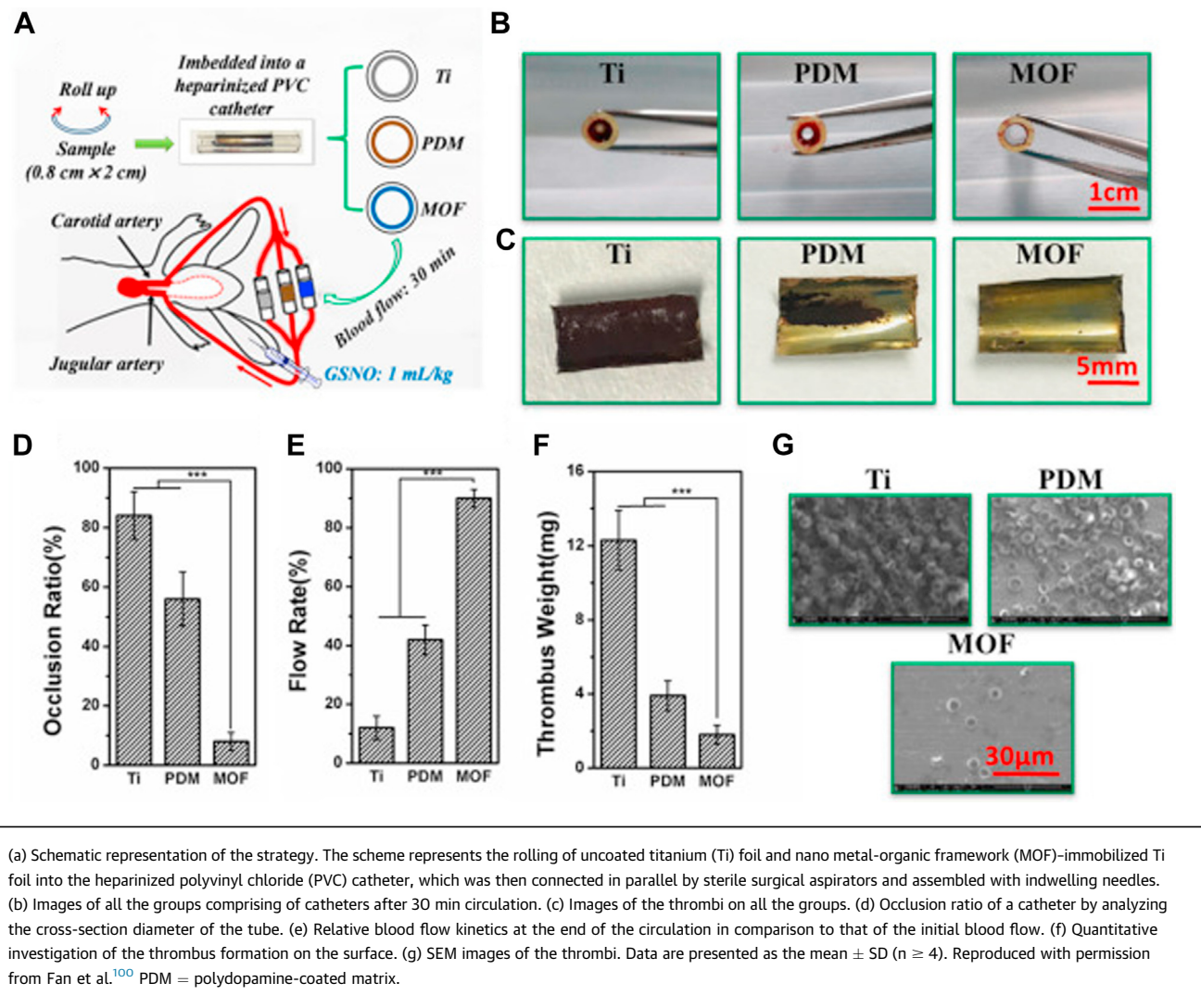
^aThe release data provided was insufficient and could not be used to calculate moles.

DETA NONOates = diethylenetriamine N-diazenuimidolates; GSH = glutathione; GSNO = S-nitrosoglutathione; HASMC = human aortic smooth muscle cell; HUASMC = human umbilical artery smooth muscle cell; HUVEC = human umbilical vein endothelial cell; MOF = metal organic framework; NO = nitric oxide; NP = nanoparticle; PCL = poly(ε-caprolactone); PCL/PK = poly(ε-caprolactone)/phosphobetainized keratin; POSS-PCU; polyhedral oligomeric silsesquioxane poly(carbonate-urea)urethane; RSNO = S-nitrosothiol; SMC = smooth muscle cell; SNAP = S-nitroso-N-acetylpenicillamine; VSMC = vascular smooth muscle cell.

properties. However, the hydrophobicity of PCL may induce thrombosis and intimal hyperplasia, for which the protective effect of NO has been investigated.¹⁰⁷

Seifalian et al^{98,107,108} have developed a class of polymeric nanocomposites, such as polyhedral oligomeric silsesquioxane poly(carbonate-urea)urethane (POSS-PCU), to modify a variety of surgical implants, aimed at releasing NO in a targeted manner. de Mel et al¹⁰⁸ reported the incorporation of SNAP and GSNO into POSS-PCU-based bypass grafts for the in situ release of NO in the presence of pulsatile flow. This study revealed that NO release from POSS-PCU helped inhibit platelet and SMC adhesion while stimulating endothelial cell adhesion tested in endothelial progenitor stem cells and SMCs. The release profile reported in this study was 10 nmol/L NO over the first 10 minutes with a continuous

diminution up to day 7. Clearly, a longer duration of NO release from vascular grafts would be desirable. Zhan et al⁸⁰ investigated the potential of electrospun Cu-MOF NPs (average size 438 nm) into PCL. MOF NPs were prepared by the reaction between organic molecules and metal ions, and vascular scaffolds were prepared by electrospinning PCL and MOF NP solution. This approach helped avoid the interaction of Cu-MOFs with serum and considerably slowed the leaching of copper ions, thereby allowing for longer-term NO catalytic capacity in serum over 6 hours. This composite promoted accelerated endothelial cell migration and supported the monolayer development of endothelial cells in HUVECs and human SMCs as well as rat abdominal artery replacement and arteriovenous shunt models. The formation and coverage of a confluent layer of endothelial cells on grafts were

FIGURE 4 Ex Vivo Assessment of the Antithrombogenic Characteristics of the Nanoscale Cu-MOF Coating in an Arteriovenous Shunt Model

(a) Schematic representation of the strategy. The scheme represents the rolling of uncoated titanium (Ti) foil and nano metal-organic framework (MOF)-immobilized Ti foil into the heparinized polyvinyl chloride (PVC) catheter, which was then connected in parallel by sterile surgical aspirators and assembled with indwelling needles. (b) Images of all the groups comprising of catheters after 30 min circulation. (c) Images of the thrombi on all the groups. (d) Occlusion ratio of a catheter by analyzing the cross-section diameter of the tube. (e) Relative blood flow kinetics at the end of the circulation in comparison to that of the initial blood flow. (f) Quantitative investigation of the thrombus formation on the surface. (g) SEM images of the thrombi. Data are presented as the mean ± SD ($n \geq 4$). Reproduced with permission from Fan et al.¹⁰⁰ PDM = polydopamine-coated matrix.

assessed by SEM, demonstrating a much higher endothelialization rate compared with the control graft.

MYOCARDIAL ISCHEMIA-REPERFUSION INJURY AND MYOCARDIAL INFARCTION. Following a myocardial infarction, timely reperfusion of the occluded coronary artery is the most effective intervention to minimize ischemic injury. However, reperfusion itself also induces injury because of a variety of cellular stresses, such as high intracellular calcium, rising pH, and generation of ROS, that culminate with mitochondrial depolarization and cardiomyocyte cell death. Such damage is termed ischemia/reperfusion (I/R) injury, and multiple lines of evidence suggest a protective effect of NO.^{109,110}

For example, canonical NO signaling via eNOS and protein kinase G helps mediate ischemic preconditioning, whereby brief periods of ischemia before an infarct reduce subsequent myocardial injury.¹¹¹ NO generation via eNOS is also integral to the RISK (Reperfusion Injury Salvage Kinase) pathway, which when stimulated during early reperfusion, ultimately inhibits mitochondrial depolarization and limits cell death.¹¹² NO is also thought to have direct cardioprotective effects via S-nitrosation of thiols in key mitochondrial proteins, in particular, complex I. Rapid reactivation of complex I early during reperfusion is a major source of H₂O₂, which contributes to oxidative damage and cell death; however, reversible S-nitrosation mitigates against this by maintaining

complex I in a low activity state.¹¹³ This protective effect has been elegantly demonstrated by the Murphy laboratory, which has created MitoSNO by covalently linking SNAP to a triphenylphosphonium cation group, providing mitochondrial targeting because of its lipophilicity and positive charge. When MitoSNO was given to Langendorff-perfused mouse hearts at the point of reperfusion, it significantly reduced infarct size and improved functional recovery.¹¹⁴ This provides proof-of-concept for the mitochondrial targeting of NO during early reperfusion, although, as with all potential I/R therapies, it is inherently difficult to target the site of injury at a time when blood flow is impaired.

Although the previous example is a small molecule approach, there is potential to target these pathways using NPs. Schoenfisch laboratory has developed and patented wide-ranging innovative NPs (porous silica, dendrimers, and other polymeric NPs) for the storage and release of NO, which have primarily been tested for the treatment of bacterial infections.²³ In 2010, they explored the ability of functionalized dendrimer NPs for reduction of I/R injury in the isolated, perfused rat heart.⁸³ Dendrimers were prepared by following a thiol-yne chemistry method. Each multi-branched dendrimer was designed to optimize cellular uptake and bioavailability and was conjugated to 64 molecules of SNAP. Hearts were also exposed to varying concentrations of reduced glutathione (GSH), which represents an important variable in vivo, because it can chemically reduce S-nitrosothiols (such as SNAP) through direct transnitrosation.¹¹⁵ Thus, NO release was found to be much higher in the presence of GSH compared with dendrimer-SNAP alone, and the GSH levels effectively determined NO release kinetics.⁸³ Optimal doses of dendrimer-SNAP and GSH were determined to establish a proof-of-principle reduction in infarct size, although low experimental numbers urge caution with interpretation of these findings. Further work is needed to determine the cellular uptake and fate of these dendrimers and for confirmation in clinically-relevant in vivo models.

It should be noted that NO may represent a double-edged sword in I/R injury. Cardioprotection depends on the timely and temporary delivery of controlled amounts of NO to the mitochondria. However, the coexistence of excess superoxide anion radicals can lead to formation of highly toxic peroxynitrite.¹¹⁶ Peroxynitrite is a powerful oxidizing and nitrating agent that can target multiple substrates resulting in membrane lipid peroxidation, mitochondrial damage, disturbances in cell signaling, apoptosis, and necrosis. Therefore, the release of NO from NPs using

exogenous NO sources will need to be fine-tuned to achieve optimal therapeutic effects for I/R injury.

TISSUE ENGINEERING. Cardiovascular tissue engineering holds promise for the repair and regeneration of injured myocardium, heart valves, and blood vessels, but this requires strong coupling with surrounding native tissues. In particular, vascular grafts can be problematic for small diameter vessels because of issues of patency, so there is interest in developing scaffolds to mimic the extracellular matrix that can either be seeded with stem cells in vitro or that promote natural angiogenesis to grow new vessels in situ. Challenges include biocompatibility, promoting endothelialization while suppressing SMC hyperplasia, and preventing hypercoagulation.¹¹⁷ Hence, it is no surprise that NO-generating/releasing scaffolds have been developed for vascular tissue engineering. Scaffolds are 3-dimensional porous networks formed from natural or synthetic materials, which provide an ideal 3-dimensional microenvironment to promote cell-cell communication, cell attachment, migration, differentiation, and proliferation. Such scaffolds for cardiac tissue engineering applications generally comprise of natural or synthetic materials, including polymers, collagens, silk, alginate, chitosan, and hydrogels, because of their good mechanical strength and favorable degradation profiles.¹¹⁸ Scaffolds have been used extensively for cardiac tissue engineering applications, specifically in ischemic heart diseases, and cardiac patches,¹¹⁹⁻¹²³ but there are limited studies using NO-based technology.

The group of Shen and colleagues has published a series of papers^{117,124-126} using an electrospun scaffold of PCL/keratin mats (size 457 ± 53 nm) functionalized with gold NPs (size 22.1 ± 4.5 nm)¹¹⁷ for use as tissue-engineered vascular grafts. This represents a typical application for cardiovascular tissue engineering where vascular or stem cells are seeded onto biodegradable scaffolds to regenerate vascular tissues instead of an autologous blood vessel.¹²⁷ In recent years, keratin, a natural component of human hair, skin, and nails, has been appreciated as a biomaterial providing excellent biocompatibility and biodegradability. Moreover, cysteine is a key component of keratin, which further facilitates the decomposition of endogenous sources of NO, catalyzed by the gold NPs. These functionalized scaffolds were able to catalyze NO generation when tested in vitro, improving HUVEC growth and inhibiting human umbilical artery smooth muscle cells viability.¹¹⁷ Further work is required to realize the potential for use in tissue engineering by testing the effects on endothelialization and SMC proliferation in vivo.

There are a few studies where NO-releasing/generating scaffolds based on hydrogels¹²⁸ or other polymers, PLGA, or PCL¹²⁹ have been studied for use in cardiovascular applications specifically in tissue-engineered vascular grafts and have been discussed elsewhere.^{130,131} In NO-releasing tissue engineering approaches, micron-sized materials have been used as NO carriers because of their ability to store high amount of NO.^{117,124,131}

OTHER APPLICATIONS OF NO-RELEASING NPs. Angiogenesis is characterized by the growth of new blood vessels sprouting from other pre-existing small vessels and plays a critical role in the response to tissue ischemia and wound healing as well as being a major goal in tissue engineering. Angiogenesis is promoted by several growth factors, such as vascular endothelial growth factor and basic fibroblast growth factor, which stimulate quiescent endothelial cells into a highly proliferative state.¹³² NO is an important regulator of endothelial function affecting angiogenesis.^{133,134} Yang et al¹³⁵ developed NONOate-incorporated methoxy poly(ethylene glycol)-b-poly(lactic-co-glycolic acid) (mPEG-PLGA) NPs of 200 nm size with NO release of ~80% in 24 hours. The induction of angiogenesis was evaluated by tube formation, which shows the formation of capillary-like structures. They demonstrated that the tubular formation increased 190% in NO-releasing NP-treated groups in comparison to the control group. The induction of angiogenesis was evaluated ex vivo using rat aorta treated with NO-releasing NPs and revealed sprouting angiogenesis. In another study, Lee et al¹³⁶ reported DETA NONOate incorporated mPEG-PLGH-thiobenzamide NPs of 140 nm size and showed that NO-releasing NPs released up to 20 nmol over 72 hours and exhibited enhanced angiogenesis compared with the control groups in both in vitro (HUVECs and 3T3-L1) and ex vivo (rat aorta) models.

Endothelial dysfunction associated with a deficiency of NO is broadly acknowledged as an integral first step in the development of atherosclerosis.¹³⁷ Hence, several groups have experimented with the systemic administration of NP NO donors. Rink et al¹³⁸ described the synthesis of RSNO phospholipid (S-nitrosylated 1,2-dipalmitoyl-sn-glycero-3-phosphonitrosothioethanol) within an outer phospholipid shell composed of a naturally abundant high-density lipoprotein (HDL). HDL NPs were synthesized by reductive methylation of apolipoprotein A-I by 3H-formaldehyde. Such NO-releasing HDL NPs retain many of the properties of natural HDLs, thereby improving biocompatibility and targeting to the vasculature. ApoE knockout mice were fed a high-

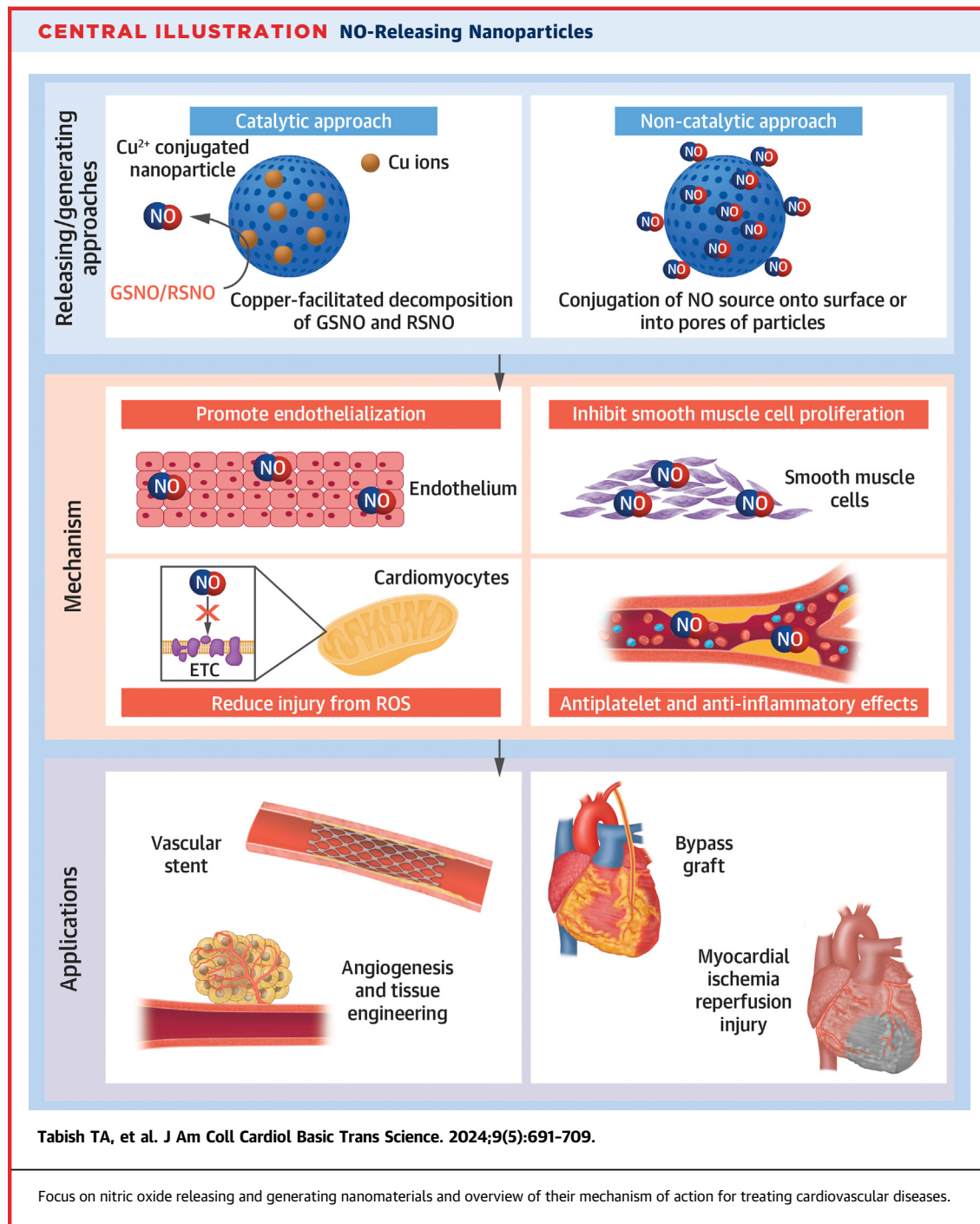
fat diet for 18 weeks, with treatment given by intravenous injection 3 times/wk from week 12 onwards. Compared with vehicle-administered control subjects, treatment with functionalized HDL NPs reduced atherosclerotic plaque burden by 42%.¹³⁸

Mohamed et al¹³⁹ developed NO-releasing polymeric NPs based on a polyvinylpyrrolidone composite incorporating nitrite and a reducing agent as the NO source. Polymeric NPs were prepared via ionotropic gelation technique. In aqueous solution, steady-state NO release was obtained within 7 minutes and lasted for 2 hours, followed by a 50% lower release phase that was sustained for at least 8 hours. NO-releasing NPs caused dose-dependent relaxations of pulmonary arteries taken from mice with hypoxia-induced pulmonary artery hypertension without altering the viability of endothelial cells.

Huang et al⁸² formulated liposomes comprising phospholipids and cholesterol that encapsulate NO gas. Liposomes were prepared by modified pressured-freeze method. NO-release kinetics could be controlled via the incorporation of argon, with formulations releasing 1.6 μmol over 60 minutes and providing sustained and slow release over 8 hours. Delivery of NO to vascular smooth muscle cells was 7-fold higher using the liposomes compared with uncaged NO, and remained high even in the presence of hemoglobin, indicating that this formulation improves bioavailability by protecting against NO scavenging. Efficacy was tested in a rabbit model of carotid artery vascular balloon injury, where NO-releasing liposomes were incubated in the artery for 2 minutes immediately after injury, and the damage was assessed by histology 2 weeks later. NO-releasing liposomes significantly reduced neointimal hyperplasia, and there was a 41% reduction in arterial wall thickening.⁸² Table 1 summarizes NO-releasing NPs for use in cardiovascular applications.

TRANSLATIONAL CONSIDERATIONS AND FUTURE OUTLOOK

This review has examined a wide range of NO-releasing and -generating NP formulations designed and tested for the potential treatment of CVD. Promising proof-of-principle data have been presented for a variety of different applications, such as vascular stents and bypass grafts, I/R injury, atherosclerosis, and tissue engineering (Central Illustration). There are currently 214 NO-related clinical trials for CVD applications registered (visited on July 24, 2022) at ClinicalTrials.gov. However, there are currently no



clinical trials on NO-releasing NPs for CVD applications, and this reflects the need for additional pre-clinical studies to overcome a number of limitations and unknowns.

For example, there are many variables in NP design that require optimization for any given application,

e.g., nanomaterial selection, structural design, physicochemical properties, and fabrication procedures. There are multiple choices for the source of NO and how these are incorporated into the NPs. Any formulation must be stable during storage and provide targeted, reproducible NO generation with

Tabish TA, et al. J Am Coll Cardiol Basic Trans Science. 2024;9(5):691-709.

clearly defined kinetics and duration. It is a major limitation that we lack methods for real-time monitoring/tracking of NO release *in vivo*, where there are also challenges with systemic administration and concerns about long-term toxicity. It is therefore important to understand issues relating to cellular accumulation, breakdown, and elimination of NPs. Large animal work is needed to generate more meaningful and translatable findings, particularly in relation to the development of stents, but also for I/R therapies.

One major barrier to progress with NO-releasing nanoformulations is the need for multidisciplinary teams spanning materials science, engineering, chemistry, biotechnology, pharmacology, and cardiovascular medicine. It is hoped that interdisciplinary fellowships will help bridge that gap. Nevertheless, we believe that recent advances in nanotechnology, particularly in relation to materials and fabrication techniques, will boost research into NO-releasing/generating formulations. For example, since the discovery of graphene in 2003, it has been widely investigated for image-guided drug delivery and sensing applications mainly for cancer and infectious diseases. However, graphene-based nanomaterials have not yet been developed for NO storage and release purposes despite highly favorable characteristics, eg, ultra-small size, exceptionally high surface area, and a wide variety of shapes and morphologies (graphene quantum dots, graphene oxide,

reduced graphene oxide, porous graphene nanosheets, graphene nanoplatelets, graphene aerogels/hydrogels, graphene foam).

NO-releasing NPs could also be extended to other CVD applications, such as angina and peripheral vascular disease. Modification of NPs may help minimize toxicity and adverse effects, eg, by favoring specific metabolic pathways or preventing drugs crossing the blood-brain barrier. It is also possible to adapt NPs as a delivery vehicle for other payloads such as hydrogen sulfide, carbon monoxide, nucleic acids, siRNA, DNA, peptides, proteins, and antibodies. Clearly this field is still in its infancy, but the detailed study of NPs for cardiovascular disease applications is an attractive prospect that promises to open up a new paradigm of highly tunable drug delivery.

FUNDING SUPPORT AND AUTHOR DISCLOSURES

This work was supported by a British Heart Foundation (BHF) Fellowship (FS/ATA/21/20015) to Dr Tabish. Work in the authors' laboratory is funded by BHF programme grant (RG/18/12/34040) to Dr Lygate. All other authors have reported that they have no relationships relevant to the contents of this paper to disclose.

ADDRESS FOR CORRESPONDENCE: Dr Tanveer A. Tabish OR Dr Craig A. Lygate, Wellcome Centre for Human Genetics, University of Oxford, Old Road Campus, Roosevelt Drive, Oxford, England OX3 7BN, United Kingdom. E-mail: tanveer.tabish@cardiov.ox.ac.uk OR craig.lygate@cardiov.ox.ac.uk.

REFERENCES

- Roth GA, Johnson C, Abajobir A, et al. Global, regional, and national burden of cardiovascular diseases for 10 causes, 1990 to 2015. *J Am Coll Cardiol*. 2017;70:1-25.
- Vanhoutte PM, Zhao Y, Xu A, Leung SW. Thirty years of saying NO: sources, fate, actions, and misfortunes of the endothelium-derived vasodilator mediator. *Circ Res*. 2016;119:375-396.
- Vanhoutte PM, Shimokawa H, Feletou M, Tang EH. Endothelial dysfunction and vascular disease - a 30th anniversary update. *Acta Physiol (Oxf)*. 2017;219:22-96.
- Bendall JK, Douglas G, McNeill E, Channon KM, Crabtree MJ. Tetrahydrobiopterin in cardiovascular health and disease. *Antioxid Redox Signal*. 2014;20:3040-3077.
- Lundberg JO, Weitzberg E. Nitric oxide signaling in health and disease. *Cell*. 2022;185:2853-2878.
- Simon JN, Duglan D, Casadei B, Carnicer R. Nitric oxide synthase regulation of cardiac excitation-contraction coupling in health and disease. *J Mol Cell Cardiol*. 2014;73:80-91.
- Naseem KM. The role of nitric oxide in cardiovascular diseases. *Mol Aspects Med*. 2005;26:33-65.
- Farah C, Michel LYM, Balligand JL. Nitric oxide signalling in cardiovascular health and disease. *Nat Rev Cardiol*. 2018;15:292-316.
- Forsythe P, Gilchrist M, Kulka M, Befus AD. Mast cells and nitric oxide: control of production, mechanisms of response. *Int Immunopharmacol*. 2001;11:1525-1541.
- Galkina E, Ley K. Immune and inflammatory mechanisms of atherosclerosis. *Annu Rev Immunol*. 2009;27:165-197.
- Tsihlis ND, Oustwani CS, Vavra AK, Jiang Q, Keefer LK, Kibbe MR. Nitric oxide inhibits vascular smooth muscle cell proliferation and neointimal hyperplasia by increasing the ubiquitination and degradation of UbcH10. *Cell Biochem Biophys*. 2011;60:89-97.
- Carpenter AW, Schoenfisch MH. Nitric oxide release: part II. Therapeutic applications. *Chem Soc Rev*. 2012;41:3742-3752.
- Broniowska KA, Hogg N. The chemical biology of S-nitrosothiols. *Antioxid Redox Signal*. 2012;17:969-980.
- Li L, Li L. Recent advances in multinuclear metal nitrosyl complexes. *Coord Chem Rev*. 2016;306:678-700.
- Burgaud JL, Ongini E, Del Soldato P. Nitric oxide-releasing drugs: a novel class of effective and safe therapeutic agents. *Ann N Y Acad Sci*. 2002;962:360-371.
- Riccio DA, Schoenfisch MH. Nitric oxide release: part I. Macromolecular scaffolds. *Chem Soc Rev*. 2012;41:3731-3741.
- El-Ferzli GT, Andukuri A, Alexander G, et al. A nitric oxide-releasing self-assembled peptide amphiphile nanomatrix for improving the biocompatibility of microporous hollow fibers. *ASAIO J*. 2015;61:589-595.
- Li X, Zhang Y, Sun J, et al. Protein nanocage-based photo-controlled nitric oxide releasing platform. *ACS Appl Mater Interfaces*. 2017;9:19519-19524.
- Jin G, Gao Z, Liu Y, et al. Polymeric nitric oxide delivery nanoplatforms for treating cancer, cardiovascular diseases, and infection. *Adv Healthc Mater*. 2021;10:e2001550.
- Zhang K, Chen X, Li H, et al. A nitric oxide-releasing hydrogel for enhancing the therapeutic effects of mesenchymal stem cell therapy for hindlimb ischemia. *Acta Biomater*. 2020;113:289-304.

- 21.** Ghalei S, Hopkins S, Douglass M, Garren M, Mondal A, Handa H. Nitric oxide releasing halloysite nanotubes for biomedical applications. *J Colloid Interface Sci.* 2021;590:277–289.
- 22.** Huang Z, Fu J, Zhang Y. Nitric oxide donor-based cancer therapy: advances and prospects. *J Med Chem.* 2017;60:7617–7635.
- 23.** Yang L, Feura ES, Ahonen MJR, Schoenfisch MH. Nitric oxide-releasing macromolecular scaffolds for antibacterial applications. *Adv Healthc Mater.* 2018;7:e1800155.
- 24.** Poh WH, Rice SA. Recent developments in nitric oxide donors and delivery for antimicrobial and anti-biofilm applications. *Molecules.* 2022;27:1–38.
- 25.** Barst RJ, Channick R, Ivy D, Goldstein B. Clinical perspectives with long-term pulsed inhaled nitric oxide for the treatment of pulmonary arterial hypertension. *Pulm Circ.* 2012;2:139–147.
- 26.** Divakaran S, Loscalzo J. The role of nitroglycerin and other nitrogen oxides in cardiovascular therapeutics. *J Am Coll Cardiol.* 2017;70:2393–2410.
- 27.** McDonagh TA, Metra M, Adamo M, et al. for the ESC Scientific Document Group. 2021 ESC guidelines for the diagnosis and treatment of acute and chronic heart failure. *Eur Heart J.* 2021;42:3599–3726.
- 28.** Cohn JN, Archibald DG, Ziesche S, et al. Effect of vasodilator therapy on mortality in chronic congestive heart failure. Results of a Veterans Administration Cooperative Study. *N Engl J Med.* 1986;314:1547–1552.
- 29.** Taylor AL, Ziesche S, Yancy C, et al. Combination of isosorbide dinitrate and hydralazine in blacks with heart failure. *N Engl J Med.* 2004;351:2049–2057.
- 30.** Munzel T, Daiber A, Mulsch A. Explaining the phenomenon of nitrate tolerance. *Circ Res.* 2005;97:618–628.
- 31.** Chen Z, Foster MW, Zhang J, et al. An essential role for mitochondrial aldehyde dehydrogenase in nitroglycerin bioactivation. *Proc Natl Acad Sci U S A.* 2005;102:12159–12164.
- 32.** Franca-Silva MS, Balarini CM, Cruz JC, Khan BA, Rampelotto PH, Braga VA. Organic nitrates: past, present and future. *Molecules.* 2014;19:15314–15323.
- 33.** Munzel T, Daiber A, Gori T. More answers to the still unresolved question of nitrate tolerance. *Eur Heart J.* 2013;34:2666–2673.
- 34.** Han B, Song M, Li L, Sun X, Lei Y. The application of nitric oxide for ocular hypertension treatment. *Molecules.* 2021;26.
- 35.** Fitzhugh AL, Keefer LK. Diazeniumdiolates: pro- and antioxidant applications of the "NON-Oates.". *Free Radic Biol Med.* 2000;28:1463–1469.
- 36.** Kevil CG, Patel RP. S-Nitrosothiol biology and therapeutic potential in metabolic disease. *Curr Opin Investig Drugs.* 2010;11:1127–1134.
- 37.** Pelegrino MT, Pieretti JC, Lange CN, et al. Foliar spray application of CuO nanoparticles (NPs) and S-nitrosoglutathione enhances productivity, physiological and biochemical parameters of lettuce plants. *J Chem Technol Biotechnol.* 2021;96:2185–2196.
- 38.** Liu S, Li G, Ma D. Controllable nitric oxide-delivering platforms for biomedical applications. *Advanced Therapeutics.* 2022;5:2100227.
- 39.** Liu R, Peng Y, Lu L, Peng S, Chen T, Zhan M. Near-infrared light-triggered nano-prodrug for cancer gas therapy. *J Nanobiotechnology.* 2021;19:443.
- 40.** Hadef F. An Introduction to nanomaterials. In: Dasgupta N, Ranjan S, Lichtfouse E, eds. *Environmental Nanotechnology. Environmental Chemistry for a Sustainable World.* Vol 14. Springer; 2018.
- 41.** Tabish TA, Hayat H, Abbas A, Narayan RJ. Graphene quantum dots-based electrochemical biosensing platform for early detection of acute myocardial infarction. *Biosensors (Basel).* 2022;12:1–11.
- 42.** Tabish TA, Dey P, Mosca S, Salimi M, Palombo F, Matousek P, Stone N. Smart gold nanostructures for light mediated cancer theranostics: combining optical diagnostics with photothermal therapy. *Adv Sci (Weinh).* 2020;7:1903441.
- 43.** Tabish TA, Chabi S, Ali M, Xia Y, Jabeen F, Zhang S. Tracing the bioavailability of three-dimensional graphene foam in biological tissues. *Materials (Basel).* 2017;10:1–13.
- 44.** Tabish TA, Zhang S, Winyard PG. Developing the next generation of graphene-based platforms for cancer therapeutics: the potential role of reactive oxygen species. *Redox Biol.* 2018;15:34–40.
- 45.** Garnett E, Mai L, Yang P. Introduction: 1D nanomaterials/nanowires. *Chem Rev.* 2019;119:8955–8957.
- 46.** Tabish TA, Narayan RJ. Crossing the blood-brain barrier with graphene nanostructures. *Mater Today.* 2021;51:393–401.
- 47.** Ali ME, Ullah M, Maamor A, Hamid SBA. Surfactant assisted ball milling: a simple top down approach for the synthesis of controlled structure nanoparticle. *Advanced Materials Research.* 2013;832:356–361.
- 48.** Manawi YM, Ihsanullah, Samara A, Al-Ansari T, Atieh MA. A review of carbon nanomaterials' synthesis via the chemical vapor deposition (CVD) method. *Materials (Basel).* 2018;11:1–36.
- 49.** Ma X-H, Cho K-H, Sung Y-M. Growth mechanism of vertically aligned SnSe nanosheets via physical vapour deposition. *CrystEngComm.* 2014;16:5080–5086.
- 50.** Lei C, Wang C, Chen W, He M, Huang B. Poly-aniline@magnetic chitosan nanomaterials for highly efficient simultaneous adsorption and in-situ chemical reduction of hexavalent chromium: Removal efficacy and mechanisms. *Sci Total Environ.* 2020;733:139316.
- 51.** Mackenzie JD, Bescher EP. Chemical routes in the synthesis of nanomaterials using the sol-gel process. *Acc Chem Res.* 2007;40:810–818.
- 52.** Yang Y, Waterhouse GIN, Chen Y, Sun-Waterhouse D, Li D. Microbial-enabled green biosynthesis of nanomaterials: Current status and future prospects. *Biotechnol Adv.* 2022;55:107914.
- 53.** Wang L, Ezazi NZ, Liu L, et al. Microfibers synthesized by wet-spinning of chitin nanomaterials: mechanical, structural and cell proliferation properties. *RSC Adv.* 2020;10:29450–29459.
- 54.** Mitchell MJ, Billingsley MM, Haley RM, Wechsler ME, Peppas NA, Langer R. Engineering precision nanoparticles for drug delivery. *Nat Rev Drug Discov.* 2021;20:101–124.
- 55.** Sadekar S, Ghandehari H. Transepithelial transport and toxicity of PAMAM dendrimers: implications for oral drug delivery. *Adv Drug Deliv Rev.* 2012;64:571–588.
- 56.** Rostamabadi H, Falsafi SR, Jafari SM. Nano-encapsulation of carotenoids within lipid-based nanocarriers. *J Control Release.* 2019;298:38–67.
- 57.** Yadav D, Sandeep K, Pandey D, Dutta RK. Liposomes for drug delivery. *J Biotechnol Biomater.* 2017;2017:1–8.
- 58.** Wigglesworth KM, Racki WJ, Mishra R, Szomolanyi-Tsuda E, Greiner DL, Galili U. Rapid recruitment and activation of macrophages by anti-Gal/alpha-Gal liposome interaction accelerates wound healing. *J Immunol.* 2011;186:4422–4432.
- 59.** Smith DJ, Chakravarthy D, Pulfer S, et al. Nitric oxide-releasing polymers containing the [NO]NO₂ group. *J Med Chem.* 1996;39:1148–1156.
- 60.** Quinn JF, Whittaker MR, Davis TP. Delivering nitric oxide with nanoparticles. *J Control Release.* 2015;205:190–205.
- 61.** Polizzi MA, Stasko NA, Schoenfisch MH. Water-soluble nitric oxide-releasing gold nanoparticles. *Langmuir.* 2007;23:4938–4943.
- 62.** Urzedo AL, Goncalves MC, Nascimento MHM, Lombello CB, Nakazato G, Seabra AB. Cytotoxicity and antibacterial activity of alginate hydrogel containing nitric oxide donor and silver nanoparticles for topical applications. *ACS Biomater Sci Eng.* 2020;6:2117–2134.
- 63.** Douglass ME, Goudie MJ, Pant J, et al. Catalyzed nitric oxide release via Cu nanoparticles leads to an increase in antimicrobial effects and hemocompatibility for short term extracorporeal circulation. *ACS Appl Bio Mater.* 2019;2:2539–2548.
- 64.** Malone-Povolny MJ, Schoenfisch MH. Extended nitric oxide-releasing polyurethanes via S-nitrosothiol-modified mesoporous silica nanoparticles. *ACS Appl Mater Interfaces.* 2019;11:12216–12223.
- 65.** Wheatley PS, Butler AR, Crane MS, et al. NO-releasing zeolites and their antithrombotic properties. *J Am Chem Soc.* 2006;128:502–509.
- 66.** Zhou Y, Yang T, Liang K, Chandrawati R. Metal-organic frameworks for therapeutic gas delivery. *Adv Drug Deliv Rev.* 2021;171:199–214.
- 67.** Taite LJ, West JL. Poly(ethylene glycol)-lysine dendrimers for targeted delivery of nitric oxide. *Journal of Biomaterials. Science, Polymer Edition.* 2012;17:1159–1172.
- 68.** Nishikawa T, Iwakiri N, Kaneko Y, et al. Nitric oxide release in human aortic endothelial cells mediated by delivery of amphiphilic polysiloxane nanoparticles to caveolae. *Biomacromolecules.* 2009;10:2074–2085.

- 69.** Saavedra JE, Shami PJ, Wang LY, Davies KM, Booth MN, Citro ML, Keefer LK. Esterase-sensitive nitric oxide donors of the diazeniumdiolate family: in vitro antileukemic activity. *J Med Chem.* 2000;43:261-269.
- 70.** Hou J, Pan Y, Zhu D, et al. Targeted delivery of nitric oxide via a ‘bump-and-hole’-based enzyme-prodrug pair. *Nat Chem Biol.* 2019;15:151-160.
- 71.** Williams DLH. Nitric oxide release from S-nitrosothiols (RSNO)-the role of copper ions. *Transition Metal Chemistry.* 1996;21:189-191.
- 72.** Jiang L, Yao H, Luo X, et al. Polydopamine-modified copper-doped titanium dioxide nanotube arrays for copper-catalyzed controlled endogenous nitric oxide release and improved re-endothelialization. *ACS Appl Bio Mater.* 2020;3:3123-3136.
- 73.** Wei H, Wang E. Nanomaterials with enzyme-like characteristics (nanozymes): next-generation artificial enzymes. *Chem Soc Rev.* 2013;42:6060-6093.
- 74.** Huang Y, Ren J, Qu X. Nanozymes: classification, catalytic mechanisms, activity regulation, and applications. *Chem Rev.* 2019;119:4357-4412.
- 75.** Du B, Li D, Wang J, Wang E. Designing metal-contained enzyme mimics for prodrug activation. *Adv Drug Deliv Rev.* 2017;118:78-93.
- 76.** Zhao Y, Ouyang X, Peng Y, Peng S. Stimuli responsive nitric oxide-based nanomedicine for synergistic therapy. *Pharmaceutics.* 2021;13:1917.
- 77.** Sortino S. Light-controlled nitric oxide delivering molecular assemblies. *Chem Soc Rev.* 2010;39:2903-2913.
- 78.** Weng Y, Song Q, Zhou Y, et al. Immobilization of selenocystamine on TiO₂ surfaces for in situ catalytic generation of nitric oxide and potential application in intravascular stents. *Biomaterials.* 2011;32:1253-1263.
- 79.** Li X, Qiu H, Gao P, Yang Y, Yang Z, Huang N. Synergetic coordination and catecholamine chemistry for catalytic generation of nitric oxide on vascular stents. *NPG Asia Materials.* 2018;10:482-496.
- 80.** Zhang X, Wang Y, Liu J, et al. A metal-organic-framework incorporated vascular graft for sustained nitric oxide generation and long-term vascular patency. *Chemical Engineering Journal.* 2021;421:129577.
- 81.** Li P, Jin D, Dou J, et al. Nitric oxide-releasing poly(epsilon-caprolactone)/S-nitrosylated keratin biocomposite scaffolds for potential small-diameter vascular grafts. *Int J Biol Macromol.* 2021;189:516-527.
- 82.** Huang SL, Kee PH, Kim H, et al. Nitric oxide-loaded echogenic liposomes for nitric oxide delivery and inhibition of intimal hyperplasia. *J Am Coll Cardiol.* 2009;54:652-659.
- 83.** Johnson TA, Stasko NA, Matthews JL, et al. Reduced ischemia/reperfusion injury via glutathione-initiated nitric oxide-releasing dendrimers. *Nitric Oxide.* 2010;22:30-36.
- 84.** Navati MS, Lucas A, Liang C, et al. Reducing ischemia/reperfusion injury by the targeted delivery of nitric oxide from magnetic-field-induced localization of S-nitrosothiol-coated paramagnetic nanoparticles. *ACS Appl Bio Mater.* 2019;2:2907-2919.
- 85.** Vosen S, Rieck S, Heidsieck A, et al. Vascular repair by circumferential cell therapy using magnetic nanoparticles and tailored magnets. *ACS Nano.* 2016;10:369-376.
- 86.** Vosen S, Rieck S, Heidsieck A, et al. Improvement of vascular function by magnetic nanoparticle-assisted circumferential gene transfer into the native endothelium. *J Controlled Release.* 2016;241:164-173.
- 87.** Pan C, Han Y, Lu J. Structural design of vascular stents: a review. *Micromachines (Basel).* 2021;12:1-26.
- 88.** Liu S, Zhi J, Li S, et al. Progress on precise regulation of vascular intimal repair by a surface coating of vascular stent. *Curr Drug Deliv.* 2021;18:862-873.
- 89.** Giustino G, Colombo A, Camaj A, et al. Coronary in-stent restenosis: JACC state-of-the-art review. *J Am Coll Cardiol.* 2022;80:348-372.
- 90.** Bink N, Mohan VB, Fakirov S. Recent advances in plastic stents: a comprehensive review. *Int J Polym.* 2019;70:54-74.
- 91.** Nicolas J, Pivato CA, Chiarito M, Beerkens F, Cao D, Mehran R. Evolution of drug-eluting coronary stents: a back-and-forth journey from the bench to bedside. *Cardiovasc Res.* 2023;119:631-646.
- 92.** Gori T. Vascular wall reactions to coronary stents-clinical implications for stent failure. *Life (Basel).* 2021;11.
- 93.** Zhuang Y, Zhang C, Cheng M, et al. Challenges and strategies for in situ endothelialization and long-term lumen patency of vascular grafts. *Bioact Mater.* 2021;6:1791-1809.
- 94.** Cai Q, Liao W, Xue F, et al. Selection of different endothelialization modes and different seed cells for tissue-engineered vascular graft. *Bioact Mater.* 2021;6:2557-2568.
- 95.** Lei J, Vodovotz Y, Tseng E, Billiar TR. Nitric oxide, a protective molecule in the cardiovascular system. *Nitric Oxide.* 2013;35:175-185.
- 96.** Dimmeler S, Zeiher AM. Nitric oxide-an endothelial cell survival factor. *Cell Death Differ.* 1999;6:964-968.
- 97.** Chug MK, Bachtar E, Narwold N, Gall K, Brisbois EJ. Tailoring nitric oxide release with additive manufacturing to create antimicrobial surfaces. *Biomater Sci.* 2021;9:3100-3111.
- 98.** Naghavi N, de Mel A, Alavijeh OS, Cousins BG, Seifalian AM. Nitric oxide donors for cardiovascular implant applications. *Small.* 2013;9:22-35.
- 99.** Elnaggar MA, Seo SH, Gobaa S, et al. Nitric oxide releasing coronary stent: a new approach using layer-by-layer coating and liposomal encapsulation. *Small.* 2016;12:6012-6023.
- 100.** Fan Y, Zhang Y, Zhao Q, et al. Immobilization of nano Cu-MOFs with polydopamine coating for adaptable gasotransmitter generation and copper ion delivery on cardiovascular stents. *Biomaterials.* 2019;204:36-45.
- 101.** Gomes AJ, Barbougli PA, Espreafico EM, Tfouni E. Trans-[Ru(NO)(NH₃)₄(py)][BF₄]₃·H₂O encapsulated in PLGA microparticles for delivery of nitric oxide to B16-F10 cells: Cytotoxicity and phototoxicity. *J Inorg Biochem.* 2008;102:757-766.
- 102.** Soraggi Cde L, Shishido SM, et al. In vitro evaluation of the safe margin, antithrombotic and antiproliferative actions for the treatment of restenosis: nitric oxide donor and polymers. *Cell Biochem Funct.* 2011;29:207-214.
- 103.** Hwang S, Meyerhoff ME. Polyurethane with tethered copper(II)-cyclen complex: preparation, characterization and catalytic generation of nitric oxide from S-nitrosothiols. *Biomaterials.* 2008;29:2443-2452.
- 104.** Seabra AB, da Silva R, de Souza GF, de Oliveira MG. Antithrombogenic polynitrosated polyester/poly(methyl methacrylate) blend for the coating of blood-contacting surfaces. *Artif Organs.* 2008;32:262-267.
- 105.** Rao J, Pan Bei H, Yang Y, Liu Y, Lin H, Zhao X. Nitric oxide-producing cardiovascular stent coatings for prevention of thrombosis and restenosis. *Front Bioeng Biotechnol.* 2020;8:578.
- 106.** He M, Wang D, Xu Y, et al. Nitric oxide-releasing platforms for treating cardiovascular disease. *Pharmaceutics.* 2022;14(7):1345.
- 107.** de Mel A, Murad F, Seifalian AM. Nitric oxide: a guardian for vascular grafts? *Chem Rev.* 2011;111:5742-5767.
- 108.** de Mel A, Naghavi N, Cousins BG, et al. Nitric oxide-eluting nanocomposite for cardiovascular implants. *J Mater Sci Mater Med.* 2014;25:917-929.
- 109.** Munzel T, Camici GG, Maack C, Bonetti NR, Fuster V, Kovacic JC. Impact of oxidative stress on the heart and vasculature: part 2 of a 3-part series. *J Am Coll Cardiol.* 2017;70:212-229.
- 110.** Perrelli MG, Pagliaro P, Penna C. Ischemia/reperfusion injury and cardioprotective mechanisms: Role of mitochondria and reactive oxygen species. *World J Cardiol.* 2011;3:186-200.
- 111.** Cohen MV, Downey JM. Signalling pathways and mechanisms of protection in pre- and post-conditioning: historical perspective and lessons for the future. *Br J Pharmacol.* 2015;172:1913-1932.
- 112.** Heusch G. Molecular basis of cardioprotection: signal transduction in ischemic pre-, post-, and remote conditioning. *Circ Res.* 2015;116:674-699.
- 113.** Chouchani ET, Methner C, Nadtochiy SM, et al. Cardioprotection by S-nitrosation of a cysteine switch on mitochondrial complex I. *Nat Med.* 2013;19:753-759.
- 114.** Prime TA, Blaikie FH, Evans C, et al. A mitochondria-targeted S-nitrosothiol modulates respiration, nitrosates thiols, and protects against ischemia-reperfusion injury. *Proc Natl Acad Sci U S A.* 2009;106:10764-10769.
- 115.** Williams DLH. The chemistry of S-nitrosothiols. *Chem Rev.* 1999;92:869-876.
- 116.** Ferdinand P, Schulz R. Nitric oxide, superoxide, and peroxynitrite in myocardial ischaemia-reperfusion injury and preconditioning. *Br J Pharmacol.* 2003;138:532-543.
- 117.** Wan X, Liu P, Jin X, et al. Electrospun PCL/keratin/AuNPs mats with the catalytic generation

- of nitric oxide for potential of vascular tissue engineering. *J Biomed Mater Res A*. 2018;106:3239–3247.
- 118.** Roacho-Pérez JA, Garza-Treviño EN, Moncada-Saucedo NK, et al. Artificial scaffolds in cardiac tissue engineering. *Life (Basel)*. 2022;12(8):1117.
- 119.** Roshandel M, Dorkoosh F. Cardiac tissue engineering, biomaterial scaffolds, and their fabrication techniques. *Polymers for Advanced Technologies*. 2021;32:2290–2305.
- 120.** Nguyen AH, Marsh P, Schmies-Henne L, et al. Cardiac tissue engineering: state-of-the-art methods and outlook. *J Biological Engineering*. 2019;13:57.
- 121.** Toyota T, Morimoto T, Shiomi H, et al. Very late scaffold thrombosis of bioresorbable vascular scaffold: systematic review and a meta-analysis. *J Am Coll Cardiol Intv*. 2017;10:27–37.
- 122.** Toong DWY, Toh HW, Ng JCK, et al. Bioresorbable polymeric scaffold in cardiovascular applications. *Int J Mol Sci*. 2020;21(10):3444.
- 123.** Tallawi M, Rosellini E, Barbani N, et al. Strategies for the chemical and biological functionalization of scaffolds for cardiac tissue engineering: a review. *J R Soc Interface*. 2015;12:20150254.
- 124.** Li P, Wang Y, Jin X, et al. Catalytic generation of nitric oxide from poly(epsilon-caprolactone)/phosphobetainized keratin mats for a vascular tissue engineering scaffold. *Langmuir*. 2020;36:4396–4404.
- 125.** Li P, Wang Y, Jin X, et al. Fabrication of PCL/keratin composite scaffolds for vascular tissue engineering with catalytic generation of nitric oxide potential. *J Mater Chem B*. 2020;8:6092–6099.
- 126.** Wang L, Xin X, Li P, Dou J, Han X, Shen J, Yuan J. Stepwise immobilization of keratin-dopamine conjugates and gold nanoparticles on PET sheets for potential vascular graft with the catalytic generation of nitric oxide. *Colloids Surf B Biointerfaces*. 2021;205:111855.
- 127.** Wan X, Liu P, Jin X, Xin X, Li P, Yuan J, Shen J. Electrospun PCL/keratin/AuNPs mats with the catalytic generation of nitric oxide for potential of vascular tissue engineering. *J Biomed Mater Res A*. 2018;106:3239–3247.
- 128.** Chen Y, Gao P, Huang L, et al. A tough nitric oxide-eluting hydrogel coating suppresses neointimal hyperplasia on vascular stent. *Nat Commun*. 2021;12:7079.
- 129.** Parent M, Boudier A, Fries I, et al. Nitric oxide-eluting scaffolds and their interaction with smooth muscle cells in vitro. *J Biomed Mater Res A*. 2015;103:3303–3311.
- 130.** Wang F, Qin K, Wang K, et al. Nitric oxide improves regeneration and prevents calcification in bio-hybrid vascular grafts via regulation of vascular stem/progenitor cells. *Cell Rep*. 2022;39:110981.
- 131.** Le Thi P, Tran DL, Hoang Thi TT, Lee Y, Park KD. Injectable reactive oxygen and nitrogen species-controlling hydrogels for tissue regeneration: current status and future perspectives. *Regen Biomater*. 2022;9:rbac069.
- 132.** Schgoer W, Theurl M, Jeschke J, et al. Gene therapy with the angiogenic cytokine secretoneurin induces therapeutic angiogenesis by a nitric oxide-dependent mechanism. *Circ Res*. 2009;105:994–1002.
- 133.** Ridnour LA, Isenberg JS, Espey MG, Thomas DD, Roberts DD, Wink DA. Nitric oxide regulates angiogenesis through a functional switch involving thrombospondin-1. *Proc Natl Acad Sci U S A*. 2005;102:13147–13152.
- 134.** Murohara T, Asahara T, Silver M, et al. Nitric oxide synthase modulates angiogenesis in response to tissue ischemia. *J Clin Invest*. 1998;101:2567–2578.
- 135.** Yang C, Hwang HH, Jeong S, et al. Inducing angiogenesis with the controlled release of nitric oxide from biodegradable and biocompatible copolymeric nanoparticles. *Int J Nanomedicine*. 2018;13:6517–6530.
- 136.** Lee J, Yang C, Ahn S, Choi Y, Lee K. Enhanced NO-induced angiogenesis via NO/H₂S co-delivery from self-assembled nanoparticles. *Biomater Sci*. 2021;9:5150–5159.
- 137.** Murad F. The excitement and rewards of research with our discovery of some of the biological effects of nitric oxide. *Circ Res*. 2003;92:339–341.
- 138.** Rink JS, Sun W, Misener S, et al. Nitric oxide-delivering high-density lipoprotein-like nanoparticles as a biomimetic nanotherapy for vascular diseases. *ACS Appl Mater Interfaces*. 2018;10:6904–6916.
- 139.** Mohamed NA, Ahmetaj-Shala B, Duluc L, et al. A new NO-releasing nanoformulation for the treatment of pulmonary arterial hypertension. *J Cardiovasc Transl Res*. 2016;9:162–164.
- 140.** Kushwaha M, Anderson JM, Bosworth CA, et al. A nitric oxide releasing, self assembled peptide amphiphile matrix that mimics native endothelium for coating implantable cardiovascular devices. *Biomaterials*. 2010;31:1502–1508.
- 141.** Zhang F, Zhang Q, Li X, Huang N, Zhao X, Yang Z. Mussel-inspired dopamine-Cu(II) coatings for sustained in situ generation of nitric oxide for prevention of stent thrombosis and restenosis. *Biomaterials*. 2019;194:117–129.
- 142.** Li X, Liu J, Yang T, Qiu H, Lu L, Tu Q, Xiong K, Huang N, Yang Z. Mussel-inspired "built-up" surface chemistry for combining nitric oxide catalytic and vascular cell selective properties. *Biomaterials*. 2020;241:119904.
- 143.** Yang Z, Yang Y, Zhang L, et al. Mussel-inspired catalytic selenocystamine-dopamine coatings for long-term generation of therapeutic gas on cardiovascular stents. *Biomaterials*. 2018;178:1–10.
- 144.** Acharya G, Lee CH, Lee Y. Optimization of cardiovascular stent against restenosis: factorial design-based statistical analysis of polymer coating conditions. *PLoS One*. 2012;7:e43100.
- 145.** Naghavi N, Seifalian AM, Hamilton G, de Mel A. Evaluation of experimental methods for nitric oxide release from cardiovascular implants; bypass grafts as an exemplar. *Ther Adv Cardiovasc Dis*. 2015;9:375–388.
- 146.** Naghavi N, Mel Ad, Cousins BG, Hamilton G, Seifalian AM. Development of nitric oxide-eluting nanocomposite materials using nanoparticles for cardiovascular applications. *Cardiovascular Pathology*. 2013;22:e41.
- 147.** Taite LJ, West JL. Sustained delivery of nitric oxide from poly(ethylene glycol) hydrogels enhances endothelialization in a rat carotid balloon injury model. *Cardiovascular Engineering and Technology*. 2011;2:113–123.
- 148.** Lee YJ, Kim YR, Jeong WY, Lee S, Shin JH, Lee GJ. Potential protective effect of nitric oxide-releasing nanofibers in hypoxia/reoxygenation-induced cardiomyocyte injury. *J Nanosci Nanotechnol*. 2019;19:6539–6545.

KEY WORDS cardiac tissue engineering, inorganic nanoparticles, nitric oxide, nitric oxide release, organic nanoparticles, stent, vascular graft

STATE-OF-THE-ART REVIEW

Advances in Clinical Imaging of Vascular Inflammation



A State-of-the-Art Review

Henry W. West, BMEDSCI, MBBS, PhD,^{a,b,*} Katerina Dangas, BA,^{a,*} Charalambos Antoniades, MD, PhD^a

HIGHLIGHTS

- Vascular inflammation is a druggable target involved in the development and rupture of atherosclerotic plaques. Noninvasive imaging methodologies that quantify vascular inflammation can help in risk stratification and guide treatments.
- Molecular imaging using PET/PET-CT/PET-MRI adds significantly to the understanding of disease pathogenesis and is considered the gold standard in visualizing inflammation noninvasively. However, the practical limitations of its clinical deployment limit its use in clinical practice.
- CT imaging allows high-resolution investigation of plaque structure, allowing detection of high-risk features. CT phenotyping of PVAT for the assessment of vascular inflammation allows detection of residual inflammatory risk. This method is used in clinical practice.
- CMR allows structural assessment of large vessels, but its limited spatial and temporal resolution restricts its use for assessment of coronary plaque or coronary inflammation.
- Ultrasound offers an attractive perspective for assessment of vascular inflammation at low cost and with no radiation, but current approaches do not offer an alternative to PET imaging- or CT imaging-based methods for assessment of coronary inflammation.

SUMMARY

Vascular inflammation is a major contributor to cardiovascular disease, particularly atherosclerotic disease, and early detection of vascular inflammation may be key to the ultimate reduction of residual cardiovascular morbidity and mortality. This review paper discusses the progress toward the clinical utility of noninvasive imaging techniques for assessing vascular inflammation, with a focus on coronary atherosclerosis. A discussion of multiple modalities is included: computed tomography (CT) imaging (the major focus of the review), cardiac magnetic resonance, ultrasound, and positron emission tomography imaging. The review covers recent progress in new technologies such as the novel CT biomarkers of coronary inflammation (eg, the perivascular fat attenuation index), new inflammation-specific tracers for positron emission tomography-CT imaging, and others. The strengths and limitations of each modality are explored, highlighting the potential for multi-modality imaging and the use of artificial intelligence image interpretation to improve both diagnostic and prognostic potential for common conditions such as coronary artery disease. (J Am Coll Cardiol Basic Trans Science 2024;9:710-732) © 2024 The Authors. Published by Elsevier on behalf of the American College of Cardiology Foundation. This is an open access article under the CC BY license (<http://creativecommons.org/licenses/by/4.0/>).

From the ^aAcute Multidisciplinary Imaging and Interventional Centre, Radcliffe Department of Medicine, University of Oxford, Oxford, United Kingdom; and the ^bCentral Clinical School, Sydney Medical School, University of Sydney, Sydney, New South Wales, Australia. *Dr West and Ms Dangas contributed equally to this work.

The authors attest they are in compliance with human studies committees and animal welfare regulations of the authors' institutions and Food and Drug Administration guidelines, including patient consent where appropriate. For more information, visit the [Author Center](#).

Manuscript received September 13, 2023; revised manuscript received October 12, 2023, accepted October 12, 2023.

Vascular inflammation plays a critical role in the development and progression of various cardiovascular diseases, most importantly atherosclerotic coronary artery disease (CAD). Accurate noninvasive assessment of vascular inflammation has been a challenge for clinicians and researchers due to the limitations of traditional imaging modalities, with invasive assessment limited to surgical patients in highly controlled research settings. With the advent of more advanced imaging technologies such as multi-detector computed tomography (CT) scanners and molecular imaging using selective radiotracers in positron emission tomography (PET), it is now possible to directly assess vascular biology and inflammation, including in the coronary tree. Furthermore, the burgeoning field of CT radiomics has the potential to augment noninvasive inflammation detection for improvements in patient care. Concurrently, molecular imaging with PET has experienced tremendous growth in recent years, with numerous radiotracers and imaging technologies being developed for the detection of vascular inflammation. Intravascular ultrasound is also becoming increasingly available during invasive angiography, presenting a significant opportunity for the use of ultrasound-based methods for the indirect detection of the high-risk (and presumably inflamed) coronary plaque.

In the current state-of-the-art review, an overview is provided of the advances in all imaging technologies used for the detection of vascular inflammation, with a specific focus on coronary artery inflammation. The review focuses on CT imaging techniques, which have seen huge interest in recent years, but it also includes dedicated discussion of magnetic resonance imaging (MRI), PET-CT and PET-MRI, and ultrasound. Highlighted also is the recent progress in human translational applications of each imaging modality, evaluating their strengths and limitations in the assessment of vascular inflammation.

INTRODUCTION TO VASCULAR INFLAMMATION

Atherosclerosis is a chronic inflammatory condition of the vasculature. It is highly patterned in its pathophysiology, forming characteristic lesions within the arterial system all around the body. Broadly, atherosclerosis encompasses the stages of endothelial dysfunction, formation of fatty streak, plaque development (atheroma and fibroatheroma), and plaque disruption and thrombosis, including the pathophysiological processes that underpin these transitions. The spectrum of disease caused by atherosclerosis is vast, including myocardial

infarction (MI), stroke, and peripheral arterial disease, which, among other related conditions, comprise cardiovascular disease, the leading cause of morbidity and mortality globally.¹

Since the pioneering work of Russell Ross, vascular inflammation has played a causal role in the pathogenesis of all stages of atherosclerosis and plaque rupture.^{2–4} However, our understanding has flourished since Ross's canonical response-to-injury hypothesis,^{5,6} which suggested that endothelial dysfunction (caused by genetics, vascular injury, elevated low-density lipoprotein [LDL-C] levels, free radicals from cigarette smoking, and hypertension, among others) causes collagen exposure and platelet adhesion, aggregation, and degranulation to initiate atherosclerosis. Adhesion markers (intercellular adhesion molecule-1, vascular cell adhesion molecule [VCAM-1]), in conjunction with chemotactic agents (chemokine [C-C motif] ligand 5) secreted by platelet degranulation, then act to stimulate neutrophil and macrophage migration and subendothelial accumulation of monocytes and LDL-C, initiating the inflammatory process.⁷ Other cytokines such as chemokine (C-C motif) ligand 2 are also released by neutrophils and smooth muscle cells (SMCs) and stimulate further leukocyte chemotaxis. The evolution of plaque then begins in the arterial intima, which contains a lipid-rich core from accumulation of LDL-C within macrophage foam cells underneath a fibrous cap formed from SMC migration and proliferation (Figure 1).

This canonical view of the initiation of atherosclerosis has been updated to reveal a complex interrelated network of pathways involving not only the innate immune system but also adaptive immunity (T- and B-cell responses), thrombo-inflammation (platelet-triggered processes), and C-mediated processes, among others. The role of B cells in atherosclerosis is complex,⁸ as some B-cell responses targeting oxidation-specific epitopes might be disease protective, whereas other downstream pathways may be pro-atherosclerotic. Furthermore, antibody-independent roles include cytokine production and T-cell regulation that secondarily mediate atherosclerosis. B-cell depletion therapies have been investigated, but further isolation of the pro-atherosclerotic pathways may be even more useful in generating targeted therapies. A role for T helper 1

ABBREVIATIONS AND ACRONYMS

¹⁸F-FDG = ¹⁸ F-fluorodeoxyglucose
¹⁸F-NaF = ¹⁸ F-sodium fluoride
⁶⁸Ga-DOTATATE = gallium-68-labeled DOTATATE
ACS = acute coronary syndromes
AI = artificial intelligence
CAD = coronary artery disease
CTA = computed tomography angiography
CMR = cardiac magnetic resonance
FAI = fat attenuation index
FRP = fat radiomic profile
HRP = high-risk plaque
LDL-C = low-density lipoprotein
MACE = major adverse cardiovascular events
MI = myocardial infarction
MRI = magnetic resonance imaging
NLRP3 = NOD-, LRR-, and pyrin domain-containing 3
PCAT = pericoronary adipose tissue
PET = positron emission tomography
PVAT = perivascular adipose tissue
SMC = smooth muscle cell
SST₂ = somatostatin receptor subtype 2
VCAM-1 = vascular cell adhesion molecule type 1

cells is also being established.⁹ Platelets have been known to be critical in the early stages of atherosclerosis by releasing chemokine (C-C motif) ligand 5, a critical chemokine for promoting monocyte adhesion; increasingly complex roles are being elucidated.¹⁰ The role of these cell-mediated pathways and others (eg, protein kinase C) have been reviewed in detail elsewhere.¹¹

The role of inflammation also extends to atherosclerotic disease progression.⁷ Activated macrophages that ingest lipid molecules subsequently secrete chemokines and cytokines and drive lipid accumulation.^{12,13} Notably, however, the role of macrophages in atherosclerosis is highly complex, with both pro- and anti-atherosclerotic functions. One recent study suggests that mural cell-driven macrophage niches may be protective against chronic inflammation.¹⁴ Furthermore, as SMCs and macrophages apoptose and a necrotic core grows, senescent SMCs release pro-inflammatory cytokines and matrix metalloproteinases.¹⁵ Oxidized LDL-C also triggers the nuclear factor κB signaling pathway, promoting the transcription of the NOD-, LRR-, and pyrin domain-containing 3 (NLRP3) inflammasome and pro-interleukin-1, triggering downstream pathways, which include the release of neutrophil extracellular traps. These traps further induce cytotoxicity by priming the NLRP3 inflammasome in macrophages and inducing platelet activation and the tissue factor pathway inhibitor.⁷

Finally, inflammation is also a critical driver of vulnerable plaque rupture, which is a key pathogenic mechanism of acute coronary syndromes (ACS). When the weakened cap breaks, procoagulant molecules in the blood are exposed to tissue factor within the lipid-rich core; platelet aggregation and thrombosis ensue. Superficial erosion is a second mechanism by which plaque progression occurs; depletion of neutrophils has been shown to prevent this process, further highlighting the role of inflammation.¹⁶

Vascular inflammation is therefore causally implicated in atherosclerosis from inception to complication. Clinical studies have concordantly confirmed the clinical relevance of inflammation in atherosclerotic cardiovascular disease. Elevation in inflammatory markers predicts outcomes in patients with ACS.^{17–19} Inflammation also affects cardiovascular risk factors, possibly by decreasing nitric oxide bioavailability in the vascular endothelium.²⁰ Vascular inflammation has furthermore been shown to affect serum lipid levels and lipoprotein function. It causes LDL-C to be more easily oxidized,²¹ as the ability of HDL to prevent the oxidation of LDL-C is diminished.

It follows that lipid-modifying statins trigger clinically significant anti-inflammatory processes.²²

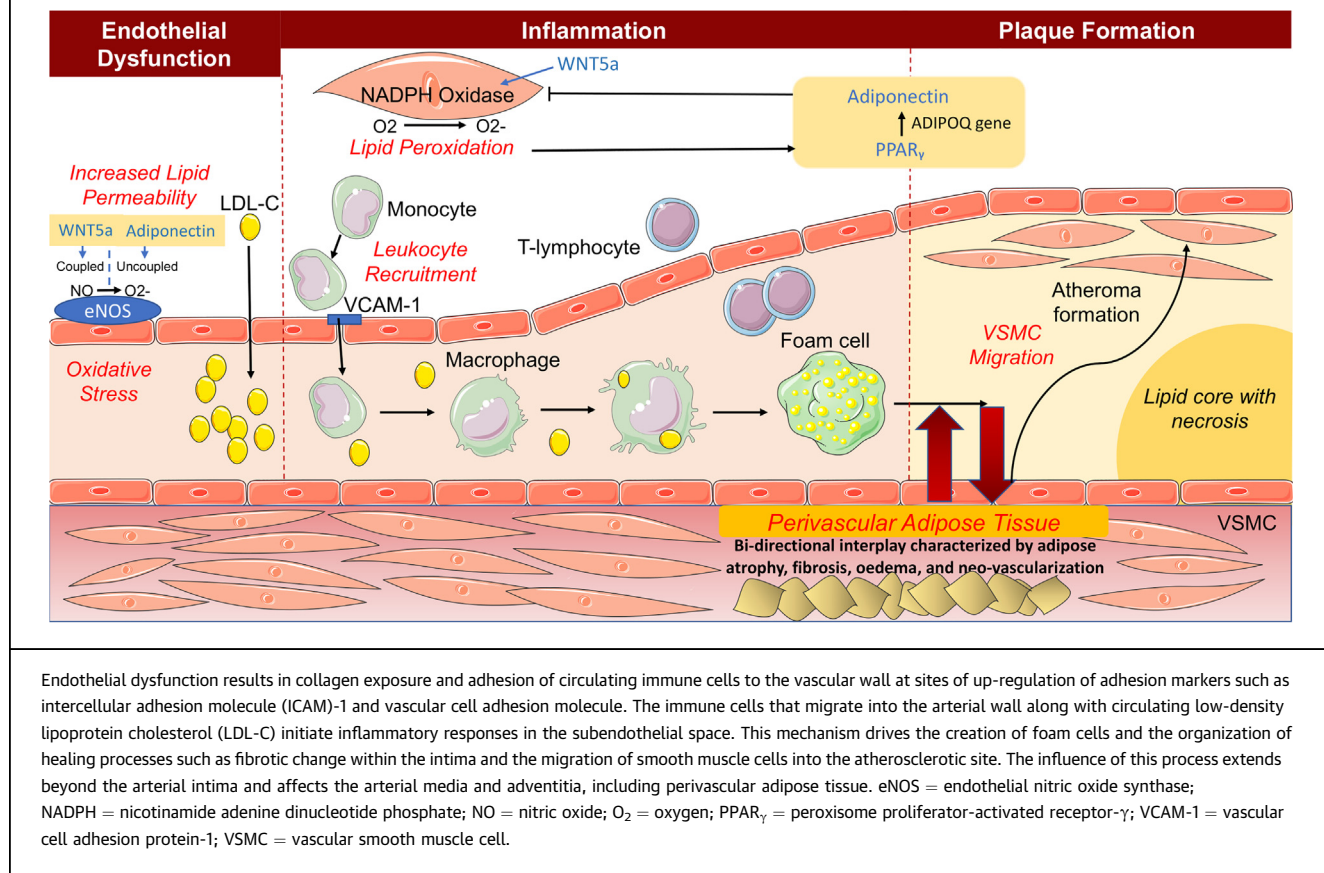
Therefore, targeting these complex pathways provides a promising route toward diagnosing and treating the disease. Our growing understanding of the complex interconnected pathways that give rise to the modern view of atherosclerosis serves as a potential avenue for precision medicine. Inflammation had been largely overlooked until recent years but has become a fast-growing target for innovation in diagnostics and treatment. In particular, the potential to further stratify CAD according to the presence of inflammation may be critical, as anti-inflammatory treatments for atherosclerosis are recommended in clinical guidelines.²³ Its potential applications are also being investigated beyond ischemic heart disease to include cardiometabolic disease.²⁴

CAUSAL RELATIONSHIPS BETWEEN INFLAMMATION AND CARDIOVASCULAR EVENTS: INSIGHTS FROM RANDOMIZED CLINICAL TRIALS

The advance in understanding of the cellular mechanisms of the chronic inflammatory process underlying atherosclerosis is increasingly being translated into actionable clinical discoveries. Phase 3, double-blind, randomized controlled clinical trials have now shown that targeting specific inflammatory pathways can improve clinical outcomes and reduce cardiovascular events in select populations. Importantly, different anti-inflammatory strategies may have varying agent-related effectiveness due to diversity in underlying mechanisms, specifically whether they prevent early disease progression, lessen plaque formation, or reduce late-stage plaque rupture to prevent acute cardiac events. This scenario highlights a major challenge in clinical trials for anti-inflammatory agents: what is the population of relevance for the specific agent, and what is the relevant outcome that the agent may modify?

The first trial to test a clinical treatment strategy based on inflammatory markers was JUPITER (Justification for the Use of Statin in Prevention: An Intervention Trial Evaluating Rosuvastatin). In 17,802 patients selected per LDL-C level <130 mg/dL and high-sensitivity C-reactive protein level ≥2 mg/L, rosuvastatin 20 mg was associated with a reduction in the rate of primary endpoint (MI, stroke, arterial revascularization, hospitalization for unstable angina, and cardiovascular death) compared with placebo (rosuvastatin vs placebo 1.31 vs 0.77).²⁵ However, it was unclear whether it was an on-target

FIGURE 1 Simplified Schematic of Vascular Inflammation Driving Atherosclerosis



Endothelial dysfunction results in collagen exposure and adhesion of circulating immune cells to the vascular wall at sites of up-regulation of adhesion markers such as intercellular adhesion molecule (ICAM)-1 and vascular cell adhesion molecule. The immune cells that migrate into the arterial wall along with circulating low-density lipoprotein cholesterol (LDL-C) initiate inflammatory responses in the subendothelial space. This mechanism drives the creation of foam cells and the organization of healing processes such as fibrotic change within the intima and the migration of smooth muscle cells into the atherosclerotic site. The influence of this process extends beyond the arterial intima and affects the arterial media and adventitia, including perivascular adipose tissue. eNOS = endothelial nitric oxide synthase; NADPH = nicotinamide adenine dinucleotide phosphate; NO = nitric oxide; O₂ = oxygen; PPAR_γ = peroxisome proliferator-activated receptor- γ ; VCAM-1 = vascular cell adhesion protein-1; VSMC = vascular smooth muscle cell.

effect due to LDL-C reduction or a pleiotropic effect of reducing inflammation, generating the need for investigation and development of targeted anti-inflammatory treatments.

Notably, CANTOS (Canakinumab Anti-inflammatory Thrombosis Outcomes Study) investigated the impact of an interleukin-1 β -targeted monoclonal antibody (canakinumab) on cardiovascular outcomes, in 10,061 patients with a previous MI and C-reactive protein level ≥ 2 mg/L.²⁶ The trial compared 3 doses (50, 150, and 300 mg) of canakinumab administered subcutaneously every 3 months vs placebo on the primary endpoint of nonfatal MI, nonfatal stroke, or cardiovascular death. Canakinumab 150 mg every 3 months was found to significantly reduce recurrent major adverse cardiovascular events (MACE) by 17% (HR: 0.83; $P = 0.005$). This study was the first to show that anti-inflammatory drug treatment reduces cardiovascular risk, although the relatively modest reduction in MACE, with no significant effect on cardiac mortality, questioned the use of high-sensitivity C-reactive protein for patient

selection; this introduced the need for more precise and sophisticated methods to identify those patients with high coronary inflammation who would benefit the most from targeted treatment. The CANTOS trial has revived the need to develop imaging biomarkers of coronary inflammation for use as a companion or complementary diagnostic tool.²⁷

However, the story is not that simple. CIRT (Cardiovascular Inflammation Reduction Trial) investigated low-dose methotrexate vs placebo in 4,786 patients with previous MI or multivessel coronary disease with diabetes or metabolic syndrome; it found no reduction in the composite primary endpoint (nonfatal MI, nonfatal stroke, or cardiovascular death) with methotrexate.²⁸ An ancillary study found that impaired coronary flow reserve was independently associated with increased inflammation and myocardial strain, which may have implications in heart failure.²⁴ The contrasting results of the CIRT and CANTOS trials show that anti-inflammatory therapies effective against atherosclerosis must be biochemically targeted to the specific inflammatory

pathways validated in the disease. Whereas the interleukin-1 β to NLRP3 inflammasome pathway targeted by canakinumab is genetically and cellularly validated as a critical driver of atherosclerosis, this is not the case for nucleic acid synthesis targeted by methotrexate. Similarly, the phospholipase inhibitor darapladib²⁹ and p38 mitogen-activated protein kinase blocker losmapimod³⁰ also yielded neutral results as they act on pathways not likely critical in the pathophysiology of atherosclerosis. Thus, additional cellular work may be a critical hypothesis generator for future drug development.

Colchicine is a potent anti-inflammatory drug targeting cyclooxygenase-2 with wide-ranging clinical utility, including in gout and pericarditis. It is an effective tubulin disruptor and also a known inhibitor of leukocyte migration and of the NLRP3 inflammasome. This drug has shown promise in mitigating vascular inflammation in 2 key trials. COLCOT (Colchicine Cardiovascular Outcomes Trial) found that 0.5 mg daily colchicine vs placebo in patients <30 days after a MI significantly reduced the risk of ischemic cardiovascular events (cardiovascular death, resuscitated cardiac arrest, MI, stroke, and urgent hospitalization for angina leading to coronary revascularization) with colchicine than placebo.³¹ The effects of colchicine also translate to patients with chronic coronary disease, as shown by the LoDoCo2 (Low-Dose Colchicine 2) trial,³² which compared 0.5 mg colchicine daily vs placebo in those with chronic coronary disease. These 2 trials confirmed that anti-inflammatory treatments can be used in cardiovascular risk management and led to the inclusion of colchicine in the European Society of Cardiology 2021 prevention guidelines (with a Class IIb indication) as a therapeutic option on top of statins, in patients at very high risk.³³

Furthermore, REDUCE-IT (Reduction of Cardiovascular Events with Icosapent Ethyl-Intervention Trial), which assessed icosapent ethyl in patients with hypertriglyceridemia, found a striking risk reduction of ischemic heart disease; however, the result was not found to be related to reduction in triglyceride level.³⁴ It is indeed possible that this effect is mediated through the anti-inflammatory effects of this agent.

Finally, the ZEUS (Effects of Ziltivekimab vs Placebo on Cardiovascular Outcomes in Participants With Established Atherosclerotic Cardiovascular Disease, Chronic Kidney Disease, and Systemic Inflammation) trial investigating the novel interleukin-6 inhibitor ziltivekimab vs placebo on primary outcomes of cardiovascular death, nonfatal MI, and nonfatal stroke is ongoing.³⁵ The results of this phase

3 trial have the potential to further shift the view of atherosclerosis from a lipid storage disease to an inflammatory one.

Overall, clinical practice changes with phase 3 randomized clinical trials. The most recent European Society of Cardiology guidelines reflect this paradigm shift by recommending colchicine in high-risk individuals with atherosclerotic cardiovascular disease.³³ However, the direction of anti-inflammatory treatments to individuals with pathology that is amenable to such therapy is paramount. The side effect profiles of many anti-inflammatory treatments are not to be neglected, including infection risk and gastrointestinal complication resulting in poor tolerability. Furthermore, biologics are expensive therapies that require increased selectivity, which can be accomplished by personalized medicine. Further work is needed to develop reliable investigations to accurately identify those patients with arterial inflammation who would respond to such therapies. Emerging imaging techniques that allow measurement of cardiovascular inflammation are expected to soon lead us to more personalized therapeutic strategies.

NONINVASIVE DETECTION OF VASCULAR INFLAMMATION

Noninvasive imaging techniques for the assessment of vascular inflammation have garnered significant interest in the research and clinical communities over recent years. As our understanding of the fundamental roles of inflammation in atherosclerosis and other vascular conditions such as vasculitis has improved, so has the impetus to use noninvasive means to assess human inflammatory load, particularly in the coronary arteries and the aorta. The noninvasive assessment of coronary artery inflammation has already been shown to provide significant opportunity for enhanced CAD risk stratification, personalized therapy decision-making, and enhanced monitoring of therapeutic efficacy³⁶ (discussed in this section of the review).

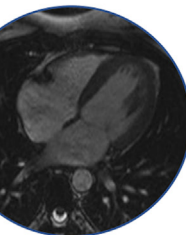
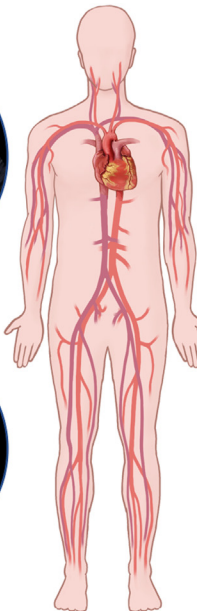
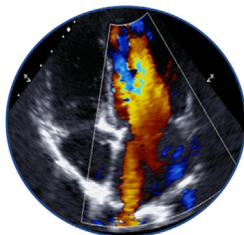
We provide a review of the major noninvasive imaging modalities available to researchers and clinicians to visualize vascular inflammation *in vivo* with a focus on both the molecular mechanisms that these imaging modalities rely upon and their clinical applications. Invasive modalities such as intravascular imaging techniques are not included in this review. The noninvasive imaging modalities for the detection of vascular inflammation discussed here are summarized in the **Central Illustration** along with their strengths and weaknesses.

CENTRAL ILLUSTRATION Imaging Modalities to Detect Vascular Inflammation

Ultrasound

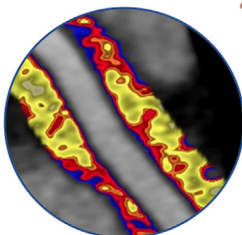
Low cost,
non-invasive

Low resolution,
no clinical use
currently for tissue
inflammation

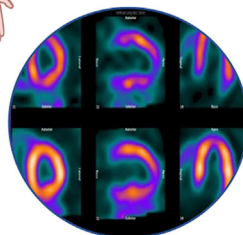


Computed tomography

Validated methods for
inflammation detection,
currently used for
coronary artery disease
diagnosis and cardio-
vascular risk assessment,
growing usage in practice



Radiation/contrast



Cardiac MRI

Can assess
structural disease

No use currently
validated for vascular
inflammation,
time consuming

PET CT/MRI

Gold standard for
inflammation with
high specificity

Lack of clinical
expertise and
availability outside
major centers

West HW, et al. J Am Coll Cardiol Basic Trans Science. 2024;9(5):710–732.

Summary of the clinical imaging modalities in use or under development for the noninvasive detection of vascular inflammation. CT = computed tomography; MRI = magnetic resonance imaging; PET = positron emission tomography.

CT IMAGING. The use of CT imaging to visualize the heart and vascular structures has increased dramatically in recent decades owing to improved imaging technology and widespread utility of CT scanners across a broad range of clinical indications.

Coronary computed tomography angiography (CTA) has become the noninvasive imaging modality of choice for the noninvasive examination of the coronary arteries. The currently accepted broad indications for coronary CTA in clinical practice that are relevant to inflammatory vascular disease include: 1) suspected or known CAD (to evaluate the severity and extent of CAD, particularly in patients with symptoms such as stable chest pain, shortness of breath, and exercise intolerance); 2) assessing the anatomy of the coronary arteries before revascularization procedures such as coronary artery bypass surgery or percutaneous coronary intervention; 3) preoperative evaluation for noncardiac surgery to assess the presence and severity of CAD in patients scheduled for noncardiac surgery; and 4) monitoring the progression of CAD or assessing the effectiveness of

treatment, including lifestyle changes, medication, or revascularization procedures.

It is important to note that coronary CTA is not always the first-line imaging modality for all these broad indications in all settings. The choice of imaging test often depends on an individual patient's disposition.

Beyond the indications listed here, the role of CT imaging has recently expanded to include the direct noninvasive imaging of vascular inflammation. CT imaging offers unparalleled potential for widespread clinical uptake of vascular inflammation assessment, upheld by the existing reliance on CT scans in clinical guidelines for the investigation of chest pain worldwide.^{37,38} Advances that allow these scans to be further utilized for the visualization of coronary inflammation would improve and streamline clinical practice and add immense value for patients and clinicians.

Currently, when plaque is visualized with coronary CTA, plaque risk is stratified to assess plaque stability and therefore risk of cardiac events. High-risk plaque (HRP) features include low attenuation, positive

remodeling, spotty calcification, and the napkin ring sign (ringlike peripheral higher attenuation with central low attenuation), among others. On the other hand, calcification signifies stability and low inflammation. However, HRP features are not reliable in assessing plaque inflammation. The absence of these features does not necessarily correlate with lack of inflammation because by the time plaque appears, vascular inflammation has been ongoing for some time. Indeed, recent studies show that the traditional stenosis-based approach has failed to identify at-risk patients (Coronary Artery Disease Reporting and Data System 2.0 [CAD-RADS 2.0])³⁹ and furthermore failed to improve clinical outcomes beyond symptom improvement in patients with stable CAD (ISCHEMIA [International Study of Comparative Health Effectiveness With Medical and Invasive Approaches]).⁴⁰ Therefore, to maximize prevention of cardiac events, imaging biomarkers specific to vascular inflammation are needed to detect coronary inflammation before plaque formation is detectable.

Perivascular adipose tissue (PVAT) can detect signals of disease emanating from the vascular wall. In brief, in conditions of cardiovascular disease, the arterial wall releases various mediators such as oxidation products (eg, 4-hydroxynonenal), which diffuse to PVAT, inducing the transformation of adipocytes from quiescent lipid-storage cells to active biosynthetic cells that secrete antioxidant adipokines such as adiponectin. These adipokines are then transported back to the vascular wall, acting as a defense mechanism against vascular oxidative damage. Inflammatory molecules originating from the vascular wall also diffuse into adjacent adipose tissue, preventing pre-adipocyte differentiation into mature adipocytes within PVAT. In addition, these inflammatory molecules stimulate perivascular lipolysis, generating a gradient of adipocyte size surrounding the inflamed artery. The adipocyte size gradient in PVAT close to the inflamed artery results in a higher lipid/water ratio in the layers of PVAT adjacent to the inflamed vascular wall. The gradient changes in PVAT's structure and composition around inflamed arteries could act as an internal "thermometer" of vascular inflammation if it can be visualized and quantified noninvasively.

One of the key advances that has facilitated CT imaging to becoming a "one-stop-shop"⁴¹ for imaging of the vasculature, particularly the coronary arteries, is the fundamental but often overlooked fact that three-dimensional medical images, like all images, are data sets.

The first major imaging technology that utilizes coronary CTA for the detection of vascular

inflammation is the perivascular fat attenuation index (FAI). This noninvasive, CT imaging-derived biomarker relies on attenuation mapping of peri-coronary adipose tissue (PCAT) composition to extract information about the inflammatory status of the adjacent coronary artery.^{42,43} The premise of this work emerges from the understanding that adipose tissue is a key regulator of cardiometabolic health.^{44,45} PVAT is the adipose tissue that forms a contiguous entity with the arterial adventitia and plays a key role in vascular homeostasis and atherosclerosis by regulating the local microenvironment through the release of bioactive adipokines,^{46,47} as well as gaseous and other lipid messengers.^{42,44}

Studies that used ¹⁸F-fluorodeoxyglucose (¹⁸F-FDG) PET-CT imaging to visualize inflammation in PVAT (as outlined later in this review) have highlighted significant relationships between this inflammation and a range of clinically significant cardiovascular disease endpoints.⁴⁸ Importantly, our group showed that the paracrine interactions between the arterial wall and the PVAT are bidirectional.^{43,46,47,49} We found that in the presence of increased vascular oxidative stress, lipid peroxidation products such as 4-hydroxynonenal are increasingly produced and diffuse from the vascular wall to the PVAT.⁵⁰ These substances activate peroxisome proliferator-activated receptor-γ signaling in PVAT adipocytes, which results in an up-regulation and increased secretion of the antioxidant adiponectin from the perivascular adipocytes.⁵¹ Adiponectin can then diffuse back to the vascular wall and proximal myocardial tissue and reduce superoxide production by suppressing the activity of nicotinamide adenine dinucleotide phosphate oxidases, as well as by improving the coupling of endothelial nitric oxide synthase in the vascular endothelium.^{46,47,52} During the process of shifting the phenotype of PVAT adipocytes from energy storing to active secretory cells, their dimensions, shape, and content change, becoming smaller in size and with reduced intracellular lipid content.

The ability to evolve in response to signals from the cardiovascular system is also shown by the ability of adipocytes to activate lipolysis and reduce adipogenesis in the presence of exogenous inflammation and circulating molecules such as brain natriuretic peptide.⁴⁹ Importantly, we have also shown that if vascular inflammation is present, the release of pro-inflammatory mediators such as tumor necrosis factor-α, interleukin-6, and interferon gamma blocks the ability of perivascular pre-adipocytes to differentiate into mature lipid-laden adipocytes.⁴³ Indeed, per results of paired PVAT biopsies from a site attached to

the right coronary artery, perivascular adipocytes were significantly smaller and less well differentiated compared with adipocytes from epicardial adipose tissue biopsies obtained >2 cm away from any coronary artery (non-PVAT); this was evidenced by a lower relative expression of the adipocyte differentiation markers peroxisome proliferator-activated receptor- γ and fatty acid binding protein-4. This gradient in PVAT composition reflects the inflammatory burden of a given coronary segment and has highlighted PVAT as a biological sensor of coronary artery inflammation. If these gradients of PVAT composition around the coronary arteries is visualized and quantified using noninvasive imaging, we would be able to detect or even quantify coronary artery inflammation noninvasively, leading to a new generation of diagnostic and prognostic biomarkers of cardiovascular events.

These laboratory findings have been translated to coronary CTA through the segmentation and analysis of PVAT along the coronary vessels using predefined validated Hounsfield unit (HU) cutoffs (-190 to -30 HU).^{43,53} The perivascular FAI utilizes coronary CTA to track spatial changes in PVAT composition that are induced by inflamed coronary vessels as outlined earlier.⁴³ The FAI relies on the concept that the inflammation-induced changes in adipocyte size are associated with a detectable shift in CT attenuation toward a less negative HU range (toward -30 HU). The perivascular FAI (calculated by using the CaRi-HEART medical device; Caristo Diagnostics⁵⁴) captures and interprets these attenuation gradients in the perivascular space, with high perivascular FAI linked to a higher inflammatory burden^{43,55} (**Figures 2A to 2E**).

Importantly, there is strong evidence that CAD is associated with a higher perivascular FAI compared with healthy individuals.⁴³ In addition, perivascular FAI is significantly increased around culprit/unstable lesions in patients presenting with acute MI, and perivascular FAI exhibits dynamic changes around culprit coronary lesions, decreasing significantly when measured 5 weeks after the index event. It is interesting to consider the concept of the vulnerable arterial plaque in light of these findings, as this has dominated clinical thinking around ACS for decades. It will be of tremendous importance whether inflammatory imaging, such as FAI, can assist in identifying coronary lesions at increased risk of rupture or, perhaps more importantly, superficial erosion.⁵⁶ Whether CT imaging will be useful in noninvasive differentiation of ACS etiology (ie, plaque erosion vs rupture) remains to be seen. However, it is important to note that perivascular FAI provides a measure of vascular inflammation and CAD risk regardless of the

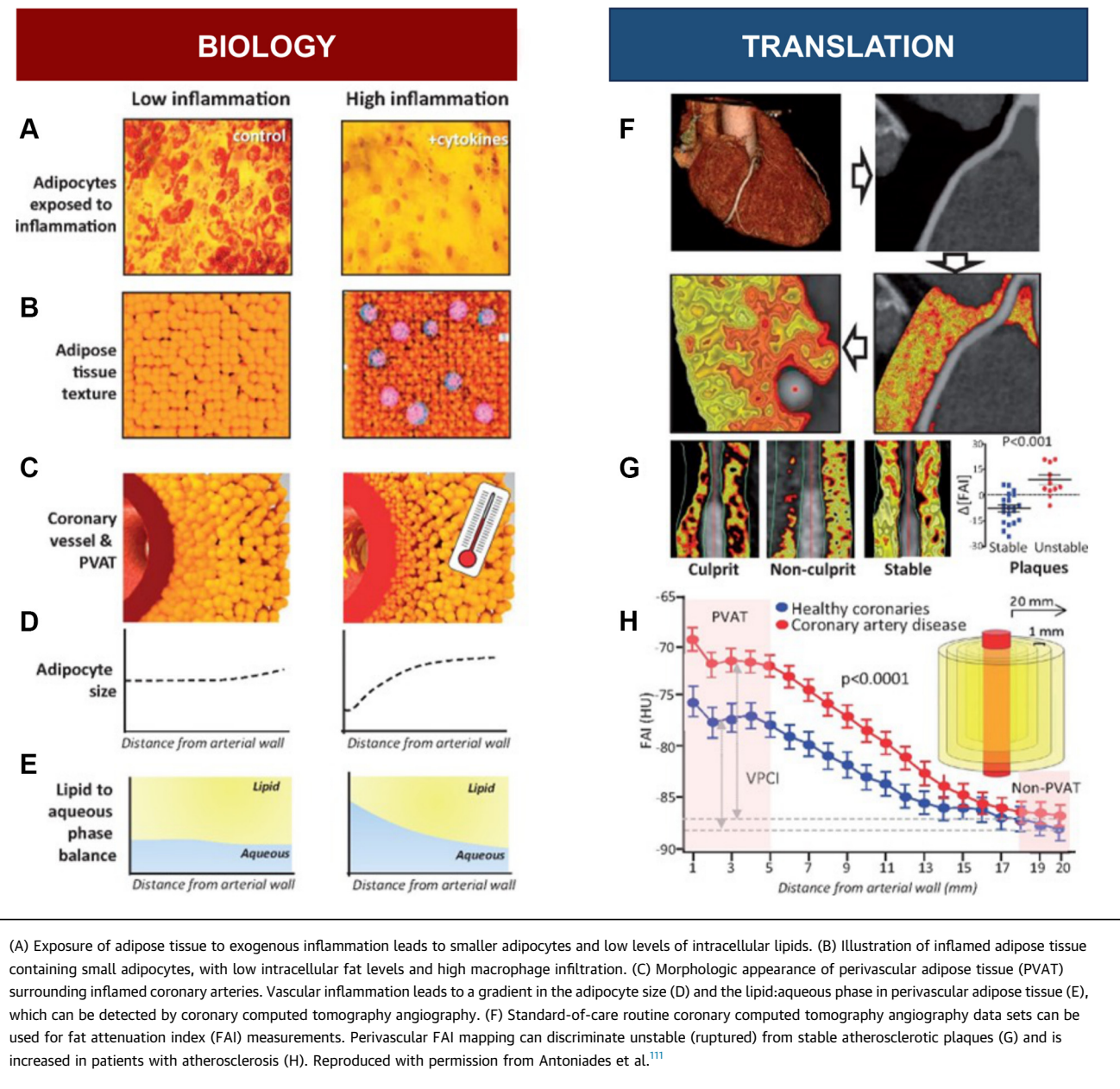
presence of any detectable coronary plaque, suggesting that patient vulnerability extends beyond immediately detectable plaque(s). This has been confirmed by others,^{56,57} including a recent study of 765 coronary lesions by Kuneman et al,⁵⁸ which found that mean unadjusted PCAT attenuation is significantly increased across culprit lesion precursors compared with non-culprit lesions in patients with ACS and vs lesions of patients with stable CAD, suggesting a higher intensity of inflammation.

Perivascular FAI has also been shown to accurately predict plaque progression⁴¹ and discriminate stable vs unstable atherosclerotic plaques in 2 independent cohorts (**Figures 2F to 2H**). These findings validate the utility of FAI for the detection of both global coronary artery inflammatory burden and clinically relevant plaques.

The utility of FAI for cardiac mortality risk prediction has also been explored. Stratifying by high vs low FAI is shown to be able to predict risk of cardiac mortality (**Figures 3A to 3D**), with high FAI being associated with higher risk. This prognostic value was even incremental to current clinical risk factors (Duke CAD Index and HRP features on coronary CTA).

Furthermore, HRP features on coronary CTA in conjunction with FAI show promise as a powerful clinically relevant merged analysis for CAD risk stratification (**Figures 3E to 3G**). A recent narrative review suggests that a technology to improve plaque risk evaluation with coronary CTA would be of great use.⁵⁹ Such findings have been confirmed by other studies, including the landmark SCOT-HEART (Scottish Computed Tomography of the Heart) trial,⁶⁰ in which PCAT attenuation of the right coronary artery was predictive of MI events (HR: 1.55; 95% CI: 1.08-2.22; $P = 0.017$, per 1 SD increment). In multivariable analysis, adding PCAT of the right coronary artery -70.5 HU or higher to model including low-attenuation plaque burden led to improved prediction of future MI (HR: 11.7; 95% CI: 3.3-40.9; $P < 0.0001$). In a 2022 meta-analysis of 9 studies by Sagris et al,⁶¹ the power of FAI to identify stable and unstable coronary plaques (via the mean difference in attenuation) was tested. FAI was found to be significantly higher in unstable plaques compared with stable plaques with a mean difference of 4.5 HU (95% CI: 1.10-7.89; $I^2 = 88\%$). Higher pericoronary FAI values offered incremental prognostic value for MACE in studies with prospective follow-up (HR: 3.29; 95% CI: 1.88-5.76; $I^2 = 75\%$) among 6,335 patients.

Other groups have investigated the application of FAI to confirm the hypothesis behind the biomarker.^{57,62} In a validation of the link between coronary artery inflammation and PVAT phenotype,

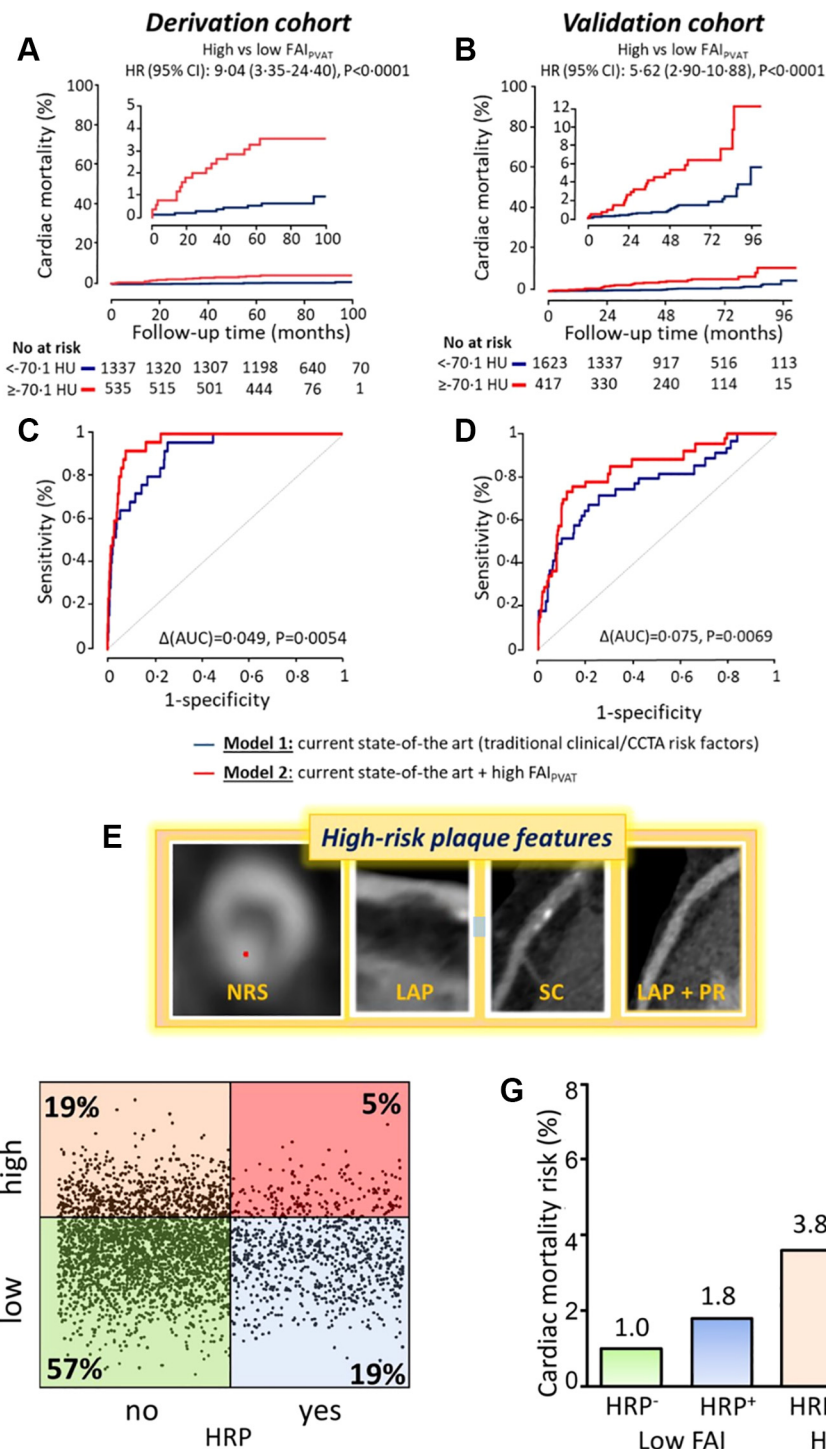
FIGURE 2 Schematic Representation of the Biology Underlying the Detection of Coronary Inflammation by Imaging PVAT

higher perivascular fat radiodensity has been shown to strongly correlate with both increased plaque inflammation as assessed by ¹⁸F-sodium fluoride (¹⁸F-NaF) uptake on PET-CT imaging⁶³ and the progression of total and noncalcified atherosclerotic plaque burden in the adjacent vessel.⁶⁴ It is noteworthy that in symptomatic patients undergoing cardiac CT imaging, the information captured by perivascular FAI is independent of coronary

calcification^{42,43} or systemic markers of inflammation such as high-sensitivity C-reactive protein.⁴²

Measuring perivascular attenuation in clinical practice is problematic, however, as it is affected by factors such as technical scan acquisition settings, image postprocessing, and local anatomical and biological factors.⁶⁵ This has led to the development of a fully corrected metric of coronary inflammation, the FAI Score, which allows us to individualize the

FIGURE 3 Prognostic Value of Perivascular FAI



Continued on the next page

inflammatory burden of each coronary artery relative to the patient and use it as a clinical biomarker of coronary inflammation.⁶⁵ Indeed, the FAI Score has received regulatory clearance (CE Mark) for use in clinical practice in the United Kingdom, Europe, and Australia, as the clinical metric of coronary inflammation obtained from coronary CTA. The medical device that measures the FAI Score (CaRi-HEART) incorporates these measurements and patient risk factors into a prognostic model of coronary atherosclerosis to generate the individualized patient risk for heart attack over a fixed period (using the CaRi-HEART risk calculator). The performance and prognostic value of the FAI Score in predicting cardiac mortality have been validated within the 2 original validation cohorts (Erlangen, n = 1,872; Cleveland Clinic, n = 2,040).⁶⁵

Pericoronary FAI has been shown to be responsive to established CAD treatments, including 3-hydroxy-3-methylglutaryl coenzyme A reductase inhibitors (ie, statins). In a retrospective analysis of 108 patients who underwent coronary CTA,⁶⁶ FAI was significantly lower in noncalcified plaques and mixed plaques when statin therapy was commenced (-68.0 ± 8.5 HU vs -71.5 ± 8.1 HU [$P < 0.001$] and -70.5 ± 8.9 HU vs -72.8 ± 9.0 HU [$P = 0.014$], respectively). This indicates potential for perivascular FAI as an imaging biomarker to monitor statin response. Indeed, **Figure 4B** presents a single case in which FAI was used to monitor the therapeutic response to statins through inflammatory burden in the right coronary artery. Currently, there is no direct noninvasive imaging test that clinicians can use to assess for potential response to such treatments.

The precise role for the perivascular FAI Score for assessment of coronary artery inflammation in clinical practice is in progress, with promising

workstreams now being developed. **Figure 4A** presents the proposed workstream for incorporating inflammatory imaging into clinical CT imaging with automated artificial intelligence (AI) performing both quantitative plaque analysis and inflammatory imaging with FAI. The associated personalized risk would then be calculated when clinical risk factors are entered by clinicians,⁶⁷ as PVAT inflammatory imaging is most powerful when integrated with plaque metrics and clinical risk factors (**Figure 4B**).

A recent clinical consensus statement from the European Society of Cardiology Working Group on Coronary Pathophysiology and Micro-circulation outlined current and future clinical applicability of AI technologies that integrate PVAT information into prognostic models.⁶⁸ The goal is to provide clinically meaningful information in primary and secondary prevention of atherosclerotic heart disease, which offers the best high-level guidance for clinicians yet.

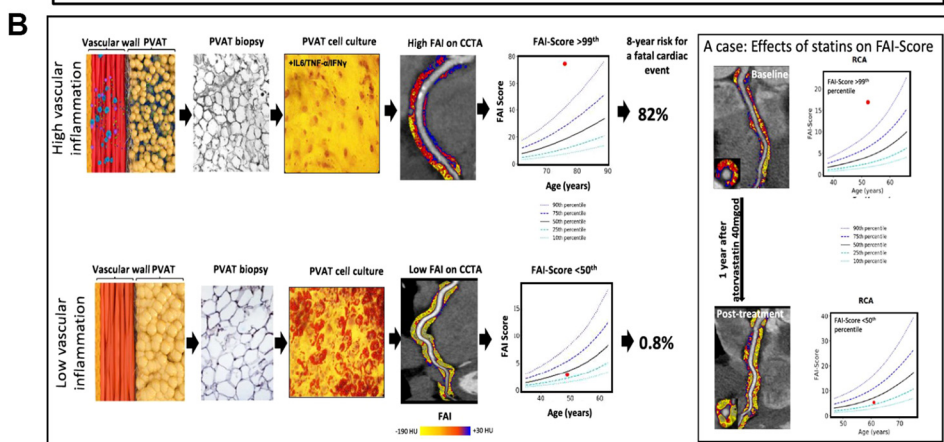
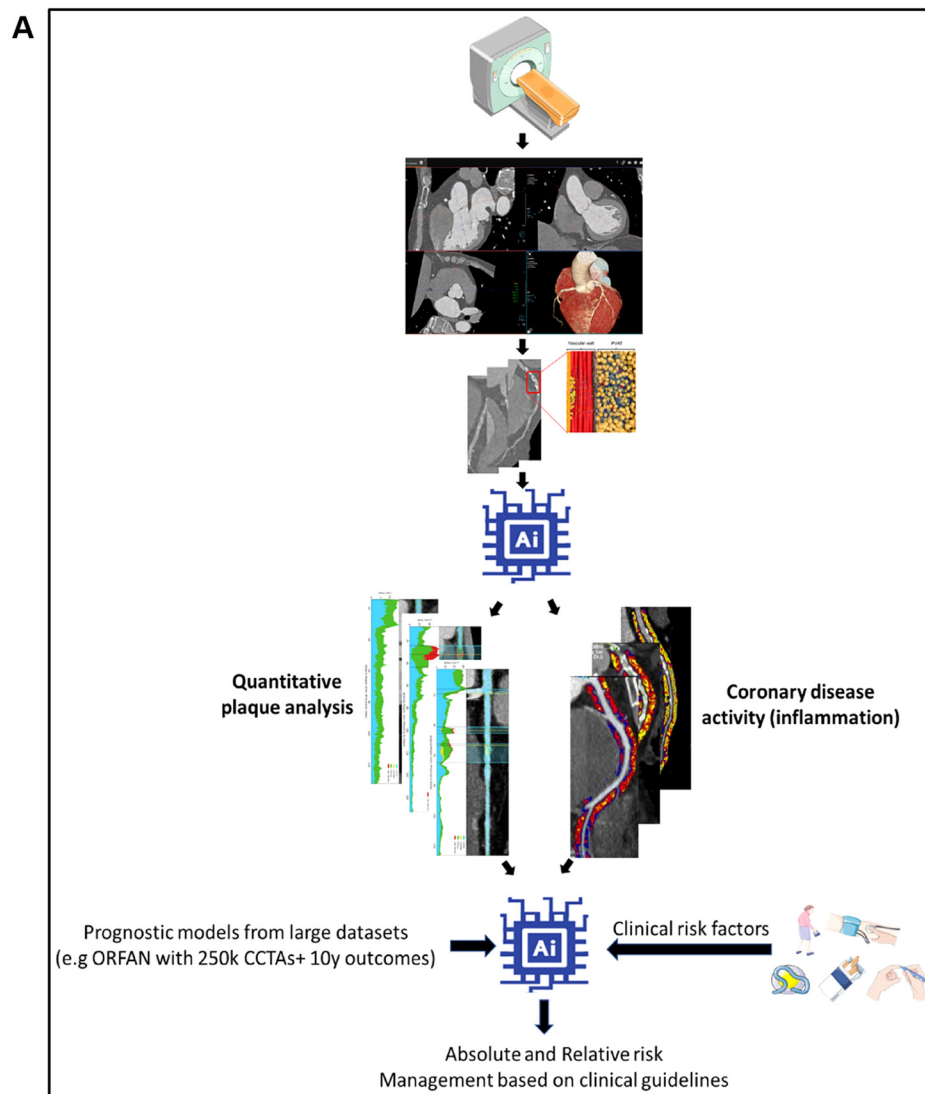
A relevant meta-analysis recently tested all current clinically available approaches to vascular inflammation detection and assessed their prognostic value.⁶⁹ The measurement of vascular inflammation in addition to clinical risk factors was found to significantly enhance risk discrimination for cardiovascular events (**Figure 5**). PVAT assessment with CT imaging yielded the highest C-index values of all means assessed. Thus, coronary CTA biomarkers such as HRP features and pericoronary fat imaging through the FAI (alone or in combination) enhance cardiovascular risk discrimination beyond circulating biomarkers of inflammation.

CT RADIOTRANSCRIPTOMICS FOR THE DETECTION OF VASCULAR INFLAMMATION. Handling CT scans as data sets for analysis rather than as images to examine with the human eye is the focus of the field of radiomics. Radiomics uses mathematical formulae

FIGURE 3 Continued

Prognostic value of perivascular FAI. (A, B) In the CRISP-CT (Cardiovascular Risk Prediction Using Computed Tomography) study, which evaluated 2 prospective clinical cohorts of 3,912 patients undergoing diagnostic coronary computed tomography angiography for clinical indications, perivascular FAI was predictive of cardiac mortality in both the derivation cohort and the validation cohort. (C, D) The FAI provided incremental prognostic value for cardiac mortality on top of traditional clinical risk factors, the Duke CAD Index, and number of high-risk plaque (HRP) features on coronary computed tomography angiography. Reproduced with permission from Oikonomou EK, Marwan M, Desai MY, et al. Non-invasive detection of coronary inflammation using computed tomography and prediction of residual cardiovascular risk (the CRISP CT study): a post-hoc analysis of prospective outcome data. *Lancet*. 2018;392:929–939. (E) HRP features on coronary computed tomography angiography are defined as the napkin-ring sign (NRS), low attenuation plaque (LAP), spotty calcification (SC), and positive remodeling (PR). (F, G) Stratification of the pooled population of CRISP-CT based on the presence of HRP and high coronary inflammatory burden as determined by the perivascular FAI and observed rates of cardiac mortality within each group. The combination of HRP and high FAI could be used to identify vulnerable patients at the highest risk who are eligible for aggressive prevention strategies; derived from post hoc data analysis of CRISP-CT data in the Oxford Academic Cardiovascular Computed Tomography Core Laboratory. Reproduced with permission from Antoniades et al.¹¹ AUC = area under the curve; other abbreviations as in **Figure 2**.

FIGURE 4 Concepts for Implementing Coronary Artery Plaque and Inflammation-Guided Management via CT Imaging in Clinical Practice



Continued on the next page

to compute many hundreds of shape-, attenuation-, and texture-related features for a given anatomical volume or segmentation.⁷⁰ Many radiomic features used together can be employed for disease diagnosis or prognostication. The field of radiomics was developed for the large-scale analysis of geospatial satellite imagery and first applied to health care in the field of cancer imaging.⁷¹ Radiomic approaches have now been implemented in coronary CTA with the aim of detecting biological mechanisms, including vascular inflammation occurring around the coronary arteries. Ultimately, the goal is to detect the residual inflammatory risk that continues to drive high morbidity and mortality associated with CAD.⁷²

Using AI for radiotranscriptomic phenotyping of PVAT in risk prediction can potentially generate more advanced biomarkers for comprehensive PVAT phenotyping. This approach promises to unlock detection of precise subtypes of vascular pathology that determine texture and composition of PVAT through perivascular lipolysis, adipogenesis, edema, fibrosis, and angiogenesis. Basic science techniques such as RNA sequencing and histology serve to establish the biological “ground truth” of vascular pathology to which the radiomic signature of PVAT on coronary CTA is trained to specifically detect.

In cardiovascular imaging, the term “radiotranscriptomic” was introduced to describe this process of training radiomic signatures against the transcriptomic profile of the tissue. **Figure 6A** outlines the development pipeline for radiotranscriptomic imaging biomarkers. Two lines of work are needed: tissue samples from relevant PVAT with deep RNA sequencing and CT imaging of the relevant PVAT segments with full radiomic feature extraction. To limit analysis to radiomic features that have potential value as imaging biomarkers, filtering steps are undertaken to exclude the following: 1) features that are not stable in test-retest analyses; 2) features that are highly correlated with each other; and 3) features that are significantly correlated with other measures of adipose tissue volume. Importantly, recursive feature

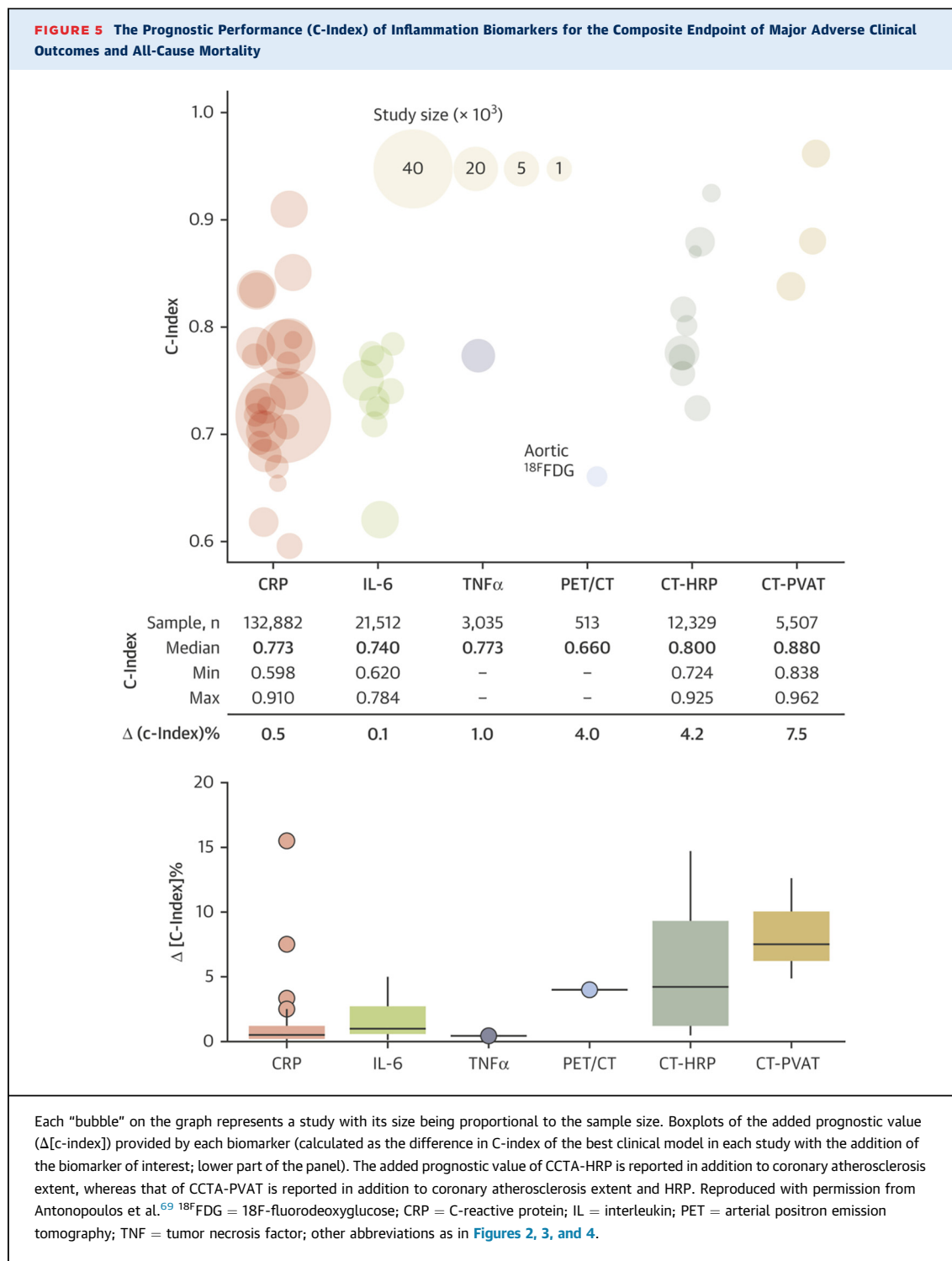
elimination with a random forest algorithm and repeated 5-times cross-validation have been shown to be a reproducible means to generate a final list of relevant radiomic features. Two examples of the development of radiotranscriptomic imaging biomarkers are outlined here, the fat radiomic profile (FRP) for CAD risk and the C19-RS for vascular inflammation attributable to COVID-19 infection.

In work that extended the use of CT radiomics beyond the power of a single radiomic feature for the assessment of changes in perivascular adipocytes that are reacting to vascular inflammation, we have reported the first study to apply complete radiomic feature quantification of coronary CTA scans for the purpose of better detection of vascular inflammation.⁷³ Radiomic signatures derived via a machine learning approach were able to detect coronary artery inflammation, and features of radiomic texture were found to be related to adipose tissue fibrosis and vascularity, as measured through gene expression in tissue samples obtained during cardiac surgery. An AI-derived algorithm, the FRP, was applied to the SCOT-HEART trial, in which it significantly improved major adverse cardiac event prediction beyond traditional risk stratification that included risk factors, coronary calcium score, coronary stenosis, and HRP features on coronary CTA ($\Delta[\text{C-statistic}] = 0.126$; $P < 0.001$).⁷⁴ This represented an improvement in cardiovascular disease risk prediction beyond the current state of the art.

Notably, it was found that FRP was unlike perivascular FAI in relation to its responsiveness to therapy, as the FRP was not altered up to 6 months after an index cardiac event while FAI was shown to improve during this time; this suggests that FRP is detecting PVAT changes beyond coronary inflammation alone, changes that are not captured by FAI and that are less susceptible to current treatment strategies for CAD. These findings have been confirmed by other groups, including Lin et al.,⁷⁵ who recently showed in a prospective case-control study that patients with acute MI have a distinct PCAT radiomic

FIGURE 4 Continued

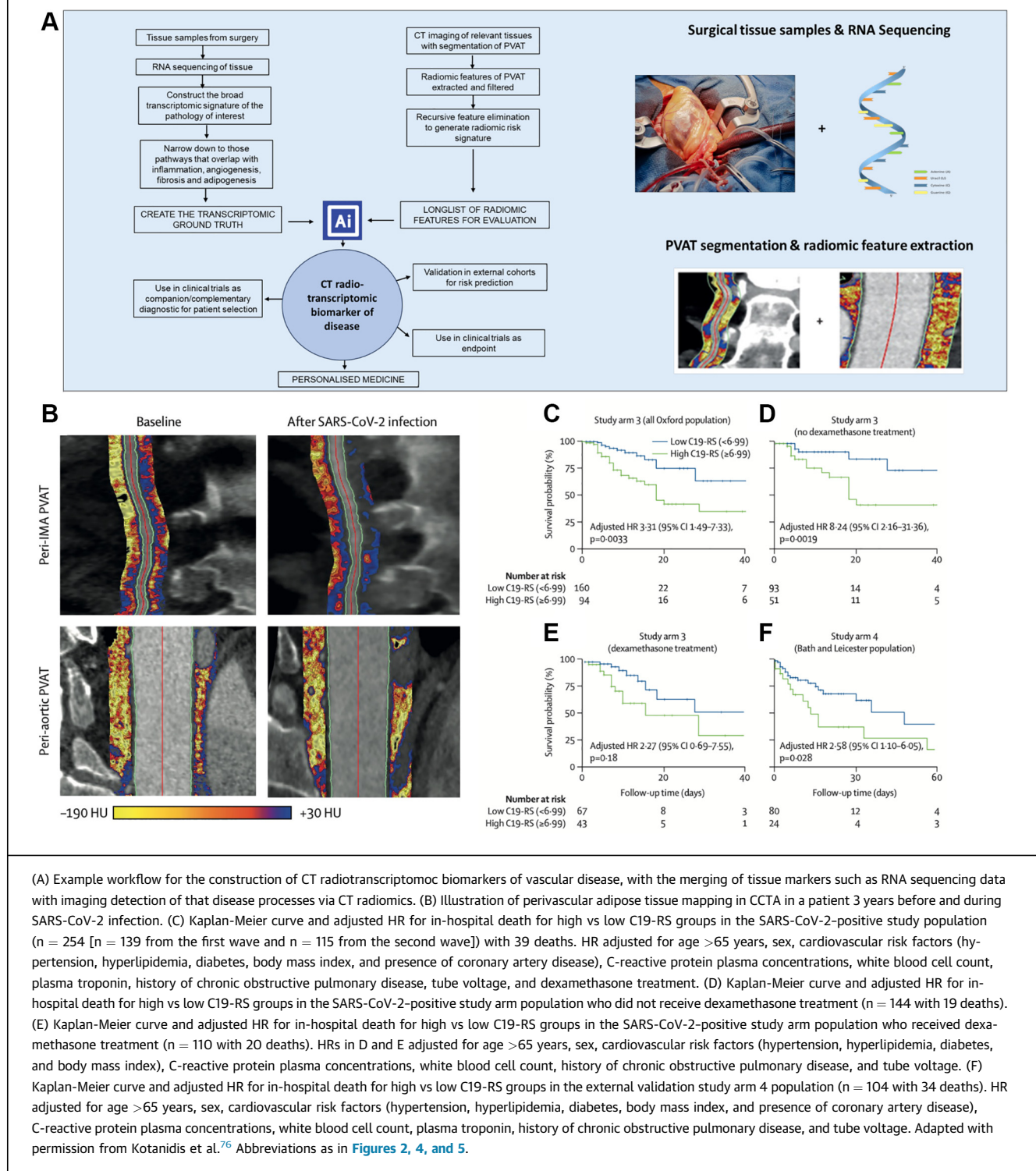
(A) Example of workflow for artificial intelligence (AI)-assisted computed tomography (CT) interpretation for the assessment of coronary artery disease, which includes automated prediction of a patient's risk of major adverse cardiovascular events and suggested medical management. (B) Schematic representation of the biology underlying the detection of coronary inflammation by imaging PVAT. Health coronary artery shown on bottom and high inflammation at top, with corresponding low and high FAI Scores, respectively. At right is an example of a single patient with a high FAI Score at baseline with reduced vascular inflammation after 1 year of treatment with atorvastatin 40 mg once daily. A is reproduced with permission from Antoniades et al.⁶⁷ B is reproduced with permission from Antoniades C et al.¹¹¹ CCTA = coronary computed tomography angiography; ORFAN = Oxford Risk Factors and Non Invasive Imaging Study; RCA = right coronary artery; other abbreviations as in **Figures 2 and 3**.



phenotype compared with patients with stable or no CAD. These findings are important in understanding the mechanistic pathways that are being detected in these radiomic analyses, most importantly inflammation and fibrosis, and the possible translational

applications of the technology into specific clinical scenarios related to the detection and monitoring of coronary artery inflammation.

In very recent work, we have also shown the role of CT radiomics for the detection of vascular

FIGURE 6 Radiotranscriptomic Detection of COVID-19 Severity Risk Using CT Detection of Perivascular Inflammation

inflammation and prognosis in patients with COVID-19 infection.⁷⁶ This is another example of how radiotranscriptomics can be harnessed for vascular inflammation in a non-atherosclerosis setting. This technology will facilitate more effective trials of treatments and could identify patients at long-term risk of complications arising from their infection who may respond to therapy. An AI-powered radiomic “fingerprint” of the perivascular space (C19-RS), trained using as ground truth a transcriptomic signature of cytokine-driven inflammation (derived from RNA sequencing of human internal mammary arteries), had a striking prognostic value in conditions triggering acute vascular inflammation such as COVID-19.⁷⁶ Technologies such as C19-RS are applicable to any type of contrast chest CT scan, gated (eg, CT coronary angiogram) or nongated (eg, CT angiogram of the pulmonary artery). It is important to note that C19-RS identifies an entirely distinct inflammatory phenotype from the pericoronary FAI and the FRP, with no overlap in radiomic features.

Indeed, patients with COVID-19 infection have much higher scores for C19-RS compared vs those without (Figure 6B). The score was found to have prognostic value for in-hospital mortality in COVID-19 in 2 testing cohorts (high [≥ 6.99] vs low [< 6.99] C19-RS; HR: 3.31 [95% CI: 1.49-7.33; $P = 0.0033$] [Figure 6C] and HR: 2.58 [95% CI: 1.10-6.05; $P = 0.028$, respectively]), adjusted for clinical factors, biochemical biomarkers of inflammation and myocardial injury, and technical parameters. C19-RS was also predictive of in-hospital death for high vs low C19-RS groups in the SARS-CoV-2-positive study arm population who did not receive dexamethasone treatment (Figure 6D) and those who did receive dexamethasone treatment (Figure 6E). HRs in Figures 6D and 6E are adjusted for age > 65 years, sex, cardiovascular risk factors (hypertension, hyperlipidemia, diabetes, and body mass index), C-reactive protein plasma concentrations, white blood cell count, history of chronic obstructive pulmonary disease, and tube voltage. The risk was validated in an external sample from geographically distinct locations for in-hospital death for high vs low C19-RS groups ($n = 104$ with 34 deaths) (Figure 6F). Finally, C19-RS was strongly associated ($R = 0.61$; $P = 0.00031$) with a whole blood transcriptional module representing dysregulation of coagulation and platelet aggregation pathways. This radiotranscriptomic signature for in-hospital mortality in acute COVID-19 worked even when applied in nongated CT angiograms of the pulmonary arteries.

Texture radiotranscriptomics can also be used to capture and quantify microcirculation in the perivascular space, in addition to lipolysis/adipogenesis,

fibrosis, and edema, offering additional prognostic value over the perivascular FAI Score for cardiac events. Machine learning/radiotranscriptomic approaches are anticipated to revolutionize the utilization of adipose tissue as a tool for exploring vascular biology.

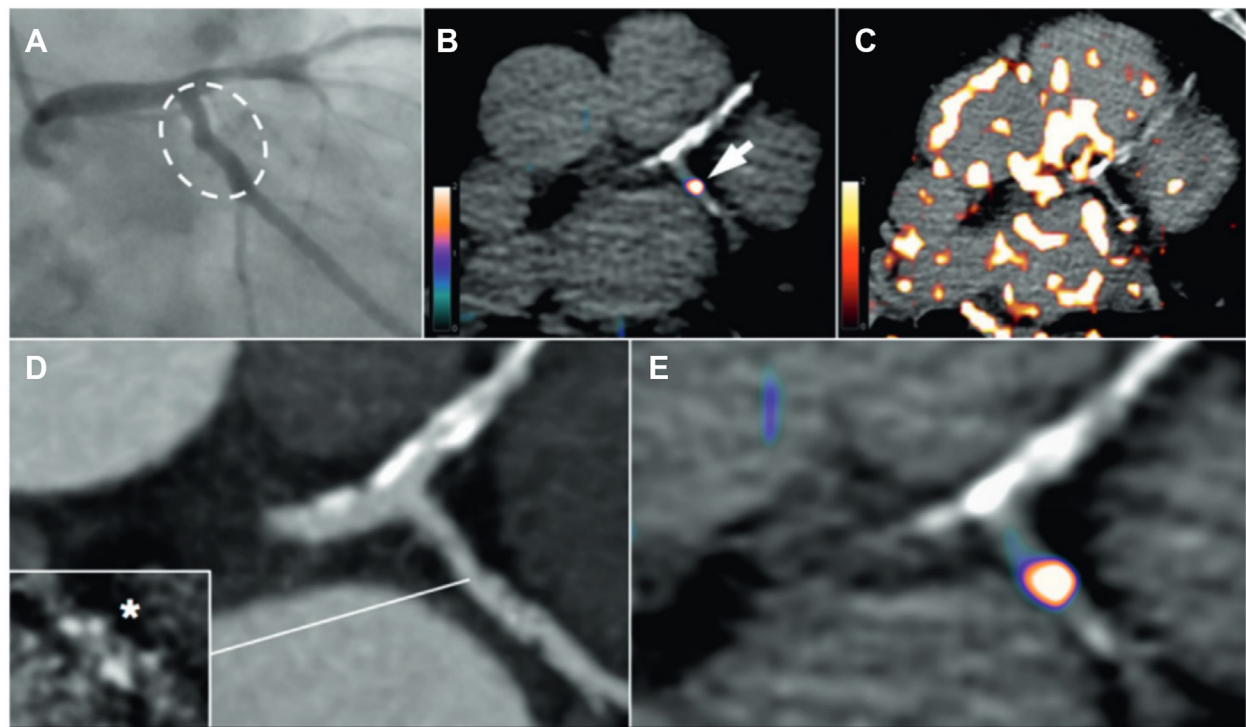
COMPETING TECHNOLOGIES

ULTRASOUND. Contrast-enhanced ultrasound has been investigated for visualization of inflammation in vessels affected by atherosclerosis. Although the techniques that have been developed have been useful in researching vascular inflammation, their clinical utility has not been fully realized. The potential future applications of ultrasound are particularly of interest as it could serve as a low-cost noninvasive modality for vascular inflammation detection.

The initial utility of ultrasound was in detection of early inflammation in the murine aorta, a classic animal model for cardiovascular disease. More recently, microbubbles targeted at VCAM type 1 (VCAM-1), a chemokine expressed by activated endothelial cells in atherosclerosis,⁷⁷ have facilitated use of ultrasound scans to evaluate arterial inflammation initially in vitro.⁷⁸ Noninvasive ultrasound has since been shown to detect VCAM-1 on human carotid arterial tissue using specialized microbubbles with a maleimide-thiol conjugation of an anti-VCAM-1 nanobody.^{79,80} Further in vitro research using contrast-enhanced ultrasound and von Willebrand factor A1-bearing microbubbles has been shown to detect activated platelets on vascular endothelium and indicate lesion severity in a rodent model of atherosclerosis.⁸¹ The use of microbubbles has not yet been validated *in vivo* in humans.

A recent translational study by Punjabi et al⁸² described the ability of VCAM-1-targeted microbubbles to detect treatment response to the glucagon-like peptide-1 agonist liraglutide by monitoring the VCAM-1 signal. This work shows the power of using biochemically targeted ultrasound imaging to prove molecular involvement *in vivo*. Intercellular adhesion molecule 1-targeted nano-ultrasonic contrast also has potential for future technological innovation to further our bottom-up understanding of atherosclerosis.⁸³

Furthermore, echocardiographic molecular imaging of vascular endothelium has recently been shown to detect reductions in pro-inflammatory signals (eg, P-selectin, VCAM-1, von Willebrand factor) as a result of anti-interleukin-1 β therapy.⁸⁴ Ultrasound therefore has the potential to evaluate the effects of

FIGURE 7 Coronary Artery PET Inflammation Imaging With ^{68}Ga -DOTATATE

Radiograph (A) and CT coronary angiograms (D) of a 67-year-old man with stable angina, showing minor left circumflex atheroma (hatched oval) with spotty calcification ([inset] *calcium scan) and calcified plaque in the left anterior descending artery. Although gallium-68-labeled DOTATATE (^{68}Ga -DOTATATE) positron emission tomography (PET) (B, E) allows unimpeded interpretation of inflammation in the left circumflex artery lesion (B, arrow), and lack of signal in the left anterior descending artery, coronary ^{18}F -fluorodeoxyglucose imaging is obscured by patchy myocardial tracer uptake (C). Adapted with permission from Tarkin et al.⁹³

preclinically validated molecules on pro-atherosclerotic inflammation, which is critical to spurring future development of inflammation-targeted therapies.

Clinically, the utility of advanced ultrasound techniques for detecting carotid disease is being increasingly appreciated. Intraplaque neovascularization is a marker of carotid instability, a known precursor to embolic stroke, but is not detectable with Doppler ultrasound; contrast-enhanced ultrasound can detect it only invasively. Recently, however, superb microvascular imaging, a noninvasive technique that removes noise while preserving low-velocity flow signal, has been shown to accurately detect intraplaque neovascularization.⁸⁵ A prospective cohort study comparing superb microvascular imaging against existing validated methods for detecting carotid plaque instability (eg, contrast-enhanced ultrasound, carotid-MRI and PET- ^{18}F -FDG, histology) is currently being conducted; the results have significant potential implications for detection

of carotid inflammation and risk prediction of carotid ischemic events beyond extent of stenosis.⁸⁶

Overall, although the results to date suggest that any ultrasound-based method of inflammation detection can be expected to have limited sensitivity relative to other imaging modalities, this is an area that could yield promising results in the future. This is especially true given that intravascular ultrasound has not yet been tested with the techniques discussed herein but could provide an exciting avenue for further research with greater resolution of the relevant tissues in real time.

MAGNETIC RESONANCE IMAGING. Along with echocardiography and PET, CMR imaging is widely considered a key tool for the diagnosis of inflammatory myocardial disease, with a Class I recommendation for the assessment of myocarditis and storage diseases in the current European Society of Cardiology guidelines for the diagnosis and treatment of acute and chronic heart failure.⁸⁷ Despite CMR being

TABLE 1 Detailed Summary of Imaging Modalities for Detection of Vascular Inflammation

	USS	Cardiac MRI	CT Imaging	PET-CT Imaging	PET-MRI
Traditional usage ^a	Assessment of heart function, including movement of myocardium and valves	Assessment of structural disease processes cardiomyopathies and pericardial disease, and myocardial viability	Assessment of coronary artery disease and congenital heart disease	Detection of ischemic and nonischemic cardiomyopathy and cardiac tumors	Not currently in widespread usage
Vascular inflammation usage	Accurate detection in murine models Nanobubbles + USS may indicate lesion severity in vitro	None validated at present	Detection of vascular inflammation via the perivascular fat attenuation index, with proposed diagnostic and prognostic usage	Detection of inflamed coronaries and residual post-MI inflammation Allows for tracking of plaque composition	Can detect active inflammation via SST ₂
Strengths	Low cost Truly noninvasive Ease of use IVUS may revolutionize	Potential for approach to vascular inflammation similar to that of myocardial inflammation	Rapid examination Validated tools for coronary artery inflammation detection	Molecular imaging with novel tracers allow targeted detection of inflammation; gold standard for tissue inflammation detection	Use of tracers allows for tissue-level resolution Resolution without radiation
Limitations	Low- resolution and no 3D analysis Clinical evidence lacking Unable to assess adipose around vessels	Low tissue-level resolution High cost Vascular assessment of large vessels only	Radiation exposure IV contrast needed	Requires access to advanced imaging center Poor spatial resolution	Lack of clinical availability and expertise Paucity of clinical evidence Cannot image adipose tissue

^aTraditional usage in brief; full indications are broader.

3D = 3-dimensional; CT = computed imaging; IV = intravenous; IVUS = intravascular ultrasound; MI = myocardial infarction; MRI = magnetic resonance imaging; PET = positron emission tomography; SST₂ = somatostatin receptor 2; USS = ultrasound scan.

shown to be an excellent noninvasive tool for the detection of myocardial inflammation in myocarditis, its utility in clinical detection of vascular inflammation has not been successfully achieved, as the means through which CMR detects myocardial disease do not map well to the pathobiology underlying the vascular inflammatory processes occurring in atherosclerosis. In detecting myocarditis, CMR does not directly assess immune cells but instead enables the assessment of macroscopic responses to inflammatory processes and myocardial injury at a low-resolution tissue level. The images acquired allow the identification of gross myocardial edema, vasodilation, fibrosis, and necrotic activity within the myocardium. Specific CMR sequences have been shown to be useful for the assessment of inflammatory pericardial disease. Such sequences include late gadolinium enhancement, T2 short tau inversion recovery, and viability phase-sensitive inversion recovery, which are also sequences that have been assessed for coronary artery inflammation detection.⁸⁸

The use of non-PET-MR specifically for early detection of vascular inflammation is therefore very limited. Researchers continue to investigate means to allow the analysis of standard CMR acquisitions to be

used for the identification of vascular inflammation as it would be an excellent addition to the clinical value achieved from this commonly performed noninvasive modality. Compared with CT imaging, CMR offers superior soft-tissue contrast, potentially allowing improved detection of HRP characteristics such as intraplaque hemorrhage, thrombus, and positive remodeling in large vessels. Importantly, CMR does not involve exposure to ionizing radiation; thus, if accurate means to assess both vascular plaque and the associated inflammation burden were discovered, they stand to be very powerful clinical tools.

PET-CT IMAGING. Molecular imaging technologies have emerged in the last decades as highly accurate techniques for the investigation of vascular inflammation in a noninvasive manner,⁸⁹ allowing detection of clinically relevant atherosclerotic inflammation,⁹⁰ with injectable tracers that bind pathophysiology-specific receptors. The tracers are then detected via PET. The exact mechanisms of the relevance of PET to cardiology have been thoroughly reviewed elsewhere.⁹¹ The most common intravenous tracer agent used in PET is ¹⁸F-FDG. This agent can noninvasively assess arterial inflammation as well as other inflammatory processes throughout the body.

^{18}F -FDG uptake reflects glucose metabolism, which is particularly increased in inflamed atherosclerotic disease exhibiting the retention of macrophages and hypoxic stress.

^{18}F -FDG has been used to assess the activity of metabolically active inflammatory cells and has shown a preference for inflamed coronary plaque in patients who have undergone proper preparation (low-carbohydrate, high-fat diet to suppress myocardial uptake of the tracer).⁹² Currently, ^{18}F -FDG PET-CT imaging is used in the clinic to assess myocardial viability and blood flow, as well as to detect and monitor noncoronary conditions such as sarcoidosis and myocarditis. It is also well validated for the identification of carotid plaque instability.⁸⁵

Another radiotracer, gallium-68-labeled DOTATATE (^{68}Ga -DOTATATE), can also provide clinically useful images of vascular inflammation. This tracer is widely used in imaging neuroendocrine tumors and binds to the somatostatin receptor subtype 2 (SST₂), which is expressed by M1 pro-inflammatory macrophages. PET-CT images using ^{68}Ga -DOTATATE have been found to produce better image quality than ^{18}F -FDG and can be used to identify inflamed coronary lesions⁹³ and residual inflammation in myocardial tissue after an acute MI.⁹⁴ Figure 7 illustrates the use of ^{68}Ga -DOTATATE for detection of coronary artery vascular inflammation compared with ^{18}F -FDG.

Several other radiotracers have also shown promise in imaging inflammation within the coronary wall. For instance, ^{18}F -NaF, which has a strong affinity for the vascular wall, has been shown to incorporate into hydroxyapatite in areas of arterial wall microcalcification. Imaging with ^{18}F -NaF has shown promising accuracy in detecting the culprit coronary lesions and abdominal aortic aneurysms,⁹⁵ with ^{18}F -NaF PET-CT imaging being the first noninvasive imaging method to identify and localize ruptured and high-risk coronary plaque.⁹⁶ ^{18}F -NaF has been used to investigate developing microcalcification in the vasculature. Work from Dweck et al⁹⁷ showed that coronary uptake was associated with cardiovascular risk, describing significant associations between coronary arterial NaF uptake and prior coronary events, angina status, and Framingham risk scores. Recent work from the same group has shown that in a small cohort of patients with established CAD pooled from a prospective observational study, ^{18}F -NaF PET provides powerful independent prediction of fatal or nonfatal MI.⁹⁸ ^{18}F -fluciclatide, a PET tracer that binds to $\alpha_v\beta_3$ integrin, is also considered a promising tool for identifying high-risk coronary plaque.⁹⁹ Indeed, small studies in humans have shown that the quantification of $\alpha_v\beta_3$ integrin expression with

^{18}F -fluciclatide PET has potential to assess plaque vulnerability and disease activity in aortic atherosclerosis.¹⁰⁰

There is early evidence to suggest that the 18 kDa translocator protein could be used as a target for imaging inflammation using a specific PET-CT tracer. For example, ^{11}C -PK11195 has been used to this end, although primarily in carotid disease cases. PET-CT imaging using ^{11}C -PK11195 has been found to distinguish between recently symptomatic and asymptomatic plaque in carotid disease populations.^{101,102}

Other experimental techniques have also been explored to visualize coronary artery inflammation using PET-CT imaging, such as visualizing chemokine receptors, which are up-regulated in pro-inflammatory macrophages, in experimental nanoplatforms,¹⁰³ or visualizing endothelial activation and inflammation using ^{18}F -labeled small VCAM-1 affinity ligands.¹⁰⁴ Magnetic resonance and optical detection technologies can be combined with PET to visualize inflammation by using ^{64}Cu -labeled 20 nm magnetofluorescent polysaccharide-containing nanoparticles,¹⁰⁵ which have been found to accumulate in macrophages in atherosclerotic lesions in apolipoprotein E knock-out mice.

Single-photon emission CT imaging/CT imaging that uses ^{111}In - and ^{123}I -radiolabeled compounds is another experimental approach to noninvasively visualize coronary artery inflammation. These compounds target activated matrix metalloproteinases and allow the detection and tracking of plaque composition in response to treatment.¹⁰⁶

Although ^{18}F -FDG PET-CT imaging and increasingly ^{18}F -NaF are widely used for myocardial assessment, the other mentioned techniques are currently experimental and restricted by their high costs, limited availability, and required expertise. As we have discussed, ^{18}F -FDG accumulation occurs with PET-CT imaging in vulnerable atherosclerotic plaque. From a clinician's perspective, the main obstacle to wider adoption of these techniques is a lack of clinical availability, lack of expertise, and, most importantly, a paucity of clinical evidence to show the translational potential of these PET-CT techniques for reduction of either primary or secondary cardiovascular risk.

PET-MRI TECHNOLOGY. As discussed earlier in relation to PET-CT imaging, ^{18}F -FDG can assess arterial inflammation *in vivo* because tracer uptake reflects, at least in part, the presence of invading inflammatory cells, including macrophages and foam cell formation.¹⁰⁷ MRI can also provide atherosclerotic plaque detection and characterization; thus, hybrid

PET-MRI technology has the potential to simultaneously provide anatomical and functional information.¹⁰⁸ However, data on vascular PET-MRI remain scarce, with the focus of research on carotid atherosclerosis.¹⁰⁹

In recent work focused on the detection of vascular inflammation in patients with large vessel vasculitis, it has been shown that PET-MRI can be used to detect active inflammation via the detection of SST₂ as a novel inflammation-specific molecular marker.¹¹⁰ SST₂ is expressed by inflammatory macrophages activated in vitro, and SST₂ staining colocalizes with CD68⁺ macrophages within inflamed atherosclerotic plaques. Of the somatostatin receptor PET tracers used for clinical neuroendocrine tumor imaging, ⁶⁸Ga-DOTATATE has the highest binding affinity for SST₂. A novel ¹⁸F click-labeled octreotide radioligand called ¹⁸F-FET-βAG-TOCA has also shown high SST₂-binding affinity and favorable tracer kinetics. SST₂ PET-MRI was found to be consistent with ¹⁸F-FDG PET-CT imaging in patients with large vessel vasculitis. Resolution of the PET-MRI clinical images was found to be suitable for coronary and intracranial arteries.

Other experimental PET-MRI probes are currently in development for inflammatory purposes. These include ¹⁸fluorine-fluoromethylcholine, which has shown better identification of atherosclerotic plaque and lower myocardial uptake compared with ¹⁸F-FDG in murine models. Current trials of this probe include a PET-MRI study recruiting those with ACS who will undergo optical coherence tomography to investigate if intravascular findings of high-risk plaque correlate with ¹⁸fluorine-fluoromethylcholine uptake on PET-MRI ([NCT03252990](#)). There are also a number of small clinical studies investigating the use of cell adhesion motifs for inflammatory imaging in atherosclerosis. One of the most advanced is tripeptide Arg-Gly-Asp (RGD), which was originally identified as the sequence within fibronectin that mediates cell attachment. The RGD motif has now been found in numerous other proteins and has been identified as a key molecule that supports cell adhesion within atherosclerotic plaque.

An ongoing ¹⁸F-FPPRGD2 study is exploring the use of these probes in both PET-MRI and PET-CT imaging in a cohort of carotid endarterectomy patients ([NCT02995642](#)).

CONCLUSIONS

The field of noninvasive clinical imaging of vascular inflammation has undergone significant advancements in recent years (**Table 1**). The integration of various imaging modalities into clinical practice such as CT and molecular imaging with PET-CT imaging has allowed for a more comprehensive and accurate assessment of the presence and extent of vascular inflammation, particularly in the coronary arteries. The application of image analysis techniques on imaging data sets (eg, perivascular FAI Score and radiotranscriptomic phenotyping from routine coronary CTA) have shown very promising results in the use of vascular inflammation as part of CAD risk stratification. Ongoing studies are expected to validate their clinical utility, economic feasibility, and overall impact on clinical management in primary and secondary prevention.

FUNDING SUPPORT AND AUTHOR DISCLOSURES

Dr Antoniades declares several patents (US10,695,023B2, PCT/GB2017/053262, GB2018/1818049.7, GR20180100490, and GR20180100510) licensed to Caristo Diagnostics. Dr Antoniades is the Chair of the British Atherosclerosis Society, as well as founder, shareholder, and director of Caristo Diagnostics, a University of Oxford spinout company. He declares past honoraria from Amarin, Silence Therapeutics, and Caristo Diagnostics; and funding from the British Heart Foundation (CH/F/21/90009 and RG/F/21/110040), the British National Institute for Health and Care Research, and the Oxford Biomedical Research Centre. All other authors have reported that they have no relationships relevant to the contents of this paper to disclose.

ADDRESS FOR CORRESPONDENCE: Dr Charalambos Antoniades, British Heart Foundation Chair of Cardiovascular Medicine, Division of Cardiovascular Medicine, University of Oxford, John Radcliffe Hospital, Headley Way, Oxford OX3 9DU, United Kingdom. E-mail: charalambos.antonides@cardiov.ox.ac.uk.

REFERENCES

- Roth GA, Mensah GA, Johnson CO, et al. Global burden of cardiovascular diseases and risk factors, 1990-2019: update from the GBD 2019 Study. *J Am Coll Cardiol.* 2020;76(25):2982-3021.
- Libby P, Ridker PM, Maseri A. Inflammation and atherosclerosis. *Circulation.* 2002;105(9):1135-1143.
- Shobeiri N, Beneck MP. Interleukin-1beta is a key biomarker and mediator of inflammatory vascular calcification. *Arterioscler Thromb Vasc Biol.* 2017;37(2):179-180.
- Madonna R, Massaro M, Scoditti E, Pescetelli I, De Caterina R. The epicardial adipose tissue and the coronary arteries: dangerous liaisons. *Cardiovasc Res.* 2019;115(6):1013-1025.
- Ross R, Glomset J, Harker L. Response to injury and atherogenesis. *Am J Pathol.* 1977;86(3):675-684.
- Ross R. Atherosclerosis—an inflammatory disease. *N Engl J Med.* 1999;340(2):115-126.
- Soehnlein O, Libby P. Targeting inflammation in atherosclerosis—from experimental insights to the clinic. *Nat Rev Drug Discov.* 2021;20(8):589-610.

- 8.** Sage AP, Tsiantoulas D, Binder CJ, Mallat Z. The role of B cells in atherosclerosis. *Nat Rev Cardiol.* 2019;16(3):180–196.
- 9.** Gistera A, Hansson GK. The immunology of atherosclerosis. *Nat Rev Nephrol.* 2017;13(6):368–380.
- 10.** Barrett TJ, Schlegel M, Zhou F, et al. Platelet regulation of myeloid suppressor of cytokine signaling 3 accelerates atherosclerosis. *Sci Transl Med.* 2019;11(517).
- 11.** Chen L, Deng H, Cui H, et al. Inflammatory responses and inflammation-associated diseases in organs. *Oncotarget.* 2017;9(6):7204–7218.
- 12.** Paulson KE, Zhu SN, Chen M, Nurmohamed S, Jongstra-Bilen J, Cybulsky MI. Resident intimal dendritic cells accumulate lipid and contribute to the initiation of atherosclerosis. *Circ Res.* 2010;106(2):383–390.
- 13.** Williams JW, Zaitsev K, Kim KW, et al. Limited proliferation capacity of aortic intima resident macrophages requires monocyte recruitment for atherosclerotic plaque progression. *Nat Immunol.* 2020;21(10):1194–1204.
- 14.** Pekayvaz K, Gold C, Hoseinpour P, et al. Murine cell-derived chemokines provide a protective niche to safeguard vascular macrophages and limit chronic inflammation. *Immunity.* 2023;56(10):2325–2341.e15.
- 15.** Gardner SE, Humphry M, Bennett MR, Clarke MC. Senescent vascular smooth muscle cells drive inflammation through an interleukin-1alpha-dependent senescence-associated secretory phenotype. *Arterioscler Thromb Vasc Biol.* 2015;35(9):1963–1974.
- 16.** Franck G, Mawson T, Sausen G, et al. Flow perturbation mediates neutrophil recruitment and potentiates endothelial injury via TLR2 in mice: implications for superficial erosion. *Circ Res.* 2017;121(1):31–42.
- 17.** Sheikh AS, Yahya S, Sheikh NS, Sheikh AA. C-reactive protein as a predictor of adverse outcome in patients with acute coronary syndrome. *Heart Views.* 2012;13(1):7–12.
- 18.** Armstrong EJ, Morrow DA, Sabatine MS. Inflammatory biomarkers in acute coronary syndromes: part I: introduction and cytokines. *Circulation.* 2006;113(6):e72–e75.
- 19.** Schmitz T, Harmel E, Heier M, Peters A, Linseisen J, Meisinger C. Inflammatory plasma proteins predict short-term mortality in patients with an acute myocardial infarction. *J Transl Med.* 2022;20(1):457.
- 20.** Tousoulis D, Kampoli AM, Papageorgiou N, et al. Pathophysiology of atherosclerosis: the role of inflammation. *Curr Pharm Des.* 2011;17(37):4089–4110.
- 21.** Boren J, Chapman MJ, Krauss RM, et al. Low-density lipoproteins cause atherosclerotic cardiovascular disease: pathophysiological, genetic, and therapeutic insights: a consensus statement from the European Atherosclerosis Society Consensus Panel. *Eur Heart J.* 2020;41(24):2313–2330.
- 22.** Antonopoulos AS, Margaritis M, Lee R, Channon K, Antoniades C. Statins as anti-inflammatory agents in atherogenesis: molecular mechanisms and lessons from the recent clinical trials. *Curr Pharm Des.* 2012;18(11):1519–1530.
- 23.** Crea F, Libby P. Acute coronary syndromes: the way forward from mechanisms to precision treatment. *Circulation.* 2017;136(12):1155–1166.
- 24.** Taqueti VR, Shah AM, Everett BM, et al. Coronary flow reserve, inflammation, and myocardial strain: the CIRT-CFR trial. *J Am Coll Cardiol Basic Transl Science.* 2023;8(2):141–151.
- 25.** Ridker PM, Danielson E, Fonseca FA, et al. Rosuvastatin to prevent vascular events in men and women with elevated C-reactive protein. *N Engl J Med.* 2008;359(21):2195–2207.
- 26.** Ridker PM, Everett BM, Thuren T, et al. Anti-inflammatory therapy with canakinumab for atherosclerotic disease. *N Engl J Med.* 2017;377(12):1119–1131.
- 27.** Antoniades C, West HW. ESC CVD Prevention Guidelines 2021: improvements, controversies, and opportunities. *Cardiovasc Res.* 2022;118(2):e17–e19.
- 28.** Ridker PM, Everett BM, Pradhan A, et al. Low-dose methotrexate for the prevention of atherosclerotic events. *N Engl J Med.* 2019;380(8):752–762.
- 29.** O'Donoghue ML, Braunwald E, White HD, et al. Effect of darapladib on major coronary events after an acute coronary syndrome: the SOLID-TIMI 52 randomized clinical trial. *JAMA.* 2014;312(10):1006–1015.
- 30.** O'Donoghue ML, Glaser R, Cavender MA, et al. Effect of losmapimod on cardiovascular outcomes in patients hospitalized with acute myocardial infarction: a randomized clinical trial. *JAMA.* 2016;315(15):1591–1599.
- 31.** Tardif JC, Kouz S, Waters DD, et al. Efficacy and safety of low-dose colchicine after myocardial infarction. *N Engl J Med.* 2019;381(26):2497–2505.
- 32.** Nidorf SM, Fiolet ATL, Mosterd A, et al. Colchicine in patients with chronic coronary disease. *N Engl J Med.* 2020;383(19):1838–1847.
- 33.** Parums DV. Editorial: the 2021 European Society of Cardiology (ESC) Guidelines on the Real-World Prevention of Atherosclerotic Cardiovascular Disease (ASCVD). *Med Sci Monit.* 2021;27:e935172.
- 34.** Bhatt DL, Steg PG, Miller M, et al. Cardiovascular risk reduction with icosapent ethyl for hypertriglyceridemia. *N Engl J Med.* 2019;380(1):11–22.
- 35.** Ridker PM. From RESCUE to ZEUS: will interleukin-6 inhibition with zilitavemab prove effective for cardiovascular event reduction? *Cardiovasc Res.* 2021;117(11):e138–e140.
- 36.** Oikonomou Evangelos K, West Henry W, Antoniades C. Cardiac computed tomography: coronary inflammation and other plaque features. *Arterioscler Thromb Vasc Biol.* 2019;39(11):2207–2219.
- 37.** Gulati M, Levy PD, Mukherjee D, et al. 2021 AHA/ACC/AES/CHEST/SAEM/SCCT/SCMR guideline for the evaluation and diagnosis of chest pain: a report of the American College of Cardiology/American Heart Association Joint Committee on Clinical Practice Guidelines. *J Am Coll Cardiol.* 2021;78(21):e187–e285.
- 38.** Kuunutti J, Wijns W, Saraste A, et al. 2019 ESC guidelines for the diagnosis and management of chronic coronary syndromes: the Task Force for the diagnosis and management of chronic coronary syndromes of the European Society of Cardiology (ESC). *Eur Heart J.* 2019;41(3):407–477.
- 39.** Curry RC, Leipsic J, Abbara S, et al. CAD-RADS 2.0–2022 Coronary Artery Disease-Reporting and Data System: an expert consensus document of the Society of Cardiovascular Computed Tomography (SCCT), the American College of Cardiology (ACC), the American College of Radiology (ACR), and the North America Society of Cardiovascular Imaging (NASCI). *J Am Coll Cardiol Img.* 2022;15(11):1974–2001.
- 40.** Maron DJ, Hochman JS. Invasive or conservative strategy for stable coronary disease. *Reply.* *N Engl J Med.* 2020;383(10):e66.
- 41.** Antoniades C, West HW. Coronary CT angiography as an 'one-stop shop' to detect the high-risk plaque and the vulnerable patient. *Eur Heart J.* 2021;42(37):3853–3855.
- 42.** Mancio J, Oikonomou EK, Antoniades C. Perivascular adipose tissue and coronary atherosclerosis. *Heart.* 2018;104(20):1654–1662.
- 43.** Antonopoulos AS, Sanna F, Sabharwal N, et al. Detecting human coronary inflammation by imaging perivascular fat. *Sci Transl Med.* 2017;9(398).
- 44.** Oikonomou EK, Antoniades C. The role of adipose tissue in cardiovascular health and disease. *Nat Rev Cardiol.* 2019;16(2):83–99.
- 45.** Badimon L, Cubedo J. Adipose tissue depots and inflammation: effects on plasticity and resident mesenchymal stem cell function. *Cardiovasc Res.* 2017;113(9):1064–1073.
- 46.** Antonopoulos AS, Margaritis M, Coutinho P, et al. Adiponectin as a link between type 2 diabetes and vascular NADPH oxidase activity in the human arterial wall: the regulatory role of perivascular adipose tissue. *Diabetes.* 2015;64(6):2207–2219.
- 47.** Margaritis M, Antonopoulos AS, Digby J, et al. Interactions between vascular wall and perivascular adipose tissue reveal novel roles for adiponectin in the regulation of endothelial nitric oxide synthase function in human vessels. *Circulation.* 2013;127(22):2209–2221.
- 48.** Ohyama K, Matsumoto Y, Takanami K, et al. Coronary adventitial and perivascular adipose tissue inflammation in patients with vasospastic angina. *J Am Coll Cardiol.* 2018;71(4):414–425.
- 49.** Antonopoulos AS, Margaritis M, Coutinho P, et al. Reciprocal effects of systemic inflammation and brain natriuretic peptide on adiponectin biosynthesis in adipose tissue of patients with ischemic heart disease. *Arterioscler Thromb Vasc Biol.* 2014;34(9):2151–2159.
- 50.** Akoumanakis I, Tarun A, Antoniades C. Perivascular adipose tissue as a regulator of vascular disease pathogenesis: identifying novel therapeutic targets. *Br J Pharmacol.* 2017;174(20):3411–3424.

- 51.** Sowka A, Dobrzn P. Role of perivascular adipose tissue-derived adiponectin in vascular homeostasis. *Cells*. 2021;10(6).
- 52.** Polkinghorne M, West H, Antoniades C. The role of perivascular fat in the diagnosis and prognosis of atherosclerosis. *Cardiometab Syndr*. 2023;3(1):8-26.
- 53.** Mancio J, Azevedo D, Saraiwa F, et al. Epicardial adipose tissue volume assessed by computed tomography and coronary artery disease: a systematic review and meta-analysis. *Eur Heart J Cardiovasc Imaging*. 2018;19(5):490-497.
- 54.** Klüner LV, Oikonomou EK, Antoniades C. Assessing cardiovascular risk by using the fat attenuation index in coronary CT angiography. *Radiol Cardiothorac Imaging*. 2021;3(1):e200563.
- 55.** Kotanidis CP, Antoniades C. Perivascular fat imaging by computed tomography (CT): a virtual guide. *Br J Pharmacol*. 2021;178(21):4270-4290.
- 56.** Libby P, Pasterkamp G, Crea F, Jang I-K. Reassessing the mechanisms of acute coronary syndromes. *Circ Res*. 2019;124(1):150-160.
- 57.** Goeller M, Achenbach S, Cadet S, et al. Pericoronary adipose tissue computed tomography attenuation and high-risk plaque characteristics in acute coronary syndrome compared with stable coronary artery disease. *JAMA Cardiol*. 2018;3(9):858-863.
- 58.** Kuneman JH, van Rosendaal SE, van der Bijl P, et al. Pericoronal adipose tissue attenuation in patients with acute coronary syndrome versus stable coronary artery disease. *Circ Cardiovasc Imaging*. 2023;16(2):e014672.
- 59.** Stone PH, Libby P, Boden WE. Fundamental pathobiology of coronary atherosclerosis and clinical implications for chronic ischemic heart disease management—the plaque hypothesis: a narrative review. *JAMA Cardiol*. 2023;8(2):192-201.
- 60.** Tzolos E, Williams MC, McElhinney P, et al. Pericoronal adipose tissue attenuation, low-attenuation plaque burden, and 5-year risk of myocardial infarction. *J Am Coll Cardiol Img*. 2022;15(6):1078-1088.
- 61.** Sagris M, Antonopoulos AS, Simantiris S, et al. Pericoronal fat attenuation index—a new imaging biomarker and its diagnostic and prognostic utility: a systematic review and meta-analysis. *Eur Heart J Cardiovasc Imaging*. 2022;23(12):e526-e536.
- 62.** Hedgire S, Baliyan V, Zucker EJ, et al. Perivascular epicardial fat stranding at coronary CT angiography: a marker of acute plaque rupture and spontaneous coronary artery dissection. *Radiology*. 2018;287(3):808-815.
- 63.** Kwiecinski J, Dey D, Cadet S, et al. Pericoronary adipose tissue density is associated with ¹⁸F-sodium fluoride coronary uptake in stable patients with high-risk plaques. *J Am Coll Cardiol Img*. 2019;12(10):2000-2010.
- 64.** Goeller M, Tamarappoo BK, Kwan AC, et al. Relationship between changes in pericoronal adipose tissue attenuation and coronary plaque burden quantified from coronary computed tomography angiography. *Eur Heart J Cardiovasc Imaging*. 2019;20(6):636-643.
- 65.** Oikonomou EK, Antonopoulos AS, Schottlander D, et al. Standardized measurement of coronary inflammation using cardiovascular computed tomography: integration in clinical care as a prognostic medical device. *Cardiovasc Res*. 2021;117(13):2677-2690.
- 66.** Dai X, Yu L, Lu Z, Shen C, Tao X, Zhang J. Serial change of perivascular fat attenuation index after statin treatment: insights from a coronary CT angiography follow-up study. *Int J Cardiol*. 2020;319:144-149.
- 67.** Antoniades C, Patel P, Antonopoulos AS. Using artificial intelligence to study atherosclerosis, predict risk and guide treatments in clinical practice. *Eur Heart J*. 2023;44(6):437-439.
- 68.** Antoniades C, Tousoulis D, Vavlikis M, et al. Perivascular adipose tissue as a source of therapeutic targets and clinical biomarkers. *Eur Heart J*. 2023;44(38):3827-3844.
- 69.** Antonopoulos AS, Angelopoulos A, Papapetrikou P, et al. Biomarkers of vascular inflammation for cardiovascular risk prognostication: a meta-analysis. *J Am Coll Cardiol Img*. 2022;15(3):460-471.
- 70.** Oikonomou EK, Siddique M, Antoniades C. Artificial intelligence in medical imaging: a radiomic guide to precision phenotyping of cardiovascular disease. *Cardiovasc Res*. 2020;116(13):2040-2054.
- 71.** El Ayach R, Giraud N, Giraud P, et al. The role of radiomics in lung cancer: from screening to treatment and follow-up. *Front Oncol*. 2021;11:603595.
- 72.** Oikonomou EK, Schottlander D, Antonopoulos AS, et al. Standardised quantification of coronary inflammation using cardiac computed tomography: the fat attenuation index score (FAI-Score). *Eur J Prevent Cardiol*. 2021;28(suppl 1):zwab061.451.
- 73.** Oikonomou EK, Williams MC, Kotanidis CP, et al. A novel machine learning-derived radio-transcriptomic signature of perivascular fat improves cardiac risk prediction using coronary CT angiography. *Eur Heart J*. 2019;40(43):3529-3543.
- 74.** Oikonomou EK, Williams MC, Kotanidis CP, et al. A novel machine learning-derived radio-transcriptomic signature of perivascular fat improves cardiac risk prediction using coronary CT angiography. *Eur Heart J*. 2019;40(43):3529-3543.
- 75.** Lin A, Kolossvary M, Yuvaraj J, et al. Myocardial infarction associates with a distinct pericoronal adipose tissue radiomic phenotype: a prospective case-control study. *J Am Coll Cardiol Img*. 2020;13(11):2371-2383.
- 76.** Kotanidis CP, Xie C, Alexander D, et al. Constructing custom-made radiotranscriptomic signatures of vascular inflammation from routine CT angiograms: a prospective outcomes validation study in COVID-19. *Lancet Digital Health*. 2022;4(10):e705-e716.
- 77.** Kaufmann BA, Carr CL, Belcik JT, et al. Molecular imaging of the initial inflammatory response in atherosclerosis. *Arterioscler Thromb Vasc Biol*. 2010;30(1):54-59.
- 78.** Kaufmann BA, Sanders JM, Davis C, et al. Molecular imaging of inflammation in atherosclerosis with targeted ultrasound detection of vascular cell adhesion molecule-1. *Circulation*. 2007;116(3):276-284.
- 79.** Punjabi M, Xu L, Ochoa-Espinosa A, et al. Ultrasound molecular imaging of atherosclerosis with nanobodies. *Arterioscler Thromb Vasc Biol*. 2019;39(12):2520-2530.
- 80.** Weinkauf CC, Concha-Moore K, Lindner JR, et al. Endothelial vascular cell adhesion molecule 1 is a marker for high-risk carotid plaques and target for ultrasound molecular imaging. *J Vasc Surg*. 2018;68(6S):1055-113S.
- 81.** Tian J, Weng Y, Sun R, et al. Contrast-enhanced ultrasound molecular imaging of activated platelets in the progression of atherosclerosis using microbubbles bearing the von Willebrand factor A1 domain. *Exp Ther Med*. 2021;22(1):721.
- 82.** Punjabi M, Kosareva A, Xu L, et al. Ligand-labeled endothelial vascular cell adhesion molecule-1 in murine atherosclerosis independent of glucose levels. *J Am Coll Cardiol Basic Trans Science*. 2023;8(2):189-200.
- 83.** Li P, Jin L, Feng L, Wang Y, Yang R. ICAM-1-carrying targeted nano contrast agent for evaluating inflammatory injury in rabbits with atherosclerosis. *Sci Rep*. 2021;11(1):16508.
- 84.** Shentu W, Ozawa K, Nguyen TA, et al. Echo-cardiographic molecular imaging of the effect of anticytokine therapy for atherosclerosis. *J Am Soc Echocardiogr*. 2021;34(4):433-442.e3.
- 85.** Zamani M, Skagen K, Scott H, Lindberg B, Russell D, Skjelland M. Carotid plaque neovascularization detected with superb microvascular imaging ultrasound without using contrast media. *Stroke*. 2019;50(11):3121-3127.
- 86.** Zamani M, Skagen K, Scott H, Russell D, Skjelland M. Advanced ultrasound methods in assessment of carotid plaque instability: a prospective multimodal study. *BMC Neurol*. 2020;20(1):39.
- 87.** Ponikowski P, Voors AA, Anker SD, et al. 2016 ESC guidelines for the diagnosis and treatment of acute and chronic heart failure: the Task Force for the diagnosis and treatment of acute and chronic heart failure of the European Society of Cardiology (ESC). Developed with the special contribution of the Heart Failure Association (HFA) of the ESC. *Eur J Heart Fail*. 2016;18(8):891-975.
- 88.** Wang TKM, Ayoub C, Chetrit M, et al. Cardiac magnetic resonance imaging techniques and applications for pericardial diseases. *Circ Cardiovasc Imaging*. 2022;15(7):e014283.
- 89.** Wang X, Peter K. Molecular imaging of atherosclerotic diseases: seeing is believing. *Arterioscler Thromb Vasc Biol*. 2017;37(6):1029-1040.
- 90.** MacAskill MG, Newby DE, Tavares AAS. Frontiers in positron emission tomography imaging of the vulnerable atherosclerotic plaque. *Cardiovasc Res*. 2019;115(14):1952-1962.
- 91.** Tarkin JM, Corovic A, Wall C, Gopalan D, Rudd JH. Positron emission tomography imaging in cardiovascular disease. *Heart*. 2020;106(22):1712-1718.

- 92.** Wykrzykowska J, Lehman S, Williams G, et al. Imaging of inflamed and vulnerable plaque in coronary arteries with 18F-FDG PET/CT in patients with suppression of myocardial uptake using a low-carbohydrate, high-fat preparation. *J Nucl Med*. 2009;50(4):563–568.
- 93.** Tarkin JM, Joshi FR, Evans NR, et al. Detection of atherosclerotic inflammation by (68)Ga-DOTATATE PET compared to [(18)F]FDG PET imaging. *J Am Coll Cardiol*. 2017;69(14):1774–1791.
- 94.** Tarkin JM, Calcagno C, Dweck MR, et al. (68)Ga-DOTATATE PET identifies residual myocardial inflammation and bone marrow activation after myocardial infarction. *J Am Coll Cardiol*. 2019;73(19):2489–2491.
- 95.** Raggi P, Senior P, Shahbaz S, et al. (18)F-sodium fluoride imaging of coronary atherosclerosis in ambulatory patients with diabetes mellitus. *Arterioscler Thromb Vasc Biol*. 2019;39(2):276–284.
- 96.** Joshi NV, Vesey AT, Williams MC, et al. 18F-fluoride positron emission tomography for identification of ruptured and high-risk coronary atherosclerotic plaques: a prospective clinical trial. *Lancet*. 2014;383(9918):705–713.
- 97.** Dweck MR, Chow MW, Joshi NV, et al. Coronary arterial 18F-sodium fluoride uptake: a novel marker of plaque biology. *J Am Coll Cardiol*. 2012;59(17):1539–1548.
- 98.** Kwiecinski J, Tzolos E, Adamson PD, et al. Coronary (18)F-sodium fluoride uptake predicts outcomes in patients with coronary artery disease. *J Am Coll Cardiol*. 2020;75(24):3061–3074.
- 99.** Ćorović A, Wall C, Mason JC, Rudd JHF, Tarkin JM. Novel positron emission tomography tracers for imaging vascular inflammation. *Curr Cardiol Rep*. 2020;22(10):119.
- 100.** Jenkins WS, Vesey AT, Vickers A, et al. In vivo alpha-V beta-3 integrin expression in human aortic atherosclerosis. *Heart*. 2019;105(24):1868–1875.
- 101.** Daghem M, Bing R, Fayad ZA, Dweck MR. Noninvasive imaging to assess atherosclerotic plaque composition and disease activity: coronary and carotid applications. *J Am Coll Cardiol Img*. 2020;13(4):1055–1068.
- 102.** Bartlett B, Ludewick HP, Lee S, Verma S, Francis RJ, Dwivedi G. Imaging inflammation in patients and animals: focus on PET imaging the vulnerable plaque. *Cells*. 2021;10(10).
- 103.** Luehmann HP, Detering L, Fors BP, et al. PET/CT imaging of chemokine receptors in inflammatory atherosclerosis using targeted nanoparticles. *J Nucl Med*. 2016;57(7):1124–1129.
- 104.** Nahrendorf M, Kelih E, Panizzi P, et al. 18F-4V for PET-CT imaging of VCAM-1 expression in atherosclerosis. *J Am Coll Cardiol Img*. 2009;2(10):1213–1222.
- 105.** Razavian M, Tavakoli S, Zhang J, et al. Atherosclerosis plaque heterogeneity and response to therapy detected by in vivo molecular imaging of matrix metalloproteinase activation. *J Nucl Med*. 2011;52(11):1795–1802.
- 106.** Hakimzadeh N, Pinas VA, Molenaar G, et al. Novel molecular imaging ligands targeting matrix metalloproteinases 2 and 9 for imaging of unstable atherosclerotic plaques. *PLoS One*. 2017;12(11):e0187767.
- 107.** Poznyak AV, Sukhorukov VN, Eremin II, Nadelyaeva II, Orekhov AN. Diagnostics of atherosclerosis: overview of the existing methods. *Front Cardiovasc Med*. 2023;10:1134097.
- 108.** von Schulthess GK, Kuhn FP, Kaufmann P, Veit-Haibach P. Clinical positron emission tomography/magnetic resonance imaging applications. *Semin Nucl Med*. 2013;43(1):3–10.
- 109.** Hyafil F, Schindler A, Sepp D, et al. High-risk plaque features can be detected in non-stenotic carotid plaques of patients with ischaemic stroke classified as cryptogenic using combined 18F-FDG PET/MR imaging. *Eur J Nucl Med Mol Imaging*. 2016;43(2):270–279.
- 110.** Ćorović A, Wall C, Nus M, et al. Somatostatin receptor PET/MR imaging of inflammation in patients with large vessel vasculitis and atherosclerosis. *J Am Coll Cardiol*. 2023;81(4):336–354.
- 111.** Antoniades C, Antonopoulos AS, Deanfield J. Imaging residual inflammatory cardiovascular risk. *Eur Heart J*. 2020;41(6):748–758.

KEY WORDS atherosclerosis, cardiac magnetic resonance, computed tomography, imaging, inflammation, positron emission tomography